

UNIVERSITY OF BIRMINGHAM

Investigation of the Phases Present in Al-7Si-0.3Mg Alloy with the Addition of Transition Metals

by

Samira Moghadam Arya

A thesis submitted to the University of Birmingham for the degree

of

DOCTOR OF PHILOSOPHY

School of Metallurgy and Materials
College of Engineering and Physical Science
University of Birmingham

March 2024

UNIVERSITY OF
BIRMINGHAM

University of Birmingham Research Archive

e-theses repository

This unpublished thesis/dissertation is copyright of the author and/or third parties. The intellectual property rights of the author or third parties in respect of this work are as defined by The Copyright Designs and Patents Act 1988 or as modified by any successor legislation.

Any use made of information contained in this thesis/dissertation must be in accordance with that legislation and must be properly acknowledged. Further distribution or reproduction in any format is prohibited without the permission of the copyright holder.

Synopsis

This research aimed to investigate the effects of the addition of the transition metals molybdenum, tungsten, and vanadium to Al-7Si-0.3Mg (2L99) and the mechanism by which their addition can improve the tensile properties of 2L99. Although the addition of certain transition metals is thought to enhance the properties of Al alloys, research has been limited on this subject.

It is known that the presence of entrapped double oxide film defects (bifilms) in the aluminium alloy has a detrimental effect on its mechanical and corrosion resistance properties. As part of this study, various alloys of 2L99 + 0.4 wt.% Mo, W and V were made using the sand-casting method. It was observed that the addition of Mo and W improved the Ultimate Tensile Strength (UTS), %Elongation and yield strength of 2L99, whilst the addition of V showed a negligible increase in these parameters. Statistical analysis showed a significant increase in the Weibull moduli of the measured tensile properties of the alloys due to the addition of all three transition metals.

Subsequent to tensile testing, SEM and EDX analyses were carried out on various alloys to study the phases of oxides, nitrides and intermetallics on each alloy's polished and fractured surfaces. Characterisation of the fractured surfaces of 2L99 alloy in as-cast condition discovered for the first time AlN patches with a different "nodular" morphology of approximately 15 μm length, which were considered to be impermeable. This discovery reinforces Nyahumwa's hypothesis on the utilisation of internal gases, indicating that the presence of AlN is likely a result of increased consumption of entrapped air within the bifilms. This process begins with converting oxygen into spinel, followed by nitrogen transformation into AlN. Furthermore, impermeable nodular AlN morphologies observed in this study are considered to prevent hydrogen diffusion into the bifilms and prevent their expansion, ultimately leading to the reduction in bifilms' size.

Sedimentation testing was carried out on 2L99 and 2L99 + Mo, W and V alloys by holding the

melt at 800°C for 1 hour, followed by air cooling of the samples. The results showed that the addition of transition metals to 2L99 encouraged the settlement of a large portion of the intermetallics and bifilms to the base of the melt. This is thought to be due to the suitability of bifilms as a potent substrate for the nucleation of most intermetallics and the higher density of the intermetallics compared to liquid Al.

Nitrogen growth test was carried out on CP-AL, 2L99, 2L99 + 0.6 wt.% Mo and 0.2 wt.% W alloys. Alloy melts were held at 850°C in a nitrogen atmosphere for various holding times. The test showed the presence of different aluminium nitride morphologies such as rod, whisker, nodular, and feather-shaped.

Phase analysis also indicated that the reduction in the amount of bifilms resulted in the improvement of tensile properties of the 2L99 alloy, likely due to a combination of the following factors: (i) Substantial settling of double oxide films to the base of the melt due to nucleation of intermetallics on bifilms, (ii) The presence of more frequent AlN patches and morphologies suggesting an increase in the rate of consumption of the internal gases inside the bifilms and subsequent reduction of their size, and (iii) Alteration of the β- Al_5FeSi morphology or its type to an α-compound intermetallic phase in 2L99, which is considered less detrimental to mechanical properties of the alloy due to its differing morphology and/or size.

The findings of this research contribute to understanding the mechanism by which the mechanical properties of 2L99 alloy are improved by the addition of Mo, W and V. Furthermore; it upholds previous research undertaken by Nyahumwa for the consumption of gases within double oxide films and the existence of nitride in the process, as well as providing evidence of different AlN morphologies in Al-Si-Mg alloys.

ACKNOWLEDGEMENTS

I would like to extend my sincere gratitude to my supervisor, Dr. W. D. Griffiths, for his excellent guidance, invaluable knowledge-sharing, supervision, and advice throughout this research.

My heartfelt appreciation goes to Professor Hanshan Dong and the Engineering and Physical Sciences Research Council (EPSRC, EP/L016206/1) for their generous financial support, which made his research possible.

I would also like to thank Professor John Campbell for his kind advice, encouragement, and dedication to the science of metallurgy and materials, which has inspired many, including myself.

I am deeply thankful to Mr. Adrian Caden and Mr. Joseph Tile for their invaluable support in the execution of the experimental works and acknowledge the use of the WD-XRF test results supplied by Dr. Christopher Waldron, Research Technology Platforms, University of Warwick (EPSRC EP/V007688/1).

I also want to express my sincere gratitude to Professor Jon Binner for his compassionate pastoral care and support during the difficult months of the COVID-19 pandemic.

And finally, I would like to thank my husband, Babak, and our son, Ryan, for their enduring patience and support, without which this work would not have been achievable.

This thesis incorporates the work that was carried out by Samira Moghadam Arya, supervised by Dr. William D. Griffiths, and was originally published in Metallurgical and Materials Transactions B [1].

CONTENTS LISTINGS

1 INTRODUCTION 1

2 LITERATURE REVIEW 3

2.1 Oxide films in Al alloys 3

2.1.1 Oxidation of Al alloys 3

2.1.2 Formation of oxide film defects 8

2.1.3 Observable characteristics of double oxide film defects 10

2.1.4 Statistical analysis of mechanical properties of the alloys 12

2.1.5 Al-7Si-0.3Mg (2L99) 18

2.1.6 Formation of the Aluminium Nitride 20

2.1.7 Formation of Mg_3N_2 32

2.1.8 Formation of hydrogen 32

2.2 The effects of transition metals Mo, W and V on oxide film defects in Al alloys 35

2.2.1 Effect of addition of Mo to Al alloys 35

2.2.2 Effect of addition of W into Al alloys 37

2.2.3 Effect of addition of V into Al alloys 40

2.3 Potential mechanisms of reduction of bifilms due to the addition of transition metal 43

2.3.1 Effect of intermetallics (mainly Fe and Mn) on the Al alloys 43

2.3.2 Consumption of internal gases 48

2.4 Summary 56

3 EXPERIMENTAL 57

3.1 Materials 57

3.1.1 XRF measurements 57
3.2 Testbar Castings 58
3.2.1 Sand Mould Preparation 58
3.2.2 Masteralloy Preparation 59
3.2.3 Casting 60
3.2.4 The Roll-over Process 61
3.2.5 T6 Heat Treatment 62
3.2.6 Tensile Testing 62
3.2.7 SEM Samples Surface Preparations 63
3.2.1 SEM Imaging 64
3.2.2 X-ray Diffraction (XRD) 64
3.3 Sedimentation 65
3.4 Nitride Growth 67
4 RESULTS 70
4.1 Mechanical Properties 70
4.1.1 Tensile testing of 2L99 alloy 71
4.1.2 Tensile testing of 2L99 + 0.4 wt.% Mo alloy 74
4.1.3 Tensile testing of 2L99+0.4 wt.% W alloy 78
4.1.4 Tensile test of 2L99 + 0.4 wt.% V alloy 81
4.1.5 Summary 84
4.2 Identification of phases 89
4.2.1 2L99 alloy 89
4.2.1.1 Characterisations of the phases on the polished surfaces of 2L99 89
4.2.1.2 Characterisations of the phases on the fractured surfaces of 2L99 98

4.2.2 2L99 + Mo alloy 113

4.2.2.1 Characterisation of the masteralloy of 2L99 + 10%Mo 113

4.2.2.1.1 Polished surfaces of 2L99 + 10 wt. % Mo testbars (Masteralloy) 113

4.2.2.1.2 Fractured surfaces of 2L99 + 10 wt. % Mo testbars (Masteralloy) 118

4.2.2.2 Characterisations of the phases on the polished surfaces of 2L99 + 0.4 wt % Mo 127

4.2.2.3 Characterisations of the phases on the fractured surfaces of 2L99 + 0.4 wt.% Mo 145

4.2.3 2L99 + W alloy 155

4.2.3.1 Characterisation of the masteralloy of 2L99+10%W 155

4.2.3.2 Fractured Surface of the Masteralloy (2L99 + 10 wt.% W) 160

4.2.3.3 Characterisations of the phases on polished surfaces of 2L99 + 0.4 wt.% W ..167

4.2.3.4 Characterisations of the phases on the fractured surfaces of 2L99 + 0.4 wt.% W 182

4.2.4 2L99 + V alloy 193

4.2.4.1 Characterisations of the phases on polished surfaces of 2L99 + 0.4 wt.% V ...193

4.2.4.2 Characterisations of the phases on the fractured surfaces of 2L99 + 0.4 wt.% V 206

4.2.5 Summary 218

4.3 Characterisation of the phases using XRD 222

4.4 Sedimentation 226

4.4.1 2L99 + Mo alloy 229

4.4.1.1 2L99 + 0.5 wt.% Mo 229

4.4.1.2 2L99 + 1.8 wt.% Mo 231

4.4.1.3 2L99 + 2.4 wt.% Mo 235

4.4.2 2L99 + W alloy 237

4.4.2.1 2L99 + 1.6 wt.% W 237

4.4.2.2 2L99 + 1.9 wt.% W 241

4.4.2.3 2L99 + 4.8 wt.% W 243
4.4.3 2L99 + V alloy 247
4.4.3.1 2L99 + 1.2 wt.% V 247
4.4.3.2 2L99 + 2.1 wt.% V 250
4.4.3.3 2L99 + 5.1 wt.% V 253
4.4.4 Summary 256
4.5 Nitride growth 258
4.5.1 Rod- Shape AlN 258
4.5.2 Whisker-shaped AlN 260
4.5.3 Nodular-shaped AlN 262
4.5.4 Feather-shaped AlN 264
4.5.5 Summary 266
5 DISCUSSION 267
5.1 Phases in 2L99 alloy 267
5.2 Phases of 2L99 + transitional alloys Mo, W and V 271
5.2.1 2L99 + Mo phases 271
5.2.2 2L99 + W phases 275
5.2.3 2L99 + V phases 279
5.3 Nitrogen growth impact on AlN morphology 283
5.4 The mechanism for improvement of mechanical properties of 2L99 with the addition of 0.4 wt.% Mo, W and V 286
6 CONCLUSION 292
6.1 Effect of alloying elements on tensile properties of 2L99 alloy 293
6.2 Effects of alloying elements on the bifilms 294
6.3 Effects of the alloying elements on nitrides 295

6.3.1 Nitrogen growth experiment 296

6.4 Effects of alloying elements on intermetallics 297

7 FUTURE WORKS 300

8 Reference 302

Appendix A 315

Tables

Table 2-1: The Weibull parameters a and b are estimators of unbiased probability [26] [34] 16

Table 2-2: Crystallographic data of Al, AlN and common oxides and borides on CP-Al at 660 °C [66] 31

Table 4-1: Composition of the alloys used in mechanical testing and phase characterisation . 70

Table 4-2: Composition of the masteralloys 71

Table 4-3: Leco sample hydrogen analyses 71

Table 4-4: UTS, %Elongation and yield strength measurements for 2L99 alloy 72

Table 4-5: Relevant statical data for UTS, %Elongation and yield stress results of 2L99 alloy . 72

Table 4-6: Summarised Weibull modulus and position parameter of 2L99 alloy 74

Table 4-7: Statistical analysis of the distribution of UTS, %Elongation and Yield of 2L99 testbars verified the Weibull distribution 74

Table 4-8: Leco sample hydrogen analyses 75

Table 4-9: UTS, %Elongation and yield strength results of 2L99 + 0.4 wt.% Mo alloy 75

Table 4-10: Relevant statical data for UTS, %Elongation and yield strength results of 2L99 + 0.4 wt.% Mo alloy 75

Table 4-11: Summarised Weibull modulus and position parameter 2L99 + 0.4 wt.% Mo alloy 77

Table 4-12: Statistical analysis of the distribution of UTS, %Elongation and yield strength of 2L99 + 0.4 wt.% Mo testbars verified the Weibull distribution 77

Table 4-13: Leco sample hydrogen analyses 78

Table 4-14: UTS, %Elongation and yield strength results of 2L99 + 0.4 wt.% W alloy 78

Table 4-15: Relevant statical data for UTS, %Elongation and yield strength results of 2L99 + 0.4 wt.% W alloy 79

Table 4-16: Summarised Weibull moduli and position parameter 2L99 + 0.4 wt.% W alloy 80

Table 4-17: Statistical analysis of the distribution of UTS, %Elongation and yield strength of 2L99 + 0.4 wt.% W testbars verified the Weibull distribution 80

Table 4-18: Leco sample hydrogen analyses 81

Table 4-19: UTS, %Elongation and yield strength results of 2L99 + 0.4 wt.% V alloy 82

Table 4-20: Relevant statical data for UTS, %Elongation and yield strength results of 2L99 + 0.4 wt.% V alloy 82

Table 4-21: Summarised Weibull moduli and position parameter 2L99 + 0.4 wt.% V alloy 84

Table 4-22: Statistical analysis of the distribution of UTS, %Elongation and yield strength of 2L99 + 0.4 wt.% V testbars verified the Weibull distribution 84

Table 4-23: Comparison of the UTS, %Elongation and Yield mean values 85

Table 4-24: Comparison of the UTS, %Elongation and yield strength Weibull modulus increase in studied alloys 87

Table 4-25: EDX element composition of the spectrum1 in Figure 4-18 (b) 90

Table 4-26: EDX elemental composition of spectrum 1 in Figure 4-19 (a) 92

Table 4-27: EDX elemental composition of Spectrum 1 and Spectrum 9 in Figure 4-20 (b) 94

Table 4-28: EDX elemental composition of the area marked as spectrum 1 in Figure 4-21 (a) 95

Table 4-29: EDX elemental composition of spectrum 1 in Figure 4-22 (b) 97

Table 4-30: Summary of the phases on a polished surface of 2L99 alloy 98

Table 4-31: Quantification of the market area, Spectrum11, in Figure 4-25 (e) is presented in (f) 100

Table 4-32: Quantification of Spectrum 2 as marked up in Figure 4-26 (d) 101

Table 4-33: Quantification of Spectrum 1 as marked in Figure 4-27 (b) 103

Table 4-34: Quantification of Spectrum 2 as marked in Figure 4-28 (b) 104

Table 4-35: EDX elemental spectra of the areas marked in Figure 4-29 (d) and (g) 106

Table 4-36: EDX elemental spectra of the areas marked in Figure 4-30 (c) 108

Table 4-37: EDX elemental spectrum of the area marked in Figure 4-31 (b) 109

Table 4-38: EDX elemental spectra of the areas marked in Figure 4-32 (a) and (b) 110

Table 4-39: EDX elemental spectra of the areas marked in Figure 4-33 (c) 112

Table 4-40: Summary of the phases on fractured surface 2L99 alloy 113

Table 4-41: EDX elemental composition of spectra in Figure 4-34 (d) 115

Table 4-42: EDX elemental composition of the points marked in Figure 4-35 (a) 116

Table 4-43: EDX elemental composition of the points marked in Figure 4-36 (a) to (c) 118

Table 4-44: EDX elemental composition of the area marked in Table 4-37 (c) 120

Table 4-45: EDX elemental composition of the area marked in Figure 4-38 (a) and (b) 121

Table 4-46: EDX elemental composition of the area marked in Figure 4-39 (a) and (b) 122

Table 4-47: EDX elemental composition of the area marked in Figure 4-40 (a) 124

Table 4-48: EDX elemental composition of the area marked in Figure 4-41 125

Table 4-49: EDX elemental composition of the area marked in Figure 4-42 (b) 126

Table 4-50: Summary of the phases on the masteralloy of Mo (2L99 + 10 wt.% Mo)..... 126

Table 4-51: EDX elemental composition of the points marked with black circles in Figure 4-43 (b) to (d)..... 128

Table 4-52: EDX elemental composition of the points marked with black circles, Spectrum1, Spectrum 5 and Spectrum 4 in Figure 4-44 (b), Figure 4-44 (c) and Figure 4-44 (d)..... 131

Table 4-53: EDX elemental composition of the areas marked in Figure 4-45 (a) 133

Table 4-54: EDX elemental composition of the areas marked in Figure 4-46 (a) 134

Table 4-55: EDX elemental composition of the areas marked in Figure 4-47 (a) 135

Table 4-56: EDX elemental composition of the areas marked in Figure 4-48 (a) 136

Table 4-57: EDX elemental composition of the areas marked in Figure 4-49 (a) 137

Table 4-58: EDX elemental composition of the areas marked in Figure 4-50 (a) 139

Table 4-59: EDX elemental composition of the areas marked in Figure 4-51 (a) 139

Table 4-60: EDX elemental composition of the areas marked in Figure 4-52 (a) 142

Table 4-61: EDX elemental composition of the areas marked in Figure 4-53 (a) 143

Table 4-62: Summary of the phases on polished surface 2L99 + 0.4 wt.% Mo alloy..... 144

Table 4-63: EDX elemental composition of the areas marked..... 145

Table 4-64: EDX elemental composition of the areas marked in Figure 4-55 (b) and (c) 147

Table 4-65: Summary of the phases on fractured surface 2L99+0.4 wt.% Mo alloy 155

Table 4-66: EDX elemental composition of spectra in Figure 4-62 (b) to (d)..... 157

Table 4-67: EDX elemental composition of spectra in Figure 4-63 (a) 158

Table 4-68: EDX elemental composition of spectra in Figure 4-64 (b)..... 160

Table 4-69: EDX elemental composition of spectra in Figure 4-65 (c) 161

Table 4-70: EDX elemental composition of spectra in Figure 4-66 (a) 162

Table 4-71: EDX elemental composition of spectra in Figure 4-67 (a) to (c) 164

Table 4-72: EDX elemental composition of spectra in Figure 4-68 (b)..... 165

Table 4-73 EDX elemental composition of spectra in Figure 4-69 (b)..... 166

Table 4-74: Summary of the phases on the masteralloy of W (2L99 + 10 wt.% W)..... 167

Table 4-75: EDX elemental composition of the points marked in black in Figure 4-70 (b) to (e) 169

Table 4-76: EDX elemental composition of the points marked in black in Figure 4-71 (b) 171

Table 4-77: EDX elemental composition of the spectra marked in Figure 4-72 (a)..... 172

Table 4-78: EDX elemental composition of the areas marked in Figure 4-73 (a) 174

Table 4-79: presents the EDX elemental composition of the spectra marked in Figure 4-74 (a) and (b) 175

Table 4-80: EDX elemental composition of the areas marked in Figure 4-75 (a) and (b) 176

Table 4-81: EDX elemental composition of the spectra marked in Figure 4-76 (a)..... 178

Table 4-82: EDX elemental composition of the areas marked in Figure 4-77 (a) 179

Table 4-83: EDX elemental composition of the areas marked in Figure 4-78 (a) 180

Table 4-84: Summary of the phases on polished flat surface 2L99 + 0.4 wt.% W alloy 182

Table 4-85: EDX elemental composition of the areas and points marked in Figure 4-83 (a) and (b) 186

Table 4-86: Summary of the phases on fractured surface 2L99 + 0.4 wt.% W alloy..... 193

Table 4-87: EDX elemental composition of the points marked with black circles in Figure 4-90(c) and (d)..... 195

Table 4-88: EDX elemental composition of the points marked with black circles in Figure 4-91 (c) and Figure 4-91 (d)..... 197

Table 4-89: EDX elemental composition of the points marked and Spectrum 3 and 4 in Figure 4-92 (a)..... 199

Table 4-90: EDX elemental composition of the Spectrum 4 in Figure 4-93 (a)..... 199

Table 4-91: EDX elemental composition of the Spectrum 3 in Figure 4-94 (a)..... 200

Table 4-92: EDX elemental composition of the Spectrum 1 in Figure 4-95 (a)..... 201

Table 4-93: EDX elemental composition of the Spectrum 1 in Figure 4-96 (a)..... 202

Table 4-94: EDX elemental composition of the Spectrum 2 in Figure 4-97 (a)..... 203

Table 4-95: EDX elemental composition of the spectra 1, 5 and 6 in Figure 4-98 (a) 204

Table 4-96: EDX elemental composition of the Spectrum 1 in Figure 4-99 (a)..... 205

Table 4-97: Summary of the phases on polished surface 2L99 + 0.4 wt.% V alloy..... 206

Table 4-98: EDX elemental spectrum of the area marked in Figure 4-100 (a) 207

Table 4-99: EDX elemental spectrum of the area marked in Figure 4-101 (a) 208

Table 4-100: EDX elemental spectrum of the area marked in Figure 4-102 (a)..... 209

Table 4-101: EDX elemental spectrum of the area marked in Figure 4-103 (a)..... 210

Table 4-102: EDX elemental spectrum of the points marked in Figure 4-104 (a) 211

Table 4-103: EDX elemental spectrum of the area marked in Figure 4-105 (a)..... 213

Table 4-104: EDX elemental spectrum of the area marked in Figure 4-106 (a)..... 214

Table 4-105: EDX elemental spectrum of the area marked in Figure 4-107 (a)..... 215

Table 4-106: EDX elemental spectrum of the area marked in Figure 4-109 (a)..... 218

Table 4-107: Summary of the phases on fractured surface 2L99 + 0.4 wt.% V alloy..... 218

Table 4-108: XRF analysis results for 2L99 + Mo alloys..... 226

Table 4-109 XRF analysis results for 2L99 + W alloys..... 227

Table 4-110 XRF analysis results for 2L99 + V alloys..... 227

Table 4-111: the amount of O measured by XRF on all studied alloys 257

Table 4-112: XRF amount and ImageJ analysis results for Mo intermetallics at the base of the sample 257

Table 4-113: XRF amount and ImageJ analysis results for W intermetallics at the base of the sample 257

Table 4-114: XRF amount and ImageJ analysis results for V intermetallics at the base of the sample 257

Table 4-115: Elemental composition of the alloys based on XRF analysis 258

Table 4-116: Quantification of spectra for Figure 4-145 (a) to (d) 260

Table 4-117: Quantification of spectra for Figure 4-146 (a) and (b) 262

Table 4-118: Quantification of spectra for Figure 4-147 (a) and (b) 263

Table 4-119: Quantification of spectra for Figure 4-148 (a) and (b) 265

Table 5-1: Oxide stability under varying temperatures and Mg concentrations from a thermodynamic perspective [121] 269

Table 5-2: Gibbs Free Energy data for oxides kJ/mol [122] 269

Table 5-3: various AlN morphologies reported by other researchers, mainly in pure Al and 2L99 + 0.4 wt.% Mo 285

Figures

Figure 2-1: Oxidation curves of Al in dry O2 [9] [10] [11] 4

Figure 2-2: The CP- Al oxidation in dry and humid air at 750 °C [11] [14] 5

Figure 2-3: TEM image of characteristic faceted γ-Al2O3 platelets [5] 6

Figure 2-4: High-resolution TEM micrograph showing a γ -Al2O3 platelet, which is faceted and twinned along its {1 1 1} crystal planes [5] 6

Figure 2-5: Oxygen pressure for formation of oxides vs. wt.% Mg at 725 °C [17] 7

Figure 2-6: (a) Electron micrograph of the surface of Al-5 wt.% Mg alloy showing large MgAl2O4 structures and small primary magnesia crystals, (b) MgAl2O4 crystals at the oxide-melt interface from the oxide side [14] 8

Figure 2-7: Sketch of a surface entrainment event [18] 9

Figure 2-8: (a) Symmetrical oxide film defects on the fractured surfaces from a tensile testbar of commercial pure Mg alloy, (b) EDX spectrum of the CP-Mg alloy [22] 11

Figure 2-9: Oxide film defects seen under reduced pressure test using X-ray radiography [24] 12

Figure 2-10: Weibull mixtures in tensile test results of IN939 alloy casting (a) 2-parameter $R^2 < R^2_{0.05}$[26] [40] (b) bimodal 2-parameter Weibull distribution [26] [39] 17

Figure 2-11: Backscattered electron microscopy (BSE) images of the three types of Fe intermetallics in Al-Si-Mg alloy(a) α and π shapes (b) β shape [3] [44] 19

Figure 2-12: Phase diagram of Al-N with composition 0 to 50 at.% N, at temperatures 500 °C to 3000 °C [55] 21

Figure 2-13: AlON phase diagram [56] 22

Figure 2-14: (a) SEM micrograph of granular AlN on CP-Al after 40 minutes hold, (b) SEM micrograph of granular AlN on 2L99 after 32 minutes hold, (c) and (d) the energy-dispersive X- ray spectra corresponding to (a) and (b) [60] 23

Figure 2-15: (a) SEM micrograph of AlN formed by bubbling N_2 directly into pure Al at 1200 °C for 6 hours (b) the EDX spectrum of the marked area in (a) [58] 24

Figure 2-16: (a) SEM micrograph of feather-shaped AlN layer (b) EDX spectrum of the whole area shown in (a) [10] [61] 24

Figure 2-17: (a) SEM micrograph of feather-shaped AlN layer (b) EDX spectrum of the area marked in (a) [11] [63] 25

Figure 2-18: (a) SEM micrograph of SP-Al cast at 750 °C with 24 hours holding time (b) the EDX quantification of the area marked in (a) [7] 26

Figure 2-19: (a) SEM micrograph of the nitrides on the fractured surface of heat-treated 2L99 + 0.4 wt.% Mo alloy (b) EDX spectrum of the marked area in (a) [3] 28

Figure 2-20: (a) and (c) low and high magnification SEM micrographs of a granular nitride layer on the surface of the 2L99 + 0.4 wt.% Mo alloy sample from the bubble-growth experiment (b) and (d) EDX spectra of the marked areas in (a) and (b) [3] [65] 29

Figure 2-21: (a) SEM micrograph of nitride inclusion particles held at (a) 750 °C and (b) 850 °C (c) the EDX spectrum of the marked areas and points in (a) and (b) [66] 30

Figure 2-22: H solubility in pure aluminium plotted against the temperature [3] [10][68] 33

Figure 2-23: Al-Mo Phase diagram [76] [75] 37

Figure 2-24: (a) and (b) low and high magnification of the SEM image of oxide particles on fractured surface of 2L99+0.4 wt.% W (c) EDX spectra of X1 marked in (a) [3] 38

Figure 2-25: Al–W phase diagram [79] 40

Figure 2-26: Aluminium-vanadium phase diagram [86] [75] 42

Figure 2-27: Consumption of the gases inside the bifilm in 2L99 alloy [12] 49

Figure 2-28: Real-time X-ray radiography utilised to observe the consumption of the trapped air bubble via reaction with the melt [10] 50

Figure 2-29: The rate of consumption of the entrained oxygen and nitrogen [59] 51

Figure 2-30: The rate of diffusion of hydrogen into bifilms [59] 51

Figure 2-31: Schematic of the double oxide film defects corresponding to the three reaction stages under different atmospheres shown (a) stage 1, (b) stage 2, and (c) stage 3 [96] 54

Figure 3-1: Sketch of the "badly designed" running system 59

Figure 3-2: shows (a) the bottom of a crucible after casting a masteralloy (b) the ingot mould 60

Figure 3-3: (a) and (b) sectioned masteralloy ingot areas for XRF test 60

Figure 3-4: (a) Roll-over device with three sand moulds 62

Figure 3-5: Sketch of the tensile testbar in mm 63

Figure 3-6: fractured testbar and the fractured and polished samples 63

Figure 3-7: Sedimentation tests cylindrical sample and subsequent sub-sampling dimensions and details 66

Figure 3-8: Nitride growth experiment equipment set-up 68

Figure 3-9: The growth nitrogen experiment set-up at the laboratory (a) placing the crucible inside the cylindrical stainless-steel tube (b) the vertical tube furnace full set-up 69

Figure 4-1: The Weibull plot of UTS of 2L99 alloy 73

Figure 4-2: The Weibull plot of % Elongation of 2L99 alloy 73

Figure 4-3: The Weibull plot of the yield stress of 2L99 alloy 73

Figure 4-4: The Weibull plot of UTS of 2L99 + 0.4 wt.% Mo alloy 76

Figure 4-5 : The Weibull plot of % Elongation of 2L99 + 0.4 wt.% Mo alloy 76

Figure 4-6: The Weibull plot of Yield of 2L99 + 0.4 wt.% Mo alloy 77

Figure 4-7: The Weibull plot of UTS of 2L99 + 0.4 wt.% W alloy 79

Figure 4-8: The Weibull plot of % Elongation of 2L99 + 0.4 wt.% W alloy 79

Figure 4-9: The Weibull plot of Yield of 2L99 + 0.4 wt.% W alloy 80

Figure 4-10: The Weibull plot of UTS of 2L99 + 0.4 wt.% V alloy 83

Figure 4-11: The Weibull plot of % Elongation of 2L99 + 0.4 wt.% V alloy 83

Figure 4-12: The Weibull plot of yield strength of 2L99 + 0.4 wt.% V alloy 83

Figure 4-13: Combined UTS Weibull distribution plot 86

Figure 4-14: Combined %Elongation Weibull distribution plot 86

Figure 4-15: Combined yield strength Weibull distribution plot 87

Figure 4-16: comparison of the mean values of the measured tensile properties of 2L99 and 2L99 + 0.4 wt.% transition alloys 88

Figure 4-17: comparison of the Weibull moduli of 2L99 and 2L99 + 0.4 wt.% transition alloys… 88

Figure 4-18: (a) Whole matrix SEM micrograph of a polished cross-section of the 2L99 alloy (low UTS 83 MPa) (b) Low magnification SEM micrograph of the flat surface in the absence of cavities 90

Figure 4-19: (a) to (d) High magnification of SEM micrographs of the main cavities in the 2L99 in (a) (e) EDX spectrum1 of the point marked in (a) 92

Figure 4-20: (a) Whole matrix SEM micrograph of a polished cross-section of the 2L99 alloy with high UTS 296 MPa. (b) Low magnification SEM micrograph of the flat surface without cavities 93

Figure 4-21: (a) High magnification SEM micrographs of the main cavities detailed in Figure 4-18 (a). (c) EDX Spectrum1 for Figure 4-19 (a) 95

Figure 4-22: (a) low magnification of SEM micrograph of the pore on the polished cross-section of the 2L99 alloy (b) high magnification of oxide particle in the pores (c) EDX spectrum 1 of the marked areas in (b) 96

Figure 4-23: EDX mapping of typical tangled bifilms and cavities on the polished surface 2L99 98

Figure 4-24: (a) and (b) depict low magnification SEM images of the fractured surfaces of an as-cast 2L99 testbar..... 99

Figure 4-25: (a) to (e) illustrate SEM micrographs of an oxide and nitride layer on the fractured surface of the as-cast 2L99 alloy (f) presents the EDX analysis of spectrum 11 in (e) 100

Figure 4-26: (a), (b), and (c) showcase high-magnification SEM images of a nitride and oxide layer on the fractured surface of the as-cast 2L99 alloy. Additionally, (d) presents the EDX analysis of Spectrum 2 101

Figure 4-27: (a) shows the cross-section of the nitride layer observed on the fractured surfaces of 2L99 with Pt Coating, (b) the same nitride area without Pt coating, (c) EDX analysis of Spectrum 1 showing both O and N as well as a small amount of Pt and Ga..... 102

Figure 4-28: (a) displays a low magnification SEM micrograph of the oxide layers and nitride on the fractured surface 2L99 in its as-cast condition. (b) a high magnification SEM micrograph of the area marked in (a). (c) the EDX analysis of Spectrum 2, as indicated in (b)..... 103

Figure 4-29: (a) SEM micrograph of the pore marked as X1 on the corner of the fractured surface of 2L99 (b), (c), (d) respective higher magnification SEM micrographs of the pore (e) and (f) EDX elemental spectra of the two areas marked in (d). (g) is the high magnification of the area marked as X2 in (a) Showing a thin layer of oxide film, (h) is the EDX analysis of the area marked in (g) 106

Figure 4-30: (a) SEM micrograph of the oxide layers and nitride on the fractured surface of 2L99 (as-cast condition) (b) High magnification SEM micrograph of the marked area in (a), (c) is the high magnification SEM micrograph of the marked area in (b), EDX analysis of Spectrum 2 and Spectrum 3 as marked in (c) 108

Figure 4-31: (a) and (b) SEM micrograph of the oxide particles (spinel) on the fractured surface of 2L99 (as-cast condition) low UTS, (c) the EDX analysis of Spectrum 2 as marked in (b) 109

Figure 4-32: (a) and (b) SEM micrograph of the oxide particles (MgO) and spinel layer on the fractured surface of 2L99, (c) and (d) EDX analysis of Spectra 1 and 3, respectively 110

Figure 4-33: (a) to (c) low to high magnification SEM micrograph of one of the secondary dendrite arms covered with oxide films on the fractured surface of 2L99 (as-cast condition), (d) to (f) EDX analysis of Spectra are marked in (c)..... 112

Figure 4-34: (a) to (d) low to high magnification SEM micrographs of a typical Mo masteralloy testbar, (e) to (h) corresponding EDX spectra of the points marked in (d) (sample 7 testbar) . 115

Figure 4-35: (a) High magnification SEM micrographs of a gas pore on the polished surface of Mo masteralloy, Figures 2. (b) to (d) Corresponding EDX spectra (1, 2 and 3) in (a) 116

Figure 4-36: (a) to (c) high magnification of different Al-Mo intermetallic compounds (blocky shape) showing $Al_{34}Si_3Mo_{11}$ intermetallic compounds on the polished surface of Mo masteralloy (d) to (f) EDX spectra of the points marked in (a) to (c), respectively..... 117

Figure 4-37: (a) low magnification SEM micrographs of a Mo masteralloy testbar, (b) high magnification of the area marked in (a), (c) high magnification of the area marked in (b), (d) BSE image of (c), (e) EDX corresponding for the area marked in (c) 119

Figure 4-38: (a) and (b) high magnification SEM images of X1 and X2 areas marked in Figure 4-37 (c), (c) and (d) EDX corresponding spectra (Spectrum 2 and Specturm1) (a) and (b) respectively 121

Figure 4-39: (a) High magnification SEM micrographs of the spherical oxide particles on 2L99 + 10 wt.% Mo, (b) High magnification SEM micrographs of the flake oxide particles on 2L99 + 10 wt.% Mo, (c) and (b) Corresponding EDX spectra in (a) and (b) 122

Figure 4-40: (a) High magnification SEM micrographs of the intermetallics in oxide particles on 2L99 + 10 wt.% Mo, (b) Corresponding EDX spectra in (a) 123

Figure 4-41: (a) and (b) low and high magnification of BSE image of the top of the Mo masteralloy ingot (c) EDX spectrum for the point marled as Spectrum 7 Figure 4-41 (b) 125

Figure 4-42: (a) and (b) low and high magnification of BEC image of the bottom of the Mo masteralloy ingot (c) EDX spectrum for the point marked as Spectrum 5 126

Figure 4-43: (a) Whole matrix SEM micrograph of a polished cross-section of the 2L99 + 0.4 wt.% Mo alloy with low UTS (191.5 MPa), (b) to (d) High magnification SEM micrographs of the main cavities detailed in (a), (e) EDX Spectrum1 for (b) to (d) 128

Figure 4-44: (a) Whole matrix SEM micrograph of a polished cross-section of the 2L99 + 0.4 wt.% Mo alloy with high UTS (292.8 MPa), (b) and (c) High magnification SEM micrographs of the main cavities detailed in (a), (d) to (f) corresponding EDX Spectrum1, Spectrum 5 and Spectrum 1131

Figure 4-45: (a) SEM micrograph of a polished surface 2L99 + 0.4 wt.% Mo alloy showing the faceted intermetallic compounds grown on the bifilm (b) to (f) EDX spectra of the areas marked in (a) 132

Figure 4-46: (a) SEM micrograph of a polished surface 2L99 + 0.4 wt.% Mo alloy showing three different faceted intermetallic compounds (blocky shape), (b) to (d) EDX spectra of the areas marked in (a) 134

Figure 4-47: (a) SEM micrograph of a polished surface 2L99 + 0.4 wt.% Mo alloy showing hexagonal intermetallic compounds, (b) to (d) EDX spectra of the areas marked in (a) 135

Figure 4-48: (a) SEM micrograph of a polished surface 2L99 + 0.4 wt.% Mo alloy showing different intermetallic compounds faceted and hexagonal shapes, (b) to (f) EDX spectra of the areas marked in (a) 136

Figure 4-49 (a): SEM micrograph of a polished surface 2L99 + 0.4 wt.% Mo alloy showing a faceted intermetallic compound grown on bifilm (b) to (f) EDX spectra of the areas marked in (a) 137

Figure 4-50: (a) SEM micrograph of a polished surface 2L99 + 0.4 wt.% Mo alloy showing the faceted intermetallic compounds (b) to (e) EDX spectra of the areas marked in (a) 138

Figure 4-51: (a) SEM micrograph of a polished surface 2L99 + 0.4 wt.% Mo alloy showing a faceted intermetallic compound, (b) EDX spectrum of the area marked in (a) 139

Figure 4-52: (a) SEM micrograph of a polished surface 2L99 + 0.4 wt.% Mo alloy showing a bifilm with oxide and nitride layers, (b) to (f) EDX spectra of the areas marked in (a) 141

Figure 4-53: (a) SEM micrograph of high magnification of X1 marked in Figure 4-52 (a) showing a bifilm with oxide and nitride layers, (b) to (f) EDX spectra of the areas marked in (a)..... 143

Figure 4-54: (a), (b) low and high magnification of SEM image of a typical nodular oxide layer (spinel) on the fractured surface of as-cast 2L99 + 0.4 wt.% Mo, (c) EDX spectra of Spectrum 2 145

Figure 4-55: (a), (b) low and high magnification of SEM image of a granular oxide layer on the fractured surface of as-cast 2L99 + 0.4 wt.% Mo, (c) high magnification of SEM image of whisker oxide, (d) and (e) EDX spectra of Spectrum 1 and Spectrum 2..... 147

Figure 4-56: (a) SEM image of oxides and AlN layer on the fractured surface of as-cast 2L99 + 0.4 wt.% Mo and (b) and (c) EDX analysis of spectrum1 of the oxide layer (d) and (e) EDX analysis of spectrum 2 of AlN layer (f) and (g) EDX analysis of spectrum 3 of the oxide..... 148

Figure 4-57: (a) and (b) SEM images of low and high magnification of feather shape nitride layers on the fractured surface of as-cast 2L99 + 0.4 wt.% Mo and (c) and (d) EDX analysis of spectrum 2 149

Figure 4-58: (a) SEM micrograph of a fractured surface of 2L99 + 0.4 wt.% Mo alloy showing Mo containing faceted intermetallic compounds (blocky shape) and oxides, (b) and (c) EDX spectrum1 intermetallic, (d) and (e) EDX Spectrum 2 for oxides and Mo intermetallic, (f) and (g) EDX Spectrum 3 for oxides..... 151

Figure 4-59: (a) SEM image of Mo intermetallic on the fractured surface of as-cast 2L99 + 0.4 wt.% Mo and (b) and (c) EDX analysis of spectrum 1 (d) and (e) EDX analysis of spectrum 6 for all the red circles marked..... 152

Figure 4-60: (a) SEM image of Mo intermetallic on the fractured surface of as-cast 2L99 + 0.4 wt.% Mo and (b) and (c) EDX analysis of spectrum 1, (d) and (e) EDX analysis of spectrum 7 for all the red circles marked..... 153

Figure 4-61: (a) Low magnification of the half of the fractured surface 2L99 + 0.4 wt.% Mo alloy with gas porosity (b) High magnification of gas porosity (c) and (d) EDX analysis of spectrum3 on gas porosity..... 154

Figure 4-62: (a) low magnification of a typical SEM micrograph of the polished surface of W masteralloy with gas porosity, (b) to (d) high magnification of different Al-W intermetallic compounds (facetted shape), (e) to (g) EDX spectra of the points marked as Spectrum 7 and Spectrum 1..... 157

Figure 4-63: (a) High magnification SEM image of one of the intermetallics on the polished W masteralloy (AlW_2), possessing a heptagon shape with a crack cutting through the middle of the particle (oxide film), (b) and (c) corresponding EDX spectra in (a)..... 158

Figure 4-64: (a) High magnification SEM micrograph of a pore on the polished W masteralloy with numerous intermetallic compounds, (b) low magnification of the area marked (tangled intermetallics with oxide films inside one of the pores) in (a), (c) to (f) corresponding EDX spectra as marked in (b)..... 160

Figure 4-65: (a) Low magnification of SEM micrograph of the fractured surface of W masteralloy with numerous gas porosities present, (b) high magnification of the area marked in (a), (c) high magnification of the area marked in (b) showing the Al_4W Intermetallic Compound on the fractured surface, (d) corresponding EDX spectrum of the area marked in (c)..... 161

Figure 4-66: (a) high magnification of the fractured surface of W masteralloy, (b) and (c) corresponding EDX spectrum of the area marked in (a)..... 162

Figure 4-67: (a) SEM micrograph, high magnification showing the spinel particle on the fractured surface, (b) high magnification showing the small spinel particle on the fractured Surface, (c) high magnification SEM micrograph showing the spinel layer on the fractured surface, (d) to (f) corresponding EDX spectrum of the area marked in (a) to (c)..... 164

Figure 4-68: (a) and (b) low and high magnification of a typical SEM micrograph of the top of the polished surface of W masteralloy ingot with gas porosity, (c) EDX spectrum for the point marled as Spectrum 2..... 165

Figure 4-69: (a) and (b) low and high magnification of SEM image of the bottom of the W masteralloy ingot (c) EDX spectrum for the point marled as Spectrum 6..... 166

Figure 4-70: (a) the whole matrix SEM micrograph of the 2L99 + 0.4 wt.% W alloy polished cross-section with low UTS value (178.7 MPa), (b) to (e) High magnification SEM micrographs of the significant cavities detailed in (a), (f) Corresponding EDX Spectrum3 for black circles marked in (b) to (e)..... 169

Figure 4-71: (a) Whole matrix SEM micrograph of a polished cross-section of the 2L99 + 0.4 wt.% W alloy with high UTS value (286.1 MPa), (b) and (c) High magnification SEM micrographs of the main cavities detailed in (a), (d) EDX Spectrumb1 as marked in (b) and (e) EDX Spectrum 2 as marked in (c)..... 170

Figure 4-72: (a) SEM micrograph of a polished surface 2L99 + 0.4 wt.% W alloy showing the faceted intermetallic compounds grown on the bifilm (b) to (d) EDX spectra marked in (a) 172

Figure 4-73: (a) SEM micrograph of a polished surface 2L99 + 0.4 wt.% W alloy showing the faceted intermetallic compounds grown on the bifilm (b) and (c) EDX spectra marked in (a) . 173

Figure 4-74: (a) and (b) SEM micrographs of a polished surface of 2L99 + 0.4 wt.% W alloy showing different single intermetallics with inverse three and flower shapes ($AlSi_{1.5}W_{1.5}$) intermetallic compounds, (c) and (d) corresponding EDX spectra marked in (a) and (b), respectively..... 175

Figure 4-75: (a) and (b) SEM micrographs of a polished surface of 2L99 + 0.4 wt.% W alloy showing different single intermetallics with inverse three and flower shapes ($AlW_{1.5}$, $AlSi_2W_{1.5}$) intermetallic compounds, (c) and (d) corresponding EDX spectra of the areas marked in (a) and (b), respectively. 176

Figure 4-76: (a) SEM micrograph of a polished surface of 2L99 + 0.4 wt.% W alloy showing different faceted shapes $AlW_{1.5}$ intermetallic compounds, (b) to (d) EDX spectra of the areas marked in (a) 178

Figure 4-77: (a) SEM micrograph of a polished surface of 2L99 + 0.4 wt.% W alloy showing small-sized Al Si_2 W and Al-Si- W intermetallic compounds, (b) EDX spectra as marked in (a) 179

Figure 4-78: (a) SEM micrograph of a polished surface of 2L99 + 0.4 wt.% W alloy showing a bifilm with oxide and nitride layers, (b) High magnification of the area marked in (a), (c) to (e) EDX spectra as marked in (b)..... 180

Figure 4-79: (a) to (f) EDX mapping of a bifilm on the polished surface of 2L99 + 0.4 wt.% W. 182

Figure 4-80: (a) Low magnification SEM image of the tensile test fractured surface of as-cast 2L99 + 0.4 wt.% W and (b) high magnification SEM image of area marked as A in Figure (a), (c) and (d)

EDX analysis of spectrum1 183

Figure 4-81: (a) SEM image of oxide inclusion on the fractured surface of as-cast 2L99 + 0.4 wt.% W, (b) and (c) EDX analysis of spectrum 2, (d) and (e) EDX analysis of spectrum 4 184

Figure 4-82: (a) SEM image of an oxide layer on the fractured surface of as-cast 2L99 + 0.4 wt.% W and (b) and (c) EDX analysis of spectrum1 185

Figure 4-83: (a) and (b) SEM image of an oxide layer nodular and whisker on the fractured surface of as-cast 2L99 + 0.4 wt.% W and (c) and (d) corresponding EDX Spectra 186

Figure 4-84: (a) SEM image of nitride layers on the fractured surface of as-cast 2L99 + 0.4 wt.% W, (b) and (c) EDX analysis of spectrum 1, (d) and (e) EDX analysis of spectrum 2, (f) and (g) EDX analysis of spectrum 3, (h) and (i) EDX analysis of spectrum 5 188

Figure 4-85: (a) SEM image of nitride layers on the fractured surface of as-cast 2L99 + 0.4 wt.% W and (b) and (c) EDX analysis of spectrum 2 189

Figure 4-86: (a) SEM image of an oxide and nitride layers on the fractured surface of as-cast 2L99 + 0.4 wt.% W, (b) and (c) EDX analysis of spectrum 1, (d) and (e) EDX analysis of spectrum 2, (f) and (g) EDX analysis of spectrum 3 190

Figure 4-87: (a) SEM image of W intermetallic on the fractured surface of as-cast 2L99 + 0.4 wt.% W and (b) and (c) EDX analysis of spectrum 2 191

Figure 4-88: (a) SEM image of W intermetallic on the fractured surface of as-cast 2L99 + 0.4 wt.% W and (b) and (c) EDX analysis of spectrum 1 192

Figure 4-89: (a) Low magnification of the half of the fractured surface 2L99 + 0.4 wt.% W alloy with gas porosity (b) High magnification of gas porosity (c) and (d) EDX analysis of spectrum1 on gas porosity 193

Figure 4-90: (a) Whole matrix SEM micrograph of a polished cross-section of the 2L99 + 0.4 wt.% V alloy with low UTS (191.5 MPa), (b) to (d) High magnification SEM micrographs of the main cavities detailed in (a), (e) EDX Spectrum 5 for (c) and (d) 195

Figure 4-91: (a) Whole matrix SEM micrograph of a polished cross-section of the 2L99 + 0.4 wt.% V alloy with high UTS (292.8 MPa), (b) High magnification SEM micrographs of the main cavities detailed in (a), (c) High magnification SEM micrographs of the few cavities described in (b) and (d) EDX spectrum of the marked points 197

Figure 4-92: (a) SEM micrograph of a polished surface of 2L99 + 0.4 wt.% V alloy showing the faceted intermetallic compounds grown on the bifilm (b) and (c) EDX spectra of the areas marked in (a) 198

Figure 4-93: (a) SEM micrograph of a polished surface of 2L99 + 0.4 wt.% V alloy showing intermetallic compounds grew on the side of the bifilm, (b) EDX spectrum of the areas marked in (a) 199

Figure 4-94: (a) SEM micrograph of a polished surface of 2L99 + 0.4 wt.% V alloy showing intermetallic compounds, (b) EDX spectrum of the areas marked in (a) 200

Figure 4-95: (a) SEM micrograph of a polished surface of 2L99 + 0.4 wt.% V alloy showing intermetallic compounds, (b) EDX spectrum of the areas marked in (a) 201

Figure 4-96: (a) SEM micrograph of a polished surface of 2L99 + 0.4 wt.% V alloy showing intermetallic compounds, (b) EDX spectrum of the areas marked in (a) 202

Figure 4-97: (a) SEM micrograph of a polished surface of 2L99 + 0.4 wt.% V alloy showing intermetallic compounds, (b) EDX spectrum of the areas marked in (a) 203

Figure 4-98: (a) SEM micrograph of a polished surface of 2L99 + 0.4 wt.% V alloy showing intermetallic compounds nucleated on the wetted side of a bifilm, (b) to (d) EDX spectra of the areas marked in Figure 4-98 (a) 204

Figure 4-99: (a) SEM micrograph of high magnification of a polished surface of 2L99 + 0.4 wt.% V alloy showing oxide and nitride layers, (b) EDX spectrum of the areas marked in (a) 205

Figure 4-100: (a) High magnification of SEM image of an oxide layer on the fractured surface of as-cast 2L99 + 0.4 wt.% V, (b) EDX analysis of Spectrum 2 207

Figure 4-101: (a) High magnification of SEM image of an oxide layer on the fractured surface of as-cast 2L99 + 0.4 wt% V, (b) EDX analysis of Spectrum 1 208

Figure 4-102: (a) High magnification of SEM image of an oxide layer on the fractured surface of as-cast 2L99 + 0.4 wt.% V, (b) EDX analysis of Spectrum 1 209

Figure 4-103: (a) SEM image of AlN layer on the fractured surface of as-cast 2L99 + 0.4 wt% V and (b) EDX analysis of Spectrum 1 210

Figure 4-104: (a) SEM image of AlN patches and spinel on the fractured surface of as-cast 2L99 + 0.4 wt% V and (b) and (c) EDX analysis of Spectrum 2 and Spectrum 8 211

Figure 4-105: (a) SEM image of AlN layer on the fractured surface of as-cast 2L99 + 0.4 wt.% V and (b) EDX analysis of Spectrum 1 213

Figure 4-106: (a) SEM image of V intermetallic on the fractured surface of as-cast 2L99 + 0.4 wt.% V and (b) EDX analysis of spectrum 3 214

Figure 4-107: (a) SEM image of V intermetallic on the fractured surface of as-cast 2L99 + 0.4 wt.% V and (b) EDX analysis of spectrum 1 215

Figure 4-108: EDX mapping of an AlN on the fractured surface of 2L99 + 0.4 wt.% V 216

Figure 4-109: (a) SEM image of porosity on the fractured surface of as-cast 2L99 + 0.4 wt.% V and (b) EDX analysis of spectrum 3 217

Figure 4-110: XRD Spectrum of 2L99 223

Figure 4-111: XRD spectrum for 2L99 + 10 wt.% Mo alloy 223

Figure 4-112: XRD spectrum for 2L99 + 0.4 wt.% Mo alloy 224

Figure 4-113: XRD spectrum for 2L99 + 10 wt.% W alloy 224

Figure 4-114: XRD spectrum for 2L99 + 0.4 wt.% W alloy 225

Figure 4-115: XRD spectrum for 2L99 + 0.4 wt.% V alloy 226

Figure 4-116: (a) to (c) separation and calculation of the area fraction occupied by gas pores and intermetallics on a 2L99 + 2.1 wt.% V sample 228

Figure 4-117: (a) and (b) Low magnification of SEM images of 2L99 + 0.5 wt.% Mo top and bottom 229

Figure 4-118: (a) High magnification SEM image of intermetallics on the top surface of a 2L99 + 0.5 wt.% Mo sample, (b) and (c)corresponding EDX elemental compositions 230

Figure 4-119: (a) High magnification SEM image of intermetallics on the bottom of a 2L99 + 0.5 wt.% Mo, (b) and (c)corresponding EDX elemental compositions 231

Figure 4-120 (a) and (b) Low magnification of SEM images of 2L99 + 1.8 wt.% Mo top and Bottom 232

Figure 4-121: (a) to (e) Intermetallics observed on the top surface of a 2L99 + 1.8 wt.% Mo sample, accompanied by their respective EDX elemental compositions 233

Figure 4-122: (a) to (f) Intermetallics observed on the bottom surface of a 2L99 + 1.8 wt.% Mo sample, accompanied by relevant EDX elemental composition 234

Figure 4-123: (a) and (b) Low magnification of SEM images of 2L99 + 2.4 wt.% Mo top and Bottom 235

Figure 4-124: (a) to (d) SEM image of the intermetallics on the top surface of a 2L99 + 2.4 wt.% Mo, (c) to (f) corresponding EDX spectra and elemental compositions 236

Figure 4-125: (a) and (b) low and high SEM images of i*ntermetallics* in the pore at the base of a 2L99 + 2.4 wt.% Mo sample, (c) and (d) corresponding EDX elemental compositions 237

Figure 4-126 (a) and (b) Low magnification of SEM images of 2L99 + 1.6 wt.% W top and bottom 238

Figure 4-127: (a) High magnification SEM image of intermetallic on the top surface of a 2L99 + 1.6 wt.% W sample, (b) and (c) corresponding EDX spectrum and elemental composition..... 239

Figure 4-128: (a) High magnification of intermetallics and spinel observed on the bottom surface of a 2L99 + 1.6 wt.% W sample, (b) to (g) corresponding EDX spectra and elemental compositions 240

Figure 4-129: (a) and (b) Low magnification SEM images of 2L99 +1.9 wt.% W top and bottom 241

Figure 4-130: (a) SEM image of a shrinkage on the top surface of a 2L99 + 1.9 wt.% W sample, (b) and (c) corresponding EDX elemental composition..... 242

Figure 4-131: (a) SEM image of intermetallics and gas pore on the bottom surface of a 2L99 + 1.9 wt.% W sample, (b) to (e) corresponding EDX spectra and elemental composition 243

Figure 4-132 (a) and (b) Low magnification of SEM images of 2L99 + 4.8 wt.% W top and bottom 244

Figure 4-133: (a) Low magnification SEM micrograph at the top surface of a 2L99 + 4.8 wt.% W (b) to (g) corresponding EDX Spectra and EDX elemental compositions 245

Figure 4-134: (a) high (b) and (C) low magnification SEM micrographs at the base of a 2L99 + 4.8 wt.% W Intermetallics, (c) to (h) corresponding EDX spectra and their elemental composition 247

Figure 4-135: (a) and (b) Low magnification of SEM images of 2L99 + 1.2 wt.% V top and Bottom 248

Figure 4-136: (a) to (c) Intermetallic observed on the top surface of a 2L99 + 1.2 wt.% V sample, accompanied by its respective EDX elemental composition..... 249

Figure 4-137: (a) SEM image of intermetallics on the bottom surface of a 2L99 + 1.2 wt.% V sample, (c) and (d) corresponding EDX spectrum and elemental composition 249

Figure 4-138: (a) and (b) Low magnification of SEM images of 2L99 + 2.1 wt.% V top and bottom 250

Figure 4-139: (a) Low magnification of SEM images of intermetallics on the top surface of a 2L99 + 2.1 wt.% V sample, (b) to (e) corresponding EDX spectra and elemental composition 251

Figure 4-140: (a) Low magnification of SEM images of intermetallics on the top surface of a 2L99 + 2.1 wt.% V sample, (c) to (f) corresponding EDX spectra and elemental compositions 252

Figure 4-141: (a) Low magnification of SEM images on the bottom surface of a 2L99 + 2.1 wt.% V sample, (b) and (c) corresponding EDX spectra and elemental composition 253

Figure 4-142: (a) and (b) Low magnification of SEM images of 2L99 + 5.1 wt.% V top and Bottom 254

Figure 4-143: (a) and (b) low magnification SEM image of intermetallics on the top surface of a 2L99 + 5.1 wt.% V sample, (c) and (d) corresponding EDX spectra and elemental composition 255

Figure 4-144: (a) and (b) SEM image of intermetallics on the bottom surface of a 2L99 + 5.1 wt.% V sample, (c) to (f) corresponding EDX spectra and elemental compositions 256

Figure 4-145: (a) to (d) SEM micrographs of rod-shaped AlN on the surface of CP- Al, 2L99 alloy, 2L99 + 0.6 wt.% Mo alloy and 2L99+0.2 wt pct W alloy, with 24 hours holding time in N at 850 °C (e) to (h) the EDX spectra for the marked areas in (a) to (d) 259

Figure 4-146: (a) to (d) SEM micrographs of whisker-shaped AlN on the surfaces of CP- Al, 2L99 alloy, 2L99 + 0.6 wt.% Mo alloy and 2L99 + 0.2 wt.% W alloy respectively, with 12 hours of holding time in N at 850 °C (e) to (h) the EDX spectra for the marked areas shown in (a) to (d) 261

Figure 4-147: (a) to (d) SEM micrographs of nodular-shaped AlN on the surfaces of CP- Al, 2L99 alloy, 2L99 + 0.6 wt.% Mo alloy and 2L99 + 0.2 wt.% W alloy, respectively, with 3 hours of holding time in N at 850 °C (e) to (h) are EDX spectra of the marked areas shown in (a) to (d) 263

Figure 4-148: (a) to (d) are SEM micrographs of feather-shaped AlN on the surfaces of CP- Al, 2L99 alloy, 2L99 + 0.6 wt.% Mo alloy and 2L99 + 0.2 wt.% W alloy, respectively, with 6 hours holding time in N at 850 °C (e) to (h) are EDX spectra of the marked areas shown in (a) to (d) 265

Figure 5-1: XRF measured wt.% of transition metal additions vs. the area occupied by the intermetallics at the base of the samples 288

Figure 5-2: XRF measured wt.% of transition metal additions vs. the percentage increase in XRF measured wt.% of O at the base of the samples compared to the top 289

1 INTRODUCTION

Aluminium is the third most abundant element in the Earth's crust, following oxygen and silicon. Moreover, it is acclaimed as one of the most cost-effective metals available. Aluminium is never found in its free state in nature. Instead, all the Earth's aluminium has reacted with other elements to form compounds. Aluminium alloys are widely utilised in numerous industries due to their desirable properties, such as light weight, high strength, and excellent corrosion resistance. Aluminium’s density is approximately one-third that of steel, making it significantly lighter. In addition to these properties, aluminium's low melting point, limited gas solubility (excluding hydrogen), and excellent surface finish make it highly suitable for casting applications and general use.

Despite being a widely used alloy, double oxide film defects (bifilms) can negatively affect the performance and reliability of aluminium alloys. These defects can lead to reduced mechanical strengths, diminished surface quality, and increased susceptibility to corrosion. Extensive research has been conducted on bifilms for several decades, ever since their initial mention by Campbell in the 1990s [2], and the impact of these defects on the casting properties of light alloys has generated growing attention.

Previous researchers have explored the addition of transition metals to aluminium alloys to relieve these issues. Adding transition metals, such as molybdenum and tungsten, has shown promising results in improving the mechanical properties of the alloys. However, reaching a definitive conclusion on this subject was difficult due to the limited amount of data available [3].

Understanding the mechanisms by which transition metals influence the reduction of the amount of bifilms is essential for optimising the design and performance of aluminium alloys. These mechanisms include:

i) The role of intermetallics,

ii) The presence of aluminium nitrides, their morphology, and their relation to the consumption of the air inside the bifilms,

iii) Also, examining the resulting microstructural changes to the bifilms and the impact of the above on the mechanical properties of alloys.

Based on the above, this study aimed to investigate the impact of transition metals molybdenum, tungsten, and vanadium on the tensile properties of Al-Si-Mg (2L99) alloys, with a specific focus on their role in reducing the amount and/or size of the bifilms. Vanadium was chosen as the third transition metal in this study due to its lower melting point compared to molybdenum and tungsten.

Furthermore, the research aimed to characterise and understand the various AlN morphologies in the alloys and the impact of various alloy melt holding times in the N atmosphere.

Overall, the investigation of transition metal effects on aluminium alloys holds great significance in advancing the understanding and application of these materials. It offers valuable insights into optimising the alloy composition and processing techniques to establish a foundation to develop enhanced aluminium alloys that exhibit improved performance and reliability.

2 LITERATURE REVIEW

2.1 Oxide films in Al alloys

2.1.1 Oxidation of Al alloys

The reaction of liquid aluminium with oxygen results in the formation of alumina (Al_2O_3) oxide layer, which has a high Gibbs Free Energy of formation [ΔG = -907.55 kJ/mole O_2] [3]. The formation of aluminium oxide on the surface of aluminium was found to proceed through a two-step process. Initially, a thin nanometer-thick layer of amorphous aluminium oxide forms instantaneously due to the reaction of the melt with O_2 [4]. This is shortly followed by the transformation of the oxide layer into a γ-Al2O3 crystal structure γ-Al_2O_3 [3][5][6], which serves as a protective barrier [7]. Further transformation of the γ-Al_2O_3 to α-Al_2O_3 was observed to occur with an increase in temperature and duration in the melt. It has been reported that after 5 hours of commercial-purity aluminium (CP-Al) incubation at 750 °C, the γ-Al_2O_3 was fully transformed to α-Al_2O_3 [3].

The rate of aluminium oxidation is subject to modification by factors such as the surface area, temperature, humidity [8] and impurities [3] of the melt. This has implications for a range of processes, including recycling, extraction, casting, and welding, as the presence of an oxide layer in the melt can impact the quality of the liquid metal [8].

The γ-alumina is stable and protects the surface of the Al alloy from further oxidation except at temperatures above 700 °C. The relationship between time and oxide growth in the melt largely depends on the temperature of the alloy, as shown in Figure 2-1. For temperatures less than 700 °C, the oxide growth vs. time curve indicated a

logarithmic pattern, whilst the oxide growth vs. time curve above 700 °C showed a parabolic rate of increase [9] [10] [11].

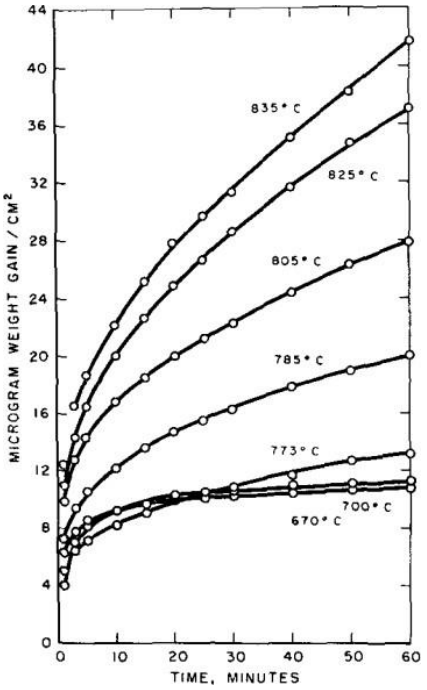


Figure 2-1: Oxidation curves of Al in dry O_2 [9] [10] [11]

As discussed, after an extended incubation period, the ɣ-alumina transforms into α-alumina (corundum), which is a thermodynamically favoured crystalline ceramic [12] [13]. The conversion to α-alumina results in a higher density and less protective oxide layer compared to ɣ-alumina and could lead to a 24% reduction in the oxide's volume, which subsequently generates stresses in both the metal and the oxide layers. This stress can cause the formation of cracks in the oxide layer, leading to an acceleration in the rate of oxidation [12].

Impey et al. [14] reported that the transformation of the phases from γ to α-alumina is largely influenced by the presence of water vapour in the air. However, the specific moisture levels and the elapsed time were not reported. They reported that the rate of formation of oxides slows down after 30-60 minutes, with the breakaway

transformation from γ to α-alumina after approximately 5 hours. This is followed by hydrogen absorption, which leads to the natural removal of hydroxyl ions, which act as a stabiliser for γ-alumina. According to Impey et al., this transformation continues for up to 24 hours and is more pronounced in dry air compared to humid air, as shown in Figure 2-2.

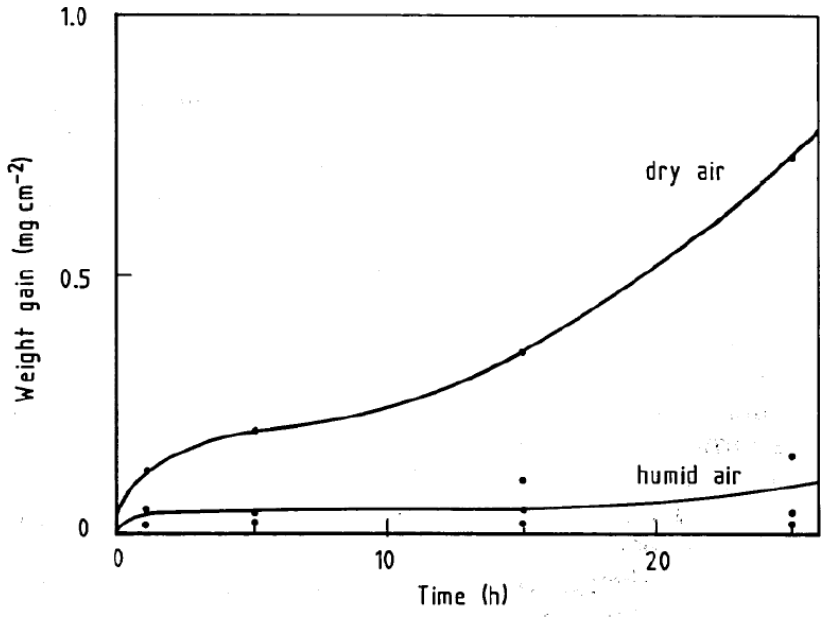


Figure 2-2: The CP- Al oxidation in dry and humid air at 750 °C [11] [14]

Stephenson [15] demonstrated that during the initial twenty minutes of exposure to humid air, liquid Al absorbs H rapidly due to the diffusion of hydroxide ions through the amorphous oxide layer on the melt surface, providing a source of hydrogen for absorption by the melt. However, the H content of the melt did not continue to increase after this period as the formation of a crystalline γ-Al_2O_3 layer at the interface between the melt and the amorphous layer further reduced hydrogen absorption. The γ-Al_2O_3 layer acted as a barrier, preventing the diffusion of hydroxide ions and thus restricting hydrogen absorption until breakaway oxidation caused cracking in the oxide layer, exposing the surface to water vapour and allowing for further reaction [11] [7].

As reported by Wang et al. [5], Transmission Electron Microscopy (TEM) analysis, supported by X-ray diffraction, revealed the presence of platelet-shaped oxide particles of γ-Al_2O_3. The platelets, as depicted in the TEM image in Figure 2-3, measured approximately 200 to 300 nm in length and 40 to 60 nm in width. High-resolution TEM further showed that these γ-Al_2O_3 platelets possessed a faceted morphology and were twinned along the faceting and twinning planes identified as {1 1 1} as seen in Figure 2-4.

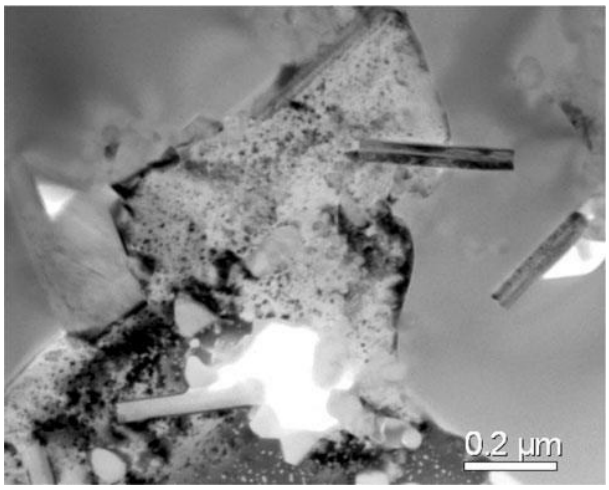


Figure 2-3: TEM image of characteristic faceted γ-Al2O3 platelets [5]

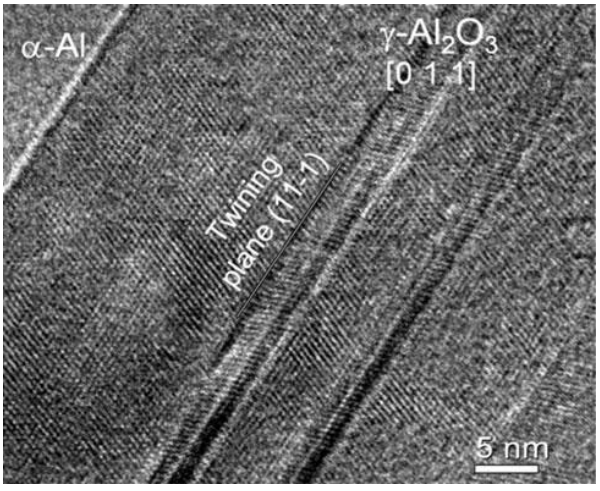


Figure 2-4: High-resolution TEM micrograph showing a γ -Al2O3 platelet, which is faceted and twinned along its {1 1 1} crystal planes [5]

Wang et al. [5] also reported that γ-Al_2O_3 and α-Al_2O_3 films are not continuous solid structures but rather consist of separate individual oxide particles. This finding helped to explain the observed fragmentation of the oxide films at the surface and reported that based on the calculation of lattice mismatch, the potent substrate for Al could be Al_3Ti (0.09%), α-Al_2O_3 (-0.048%), $MgAl_2O_4$ (1.41%), γ-Al_2O_3 (3.38%) and TiB_2 (-4.22%) in nucleation potency order [5].

The addition of magnesium to aluminium is reported to enhance the hardening characteristics of Al; however, it may also result in Mg loss in the aluminium melt during the oxidation process [16]. According to Sylvia and Talbot [17], MgO is the most stable form of oxide for Mg contents over 1.5 wt.% as it is in equilibrium with the lowest oxygen pressure, as demonstrated in Figure 2-5. For Mg contents ranging from 0.02 to 1.5 wt.%, $MgAl_2O_4$ is the most stable form of oxide [17] [14],

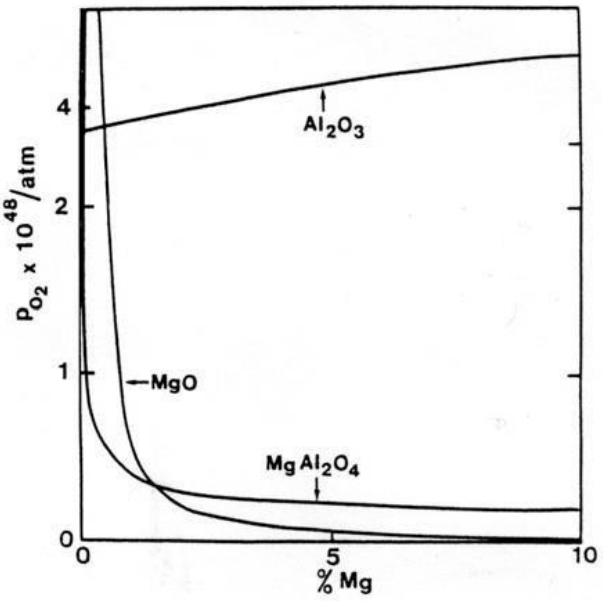


Figure 2-5: Oxygen pressure for formation of oxides vs. wt.% Mg at 725 °C [17]

The reduction of Mg concentration at the melt-oxide interface during oxidation can cause the formation of magnesium aluminate crystals, which can grow into large

particles and introduce extra stress into the oxide layer, making it more vulnerable to rupture. This phenomenon has been confirmed by SEM and TEM studies by Impey et al. [3], who observed the nucleation and growth of $MgAl_2O_4$ crystals [10] at the oxide-melt interface, as shown in Figure 2-6. The breakaway oxidation of Mg-containing alloys is a result of these crystals causing local failure at the oxide-melt interface, as noted by Impey [14].

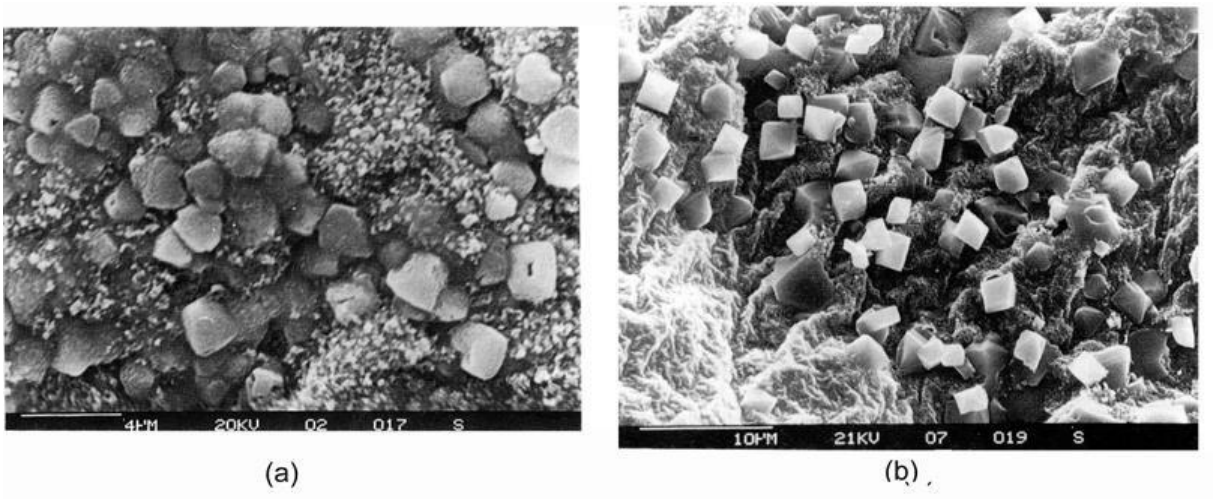


Figure 2-6: (a) Electron micrograph of the surface of Al-5 wt.% Mg alloy showing large MgAl2O4 structures and small primary magnesia crystals, (b) MgAl2O4 crystals at the oxide-melt interface from the oxide side [14]

2.1.2 Formation of oxide film defects

Many Molten metals, such as aluminium, react with oxygen, forming an oxide layer on the surface of the melt. During casting, the surface folds as waves and droplets form and merge back into the melt. In this case, the oxide film formed on the surface becomes entrained inside the bulk liquid, as shown in Figure 2-7 [18]. Campbell referred to this process as “entrainment”[19].

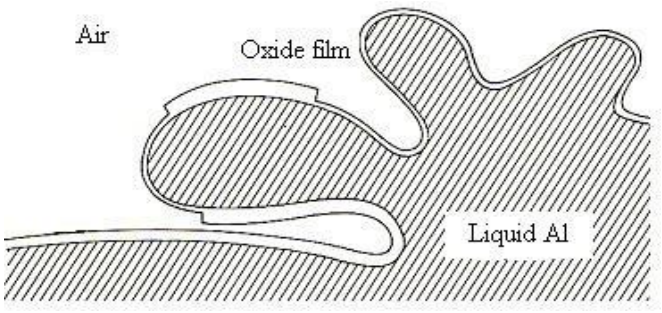


Figure 2-7: Sketch of a surface entrainment event [18]

The entrainment process in aluminium occurs due to two types of action:

- folding
- molten Al droplets coalescing back into the melt.

It is reasonable to assume that the oxide layers (films) join from the dry side to the dry side, forming what is called a bifilm. As shown in Figure 2-7, the submerged surface films are double and due to the weak bonding between the dry surfaces, the bifilm defect forms a weakly bonded surface [18]. The formation of bifilms results in the appearance of cracks of varying sizes and shapes in the liquid, which have the potential to escalate into more substantial defects in the final casting. In addition, the occurrence of cracks extending from wall to wall of the casting can lead to leakage, compromising the leak-tight nature of the material. Oxide films are the cause of casting porosity and cracks that reduce the ductility, strength, and corrosion resistance of aluminium alloy castings [5].

The increase in bifilm content leads to a decrease in toughness and an increase in the scatter of the results. To produce high-quality castings, it is essential to maintain the lowest possible bifilm content in the melt [20].

Once the bifilm is submerged, it becomes subject to bulk turbulence beneath the surface, causing it to crumple and compact. However, re-establishing quiescent conditions during solidification enables the bifilm to unfold and form a planar crack [21].

The transformation of the defects from a compact to an open crack is believed to be influenced by several mechanisms. (i) Precipitation of hydrogen in the gas layer between the films [21], (ii) Films being pulled apart due to shrinkage, (iii) Precipitation of β-phase iron in Al-Si alloys, and (iv) The formation of larger grain sizes encouraging the pushing of dendrites that straighten the films [21][10].

2.1.3 Observable characteristics of double oxide film defects

Due to the small thickness of the bifilms, which is less than a few micrometers, the detection of bifilms using routine techniques such as X-ray and ultrasound scanning is challenging and often not possible [2]. To resolve this problem, two methods have been developed in recent years to provide evidence for bifilms.

The first method involves breaking a cast testbar in a tensile or fatigue test. If bifilm defects are present in the testbar, the oxide film beneath at the weakest point appears symmetrically on both fractured surfaces. It can be identified as oxide using scanning electron microscopy (SEM) and energy-dispersive X-ray analysis (EDX) [2], as illustrated in Figure 2-8 (a) and Figure 2-8 (b).

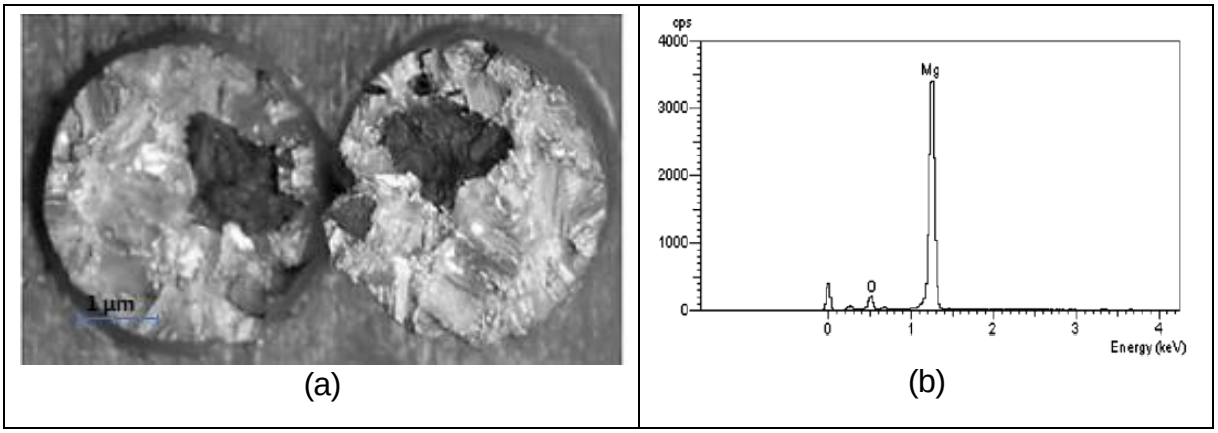


Figure 2-8: (a) Symmetrical oxide film defects on the fractured surfaces from a tensile testbar of commercial pure Mg alloy, (b) EDX spectrum of the CP-Mg alloy [22]

The second method was reported by Fox and Campbell [23] for the detection of bifilms with x-ray radiography using the Reduced Pressure Test (RPT) [3]. Bifilm defects have a volume that contains the atmosphere present at the time of their formation. The atmospheric pressure present during the solidification of the bifilm has an essential effect on the volume of the bifilm and the possibility of its detection by X-ray radiography. This can be explained by Boyle's law, which states that the product of volume and pressure is a constant ($v_1p_1 = v_2p_2$). Thus, for a sample solidified under 0.1 bar pressure, the volume of the internal atmosphere would expand by a factor of 10, allowing the defects to be more easily detected by X-ray.

To illustrate this further, liquid Al metal was allowed to solidify within a range of atmospheric pressures, varying from 0.005 atm to 0.25 atm. The intention behind employing negative internal pressure was to facilitate the expansion of the internal atmosphere within an oxide film defect. This expansion would result in the revelation of the defect itself, making it more visible in X-ray imagery. Furthermore, a reduced pressure condition may induce the migration of hydrogen content from the molten material into the internal atmosphere within a double oxide film defect. This migration,

in turn, causes the expansion of the bifilm. Figure 2-9 illustrates how the reduction in pressure enhances the clarity of the oxide film in X-ray images [24].

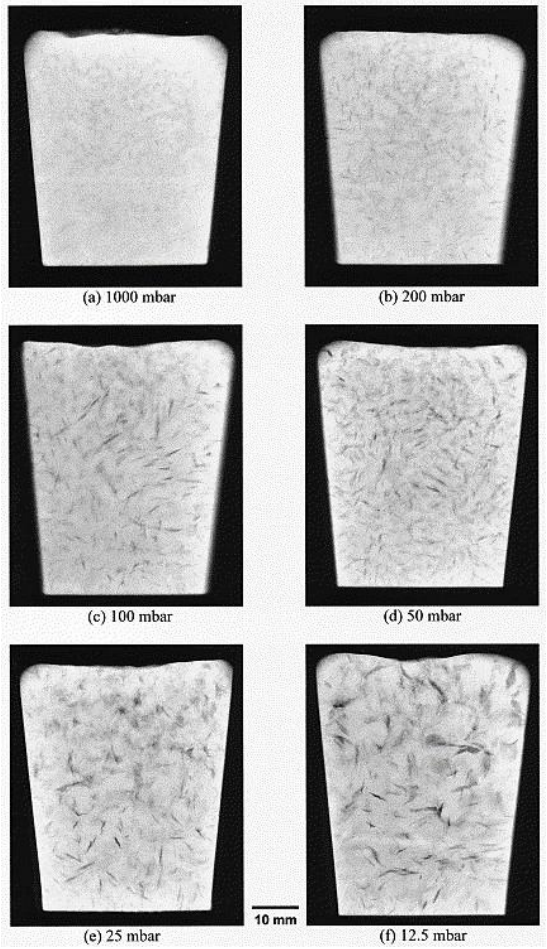


Figure 2-9: Oxide film defects seen under reduced pressure test using X-ray radiography [24]

2.1.4 Statistical analysis of mechanical properties of the alloys

The presence of oxide film defects entrapped in a casting can cause significant structural weakness, resulting in a reduction of the material's mechanical properties, such as tensile strength or fatigue resistance. Furthermore, the scatter of mechanical properties is increased in the presence of oxide film defects due to their random orientation and distribution, leading to a lack of uniformity and reproducibility of casting properties [24].

It is, therefore, essential to design alloys that are free of bifilm defects to ensure their reliability in terms of mechanical properties. The reproducibility of mechanical properties of cast alloys obtained through different casting methodologies can be represented by the Weibull modulus. This value signifies the variability in properties, where a greater Weibull modulus indicates a more limited range of defects and, subsequently, fewer defects in the final cast products [26]. [27].

The Weibull statistical distribution is a commonly used empirical method to analyse the failure properties of metals declared by Weibull [25]. In comparison to the normal distribution, this data set shows irregularity and a higher concentration of data towards the lower end of the range [3] [26].

It relies on the "weakest link" concept, originally proposed by Pierce [27], which explains the likelihood of failure in a chain composed of numerous links, considering the weakest link's failure probability. The Weibull distribution is frequently employed for characterising the reliability and lifespan of engineered components [26][28][29]. The subsequent equation (2-1) defines the Weibull cumulative distribution function [3]:

$$F_w = 1 - exp\left[-\left(\frac{x-x_T}{x_0}\right)^m\right] \quad (2\text{-}1)$$

The aggregate proportion of failure, denoted by "F_w", for an assumed value of x (such as strength) is modelled using the Weibull parameters m, x_T, and x_0. m denotes the Weibull modulus for the dataset, x_T stands for the lower strength limit where none of the samples experienced failure, and x_0 represents the location parameter where 63% of the data could fail [3] [26].

The Weibull modulus and distribution model is a valuable method for statistical analysis of casting failures with defects [30]. At the upper end of the model, there is a limit to

the material's mechanical property is represented by a cut-off value. Cast components also show the same behaviour, such as the accumulation of tensile testing results at the upper extremity of the distribution. Nonetheless, in the case of testbars containing significant defects leading to lower values, the results will tend to cluster at the lower extremity of the distribution [3] [26].

The utilisation of the Weibull distribution is made easier by assuming the threshold (x_T) to be zero, reducing the number of unknown variables from three to two [26]. This version of the distribution is referred to as the 2-parameter Weibull, and its cumulative distribution function can be expressed as follows equation (2-2):

$$F_w = 1 - exp\left[-\left(\frac{x}{x_0}\right)^m\right] \quad (2\text{-}2)$$

The above equation (2-2) has the potential to be restated as equation (2-3):

$$\ln[\ln(1/(1 - F_w)] = m\ln(x) - m\ln(x_0) \quad (2\text{-}3)$$

m: the slope of the line

$m\ln(x_0)$: the intercept

The equation can now be transformed into a linear form and represented as a straight line. The scale parameter (x_0) and Weibull modulus (m) of the 2-parameter Weibull can be calculated by plotting $\ln[\ln(1/(1\text{-}F_w)]$ against $\ln(x)$ [26].

To analyse the mechanical properties (such as UTS, %Elongation, or fatigue life) of the castings, the values (x_n) must be sorted in ascending order as follows equation (2-4):

$$x_1 < x_2 < x_3 < \ldots < x_{n-1} < x_n \quad (2\text{-}4)$$

A failure probability (P_n) between 0 and 1 is derived based on the following equation

(2-5):

$$P_1 < P_2 < P_3 < \ldots < P_{n-1} < P_n \quad (2\text{-}5)$$

To calculate the probability values, the equation (2-6) is normally constructed as :

$$P_n = \frac{n-a}{N+b} \quad (2\text{-}6)$$

Four more commonly used equations (2-7 to 2-10) [31] [32]:

$$P_n = \frac{n-0.5}{N} \quad (2\text{-}7)$$

$$P_n = \frac{n}{N+1} \quad (2\text{-}8)$$

$$P_n = \frac{n-0.3}{N+0.4} \quad (2\text{-}9)$$

$$P_n = \frac{n-0.5}{N+0.25} \quad (2\text{-}10)$$

According to Khalili and Kromp [33], equation 2-8 was found to have the least accurate results, whereas equation 2-10 provided a better estimation for the assigned probability of failure [3]. Tiryakioglu et al. [34] utilised Monte Carlo simulation to derive a and b estimators, presented in Table 2-1. Tiryakioglu et al. [35] also studied if the Weibull distribution could be used to determine a pattern in the mechanical property test values. A goodness-of-fit test can be performed (at 95% confidence) using equations 2-11 by calculating the coefficient of determination (R^2) for a wide range of sample numbers between 5 and 100. This value is compared to the R^2 of the linear regression obtained from the Weibull probability plot. If R^2 is below $R^2_{0.05}$, it suggests that the data does not adhere to the 2-parameter Weibull distribution. Conversely, if R^2 exceeds $R^2_{0.05}$, it implies that the data does align with equation 2-11, which represents a 2-parameter Weibull distribution [26].

$$R^2_{0.05} = 1.0637 - \frac{0.4174}{n^{0.3}} \quad (2\text{-}11)$$

Table 2-1: The Weibull parameters a and b are estimators of unbiased probability [26] [34]

N	a	b	N	a	b
5	0.173	0.500	27	0.448	0.000
6	0.243	0.390	30	0.455	0.000
7	0.280	0.310	32	0.460	0.000
8	0.309	0.251	35	0.465	0.000
9	0.322	0.210	40	0.472	0.000
10	0.348	0.190	45	0.481	0.000
11	0.367	0.160	50	0.486	0.000
12	0.371	0.130	55	0.499	0.000
13	0.382	0.110	60	0.503	0.000
14	0.388	0.100	65	0.509	0.000
15	0.394	0.080	70	0.518	0.000
17	0.407	0.050	75	0.522	0.000
20	0.417	0.030	80	0.516	0.000
22	0.430	0.000	90	0.518	0.000
25	0.443	0.000	100	0.519	0.000

Green and Campbell [36] utilised a 2-parameter Weibull distribution to characterise the fracture strength distribution in Al-7Si-0.35Mg alloy[26] [36]. They suggested that the Weibull distribution provided a more accurate representation of the data than both the Type 1 extreme value and Normal distributions[26] [3]. A comparable finding was reported by Byczynski [37] on Al-Si-Cu-Mg (A319) alloy.

Nyahumwa et al. [12] [38] also applied this method to examine the effects of surface turbulence filling and other defects on the fatigue life of cast Al-Si-Mg alloys.

It was proposed that even if the goodness-of-fit criterion is not met, a 2-parameter Weibull distribution may still apply to the data set. Weibull plots may exhibit two distinct Weibull distributions, also known as Weibull mixtures [39]. The occurrence of a bimodal distribution becomes apparent when there are multiple varieties of defects resulting in

the reduction of the R^2 value. The data pattern exhibits inflection points, as depicted in Figure 2-10 (b). This inflexion is attributed to the presence of two distinct types of defect distributions [40]. Consequently, when the data sets were analysed as a unified group, the R^2 value was lower than $R^2_{0.05}$, as illustrated in Figure 2-10 (a). Hence, in order to provide a more accurate depiction of the data, Cox et al. proposed the utilisation of two distinct Weibull distributions with different slopes [40].

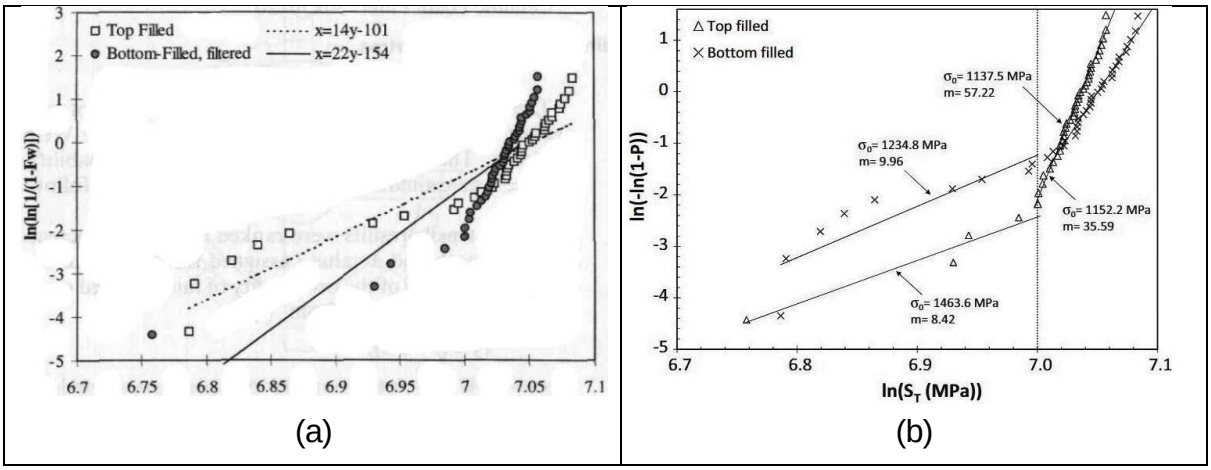


Figure 2-10: Weibull mixtures in tensile test results of IN939 alloy casting (a) 2-parameter $R^2 < R^2_{0.05}$[26] [40] **(b) bimodal 2-parameter Weibull distribution** [26] [39]

Nyahumwa et al. [41] [26]observed a similar phenomenon in their investigation of the fatigue life of an Al-7Si-0.35Mg alloy. The authors theorised that the Weibull mixtures in the alloy were the result of multiple sources of failure, including young oxide bifilm defects, old oxide bifilm defects, oxide bifilms that formed within pores, and slip planes. The reduced distribution was attributed to pre-existing bifilms formed before the mould-filling process, while the increased distribution was attributed to recently formed, or "young," bifilms [26].

The 2-parameter Weibull distribution is a commonly used approach to assess the reliability of mechanical property data for castings. However, if the 2-parameter Weibull plot exhibits non-linearity, the goodness-of-fit criteria will not be satisfied. This could be due to the assumption in equation 2-1 that $x_T = 0$ is invalid, meaning that the minimum limit of the data set's strength cannot be presumed to be zero. In such cases, the plot turns into a Weibull distribution with three parameters, as per equation (2-12) [26] [30].

$$\ln[\ln(1/(1-F_w)] = m\ln(x-x_T) - m\ln(x_0) \quad (2\text{-}12)$$

$\ln[-\ln(1-F_w)]$ represents the vertical axis, and $\ln(x-x_T)$ represents the horizontal axis of a Weibull plot. Once the plot is generated, a curve has to be fit to optimise the values of the following undetermined parameters: m, x_0, and x_T [26] [42].

Caution must be exercised when the Weibull modulus is derived from a small number of test results. Tiryakioglu and Hudak [34] demonstrated a reduction in the number of samples from 100 to 5 can result in a wider spread of the Weibull modulus confidence limit and decrease the accuracy of the estimated value of m.

Whilst Campbell [26] [30] suggested that a sample size of 30 is typically enough to produce a highly reliable Weibull plot, as the results do not weaken significantly with the introduction of more samples [26].

2.1.5 Al-7Si-0.3Mg (2L99)

Al-7Si-0.3Mg is one of the most widely used alloys of Aluminium. 2L99 has excellent characteristics, including castability, corrosion resistance and fluidity [43]. The mechanical properties of 2L99 and its microstructure are dependent upon the melt

treatment, feeding system efficiency, heat treatment, cooling rate, and composition of each element in the alloy [43].

The most damaging impurity for 2L99 is the presence of iron (Fe), as it forms three different types of intermetallic compounds. These are i) α(Fe_2SiAl_8), which generally has a plate-like morphology; ii) β($FeSiAl_5$), which has a needle-shaped morphology; and iii) π($FeMg_3Si_6Al_8$), which has a porous morphology as shown in Figure 2-11 [3][44]. It has been reported that the plate-shaped β compounds lead to the most significant reduction in the mechanical properties of the 2L99 alloy, specifically fracture toughness and ductility due to their size and shape. Also, the addition of 0.2 wt.% Cr,
0.5 wt.% Mo or W and 0.8 wt.% V to Al-Si alloys has been reported to increase the crystallisation of the α-Al(Fe, M)Si phase, leading to a reduction in the amount of β compounds [45].

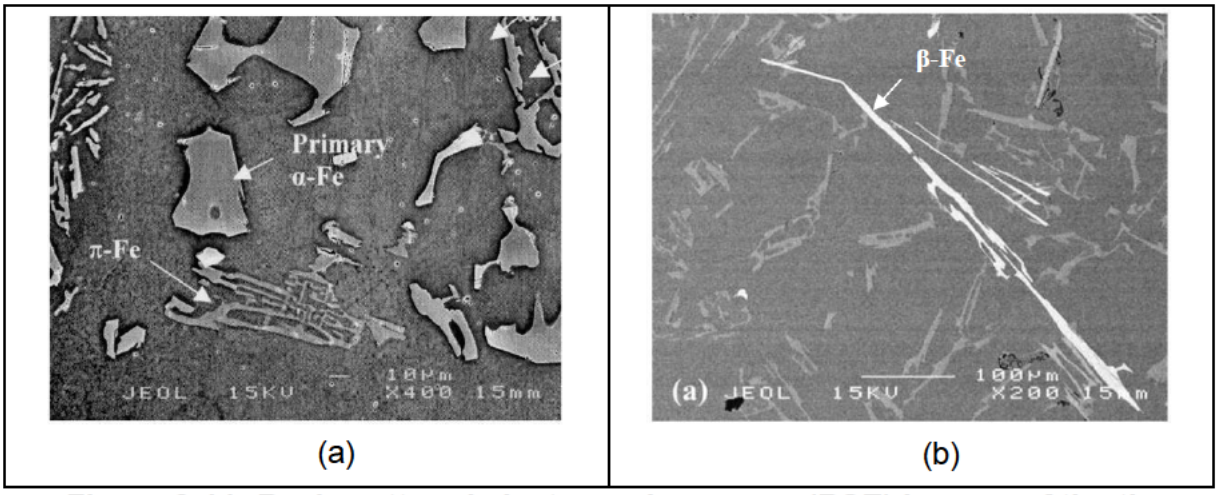


Figure 2-11: Backscattered electron microscopy (BSE) images of the three types of Fe intermetallics in Al-Si-Mg alloy(a) α and π shapes (b) β shape [3] [44]

Magnesium at 0.2 to 0.6 wt.%, when combined with Si, forms Mg_2Si, which precipitates during an age-hardening process serving to strengthen the alloy. Mg_2Si is an intermetallic compound with excellent characteristics, including great hardness (4.5×10^9 N/m^2) and low density (1.99 g/cm^3) [46][47]. It's important to highlight that the

shape, size, and distribution of Mg_2Si phases employ a significant influence on their mechanical properties [47]. In Al-Si-Mg alloys, the crystallisation of Mg_2Si phases aligns with the composition ratio of Si and Mg. In their as-cast state, Mg_2Si phases tend to be a coarse dendritic structure [47][48]. This coarse dendritic morphology in Mg_2Si phases leads to uneven stress concentration, ultimately compromising the mechanical characteristics of the aluminium alloys. One way to improve the morphology of Mg_2Si phases is the addition of elements such as P [48][49], Na [50], TiB_2 [49], Ca or Sb [51][47].

It is important to note that the increased affinity of Mg to oxygen can result in over-oxidation of Mg, which makes it challenging to retain the Mg content within the limits required for the 2L99 alloy. Mg over-oxidation can also lead to the reduction of the mechanical properties of 2L99 [43].

During the process of 2L99 solidification, the primary α-Al phase develops as dendrites form and are surrounded by the liquid melt, which is rich in Si. The liquid solidifies at the eutectic temperature, forming eutectic Al and Si phases. The morphology of the eutectic Si is coarse (platelets or acicular needles), having a random distribution with slow cooling rates. As a result, the sharp edges of the Si needles increase the stress and lower the mechanical properties of the alloy [43]. Solidification rate, however, influences the eutectic Si shape, size, and length of intermetallic iron compounds and alloy porosity, in addition to dendrite arm spacing [43].

2.1.6 Formation of the Aluminium Nitride

^{1}AlN can form when liquid Al reacts with nitrogen gas as per equation (2-13). By blowing N gas into the melt at a pre-determined rate, researchers have claimed AlN to have been

formed in the aluminium melt, producing a reinforced Metal Matrix Composite (MMC) of AlN [52][53][54].

$$2Al + N_2 \rightarrow 2AlN \quad (2\text{-}13)$$

The Al-N phase diagram shown in Figure 2-12 displays the composition ranging from 0 to 50 at.% N, and the temperatures range from 500 °C to 3000 °C. AlN is composed of covalent bonds, displaying a hexagonal wurtzite crystal structure. Its melting and boiling points are recorded as 2200 °C and 2517 °C, respectively [55].

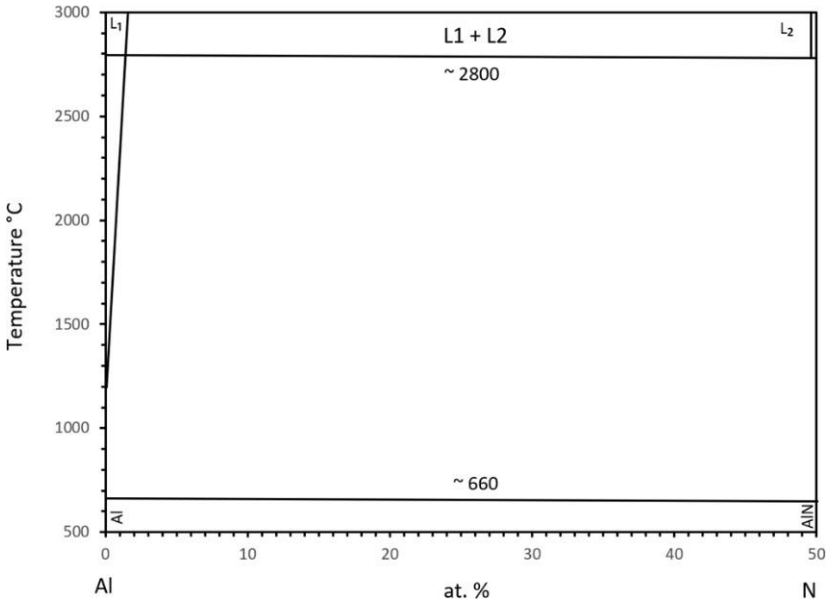


Figure 2-12: Phase diagram of Al-N with composition 0 to 50 at.% N, at temperatures 500 °C to 3000 °C [55]

It is also possible for AlON to form, aside from alumina, spinel, and MgO. However, the eutectoid Al_2O_3-AlN phase diagram, as shown in Figure 2-13, reveals that AlON is unlikely to exist at temperatures below 1640 °C [56]. At normal room temperature, AlON is unstable and can only be found under extremely limited pressures of O and N of around 10^{-10} bar [57].

[1] The literature review presented in this section has been published by the author in the paper provided in Appendix A.

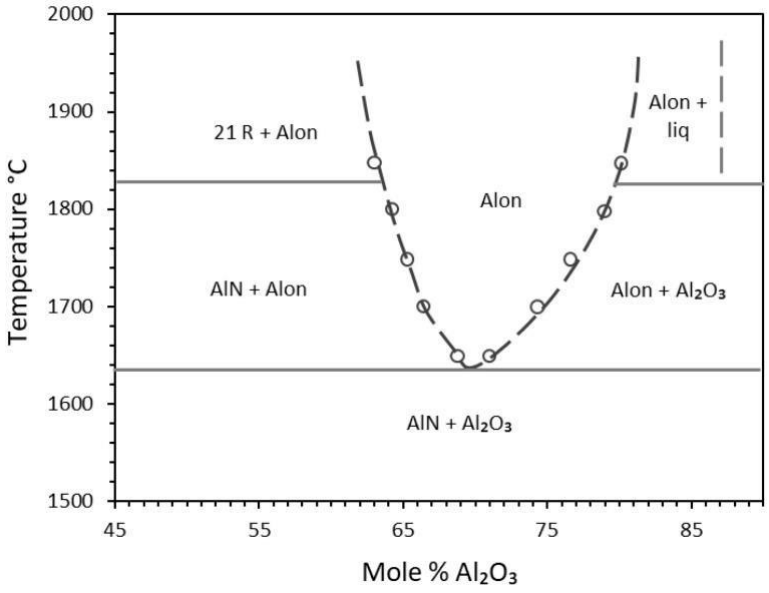


Figure 2-13: AlON phase diagram [56]

The formation of AlN can be negatively impacted by the presence of oxygen. By comparing the nitrogen bubbling between commercial purity and high-purity nitrogen, Zheng et al. [58] suggested that AlN only formed when the partial pressure of oxygen was low [3].

Nyahumwa et al. proposed that the internal gases in air bubbles were consumed in the following order. First, oxygen reacted to form Al_2O_3 in pure Al, or $MgAl_2O_4$ in the case of 2L99, or MgO in Al-5Mg alloy, followed by a nitrogen reaction to form AlN [59]. They observed nodular AlN structures on CP-Al (held for 40 minutes) and 2L99 (held for 32 minutes) at 720 °C, as shown in Figure 2-14 (a) and Figure 2-14 (b) and confirmed by the EDX spectra in Figure 2-14 (c) and Figure 2-14 (d). Additionally, El Sayed et al. [60] noted that hydrogen diffusion into the entrapped bifilm defects may occur during their presence in the melt.

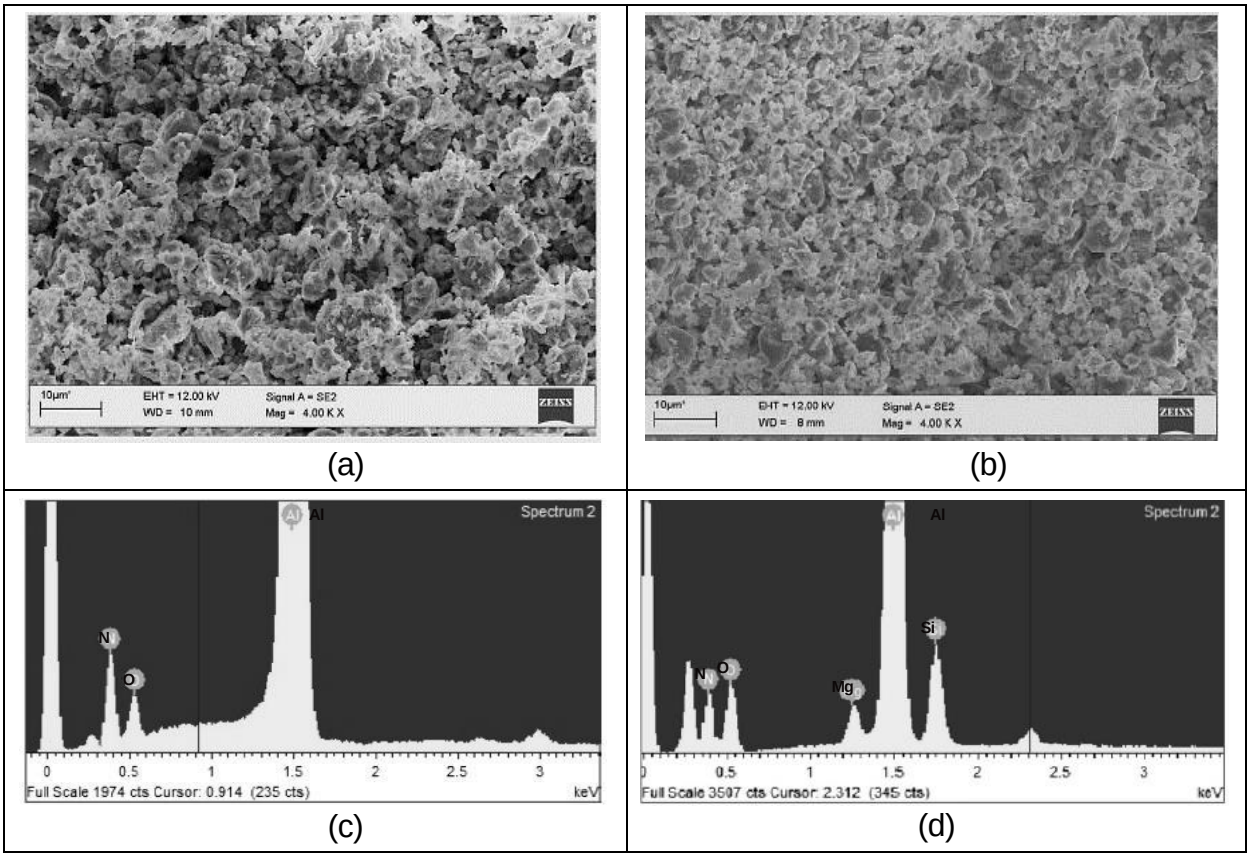


Figure 2-14: (a) SEM micrograph of granular AlN on CP-Al after 40 minutes hold, (b) SEM micrograph of granular AlN on 2L99 after 32 minutes hold, (c) and (d) the energy-dispersive X-ray spectra corresponding to (a) and (b) [60]

Zheng et al. [58] reported the formation of spherical dendritic AlN particles, smaller than 10 µm, as depicted in Figure 2-15 (a) through direct bubbling of N_2 into a pure Al melt for a duration of 6 hours at a temperature of 1200 °C. The EDX spectrum of the area marked in Figure 2-15 (a) is shown in Figure 2-15 (b).

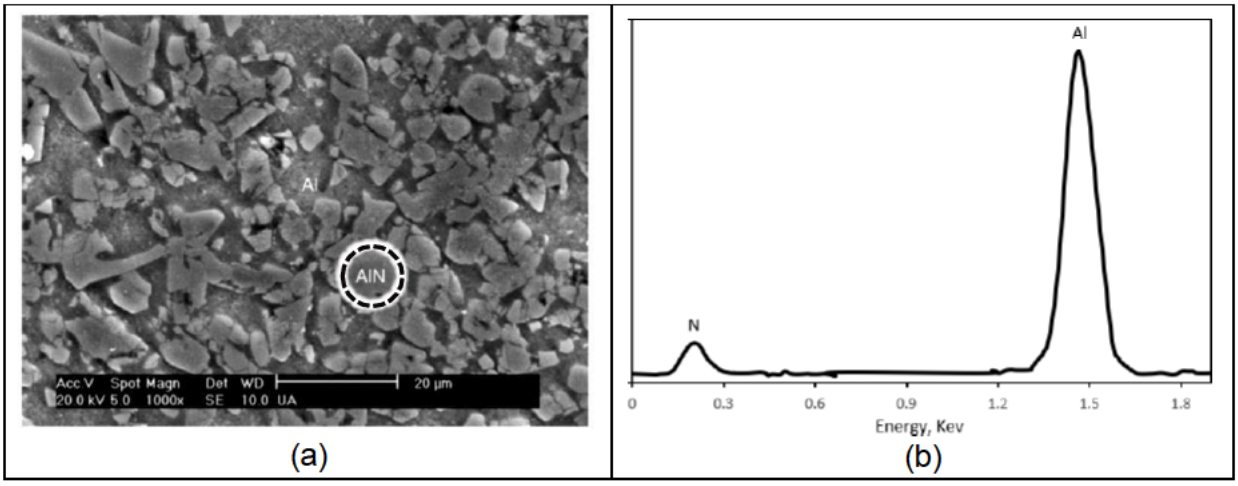


Figure 2-15: (a) SEM micrograph of AlN formed by bubbling N_2 directly into pure Al at 1200 °C for 6 hours (b) the EDX spectrum of the marked area in (a) [58]

Raiszadeh and Griffiths [10][61] investigated the reaction rate of an entrapped air bubble in CP-Al liquid, using real-time x-ray radiography, to observe the changes in air volume when in contact with the liquid Al at 850 °C. They determined that the O was consumed entirely within four hours and N was completely consumed within the next four hours, resulting in the formation of feather-like AlN of about 10 µm in length, as seen in Figure 2-16 (a). Figure 2-16 (b) presents the EDX spectrum of the entire area shown in Figure 2-16 (a).

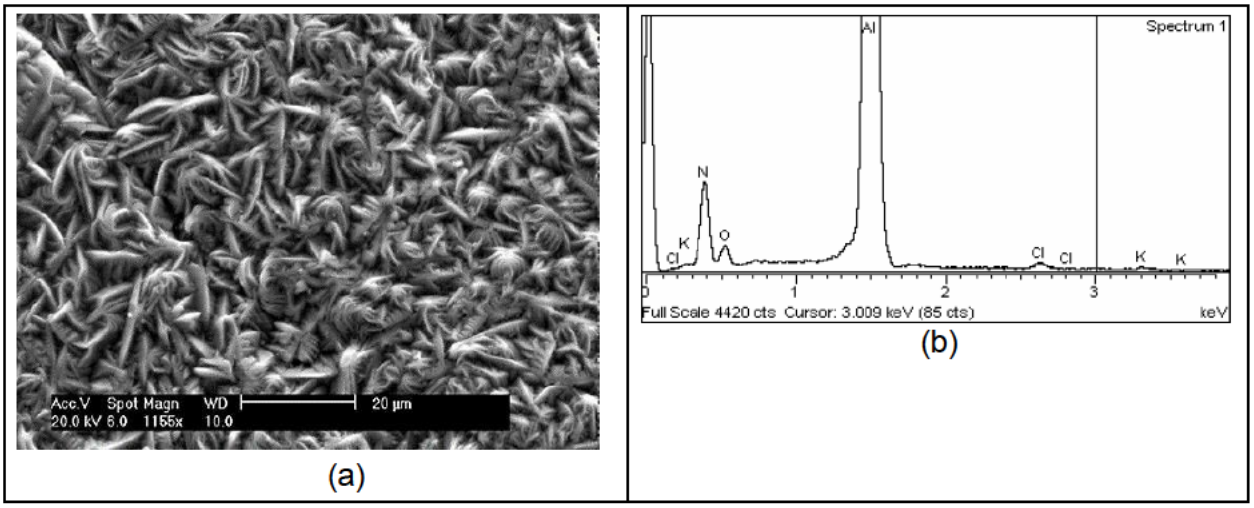


Figure 2-16: (a) SEM micrograph of feather shaped AlN layer (b) EDX spectrum of the whole area shown in (a) [10] [61]

As shown in Figure 2-17 (a), Gerrard et al. [11] [62] observed feather-shaped AlN in CP-Al by degassing a LECO sample to remove hydrogen and heating the sample to 700 °C in a N atmosphere for 15 mins. Figure 2-17 (b), the EDX spectrum of the area marked in Figure 2-17 (a), shows the presence of oxides (5 wt.%), nitrides (12 wt.%), Fe (2 wt.%) and Al (81 wt.%).

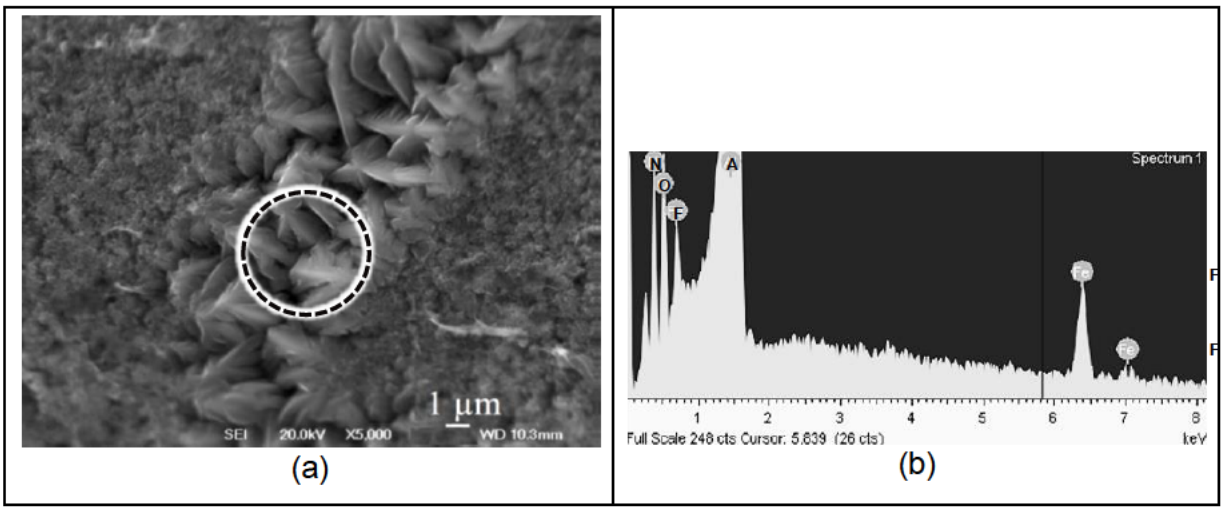


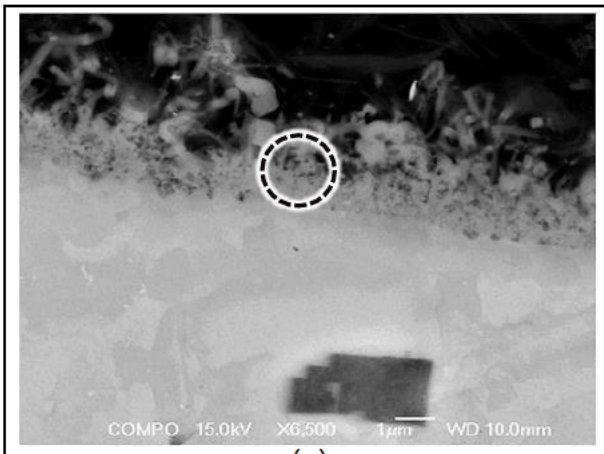
Figure 2-17: (a) SEM micrograph of feather-shaped AlN layer (b) EDX spectrum of the area marked in (a) [11] [63]

Griffiths et al. [64] conducted an examination of the fractured surfaces of CP-Al and Al-5Mg alloy. They discovered whisker-like structures of alumina and MgO within pores after a 20-minute holding period in the melt. Their findings indicate that these whisker shapes might have arisen from the evaporation of oxides inside the pores, followed by their subsequent condensation.

Hinton [7] examined the development of oxides and nitrides in various Al alloys (SP- Al, 2L99, and Al-4wt.%Mg) by melting the alloys in air and nitrogen atmospheres and holding the melts at 750 °C inside an airtight cylindrical furnace. Gases were circulated through the furnace at a rate of approximately 13 cm^3/min, and the samples were kept under nitrogen for 5 minutes, 1 hour, and 24 hours. Different cooling techniques, such

as air cooling or quenching in water were employed in both oxygen and nitrogen atmospheres. The cross-sections of the samples were analysed using a FEG-SEM [7].

Hinton [7] also reported the observation of feather-like nitride morphologies with an average height of 3.7 µm on the surface of SP-Al after a holding time of 24 hours in nitrogen gas, as depicted in Figure 2-18 (a). The EDX quantification of the marked region in Figure 2-18 (a) indicated the presence of AlN, with the highest nitride concentration of approximately 14 wt.% N, 4 wt.% O and 82 wt.% Al detected in SP-Al [7].



(a)

Element	Weight%
O	3.83
Al	82.24
N	13.93
Total	100

(b)

Figure 2-18: (a) SEM micrograph of SP-Al cast at 750 °C with 24 hours holding time (b) the EDX quantification of the area marked in (a) [7]

It is noteworthy that the feather-like characterisation of AlN by Hinton [7] differed from other researchers, as shown in Figure 2-16 (a) and Figure 2-17 (b). In Hinton's study, nitrides were not detected on SP-Al at 5 minutes and 1 hour short holding times, which was attributed to the EDX's low sensitivity in detecting nitrogen at low amounts.

After attempting to grow AlN in 2L99, Hinton did not detect any nitrogen signals with EDX in samples with various holding times (5 minutes, 1 hour and 24 hours). Hinton concluded that this could be due to the small concentration of nitrogen in the samples and the EDX's lack of sensitivity [7].

Hinton reported tests on 2L99 alloy where the oxide and nitride growth was attempted in air, after which the oxide layers grew on average from 0.6 μm to 1.5 μm between 5 minutes and 24 hours. Although the oxide growth in 2L99 had a similar pattern to SP-Al, the oxide layer observed on 2L99 measured 1.5 μm and was thicker than the 0.4 μm oxide thickness observed on SP-Al.

Chen and Griffiths [3] [65] noted the presence of feather-shaped AlN, with a thickness of approximately 14 μm, on the fractured surfaces of 2L99 + 0.4 wt.% Mo, cast at 730 °C and T6 heat treated. They also reported a granular AlN structure on the surface of the same alloy, which was produced using the entrapped air bubble technique held for 1 hour at 725 °C. The addition of 0.4 wt.% Mo to the 2L99 alloy was found to improve the Weibull modulus of the UTS by 9.7% and the %Elongation by 70%.

The feather-shaped AlN morphology depicted in Figure 2.21 (a) is considered permeable, which has the potential to facilitate the consumption of entrapped gases and result in a reduction in the size of bifilms. This size reduction is expected to engender a degree of bonding between the two un-wetted oxide surfaces, thus enhancing the mechanical properties of the alloy. The EDX spectrum of the area marked in Figure 2-19 (a) is presented in Figure 2-19 (b). The EDX analysis of this area revealed the presence of O at 9 at.%, N at 36 at.%, Al at 50 at.%, Si at 5 at.% and Mg at 0.4 at.% [3].

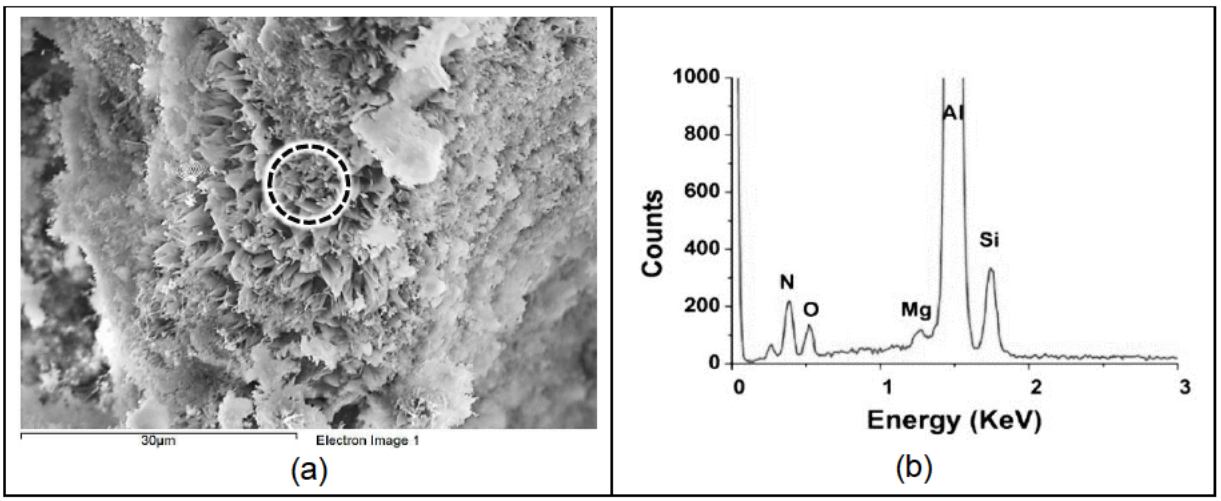
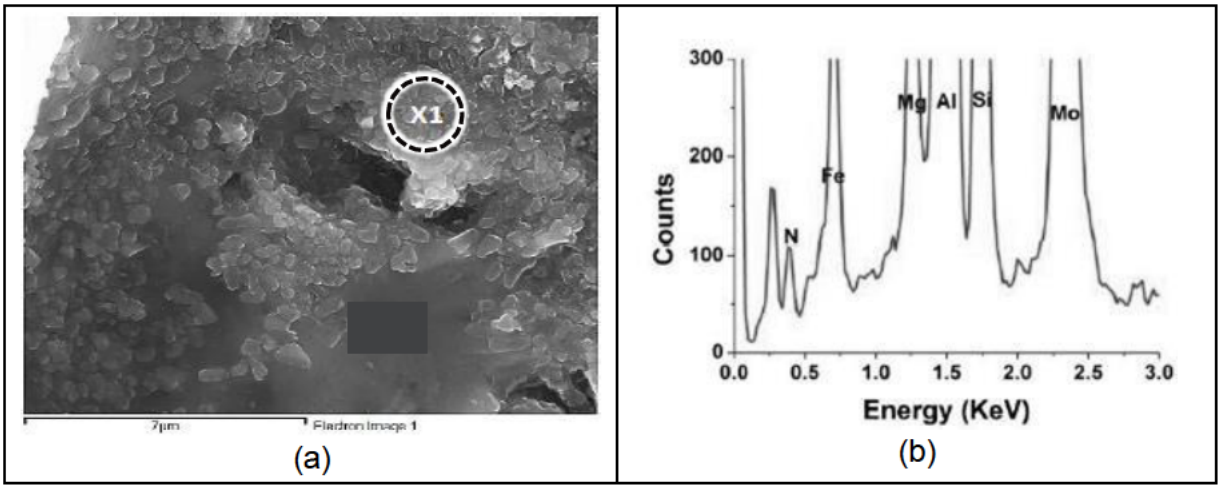


Figure 2-19: (a) SEM micrograph of the nitrides on the fractured surface of heat-treated 2L99 + 0.4 wt.% Mo alloy (b) EDX spectrum of the marked area in (a) [3]

Figure 2-20 (a) and Figure 2-20 (c) present low and high-magnification images of a sub-micron granular AlN structure observed in a sample of 2L99 + 0.4 wt.% Mo subject to a bubble growth experiment. In contrast to the feather-shaped morphology depicted in Figure 2-20 (a), this structure was reported to be considered impermeable. Figure 2-20 (b) and Figure 2-20 (d) represent EDX spectra for the AlN in Figure 2-20 (a) and Figure 2-20 (c), respectively. The researchers based their desired permeability assessment on the appearance of the AlN morphologies observed [3].



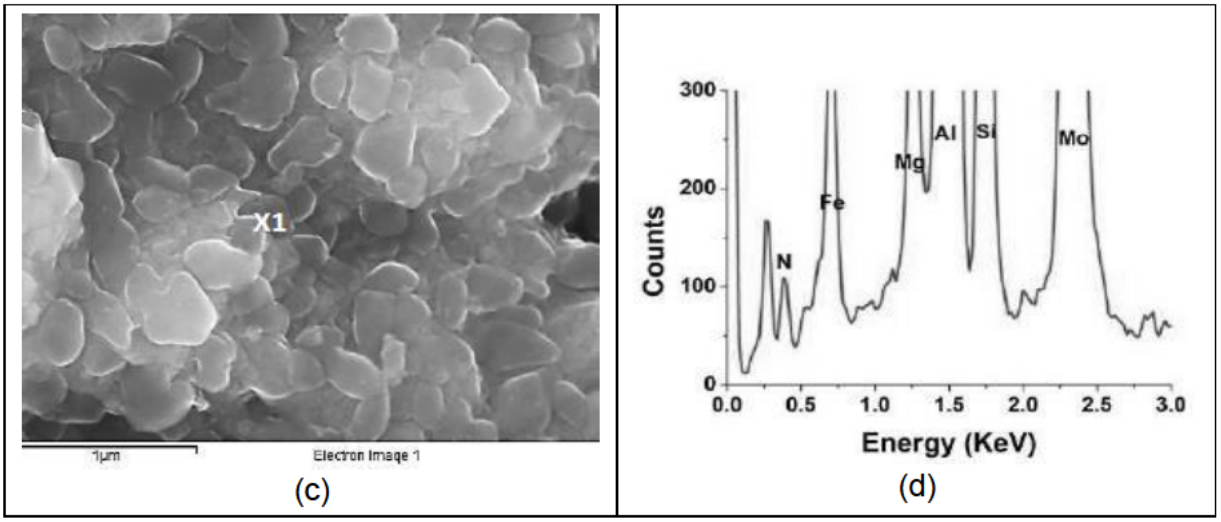


Figure 2-20: (a) and (c) low and high magnification SEM micrographs of a granular nitride layer on the surface of the 2L99 + 0.4 wt.% Mo alloy sample from the bubble-growth experiment (b) and (d) EDX spectra of the marked areas in (a) and (b) [3] [65]

Wang and Fan [66] studied the formation of nitride particles in CP-Al at temperatures of 750 °C and 850 °C, as evidenced by Figure 2-21 (a) and Figure 2-21 (b). Characterisation was performed using analytical electron microscopy on the samples obtained by a pressure melt filtration technique using a Prefil-Footprinter device. Figure 2-21 (c) displays the EDX spectra for the particles marked in Figure 2-21 (a) and Figure 2-21 (b). The AlN particles were found to have a rod-like morphology, with lengths of about 104 nm and 375 nm and widths of 1µm. The particles were identified as hexagonal wurtzite AlN with a close- packed plane structure. From Figure 2-21 (a) and Figure 2-21 (b), it may be inferred that the AlN particles likely nucleated on the oxide layers.

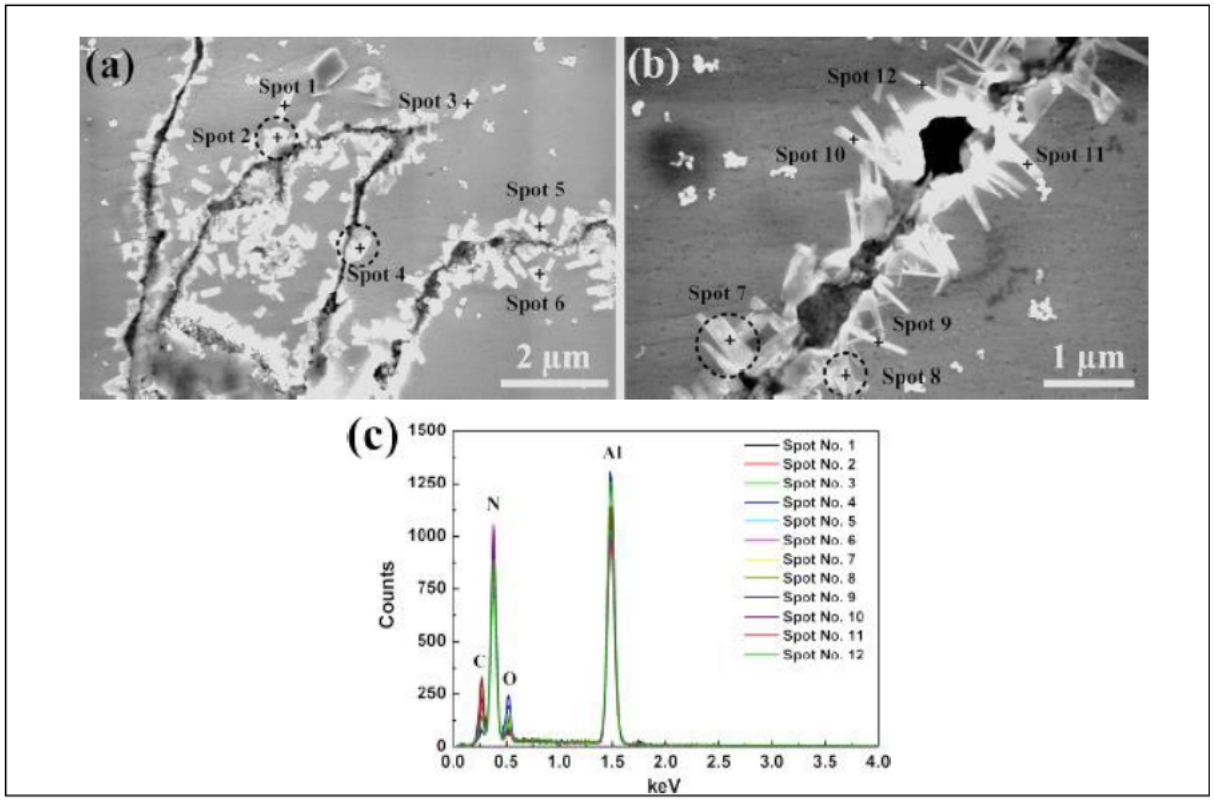


Figure 2-21: (a) SEM micrograph of nitride inclusion particles held at (a) 750 °C and (b) 850 °C (c) the EDX spectrum of the marked areas and points in (a) and (b) [66]

Using Equations (2-14) and (2-15), the authors based their calculation of the lattice-matching potential of the AlN particles as a nucleation substrate for α-Al grains on the crystallography of the observed particles.

$$fr = rAl - rp * \frac{1}{rp} \times 100pct \tag{2-14}$$

$$fd = dAl - dp * \frac{1}{dp} \times 100pct \tag{2-15}$$

In Wang and Fan's study [66], the interatomic spacings along the most closely packed directions (rAl and rp) and the interplanar spacings of the most closely packed planes (dAl and dp) of Al, oxides, borides, and AlN were analysed. The interatomic spacing misfit was represented by f_r, and the interplanar misfit of closely packed planes was

represented by f_d. It was calculated that the f_r for AlN and Al in the closely packed directions of planes was 6.66%, which indicated that AlN was a suitable nucleating substrate for α-Al grains with an f_r of less than 7%. However, when comparing the size of AlN particles with those of other particles ($MgAl_2O_4$, γ-Al_2O_3, TiB_2, α-Al_2O_3) in the melt, as shown in Table 2-2, Wang and Fan concluded that AlN was not as potent for nucleation as other phases ($MgAl_2O_4$, γ-Al_2O_3, TiB_2, α-Al_2O_3) [66].

Similarly, Simensen and Berg [66] noted that the amounts of nitrides (3 ppm to 12 ppm) in commercial Al are similar to that of oxides (6 ppm to 16 ppm). As nitride particles are identical in size, morphology, and density to oxide particles, they should have similar properties in a CP-Al alloy. However, their study reported that AlN particles were much less likely to be observed than oxide particles, indicating that the densities of AlN particles were probably much lower than the oxide particles. They suggested this might be due to the lower density of the AlN compared to oxide particles in the melt; however, they concluded that this needs further investigation.

Table 2-2: Crystallographic data of Al, AlN and common oxides and borides on CP-Al at 660 °C [66]

Phase	Structure	Lattice Parameter		Close-Packed Plane	$d_{(hkl)}$(nm)	fd (%)	$r_{[uvw]}$nm	fr (%)
		a	*C*					
Al	Cubic	0.4121	-	<110>	{111} 0.2379	N/A	0.2914	N/A
AlN	Hexagonal	0.3122	0.4992	<2110>	{0002} 0.2496	4.67	0.3122	6.66
γ-Al_2O_3	Cubic	0.7963	-	<110>	{222} 0.2299	3.50	0.2815	3.50
α-Al_2O_3	Rhomb	0.4782	1.3057	<1100>	{0006} 0.2176	9.33	0.2761	5.54
$MgAl_2O_4$	Cubic	0.8126	-	<110>	{222} 0.2346	1.43	0.2873	1.43
TiB_2	Hexagonal	0.3037	0.3237	<2110>	{0001} 0.3237	26.49	0.3037	4.05

2.1.7 Formation of Mg_3N_2

As reported by Gerrard, the Gibbs Free Energy of Formation was calculated for both Mg_3N_2 and AlN. AlN was the preferred nitride to form, as its Gibbs Free Energy of Formation (-423 kJ/mol) [10] was lower than that of Mg_3N_2 (-257.14 kJ/Mol) [11], on the surface of the 2L99 alloy, which included 0.2 to 0.45 wt.% Mg, there was no sign of nitride development [11].

It appears that alloys with low levels of Mg do not form nitrides with ease, and it is proposed that this may be due to Mg inhibiting nucleation of Mg_3N_2 and AlN, an effect evidenced by El-Sayed [59] with the surface spinel layer being slightly effective in preventing hydrogen diffusion similar to that found with an Al_2O_3 film. The MgO that was formed in Al - 4wt.% Mg alloy has a porous structure, making it ideal for sealing up any defects in the oxide film and allowing the passage of gases [11].

2.1.8 Formation of hydrogen

Hydrogen as a soluble gas in Al alloys arises from the interaction between water vapour and the Al melt [3] [10] [67], as described in Equation (2-16):

$$2Al + 3H_2O = Al_2O_3 + 3H_2 \quad (2\text{-}16)$$

The main source of H is thought to be the presence of moisture on different casting equipment, such as crucibles, refractories, and charge materials, as well as the water vapour in the air [10].

Ransley and Neufeld [68] examined the solubility of hydrogen in Al melt and, as shown in Figure 2-22, concluded that H is soluble in liquid Al at a much higher rate by a factor of 20 compared to Al in a solid state [10]. While solidification occurs and the dendritic front progresses, hydrogen situated at the solid-liquid interface is pushed into the liquid,

causing a rise in the hydrogen concentration within the remaining liquid [3] [10] [68].

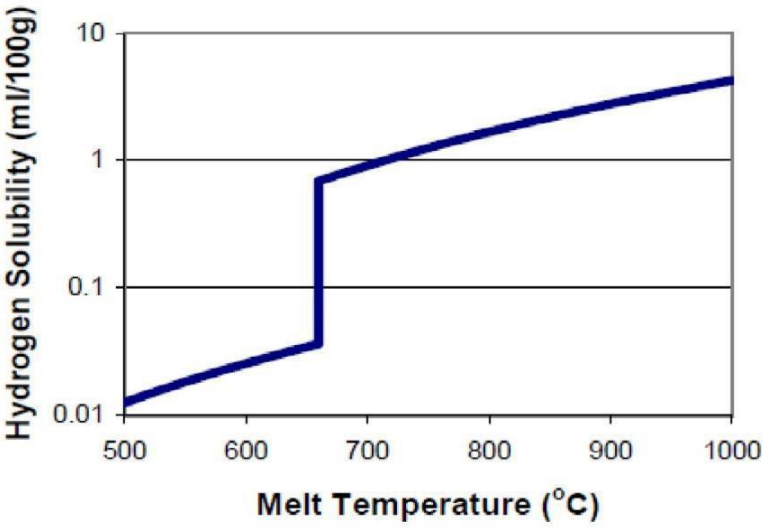


Figure 2-22: H solubility in pure aluminium plotted against the temperature [3] [10][68]

Zhou et al. [69] suggested that the hydrogen content in the melt during solidification is directly proportional to the fraction of the solids present. In pure liquid Al, absorption of H occurs quickly due to the oxidation of water vapour at the surface of the Al melt. However, the formation of a protective oxide layer on the surface of the melt restricts this absorption [11]. Bifilms play a key role in the formation of H porosity and inflate, as the hydrogen dissolved in the Al melt penetrates the interior atmosphere of the bifilm. However, this contrasts with previous evidence suggesting hydrogen cannot diffuse through alumina [11].

Gerrard et al. [60] [63] proposed that hydrogen can penetrate through the alumina layer into a bifilm, though slowly, and hydrogen porosity is formed due to the pre-existing pores. The small pores observed could be the result of newly forming pores.

The results indicated that aluminium oxide is less permeable than AlN due to AlN's more open structure, leading to a higher rate of diffusion. Older oxide films with AlN interfaces may be a more likely source of hydrogen porosity in Al alloys than younger double oxide film defects with retained oxygen.

According to El-Sayed [70], the solubility of hydrogen in aluminium castings has been found to have an impact on their mechanical properties. As H content increased from 0.05 cm^3/100 g to 0.18 cm^3/100 g, the Weibull moduli of the UTS of the 2L99 alloy decreased from 21 to 5 [3].

Campbell [2] proposed hydrogen could only form bubbles if it penetrated through an oxide film defect. El-Sayed et al. [70] further suggested that castings with low H content have smaller oxide film defects compared to those with high H content, supporting the idea that H causes these defects to expand [3].

Gerrard and Griffiths [71] reported that continuous aluminium oxide and feather-like aluminium nitride permit hydrogen diffusion. The latter was found to have twice the H absorption rate compared to the former. Raeiszadeh [10] suggested that H can diffuse into oxide film defects through permeable nitrides formed to reseal the defects or by rupturing the film at any point [3].

2.2 The effects of transition metals Mo, W and V on oxide film defects in Al alloys

2.2.1 Effect of addition of Mo to Al alloys

Molybdenum (Mo) plays a crucial role in a range of alloys, including stainless steels, alloyed cast irons, and superalloys, facilitating essential hardenability to heat-treatable alloys like pressure vessel steels [72]. Although Mo has poor solubility in aluminium (up to 850 °C) temperatures, it has not been frequently used in aluminium alloys.

Nonetheless, according to Bourkhina [73], the incorporation of 0.3 wt.% of Mo and Co altered the morphology of Fe-containing phases, leading to the formation of a more consolidated Fe-Mo-Co phase, consequently mitigating the detrimental impacts of Fe-containing phases. Additionally, Kawahara [74] proposed that the introduction of 0.05 to 0.3 wt.% Mo decreased the oxidation rate in solid Al-Mg alloys [3].

Griffiths et al. [72] claimed that incorporating 0.45 wt.% Mo or W into Al-Si-Mg alloy resulted in a reduction of the variation in tensile strength by half. Additionally, the rate of the internal reaction between O and N and the surrounding metal increased, as evidenced by the formation of AlN on the fractured surfaces of 2L99 alloy. They also claimed that the reduction in the size of the bifilms due to the consumption of internal O and N gases might alter the double oxide film morphology and enhance mechanical properties [72].

Chen [3] suggested the presence of nitride on the fractured surface is infrequent and indicated that the interior atmosphere trapped in a bifilm might have been depleting faster than the Mo-free casting. The reduction in the double oxide film defect volume

and the bonding effect would have likely had a positive effect on the mechanical properties.

Cross-sectional SEM images of the bifilm defects indicated that the nitride layer on the fractured surface of a Mo-containing casting could reach a thickness of up to 14 μm, being significantly greater than the oxide found in the 2L99 bifilm, which varied between 50 nm and 500 nm. The permeable nature of the nitride layer would likely have allowed the internal atmosphere to permeate the surface layer more easily, enabling it to react more readily with the surrounding liquid metal. As a result, this could accelerate the consumption rates of the gases inside the bifilm and potentially reduce the size of the bifilm defect [3].

TEM analysis revealed that the nitride layer identified on the fractured surface of a 2L99 + Mo testbar was composed of a duplex layer, with nitride particles observed at the base of the layer and fine-sized spinel particles or whiskers found at the top of the layer [3].

Furthermore, Chen [3] found that adding a masteralloy containing Mo resulted in forming an intermetallic phase, such as Al_4Mo or $Al_{12}Mo$. Additionally, oxide inclusions introduced by the masteralloy and the masteralloy itself provided a favourable surface for the nucleation of Al grains [3].

The determination of the grain restriction factor for a Mo intermetallic also demonstrated a minor enhancement in grain size within CP-Al. However, in the case of the 2L99 alloy, there was no observable enhancement in grain size, possibly due to $Mo(Si, Al)_2$, the compound that developed in this alloy, which may not be a suitable substrate for the nucleation of Al and Si eutectic grains. Also, this revealed that the presence of Mo did not obstruct the grain refiner addition and had no impact on the grain size enhancement brought about by TiB_2 in the alloy [3].

As shown in the Al-Mo phase diagram depicted in Figure 2-23, the maximum solubility of Mo in aluminium was 20 at.% at approximately 2150 °C [3][75]. The primary crystallisation phases are a result of peritectic transformations, including AlMo, $AlMo_3$, $Al_{17}Mo_4$, $Al_{22}Mo_5$, Al_3Mo, Al_4Mo, $Al_{63}Mo_{37}$, Al_5Mo and $Al_{12}Mo$. A further phase, Al_8Mo_3, forms at 1546 °C, corresponding to a Mo content of approximately 27.3 at.%. Thus, similar to V, adding Mo was also found to raise the crystallisation temperature of aluminium alloys [75].

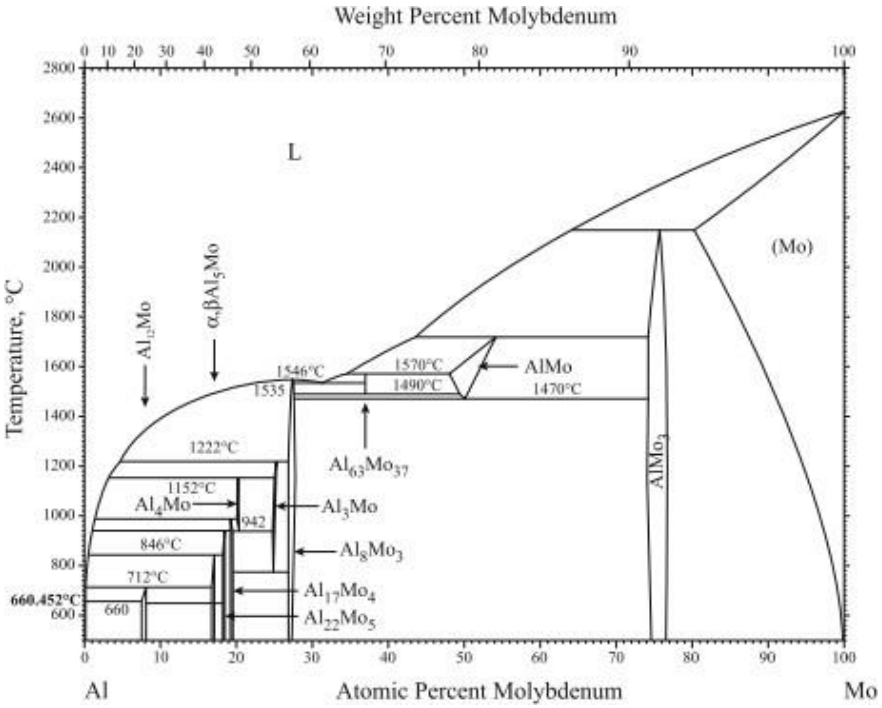


Figure 2-23: Al-Mo Phase diagram [76] [75]

2.2.2 Effect of addition of W into Al alloys

Tungsten is mostly used in high-temperature applications and is an uncommon addition to aluminium; however, it has been reported that adding W can enhance alloy corrosion behaviour [3]. There is evidence that W particles have been incorporated as a reinforcing phase in aluminium-based matrix composites, leading to significant improvements in the hardness and strength of these metal composites [77]. Chen [3] reported that the

addition of 0.4 wt.% W to 2L99 resulted in an increase of 8% in the mean UTS value (from 268 MPa to 289 MPa) and 19% in %Elongation (from 1.9% to 2.26%). The analysis indicated a statistically significant improvement in the Weibull moduli of the UTS compared to 2L99 alloy.

SEM examination revealed no substantial differences in the composition of the bifilms on 2L99+.4 wt.% W. However, spinel particles ranging from 500 nm to 3 μm in size were commonly observed on the fractured surface of 2L99 + 0.4 wt.% W as shown in Figure 2-24. It is feasible that the oxide layer in the 2L99 + W casting contained a high concentration of oxide particles with a non-uniform size [3].

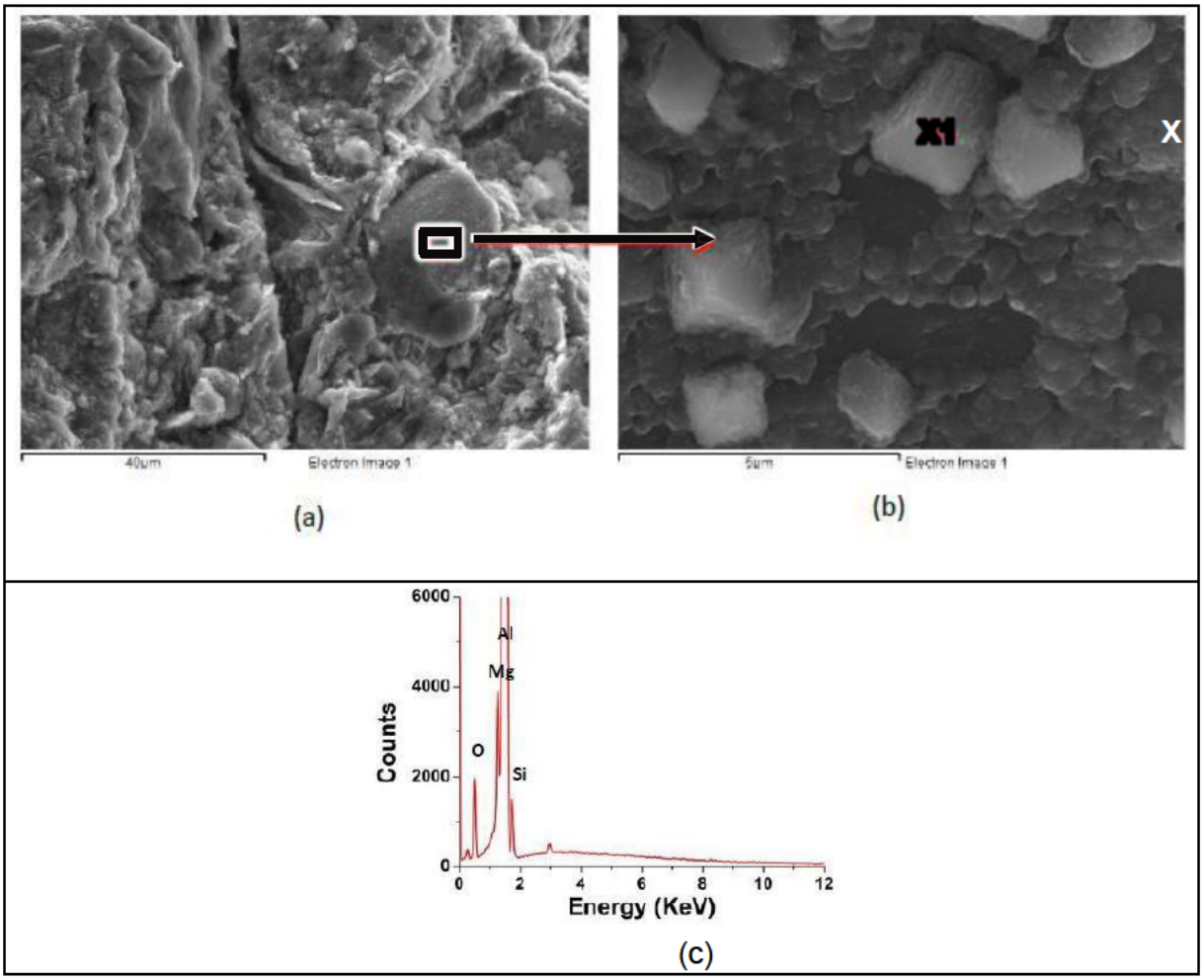


Figure 2-24: (a) and (b) low and high magnification of the SEM image of oxide particles on fractured surface of 2L99+0.4 wt.% W (c) EDX spectra of X1 marked in (a) [3]

A 200 nm thin oxide film with 350 nm W-containing particles precipitated into the formation of oxide or oxide film nucleation was observed by Chi. These oxide particles may have contributed to the cracking of the double oxide films. Intermetallic compounds containing W were also observed growing along the edges of the bifilm defects. As with intermetallic compounds containing Mo, a significant Si peak was observed, indicating the presence of WSi_2 [3]. The high density of WSi_2 (9.3 g/cm^3) may be the reason why it tended to nucleate on the oxide film; WSi_2 is the most abundant solid in the liquid solution, resulting in the sinking of the oxide films instead of floating to the surface. This could also explain why the oxide observed was small (approximately 1.5 µm in length) despite being associated with poor mechanical properties. Fewer defects in the double oxide film could result in improved mechanical properties of the casting, as suggested by Cao and Campbell [78].

The addition of 0.4 wt.% of tungsten to the 2L99 alloy resulted in a 91% increase in the Weibull moduli of the ultimate tensile strength (UTS) and a 13% increase in the %Elongation. Statistical analysis showed that the tungsten addition positively impacted the UTS Weibull moduli, but no significant benefit was found for the Weibull moduli of % Elongation. On average, the UTS and %Elongation of the 2L99 alloy with the tungsten addition showed a 10% and 19% increase, respectively [3].

An intermetallic phase containing W was identified on the edges of double oxide film defects. EDX analysis indicated a W:(Si, Al) ratio of 1:2, suggesting the presence of WSi_2 with Al in the structure. Due to its density of 9.2 g/cm^3, WSi_2 could pull an attached oxide film towards the bottom of a liquid metal, potentially reducing the negative impact of oxide film defects on casting characteristics [3]. The binary phase diagram of Al-W is shown in Figure 2-25.

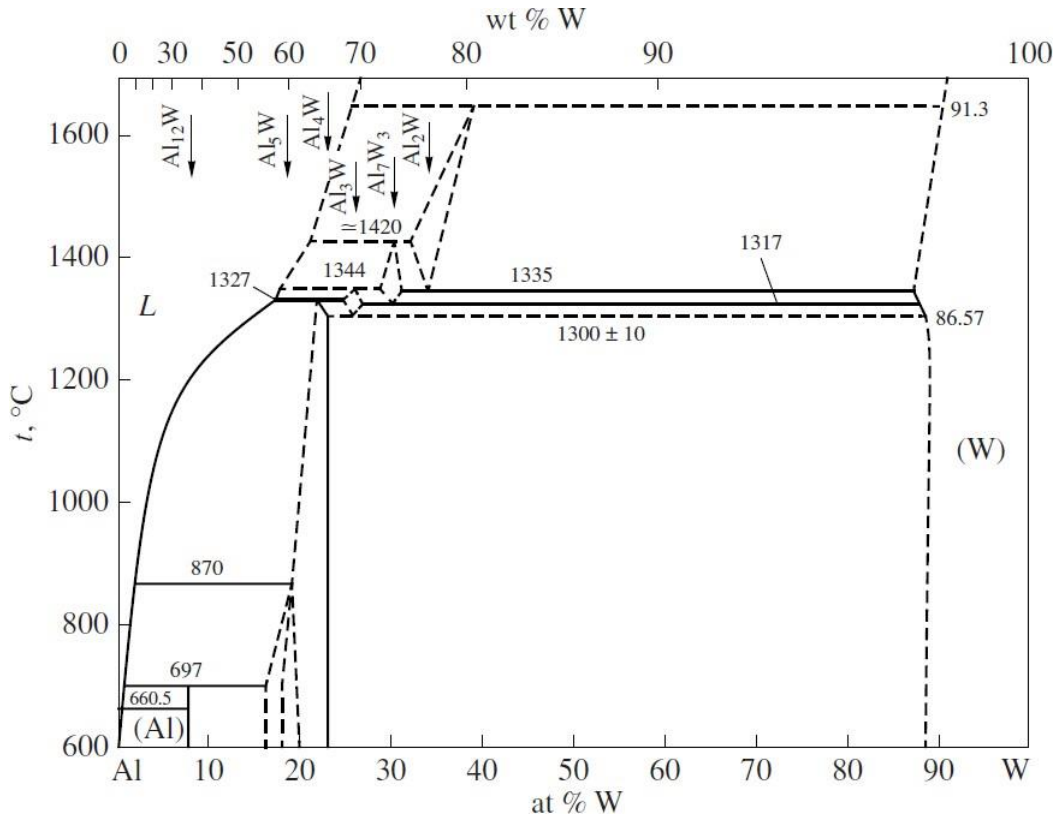


Figure 2-25: Al–W phase diagram [79]

2.2.3 Effect of addition of V into Al alloys

Vanadium is classified as a transition metal, yet it distinguishes itself from tungsten, with a melting point of 3422°C and molybdenum, with a melting point of 2623°C due to its lower melting point of 1910 °C. Furthermore, one of its stable oxide forms, vanadium oxide (V_2O_5), exhibits a notably lower melting point at 690 °C in contrast to MoO_3 (795 °C), MoO_2 (1100 °C), WO_3 (1473 °C), and WO_2 (1700 °C).

According to Elhadari et al. [80], V in aluminium exhibits low solid solubility and diffusivity and has the potential to form thermally stable phases during heat treatment. V is often added to wrought aluminium alloys as Al-V masteralloys. Still, the quality of such masteralloys available in the market may vary based on the type and shape of the

vanadium-containing phases. There are currently limited standards and evaluations of the quality of Al-V masteralloys [81]. Studies of the 6xxx series Al alloys containing copper showed the addition of 0.2 wt.% V improved the %Elongation of the tested alloys approximately by two folds [82]. After an ageing period of 4 hours, a change in the morphology of the Mg_2Si material phases was observed in the absence of added V, compared to alloys containing 0.2 wt.% V. Additionally, the Mg_2Si dispersoids in the alloys containing V were found to be larger and less dispersed within the Al matrix. The addition of V increased the number of small precipitates and altered their shape [83].

It is known that the addition of V can lead to grain refinement, decreased conductivity and increased recrystallisation temperature. A study of the 6063 alloy with 0.1 wt.% V addition was found to enhance precipitation kinetics of the Mg-Si phases (β' and β''), resulting in improved material yield and tensile strength with T6 heat treatment [83].

Further research into the precipitation hardening of Al-Mg-Si alloys indicated that a V addition of 0.15 wt.% reduced grain size and yield strength while concurrently increasing tensile strength by around 10% [83], which is in contrast with other studies [6]. Other research showed that the addition of 0.1 wt.% V to the commercial Al-6063 alloy with T5 and T6 heat treatment showed that the introduction of V adversely affected the yield strength and maximum tensile strength for the various ageing treatments [84] [85].

The solubility of V in aluminium (in its solid state) is 0.37 wt.% at around 660 °C, and up to approximately 9 wt.%, the $Al_{21}V_2$ phase is observed [83]. Investigations into 6xxx series Al alloys [83] containing copper showed that the addition of 0.2 wt.% V improved the %Elongation. After an ageing period of four hours, a difference in the morphology of the Mg_2Si material phases was noted in the absence of V, compared to alloys containing 0.2 wt.% V. The Al alloys containing V were found to have Mg_2Si dispersoids that were

not only larger but also less dispersed within the aluminium matrix [83].

As a result of the limited solubility of elements such as V, Cr, Mo, and W in Al, the presence of these elements in solid-state Silumin intermetallic phases significantly enhances the brittleness of the alloys [75].

The solubility of V in aluminium is limited, with a maximum of approximately 0.2 at.% or 0.6 wt.% [75]. At a temperature of 1670 °C, the maximum solubility of aluminium in vanadium is 54 wt.% [75]. Adding a small amount of vanadium increased the solidification temperature of Al-V alloys, as the Al-V phase diagram demonstrated in Figure 2-26 [75].

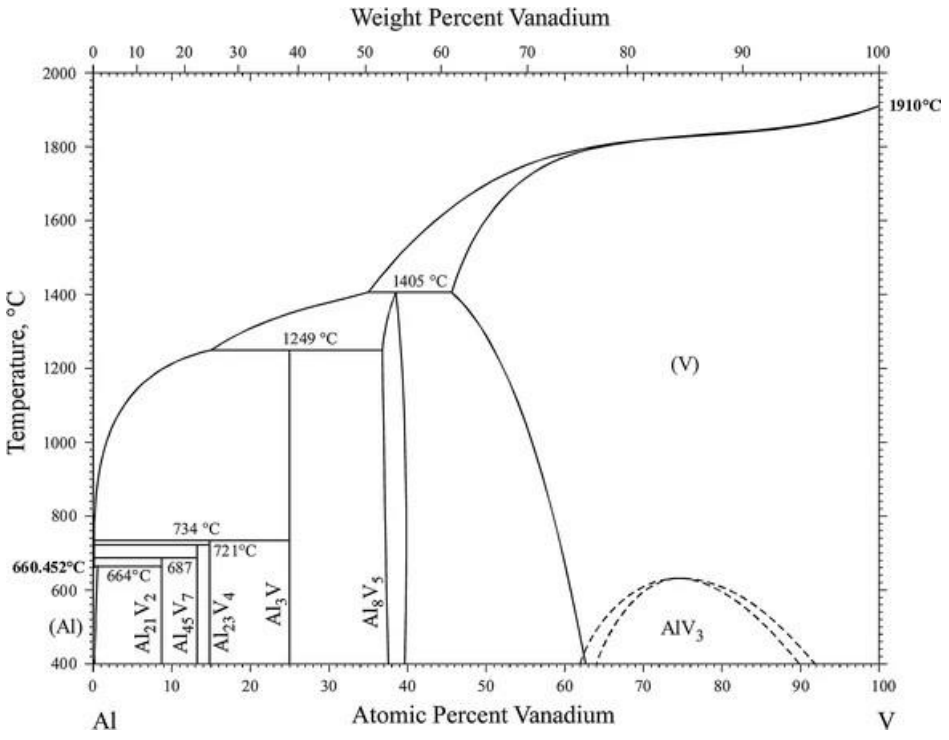


Figure 2-26: Aluminium-vanadium phase diagram [86] [75]

V is a transition metal with a low diffusion coefficient [87]. At its peritectic temperature, the maximum solid solubility of vanadium in aluminium is around 0.4 wt.%. The formation of V intermetallic compounds is unlikely at concentrations below 0.1 wt.%. The addition of vanadium up to 0.04 wt.% does not affect the phase composition of AA6063 [87].

2.3 Potential mechanisms of reduction of bifilms due to the addition of transition metals

2.3.1 Effect of intermetallics (mainly Fe and Mn) on the Al alloys

Cao and Cambell's studied the possible effect of bifilms on the precipitation of Fe-rich phases from liquid metals in Al-11.5Si-0.4Mg alloys [44]. Oxide films were entrained to be incorporated into the melts with an enfolding mechanism. The crumpled bifilms in melts consisted of two sides, wetted exterior surfaces and inner surfaces that were dry and unbonded. The exterior interfaces appeared to preferentially act as substrates for growth and nucleation of certain Fe-rich phases. Good atomic contact existed between the exterior wetted film sides and the aluminium matrix or Fe-rich phases. However, the gap between two dry sides in a double film created a crack, explaining the cracks commonly observed in these types of intermetallics and within the aluminium matrix [44]. Analytical computations aimed at evaluating planar misfit between the α-Fe phase and common oxides in Al alloys revealed that α-Al_2O_3, MgO, γ-Al_2O_3, and $MgAl_2O_4$ have the potential to serve as favourable substrates for initiating α-Fe phase nucleation [44].

The interplanar misfit, quantified as described in Campbell's reinterpretation of Bramfitt's data, with a focus on materials that are predominantly metallically bonded, demonstrates that a lattice mismatch of < 23% would aid nucleation to a certain degree, though

effectiveness was poor at disregistries levels of higher than 12%; if it was assumed that the bonding contribution to interface energy was favourable, then planar disregistries of below 12% would indicate a potent nucleating agent [44].

Bangyikhan [88] also studied Fe behaviour in Al-7Si-0.3Mg alloy and, using SEM, concluded that the β-Fe phase could nucleate on the bifilm defects [3].

Lu and Dahl incorporated alloying elements, such as manganese, chromium, cobalt, rhodium, and ruthenium. They observed that the addition of these elements modifies the needle-shaped morphology of the β-Al_5FeSi phase to a blunter shape, reducing the negative impact of the β-Fe-rich phase [89]. However, they observed that the addition of excessive alloying elements may lead to intermetallic compound formation and machining difficulties. Mn addition was found to positively impact Fe-rich phases, which could be separated and removed by sedimentation or filtration [89].

According to the study by Cao and Campbell [44], iron intermetallics such as $Al_{15}(FeMnCr)_3Si_2$ and $Al_{15}(FeMn)_3Si$ have been observed on wetted surfaces of bifilms which were in contact with liquid aluminium.

It has been suggested by Park [90] that brittle intermetallics that develop on wetted oxide surfaces facilitate the unwinding of bifilms. Campbell proposed that growing intermetallics, specifically β-Fe plates, untangle bifilms. This was thought to be due to the intermetallics on the oxide surface being thin enough to bend. The intermetallics tend to be flat, with their growth generating sufficient force to straighten and deform the shape of oxides.

According to Callegari et al., in order to counter the detrimental influence of the needle-shaped β-AlFeSi phase in Al-Si alloys, the introduction of manganese appears to be the most straightforward remedy, particularly given its cost-effectiveness and widespread availability. Despite the commonly used Fe: Mn = 2:1 guideline, relatively elevated Mn concentrations, typically in the range of 0.1 to 0.2 wt.%, have proven to be successful. Additionally, other elements like Ni, Mo, W, V and Cr can also serve in this modifying capacity and influence the microstructure and characteristics of these alloys [91].

According to Callegari et al., the ongoing challenge revolves around determining the optimal quantities to be added to the alloy to ensure the complete neutralisation of the adverse phase while preventing the formation of excessive and overly coarse intermetallic phases, which can be equally detrimental to the alloy's performance. This is crucial, particularly in Al alloy recycling, as recycled Al alloys typically contain even higher levels of iron [91].

They concluded that numerous elements, particularly those falling within the category of transition elements and rare earth elements, can be employed to enhance both strength and thermal stability. Incorporating these elements prevents the formation of large, ineffective precipitates and aggregates that do not contribute significantly to the final material's properties [91].

2.3.2 Settling Mechanism in Fe and Mn

Gravity segregation, where a second phase with a different density from the melt is found in the melt, is a widely recognised phenomenon. The second phase can be in-situ immiscible substances, inclusions, or primary phases in liquid metal [92].

In Mg-Al alloys, Al_8Mn_5 compounds are the primary solidification phases, which are crucial in enhancing corrosion resistance. Nevertheless, an excessive occurrence of these compounds above the α-Mg liquidus temperature can result in the formation of sludge. When Al_8Mn_5 compounds gather on oxide films, this can give rise to detrimental casting [93].

However, Al8Mn5 compounds were commonly attached directly to the oxides in samples with entrained oxide and sludge formation and sedimentation of Al_8Mn_5 particles were observed directly [93]. The sedimentation data obtained reasonably agrees with Stokes' law when corrected for non-spherical particles, internal liquid channels, and thin sample geometry. Direct observation confirmed the ability of entrained oxides to act as filters for Al_8Mn_5 compounds, trapping them during sedimentation [93].

Additionally, it was found that Al_8Mn_5 compounds are seen to nucleate on bifilms, continuing to grow upon cooling and resulting in large intermetallic compound clusters [93].

Cao et al. concluded that the convection-free experimental design proved to be successful in settling primary α-Al(FeMn)Si compounds and oxide films in the bulk melt. However, some oxide films could still stick to the mould wall or the top surface of the melt in the narrow tube mould, hindering sedimentation near the walls [94].

Although not all intermetallics settle at the bottom of the melt, it is still considered a useful method to separate the primary α-Al(FeMn)Si particles and remove some oxide films. The weight, number, and size of the precipitated primary α-Al(FeMn)Si phase depend on the Fe and Mn content in the original alloys and the precipitation temperature [94].

According to Dhinakar et al. [89], the addition of certain elements, such as Sr, could delay the formation of intermetallics. In contrast, the presence of Mn and Cr could promote the formation of specific intermetallics with slow cooling rates or extended holding times. The addition of Mn enhanced the formation of α-Al_{15}(Fe, Mn)$_3Si_2$ at the expense of β-Al_5FeSi, and a Mn/Fe ratio greater than 0.5 resulted in more compact and larger particles [95]. However, Mn addition led to lower iron removal rates and higher residual amounts in the melt compared to the addition of Cr. Combining 1 wt.% of each chromium and manganese in the A356 alloy improved iron removal through sediment separation.

In conclusion, the rate of settling in experiments was affected by various factors, such as the temperature of the alloy, the holding time, the cooling rate, the addition of specific elements, and particle size. Inclusions can enter the melt through various means, such as sand or ceramic materials from the furnace, dust generated from chemical reactions and equipment, and during holding and melting processes. These inclusions can be effectively removed through degassing and the use of mould filters. Intermetallics may occasionally be observed on the oxide's wetted side [11].

Moreover, the quality of the final casting was directly influenced by a range of casting parameters, including the pouring temperature, holding duration, solidification rate, and various casting practices such as filtration, cleanliness, and turbulence. Additionally, heat treatment conditions played an important role in determining both the quality of the end product and the formation of its microstructure [91].

2.3.3 Consumption of internal gases

Nyahumwa et al. [12] investigated the impact of surface turbulence during casting on the fatigue life of the commercially available A356 (Al-7Si-Mg) aluminium alloy. Their research proposed that the gradual depletion of entrapped gases (air) in the bifilms was a result of the reaction between the internal gases and the surrounding liquid metal, as illustrated in Figure 2-27.

They proposed the hypothesis that, initially, oxygen reacted with the liquid metal to produce spinel, followed by the reaction between the liquid metal and the entrapped N_2, resulting in the formation of AlN. It was concluded that the consumption of N to form AlN could seal the bifilms, reducing their size and thus limiting their adverse impact on mechanical properties.

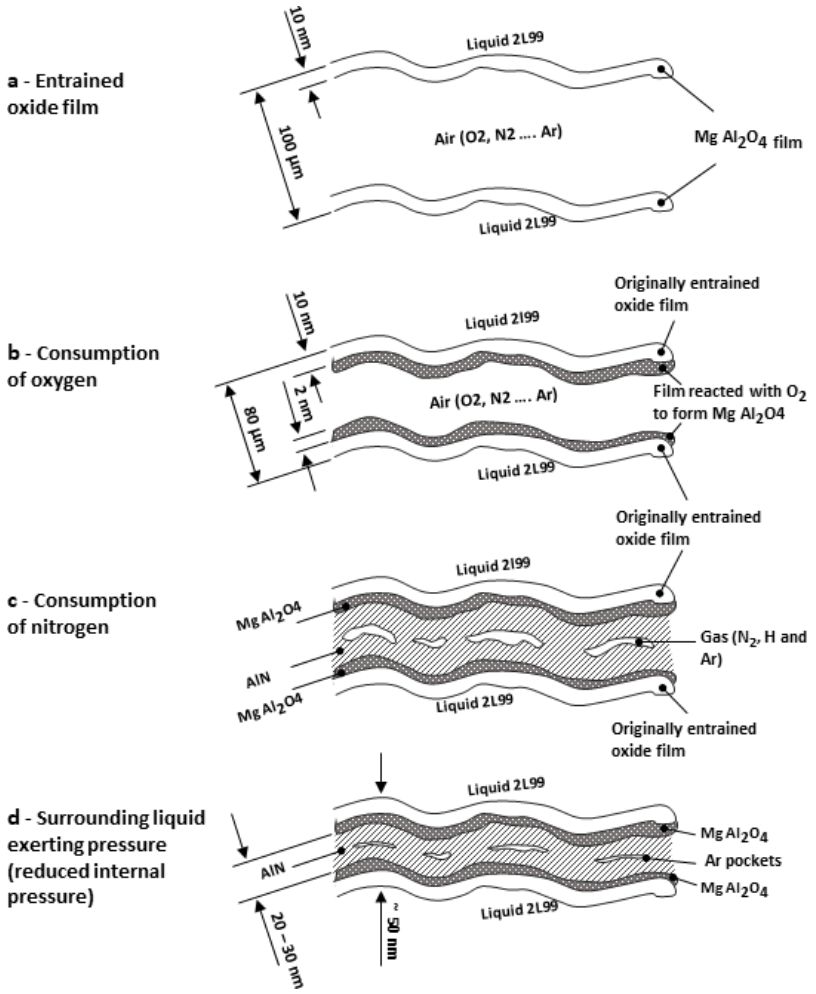


Figure 2-27: Consumption of the gases inside the bifilm in 2L99 alloy [12]

Raeiszadeh [10] conducted a study to investigate the consumption of air trapped within a bifilm on CP-Al. An air bubble was created in a CP-Al melt by inserting a silicon nitride tube with a hole at one end into the melt. Air consumption was observed live using X- ray radiography for 8 hours, as shown in Figure 2-28.

The sample containing the reaction product of the liquid metal and trapped air was analysed using SEM and EDX techniques. The experiment suggested that O reacted with the liquid Al for the first four hours, forming Al_2O_3. Subsequently, the N in the air bubble reacted with the Al, resulting in the formation of AlN [10].

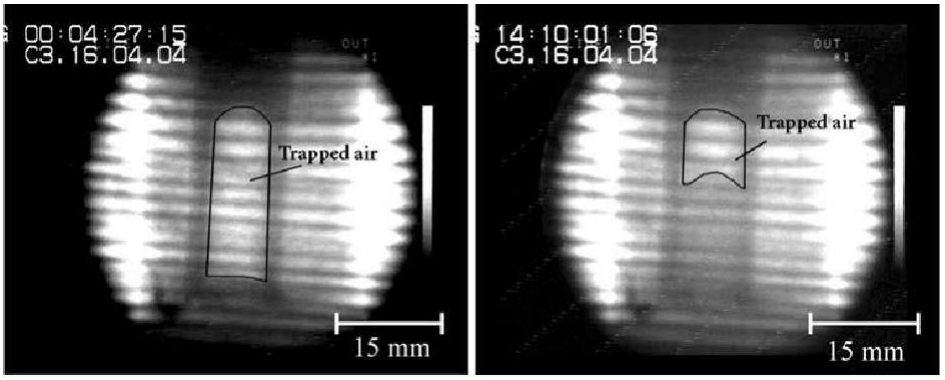


Figure 2-28: Real-time X-ray radiography utilised to observe the consumption of the trapped air bubble via reaction with the melt [10]

El-Sayed [59] performed a similar experiment to examine the rate of change in gas composition in a trapped bubble. Steel strips featuring blind holes on both sides were subjected to immersion in three different aluminium alloys, including pure commercial aluminium, 2L99, and Al-5wt.%Mg. The melt was allowed to react with the trapped air prior to solidification, followed by analysis of the composition of the air bubbles using a mass spectrometer. The results of the experiment concurred with the conclusions reached by Raeiszadeh [10]. Furthermore, El Sayed et al. [60] suggested that the type of oxide formed, determined by the composition of the alloy, affected the consumption rate of oxygen and nitrogen and the rate of hydrogen diffusion into the bifilm. The estimated time for the consumption of O and N in a bifilm defect in Al-5wt.%Mg alloy was reported to be around 6 minutes, for CP-Al approximately 9 minutes, and for 2L99 alloy approximately 25 minutes.

The consumption of the entrapped atmosphere began with oxygen, followed by nitrogen. Among the three alloys, Al-5wt.%Mg had the fastest rate of gas consumption for both oxygen and nitrogen, as depicted in Figure 2-29 [59].

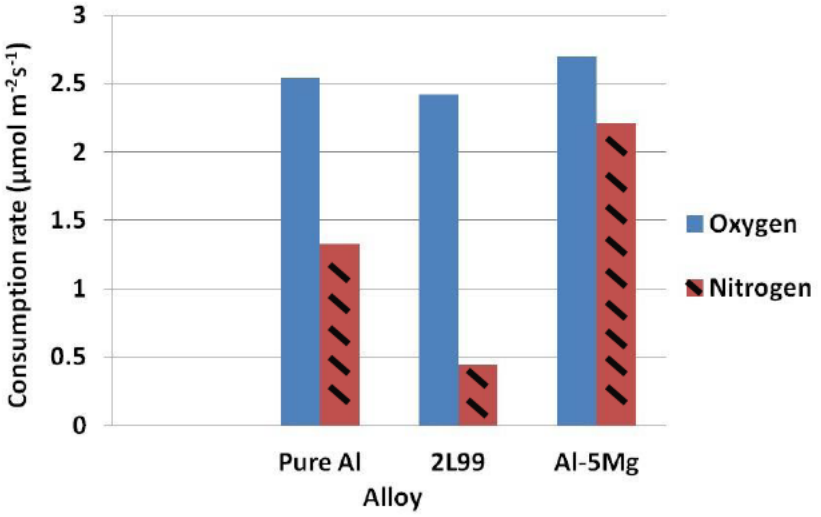


Figure 2-29: The rate of consumption of the entrained oxygen and nitrogen [59]

It was also indicated that hydrogen continued to diffuse into oxide films. In terms of hydrogen diffusion rate, Al-5wt.%Mg was the fastest, followed by pure aluminium and then 2L99, as shown in Figure 2-30 [59].

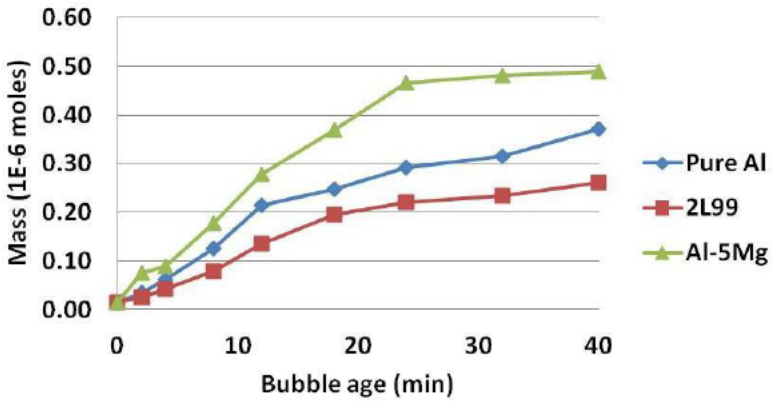


Figure 2-30: The rate of diffusion of hydrogen into bifilms [59]

El-Sayed [59] suggested the same as Nyahumwa et al. 's hypothesis in that initially, oxygen reacts with the liquid metals such as pure Al, Al-5wt.%Mg and 2L99 to produce the relevant oxides such as Al_2O_3, MgO and $MgAl_2O_4$, respectively [12][59], followed by the reaction between the liquid metal and the entrapped N_2, resulting in the formation of AlN.

Initially, the consumption of oxygen led to the production of $MgAl_2O_4$, MgO or Al_2O_3 in 2L99, Al-5Mg and pure Al. The oxygen consumption rates were concluded as 2.4 x 10^{-6}, 2.7 x 10^{-6} $mol.m^{-2}s^{-1}$ and 2.5 x 10^{-6} $mol.m^{-2}s^{-1}$ for 2L99, Al-5Mg and pure Al, respectively.

Though the nitrogen consumption rate was calculated as 4.4 x 10^{-7}, 2.2 x $10^{-6,}$ and 1.3 x 10^{-6} $mol.m^{-2}s^{-1}$ [60].

Hydrogen diffusion increased with an increase in holding time in the melt. At constant relative humidity of approximately 65%, it was estimated that diffusion rates were 2.3 x 10^{-7}, 4.6 x $10^{-7,}$ and 3.4 x 10^{-7} $mol.m^{-2}s^{-1}$, for 2L99, Al-5wt.%Mg and pure Al, alloy melts, respectively [60].

Examination via SEM indicated that the porosity interiors connected with film defects of double oxides may develop interconnections that are whisker-shaped. These were identified in castings of Al-5Mg and pure Al alloys, which were held inside the melt before solidification for 20 minutes [60].

Holding aluminium alloy melts for 10 minutes at 800 °C prior to solidification improved the %Elongation and the UTS Weibull moduli of castings by 29% and 18%, respectively. It was proposed that this occurred as a result of atmosphere consumption of the bifilms, reducing bifilm size and altering their mechanical properties [60].

Increasing the holding time to 20 minutes led to increased hydrogen diffusion in the bifilms, potentially resulting in oxide-related porosity associated with the amount of hydrogen contained. This led to a reduction in UTS and %Elongation Weibull moduli of approximately 17% and 24% respectively [60].

Raiszadeh and Griffiths [96] aimed to enhance the quality of aluminium (Al) castings by

increasing the melt holding time in order to reduce the void volume within entrainment defects. This was planned to be achieved by allowing the entrained gas to react adequately with the surrounding Al-alloy melt. They reported that the double oxide films within the defects bonded because of a connection between the two oxide surfaces. However, the reproducibility of their Al-alloy castings was not significantly enhanced despite the longer holding time. This is likely due to the difficulty in reacting nitrogen within the entrained gas (78% of air) with liquid Al-alloys [96].

Li et al. [96] recently investigated the gas utilisation within bifilms in Mg alloy using a pore gas analyser. Their results disclosed that the gases confined within the defects included H_2 and N_2 obtained from the air. As these trapped gases interacted with the liquid Mg alloy, they merged oxide film defects in the melt. The transformation of entrapped gas into solid-phase compounds could potentially decrease the void volume of defects, thus alleviating their harmful impact on casting quality [96].

Li et al. [96] also observed that compared to Al alloys, Mg alloys reveal higher reactivity with typical components, especially nitrogen, in entrained atmospheres, termed "nitrogen burning" in the Mg casting industry. Therefore, the reduction of void volume in entrainment defects in Mg-alloy castings via entrained gas consumption might be more manageable. The bonding of the entrainment defect, specifically the oxide film, as mentioned by Raiszadeh and Griffiths, is feasible in Mg alloy castings. However, the casting process for Mg alloys demands a cover gas to prevent activation, introducing complexity to the defect evolution process. Moreover, the entrained gas in Mg-alloy castings may include the cover gas used during casting rather than just air, adding extended complexity to the defect growth process [96].SF_6 is a standard cover gas used in Mg-alloy casting processes. It is widely used globally, especially in countries leading

Mg-alloy production, such as China, Brazil, and India, although its use has been restricted in European Mg-alloy foundries. SF_6 forms a protective film on top of the melt, which has previously been studied and reported to be a simple-structured surface film composed of MgF_2/MgO [96]. However, in this study, an unlimited supply of cover gas was continuously directed onto the melt surface, which is different from the finite amount of entrained gas within the defects. Despite the confirmed negative effects of entrainment defects in Mg-alloy castings, research on their behaviour and evolution is still limited [96].

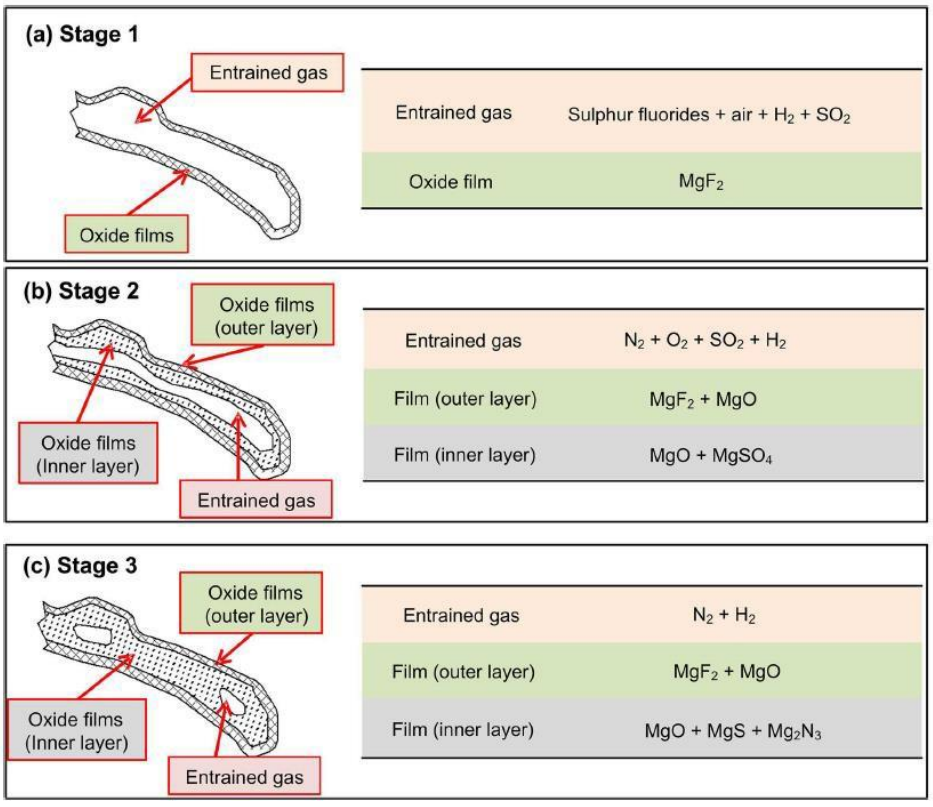


Figure 2-31: Schematic of the double oxide film defects corresponding to the three reaction stages under different atmospheres shown (a) stage 1, (b) stage 2, and (c) stage 3 [96]

The study of the development of entrainment defects during the casting process of Mg alloy was conducted through experiments and thermodynamic calculations, mainly in an

SF_6/air environment. Fluorides in the entrained gases were observed to be depleted, while sulphur was collected in the residual gases, as shown in Figure 2-31. The oxide film within the defects showed varying structures and compositions depending on the stage of the reaction. Depletion of entrained gases in the defects could lead to a “sandwich-like” structure, potentially reducing entrainment defects and enhancing the quality of Mg castings [96].

Entrained SF_6/air gases were consumed quicker than those in SF_6/CO_2, leading to a faster-growing oxide film with a higher potential to minimise entrainment defects' size and void volume[96].

The healing of a large double oxide film defect was explored by Aryafar et al. and Bakhtiarani and Raiszadeh [96]. Both studies involved stacking two Al alloy billets together in the liquid state and analysing the bonding after different isothermal holding times. The results showed that bonding improved with increased holding time and was only achieved when the oxygen and nitrogen between the two oxide layers were completely consumed [96].

The authors also suggested that cracks in the oxide layers, which may have arisen from the transformation of γ- Al_2O_3 to α-Al_2O_3, might contribute to bonding by allowing liquid Al to interact with the trapped oxygen and nitrogen. According to Campbell, based on the work of Raiszadeh and Griffiths, applying pressure to the casting metal prior to solidification could potentially speed up the healing process. However, limited research has been conducted in this area [96].

In conclusion, the entrained bifilm defects theory presents a fresh perspective on foundry practices and castings' mechanical properties. While the impact of such defects

on the mechanical properties of some alloy systems may be negligible, as noted by Knott et al., the concept has been widely accepted as trustworthy based on the available literature [96].

2.4 Summary

This chapter comprehensively reviews available literature on bifilms and their formation. It explored the evidence supporting their formation, the characterisation method utilising Weibull distributions, and strategies for minimising the occurrence of this defect.

To gain a deeper understanding of this subject, extensive research has been carried out on the oxidation process of liquid aluminium and the formation of AlN, providing a comprehensive description of AlN morphologies and their specifications.

The review of the literature also aimed at summarising previous research into mechanisms of reducing oxide film defects by adding transition metals, considering the effect of intermetallics on Al alloys, as well as analysing the settling mechanism in Fe and Mn, and investigating the consumption of the internal gases within the bifilms.

3 EXPERIMENTAL

3.1 Materials

The base materials used in this study were 2L99 (Al-7wt.%Si-0.3wt.%Mg) and CP-Al (commercial pure aluminium) alloys. Additionally, various experiments used Mo, W, or V for different purposes. To create a masteralloy, 2L99 was combined with 10 wt.% Mo, 10 wt.% W, or 10 wt.% V, resulting in 2L99 + 10 wt.% Mo, 2L99 + 10 wt.% W, and 2L99 + 10 wt.% V alloys. The masteralloys were made and diluted for various experiments to obtain the desired alloy compositions in the cast testbars.

3.1.1 XRF measurements

The masteralloys' composition and the resulting testbars were evaluated using a BRUKER S8 Tiger wavelength dispersive X-ray fluorescence (XRF) instrument. Before testing, samples were prepared by grinding their surfaces to 800 grit. During XRF testing, a Collimator mask with a spot size of 8 mm was used to determine the composition of an equivalent 50.24 mm^2 area on the sample surface. The XRF testing process for each sample took seven minutes. Table 4-1 and Table 4-2 present the elemental composition of the alloys used in the mechanical testing and phase characterisation. Table 4-115 presents the composition of the alloys used in the nitrogen growth experiments.

Wavelength-dispersive X-ray Fluorescence (WD-XRF) spectroscopy was conducted on sedimentation test samples (section 4.4) by the Department of Physics at the University of Warwick, using a Rigaku Primus IV system equipped with a 4 kW Rh tube. The sample preparation was the same as detailed for the BRUKER S8 Tiger wavelength

dispersive X-ray fluorescence instrument. Samples were analysed using a 10 mm spot size employing an ‘EZ Scan’ protocol, which performed an element sweep from B-Cm with an expected error of <5% according to the instrument’s manufacturer.

Each XRF test took approximately 20 minutes per sample. In contrast to the BRUKER S8 Tiger, the WD-XRF instrument performed an element sweep from Na-U. Table 4-108, Table 4-109 and Table 4-110 present the WD- elemental composition of the samples from the sedimentation test experiments.

3.2 Testbar Castings

3.2.1 Sand Mould Preparation

[2]Testbars were cast using the sand-casting method. The sand moulds schematically shown in Figure 3-1 used grade 60 silica sand and two types of resin, 5230 and 5112, each added at 0.6 wt.% to the sand. To minimise the potential of H porosity in the cast, the sand moulds were prepared two weeks prior to casting to allow for evaporation of hydrogen content in the resin. Corfix 22 foundry adhesive was used to glue the two halves of the sand mould together. The crucible used was a C80 clay-graphite type.

[2] The experimental procedure presented in this section has been published by the author in the paper provided in Appendix A.

Figure 3-1 depicts the mould used, which is intentionally designed to create a poor running system. The use of a poorly designed mould created a greater number of bifilm defects as the liquid metal would experience increased surface turbulence and exposure to atmospheric gases such as O during the cast. The runner system was employed to feed the testbar and to prevent the formation of shrinkage porosities.

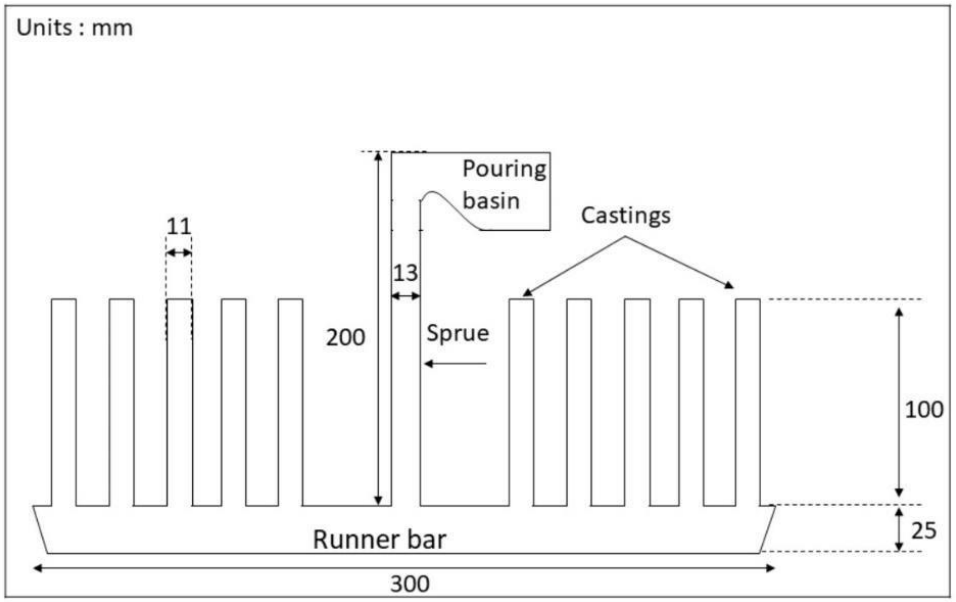


Figure 3-1: Sketch of the "badly designed" running system

3.2.2 Masteralloy Preparation

To incorporate Mo, W, or V into the 2L99 alloy, 2L99 + 10wt.% Mo, 2L99 + 10 wt.% W, and 2L99 + 10 wt.% V masteralloys were produced. To produce the masteralloys, 200 g of pure Mo, W, or V were added to 1800 g of 2L99 alloy, which was then held at 1300 °C in a 45-kW induction furnace for 40 minutes before being cast into an ingot mould.

The purity of the Mo, W and V used for the masteralloys was confirmed at 99.9%. Figure 3-2 (a) displays the bottom of the crucible after casting a masteralloy, and Figure 3-2 (b) shows the masteralloy ingot after casting.



(a)



(b)

Figure 3-2: shows (a) the bottom of a crucible after casting a masteralloy (b) the ingot mould

Figure 3-3 (a) and Figure 3-3 (b) present the cutting details of various parts of the masteralloy ingot for subsequent XRF analysis.



(a)



(b)

Figure 3-3: (a) and (b) sectioned masteralloy ingot areas for XRF test

3.2.3 Casting

To cast the 2L99 testbars, 2L99 alloy (2200 g) was placed in a C80 clay graphite crucible and melted at 730 °C in an induction furnace (175 kW). The furnace's power was initially set to 75 kW for heating the alloy in the crucible to attain a temperature of 730 °C. When

this temperature was reached, the power of the induction furnace was reduced to 10 kW, and the temperature of 730 °C was maintained for a further period of 40 minutes.

Argon lance degassing at 640 °C was used for 20 minutes to reduce the hydrogen content within the alloy melt. Although the solubility of hydrogen in liquid aluminium is low, at a temperature of 660 °C hydrogen still dissolves at around 0.69 ppm in Al, whilst in solid aluminium, hydrogen dissolves at 0.039 ppm [97], which necessitates the use of Ar degassing in order to avoid the formation of unwanted gas pores during the process of solidification [97]. Due to the limited availability of the Severn Science hydrogen gas analyser, Ar degassing with H content measurement to reduce the H content to less than 0.1 mm^3 per 100 g was carried out only on the testbars, the results of which are represented in Figure 4-24 to Figure 4-28, and all the samples cast for the N growth experiment.

The 2L99 + 0.4 wt.% Mo, 2L99 + 0.4 wt.% W and 2L99 + 0.4 wt.% V testbars were cast similarly to 2L99 and the masteralloys by the addition of the masteralloys of Mo, W and V to 2L99 at 730 °C.

3.2.4 The Roll-over Process

The roll-over device was used to reduce the possibility of shrinkage porosity formation in the casts. Figure 3-4 shows images of the roll-over device. Three moulds were fixed on the roll-over device before casting. After pouring the melt inside the moulds, chill bars made of the same composition as the alloy being cast were inserted into the downsprue of the moulds to prevent the liquid metal from pouring out during the roll- over, and the moulds were rotated immediately after pouring and insertion of the chill bars. Once the moulds were rotated by 180°, the melt was poured from the runner bar into

the testbar pockets within the mould and the process is designed to minimise the risk of shrinkage porosity.



Figure 3-4: (a) Roll-over device with three sand moulds

3.2.5 T6 Heat Treatment

After cooling, all castings were subjected to T6 heat treatment before machining. T6 heat treatment involved 12 hours of solution treatment at 540 °C, followed by quenching at 65 °C in water and ageing for 3.5 hours at 155 °C [110]. The heat treatment temperatures at all stages were controlled to remain within +/-3 °C.

3.2.6 Tensile Testing

Following the machining of the cast testbars, a Zwick^{TM} tensile strength testing machine equipped with a micro-extensometer attachment subjected the testbars to tension at a 1 mm/min rate of strain until they reached failure. Figure 3-5 illustrates the dimensions of the machined testbars.

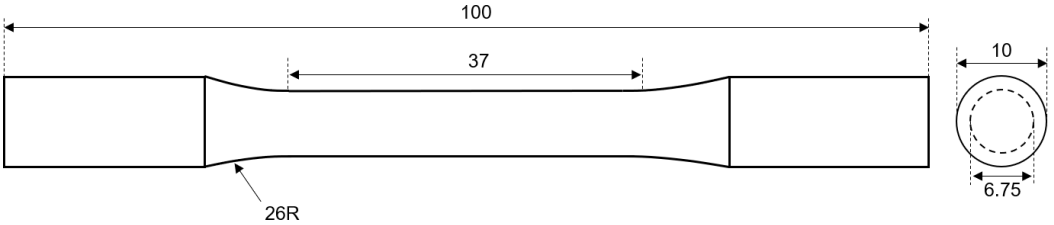


Figure 3-5: Sketch of the tensile testbar in mm

3.2.7 SEM Samples Surface Preparations

To examine the surfaces of the testbars following completion of the UTS tests, a sample measuring 5 mm in thickness was cut from below the fractured surface of the alloy, as shown in Figure 3-6. This sample, called “fractured surface”, was subsequently analysed using Scanning Electron Microscopy (SEM). The observed fractured surfaces were presumed to accurately represent the regions containing the most significant defects in the alloy.

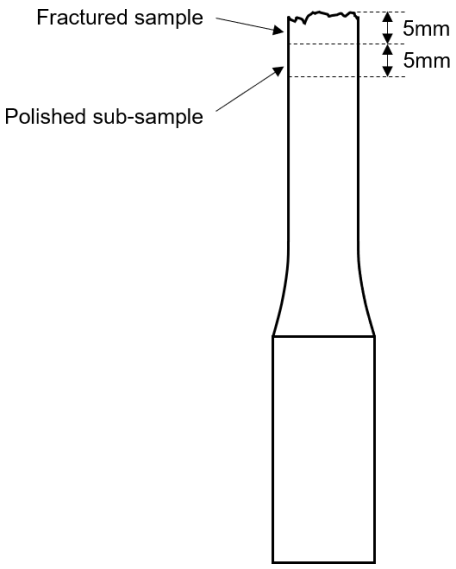


Figure 3-6: fractured testbar and the fractured and polished samples

Polished samples were obtained by cutting a 5 mm section beneath the first cut surface to facilitate the examination of the cross-section, as shown in Figure 3-6. This resulted in a cylindrical sample with a diameter of 6.75 mm and a height of 5 mm.

These samples were securely placed on a sample grip to which conductive Bakelite was added using an automatic hot mounting press, Opal 460. Subsequently, the surface of the samples underwent a grinding process using various grinding papers of different grit sizes, including 120#, 320#, 400#, 800#, 1200#, and 2500#. Following the grinding stage, the samples were polished using diamond paste with particle sizes of 6µm, 3µm, and 1 µm to create a highly reflective and mirror-like surface finish, which is referred to as a “polished surface”.

3.2.1 SEM Imaging

All surfaces were characterised using SEM equipped with EDX. An additional study of the morphology of AlN on fractured surfaces was carried out using a Focused Ion Beam (FIB) XL30 ESEM FEG instrument equipped with an INCA Oxford Electron Dispersive X-ray.

3.2.2 X-ray Diffraction (XRD)

A Proto XRD benchtop diffractometer with a CuK_{α} radiation source (λ = 0.15406 nm) at 40 kV and 40 mA was used to observe the crystal structure of the surfaces of the polished testbars. The sample preparation was similar to the SEM samples described in section 3.2.7. To facilitate the observation of the surfaces of the testbars, each sample was tested for 2θ values between 20˚ and 90˚ with a step size of 0.02 and a 1.5 second dwell time. The spectra were analysed using HighScore Plus version 3.0e (3.0.5) software.

3.3 Sedimentation

Sedimentation experiments were carried out in order to investigate the behaviour of different amounts of intermetallics of Mo, W or V on the settlement behaviour of different phases in the 2L99 alloys. The testbars were characterised using SEM to study their morphology and WD-XRF to determine their composition at the top and bottom sections, as shown in Figure 3-7.

The 2L99 + 10 wt.% of Mo, W or V masteralloys were used to cast various 2L99 + Mo, W or V. Due to the unavailability of the XRF equipment at the time of casting, samples were sent to the Department of Physics at Warwick University for XRF analysis. The masteralloys were cast at 1300 °C, whilst the 2L99 alloys were cast at 730 °C, with a pouring temperature of 800 °C to allow for the time required to transfer the melt from the Ema induction furnace to the resistance furnace and to prevent solidification of the melt during this transfer.

A mild steel cylindrical mould (inner diameter 68 mm and 250 mm in length) was painted with boron nitride to avoid wetting and left to dry at room temperature for 24 hours prior to use. The cylindrical steel mould was held for a period of less than 20 minutes (to avoid oxidation) at 800 °C to reduce the risk of the alloy melt solidification and to ensure a consistent temperature throughout the mould during pouring, as well as to minimise hydrogen absorption from the melt.

When the melt temperature reached 800 °C in the Ema furnace, the melt was poured into the cylindrical steel mould and placed into the resistance furnace. The resistance furnace was switched on 1 hour earlier to ensure a stable temperature of 800 °C. The melt was kept in the resistance furnace at 800 °C for a period of one hour. The cylindrical mould was removed after one hour and placed in a water-filled tray covering the lower 5

cm section of the mould to achieve a consistent cooling effect compared to the air-cooled top surface of the sample.

Once cooled, 1 mm of the bar's outer surface was machined using a diamond tool to obtain a smooth finished surface. This resulted in cylindrical samples, measuring approximately 190 mm in height and 66 mm in diameter, which were further sub-sampled from the top and bottom, as shown in Figure 3-7, resulting in two disc-shaped sub-samples at the top and the bottom of each sample.

The disc-shaped sub-samples were cut using the Startrite Sabre Vertical Bandsaw, and a minor wedge of the disc was obtained, measuring approximately 20 mm in radius and 15 mm in arc length, as shown in Figure 3-7. These samples were subsequently mounted, ground, and polished to enable observation of the different phases by the SEM.

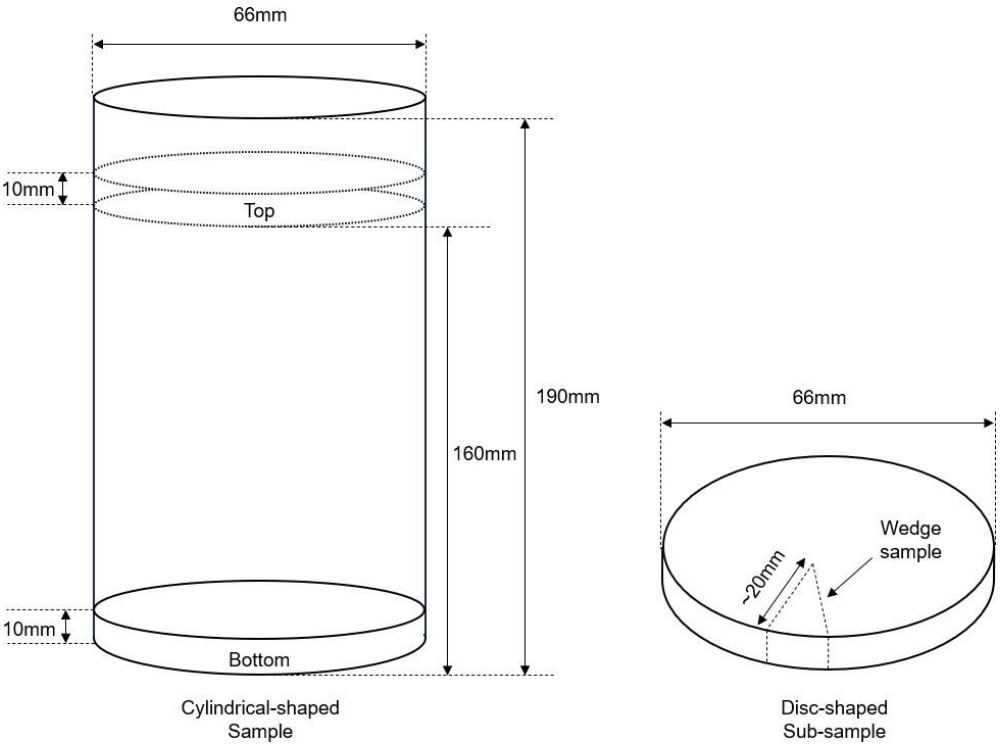


Figure 3-7: Sedimentation tests cylindrical sample and subsequent sub-sampling dimensions and details

3.4 Nitride Growth[3]

The alloys employed in this study consisted of CP-AL, 2L99, 2L99 + 0.6 wt.% Mo, and 2L99 + 0.2 wt.% W. These alloy compositions were selected to correspond with the alloys previously identified to contain AlN in earlier research. Table 4-115 shows the alloy compositions measured using X-ray fluorescence (XRF) (BRUKER S8 Tiger) during a 7-minute test duration.

The casting method for preparation of CP-Al, 2L99, 2L99 + 0.2 wt.% W and 2L99 + 0.6 wt.% Mo testbars for this experiment were the same as in section 3.2.3, including Ar degassing with hydrogen gas measurement.

Each casting per alloy resulted in ten testbars, which were T6 heat-treated and machined to form cylindrical samples measuring 15 mm in diameter and 25 mm in height. Each sample alloy was subsequently placed into a sintered cylindrical alumina crucible with an outer diameter of 20 mm, inner diameter of 16 mm and a height of 30 mm. The crucible was placed in a cylindrical stainless-steel tube, positioned vertically inside a sealed vertical tube furnace made by Carbolite (SN8/97/1843, type 15/50/175). As shown in Figure 3-8, the experimental equipment was set up such that the melting atmosphere of the furnace could be controlled. A photograph of the experimental equipment set-up is shown in Figure 3-9.

The lid of the vertical tube furnace was sealed using screws and an O-ring. A thermocouple of 0.5 mm diameter was placed through a valve into the furnace adjacent to the crucible. Nitrogen gas was added by an inlet valve using a high-pressure tube

[3] The nitride growth methodology presented in this section has been published by the author in the paper provided in Appendix A.

at ~13 cm^3/min flow rate, with a high-pressure hose joined to an outlet valve to discharge the nitrogen. The furnace temperature was set to 850 ˚C and held for approximately 15 minutes to ensure a stable temperature.

Samples were subsequently held at various holding times of 1.5, 3, 6, 12 and 24 hours. At the end of the experiment, the furnace was switched off, and both inlet and outlet valves were shut. Samples were left in the furnace to cool down. Following removing the samples from the crucible, the top surface of the samples was analysed using SEM and EDX.

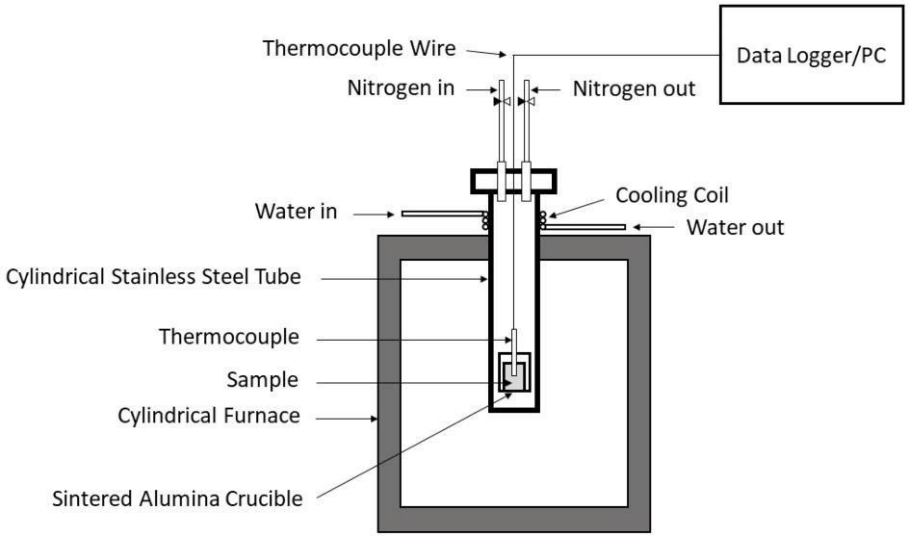


Figure 3-8: Nitride growth experiment equipment set-up



(a)



(b)

Figure 3-9: The growth nitrogen experiment set-up at the laboratory (a) placing the crucible inside the cylindrical stainless-steel tube (b) the vertical tube furnace complete set-up

4 RESULTS

This section presents the results of various tests and investigations carried out on the Al alloys as described in section 3, including mechanical, phase characterisation, sedimentation, and nitrogen growth.

4.1 Mechanical Properties

This section presents the results of the mechanical testing carried out on various alloys to measure the effects of the addition of transition alloys and the tensile properties of 2L99, namely the UTS, %Elongation and yield strength. Statistical analysis was also undertaken to measure the Weibull moduli of the results, as presented in this section. Table 4-1 and Table 4-2 show the elemental composition of the alloys (using XRF) used in the mechanical properties testing and phase characterisation as reported in Sections 4.1 and 4.2.

Table 4-1: Composition of the alloys used in mechanical testing and phase characterisation

Element Weight%	Mo	W	V	Mg	Si	Fe	Ti	Cu	Zn	Pb	Sn	Rh	Se	La	Al
2L99	0	0	0	0.3	9.8	0.03	0.14	0	0	0	0	0	0	0	Bal.
Pure Mo	Bal.	0	0	0	0	0.06	0	0.05	0	0	0	0.1	0	0.1	0
Pure W	0	Bal.	0	0	0	0	0	0	0	0	0	0	1.4	0.1	0
Pure V	0	0	Bal.	0	0.04	0.03	0	0	0	0	0	0	0	0	0
2L99 ingot raw from the foundry	0	0	0	0.33	10.9	0.04	0.12	0	0	0	0	0	0	0	Bal
2L99 + 0.4 wt.% Mo	0.37	0	0.04	0.25	10.4	0.04	0.10	0.01	0.01	0	0.01	0	0	0	Bal
2L99 + 0.4 wt.% W	0	0.36	0	0.28	8.10	0.04	0.05	0.01	0	0	0	0	0	0	Bal
2L99 + 0.4 wt.% V	0	0	0.37	0.27	9.14	0.04	0.12	0.01	0	0	0	0	0	0	Bal

Table 4-2: Composition of the masteralloys

Alloys	2L99 + 10wt. %V					2L99 + 10wt. %W				2L99 + 10wt. %MO				
Element Weight%	Al	Si	V	Ti	Mg	Si	W	Fe	Mg	Si	Mo	Ti	Fe	Mg
Top	Bal.	8.24	7.61	0.10	0.2	6.75	3.16	0.75	0.15	4.93	6.22	0.12	0.03	0.30
Middle	Bal.	7.58	8.09	0	0.22	7.20	9.02	0.79	0.19	6.18	9.22	0.12	0.06	0.23
Bottom	Bal.	8.43	13.4	0.13	0.23	6.92	15.4	0.92	0.27	7.57	12.2	0.10	0.07	0.21

4.1.1 Tensile testing of 2L99 alloy

For this experiment, three moulds of 2L99 alloy were cast in order to produce 30 testbars with a poor running system. It was not possible to measure the melt's hydrogen content at the time of casting as the Severn Science hydrogen gas analyser was faulty. A roll-over device was used to reduce shrinkage in the testbars, followed by a T6 heat treatment (detailed in section 3.2.5). A section of the runner bar was sent to measure H content to AMG Superalloys UK Ltd., showing a result of 6 ppm, as shown in Table 4-3. The UTS, %Elongation and yield stress for the 2L99 testbars are presented in Table 4-4.

Table 4-3: Leco sample hydrogen analyses

Material: 2L99 alloy	
Element	Result (ppm)
H	6

Table 4-4: UTS, %Elongation and yield strength measurements for 2L99 alloy

Sample Number	UTS MPa	Elongation %	Yield MPa	Sample Number	UTS MPa	Elongation %	Yield MPa
1	254.8	0.76	252.2	16	185.2	0.53	178.9
2	207.0	0.42	206.5	17	152.8	0.30	150.7
3	249.8	0.62	237.0	18	183.8	0.48	179.9
4	277.4	1.52	238.8	19	115.4	0.22	112.1
5	247.0	0.64	230.1	20	83.0	0.20	80.8
6	258.8	1.20	226.2	21	282.1	2.22	257.4
7	281.3	2.64	252.1	22	284.0	2.35	229.2
8	249.3	0.96	221.8	23	295.8	3.37	233.3
9	235.6	0.54	226.2	24	257.5	1.27	222.7
10	276.0	1.76	250.0	25	286.0	2.56	229.2
11	203.4	0.42	201.1	26	285.6	2.89	230.2
12	140.3	0.12	138.1	27	251.5	0.88	226.6
13	188.9	0.33	143.1	28	228.6	0.60	215.0
14	173.4	0.27	121.5	29	247.6	0.86	220.4
15	180.0	0.30	172.6	30	248.3	0.89	221.8
				Mean	227	1.07	203.5

The UTS, %Elongation and yield stress' mean, minimum, maximum, median and count for 2L99 are shown in Table 4-5.

Table 4-5: Relevant statical data for UTS, %Elongation and yield stress results of 2L99 alloy

	Mean	Minimum	Maximum	Median	Count
UTS (MPa)	227	82.9	295.7	247.6	30
%Elongation	1.07	0.12	3.37	0.64	30
Yield Stress (MPa)	203.5	80.8	257.4	222.3	30

The Weibull plots of the UTS, %Elongation and yield stress of 2L99 alloy are shown in Figure 4-1, Figure 4-2 and Figure 4-3, as well as the summary of Weibull modulus and position parameters, which are presented in Table 4-6.

The R^2 values of the Weibull plots of UTS, %Elongation and yield stress were 95%, 94% and 92%, which all were higher than the $R^2_{0.05}$ = 91.3%, suggesting that all data sets are acceptable based on two-parameter Weibull analysis as shown in Table 4-7.

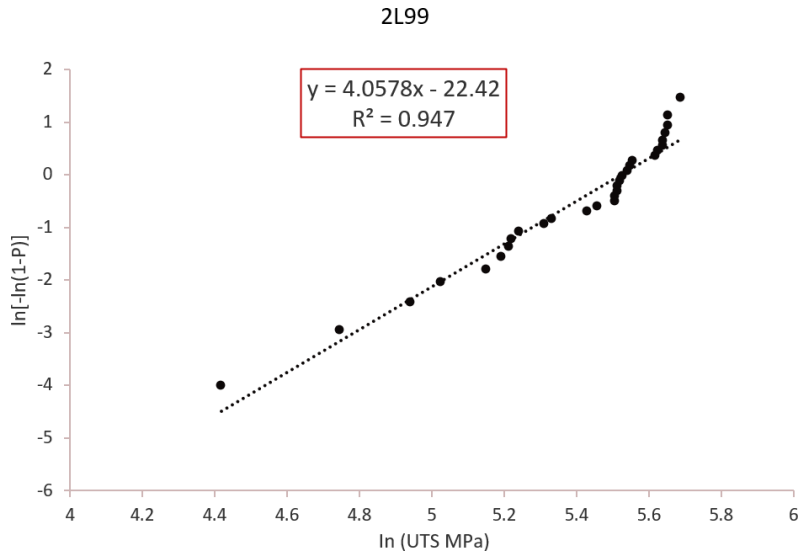


Figure 4-1: The Weibull plot of UTS of 2L99 alloy

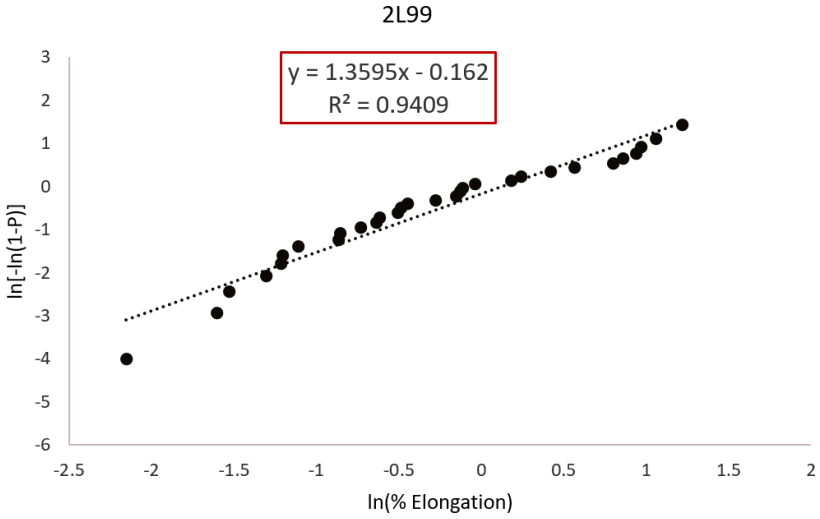


Figure 4-2: The Weibull plot of % Elongation of 2L99 alloy

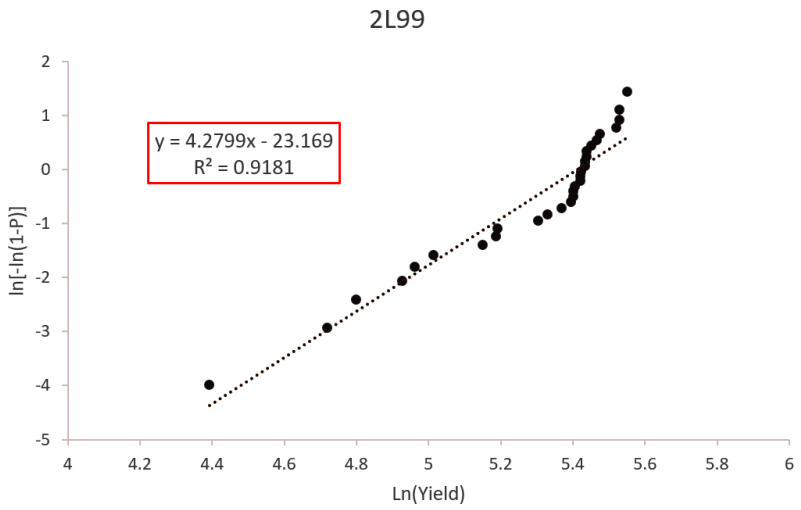


Figure 4-3: The Weibull plot of the yield stress of 2L99 alloy

Table 4-6: Summarised Weibull modulus and position parameter of 2L99 alloy

	Weibull modulus of UTS	Position parameter for UTS	Weibull modulus of %Elongation	Position parameter for %Elongation	Weibull modulus of Yield	Position parameter for Yield
2L99	4	251.5	1.35	0.89	4.28	226.6

Table 4-7: Statistical analysis of the distribution of UTS, %Elongation and Yield of 2L99 testbars verified the Weibull distribution.

	Sample number	R^2 (0.05)	R^2 for UTS	Does R^2 accept with Weibull distribution?	R^2 for %Elongation	Does R^2 accept with Weibull distribution?	R^2 for Yield	Does R^2 accept with Weibull distribution?
2L99	30	91.3%	95%	Yes	94%	Yes	92%	Yes

In this study, the minimum UTS for 2L99 alloy was measured at 82.9 MPa with a Weibull modulus of 4.06 and %Elongation at 0.12 with a Weibull modulus of 1.35. However, Chen [3] reported a minimum UTS of 204.2 MPa and UTS Weibull modulus of 16 and used the same casting method for 2L99 testbars, which were observed to be different from those in this project. The difference with respect to the experimental methodology was that Chen [3] used a Severn Science hydrogen gas analyser during casting. Chen [3] also reported a UTS mean value of 267.6 MPa and a %Elongation mean value of 1.9 for 2L99 alloy. In contrast, a lower UTS mean value of 227 MPa and a lower %Elongation mean value of 1.07 were obtained in this study.

4.1.2 Tensile testing of 2L99 + 0.4 wt.% Mo alloy

For this experiment, three moulds of 2L99 + 0.4 wt.% Mo alloys were cast to produce 30 testbars. As described in section 4.1.1, it was impossible to measure the melt's hydrogen content at the time of casting as the Severn Science hydrogen gas analyser was faulty. Similar to the 2L99 samples, the roll-over device was used to reduce the shrinkage in the testbars, and this was followed by a T6 heat treatment. A section of the runner bar was sent to AMG Superalloys UK Ltd. for hydrogen measurement and

the result of which is shown in Table 4-8. UTS, %Elongation and yield strength results of the 2L99 + 0.4 wt.% Mo testbars have been presented in Table 4-9.

Table 4-8: Leco sample hydrogen analyses

Material: 2L99 + 0.4 wt.% Mo alloy	
Element	Result (ppm)
H	8.0

Table 4-9 : UTS, %Elongation and yield strength results of 2L99 + 0.4 wt.% Mo alloy

Sample Number	UTS MPa	Elongation %	Yield MPa	Sample Number	UTS MPa	Elongation %	Yield MPa
1	228.2	1.49	214.8	16	249.2	0.85	231.5
2	287.0	2.27	232.2	17	247.4	1.05	227.2
3	262.6	2.01	227.3	18	242.0	1.22	234.7
4	283.7	0.89	234.6	19	274.9	0.92	238.2
5	259.4	0.80	224.7	20	245.5	0.61	234.3
6	215.7	0.41	212.5	21	246.6	1.07	222.6
7	252.6	0.92	230.0	22	191.5	1.09	171.9
8	208.2	1.13	205.3	23	239.0	0.78	220.4
9	292.8	0.94	243.3	24	279.6	0.77	234.5
10	227.8	1.44	216.7	25	208.4	0.43	202.7
11	288.9	2.11	235.8	26	240.7	0.80	222.0
12	258.3	0.35	226.9	27	214.9	1.05	204.7
13	241.2	2.03	224.5	28	216.4	3.04	209.1
14	240.2	1.96	221.4	29	242.6	1.47	221.9
15	204.5	1.73	201.0	30	242.3	0.53	236.5
				Mean	244.4	1.21	222.1

The UTS, %Elongation and yield stress' mean, minimum, maximum, median and count have been shown in Table 4-10.

Table 4-10: Relevant statical data for UTS, %Elongation and yield strength results of 2L99 + 0.4 wt.% Mo alloy

	Mean	Minimum	Maximum	Median	Count
UTS (MPa)	244.4	191.5	292.8	242.3	30
%Elongation	1.21	0.35	3.04	1.05	30
Yield Stress (MPa)	222.1	171.9	243.3	224.6	30

The Weibull plots of the UTS, %Elongation and yield stress are shown in Figure 4-4, Figure 4-5 and Figure 4-6. Also, the summary of the Weibull moduli and position parameter have been presented in Table 4-11.

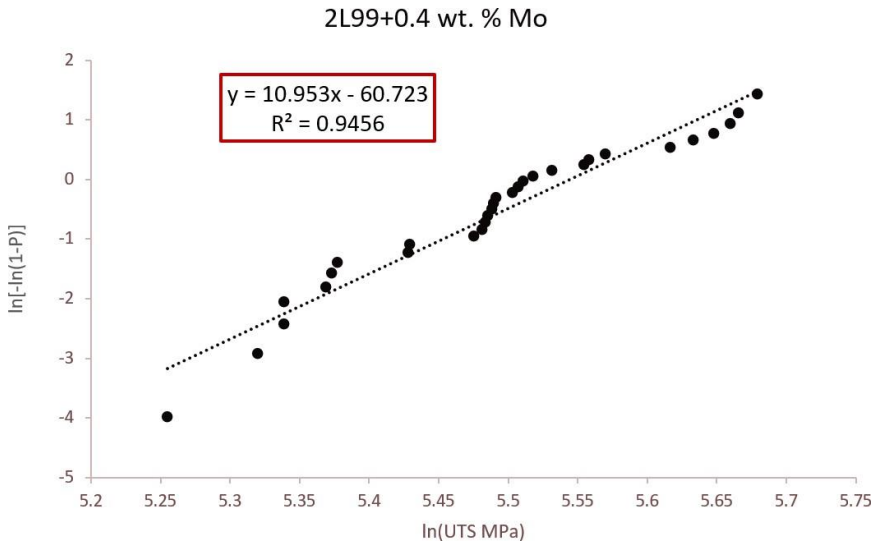


Figure 4-4: The Weibull plot of UTS of 2L99 + 0.4 wt.% Mo alloy

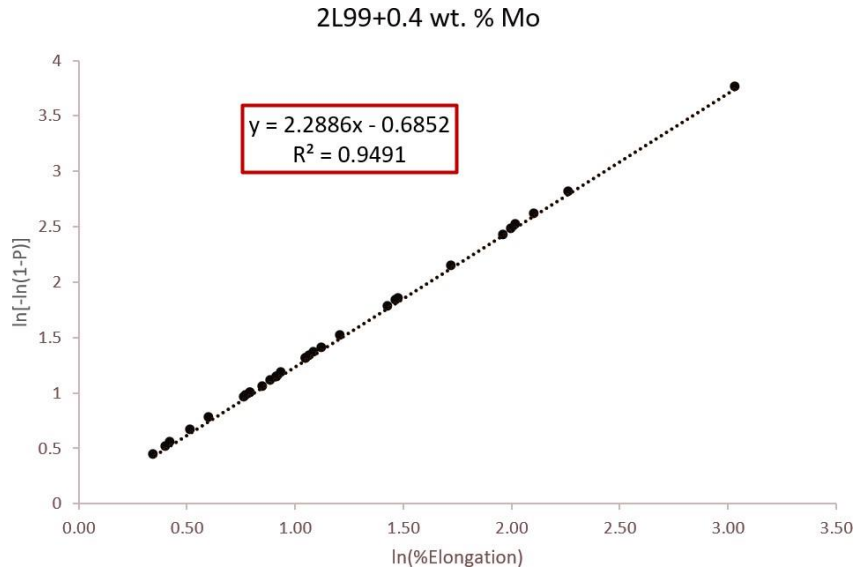


Figure 4-5 :The Weibull plot of % Elongation of 2L99 + 0.4 wt.% Mo alloy

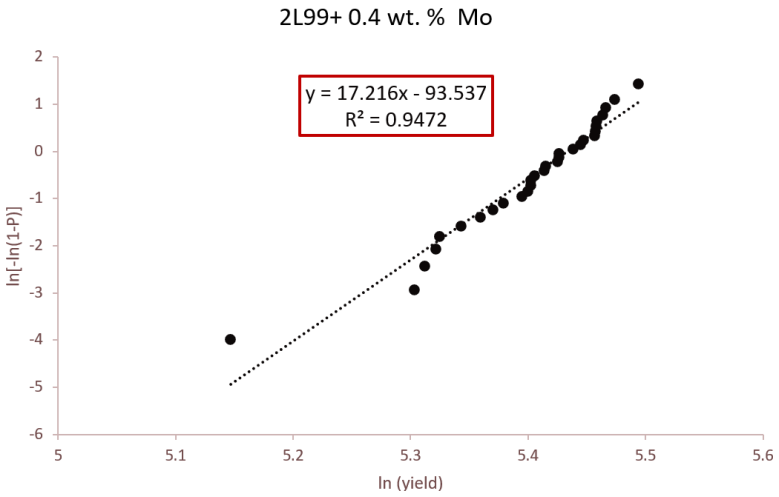


Figure 4-6: The Weibull yield plot of 2L99 + 0.4 wt.% Mo alloy

Table 4-11: Summarised Weibull modulus and position parameter 2L99 + 0.4 wt.% Mo alloy

	Weibull modulus of UTS	Position Parameter for UTS	Weibull modulus of %Elongation	Position Parameter for %Elongation	Weibull modulus of Yield	Position Parameter for Yield
2L99 + 0.4 wt.% Mo	10.95	244.4	2.28	1.13	17.21	227.3

The R^2 values of the Weibull plots of the UTS, %Elongation and yield strength were calculated to be 95%. All three R^2 values were higher than the $R^2_{0.05}$ = 91%, suggesting that the data sets were valid based on the two-parameter Weibull analysis, as shown in Table 4-12.

Table 4-12: Statistical analysis of the distribution of UTS, %Elongation and yield strength of 2L99 + 0.4 wt.% Mo testbars verified the Weibull distribution

	Sample number	R^2 (0.05)	R^2 for UTS	Does R^2 accept with Weibull distribution?	R^2 for %Elongation	Does R^2 accept with Weibull distribution?	R^2 for Yield	Does R^2 accept with Weibull distribution?
2L99 + 0.4wt.% Mo	30	91%	0.95	Yes	95%	Yes	95%	Yes

The minimum UTS of 2L99 + 0.4 wt.% Mo was measured at 191.5 MPa, with the UTS Weibull modulus calculated as 10.95.

4.1.3 Tensile testing of 2L99+0.4 wt.% W alloy

Three moulds of 2L99 + 0.4 wt.% W alloys were cast in order to produce 30 testbars. It was impossible to measure the melt's hydrogen content at the time of casting due to the unavailability of the Severn Science hydrogen gas analyser. The roll-over device was used to decrease shrinkage formation in the testbars, followed by a T6 heat treatment. A sample from the runner bar area of the mould was sent to AMG Superalloys UK Ltd. for hydrogen measurement, the result of which is presented in Table 4-13 (8 ppm). UTS results and %Elongation for the 2L99 + 0.4 wt.% W testbars are presented in Table 4-14.

Table 4-13: Leco sample hydrogen analyses

Material: 2L99 + 0.4 wt.% W alloy	
Element	Result (ppm)
H	8

Table 4-14: UTS, %Elongation and yield strength results of 2L99 + 0.4 wt.% W alloy

Sample Number	UTS MPa	Elongation %	Yield MPa	Sample Number	UTS MPa	Elongation %	Yield MPa
1	228.2	0.74	214.8	16	167.1	0.21	163.0
2	287.0	3.04	232.2	17	216.2	0.73	201.7
3	262.6	1.47	227.3	18	224.1	0.56	210.6
4	283.7	2.62	234.6	19	191.7	0.45	189.1
5	259.4	1.44	224.7	20	235.8	0.84	212.3
6	215.7	0.52	212.5	21	241.8	0.82	219.0
7	252.6	0.88	230.0	22	202.2	0.33	186.4
8	208.2	0.33	205.3	23	237.8	1.09	209.7
9	292.8	3.07	243.3	24	189.3	0.45	185.5
10	227.8	0.62	219.5	25	213.4	0.67	202.7
11	283.1	2.96	226.4	26	272.7	2.43	223.3
12	271.6	1.59	233.3	27	281.5	3.03	227.7
13	279.8	2.44	233.6	28	271.9	1.96	226.9
14	256.1	1.02	230.8	29	279.2	2.69	224.3
15	237.2	0.82	225.0	30	280.1	3.05	223.1
				Mean	245.0	1.43	216.6

The UTS, %Elongation and yield stress' mean, minimum, maximum, median and count have been shown in Table 4-15.

Table 4-15: Relevant statical data for UTS, %Elongation and yield strength results of 2L99 + 0.4 wt.% W alloy

	Mean	Minimum	Maximum	Median	Count
UTS (MPa)	245.0	167.1	292.8	247.2	30
%Elongation	1.43	0.21	3.07	0.95	30
Yield Stress (MPa)	245.0	167.1	292.8	247.2	30

The Weibull plots of the UTS, %Elongation and yield strength have been shown in Figure 4-7, Figure 4-8 and Figure 4-9. Also, the summary of the Weibull moduli and position parameter are presented in Table 4-16.

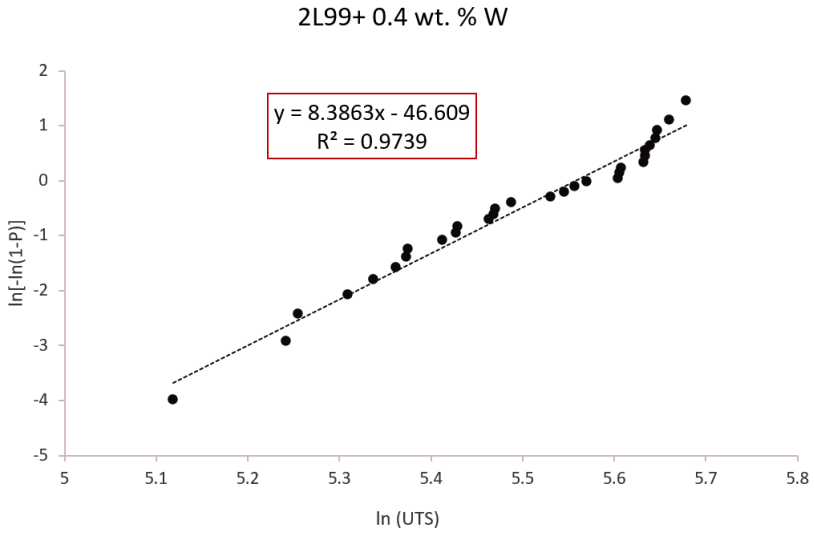


Figure 4-7: The Weibull plot of UTS of 2L99 + 0.4 wt.% W alloy

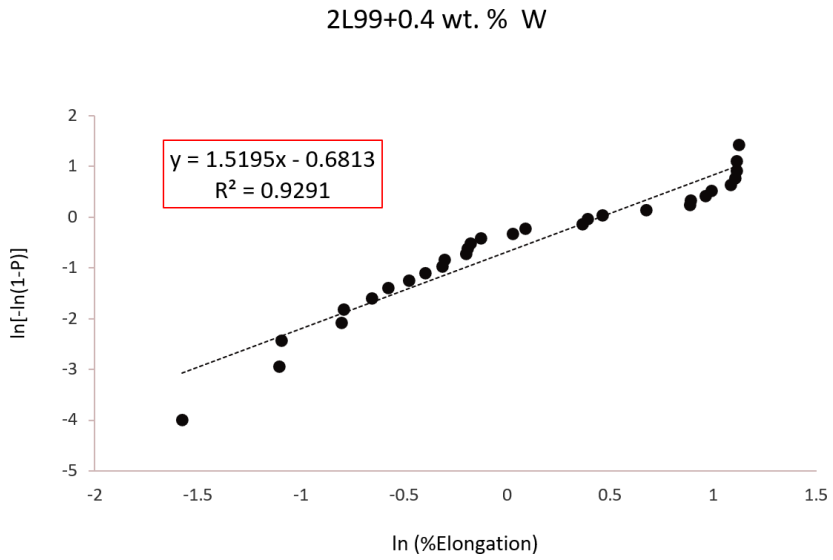


Figure 4-8: The Weibull plot of % Elongation of 2L99 + 0.4 wt.% W alloy

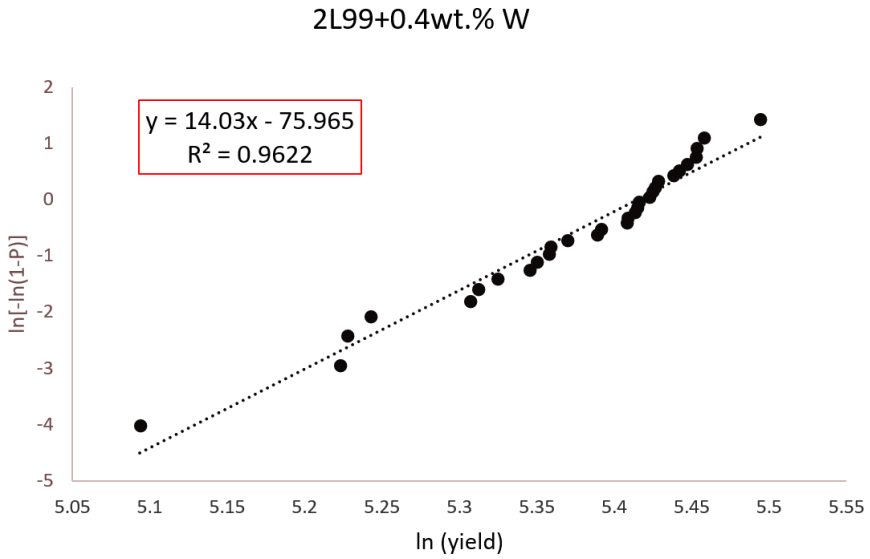


Figure 4-9: The Weibull plot of yield of 2L99 + 0.4 wt.% W alloy

The R^2 values of the UTS, %Elongation and yield strength were calculated as 97%, 93% and 96%, respectively. All three R^2 values were higher than the $R^2_{0.05}$ = 91%, suggesting that the data sets are valid based on the two-parameter Weibull analysis, as shown in Table 4-17.

Table 4-16: Summarised Weibull moduli and position parameter 2L99 + 0.4 wt.% W alloy

	Weibull modulus of UTS	Position Parameter for UTS	Weibull modulus of %Elongation	Position Parameter for %Elongation	Weibull modulus of Yield	Position Parameter for Yield
2L99 + 0.4 wt.% W	8.39	262.58	1.52	1.47	14.03	225.0

Table 4-17: Statistical analysis of the distribution of UTS, %Elongation and yield strength of 2L99 + 0.4 wt.% W testbars verified the Weibull distribution

	Sample number	R^2 (0.05)	R^2 for UTS	Does R^2 accept with Weibull distribution?	R^2 for %Elongation	Does R^2 accept with Weibull distribution?	R^2 for Yield	Does R^2 accept with Weibull distribution?
2L99 + 0.4 wt.% W	30	91%	0.97	Yes	93%	Yes	96%	Yes

In this study, the minimum UTS for 2L99 + 0.4 wt.% W was measured at 167.1 MPa, and the Weibull modulus of UTS was 8.39.

4.1.4 Tensile test of 2L99 + 0.4 wt.% V alloy

For this experiment, three moulds of 2L99 + 0.4 wt.% V alloys were cast in order to produce 30 testbars with T6 heat treatment. Similar to previous alloys studied (2L99, 2L99 + 0.4 wt.% Mo and 2L99 + 0.4 wt.% W), measuring the melt's hydrogen content was impossible. AMG Superalloys UK Ltd. tested a section of the runner bar for hydrogen measurement, the result of which is shown in Table 4-18 (8 ppm).

Table 4-18: Leco sample hydrogen analyses

Material: 2L99 + 0.4 wt.% V alloy	
Element	Result (ppm)
H	8

UTS, %Elongation and yield strength for the 2L99 + 0.4 wt.% V testbars are presented in Table 4-19. The UTS, % Elongation and yield strength's mean, minimum, maximum, median and count have been shown in Table 4-20.

Table 4-19: UTS, %Elongation and yield strength results of 2L99 + 0.4 wt.% V alloy

Sample Number	UTS MPa	Elongation %	Yield MPa	Sample Number	UTS MPa	Elongation %	Yield MPa
1	234.2	0.69	222.4	16	193.8	0.33	179.0
2	286.1	2.80	235.9	17	238.1	0.98	217.6
3	280.0	2.48	232.7	18	234.5	1.06	210.0
4	244.9	0.89	225.1	19	212.5	0.45	209.6
5	213.8	0.98	193.7	20	264.8	1.68	227.9
6	178.7	0.51	170.9	21	251.8	1.07	227.3
7	182.0	0.52	181.1	22	204.6	0.61	200.9
8	225.8	1.39	193.3	23	224.8	0.75	214.3
9	216.6	1.16	189.6	24	241.8	0.92	222.2
10	228.9	1.77	191.1	25	243.1	1.61	211.6
11	189.1	0.83	177.8	26	238.8	0.97	220.6
12	250.3	1.33	223.0	27	246.9	0.95	228.9
13	247.7	1.35	219.1	28	216.2	0.73	206.7
14	223.5	0.64	214.3	29	255.5	1.42	226.2
15	240.7	0.95	229.4	30	226.0	0.65	219.2
				Mean	231.2	1.08	210.7

Table 4-20: Relevant statical data for UTS, %Elongation and yield strength results of 2L99 + 0.4 wt.% V alloy

	Mean	Minimum	Maximum	Median	Count
UTS (MPa)	231.2	178.72	286.11	234.2	30
%Elongation	1.08	0.33	2.80	0.96	30
Yield Stress (MPa)	210.7	170.9	235.9	215.9	30

The Weibull plots of the UTS, %Elongation and yield strength are shown in Figure 4-10, Figure 4-11 and Figure 4-12, respectively. The summary of Weibull moduli and position parameters are presented in Table 4-21.

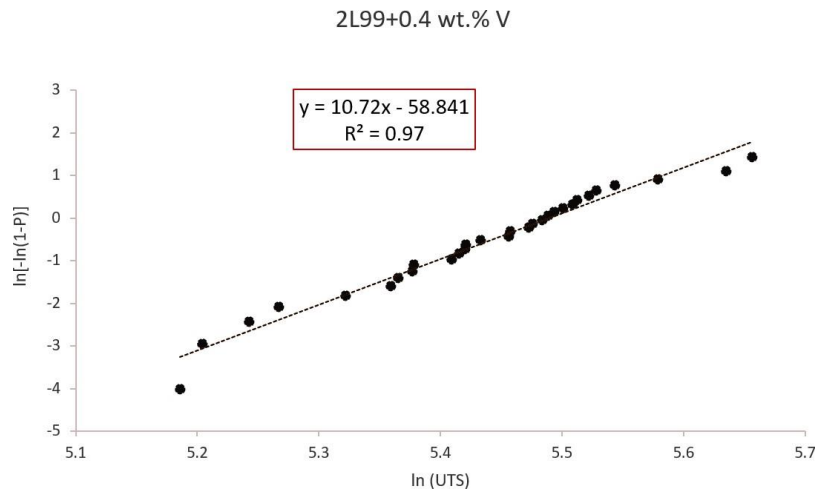


Figure 4-10: The Weibull plot of UTS of 2L99 + 0.4 wt.% V alloy

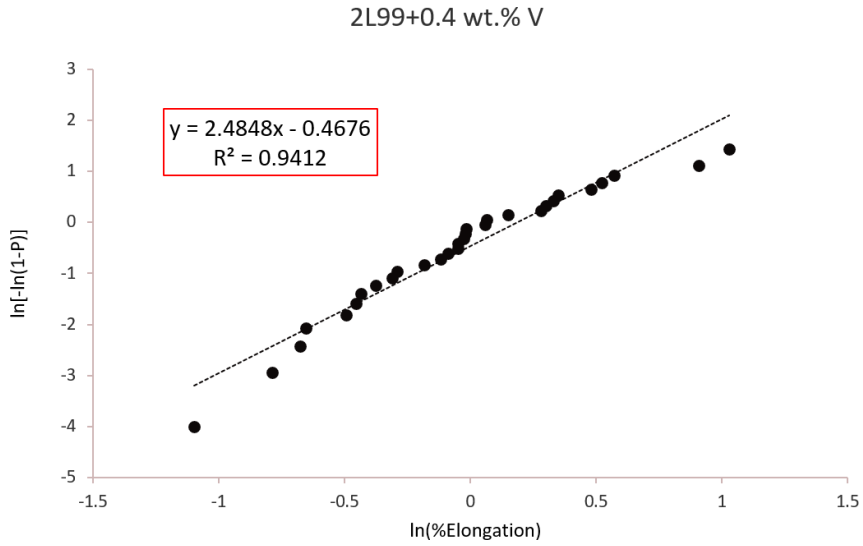


Figure 4-11: The Weibull plot of % Elongation of 2L99 + 0.4 wt.% V alloy

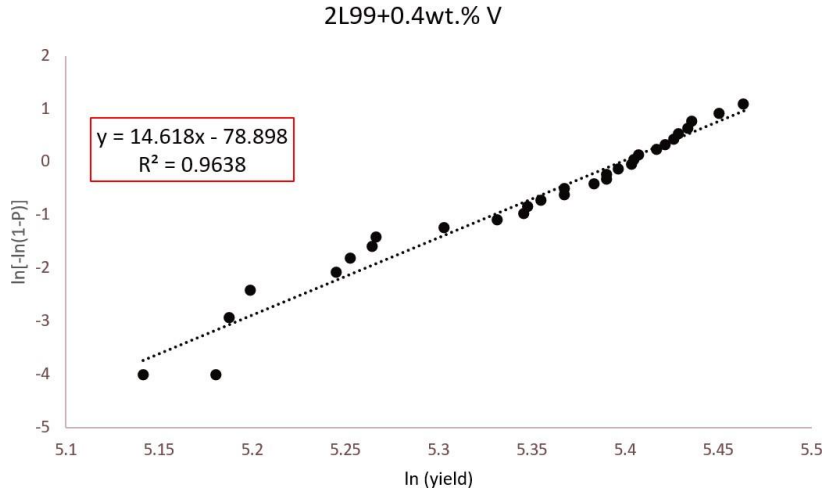


Figure 4-12: The Weibull plot of yield strength of 2L99 + 0.4 wt.% V alloy

Table 4-21: Summarised Weibull moduli and position parameter of 2L99 + 0.4 wt.% V alloy

	Weibull modulus of UTS	Position Parameter for UTS	Weibull modulus of %Elongation	Position Parameter for %Elongation	Weibull modulus of Yield	Position Parameter for Yield
2L99 + 0.4 wt.% V	10.72	240.7	2.48	1.06	14.62	220.6

The R^2 values of the Weibull plot UTS, %Elongation and yield were 97%, 94% and 94%, respectively. All three R^2 values were higher than the $R^2_{0.05}$ = 91%, suggesting that the data sets are valid based on the two-parameter Weibull analysis, as shown in Table 4-22.

Table 4-22: Statistical analysis of the distribution of UTS, %Elongation and yield strength of 2L99 + 0.4 wt.% V testbars verified the Weibull distribution

	No. of samples	R^2 (0.05)	R^2 for UTS	Does R^2 accept with Weibull distribution?	R^2 for %Elongation	Does R^2 accept with Weibull distribution?	R^2 for Yield	Does R^2 accept with Weibull distribution?
2L99 + 0.4 wt.% V	30	91%	97%	Yes	94%	Yes	96%	Yes

The minimum UTS for 2L99 + 0.4 wt.% V was measured at 178.7 MPa, and the Weibull modulus of the UTS was calculated to be 10.72.

4.1.5 Summary

Table 4-23 presents mean values of the UTS, %Elongation and yield strength for various alloys and the calculated increase in the results. Combined Weibull plots for the UTS, %Elongation and yield strength have also been presented in Figure 4-13, Figure 4-14 and Figure 4-15, respectively. The calculated Weibull moduli of the UTS, %Elongation and yield strength results are presented and compared in Table 4-24.

Table 4-23: Comparison of the UTS, %Elongation and yield mean values

Alloy	UTS Mean (MPa)	UTS % Increase	%Elongation Mean	%Elongation % Increase	Yield Mean (MPa)	Yield Strength % Increase
2L99	227	-	1.07	-	203.5	-
2L99+0.4 wt.% Mo	244.4	+7	1.21	+13	222.1	+8
2L99+0.4 wt.% W	245.0	+7	1.43	+33	216.6	+6
2L99+ 0.4 wt.% V	231.2	+2	1.08	Negligible	210.7	+3

Table 4-23 shows the effects of adding different alloying elements to 2L99 on the mean values of UTS, %Elongation and yield strength. It is important to note that the H content of the alloys was measured to be 6ppm for 2L99 and 8ppm for all other alloys. This is considered a significantly high H content, which is usually reduced during casting using Ar degassing to less than 0.2%. The results suggested that adding Mo and W to 2L99 achieves the highest amount of UTS improvement of 7.7%, while the addition of V had the lowest UTS mean value increase of 2%.

For %Elongation, the addition of W showed the highest increase in the mean %Elongation of 33%, followed by Mo of 13%, whilst the addition of V showed no improvement in the %Elongation mean value of 2L99 alloy. The positive effect of the addition of the alloying elements on the mean yield strength value was also significant. The addition of Mo resulted in an 8% increase, W in a 6% increase, whilst V resulted in an improvement of 3%.

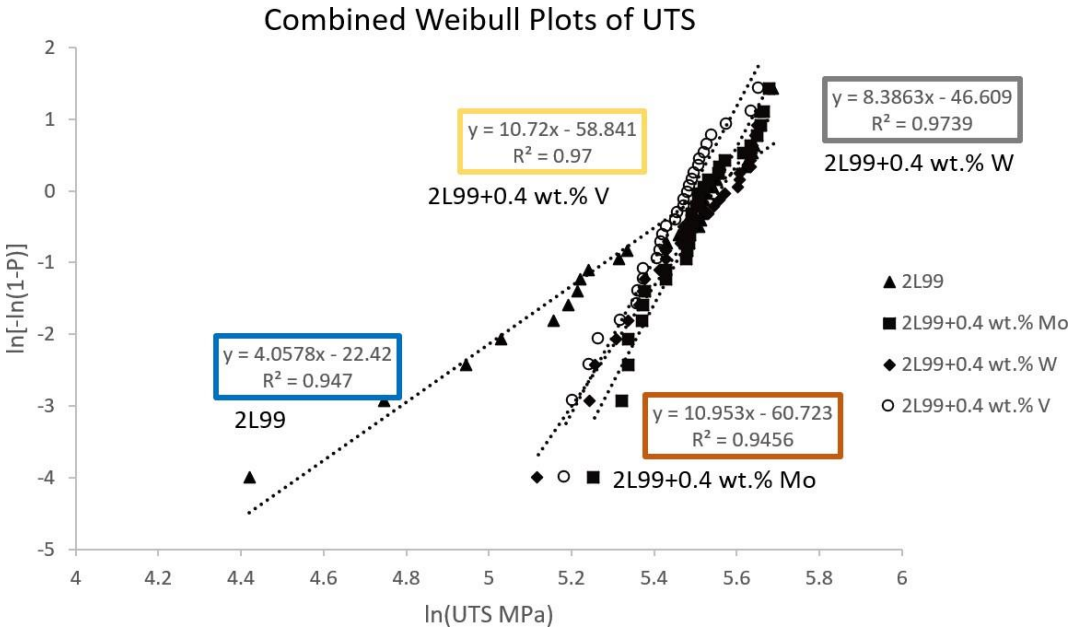


Figure 4-13: Combined UTS Weibull distribution plot

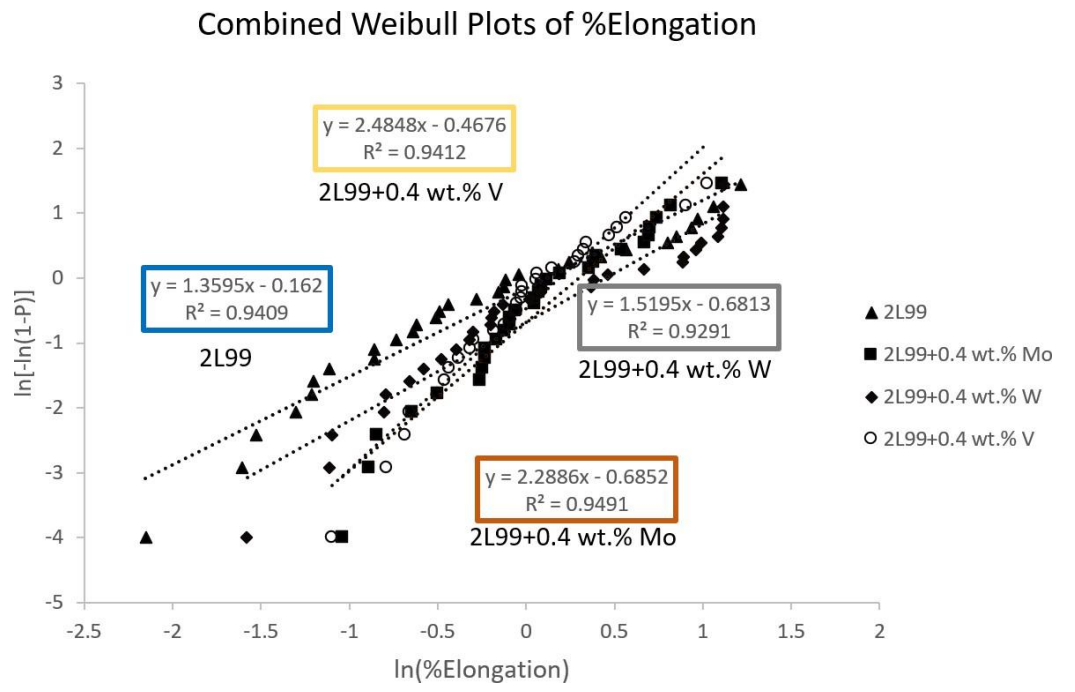


Figure 4-14: Combined %Elongation Weibull distribution plot

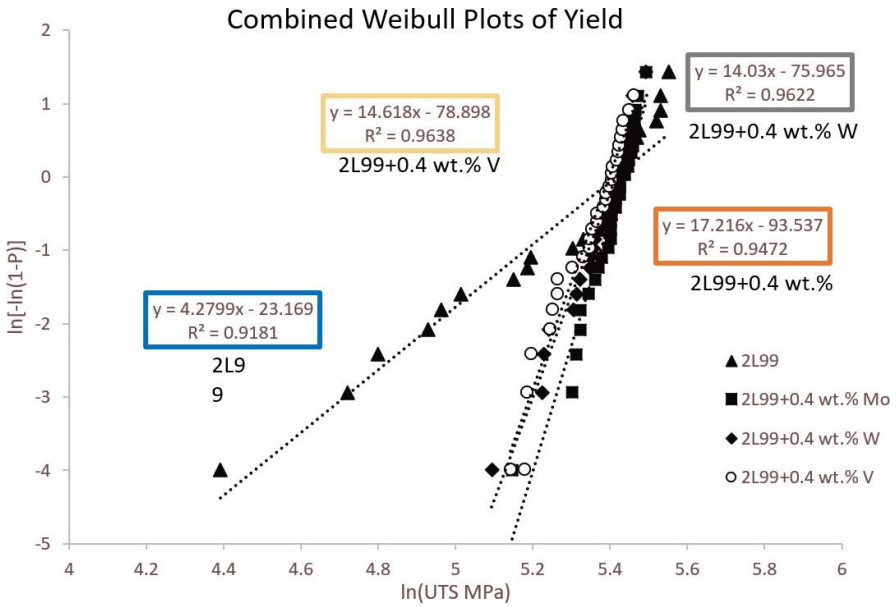


Figure 4-15: Combined yield strength Weibull distribution plot

Table 4-24: Comparison of the UTS, %Elongation and yield strength Weibull modulus increase in studied alloys

Alloy	Weibull modulus of UTS	UTS % Increase	Weibull modulus of %Elongation	%Elongation % Increase	Weibull modulus of Yield	Yield strength % Increase	H Content ppm
2L99	4	-	1.35	-	4.28	-	6
2L99 + 0.4 wt.% Mo	10.95	+173	2.28	+68	17.22	+302	8
2L99 + 0.4 wt.% W	8.39	+109	1.52	+12	14.03	+227	8
2L99 + 0.4 wt.% V	10.72	+168	2.48	+83	14.62	+241	8

As shown in Table 4-24, Figure 4-16 and Figure 4-17, the greatest increase in Weibull modulus of the UTS was 173% which occurred due to Mo addition to 2L99. It is important to note that this increase is very close to the increase resulting from adding V (168%) to 2L99. The Weibull modulus % increase by adding W was calculated to be 109%, which was lower than the Mo and V addition to 2L99.

The Weibull modulus increase for %Elongation was highest in the case of the addition of V to 2L99 at 83%. This was followed by the Weibull modulus increase obtained by adding Mo to 2L99 at 68% increase and W at 12% increase. The yield strength increase

by 302% upon adding Mo, followed by 241% upon adding V and 227% upon adding W.

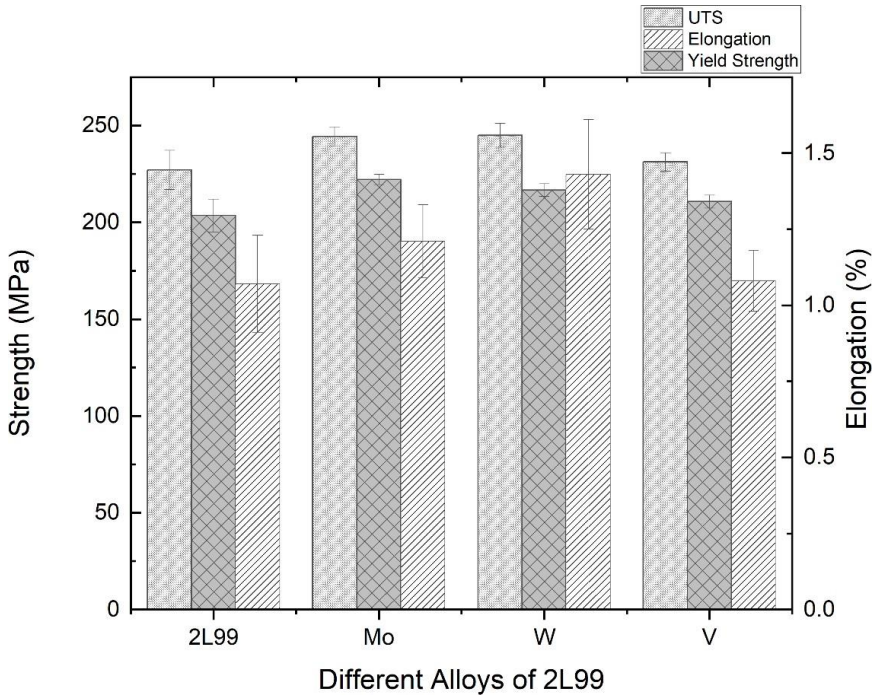


Figure 4-16: comparison of the mean values of the measured tensile properties of 2L99 and 2L99 + 0.4 wt.% transition alloys

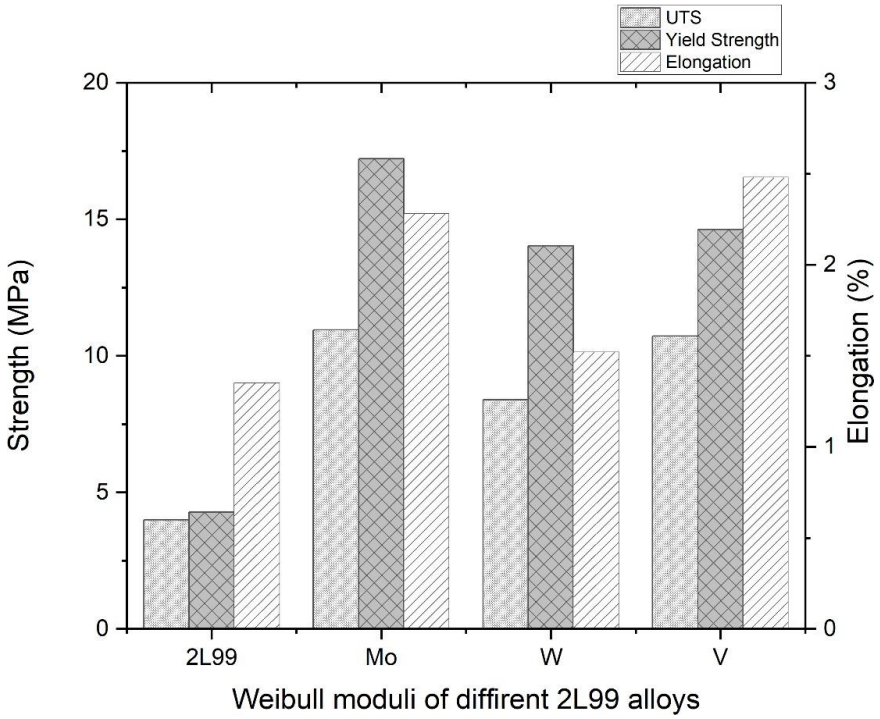


Figure 4-17: comparison of the Weibull moduli of 2L99 and 2L99 + 0.4 wt.% transition alloys

4.2 Identification of phases

SEM and EDX characterisation tests were conducted on 40% (12/30) of the polished and fractured surfaces of testbars of 2L99 and 2L99 plus transition metals at varying alloying percentages. Characterisation was carried out by SEM and EDX of routine phases of oxides, nitrides and intermetallics, as well as any unexpected phases that might have an impact on the results of the study. All the testbars were made using a poorly designed running system, rolled over, and subjected to T6 heat treatment. However, except for the samples used in growth experiments and the characterised testbars shown in Figure 4-24 to Figure 4-28, all were cast with Ar lance degassing but not measured hydrogen with Sevren Science.

It is important to note that the EDX spectra, in some cases, exhibited carbon peaks, which were suspected to result from atmospheric contamination within the SEM due to residual oil causing detector contamination [98]. Therefore, the carbon peaks were removed from the spectra whenever EDX was used to calculate elemental composition. Furthermore, the EDX showed double peak positions of Al where Al content was high. The second Al peak can be seen in the EDX spectrum; however, the Inca software did not label this second peak.

4.2.1 2L99 alloy

4.2.1.1 Characterisations of the phases on the polished surfaces of 2L99

SEM low magnification images for the matrix of the polished surface of a 2L99 alloy testbar (low UTS 83 MPa) are presented in Figure 4-18 (a) and Figure 4-18 (b).

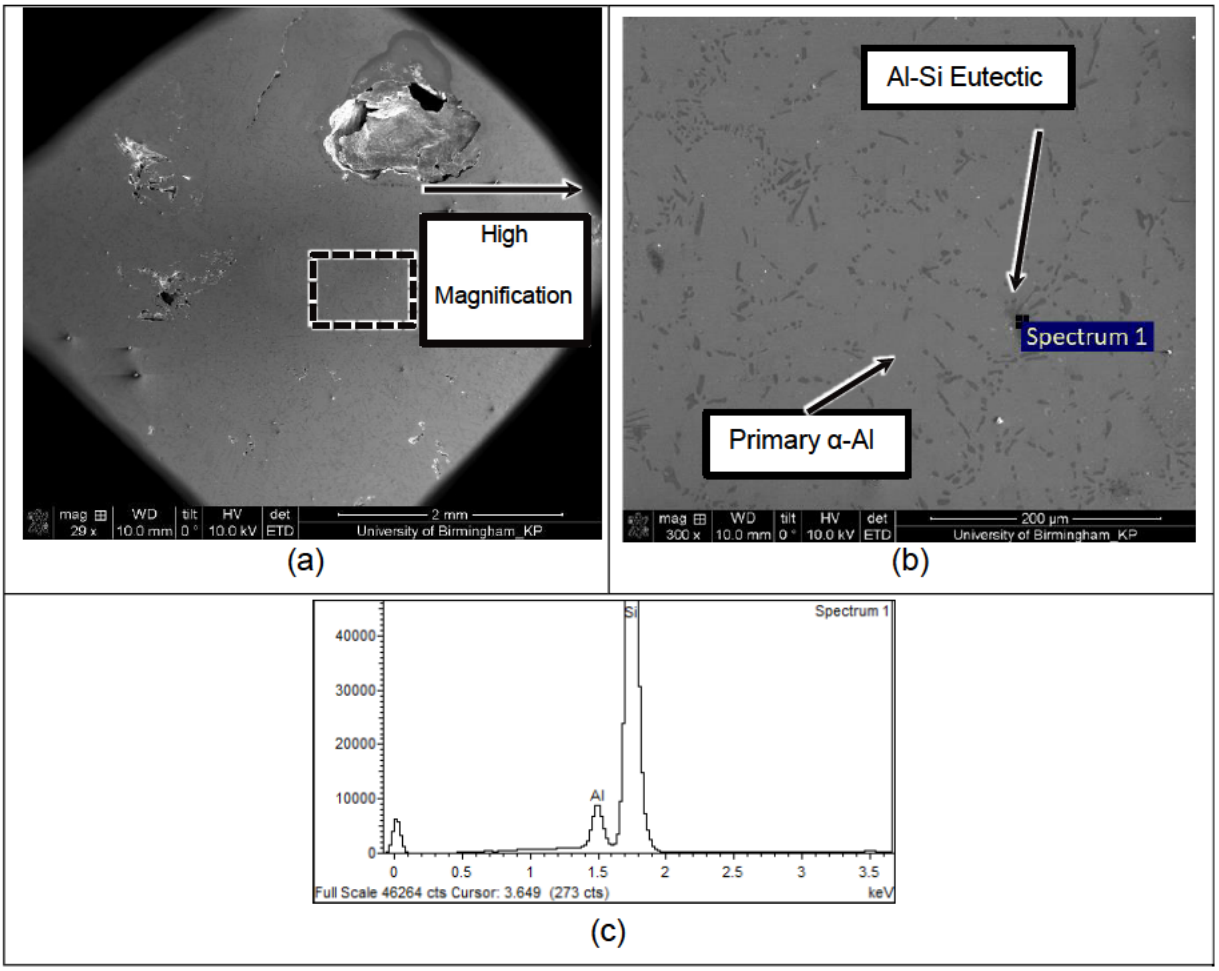


Figure 4-18: (a) Low magnification of the whole matrix SEM micrograph of a polished cross-section of the 2L99 alloy (low UTS 83 MPa) (b) High magnification SEM micrograph of the flat surface in the absence of cavities (c) EDX spectrum1 of the marked point

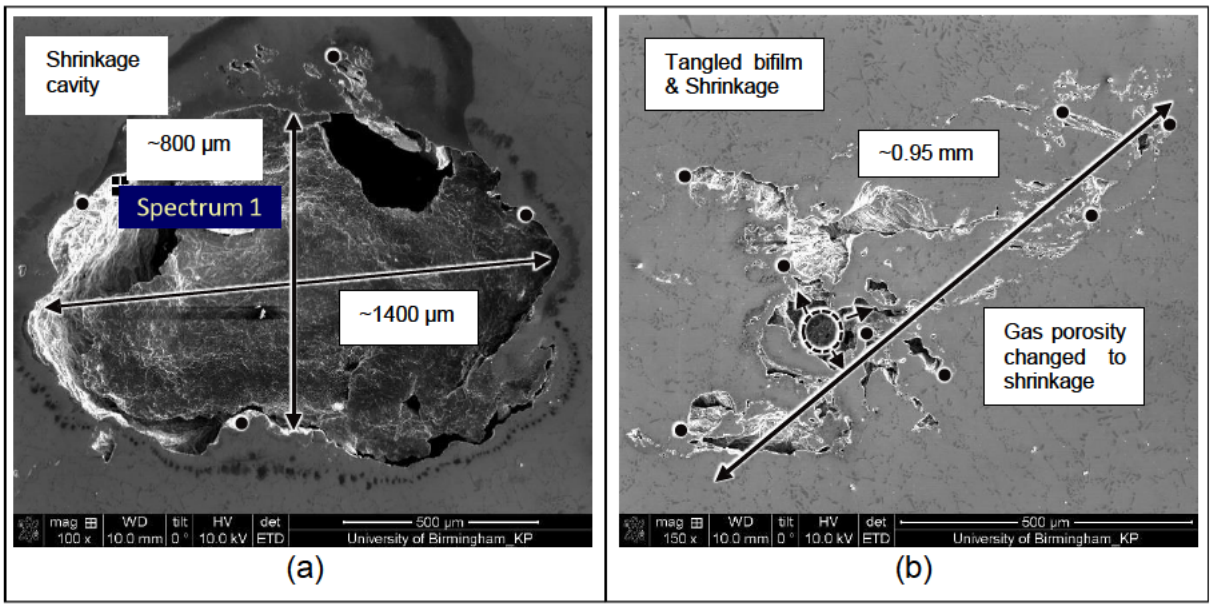
Table 4-25: EDX element composition of the spectrum1 in Figure 4-18 (b)

	Spectrum 1	
Element	Weight%	Atomic%
Al K	6.41	6.66
Si K	93.59	93.34

The main matrix of the 2L99 alloy sample consisted of primary α-Al dendrites plus eutectic Si surrounded by numerous defects, including shrinkage cavities, gas porosities and cracks, possibly resulting from bifilm formation and hydrogen gas diffusion.

The high magnification of the largest cavity seen in Figure 4-18 (a) is presented in Figure 4-19 (a) to Figure 4-19 (d). As reported above, the defects on the polished flat samples of the 2L99 surfaces varied in type, size, and orientation. The defects observed in this sample consisted of large cavities, tangled bifilms, gas porosities, or a mixture of the above.

The longest shrinkage cavity measured was 1.4 mm long and 0.8 mm wide, and the average length of the bifilm was 700 µm. Figure 4-19 (b) showed a tangled bifilm, a shrinkage pore and gas porosity, demonstrating the division of a gas pore into a shrinkage pore as a result of the solidification process [99]. These defects were located in different positions and orientations from the middle to the circumference of the fractured testbar. Figure 4-19 (e) shows an example of an EDX spectrum composition taken at the periphery of the defects in Figure 4-19 (a) to (d) (marked with black circles and Spectrum 1) detecting approximately similar amounts of O as well as other elements of the main matrix (Al, Si and Mg), indicating that these defects were oxide film defects (probably spinel). The EDX results of the points marked with the black circles and Spectrum 1 were the same, as presented in Table 4-26.



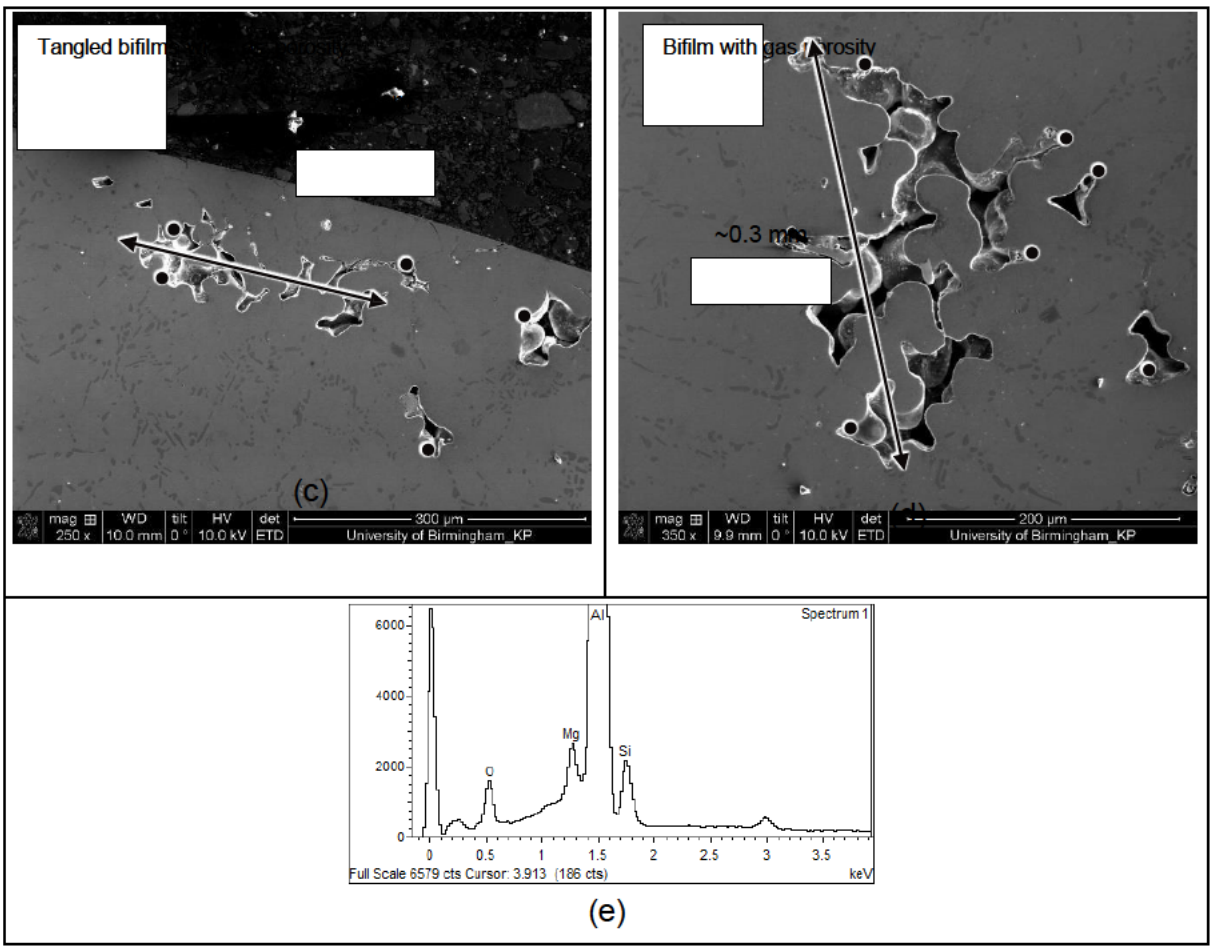


Figure 4-19: (a) to (d) High magnification of SEM micrographs of the main cavities in the 2L99 in (a) (e) EDX spectrum1 of the point marked in (a)

Table 4-26: EDX elemental composition of spectrum 1 in Figure 4-19 (a)

	Spectrum 1	
Element	Weight%	Atomic%
O K	3.74	6.15
Mg K	1.50	1.63
Al K	91.09	88.78
Si K	3.67	3.43

SEM analysis showed an additional flat surface of 2L99 alloy (high UTS, 296 MPa) was observed, employing the SEM, as shown in Figure 4-20 (a) and (b). In Figure 4-20 (b), Spectrum 1 displays Al_7SiFe intermetallics of approximately 60 µm, which closely resemble one of the most detrimental Fe-rich intermetallics found in Al-Si alloys, namely β-Al_5SiFe with a monoclinic crystal structure [3] [100] [101]. The intermetallic

shown in Spectrum 1 could potentially be β-Al_5SiFe, as the EDX spectra detected a significantly higher amount of Al from the underlying substrate due to an interaction volume of approximately 5 µm.

Mg_2Si compounds with "Chinese script" morphology were found (approximately 60 µm long) on some of the polished 2L99 alloy surfaces, one of which is presented in Figure 4-20 (b). It is considered a detrimental intermetallic in terms of the ductility of the 2L99 alloy [100]. EDX analysis of the points marked as Spectrum 1 and Spectrum 9 in Figure 4-20 (b) are shown in Figure 4-20 (c) and Figure 4-20 (d), and the EDX elemental composition is shown in Table 4-27.

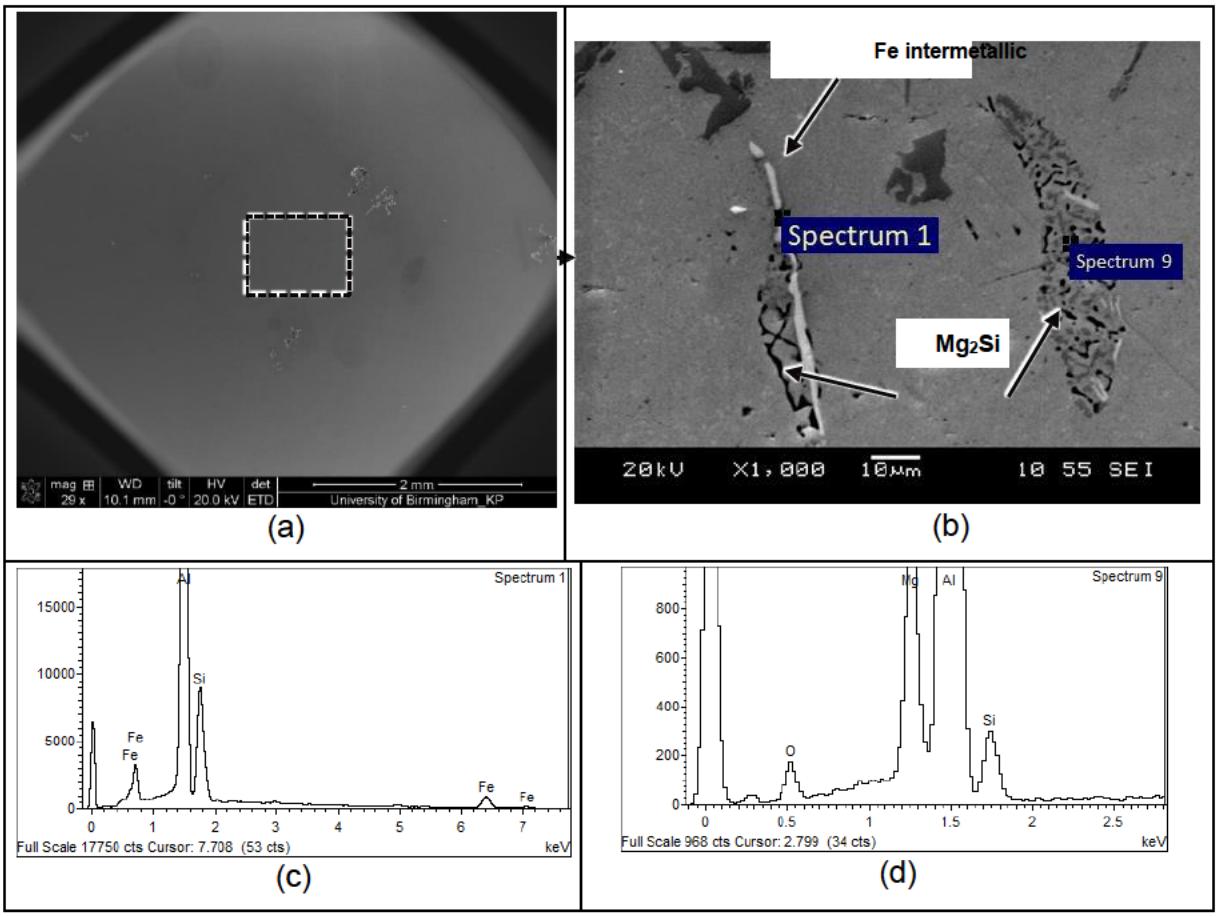


Figure 4-20: (a) Whole matrix SEM micrograph of a polished cross-section of the 2L99 alloy with high UTS 296 MPa. (b) Low magnification SEM micrograph of the flat surface without cavities

Table 4-27: EDX elemental composition of points on 2L99 polished marked as Spectrum 1 and Spectrum 9 in Figure 4-20 (b)

	Spectrum 1		Spectrum 9	
Element	Weight%	Atomic%	Weight%	Atomic%
O	0.00	0.00	7.41	11.83
Mg	0.00	0.00	6.89	7.24
Al	66.33	74.34	80.55	76.25
Si	13.88	14.95	5.15	4.68
Fe	19.78	10.71	0.00	0.00

The high magnification of the most significant shrinkage cavities and bifilms (probably spinel, shown in Figure 4-20 (a)) are presented in Figure 4-21 (a) to Figure 4-21 (c). The defects on the polished flat sample surface for 2L99 varied in type, size, and orientation. The defects consisted of relatively large shrinkage cavities, tangled bifilms, gas porosity, or a mixture of all of these. The largest bifilm and shrinkage cavity was 1250 µm long, and the average length of the bifilms was 0.5 mm.

These defects were located in different positions and orientations from the middle to the corner of the testbars. Similar to Figure 4-19, the EDX composition of the points marked with black circles on these figures indicated that the edges of the defects were the same as in Spectrum 1; an example of the spectrum is shown in Figure 4-21 (c), whilst Table 4-28 present the EDX spectrum composition of the marked points.

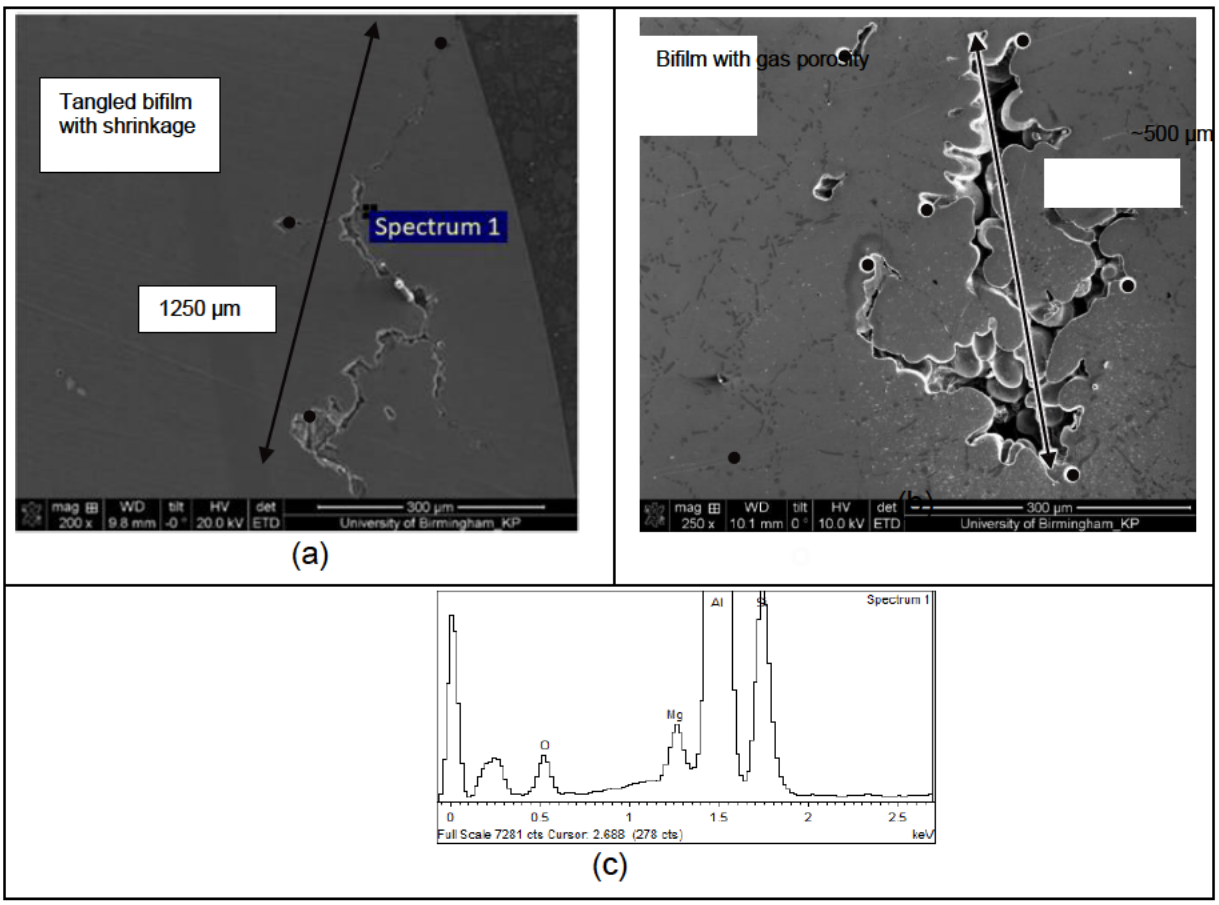


Figure 4-21: (a) High magnification SEM micrographs of the main cavities detailed in Figure 4-18 (a). (c) EDX Spectrum1 for Figure 4-19 (a)

Table 4-28: EDX elemental composition of the area marked as spectrum 1 in Figure 4-21 (a)

	Spectrum 1	
Element	Weight%	Atomic%
O K	5.57	9.09
Mg K	2.45	2.63
Al K	73.68	71.27
Si K	18.30	17.01

It is important to note that these samples showed that the size and orientation of bifilms and other defects differed, as fewer defects were observed than those for low UTS, as shown in Figure 4-18 (a).

Moreover, cubic oxide particles were observed on one of the pores of the flat surface of a 2L99 sample shown in Figure 4-22 (a) and Figure 4-22 (b). The cuboid oxide particles were thought to be spinel considering their Mg content and were observed to be

approximately 1 µm in length and located inside one of the pores on the 2L99 cross-section of a polished flat surface. The cuboid spinel particles covered an area of approximately 25 µm in length inside the pore.

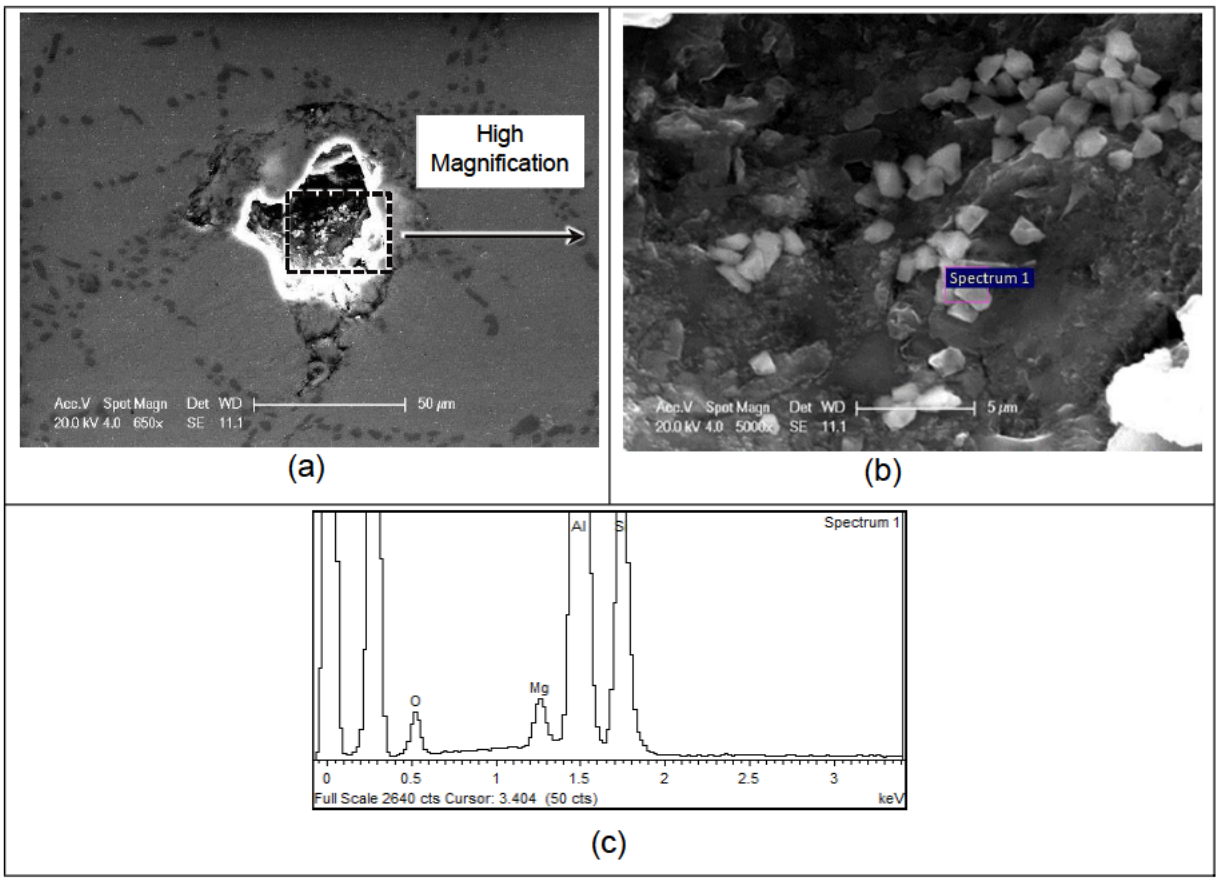


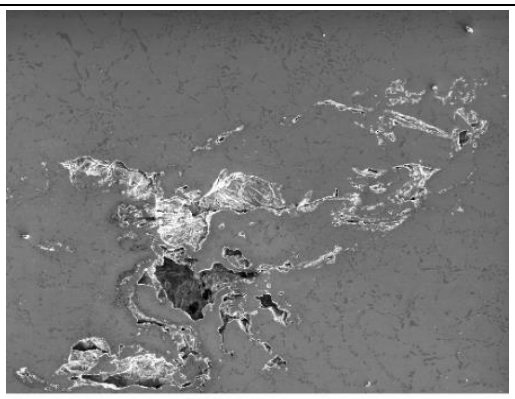
Figure 4-22: (a) low magnification of SEM micrograph of the pore on the polished cross-section of the 2L99 alloy (b) high magnification of oxide particle in the pores (c) EDX spectrum 1 of the marked areas in (b)

Table 4-29 shows the EDX spectrum elemental composition for the area marked in Figure 4-22 (b). These cubic oxide particles were considered spinel ($MgA1_2O_4$) as their morphologies were similar to the spinel particles reported by Impey [14] on an Al-5wt.%Mg alloy. This conclusion was also consistent with Campbell's naming of the spinel as an "irregular jumble crystal" [102].

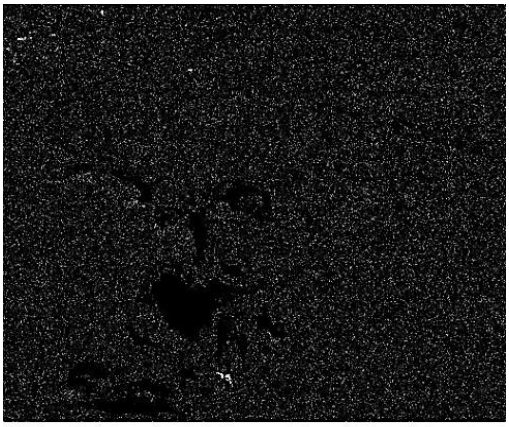
Table 4-29: EDX elemental composition of spectrum 1 in Figure 4-22 (b)

	Spectrum 1	
Element	Weight%	Atomic%
O K	13.71	21.33
Mg K	2.33	2.39
Al K	52.65	48.55
Si K	31.30	27.73

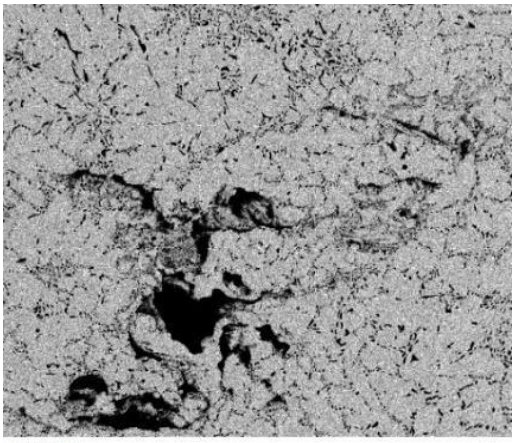
The EDX mapping of one of the typically tangled bifilms with cavities on the flat surfaces of the 2L99 testbar is shown in Figure 4-23. EDX mapping of the tangled bifilm showed the distribution of oxygen as well as the other three elements of the main matrix of 2L99, Al, Si and Mg. Table 4-30 presents the summary of the phases observed on a polished surface of 2L99 alloy in this research.



(a)



(b)



(c)

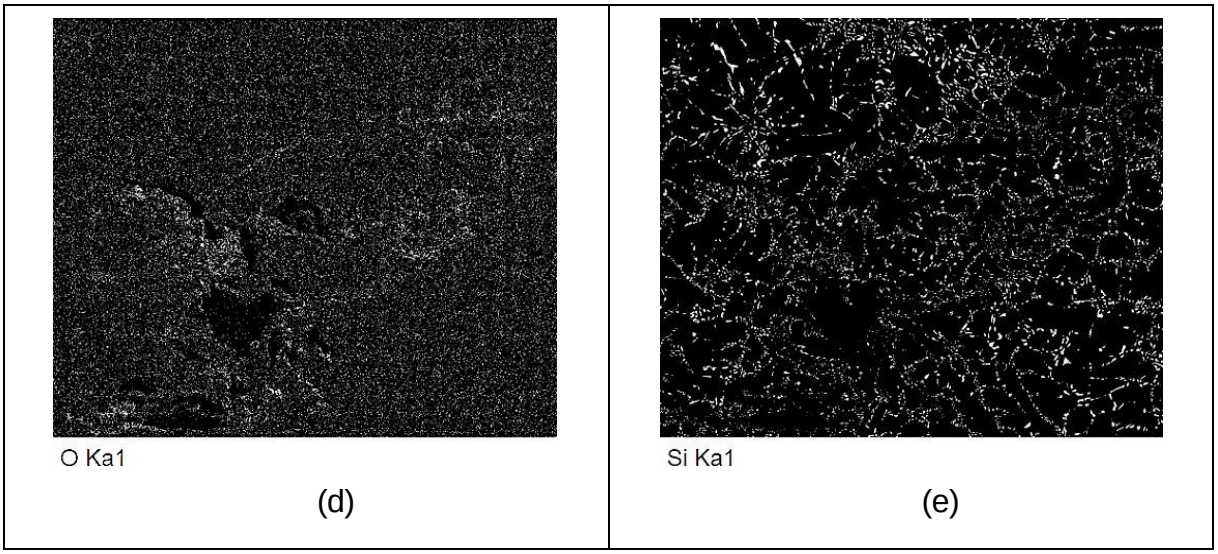


Figure 4-23: EDX mapping of typical tangled bifilms and cavities on the polished surface 2L99

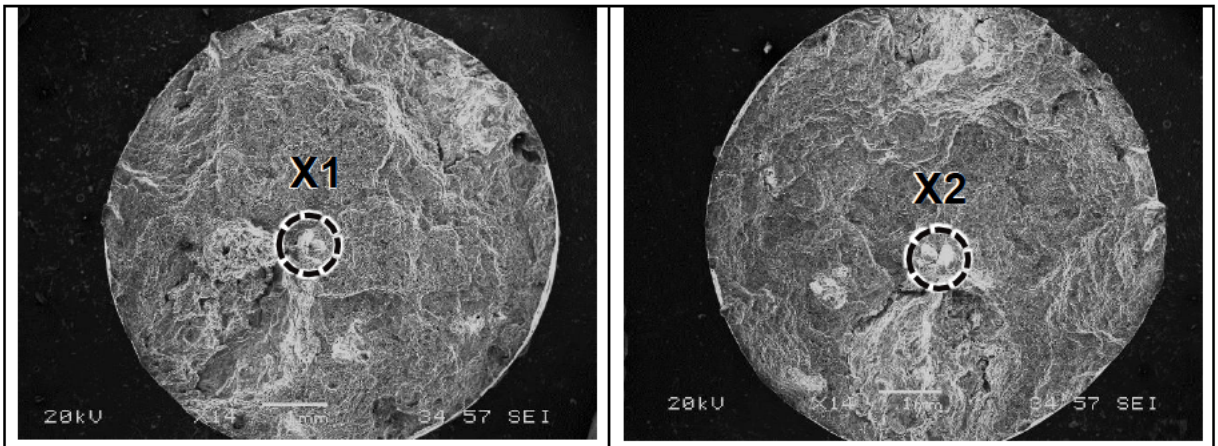
Table 4-30: Summary of the phases on a polished surface of 2L99 alloy

Polished 2L99	Name	Size
Oxides	spinel layers and particles	Cuboid oxide particle ~1 µm Covered an area of 25 µm in length inside a pore.
Intermetallic compounds	Mg_2Si Al_5SiFe	~60 µm ~60 µm

4.2.1.2 Characterisations of the phases on the fractured surfaces of 2L99

[4]Figure 4-24 (a) and (b) display low magnification SEM images of two halves of a testbar fractured surface from the as-cast 2L99 alloy with Ar lance degassing and T6 heat treatment. Figure 4-25 and Figure 4-28 present high-magnification SEM images and EDX elemental spectra of areas labelled X1 and X2 in Figure 4-24 (a) and Figure 4-24 (b). These areas revealed the existence of 220 µm long bifilms and small patches of nitrides approximately 15 µm in length. This observation confirms the presence of symmetrical oxides and nitrides on both halves of the fractured surfaces in the as-cast 2L99 alloy.

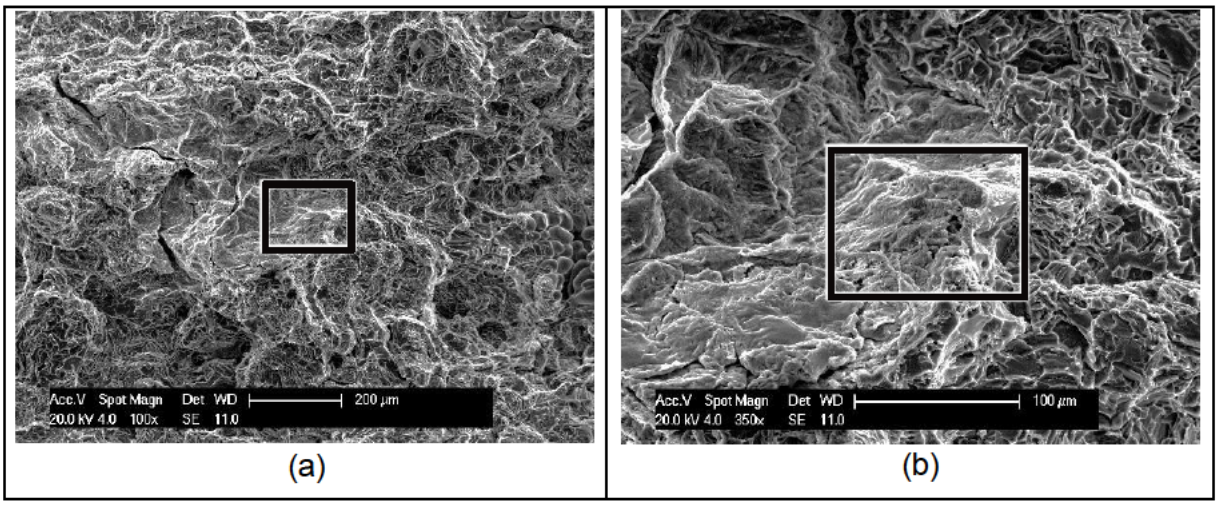
[4] Figures 4-24 to 4-28 have been included in a previous publication by the author as provided in Appendix A.



(a) (b)

Figure 4-24: (a) and (b) depict low magnification SEM images of the fractured surfaces of an as-cast 2L99 testbar

Figure 4-25 (a) to Figure 4-25 (f) exhibited high magnification morphology and EDX results of the nitride (AlN) and oxide (spinel) patches found on the fractured surface of the 2L99 testbar, as shown in Figure 4-24 (a) and Figure 4-24 (b). The composition table (Table 4-31) indicates that the marked area in Figure 4-25 (e) contains 14 at.% of oxide and 20 at.% of nitrides. The nitride patches were observed to have a nodular shape and covered approximately 15 µm of the fractured surface (Figure 4-25 (e)).



(a) (b)

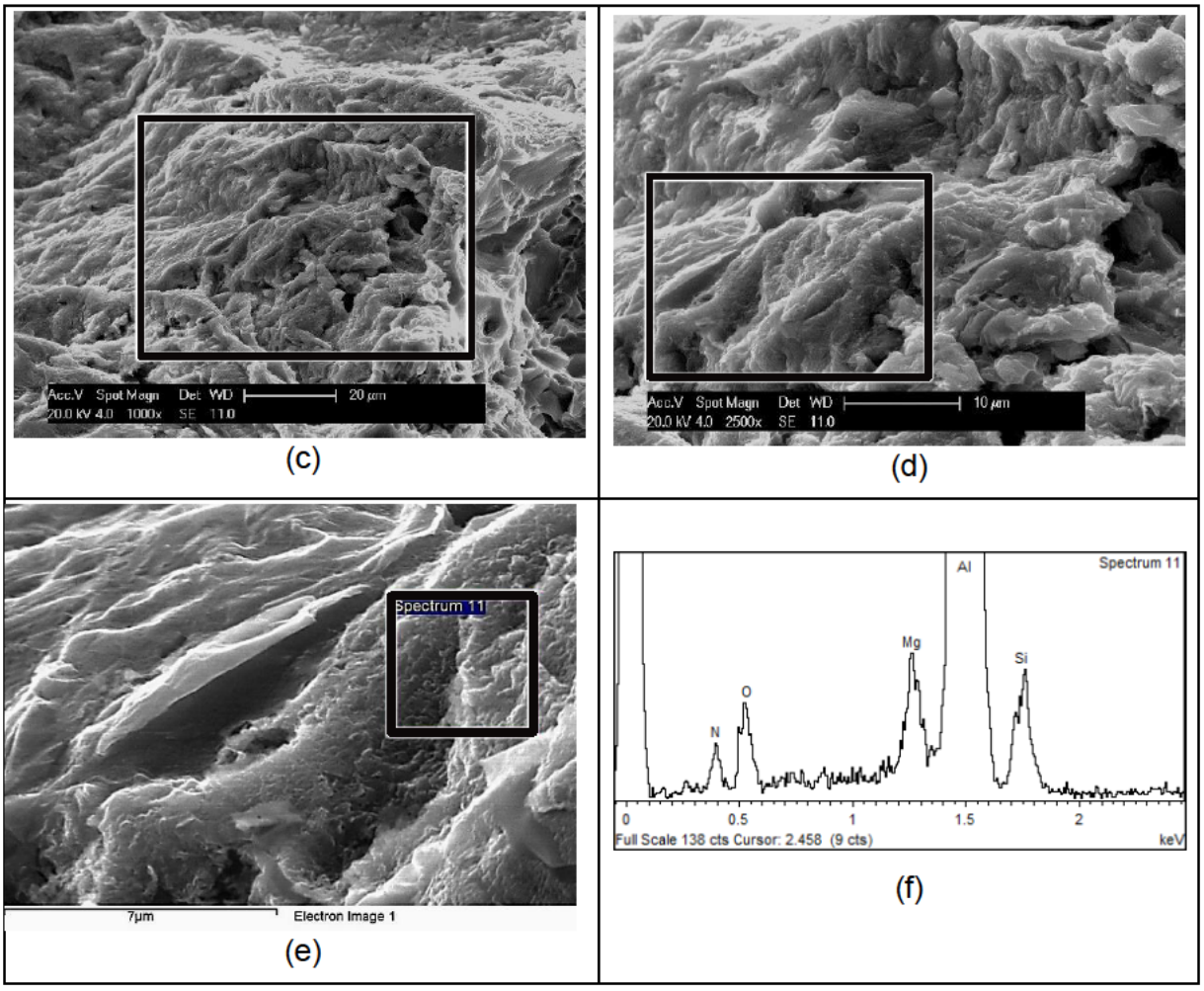


Figure 4-25: (a) to (e) illustrate SEM micrographs of an oxide and nitride layer on the fractured surface of the as-cast 2L99 alloy (f) presents the EDX analysis of spectrum 11 in (e)

Table 4-31: Quantification of the market area, Spectrum11, in Figure 4-25 (e) is presented in (f)

Element	Spectrum11	
	Weight %	Atomic %
N	12.54	20.39
O	10.04	14.29
Mg	1.43	1.34
Al	71.98	60.73
Si	4.01	3.25

The area marked in Figure 4-25 (e) was characterised using SEM at a series of higher magnifications, as shown in Figure 4-26 (a) to Figure 4-26 (c). The high magnification images confirmed the presence of nodular nitrides (AlN) morphology, with each nodule measuring approximately 250 nm and spinel oxides. Figure 4-26 (d) shows the

EDX analysis of Spectrum 2, whilst Table 4-32 presents the quantification of Spectrum 2.

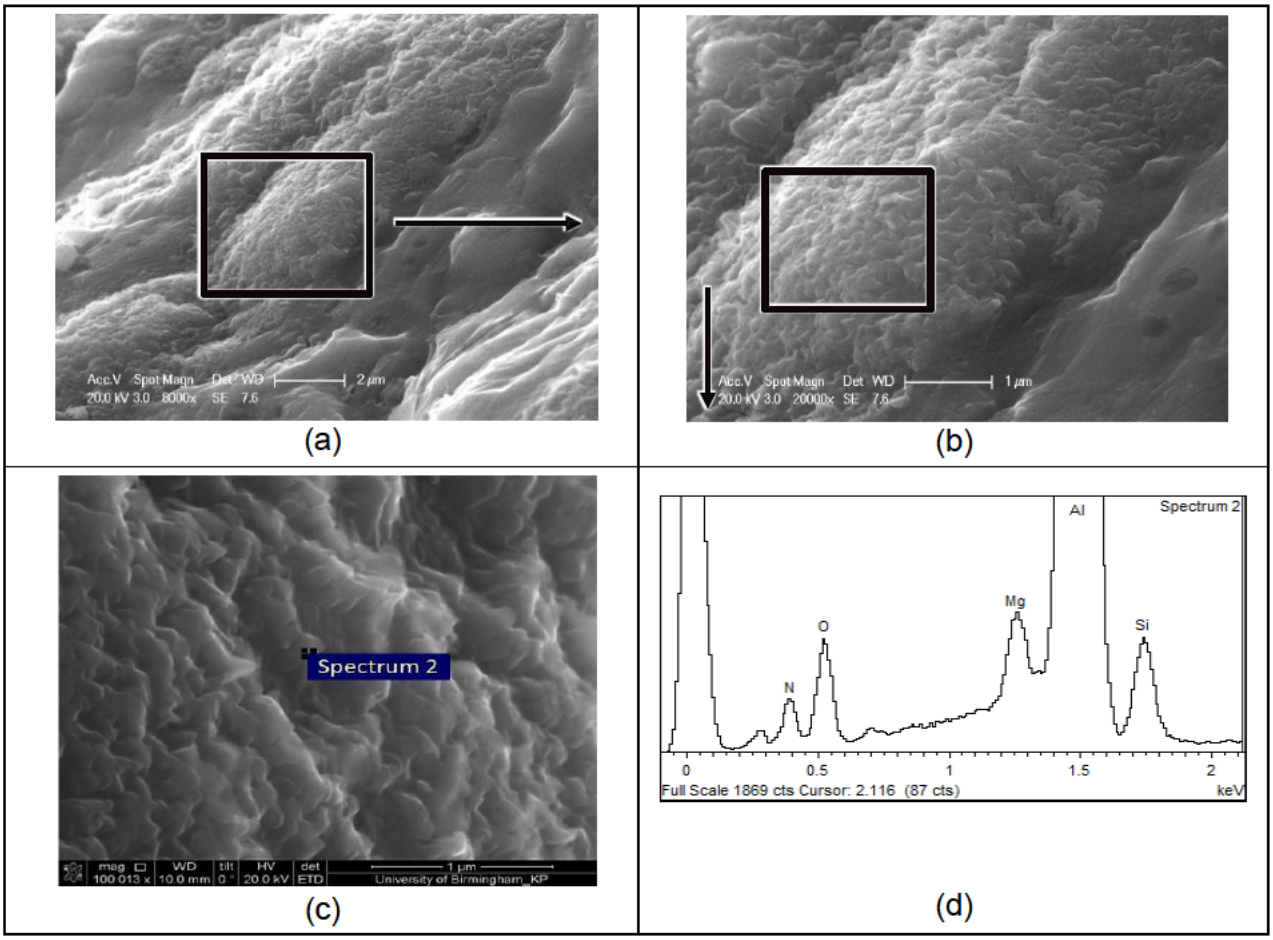


Figure 4-26: (a), (b), and (c) showcase high-magnification SEM images of a nitride and oxide layer on the fractured surface of the as-cast 2L99 alloy. Additionally, (d) presents the EDX analysis of Spectrum 2

Table 4-32: Quantification of Spectrum 2 as marked up in Figure 4-26 (d)

Element	Spectrum2	
	Weight %	Atomic %
N	10.93	17.95
O	10.53	15.13
Mg	1.02	0.96
Al	74.62	63.59
Si	2.90	2.38

To observe the thickness of the nitride layer on the as-cast 2L99 samples discussed earlier, the area was initially coated with Pt before milling by FIB, as depicted in Figure 4-27 (a). However, the presence of the Pt cover hindered the determination of the AlN

layer's thickness. To overcome this issue, as shown in Figure 4-27 (b), FIB milling was conducted without a Pt coating, which successfully allowed the measurement of the AlN layer which was found to be approximately 0.7 µm thick. Figure 4-27 (a) and Figure 4-27 (b) provide a cross-section view of Figure 4-26 (c) and Figure 4-27 (c) shows the corresponding EDX analysis. Table 4-33 specifies the quantification of spectrum 1 as marked in Figure 4-27 (b), showing the presence of oxides (spinel) and nitrides.

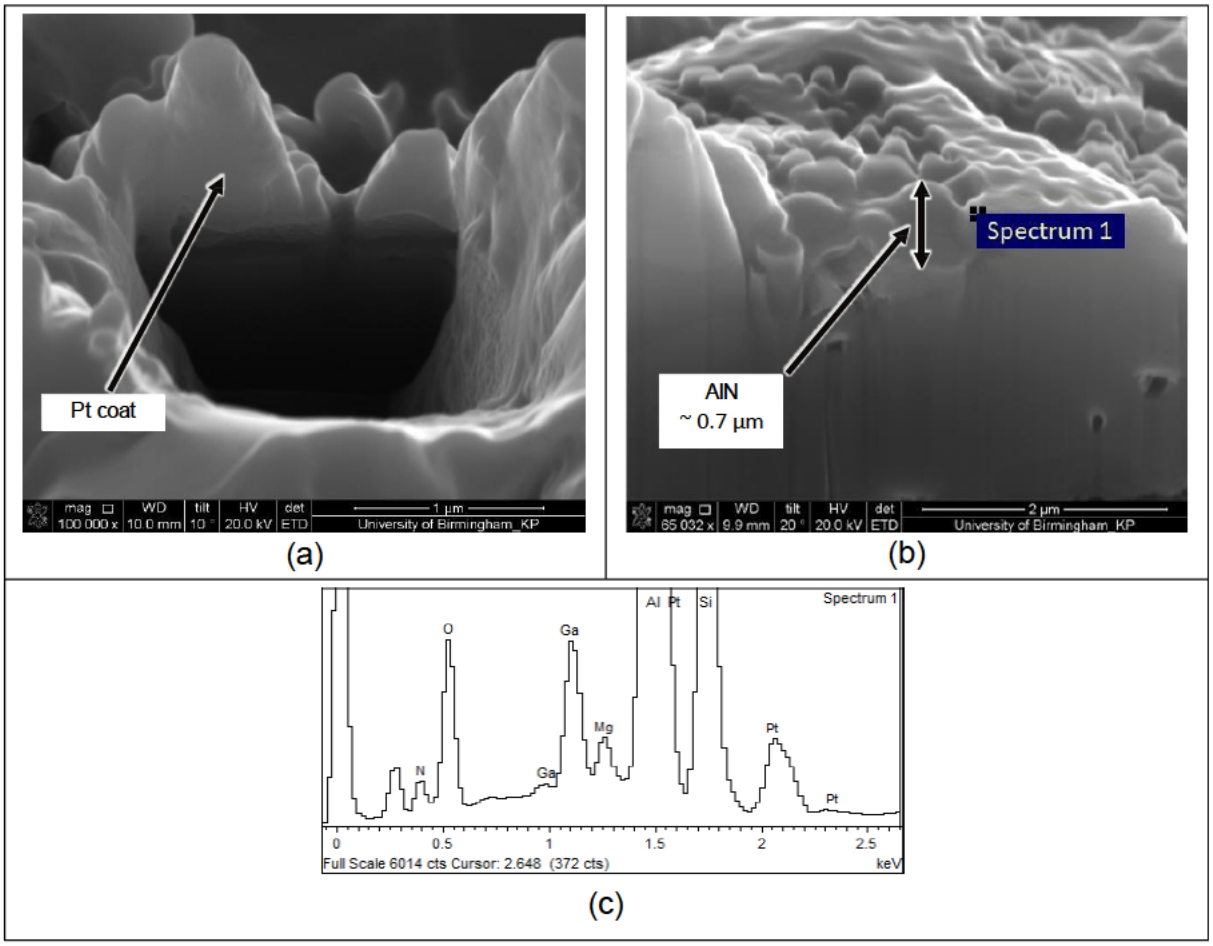


Figure 4-27: (a) shows the cross-section of the nitride layer observed on the fractured surfaces of 2L99 with Pt Coating, (b) the same nitride area without Pt coating, (c) EDX analysis of Spectrum 1 showing both O and N as well as a small amount of Pt and Ga

Table 4-33: Quantification of Spectrum 1 as marked in Figure 4-27 (b)

Element	Spectrum1	
	Weight%	Atomic %
N	10.93	17.95
O	10.53	15.13
Mg	1.02	0.96
Al	74.62	63.59
Si	2.90	2.38
Ga	4.33	1.50
Pt	7.00	0.87

The area labelled in Figure 4-28 (a) corresponds to the nitride layers (AlN) and oxides (spinel) observed on the other half of the testbar displayed in Figure 4-24 (b). Figure 4-28 (b) presents a high-magnification image of the marked area in Figure 4-28 (a). Figure 4-28 (c) provides the EDX quantification of Spectrum 2, and Table 4-34 contains the quantification data of Spectrum 2 marked in Figure 4-28 (b).

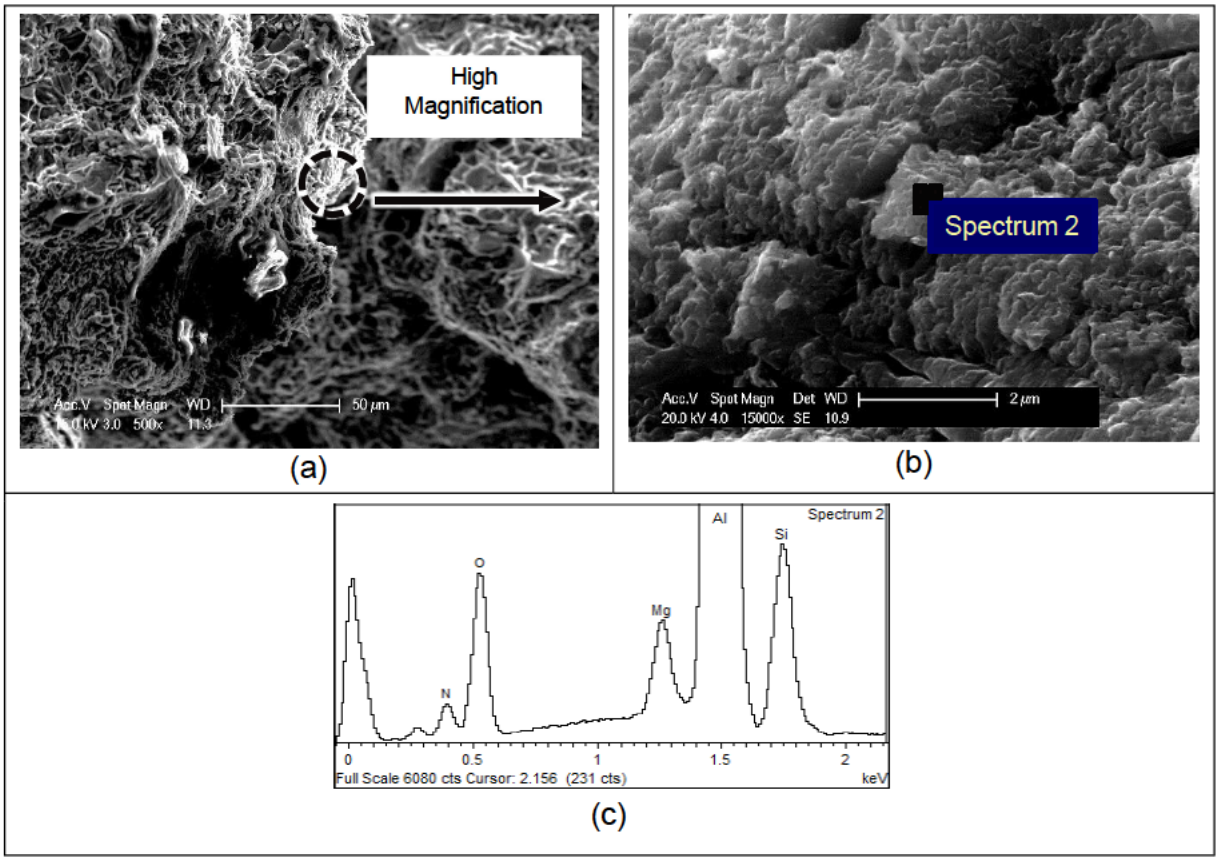


Figure 4-28: (a) displays a low magnification SEM micrograph of the oxide layers and nitride on the fractured surface 2L99 in its as-cast condition. (b) a high magnification SEM micrograph of the area marked in (a). (c) the EDX analysis of Spectrum 2, as indicated in (b)

Table 4-34: Quantification of Spectrum 2 as marked in Figure 4-28 (b)

Element	Spectrum 2	
	Weight%	Atomic %
N	11.44	17.43
O	23.19	30.93
Mg	1.88	1.65
Al	56.25	44.49
Si	7.25	5.51

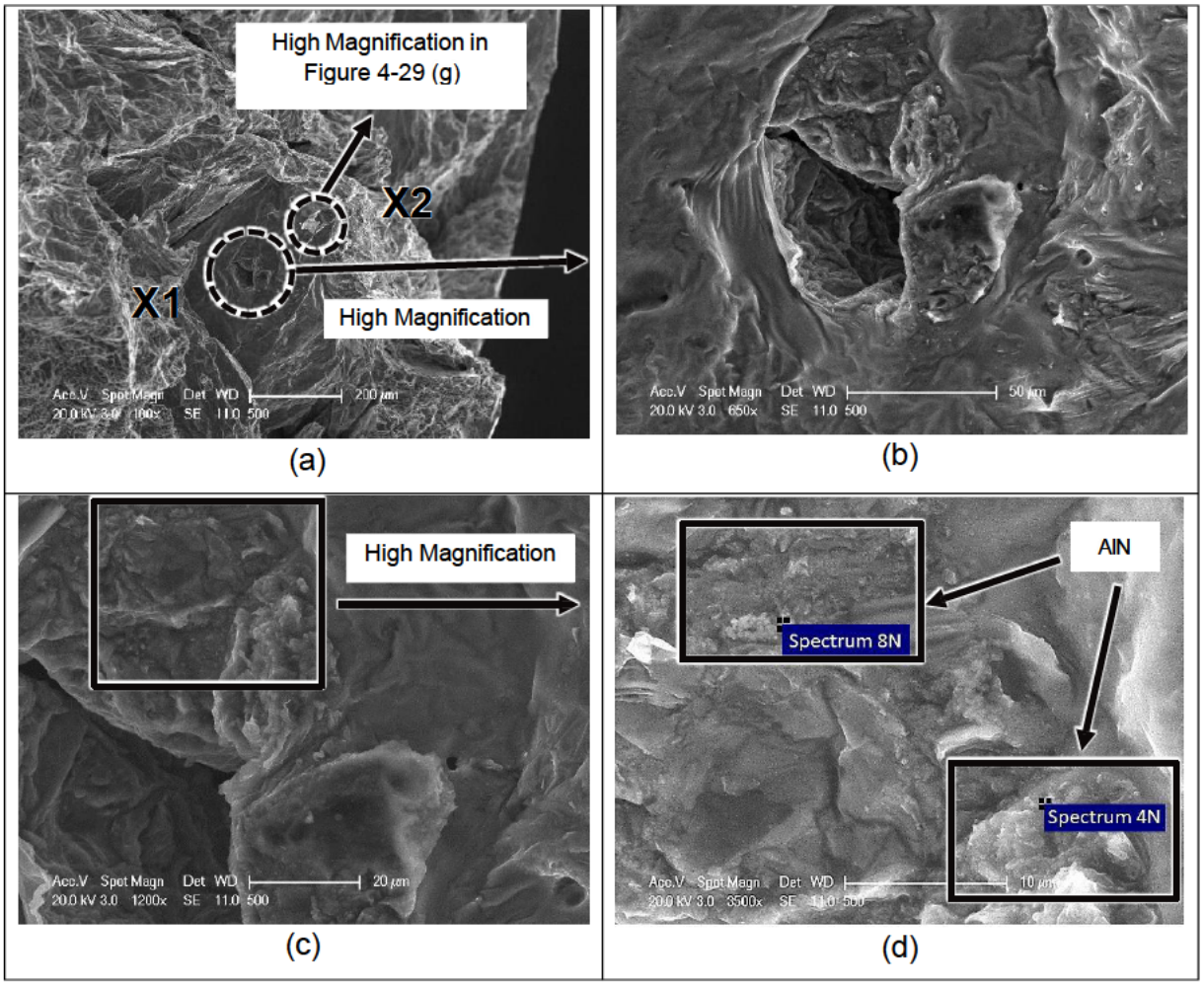
The fractured surface of one of the testbars with the lowest UTS 83 MPa was investigated further to observe the presence of any bifilms or nitrides. Figure 4-29 (a) to Figure 4-29 (d) show SEM images of one of the corners of the fractured surfaces ranging in magnification from low to high.

Figure 4-29 (a) and Figure 4-29 (b) show the SEM micrograph of the pore marked as X1 located on the fractured surface of the 2L99 testbar (with Ar lance degassing without hydrogen contents measurements) and near the edge of the sample. Numerous bifilms (spinel) and a small number of nitride patches were observed in this area. Figure 4-29 (c) and Figure 4-29 (d) show the morphology of these nitrides, which were nodular in shape. The corresponding EDX spectra for these nitrides marked in Figure 4-29 (d) are presented in Figure 4-29 (e) and Figure 4-29 (f).

The EDX results show a high amount of oxygen with a small amount of nitrogen as well as Al, Si and Mg. In contrast to nitrides, which were interspersed in small separate patches across the surface, oxides can be observed to form a continuous layer or easily identifiable particles. The nitride patches were nodular in shape and measured an average of 10 µm in width or length.

The nitrogen peaks in the two EDX spectra shown in Figure 4-29 (e) and Figure 4-29 (f) were generally observed alongside a strong oxygen peak. The EDX analysis, as shown in Table 4-32, quantifies the average amount of oxygen at 20 at.% and the average amount of nitrogen at 6.5 at.%.

Figure 4-29 (g) shows a thin wrinkle layer of oxide film (MgO) morphology of 20 μm length. This was considered comparable to the oxide film reported by Campbell found on Al-5Mg alloys [103]. Figure 4-29 (h) presents the EDX result of Spectrum 1 as marked in Figure 4-29 (g).



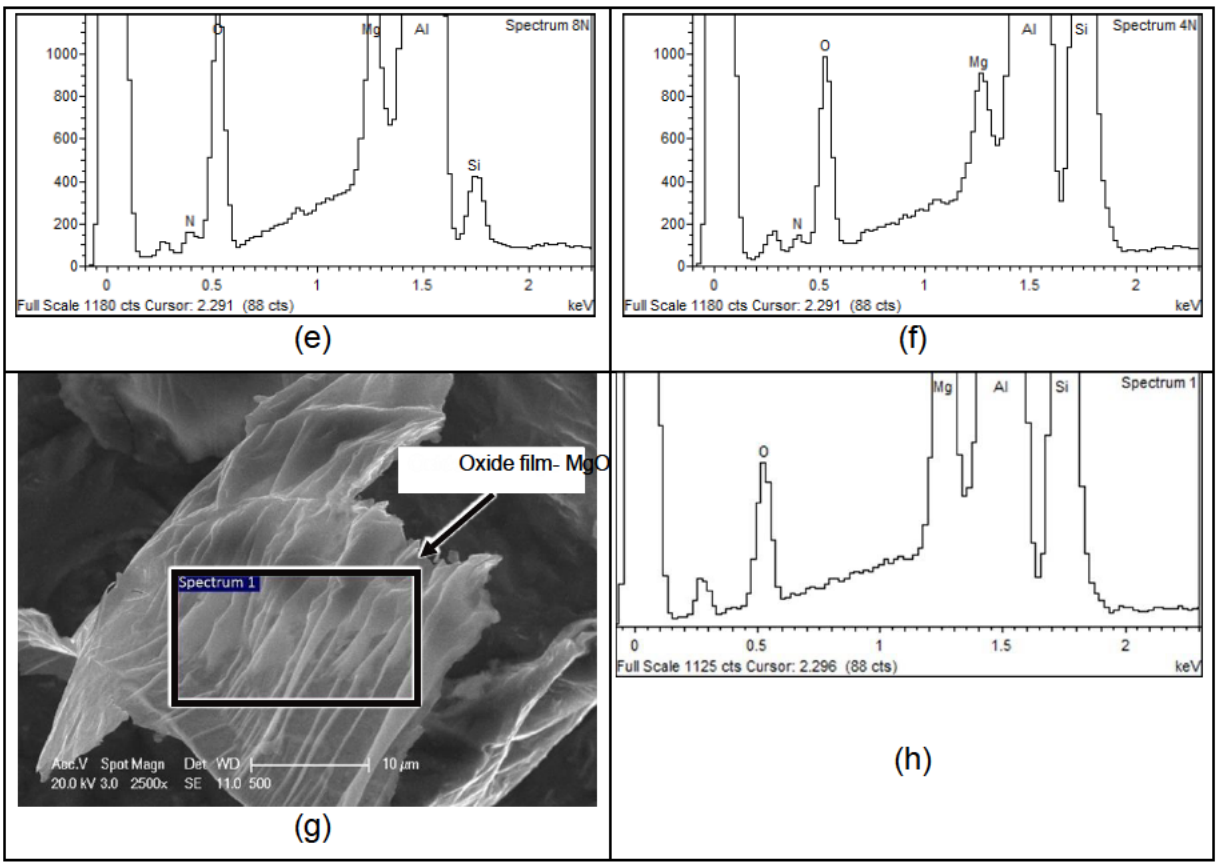


Figure 4-29: (a) SEM micrograph of the pore marked as X1 on the corner of the fractured surface of 2L99 (b), (c), (d) respective higher magnification SEM micrographs of the pore (e) and (f) EDX elemental spectra of the two areas marked in (d). (g) is the high magnification of the area marked as X2 in (a) Showing a thin layer of oxide film, (h) is the EDX analysis of the area marked in (g)

Table 4-35 shows the EDX values for Spectrum 8N, Spectrum 4N and Spectrum 1, which are marked in Figure 4-29 (d) and Figure 4-29 (g), respectively.

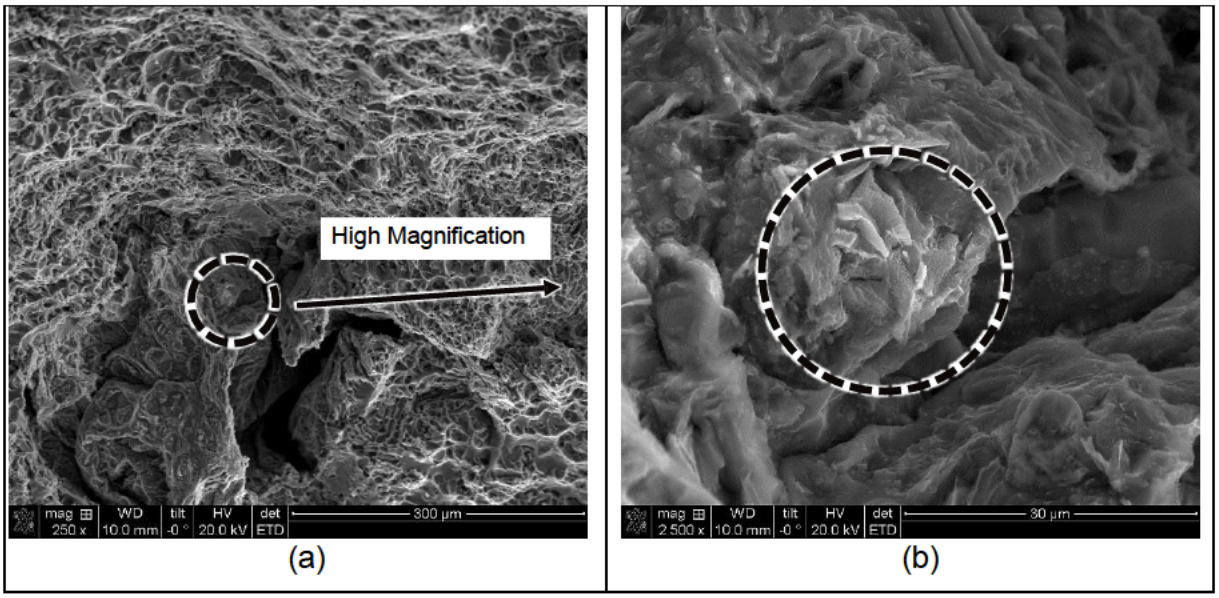
Table 4-35: EDX elemental spectra of the areas marked in Figure 4-29 (d) and (g)

	Spectrum 8N		Spectrum 4N		Spectrum 1	
Element	Weight%	Atomic%	Weight%	Atomic%	Weight%	Atomic%
N K	4.16	7.05	3.02	5.26	0.00	0.00
O K	14.29	21.18	21.84	28.09	9.34	14.84
Mg K	1.43	1.40	0.83	0.84	2.97	3.11
Al K	78.65	69.13	68.79	62.31	71.79	67.65
Si K	1.47	1.24	5.52	4.50	15.90	14.39

Figure 4-30 (a) to Figure 4-30 (c) show an SEM micrograph of the fractured surface of one of the testbars measuring the highest UTS of 296 MPa. The micrographs show

the presence of oxide films and nitride patches. Figure 4-30 (b) is the high magnification image of the area marked in Figure 4-30 (a). It has been shown in Figure 4-30 (c), which is a high magnification of the area marked in Figure 4-30 (b), that oxide films can be seen to be present at the edge of the ridges, whilst nodular nitride patches and oxides (spinel) can be observed to the sides of the ridges, with each patch on average having a length of 10 μm. As shown in Figure 4-30 (b), the marked area overall was measured to be approximately 37 μm in diameter, made up of smaller patches.

Figure 4-30 (d) and Figure 4-30 (e) represent the EDX results of Spectrum 2 and Spectrum 3 as marked in Figure 4-30 (c). Table 4-36 shows the EDX elemental values for spectra 2 and 3, which are marked in Figure 4-30 (c).



(a) (b)

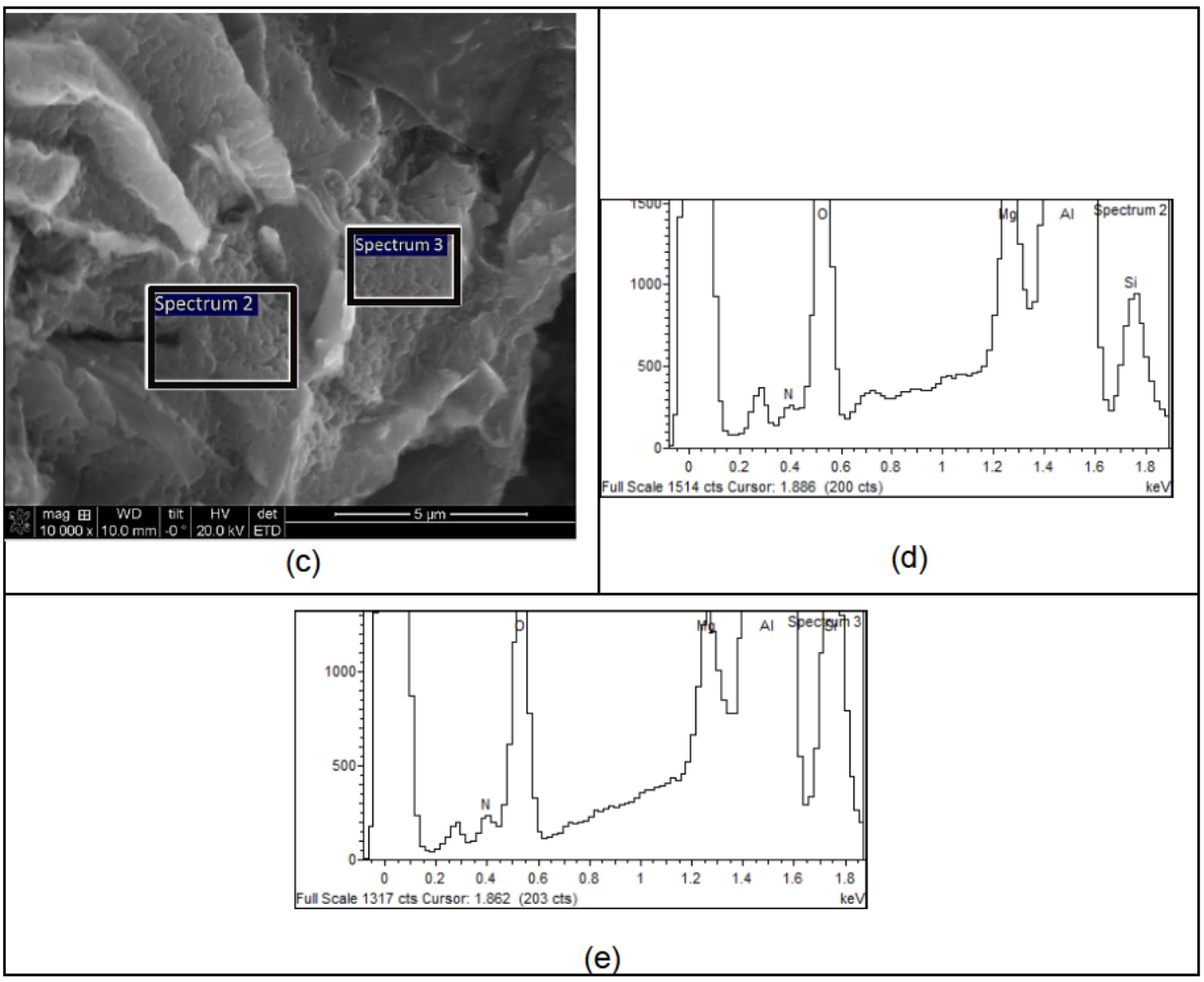


Figure 4-30: (a) SEM micrograph of the oxide layers and nitride on the fractured surface of 2L99 (as-cast condition) (b) High magnification SEM micrograph of the marked area in (a), (c) is the high magnification SEM micrograph of the marked area in (b), EDX analysis of Spectrum 2 and Spectrum 3 as marked in (c)

Table 4-36: EDX elemental spectra of the areas marked in Figure 4-30 (c)

	Spectrum 2		Spectrum 3	
Element	Weight%	Atomic%	Weight%	Atomic%
N K	3.25	5.45	4.36	7.39
O K	17.04	25.05	14.26	21.16
Mg K	1.39	1.34	1.13	1.10
Al K	76.01	66.23	73.74	64.85
Si K	2.31	1.94	6.51	5.50

Figure 4-31 (a) and Figure 4-31 (b) show low to high-magnification SEM micrographs of a 2L99 fractured surface with a low UTS of 83 MPa showing irregular granular oxides (SiO_2) morphology and defects. Further study of the morphology resulted in the observation of oxide particles (SiO_2) seen in Figure 4-31 as bright semi-rounded

granules entrained inside the cavities as bifilm inclusions. It is important to note that foundry sand has the potential to serve as a silica source [104]. These particles vary from 100 µm to 300 µm in length, showing oxygen 67 at.%, Al 2 at.%, Si 31 at.% and Mg 0.4 at.%, as shown in the EDX elemental spectrum in Figure 4-31 (c). Table 4-37 shows the EDX elemental values for spectrum 2, which is marked in Figure 4-31 (b).

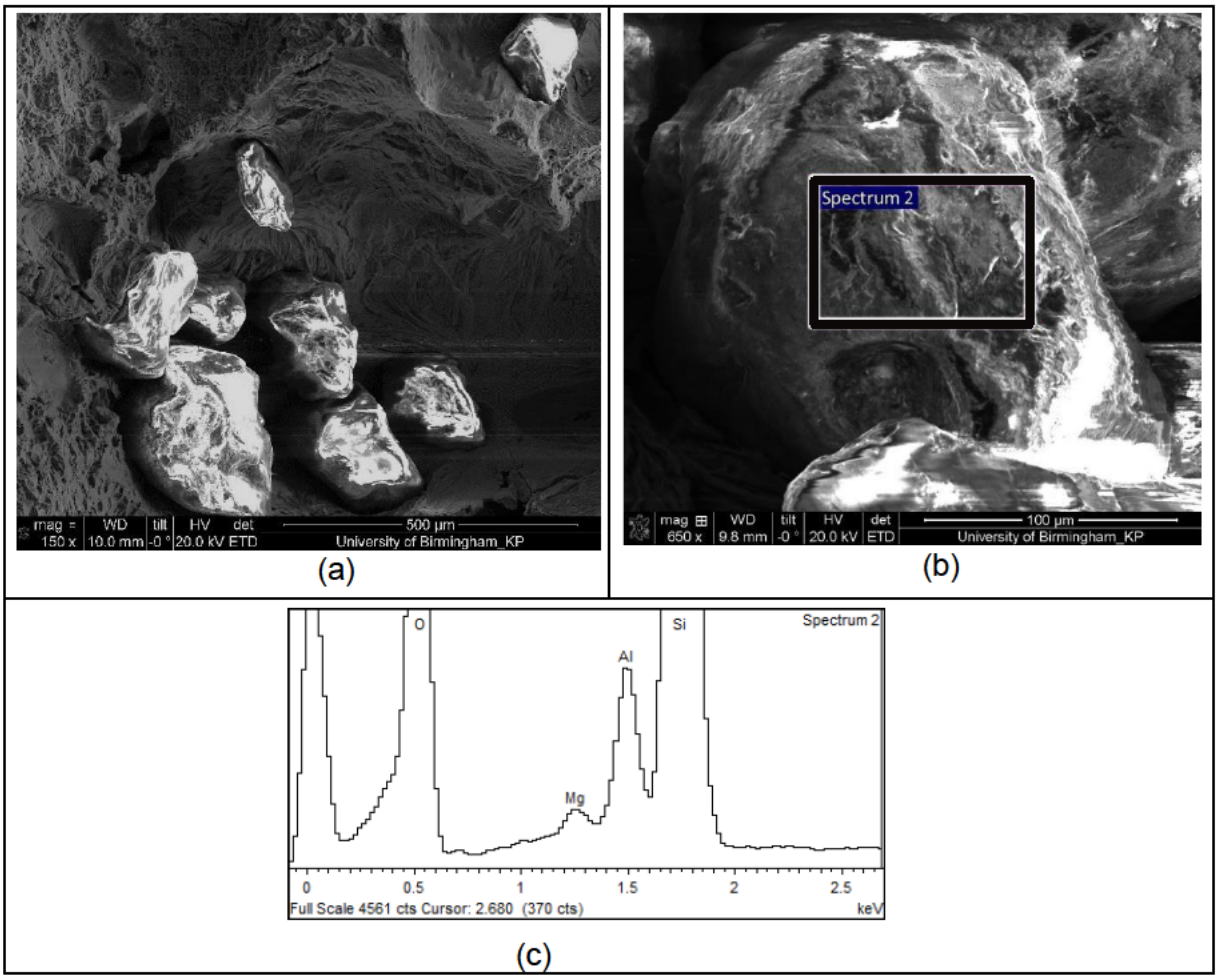


Figure 4-31: (a) and (b) SEM micrograph of the oxide particles (spinel) on the fractured surface of 2L99 (as-cast condition) low UTS, (c) the EDX analysis of Spectrum 2 as marked in (b)

Table 4-37: EDX elemental spectrum of the area marked in Figure 4-31 (b)

	Spectrum 2	
Element	Weight%	Atomic%
O K	53.37	66.67
Mg K	0.53	0.44
Al K	3.15	2.33
Si K	42.95	30.56

Other oxides present on the fractured surface of the 2L99 as-cast alloy are shown in Figure 4-32 (a) and Figure 4-32 (b). The area marked as Spectrum 1 in Figure 4-32 (a) reveals MgO particles 0.5 µm in size, while the area marked as Spectrum 3 in Figure 4-32 (b) displays spinel oxide (nodular shape) according to the EDX results, presented in Figure 4-32 (c) and Figure 4-32 (d) respectively. Detailed composition is provided in Table 4-38.

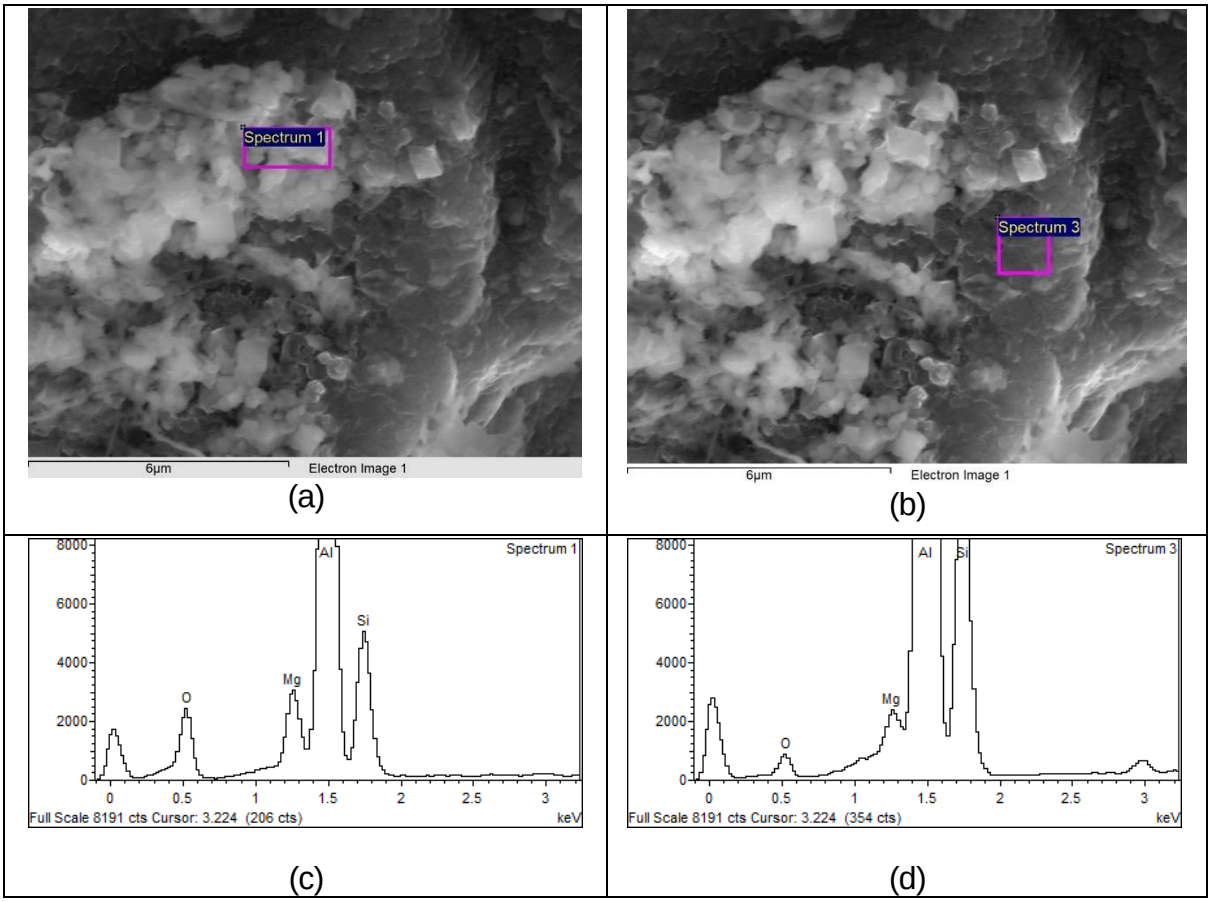


Figure 4-32: (a) and (b) SEM micrograph of the oxide particles (MgO) and spinel layer on the fractured surface of 2L99, (c) and (d) EDX analysis of Spectra 1 and 3, respectively

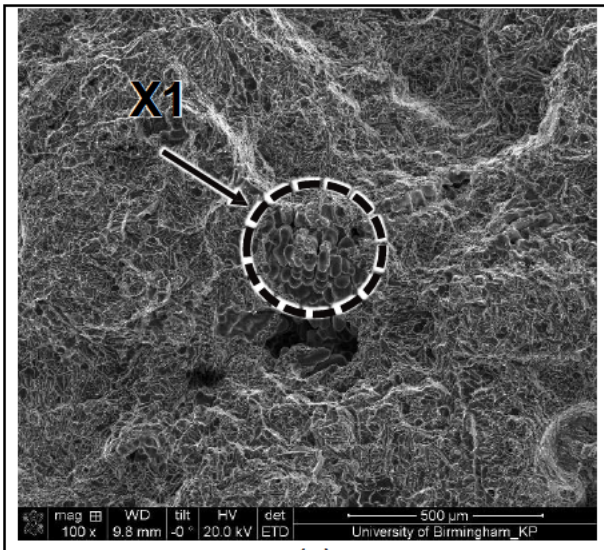
Table 4-38: EDX elemental spectra of the areas marked in Figure 4-32 (a) and (b)

	Spectrum 1		Spectrum 3	
Element	Weight%	Atomic%	Weight%	Atomic%
O K	26.57	37.95	6.42	10.46
Mg K	5.16	4.85	1.31	1.40
Al K	50.15	42.47	66.19	63.93
Si K	18.12	14.74	26.08	24.20

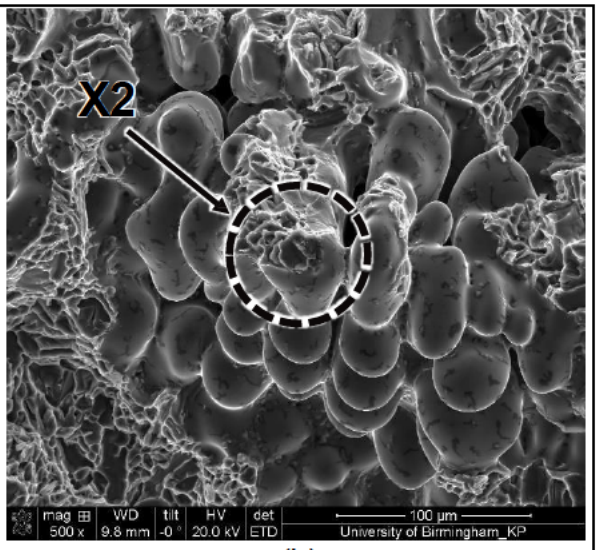
Figure 4-33 (a) shows an SEM micrograph of a typical gas porosity shrinkage observed on the fractured surface of a 2L99 testbar, marked as X1 on Figure 4-33 (a). Figure 4-33 (b) shows a higher magnification of the area marked as X1 in Figure 4-33 (a), where the secondary dendrite is covered with an oxide film, resulting in the appearance of shrinkage pores.

Figure 4-33 (c) is a high magnification of the area marked as X2 in Figure 4-33 (b), which shows the dendrite in a close-up. EDX analysis was carried out on various locations on the dendrite. On the surface of the dendrite were oxides (spinel), whilst the body of the dendrites (inside and outside) were made of Al and Si. The bright edges of the dendrite's pore also show the presence of oxides.

Figure 4-33 (d) to Figure 4-33 (f) show the EDX elemental spectra of the Spectrum 1, 3 and 5 as marked up in Figure 4-33 (c). The EDX elemental values for all 1, 3 and 5 spectra are marked in Figure 4-33 (c) and are presented in Table 4-39. Table 4-40 provides a summary of all the phases observed on fractured surface 2L99 alloy testbars in this study.



(a)



(b)

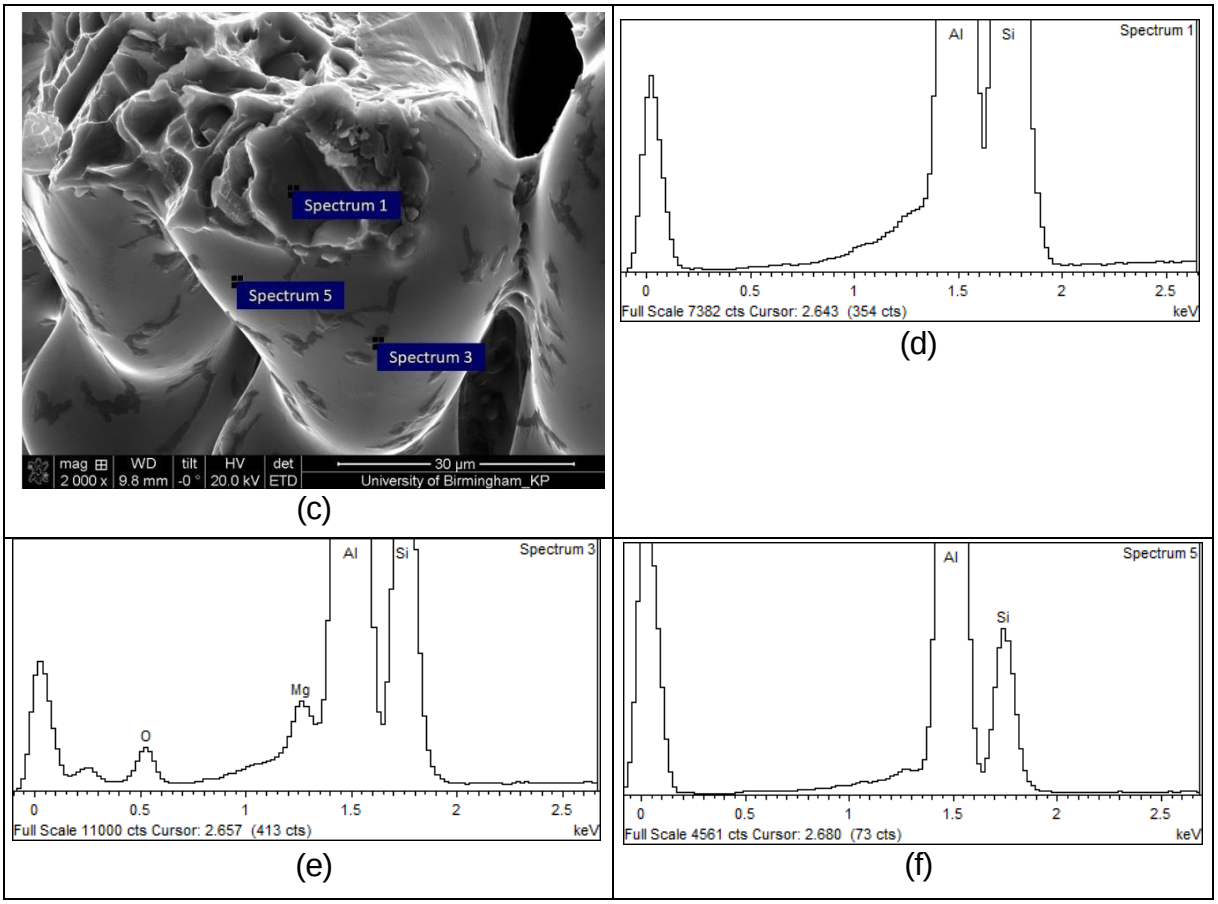


Figure 4-33: (a) to (c) low to high magnification SEM micrograph of one of the secondary dendrite arms covered with oxide films on the fractured surface of 2L99 (as-cast condition), (d) to (f) EDX analysis of Spectra are marked in (c)

Table 4-39: EDX elemental spectra of the areas marked in Figure 4-33 (c)

	Spectrum 1		Spectrum 3		Spectrum 5	
Element	Weight%	Atomic%	Weight%	Atomic%	Weight%	Atomic%
O K	0.00	0.00	8.09	13.04	0.00	0.00
Mg K	0.00	0.00	1.21	1.28	0.00	0.00
Al K	40.20	41.16	62.73	59.98	71.30	72.12
Si K	59.80	58.84	27.97	25.69	28.70	27.88

Table 4-40: Summary of the phases on fractured surface 2L99 alloy

Fractured 2L99	Name	Size
Oxides	Mostly spinel layers nodular Thin wrinkle layer of MgO MgO particle Irregular granular SiO_2	Approximately 100 µm 20 µm in length 0.5 µm in size These particles vary from 100 µm to 300 µm in length
Nitrides	AlN nodular shape	Approximately 15 µm in length (patch)
Intermetallic Particles on Polished samples	Al_5FeSi Mg_2Si	60 µm long 60 µm long
Gas porosity	H gas porosity	500 µm in size

4.2.2 2L99 + Mo alloy

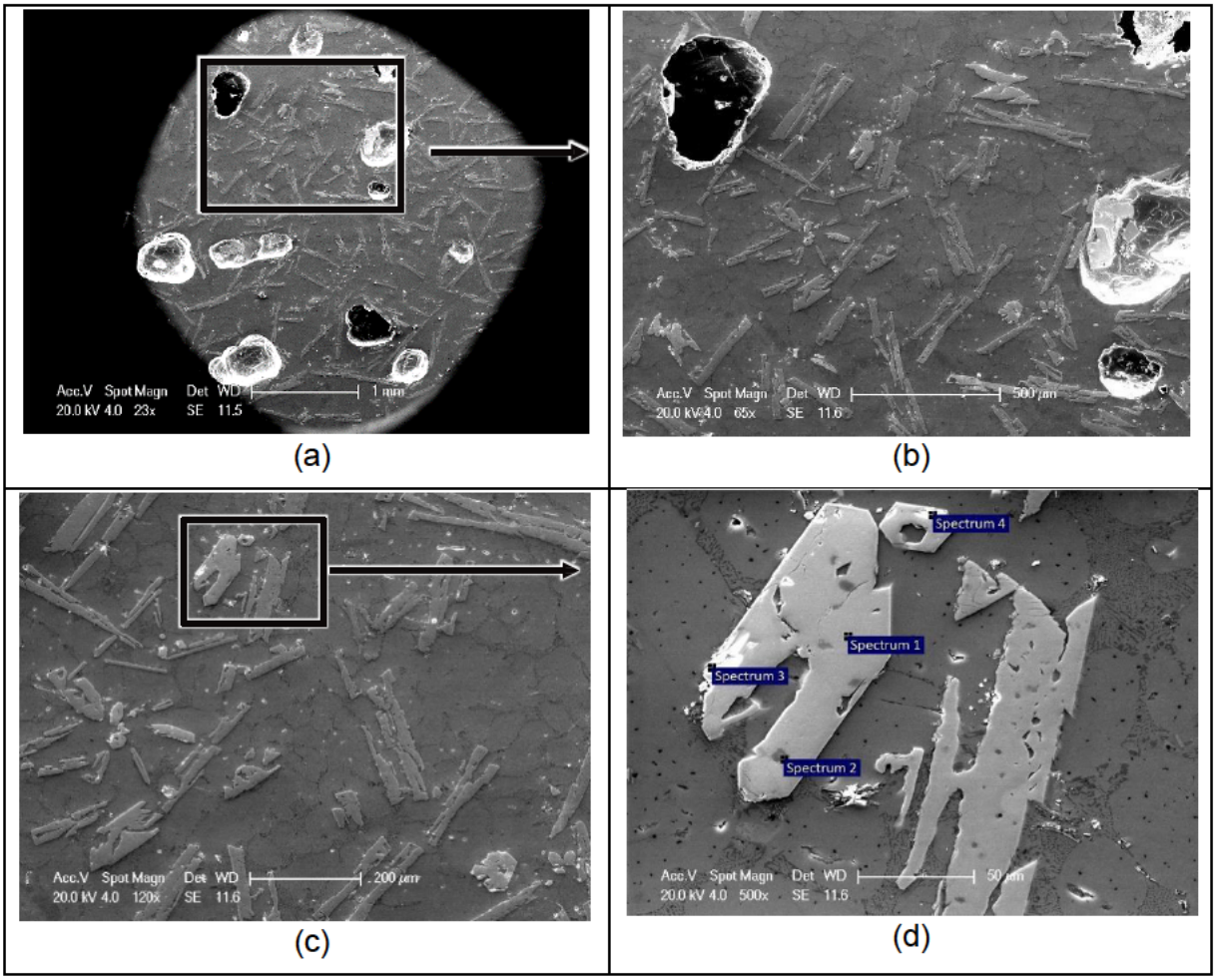
4.2.2.1 Characterisation of the masteralloy of 2L99 + 10%Mo

Characterisation of the masteralloys was carried out to investigate the potential formation of AlN within the masteralloys and its subsequent presence in the as-cast alloy. This required comprehensive characterisation efforts, including surface analysis of both the top and bottom of the ingot's polished surfaces, as well as characterisation of the polished and fractured surfaces of the masteralloy testbars.

4.2.2.1.1 Polished surfaces of 2L99 + 10 wt. % Mo testbars (Masteralloy)

Low to high-magnification SEM micrographs of a typical polished surface of a Mo masteralloy testbar have been presented in Figure 4-34 (a) to Figure 4-34 (d). Micrographs showed the presence of numerous cavities caused by gas porosity in the matrix, as well as numerous intermetallic compounds in various shapes, as shown in Figure 4-34 (b) to Figure 4-34 (d).

The high magnification micrographs of the polished surface of the masteralloy, along with corresponding EDX spectra, have been shown in Figure 4-34 (b) to Figure 4-34 (h). Table 4-41 presents the elemental composition of all the spectra in Figure 4-34 (d). The intermetallic compounds observed in the masteralloy were formed at various angles with a primarily rectangular shape varying from 25 µm to 100 µm in width and length. Spectra 1 to 4 in Figure 4-34 (d) showed multi-facetted and α-shaped Mo particles ($Mo_{1.5}AlSi_2$) based on EDX results.



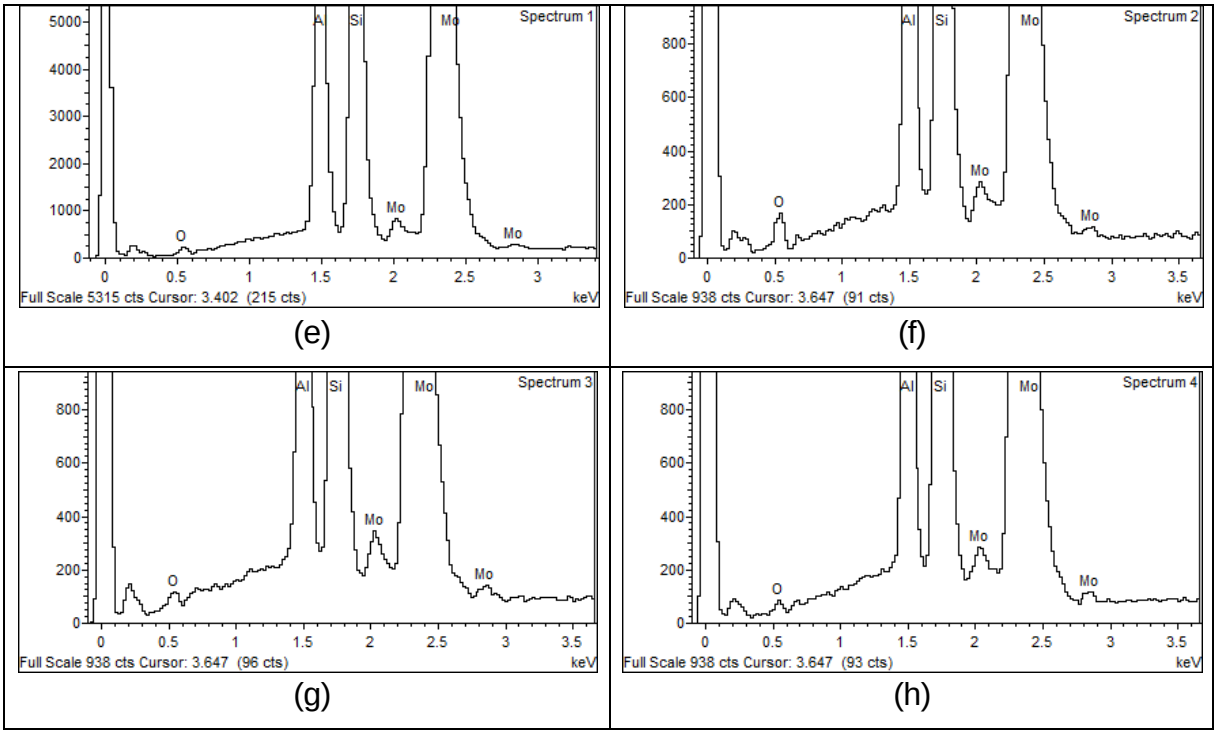


Figure 4-34: (a) to (d) low to high magnification SEM micrographs of a typical Mo masteralloy testbar, (e) to (h) corresponding EDX spectra of the points marked in (d) (sample 7 testbar)

Table 4-41: EDX elemental composition of spectra in Figure 4-34 (d)

	Spectrum 1		Spectrum 2		Spectrum 3		Spectrum 4	
Element	Weight%	Atomic%	Weight%	Atomic%	Weight%	Atomic%	Weight%	Atomic%
O	1.62	5.06	5.10	14.81	2.03	6.26	1.58	4.89
Al	11.36	21.94	9.50	16.37	11.95	21.84	9.96	18.34
Si	22.81	42.31	23.43	38.79	22.27	39.12	24.79	43.82
Mo	65.83	35.75	61.97	30.03	63.75	32.78	63.68	32.96

Low-magnification SEM micrographs of one of the cavities (gas porosity) is shown in Figure 4-35 (a). EDX composition of various spectra, as marked in Figure 4-35 (a), are presented in Figure 4-35 (b) to Figure 4-35 (d). The EDX of the spectra are presented in Table 4-42. The SEM micrographs showed the presence of intermetallic compounds connected to cavities, as shown in Figure 4-35 (a). This suggested the nucleation of intermetallic particles on the oxide film at the edge of the shrinkage or the edge of gas porosity, as EDX suggested strong peaks for O with 24 at.% and 12 at.%.

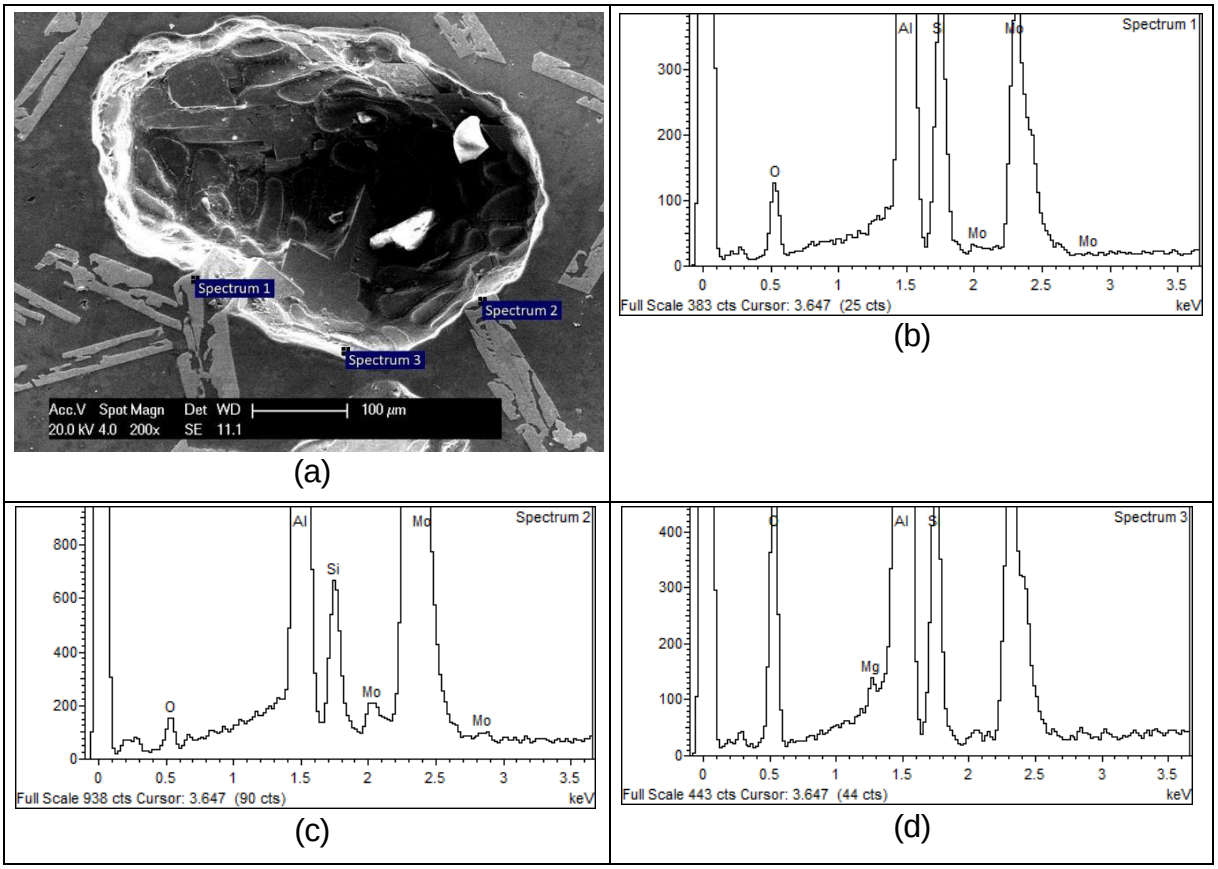


Figure 4-35: (a) High magnification SEM micrographs of a gas pore on the polished surface of Mo masteralloy, Figures 2. (b) to (d) Corresponding EDX spectra (1, 2 and 3) in (a)

Table 4-42: EDX elemental composition of the points marked in Figure 4-35 (a)

	Spectrum 1		Spectrum 2		Spectrum 3	
Element	Weight%	Atomic%	Atomic%	Weight%	Atomic%	Weight%
O K	12.94	24.50	4.96	12.22	25.27	36.44
Mg K	0.00	0.00	0.00	0.00	0.30	0.29
Al K	49.42	55.49	42.72	62.41	62.96	53.85
Si K	10.65	11.49	3.90	5.48	11.46	9.42
Mo L	26.99	8.52	48.42	19.89	0.00	0.00

Higher magnification SEM images of a number of intermetallic compounds have been presented in Figure 4-36 (a) to Figure 4-36 (c), showing the intermetallic compounds ($Mo_4Al_{11}Si$ based on EDX results) possess a long facetted rectangular shape (or β shape) varying from 50 µm to 100 µm in width and length.

The corresponding EDX elemental compositions to the points marked in Figure 4-36 (a) to (c) have been shown in Figure 4-36 (d) to Figure 4-36 (f), respectively, and have been presented in Table 4-43.

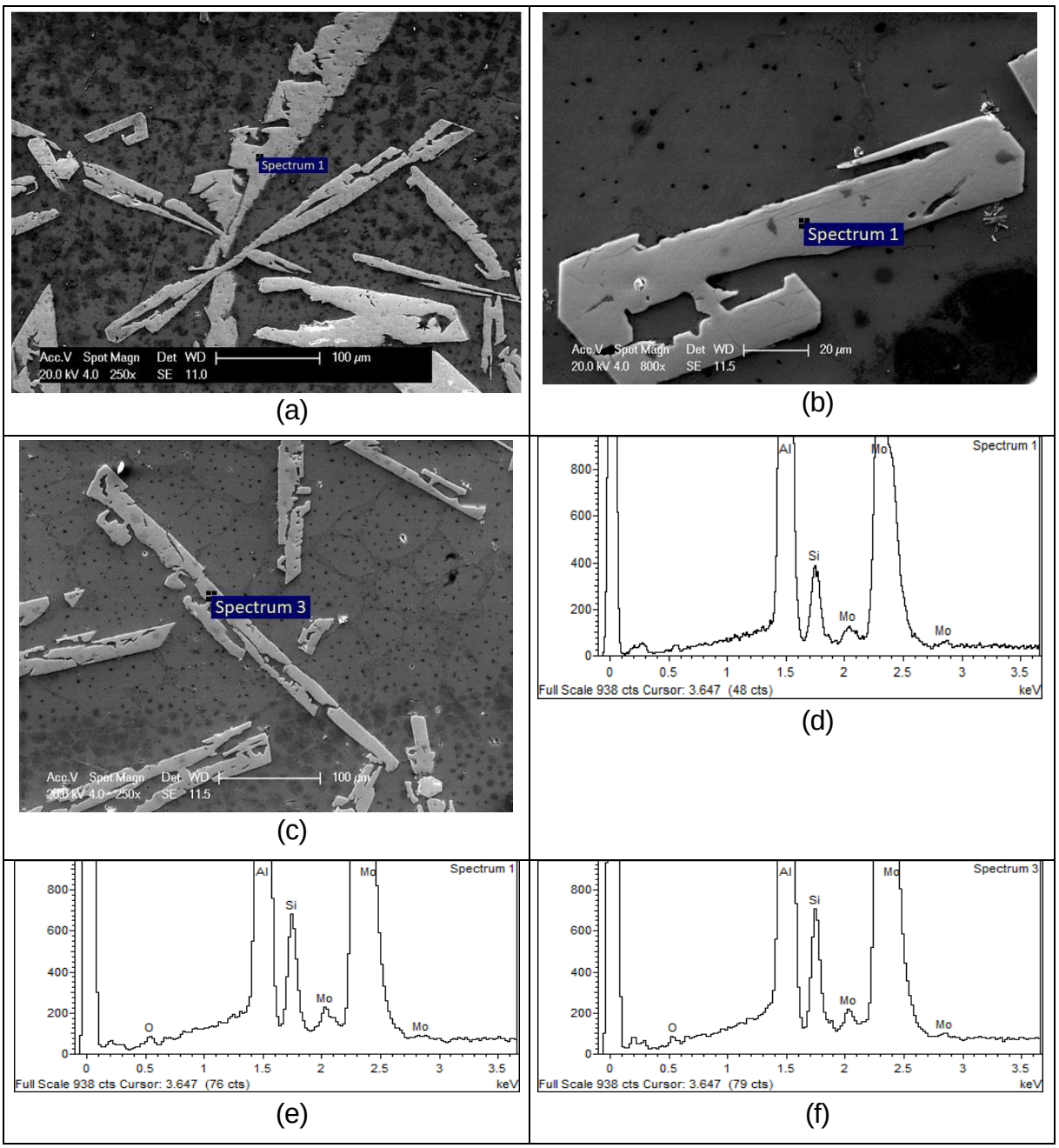


Figure 4-36: (a) to (c) high magnification of different Al-Mo intermetallic compounds (blocky shape) showing $Al_{34}Si_3Mo_{11}$ intermetallic compounds on the polished surface of Mo masteralloy (d) to (f) EDX spectra of the points marked in (a) to (c), respectively

Table 4-43: EDX elemental composition of the points marked in Figure 4-36 (a) to (c)

	Spectrum 1		Spectrum 1		Spectrum 3	
Element	Weight%	Atomic%	Weight%	Atomic%	Weight%	Atomic%
O K	0.00	0.00	1.48	3.84	1.52	3.93
Al K	45.07	71.39	44.37	68.43	44.66	68.52
Si K	3.85	5.86	4.04	5.99	4.15	6.11
Mo L	51.08	22.75	50.11	21.74	49.68	21.44

4.2.2.1.2 Fractured surfaces of 2L99 + 10 wt. % Mo testbars (Masteralloy)

Low to high-magnification SEM micrographs of a fractured surface of a Mo masteralloy testbar are presented in Figure 4-37 (a) to Figure 4-37 (d). The low magnification micrograph shown in Figure 4-37 (a) showed the presence of a crack of approximately 700 µm in length. Figure 4-37 (b) to Figure 4-37 (d) show progressively higher magnification images of the area marked in Figure 4-37 (a). Figure 4-37 (c) shows the presence of an oxide particle (SiO_2) of 150 µm in diameter.

Figure 4-37 (d) shows the SEM backscatter image of Figure 4-37 (c), which clearly indicates the presence of intermetallic compounds seen as white, roughly rod-shaped particles. The EDX elemental composition of the area marked as Spectrum 4 in Figure 4-37 (c) has been presented in Figure 4-37 (e), and EDX elemental composition is shown in Table 4-44, which showed SiO_2 with Al 0.6 at.% and Mg 4 at.%.

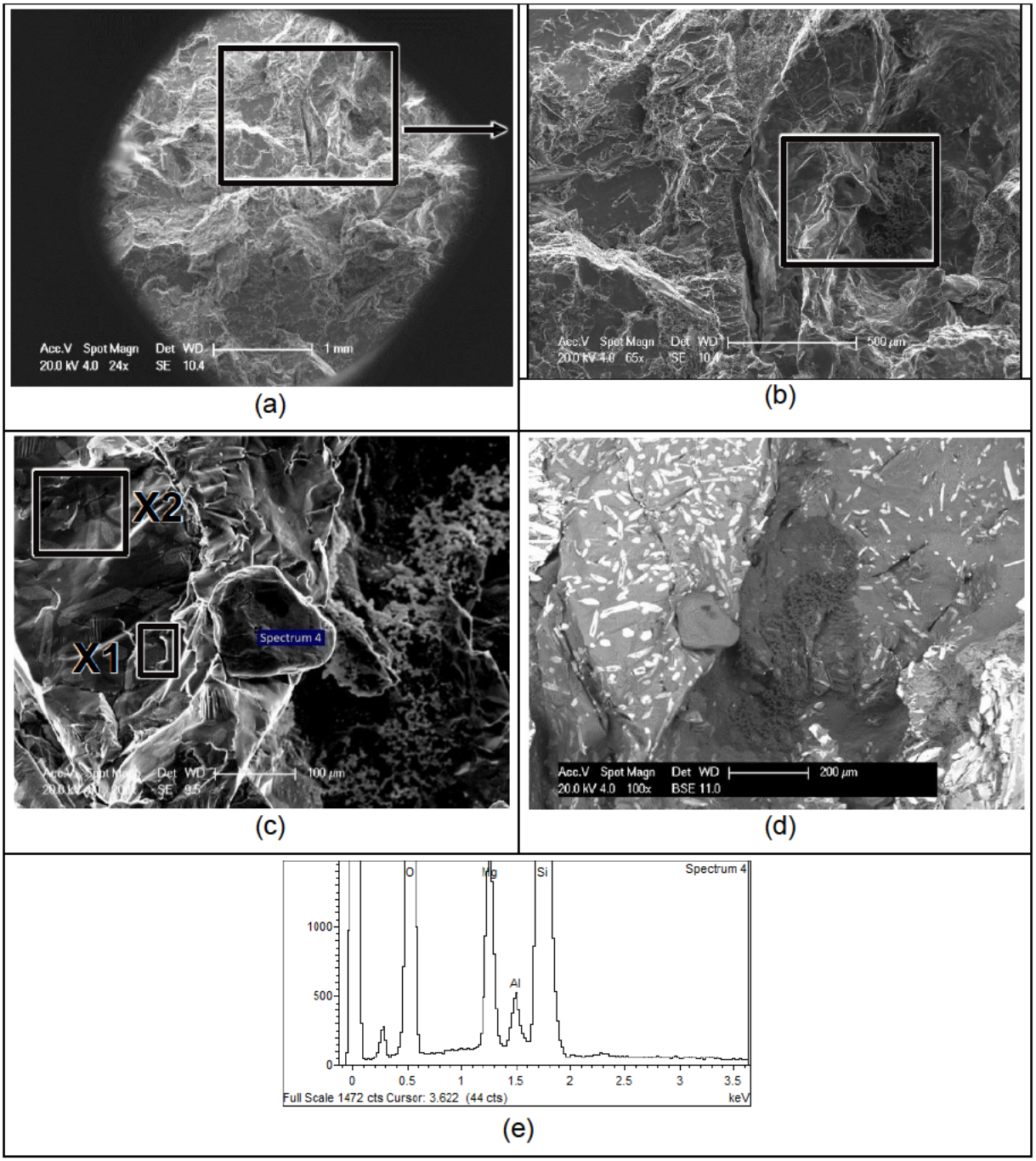
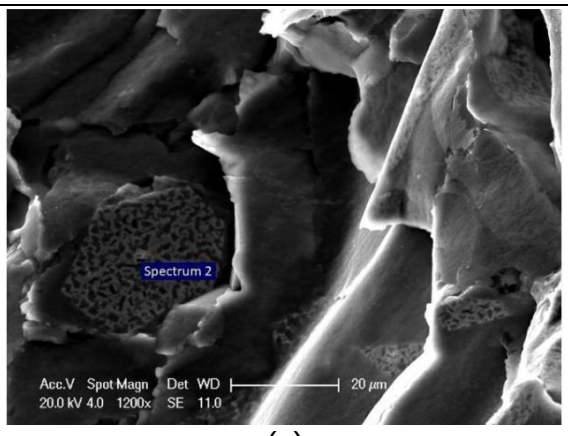


Figure 4-37: (a) low magnification SEM micrographs of a Mo masteralloy testbar, (b) high magnification of the area marked in (a), (c) high magnification of the area marked in (b), (d) BSE image of (c), (e) EDX corresponding for the area marked in (c)

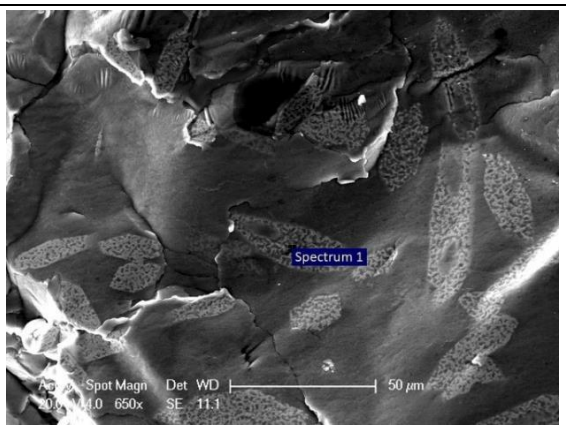
Table 4-44: EDX elemental composition of the area marked in Table 4-37 (c)

	Spectrum 4	
Element	Weight%	Atomic%
O K	59.70	71.84
Mg K	4.82	3.81
Al K	0.96	0.68
Si K	34.52	23.66

High-magnification SEM micrographs of the areas marked as X1 and X2 in Figure 4-37 (c) have been shown in Figure 4-38 (a) and Figure 4-38 (b). Figure 4-38 (a) showed the presence of ($MoAl_2Si$), a hexagonal intermetallic compound (approximately 32 µm in length and 20 µm in width) and oxide (spinel). Figure 4-38 (b) showed the presence of $MoAl_2Si$ (elliptical-shaped intermetallic compounds of approximately 50 µm in length and 20 µm in width) and oxide (spinel). Figure 4-38 (c) and Figure 4-38 (d) show the corresponding EDX spectra of the areas marked in Figure 4-38 (a) and Figure 4-38 (b), respectively. The EDX spectra for the area marked in Figure 4-38 (a) and Figure 4-38 (b) are presented in Table 4-45.



(a)



(b)

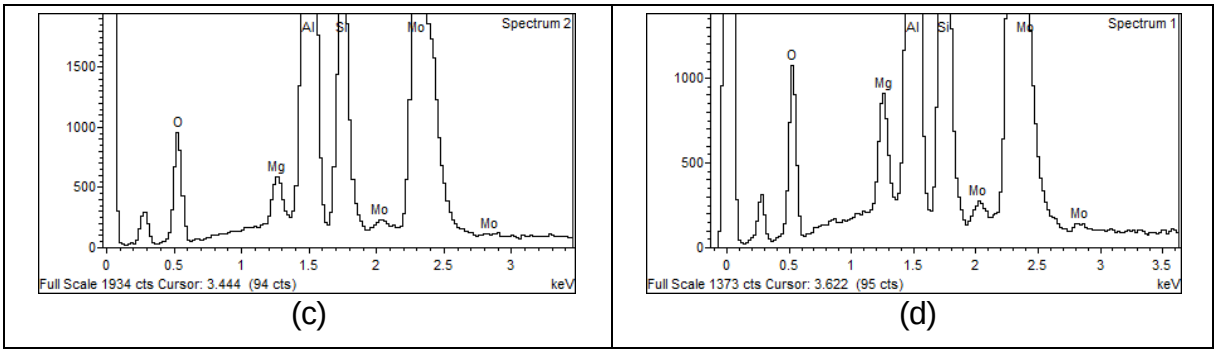


Figure 4-38: (a) and (b) high magnification SEM images of X1 and X2 areas marked in Figure 4-37 (c), (c) and (d) EDX corresponding spectra (Spectrum 2 and Specturm1) (a) and (b) respectively

Table 4-45: EDX elemental composition of the area marked in Figure 4-38 (a) and (b)

	Spectrum 2		Spectrum 1	
Element	Weight%	Atomic%	Weight%	Atomic%
O K	20.46	36.93	21.95	42.78
Mg K	1.29	1.66	2.29	2.94
Al K	28.53	36.01	23.31	26.94
Si K	11.72	13.03	13.11	14.55
Mo L	37.98	12.36	39.34	12.79

The morphology of the oxides observed as spinel (with Mg content of approximately 0.8 at.%), and alumina oxide on the fractured surface of the Mo masteralloy are shown in Figure 4-39 (a) and Figure 4-39 (b). The oxide particles (spinel) observed in Figure 4-39 (a) were of a spherical shape, measuring less than 1 µm in diameter. Figure 6 (b) shows the oxides (alumina) with a flake-shape morphology.

The EDX elemental composition of spectra marked in Figure 4-39 (a) and Figure 4-39 (b) are shown in Figure 4-39 (c) and Figure 4-39 (d), respectively. The EDX spectra for the points marked in Figure 4-39 (a) and Figure 4-39 (b) are presented in Table 4-46.

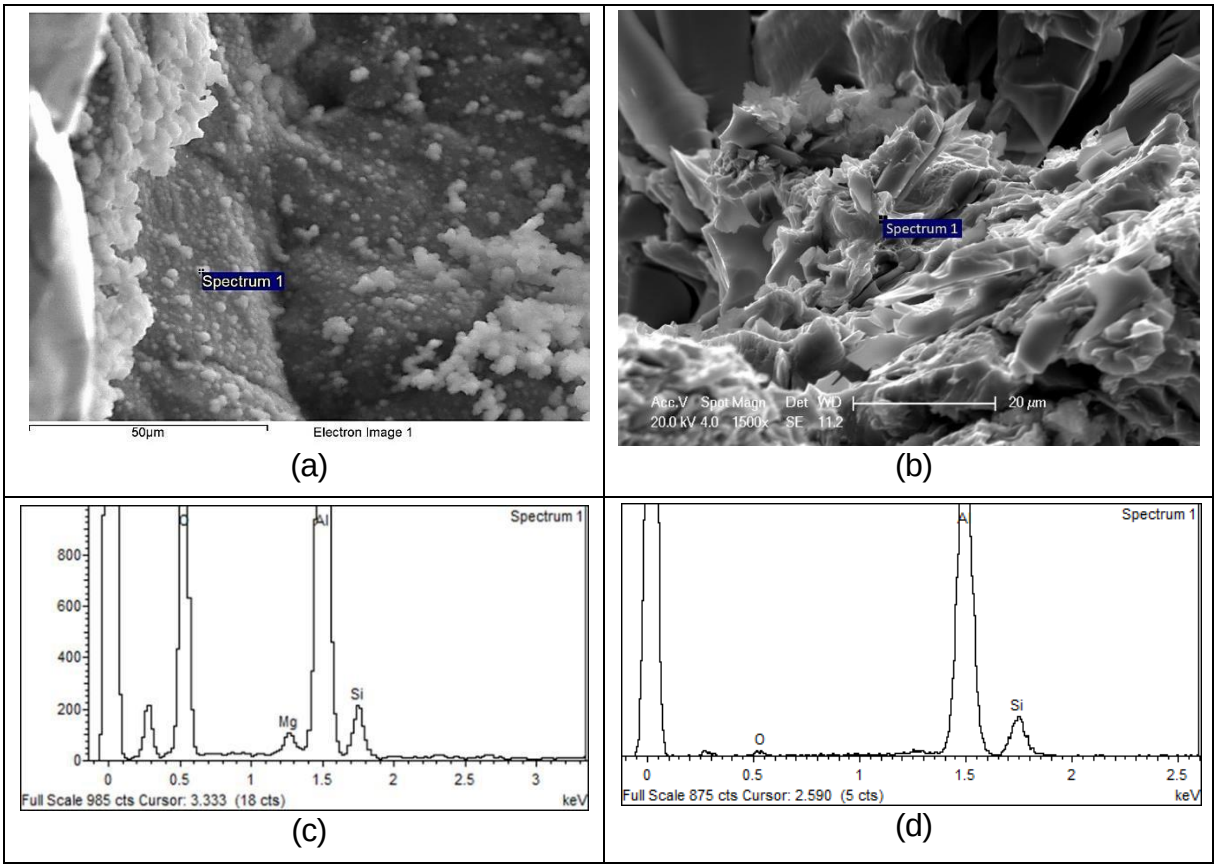


Figure 4-39: (a) High magnification SEM micrographs of the spherical oxide particles on 2L99 + 10 wt.% Mo, (b) High magnification SEM micrographs of the flake oxide particles on 2L99 + 10 wt.% Mo, (c) and (b) Corresponding EDX spectra in (a) and (b)

Table 4-46: EDX elemental composition of the area marked in Figure 4-39 (a) and (b)

	Spectrum 1 marked in Figure 4-39 (a)		Spectrum 1 marked in Figure 4-39 (b)	
Element	Weight%	Atomic%	Weight%	Atomic%
O K	55.91	68.18	6.86	11.15
Mg K	1.04	0.83	0	0
Al K	38.32	27.71	71.44	68.79
Si K	4.73	3.28	21.70	20.07

An SEM backscatter (BSE) micrograph of an area inside one of the pores on the fractured surface of a Mo masteralloy is shown in Figure 4-40 (a). The distinction between the atomic number of various elements showed the presence of Mo intermetallic compounds as white rod-shaped particles nucleated in the Al-Si eutectic

boundary between the Al grains. The rod-shaped Mo particles ($Mo_{1.5}AlSi_2$) were measured to be 4 µm x 20 µm on average. The EDX elemental compositions of the spectra marked in Figure 4-40 (a) are shown in Figure 4-40 (b) to Figure 4-40 (e) and Table 4-47.

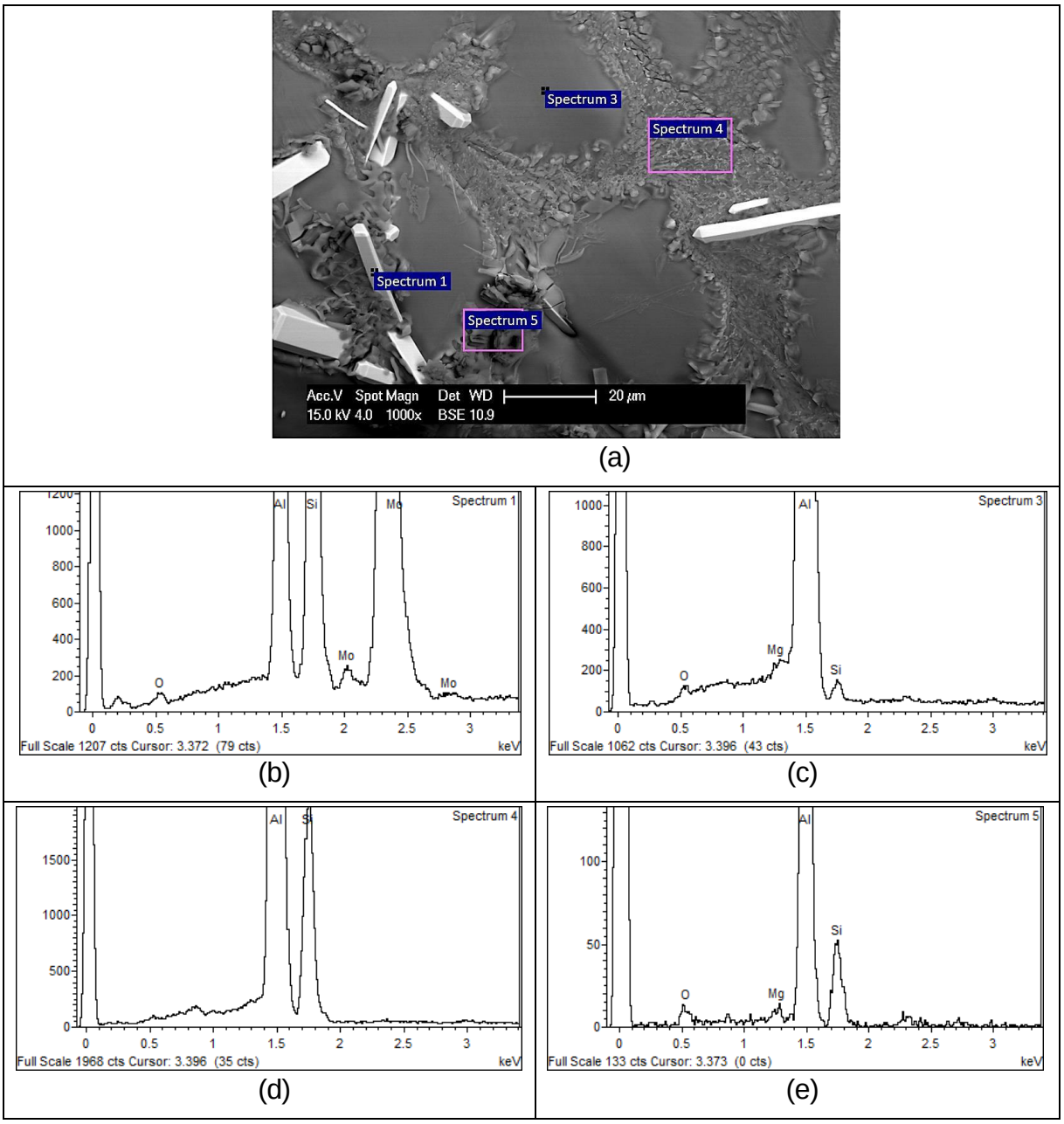


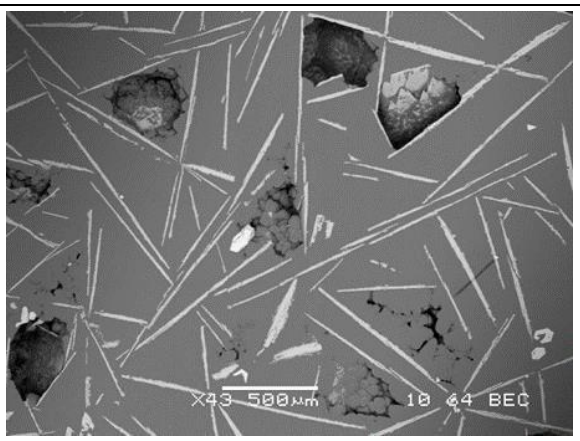
Figure 4-40: (a) High magnification SEM micrographs of the intermetallics in oxide particles on 2L99 + 10 wt.% Mo, (b) Corresponding EDX spectra in (a)

Table 4-47: EDX elemental composition of the area marked in Figure 4-40 (a)

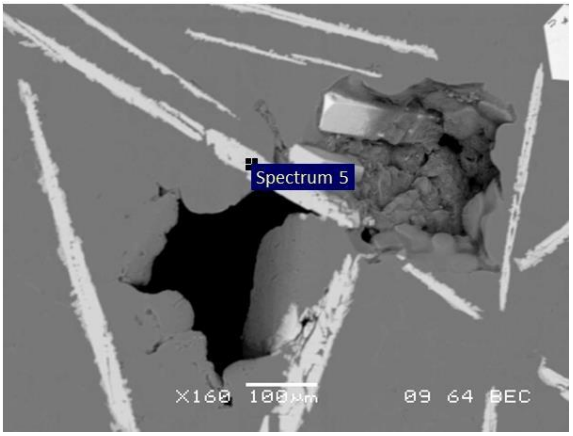
	Spectrum 1		Spectrum 3		Spectrum 4		Spectrum 5	
Element	Weight%	Atomic%	Weight%	Atomic%	Weight%	Atomic%	Weight%	Atomic%
O	1.45	4.37	1.02	1.71	0.00	0.00	6.85	11.10
Mg	0.00	0.00	0.05	0.06	0.00	0.00	1.04	1.11
Al	15.12	27.09	97.82	97.18	80.16	80.79	73.73	70.83
Si	21.77	37.47	1.10	1.05	19.84	19.21	18.38	16.96
Mo	61.66	31.07	0.00	0.00	0.00	0.00	0.00	0.00

Top and bottom of the 2L99 + 10 wt.% Mo ingot was characterised and showed the presence of cavities caused by gas porosity in the matrix, as well as numerous intermetallic compounds as needle and blocky faceted shapes. Low and high-magnification SEM micrographs of a typical top polished surface of the Mo masteralloy ingot are presented in Figure 4-41 (a) and Figure 4-41 (b).

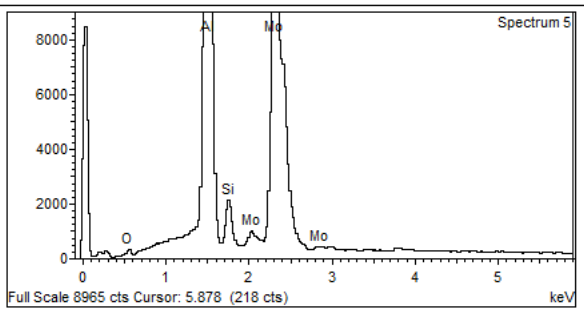
Figure 4-41 (b) shows needle-shaped β-phase ($Mo_{7.3}Al_{24}Si$) having a length range of varying from 100 µm to 900 µm and marked as Spectrum 5, the EDX spectrum 5 is shown in Figure 4-41 (c), and EDX elemental compositions are presented in Table 4-48.



(a)



(b)



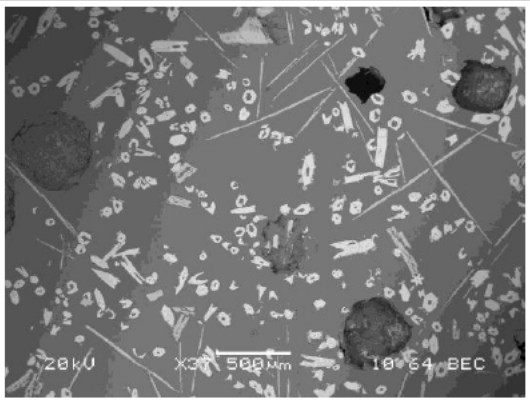
(c)

Figure 4-41: (a) and (b) low and high magnification of BSE image of the top of the Mo masteralloy ingot (c) EDX spectrum for the point marled as Spectrum 7 Figure 4-41 (b)

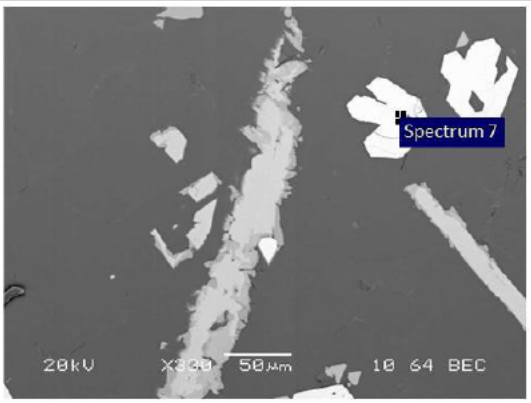
Table 4-48: EDX elemental composition of the area marked in Figure 4-41

	Spectrum 5	
Element	Weight%	Atomic%
O K	1.21	3.14
Al K	46.54	71.77
Si K	2.32	3.43
Mo L	49.94	21.66

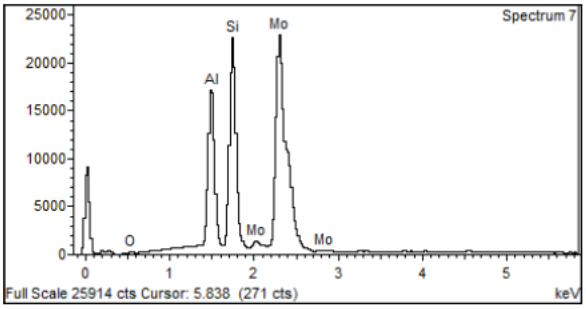
Low and high-magnification SEM micrographs of a typical bottom polished surface of the Mo masteralloy ingot are presented in Figure 4-42 (a) to Figure 4-42 (b). Figure 4-42 (b) shows the α- phase ($Mo_{1.2}AlSi_{1.5}$) as a blocky faceted shape marked in Spectrum 7 with a length varying range of 30 µm to 150 µm. The EDX spectrum is shown in Figure 4-42 (c), and the EDX elemental compositions are presented in Table 4-49. A summary of morphology and composition phases found in 2L99 + 10 wt.% Mo are presented in Table 4-50.



(a)



(b)



(c)

Figure 4-42: (a) and (b) low and high magnification of BEC image of the bottom of the Mo masteralloy ingot (c) EDX spectrum for the point marked as Spectrum 5

Table 4-49: EDX elemental composition of the area marked in Figure 4-42 (b)

	Spectrum 7	
Element	Weight%	Atomic%
O K	1.48	4.51
Al K	14.15	25.52
Si K	22.19	38.43
Mo L	62.18	31.53

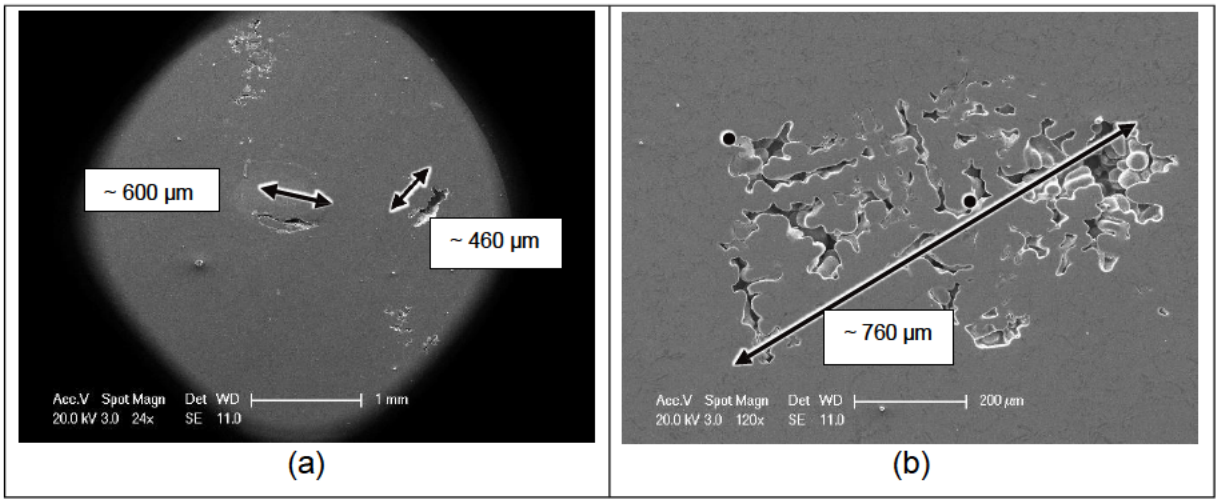
Table 4-50: Summary of the phases on the masteralloy of Mo (2L99 + 10 wt.% Mo)

Masteralloy 2L99 + 10 wt.% Mo	Name	Size
Oxides on the fractured surface of the masteralloy	Mostly spinel	- spherical spinel less than 1 µm in diameter
	slightly alumina	-An oxide layer, probably alumina 80 µm in length
	slight SiO_2	-SiO2 150 µm in diameter
Nitrides	None	NA
Intermetallic particles on the polished surface of the masteralloy	$Mo_{1.5}AlSi_2$	They are varying from 25 µm to 100 µm in width and length.
	β- shape $Mo_4Al_{11}Si$	They are varying from 50 µm to 100 µm in width and length.
Intermetallic particles on the fractured surface of the masteralloy	$MoAl_2Si$	approximately 32 µm in length and 20 µm in width
	$MoAl_2Si$	approximately 50 µm in length and 20 µm in width
	$Mo_{1.5}AlSi_2$	average range 4 µm* 20 µm.
Intermetallic particles on the ingot of the masteralloy 2L99 + 10 wt.% Mo top and bottom	Blocky $Mo_{1.2}AlSi_{1.5}$	varying from 30 µm to 150 µm
	β- shape $Mo_{7.3}Al_{24}Si$	varying from 100 µm to 900 µm long

4.2.2.2 Characterisations of the phases on the polished surfaces of 2L99 + 0.4 wt % Mo

Polished surfaces of 2L99 + 0.4 wt.% Mo alloys were investigated using SEM and EDX in order to study the morphology and composition of various phases such as oxides, nitrides and intermetallic compounds. Figure 4-43 (a) to Figure 4-43 (d) show low to high magnification SEM micrographs of a representative low UTS (191.5 MPa) 2L99 + 0.4 wt.% Mo alloy testbar. Various bifilm defects with shrinkage porosities were observed, as shown in Figure 4-43 (a), ranging in length from 300 µm to 1500 µm (average 660 µm) with different orientations.

Figure 4-43 (b) to Figure 4-43 (d) show high-magnification SEM micrographs of three of the largest bifilms. EDX elemental composition of the points marked with black circles on these figures showed the edge of the defects to be oxides (spinel) with an average O content of 10 at.%. Figure 4-43 (e) shows a representative EDX composition of the points marked in Figure 4-43 (b) to Figure 4-43 (d).



(a) (b)

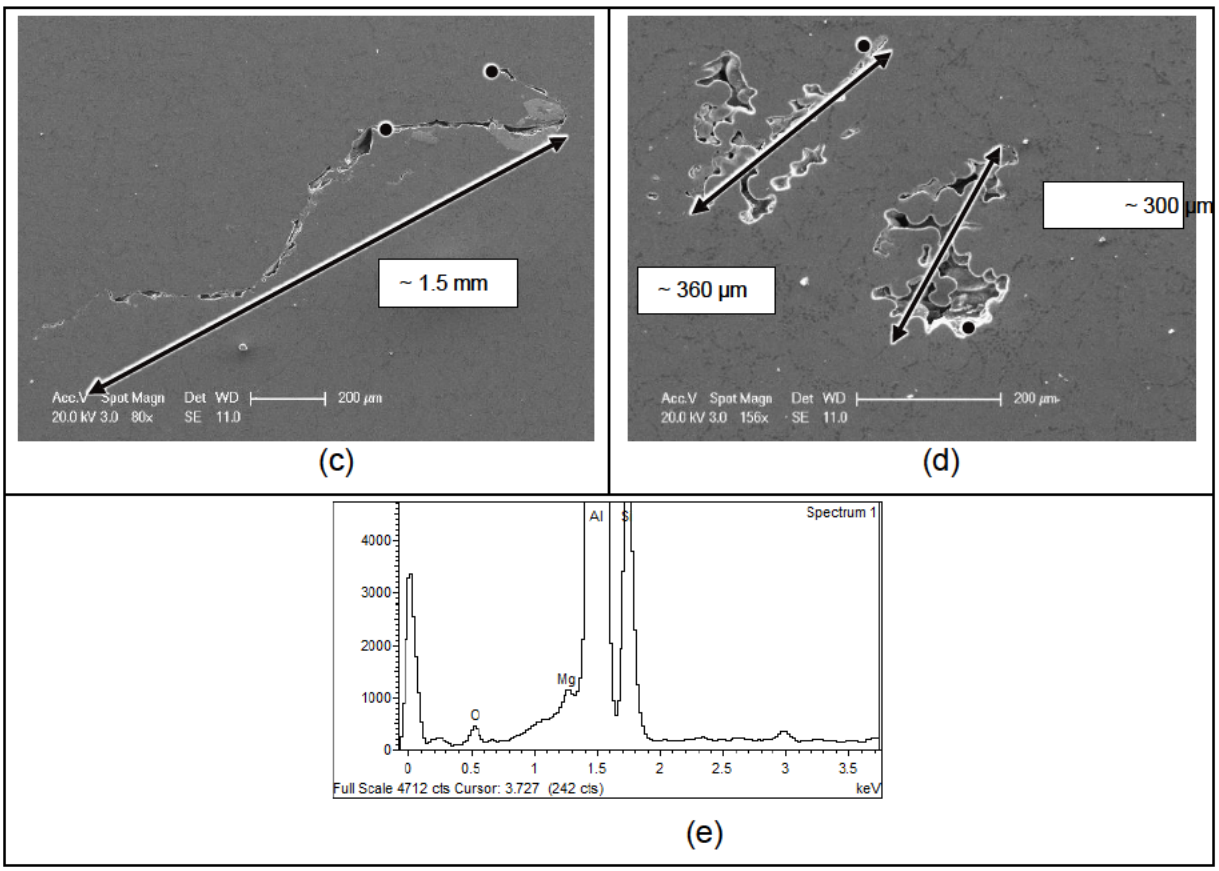


Figure 4-43: (a) Whole matrix SEM micrograph of a polished cross-section of the 2L99 + 0.4 wt.% Mo alloy with low UTS (191.5 MPa), (b) to (d) High magnification SEM micrographs of the main cavities detailed in (a), (e) EDX Spectrum1 for (b) to (d)

Table 4-51: EDX elemental composition of the points marked with black circles in Figure 4-43 (b) to (d)

	Spectrum 1	
Element	Weight%	Atomic%
O K	4.51	7.43
Mg K	0.55	0.60
Al K	73.87	72.19
Si K	21.06	19.78

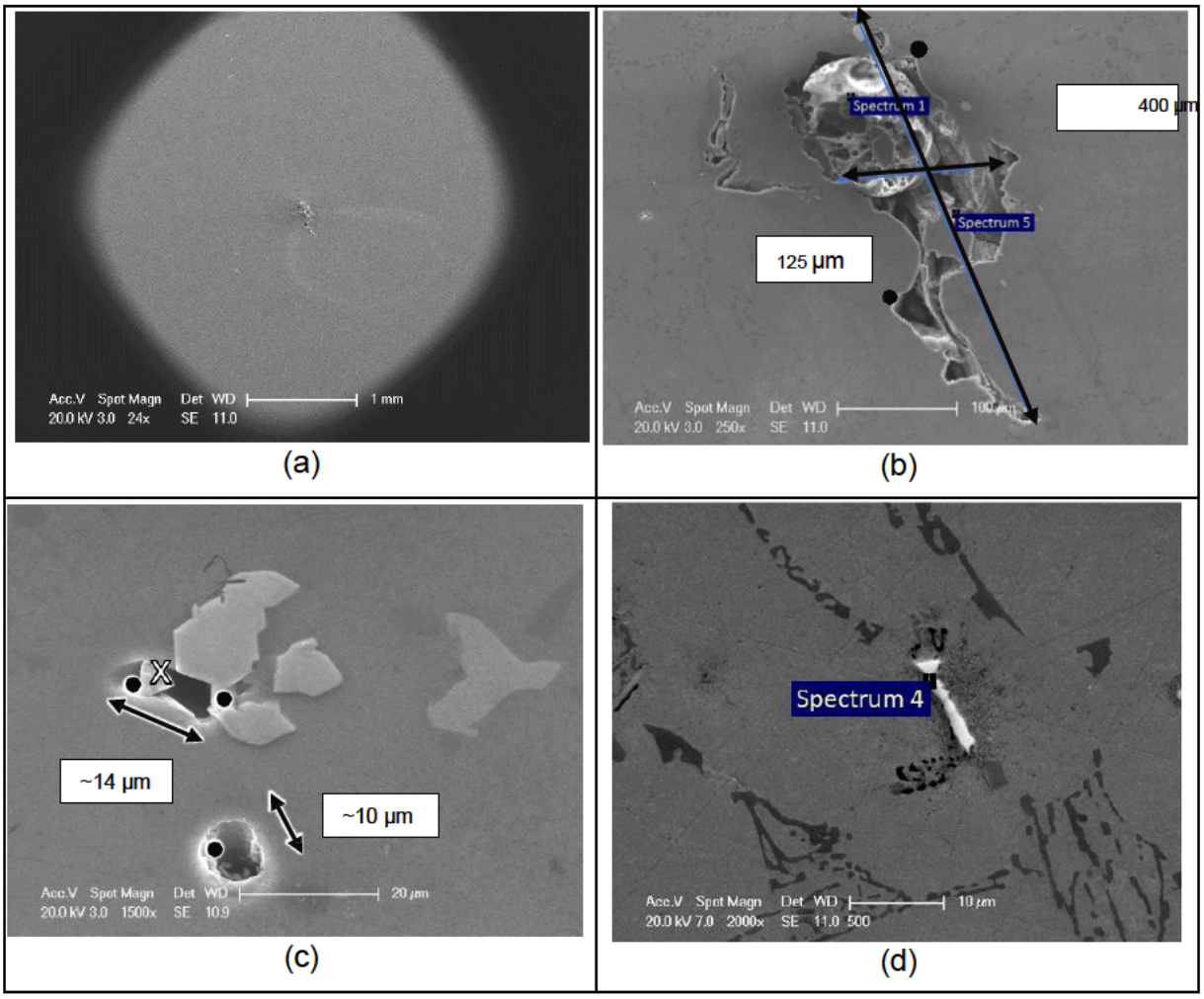
A low magnification SEM micrograph of the polished surface of a high UTS (292.8 MPa) 2L99 + 0.4 wt.% testbar has been shown in Figure 4-44 (a). Compared to the low UTS testbar presented in Figure 4-43, the study of high UTS testbars showed the observed defects to be less frequent and smaller in length, ranging from 10 µm to 400 µm (average 140 µm).

Figure 4-44 (b) shows a bifilm of 125 µm in width and 400 µm in length, with a spherical inclusion (slag) inside the bifilm marked as Spectrum. EDX analysis suggested the particle contains MgO with Na, Fe and Ca elements, which could be coming from the casting process. Slag inclusions are considered common and typically arise from improper removal of the cast alloys from the mould or accidental introduction into the casting process via other avenues, such as contaminated casting materials. The corresponding chemical analyses are presented in Figure 4-44 (d) and Table 4-52. The EDX Spectrum 1, represented all the black circles marked on the inclusion defects in Figure 4-44 (b) and Figure 4-44 (c). EDX spectrum was similar for all particles and showed the presence of O, Mg and Al at 5 at.%, 0.3 at.% and 72 at.%, respectively (spinel), as presented in Figure 4-44 (f).

Furthermore, the EDX spectrum of the point marked as Spectrum 5 in Figure 4-44 (b) showed the presence of nodular nitrides covering an area of 20 µm by 20 µm with N content of 8 at.%. It is likely that the presence of nitrides in this area results from significant consumption of oxygen, resulting in the formation of nitrides and reduction of the size of the bifilm.

Figure 4-44 (e) and Figure 4-44 (g), as well as Table 4-52, show the EDX spectra and composition of the marked areas in Spectrum 1 and Spectrum 5, marked presented in Figure 4-44 (b). Figure 4-44 (c) also shows a circular defect of approximately 10 µm diameter likely to be a gas porosity defect on the polished surface 2L99 + 0.4 wt.% Mo. Furthermore, intermetallic compounds were observed on the surface of 2L99 +0.4wt.% Mo shown in Figure 4-44 (c). Intermetallic particles nucleated on the wetted side of the bifilm, as marked in Figure 4-44 (c). This micrograph also showed nucleation of an intermetallic compound on both wetted sides of the bifilm marked as X (Spectrum 2 in

Figure 4-45 (a) and in Figure 4-44 (c)), possibly connecting both sides of the bifilm. Iron intermetallic with Mo ($Al_2FeSi_{2.6}$) was observed on the surface of 2L99+0.4wt.% Mo and shown in Figure 4-44 (d) with 10 µm length. The corresponding EDX spectrum is shown in Figure 4-44 (h).



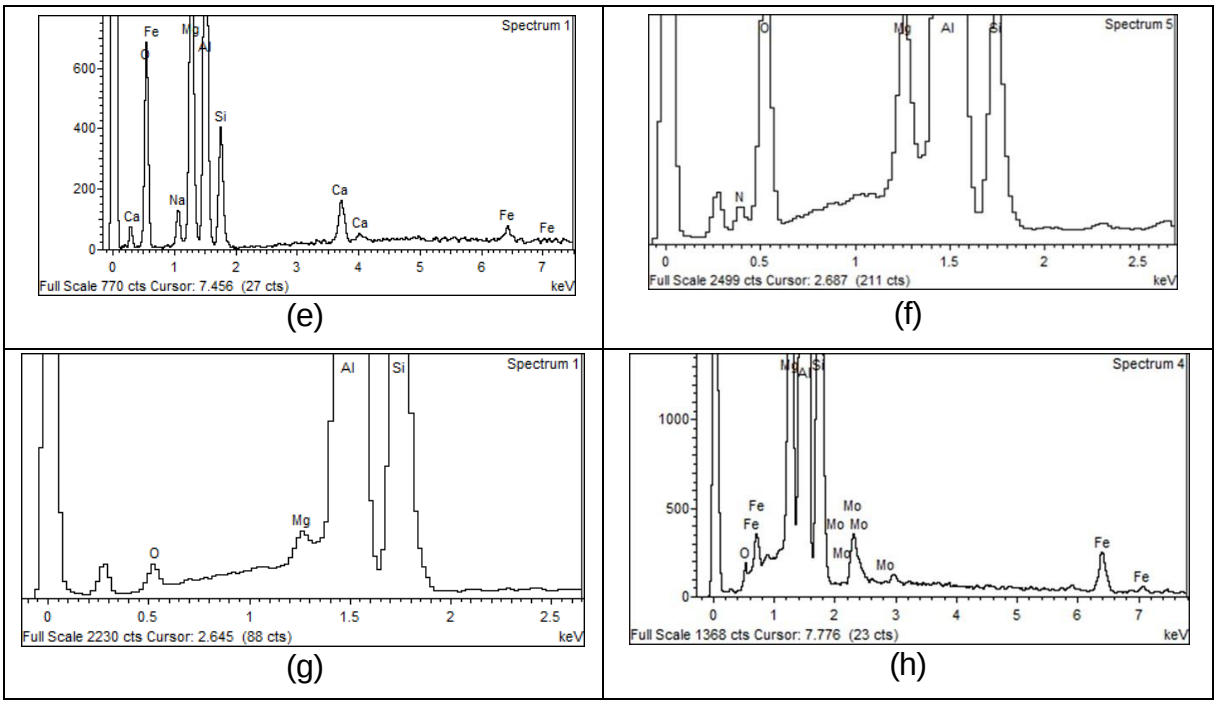


Figure 4-44: (a) Whole matrix SEM micrograph of a polished cross-section of the 2L99 + 0.4 wt.% Mo alloy with high UTS (292.8 MPa), (b) and (c) High magnification SEM micrographs of the main cavities detailed in (a), (d) to (f) corresponding EDX Spectrum1, Spectrum 5 and Spectrum 1

Table 4-52: EDX elemental composition of the points marked with black circles, Spectrum1, Spectrum 5 and Spectrum 1 in Figure 4-44 (b), Figure 4-44 (c) and Figure 4-44 (d)

	Spectrum 1		Spectrum 5		Spectrum 1		Spectrum 4	
Element	Weight%	Atomic%	Weight%	Atomic%	Weight%	Atomic%	Weight%	Atomic%
N K	0.00	0.00	5.32	8.60	0.00	0.00	0.00	0.00
O K	36.72	49.63	20.72	29.34	3.09	5.14	2.89	5.01
Mg K	16.20	14.41	1.76	1.64	0.32	0.36	5.96	6.81
Al K	31.47	25.22	66.27	55.64	72.75	71.88	32.41	34.24
Si K	8.08	6.22	5.93	4.78	23.84	22.62	40.36	40.12
Na K	2.02	1.90	0.00	0.00	0.00	0.00	0.00	0.00
Ca K	3.24	1.75	0.00	0.00	0.00	0.00	0.00	0.00
Fe K	2.26	0.88	0.00	0.00	0.00	0.00	18.76	15.22
Mo L	0.00	0.00	0.00	0.00	0.00	0.00	4.13	1.20

EDX compositions of the intermetallic compounds observed in Figure 4-44 (c) are presented in Figure 4-45. Figure 4-45 (b) to Figure 4-45 (f) and Table 4-53 show the EDX spectra and quantification of the areas marked in Figure 4-45 (a). The intermetallic

compounds observed had different facetted morphologies, such as $Mo_{1.5}Al\ Si_2$, $MoAl_8Si_3$, and $MoAl_{10}Si$, with a small amount of Fe (0.1 at.%). The size of the intermetallic compounds varied between 4 µm and 15 µm in length.

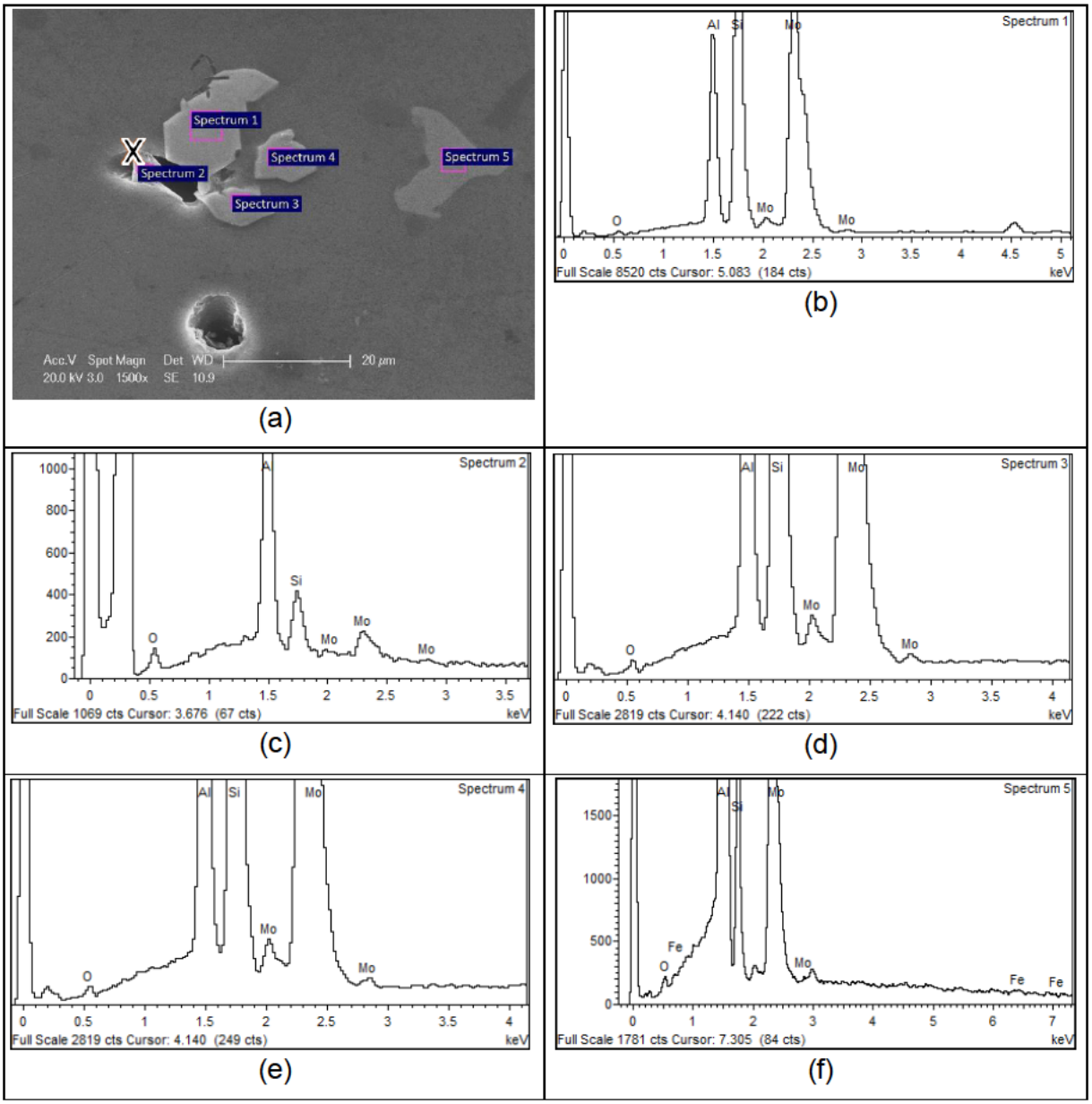
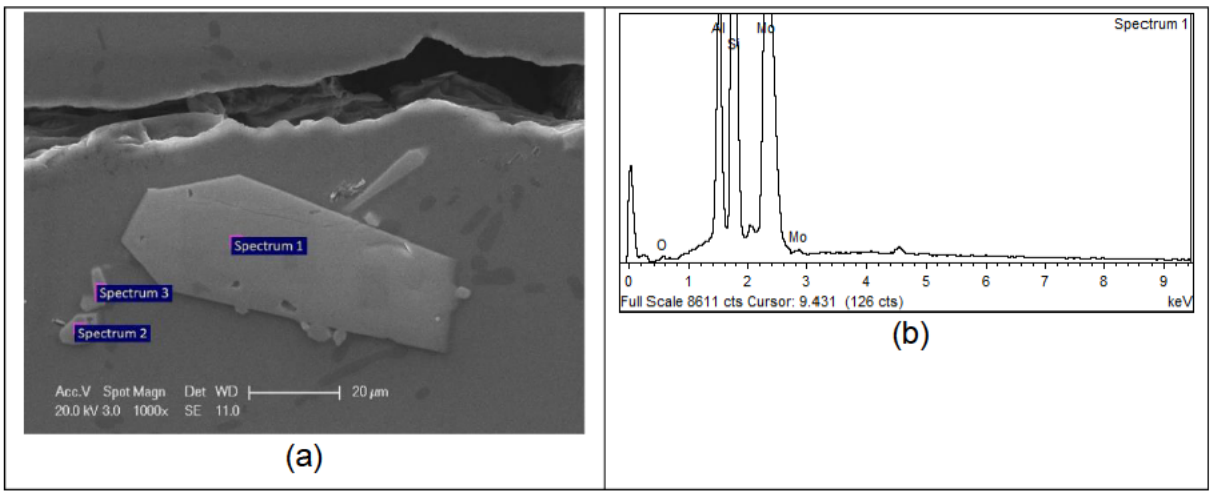


Figure 4-45: (a) SEM micrograph of a polished surface 2L99 + 0.4 wt.% Mo alloy showing the faceted intermetallic compounds grown on the bifilm (b) to (f) EDX spectra of the areas marked in (a)

Table 4-53: EDX elemental composition of the areas marked in Figure 4-45 (a)

	Spectrum 1		Spectrum 2		Spectrum 3		Spectrum 4		Spectrum 5	
Element	Weight %	Atomic %	Weight %	Atomic %	Weight %	Atomic %	Weight %	Atomic %	Weight %	Atomic %
O K	1.74	5.26	21.90	36.20	1.48	4.47	1.17	3.53	1.19	2.39
Al K	10.63	19.05	45.96	45.04	10.37	18.56	11.21	20.07	68.94	81.95
Si K	25.91	44.59	14.87	14.00	26.81	46.09	26.52	45.62	6.96	7.95
Fe K	0	0	0	0	0	0	0	0	0.19	0.11
Mo L	61.72	31.10	17.27	4.76	61.34	30.87	61.11	30.78	22.72	7.59

Further intermetallic compounds were observed on the polished surfaces of 2L99 + 0.4 wt.% Mo, as shown in Figure 4-46 to Figure 4-52, along with their EDX composition. Figure 4-46 (a) showed a large irregular hexagonal intermetallic of $Mo_{1.5}$ Al Si_2 of 80 µm by 40 µm in length and width marked as Spectrum 1 found approximately 10 µm from the bifilm above, and two smaller compounds of $Mo_{0.6}$(Al, Si), Mo (Al, Si_2)$_2$ (Spectra 2 and 3 respectively) of approximately 5 µm in length. The EDX spectra and quantification of the areas marked in Figure 4-46 (a) are provided in Figure 4-46 (b) to Figure 4-46 (d) and Table 4-54.



(a) (b)

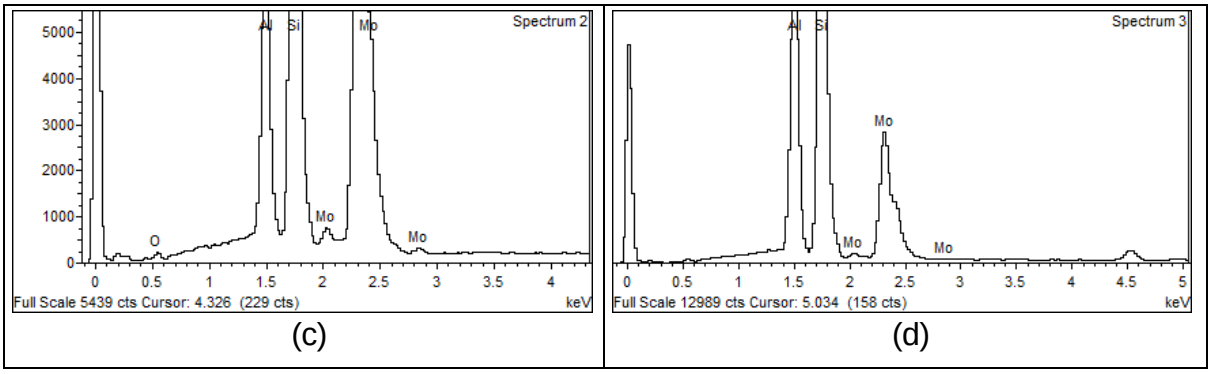


Figure 4-46: (a) SEM micrograph of a polished surface 2L99 + 0.4 wt.% Mo alloy showing three different faceted intermetallic compounds (blocky shape), (b) to (d) EDX spectra of the areas marked in (a)

Table 4-54: EDX elemental composition of the areas marked in Figure 4-46 (a)

	Spectrum 1		Spectrum 2		Spectrum 3	
Element	Weight%	Atomic%	Weight%	Atomic%	Weight%	Atomic%
O K	3.69	4.49	0.54	1.24	0.00	0.00
Al K	30.24	21.82	19.32	33.55	18.62	26.03
Si K	58.34	40.44	22.94	37.26	44.18	59.34
Mo L	163.84	33.25	57.74	28.20	37.20	14.63

Figure 4-47 (a) showed a large irregular hexagonal intermetallic of $Mo_7Al_5Si_8$ of 70 µm by 150 µm in length and width marked as Spectrum 1 grown on the small bifilms below the compound, and two smaller compounds of $Mo_2Al\ Si_2$ and $Mo_7Al_5Si_8$ (Spectra 6 and 7 respectively) of approximately 5 µm and 10 µm in length. The intermetallic compounds' regular or irregular hexagonal shapes were the most frequent shapes observed in the 2L99 + 0.4 wt.% Mo.

The EDX spectra and quantification of the areas are marked in Figure 4-47 (a) and are provided in Figure 4-47 (b) to Figure 4-47 (d) and Table 4-55.

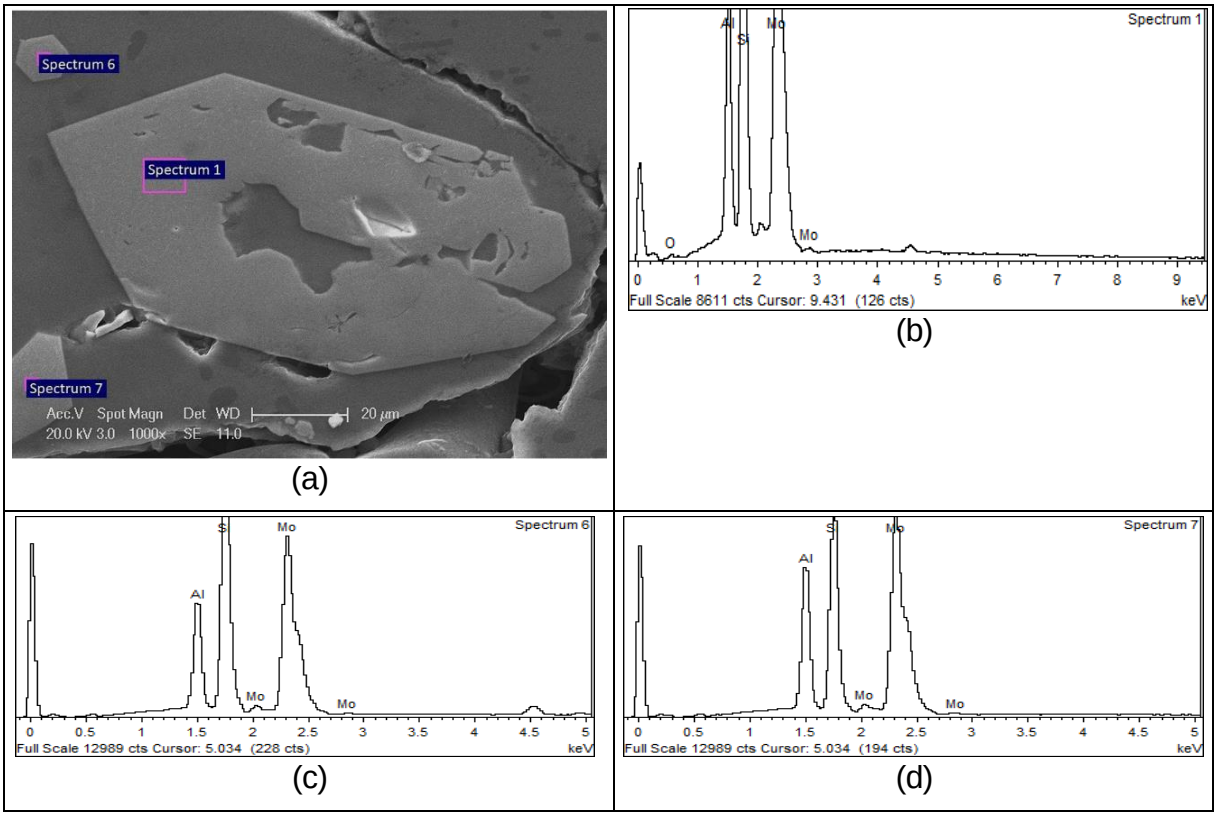


Figure 4-47: (a) SEM micrograph of a polished surface 2L99 + 0.4 wt.% Mo alloy showing hexagonal intermetallic compounds, (b) to (d) EDX spectra of the areas marked in (a)

Table 4-55: EDX elemental composition of the areas marked in Figure 4-47 (a)

	Spectrum 1		Spectrum 6		Spectrum 7	
Element	Weight%	Atomic%	Weight%	Atomic%	Weight%	Atomic%
O K	0.69	1.09	0.00	0.00	0.00	0.00
Al K	13.07	25.20	9.83	18.12	12.78	24.53
Si K	21.10	38.10	28.01	49.63	21.77	40.14
Mo L	65.83	35.70	62.17	32.25	65.45	35.33

Figure 4-48 (a) shows various irregular multi-faceted and hexagonal intermetallic compounds between 20 µm and 60 µm in length. Spectra 1 and 2 had the same composition ($Mo_{1.5}AlSi_2$). As spectra 3 and 5 ($Mo_7Al_5Si_8$) also had the same composition and Spectrum 4 suggested $Mo_5Al_5Si_6$. The EDX spectra and quantification of the areas marked in Figure 4-48 (a) are provided in Figure 4-48 (b) to Figure 4-48 (f) and Table 4-56. The EDX quantification of spectra 1, 2, 3 and 5 showed the presence of O at approximately 6 at.%. The O content was 30 at.% in 2L99+0.4 wt.% Mo, as shown in spectrum 4.

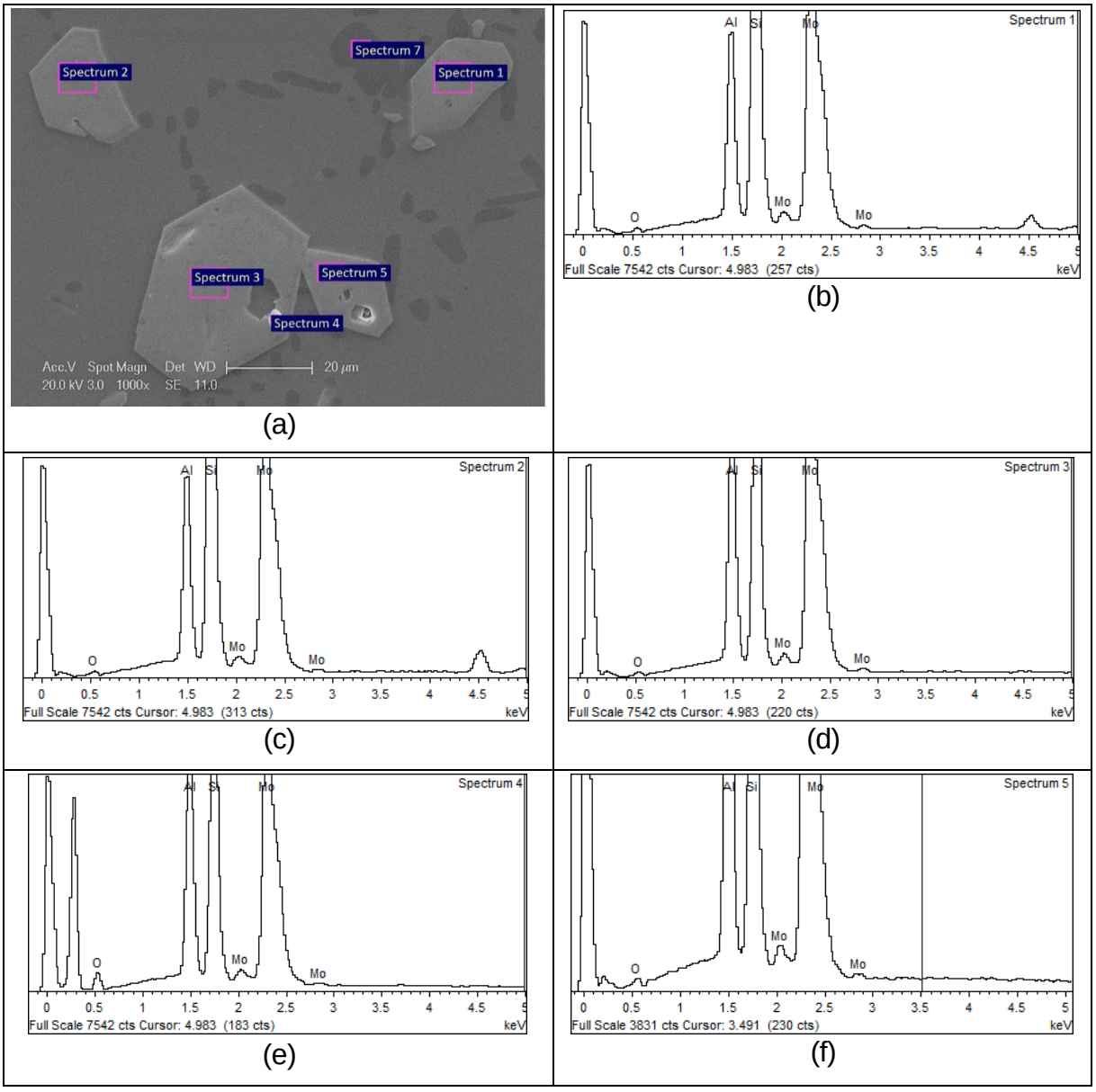


Figure 4-48: (a) SEM micrograph of a polished surface 2L99 + 0.4 wt.% Mo alloy showing different intermetallic compounds faceted and hexagonal shapes, (b) to (f) EDX spectra of the areas marked in (a)

Table 4-56: EDX elemental composition of the areas marked in Figure 4-48 (a)

	Spectrum 1		Spectrum 2		Spectrum 3		Spectrum 4		Spectrum 5	
Element	Weight %	Atomic %	Weight %	Atomic %	Weight %	Atomic %	Weight %	Atomic %	Weight %	Atomic %
O K	1.88	5.66	1.93	5.72	2.06	6.40	11.69	29.74	2.03	6.26
Al K	9.50	16.98	9.71	17.05	13.12	24.18	12.47	18.81	12.71	23.24
Si K	27.05	46.42	28.15	47.49	20.33	35.99	18.80	27.25	21.43	37.66
Mo L	61.57	30.94	60.21	29.73	64.49	33.43	57.04	24.20	63.84	32.84

Figure 4-49 (a) shows a multi-faceted intermetallic compound of $Mo_7Al_5Si_8$ measuring 40 µm by 150 µm in length and width marked as Spectrum 1, grown on the small bifilms (spinel) below the compound marked as Spectrum 3. Bifilms have also been shown in Figure 4-49 (a) marked as spectra 2 and 3 with O content of 10 and 4 at.%, respectively. The EDX spectra and quantification of the areas marked in Figure 4-49

(a) are provided in Figure 4-49 (b) to (d) and Table 4-57.

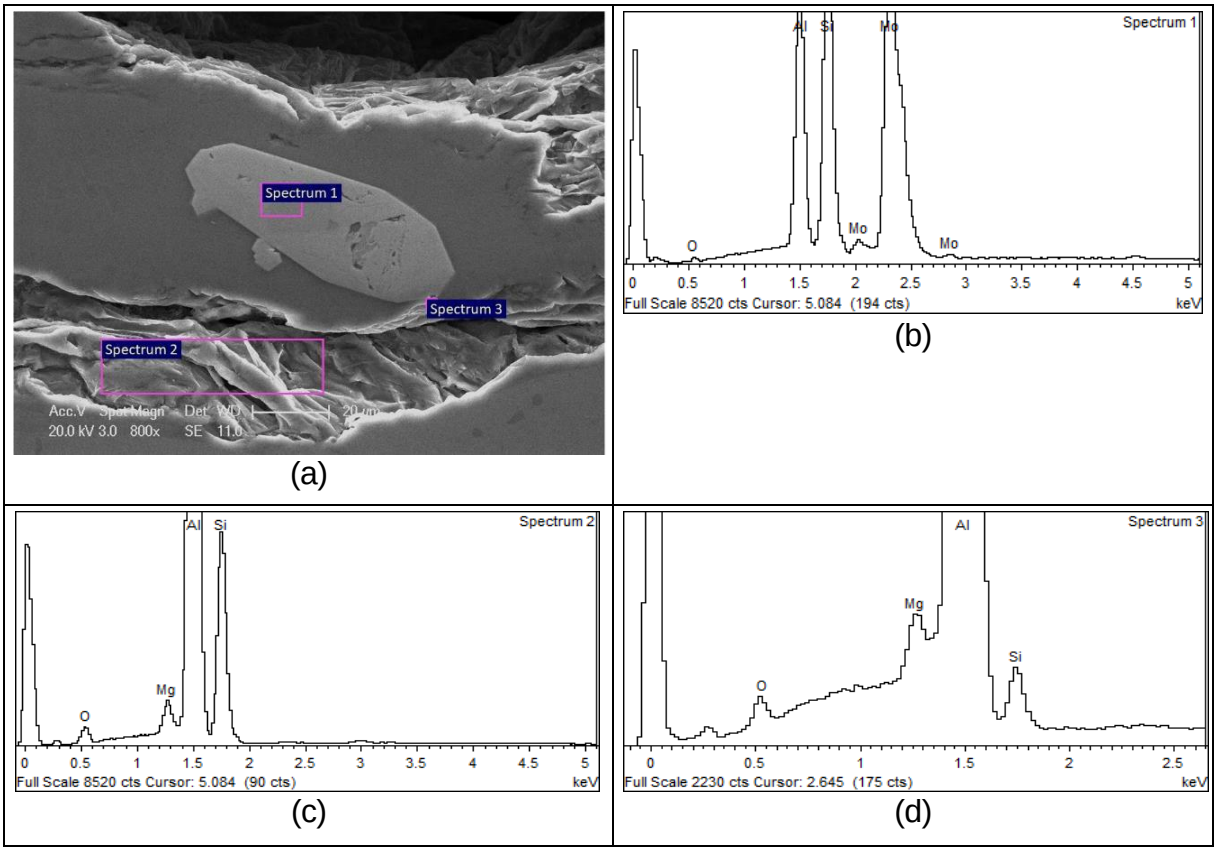


Figure 4-49 (a): SEM micrograph of a polished surface 2L99 + 0.4 wt.% Mo alloy showing a faceted intermetallic compound grown on bifilm (b) to (f) EDX spectra of the areas marked in (a)

Table 4-57: EDX elemental composition of the areas marked in Figure 4-49 (a)

	Spectrum 1		Spectrum 2		Spectrum 3	
Element	Weight%	Atomic%	Weight%	Atomic%	Weight%	Atomic%
O K	1.68	5.17	6.65	10.82	2.47	4.09
Mg K	0.00	0.00	1.47	1.58	0.46	0.50
Al K	13.99	25.54	67.39	64.94	95.05	93.49
Si K	20.95	36.74	24.48	22.67	2.02	1.91
Mo L	63.38	32.54	0.00	0.00	0.00	0.00

Figure 4-50 (a) showed various irregular multi-facetted intermetallic compounds of Mo as indicated by EDX. Spectra 1, 2 and 3 had the same composition ($Mo_{1.5}AlSi_2$) and were between 5 µm and 20 µm in length, and the EDX (Spectrum 4) suggested Mo(Al, Si)$_2$, which were of 2 µm length. EDX spectra and quantification of the areas marked in Figure 4-50 (a) are provided in Figure 4-50 (b) to (e) and Table 4-58. The EDX quantification of spectra in this figure showed the presence of O at approximately 3 at.%.

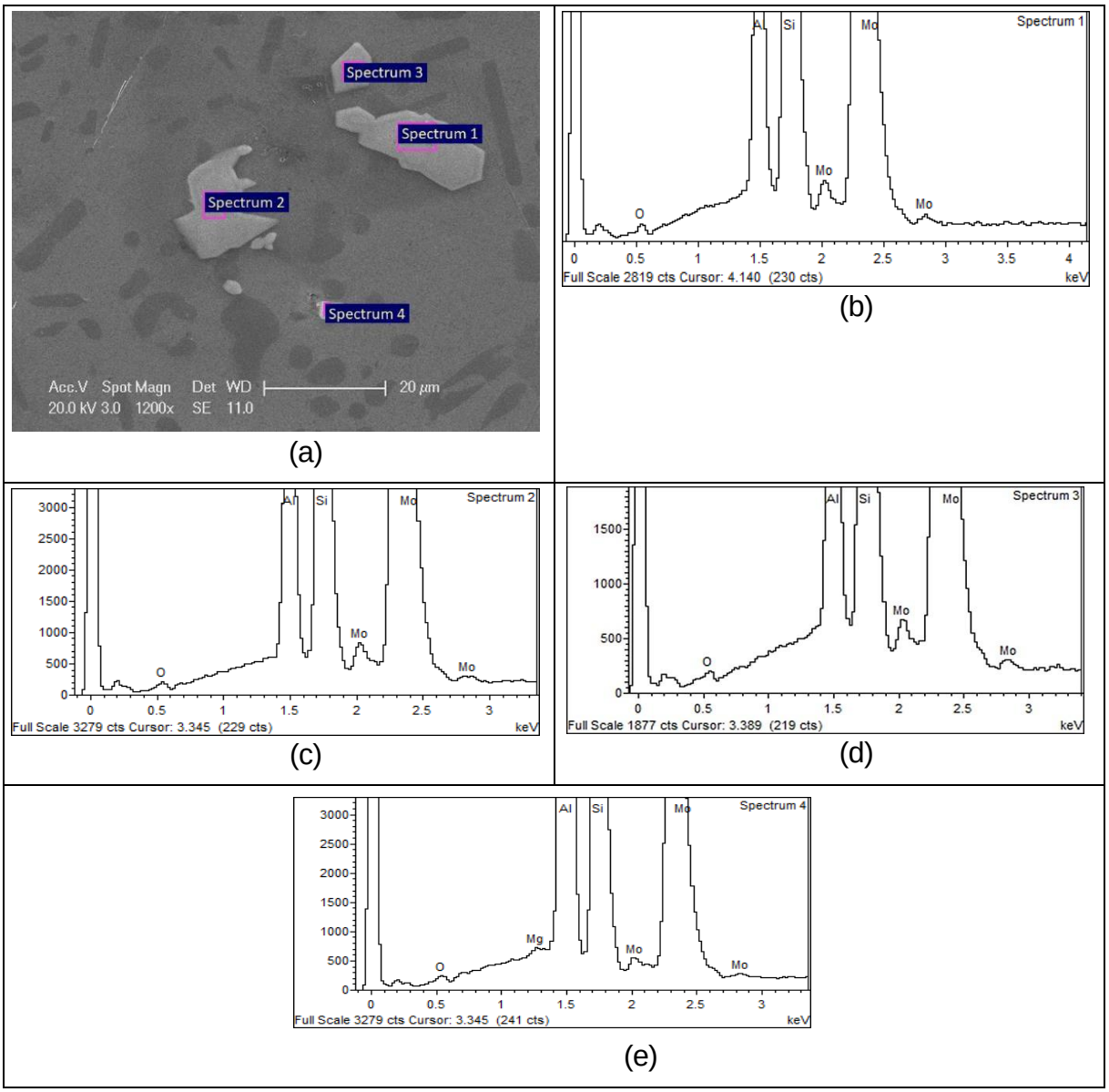


Figure 4-50: (a) SEM micrograph of a polished surface 2L99 + 0.4 wt.% Mo alloy showing the faceted intermetallic compounds (b) to (e) EDX spectra of the areas marked in (a)

Table 4-58: EDX elemental composition of the areas marked in Figure 4-50 (a)

	Spectrum 1		Spectrum 2		Spectrum 3		Spectrum 4	
Element	Weight%	Atomic%	Weight%	Atomic%	Weight%	Atomic%	Weight%	Atomic%
O K	1.22	3.67	1.61	4.87	1.02	2.86	3.29	4.89
Mg K	0.00	0.00	0.00	0.00	0.00	0.00	0.11	0.17
Al K	8.64	15.40	10.30	18.54	11.01	18.37	28.96	39.82
Si K	29.46	50.49	26.13	45.21	33.08	53.02	29.58	39.05
Mo L	60.69	30.45	61.96	31.38	54.89	25.75	40.05	16.07

Figure 4-51 (a) shows a multi-faceted intermetallic $Mo_{1.5}AlSi_2$ of 20 µm by 10 µm in length and width marked as Spectrum 1. EDX spectrum and quantification of the area marked in Figure 4-51 (a) provided in Figure 4-51 (b) and Table 4-59 showed O content of 4.78 at.%.

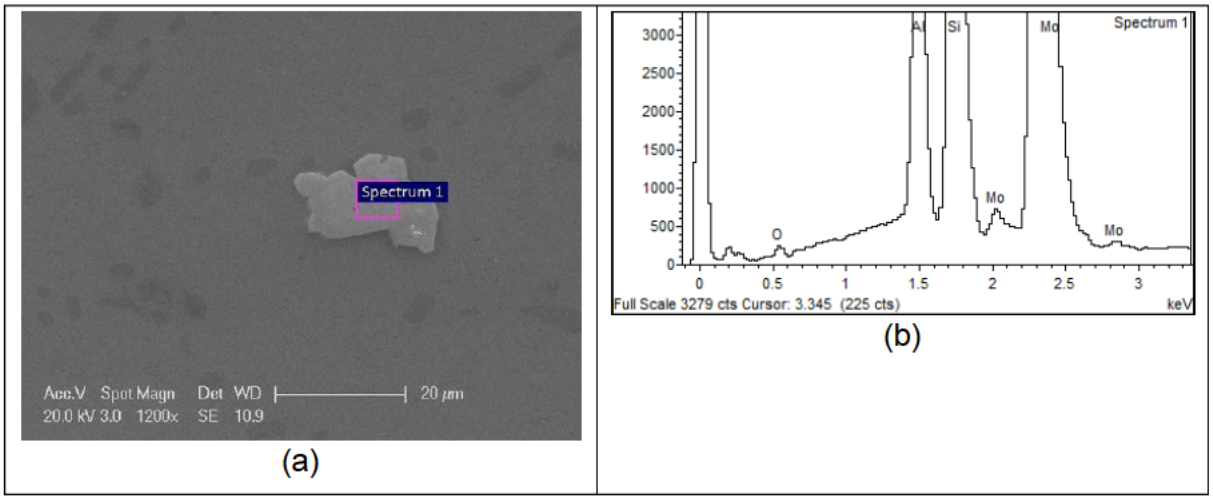


Figure 4-51: (a) SEM micrograph of a polished surface 2L99 + 0.4 wt.% Mo alloy showing a faceted intermetallic compound, (b) EDX spectrum of the area marked in (a)

Table 4-59: EDX elemental composition of the areas marked in Figure 4-51 (a)

Element	Weight%	Atomic%
O K	1.60	4.78
Al K	9.23	16.31
Si K	28.83	48.94
Mo L	60.34	29.98

A high magnification SEM micrograph of the inside of a bifilm defect observed on the polished surface of 2L99 + 0.4 wt.% Mo is shown in Figure 4-52 (a). The bifilm was thoroughly characterised using SEM and EDX to understand their morphology and composition, including a higher magnification study of an area marked as X1, shown in Figure 4-53 (a). As shown in Figure 4-52 (a) and based on EDX compositions, the bright surface around the bifilm was characterised as an oxide layer (spinel) with an average O content of 23 at.%. Furthermore, the EDX composition of Spectrum 1, as shown in Figure 4-52 (b), showed an O content of 35 at.%, Mg of 4 at.% and nitrogen content of 5 at % which suggest MgO and AlN. Spectra 2 and 3 in Figure 4-52 (c) and (d) showed a high amount of O of 60 at.% and 32 at.%, respectively. EDX composition also showed Mg (likely spinel) of 0.2 at.% and 1.3 at.%, respectively.

Spectrum 4 showed both O and Mg contents of 28 at.% and 1.2 at.%, respectively, with 10 at.% nitrogen, significantly higher than the nitrogen observed in 2L99+ 0.4wt.% Mo as the area marked as spectrum 1. Similarly, the composition of the area marked as spectrum 8 in Figure 4-52 (f) showed a high nitrogen content of 8 at.%, with O and Mg contents of 30 at.% and 1.7 at.%, respectively.

As observed in Figure 4-52 (a), the size of the bifilm around the area marked as spectrum 1 ~55 µm in width, where the nitrogen content was significantly lower than the rest of the bifilm (~20 µm width). This could suggest a reduction in the size of the bifilm following the consumption of most of the O and the subsequent formation of nitrides. Table 4-60 presents the quantification of the area marked as spectra 1,2,3,4 and 8 shown in Figure 4-52 (a). All the oxides marked in Spectra 2, 3, 4 and 8 were spinel; however, Spectrum 1 oxide was MgO.

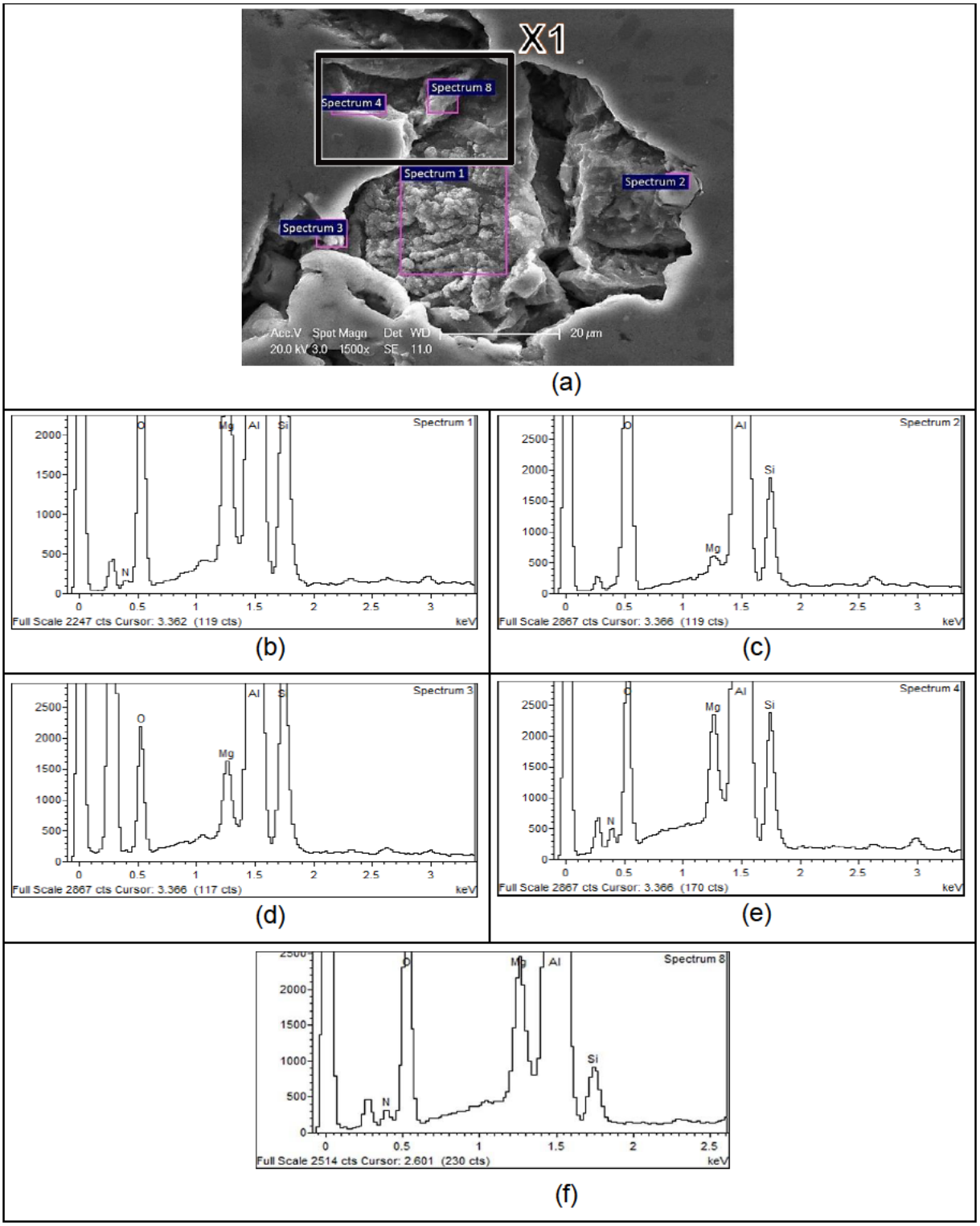


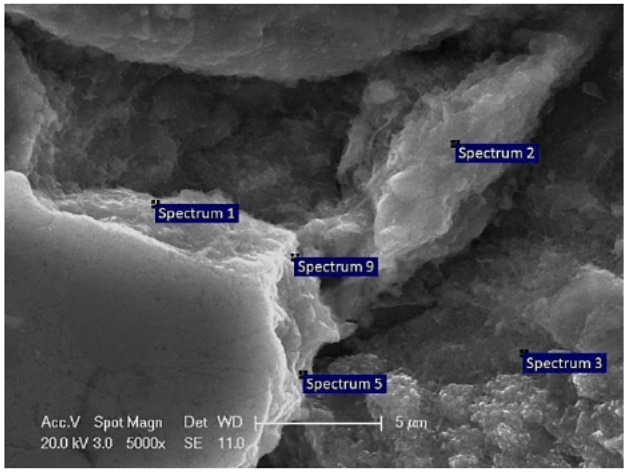
Figure 4-52: (a) SEM micrograph of a polished surface 2L99 + 0.4 wt.% Mo alloy showing a bifilm with oxide and nitride layers, (b) to (f) EDX spectra of the areas marked in (a)

Table 4-60: EDX elemental composition of the areas marked in Figure 4-52 (a)

	Spectrum 1		Spectrum 2		Spectrum 3		Spectrum 4		Spectrum 8	
Element	Weight %	Atomic %	Weight %	Atomic %	Weight %	Atomic %	Weight %	Atomic %	Weight %	Atomic %
N K	2.79	4.49	0.00	0.00	0.00	0.00	6.40	10.31	5.17	8.31
O K	24.51	34.59	47.65	60.62	21.65	31.87	19.88	28.04	21.85	30.73
Mg K	4.21	3.91	0.31	0.26	1.88	1.83	1.37	1.28	1.91	1.77
Al K	60.24	50.58	47.83	36.07	63.37	55.31	67.91	56.81	69.06	57.59
Si K	9.26	7.44	4.21	3.05	13.10	10.99	4.44	3.57	2.00	1.61

The high-magnification SEM micrograph of the area is marked as X1 in Figure 4-52 (a) is shown in Figure 4-53 (a) to observe the morphology of the nitride patches. The EDX composition of spectra 1, 2, 5 and 9 (shown in Figure 4-53 (b), (c), (e) and (f)) showed the content of nitrides in the range of 7.6 at.% to 9.4 at.%, varying in length between 5 µm and 10 µm, with a nodular morphology and O content of 20 to 30 at.%.

The EDX analysis of spectrum 3, as shown in Figure 4-53 (d), indicated the presence of oxides (spinel) at this location with O content of 4 at.% and Mg content of 0.5 at.%. Table 4-61 presents the EDX quantification of the spectra marked in Figure 4-53 (a).



(a)

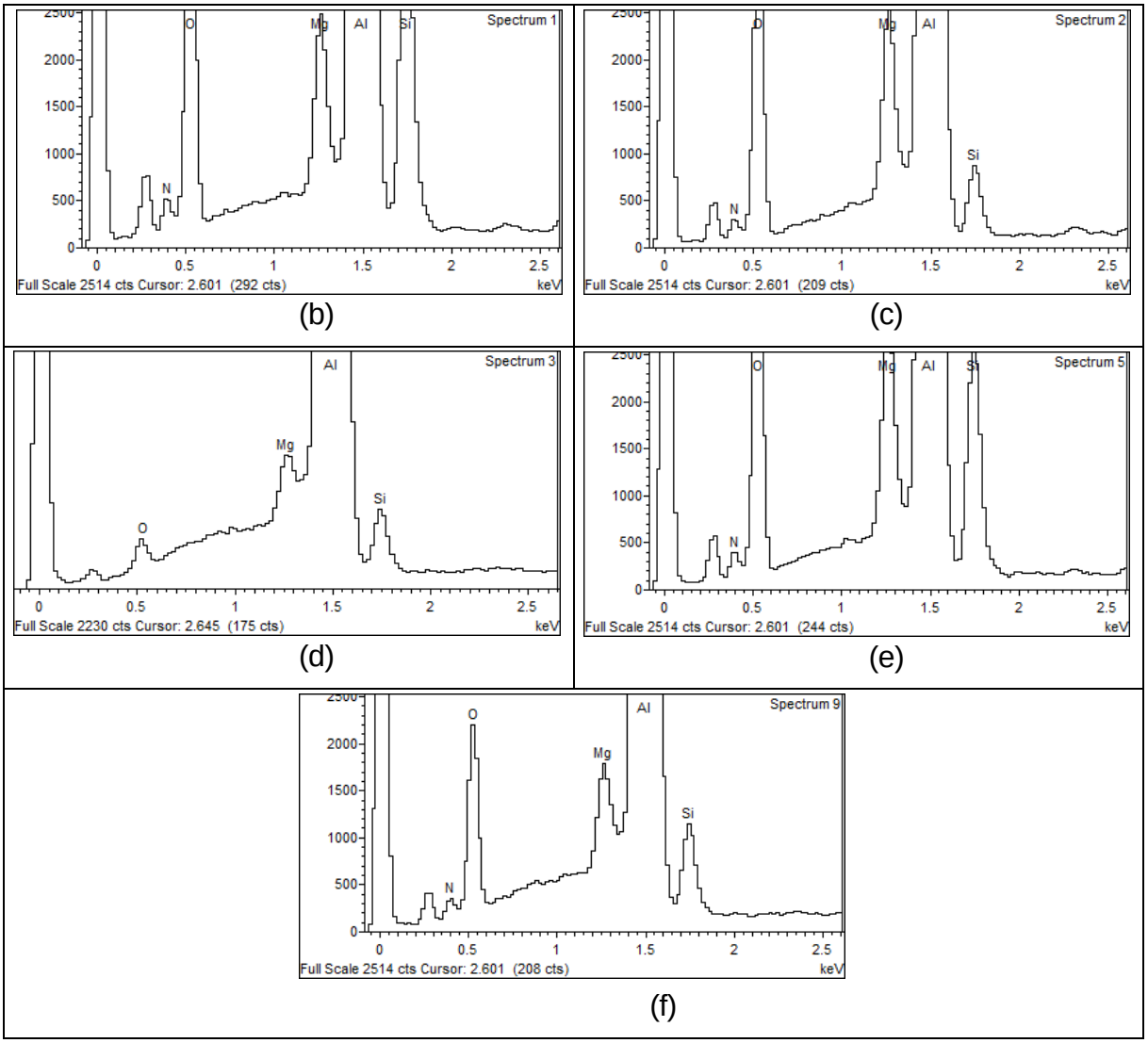


Figure 4-53: (a) SEM micrograph (2L99+0.4 wt.% Mo) of high magnification of X1 marked in Figure 4-52 (a) showing a bifilm with oxide and nitride layers, (b) to (f) EDX spectra of the areas marked in (a)

Table 4-61: EDX elemental composition of the areas marked in Figure 4-53 (a)

	Spectrum 1		Spectrum 2		Spectrum 3		Spectrum 5		Spectrum 9	
Element	Weight %	Atomic %	Weight %	Atomic %	Weight %	Atomic %	Weight %	Atomic %	Weight %	Atomic %
N K	5.95	9.42	4.73	7.65	0.00	0.00	5.45	8.74	4.76	8.06
O K	23.67	32.81	21.16	29.98	2.47	4.09	21.94	30.80	13.69	20.28
Mg K	1.52	1.39	1.96	1.83	0.46	0.50	2.13	1.96	0.89	0.87
Al K	61.58	50.63	70.28	59.04	95.05	93.49	65.23	54.30	78.34	68.83
Si K	7.28	5.75	1.87	1.51	2.02	1.91	5.25	4.20	2.32	1.96

In summary, various phases were observed on the polished surfaces of 2L99 + 0.4 wt.% Mo alloys. (i) Bifilms (spinel) of various sizes and morphologies, averaging 660 µm to 140 µm in length with O, Mg, Al, and Si content at 6 at.%, 0.4 at.%, 72 at.% and 21 at.%, respectively. (ii) Patches of nitrides were observed for the first time on the polished surface of 2L99+0.4wt.% Mo alloys with a nodular morphology with 20 µm length average. The size of the bifilms was observed to be significantly reduced in the vicinity of the nitride patch, suggesting almost total O consumption inside the bifilm followed by nitrogen consumption, leading to a reduction in the size of the bifilm. (iii) Intermetallic compounds with varying shapes, such as irregular pentagons and hexagons, as well as multi-faceted shapes, length on average from 30 to 40µm, with eight of which one different composition. A summary of all the phases of 2L99 + 0.4 wt.% Mo alloys are presented in Table 4-62.

Table 4-62: Summary of the phases on polished surface 2L99 + 0.4 wt.% Mo alloy

Polished 2L99 + 0.4 wt.% Mo	Name	Size
Oxides	Mainly spinel MgO	averaging ranging from 660 µm to 140 µm in length 25 µm in length
Nitrides	AlN nodular shape	average of 20 µm in length in a cavity on the polished surface
Intermetallic Particles	$Mo_{1.5}AlSi_2$	Varied between 10 µm to 80 µm in length
	$MoAl_8Si_3$	4 µm in length
	$MoAl_{10}Si$	10 µm in length
	$Mo_{0.6}(Al, Si)$	5 µm in length
	$Mo\ (Al, Si_2)_2$	5 µm in length
	$Mo_7Al_5Si_8$	Varied between 10 µm to 150 µm in length
	$Mo_2Al\ Si_2$	5 µm in length
	$Mo(Al, Si)_2$	2 µm in length
	$Al_2\ FeSi_{2.6}$	10 µm in length

4.2.2.3 Characterisations of the phases on the fractured surfaces of 2L99 + 0.4 wt.% Mo

Figure 4-55 (a) and Figure 4-55 (b) show low and high-magnification SEM images of a typical nodular oxide layer morphology (spinel) on the fractured surface of 2L99 + 0.4 wt.% Mo, an approximately 120 µm length. Figure 4-55 (c) shows the spectrum, and Table 4-63 shows the EDX elemental composition of Spectrum 2, which is spinel.

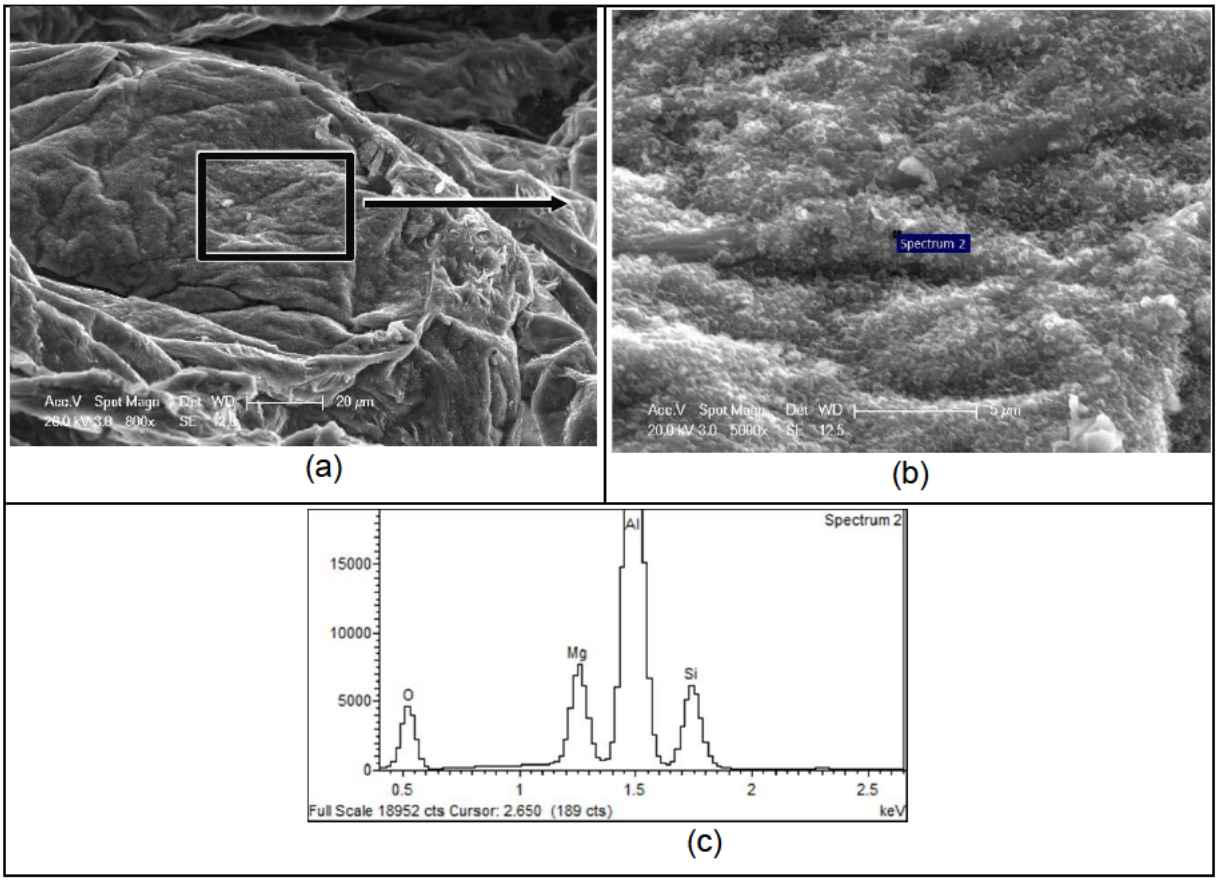
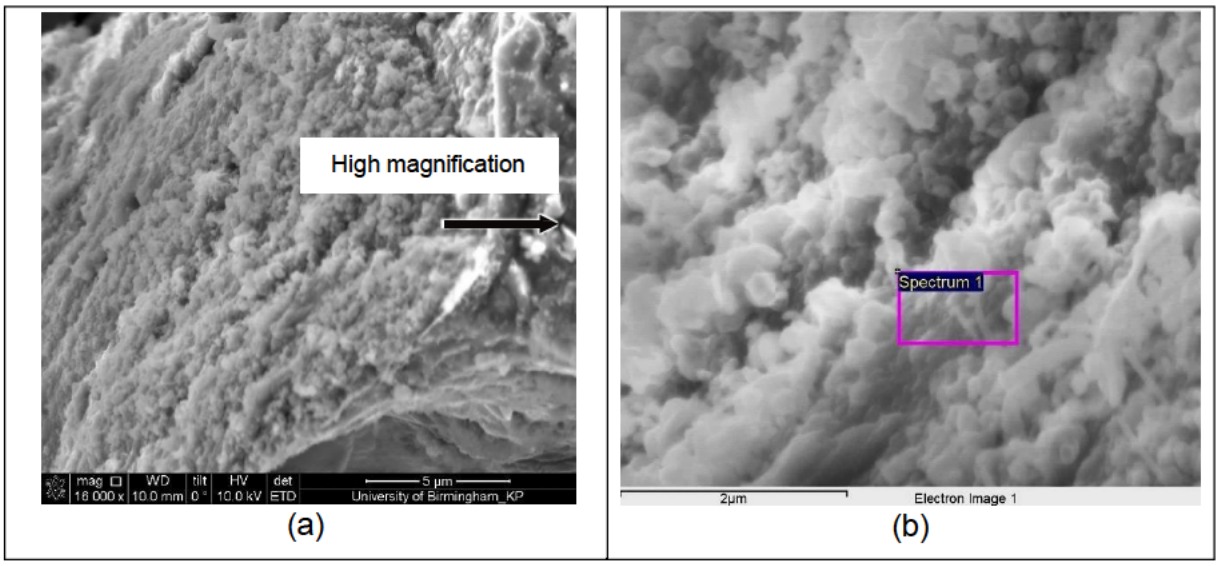


Figure 4-54: (a), (b) low and high magnification of SEM image of a typical nodular oxide layer (spinel) on the fractured surface of as-cast 2L99 + 0.4 wt.% Mo, (c) EDX spectra of Spectrum 2

Table 4-63: EDX elemental composition of the areas marked

	Spectrum 2	
Element	Weight%	Atomic%
O K	28.44	39.99
Mg K	1.75	1.10
Al K	55.80	47.69
Si K	14.00	11.22

Figure 4-55 shows different oxide morphologies on the fractured surface of 2L99 + 0.4 wt.% Mo might be due to variations in O and Mg concentrations. Figure 4-55 (a) and (b) exhibit low and high-magnification images of the same smooth granular Al oxide layer with an approximate diameter of 0.25 µm. These oxides (MgO) contained a high concentration of Mg (21.7 at. %) and revealed the presence of O, Al, and Si at 16 at.%, 57 at.%, and 5 at.%, respectively. Figure 4-55 (c) shows the whisker shape of the oxide layer covering approximately 40 µm of the fractured surface. Based on EDX results, the oxygen amount of the whisker-shaped oxide was twice the amount of O in the granular-shaped oxides, but the Mg concentration was one-fourth of the granular oxide. The EDX spectra for both oxides are shown in Figure 4-55 (d) and Figure 4-55 (e), and the concentration of EDX elements is in Table 4-64.



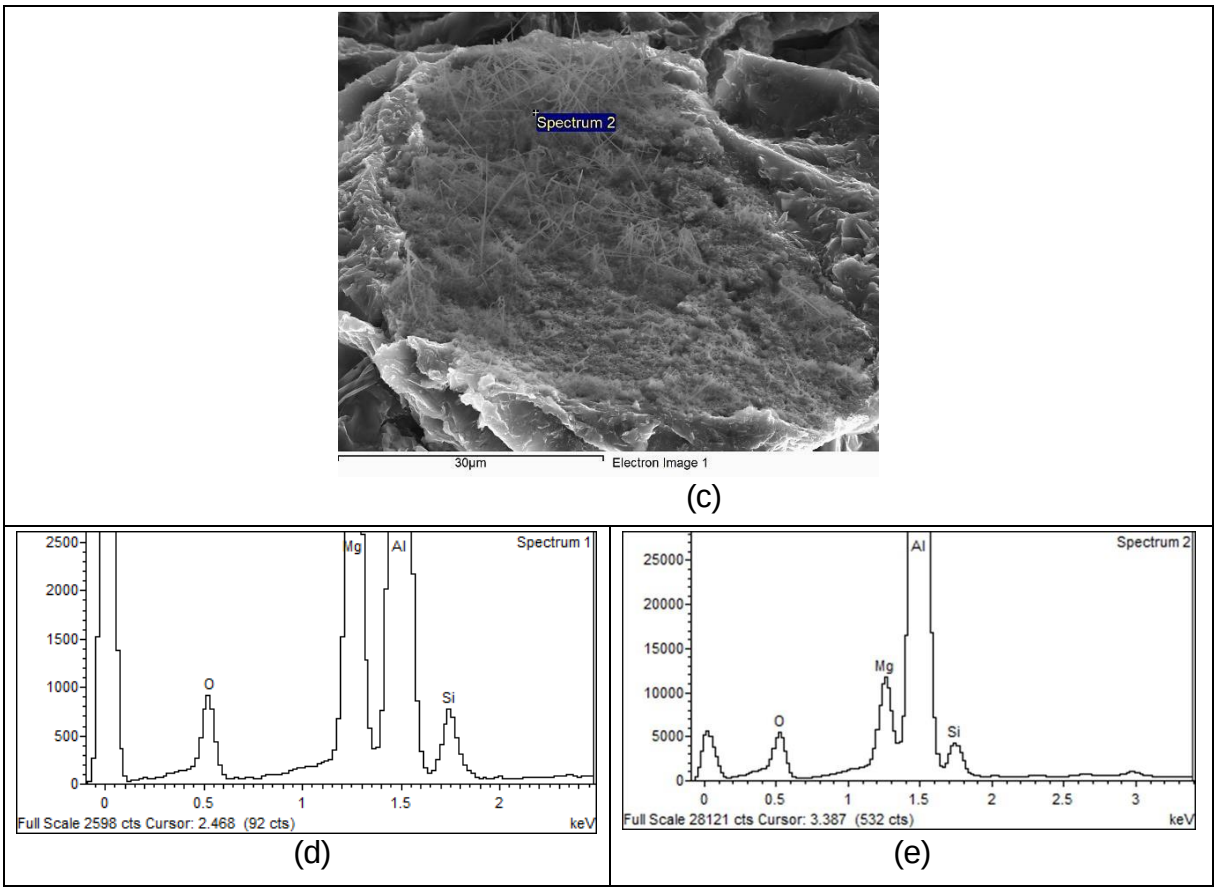


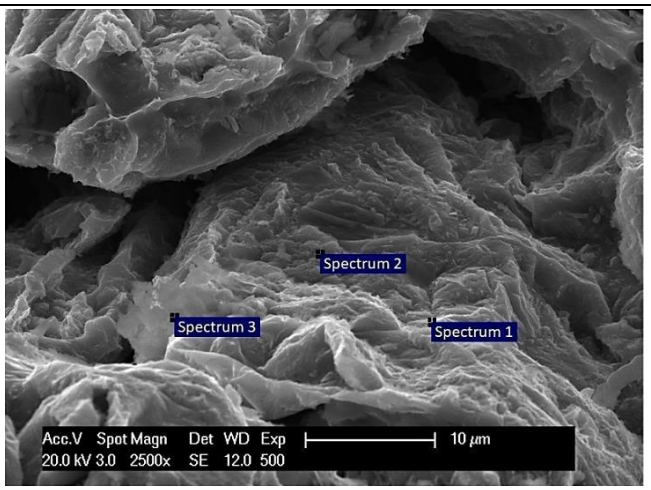
Figure 4-55: (a), (b) low and high magnification of SEM image of a granular oxide layer on the fractured surface of as-cast 2L99 + 0.4 wt.% Mo, (c) high magnification of SEM image of whisker oxide, (d) and (e) EDX spectra of Spectrum 1 and Spectrum 2

Table 4-64: EDX elemental composition of the areas marked in Figure 4-55 (b) and (c)

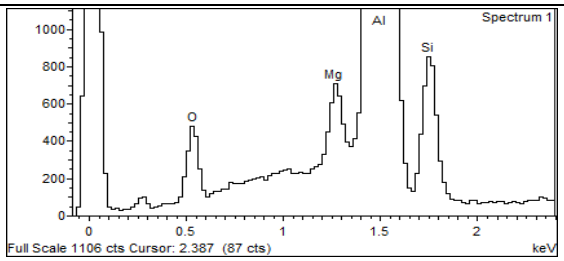
	Spectrum 1		Spectrum 2	
Element	Weight%	Atomic%	Weight%	Atomic%
O K	10.23	15.82	19.02	28.27
Mg K	21.33	21.70	5.65	5.52
Al K	62.43	57.21	70.07	61.75
Si K	6.00	5.28	5.25	4.45

Both oxide and AlN layers were present on the fractured surface of 2L99 + 0.4 wt.% Mo, as shown in Figure 4-56 (a). Spectrum 1 shows a wrinkled-shaped spinal, and Spectrum 3 shows aggregate flake-shaped spinel; both contain approximately the same amount of O, Mg, Al, and Si. Spectrum 2 showed the nodular shape AlN layer with N (28 at.%), O (12 at.%), Mg (0.5 at.%), Al (56 at.%) and Si (1.8 at.%). The AlN covered

approximately 8 µm of the fractured surface captured, as shown in Figure 4-56 (a).



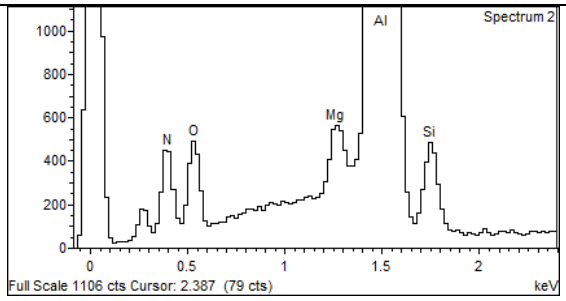
(a)



(b)

Element	Weight%	Atomic%
O K	8.29	13.25
Mg K	1.01	1.06
Al K	84.51	80.06
Si K	6.19	5.64

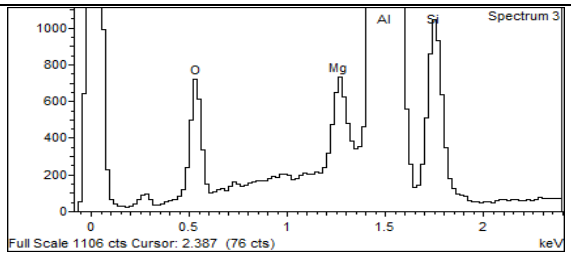
(c)



(d)

Element	Weight%	Atomic%
N K	18.07	28.32
O K	9.05	12.41
Mg K	0.64	0.58
Al K	69.95	56.90
Si K	2.29	1.79

(e)



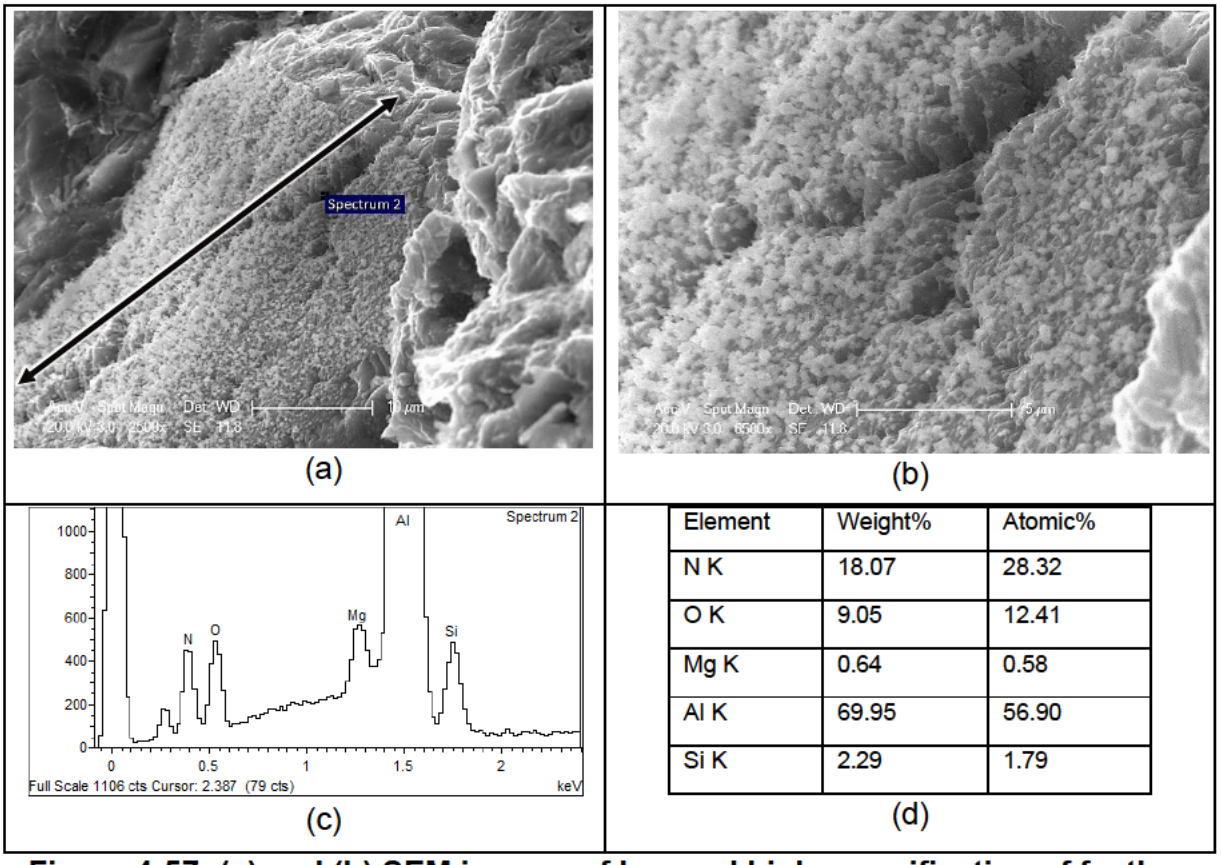
(f)

Element	Weight%	Atomic%
O K	12.56	19.53
Mg K	1.26	1.29
Al K	78.80	72.65
Si K	7.38	6.53

(g)

Figure 4-56: (a) SEM image of oxides and AlN layer on the fractured surface of as-cast 2L99 + 0.4 wt.% Mo and (b) and (c) EDX analysis of spectrum1 of the oxide layer (d) and (e) EDX analysis of spectrum 2 of AlN layer (f) and (g) EDX analysis of spectrum 3 of the oxide

Figure 4-57 (a) and Figure 4-57 (b) show low and high-magnification SEM images of AlN on the fractured surfaces of a 2L99 + 0.4 wt.% Mo. The area surrounding the oxide layer patch was observed to be AlN. The amount of N measured was relatively high (28 at.%), with Al (57 at.%), O (12 at.%), Si (2 at.%) and a small amount of Mg (0.5 at.%). The EDX analyses are shown in Figure 4-57 (c) and Figure 4-57 (d). The presence of the AlN could be due to an increase in the rate of interaction of the gases inside the bifilm by consumption of oxygen first and, subsequently, the reaction of nitrogen with the surrounding melt [1] [3]. The AlN observed in Figure 4-57 (a), and Figure 4-57 (b) showed a permeable feather-like morphology with a length of approximately 30 µm, which can enable H diffusion into the bifilms more easily.



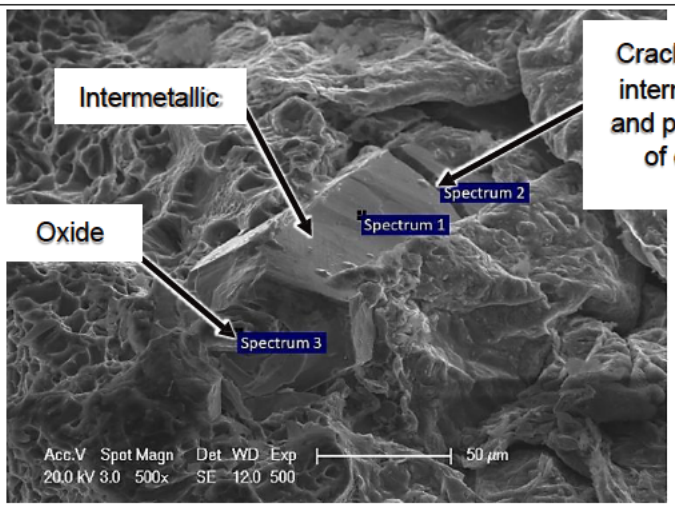
Element	Weight%	Atomic%
N K	18.07	28.32
O K	9.05	12.41
Mg K	0.64	0.58
Al K	69.95	56.90
Si K	2.29	1.79

Figure 4-57: (a) and (b) SEM images of low and high magnification of feather shape nitride layers on the fractured surface of as-cast 2L99 + 0.4 wt.% Mo and (c) and (d) EDX analysis of spectrum 2

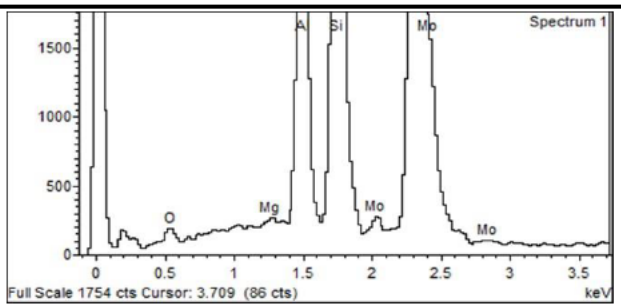
Figure 4-58 shows blocky faceted Mo containing intermetallic and oxide layers on the fractured surfaces of a 2L99 + 0.4 wt.% Mo. The point marked as Spectrum 1 showed Mo containing intermetallic ($MoAlSi_2$) with a size of 50 µm x 80 µm and the amount of Mo at 25 at.%, Al at 20 at.%, Si at 44 at.% and O at 12 at.%. The EDX spectrum and quantification are shown in Figure 4-58 (b) and Figure 4-58 (c). The point marked as Spectrum 2 revealed the presence of a Mo intermetallic, $MoAl_2Si_2$, with the composition of O at 15 at.%, Mo 15 at.%, Al 37 at.%, Si 32 at.% and Mg 0.4 at.%. The corresponding EDX spectrum and quantification are shown in Figure 4-58 (d) and Figure 4-58 (e).

The point marked as Spectrum 3 revealed oxide layers (spinal) with O, containing 23 at.%, Al 55 at.%, Si 20 at.% and Mg 2 at.%. The EDX spectrum and quantification are shown in Figure 4-58 (f) and Figure 4-58 (g). Furthermore, Figure 4-58 shows Mo intermetallic growth on the side of the oxide layer, as shown in the point marked as Spectrum 2. The corresponding EDX analysis is shown in Figure 4-58 (d) and Figure 4-58 (e).

This is in line with Campbell [105], who suggested that the initiation sites for most failures of metals, such as pores and cracks, can only occur at unbonded interfaces. These unbonded defects are introduced into metals exclusively through extrinsic mechanisms, specifically through production processes such as melting, casting, and cracking. Among these mechanisms, only entrained inclusions, particularly bifilms, possess unbonded interfaces that can open to form “Griffiths” cracks.



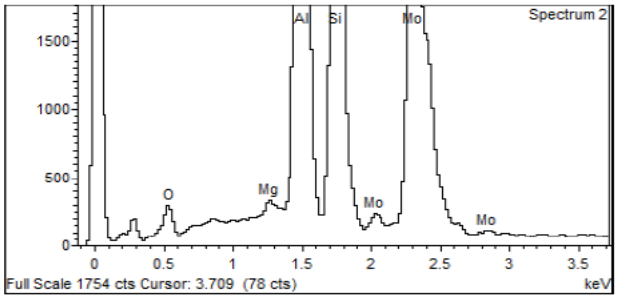
(a)



(b)

Element	Weight%	Atomic%
O K	4.32	11.66
Mg K	0.20	0.35
Al K	11.92	19.08
Si K	28.77	44.24
Mo L	54.79	24.67

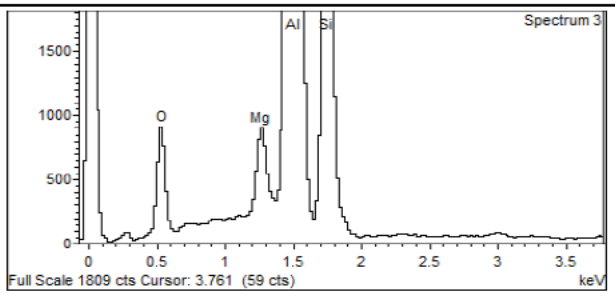
(c)



(d)

Element	Weight%	Atomic%
O K	6.77	15.34
Mg K	0.29	0.43
Al K	27.40	36.80
Si K	24.85	32.06
Mo L	40.69	15.37

(e)



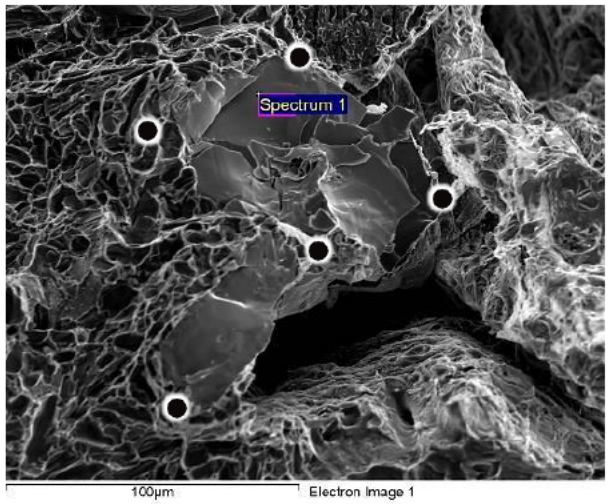
(f)

Element	Weight%	Atomic%
O K	15.17	23.31
Mg K	1.64	1.66
Al K	60.91	55.51
Si K	22.29	19.52

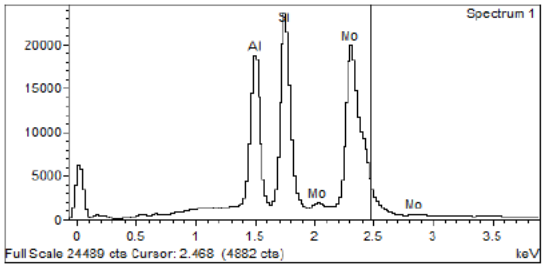
(g)

Figure 4-58: (a) SEM micrograph of a fractured surface of 2L99 + 0.4 wt.% Mo alloy showing Mo containing faceted intermetallic compounds (blocky shape) and oxides, (b) and (c) EDX spectrum1 intermetallic, (d) and (e) EDX Spectrum 2 for oxides and Mo intermetallic, (f) and (g) EDX Spectrum 3 for oxides

Another Mo intermetallic, $Mo_7Al_5Si_7$, is shown in Figure 4-59 (a) with approximate dimensions of 65 µm x 65 µm. The Mo intermetallic exhibited many cracks and oxide film defects (MgO), as revealed by EDX analysis. The representative EDX analysis of the areas marked with black circles is shown in Figure 4-59 (d) and Figure 4-59 (e). The EDX analysis specifically focused on intermetallics is presented in Figure 4-59 (b) and Figure 4-59 (c).



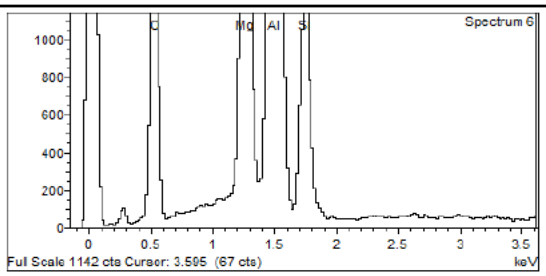
(a)



(b)

Element	Weight%	Atomic%
Al K	13.27	25.69
Si K	20.59	38.29
Mo L	66.15	36.02

(c)



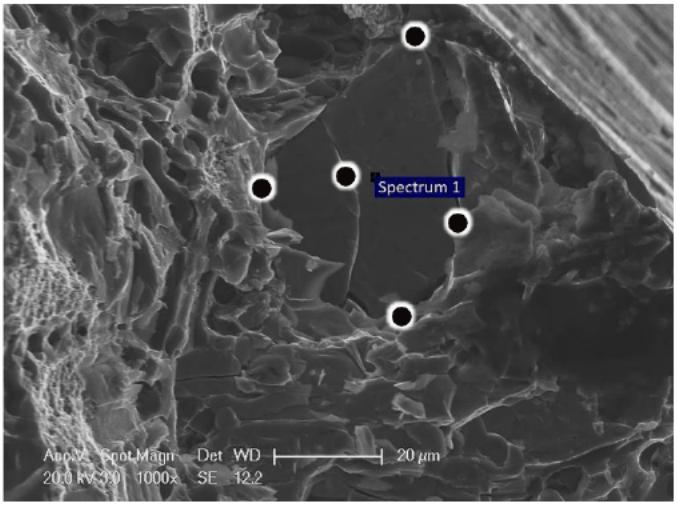
(d)

Element	Weight%	Atomic%
O K	27.18	38.34
Mg K	11.20	10.40
Al K	53.37	44.64
Si K	8.25	6.63

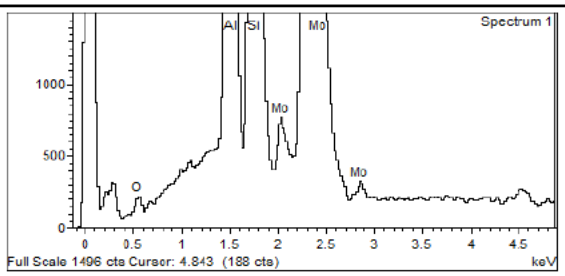
(e)

Figure 4-59: (a) SEM image of Mo intermetallic on the fractured surface of as-cast 2L99 + 0.4 wt.% Mo and (b) and (c) EDX analysis of spectrum 1 (d) and (e) EDX analysis of spectrum 6 for all the red circles marked

Another Mo intermetallic was detected on a fractured surface of 2L99 + 0.4 wt.% Mo alloy which is shown in Figure 4-60 (a) $Mo_6Al_5Si_8$, with approximately 35 µm x 52 µm size. The Mo intermetallic shows a vertical crack characterised as bifilm, confirmed by the EDX analysis. EDX analysis of the points marked with black circles is shown in Figure 4-60 (d) and Figure 4-60 (e). The representative EDX analysis of the areas marked as Spectrum1 is shown in Figure 4-60 (b) and Figure 4-60 (c).



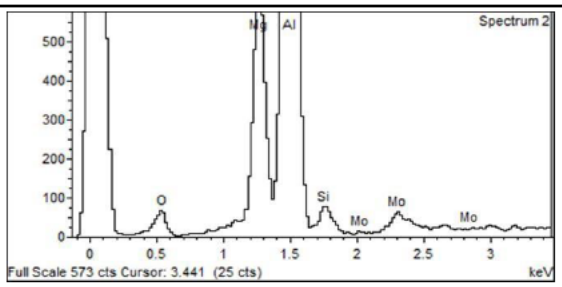
(a)



(b)

Element	Weight%	Atomic%
O K	1.93	5.86
Al K	13.34	24.06
Si K	22.12	38.33
Mo L	62.61	31.75

(c)



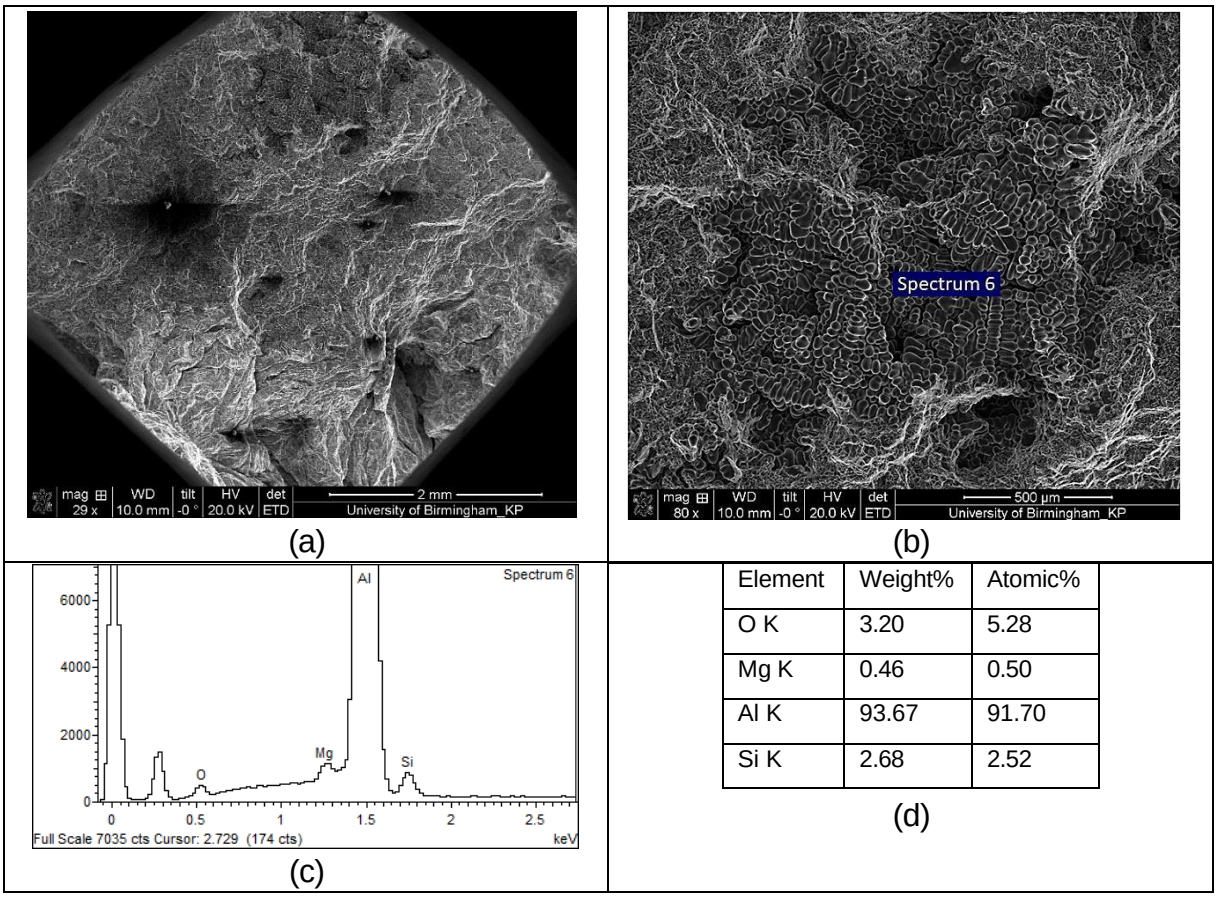
(d)

Element	Weight%	Atomic%
O K	11.40	18.23
Mg K	9.29	10.09
Al K	64.00	60.68
Si K	3.91	3.56
Mo L	5.40	1.44

(e)

Figure 4-60: (a) SEM image of Mo intermetallic on the fractured surface of as-cast 2L99 + 0.4 wt.% Mo and (b) and (c) EDX analysis of spectrum 1, (d) and (e) EDX analysis of spectrum 7 for all the red circles marked

Figure 4-61 (a) and Figure 4-61 (b) revealed gas porosity defects on a fractured surface 2L99 +0.4 wt.% Mo alloy approximately 1.7 mm in diameter. No oxygen was detected within these porosities using EDX analysis. The presence of H porosity in these porosities was probably due to the formation of defects in the expanded oxide films. A small amount of O was detected by EDX.



Element	Weight%	Atomic%
O K	3.20	5.28
Mg K	0.46	0.50
Al K	93.67	91.70
Si K	2.68	2.52

(d)

Figure 4-61: (a) Low magnification of the half of the fractured surface 2L99 + 0.4 wt.% Mo alloy with gas porosity (b) High magnification of gas porosity (c) and (d) EDX analysis of spectrum3 on gas porosity

A summary of the phases found in the fractured surface 2L99 + 0.4 wt.% Mo is presented in Table 4-65.

Table 4-65: Summary of the phases on fractured surface 2L99+0.4 wt.% Mo alloy

Fractured 2L99 + 0.4 wt.% Mo	Name	Size
Oxides	Mainly spinel (nodular and granular shape) Whisker shape MgO	Granular~0.25 µm in diameter covered 30 µm
Nitrides	AlN nodular feather shape	8 µm 30 µm
Intermetallic Particles	$MoAlSi_2$ $Mo_7Al_5Si_7$ $Mo_6Al_5Si_8$	80x50 µm 65 x 65 µm 35 x 52 µm
Gas porosity	H gas porosity	1.7 mm

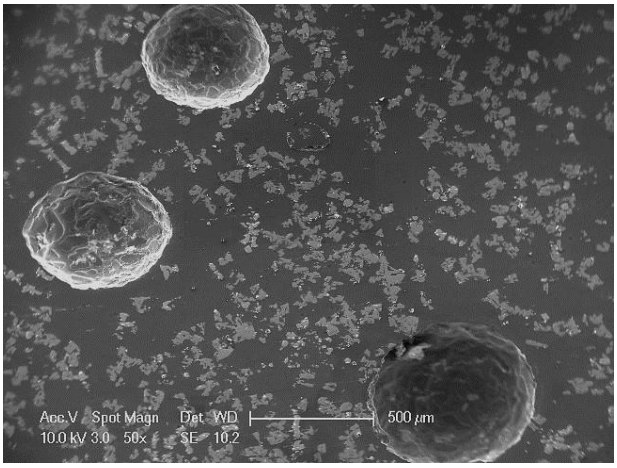
4.2.3 2L99 + W alloy

4.2.3.1 Characterisation of the masteralloy of 2L99+10%W

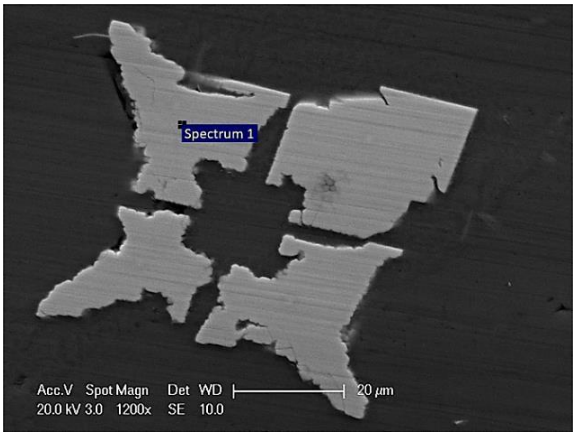
A low-magnification SEM micrograph of a polished surface of the W masteralloy has been shown in Figure 4-62 (a). The image showed a number of gas porosities as spherical cavities and intermetallic compounds scattered over the polished surface and on the surface of the gas porosities of the masteralloy testbar.

High-magnification images of some intermetallic compounds with oxides (alumina) have been presented in Figure 4-62 (b) to (d), showing the intermetallic compounds to possess a facetted shape varying from 10 µm to 50 µm in width and length.

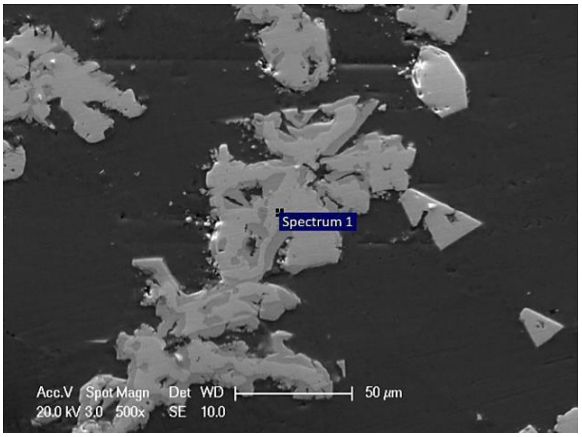
The corresponding EDX elemental compositions to the points marked as Spectrum 1 in Figure 4-62 (b) to Figure 4-62 (d) have been shown in Figure 4-62 (e) to Figure 4-62 (g), respectively and presented in Table 4-66. These intermetallics, as shown in Figure 4-62 (b) to (d), were $W_4Al_{14}Si$, $W_4Al_{14}Si$ and Al_3W.


Acc.V Spot Magn Det WD
10.0 kV 3.0 50x SE 10.2
500 µm

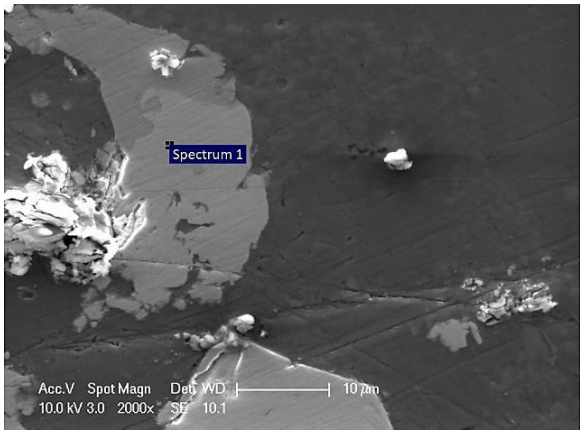
(a)


Spectrum 1
Acc.V Spot Magn Det WD
20.0 kV 3.0 1200x SE 10.0
20 µm

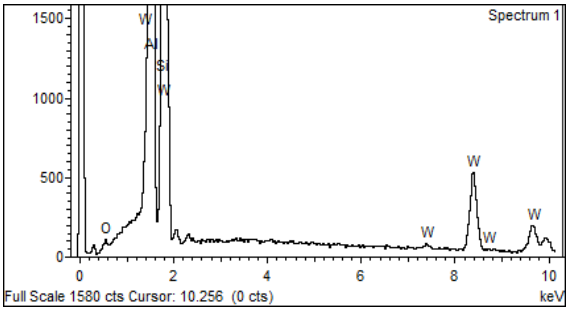
(b)


Spectrum 1
Acc.V Spot Magn Det WD
20.0 kV 3.0 500x SE 10.0
50 µm

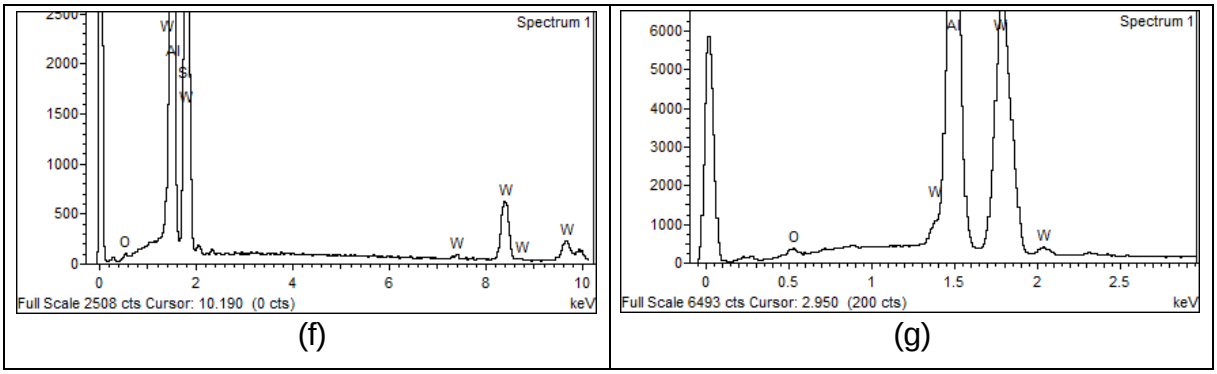
(c)


Spectrum 1
Acc.V Spot Magn Det WD
10.0 kV 3.0 2000x SE 10.1
10 µm

(d)


Spectrum 1
1500
1000
500
0
W
Al
Si
W
O
W
W
W
0
2
4
6
8
10
Full Scale 1580 cts Cursor: 10.256 (0 cts)
keV

(e)



(f) (g)

Figure 4-62: (a) low magnification of a typical SEM micrograph of the polished surface of W masteralloy with gas porosity, (b) to (d) high magnification of different Al-W intermetallic compounds (facetted shape), (e) to (g) EDX spectra of the points marked as Spectrum 7 and Spectrum 1

Table 4-66: EDX elemental composition of spectra in Figure 4-62 (b) to (d)

	Spectrum 7		Spectrum 1		Spectrum 1		Spectrum 1	
Element	Weight%	Atomic%	Weight%	Atomic%	Weight%	Atomic%	Weight%	Atomic%
O K	1.35	6.13	1.18	3.45	1.17	4.25	1.11	4.42
Al K	7.91	21.21	43.56	75.48	32.80	70.65	30.54	71.96
Si K	16.56	42.69	4.97	8.28	2.41	4.99	0.00	0.00
W M	73.51	28.95	50.29	12.79	63.62	20.11	68.34	23.63

A high-magnification SEM micrograph of an intermetallic particle on the polished surface of the W masteralloy has been shown in Figure 4-63 (a). The particle observed was heptagonal in shape (AlW_2), grown over a layer of bifilm (MgO as the Mg content is higher than 2.5 wt.%), resulting in the straightening of the bifilm and formation of a crack cutting through the intermetallic compound, as seen in Figure 4-63 (a).

Figure 4-63 (b) and Figure 4-63 (c) showed the EDX elemental composition of the points marked as Spectrums 1 and 2 in Figure 4-63 (a), respectively. Table 4-67 provides the composition percentages of Spectrums 1 and 2.

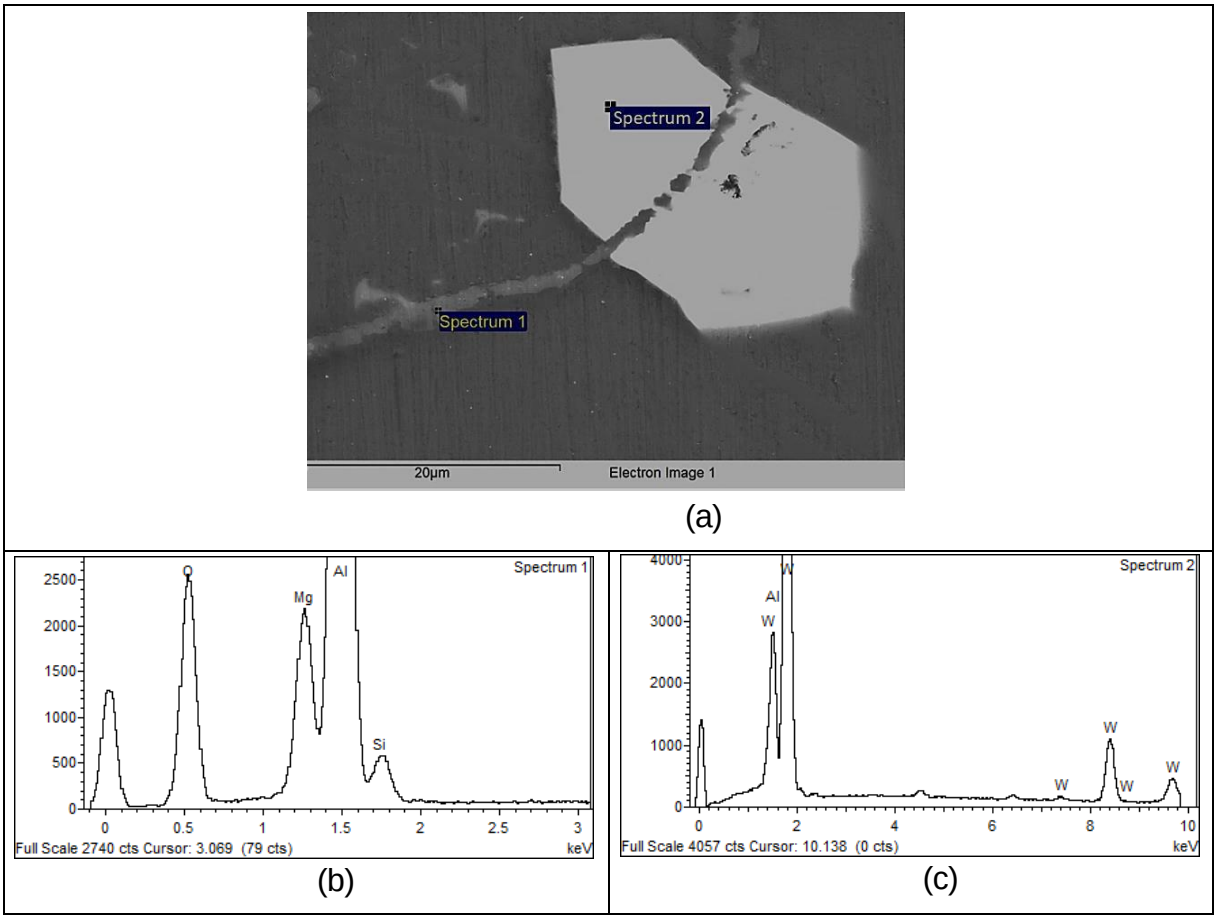


Figure 4-63: (a) High magnification SEM image of one of the intermetallics on the polished W masteralloy (AlW_2), possessing a heptagon shape with a crack cutting through the middle of the particle (oxide film), (b) and (c) corresponding EDX spectra in (a)

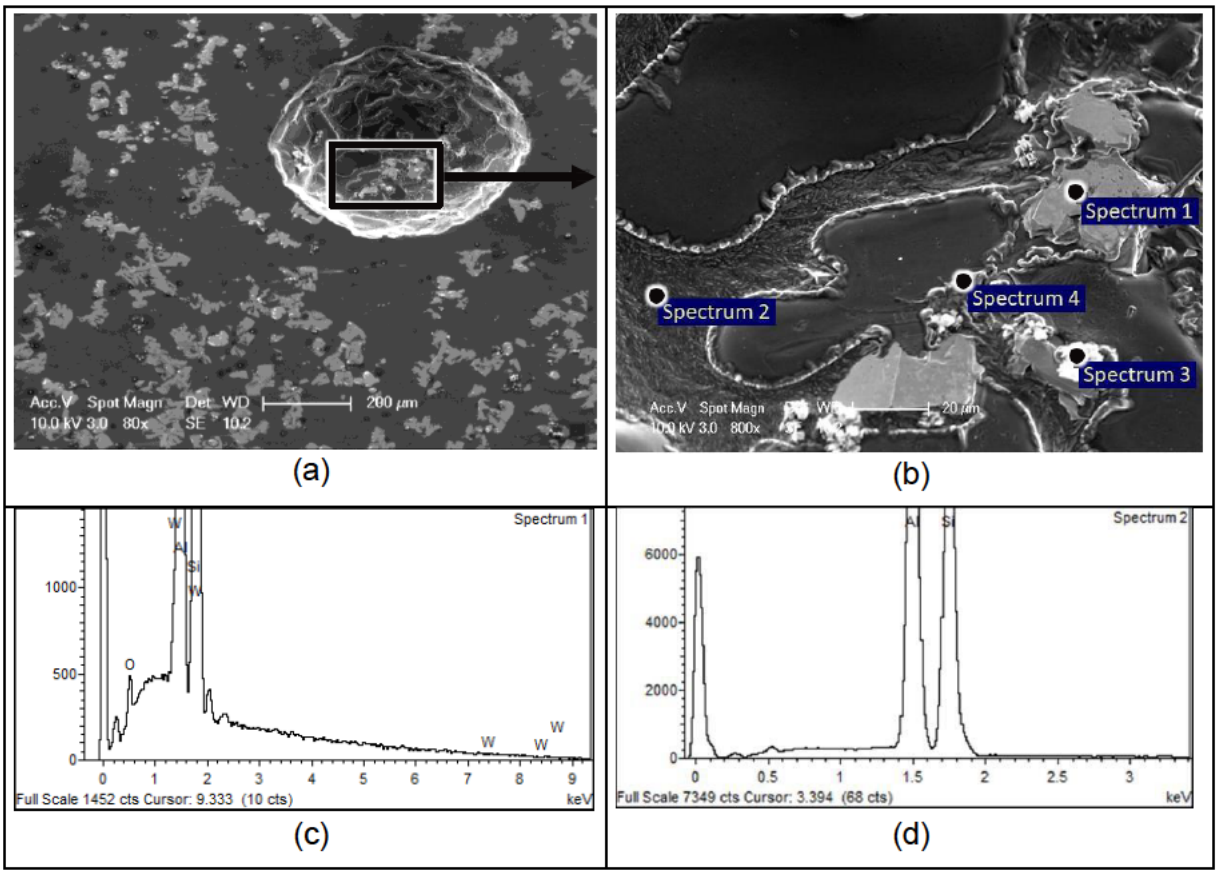
Table 4-67: EDX elemental composition of spectra in Figure 4-63 (a)

	Spectrum 1		Spectrum 2	
Element	Weight%	Atomic%	Weight%	Atomic%
O K	39.00	51.57	0.00	0.00
Mg K	8.46	7.36	0.00	0.00
Al K	48.76	38.22	37.66	37.66
Si K	3.78	2.85	0.00	0.00
W	0.00	0.00	91.86	62.34

Figure 4-64 (a) shows a low magnification SEM micrograph of a gas porosity on the polished surface of a W masteralloy. The image showed the presence of different intermetallic compounds, as shown in high magnification in Figure 4-64 (b). In this Figure using EDX, the area marked as Spectrum 1 was identified as a W intermetallic

compound ($W_4Al_{14}Si$), Spectrum 2 was identified as Al-Si eutectic, Spectrum 3 was identified as oxide (spinel), and Spectrum 4 was identified as a bifilm (alumina) with a small amount of W. The particles observed as part of spectra 1 and 4 in Figure 4-64 (b) suggested that intermetallic compounds nucleated on the wetted side of the bifilms and unfurled the tangled bifilm in the process.

The EDX elemental composition of the spectra marked in Figure 4-63 (b) have been presented in Figure 4-64 (c) to Figure 4-64 (f), along with composition percentages in Table 4-68.



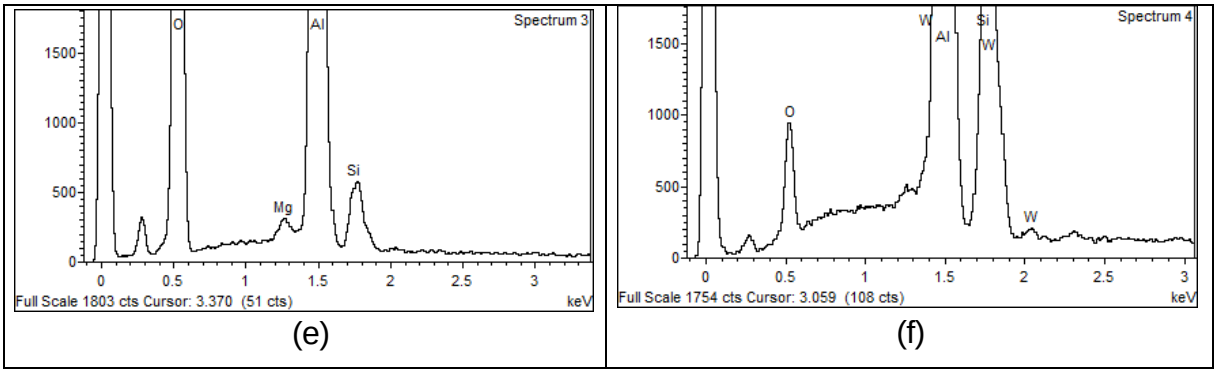


Figure 4-64: (a) High magnification SEM micrograph of a pore on the polished W masteralloy with numerous intermetallic compounds, (b) low magnification of the area marked (tangled intermetallics with oxide films inside one of the pores) in (a), (c) to (f) corresponding EDX spectra as marked in (b)

Table 4-68: EDX elemental composition of spectra in Figure 4-64 (b)

	Spectrum 1		Spectrum 2		Spectrum 3		Spectrum 4	
Element	Weight%	Atomic%	Weight%	Atomic%	Weight%	Atomic%	Weight%	Atomic%
O K	1.65	6.16	0.00	0.00	48.05	60.96	5.82	11.94
Mg K	0.00	0.00	0.00	0.00	0.46	0.38	0.00	0.00
Al K	30.32	67.27	49.35	50.35	49.08	36.92	64.06	77.97
Si K	2.45	5.22	50.65	49.65	2.41	1.74	4.75	5.55
W	65.58	21.35	0.00	0.00	0.00	0.00	25.38	4.53

4.2.3.2 Fractured Surface of the Masteralloy (2L99 + 10 wt.% W)

A low magnification SEM micrograph of a fractured surface of W masteralloy has been shown in Figure 4-65 (a) and showed the presence of numerous gas porosities with an average diameter of 500 µm.

The high magnification SEM micrograph shown in Figure 4-65 (c) indicated the presence of Al_4W intermetallic compounds with O (approximately 50µm in length) on the fractured surfaces of the 2L99 + 10 wt.% W alloy (unlike the polished surface), which matched the phases of Al-W [79]. The EDX analysis of the Al_4W with O marked as Spectrum 4 in Figure 4-65 (c) showed the amount of Al and W to be 78.56 at.% and 21.44 at.%, respectively, as shown in Table 4-69.

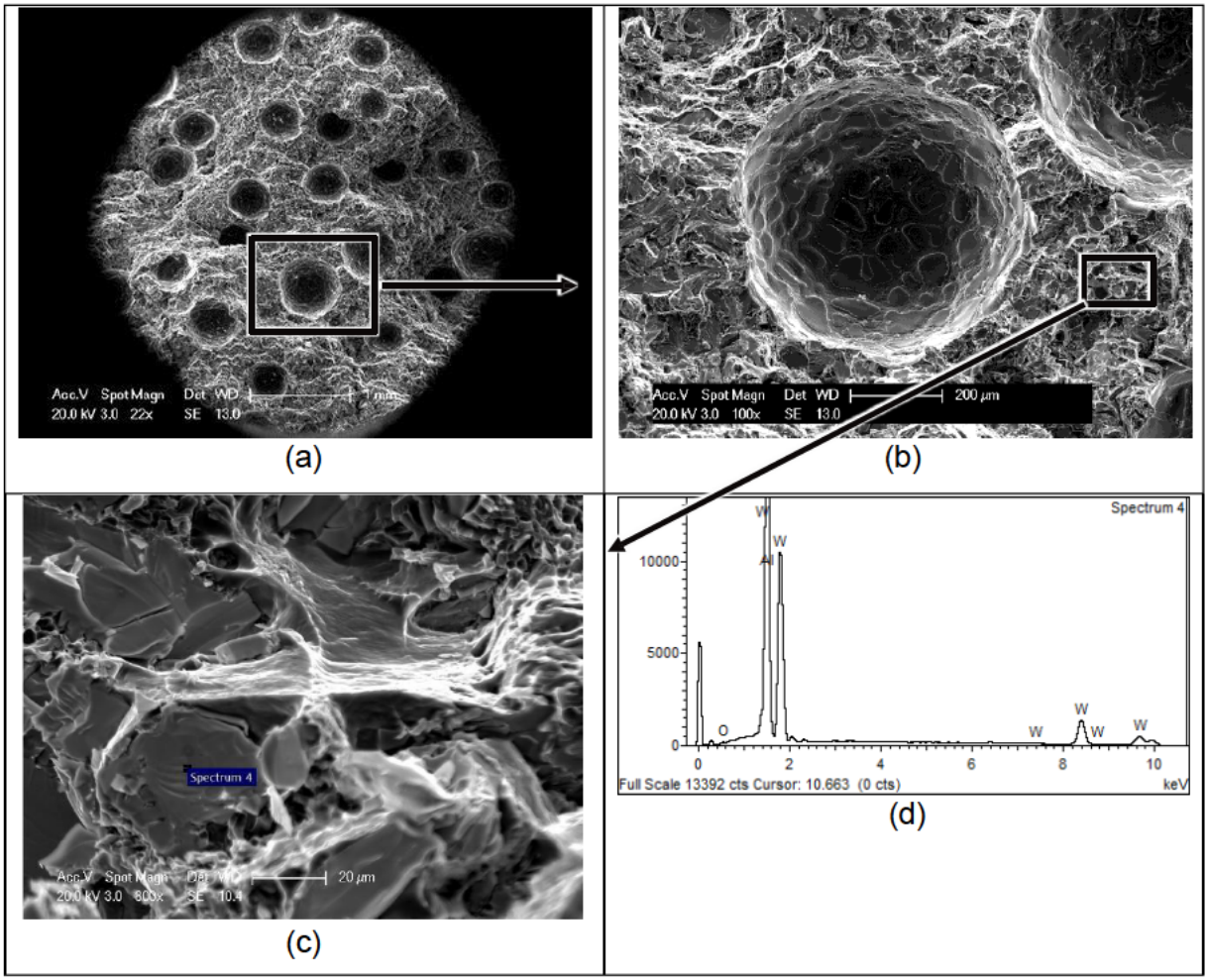


Figure 4-65: (a) Low magnification of SEM micrograph of the fractured surface of W masteralloy with numerous gas porosities present, (b) high magnification of the area marked in (a), (c) high magnification of the area marked in (b) showing the Al_4W Intermetallic Compound on the fractured surface, (d) corresponding EDX spectrum of the area marked in (c)

Table 4-69: EDX elemental composition of spectra in Figure 4-65 (c)

	Spectrum 4	
Element	Weight%	Atomic%
O K	0.87	3.36
Al K	32.57	74.35
W M	66.56	22.30

Another high magnification SEM image on the fractured surface of a W masteralloy with two facetted W intermetallic compounds ($W_{1.5}AlSi_2$ and $W_4Al_{14}Si$) with O has been shown in Figure 4-66 (a).

EDX elemental composition of the spectra marked in Figure 4-66 (a) have been presented in Figure 4-66 (b) to Figure 4-66 (c), along with composition percentages in Table 4-70.

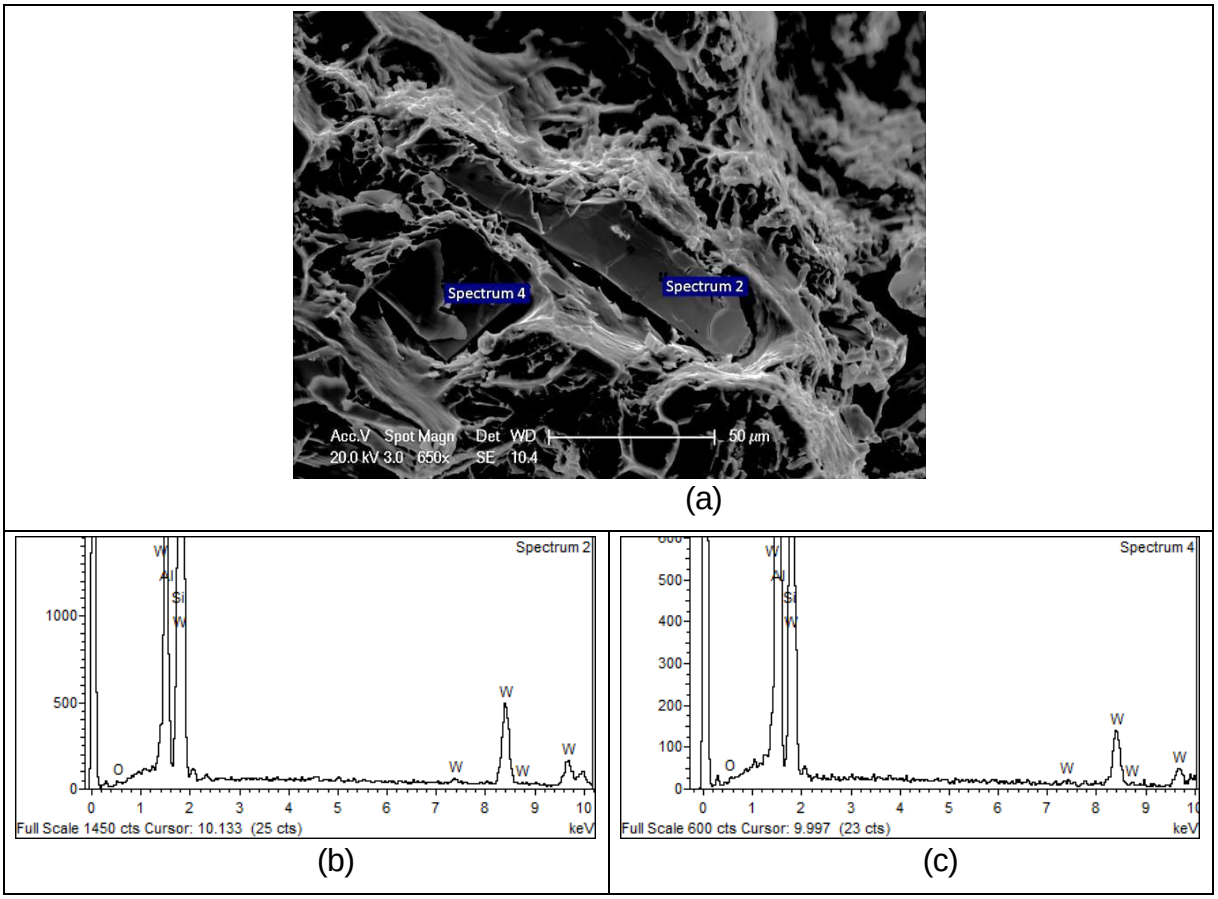


Figure 4-66: (a) high magnification of the fractured surface of W masteralloy, (b) and (c) corresponding EDX spectrum of the area marked in (a)

Table 4-70: EDX elemental composition of spectra in Figure 4-66 (a)

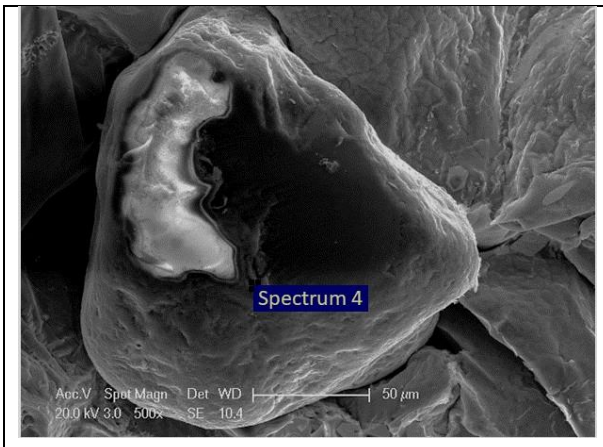
	Spectrum 2		Spectrum 4	
Element	Weight%	Atomic%	Weight%	Atomic%
O K	1.10	4.93	0.40	1.18
Al K	11.80	31.25	42.59	75.07
Si K	13.91	35.38	6.27	10.62
W	73.19	28.45	50.74	13.13

Figure 4-67 (a) to Figure 4-67 (c) show the morphology of various oxides observed on the fractured surface of a W masteralloy. Figure 4-67 (a) shows an oxide

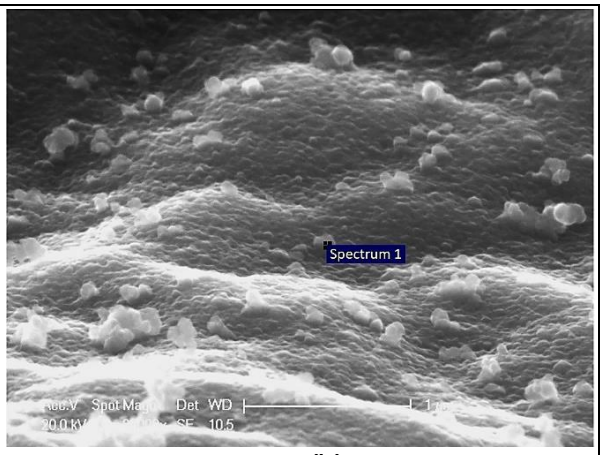
particle (SiO_2) of approximately 100 µm width comprising 32 at.% Si, 65 at.% O, 2.5 at.% Mg and only 0.5 at.% Al. Numerous oxides of approximately 100 nm in length and cubic in shape were observed, as shown in Figure 4-67 (b). The EDX analysis of the oxide particles (MgO) showed strong peaks corresponding to O and Al at 43.64 at.% and 28.86 at.%, respectively, along with weak peaks corresponding to Mg 2.88 at.% and Si 6.86 at.%.

Layers of oxides (MgO) were observed in the high magnification SEM micrograph of the fractured surface of W masteralloy, as shown in Figure 4-67 (c). The oxide layers were measured to have a width of 12 µm with strong peaks of O and Al at 42.45 at.% and 30.79 at.%, respectively, along with a weak pick of Mg 2.65 at.% and Si 8.7 at.%.

The EDX elemental composition of the spectra, as marked in Figure 4-67 (a) to Figure 4-67 (c), have been shown in Figure 4-67 (d) to Figure 4-67 (f), respectively, along with the composition percentages in Table 4-71.



(a)



(b)

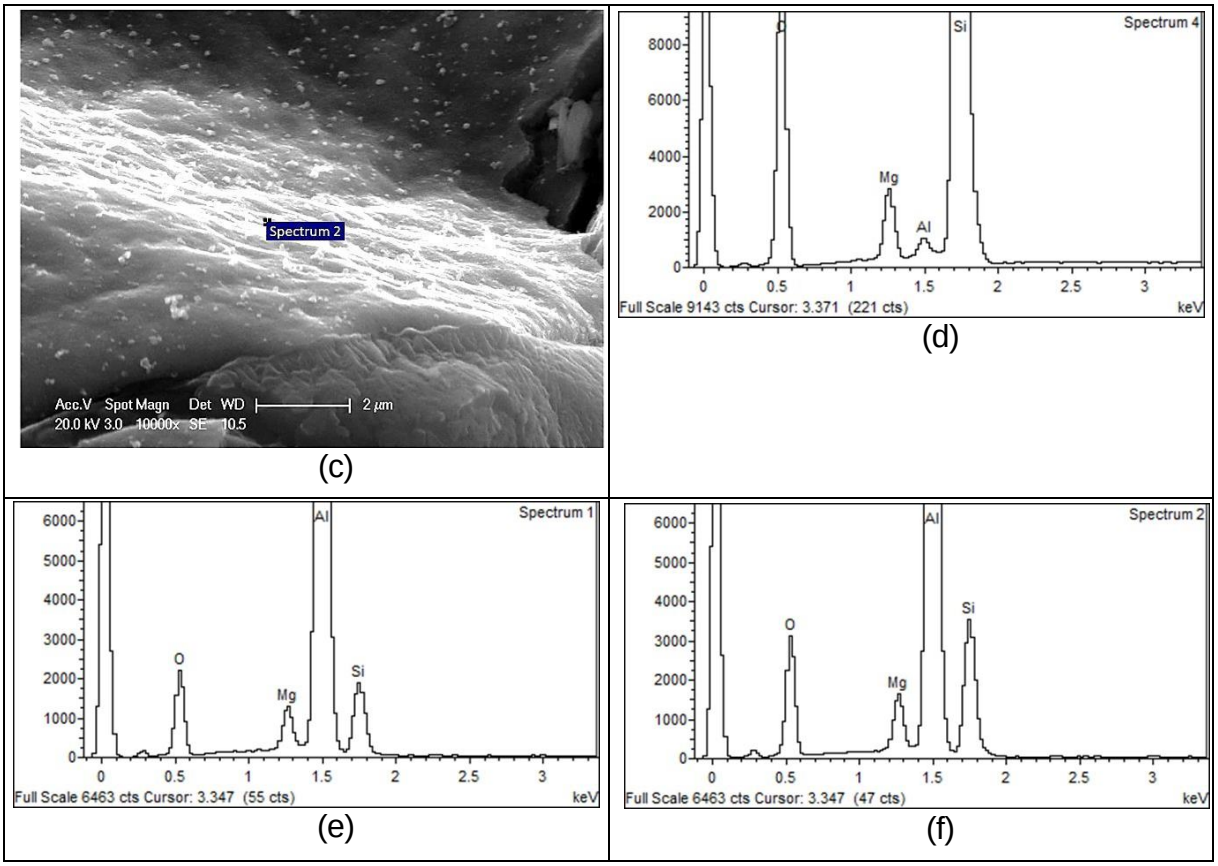


Figure 4-67: (a) SEM micrograph of fracture surfaces of W masteralloy, high magnification showing the spinel particle on the fractured surface, (b) high magnification showing the small spinel particle on the fractured Surface, (c) high magnification SEM micrograph showing the spinel layer on the fractured surface, (d) to (f) corresponding EDX spectrum of the area marked in (a) to (c)

Table 4-71: EDX elemental composition of spectra in Figure 4-67 (a) to (c)

	Spectrum 4		Spectrum 1		Spectrum 2	
Element	Weight%	Atomic%	Weight%	Atomic%	Weight%	Atomic%
O K	51.43	64.79	28.99	40.80	34.73	47.37
Mg K	3.04	2.52	2.94	2.73	3.59	3.23
Al K	0.64	0.48	58.34	48.68	46.99	38.00
Si	44.89	32.21	9.73	7.80	14.68	11.40

Top and bottom surfaces of 2L99 + 10 wt.% W ingot were characterised and showed the presence of cavities caused by gas porosity in the matrix, as well as intermetallic compounds of numerous sizes with blocky faceted (α shape), not needle-shaped (β shape) intermetallic compounds as compared with Mo masteralloys. Low and high-

magnification SEM micrographs of a typical top polished surface of the W masteralloy ingot are presented in Figure 4-68 (a) to Figure 4-68 (b).

Figure 4-68 (b) shows Al_3W with O varying from 6 µm to 50 µm in length, blocky shaped and marked as Spectrum 2; the corresponding marked EDX spectrum is shown in Figure 4-68 (c) and EDX elemental compositions are presented in Table 4-72.

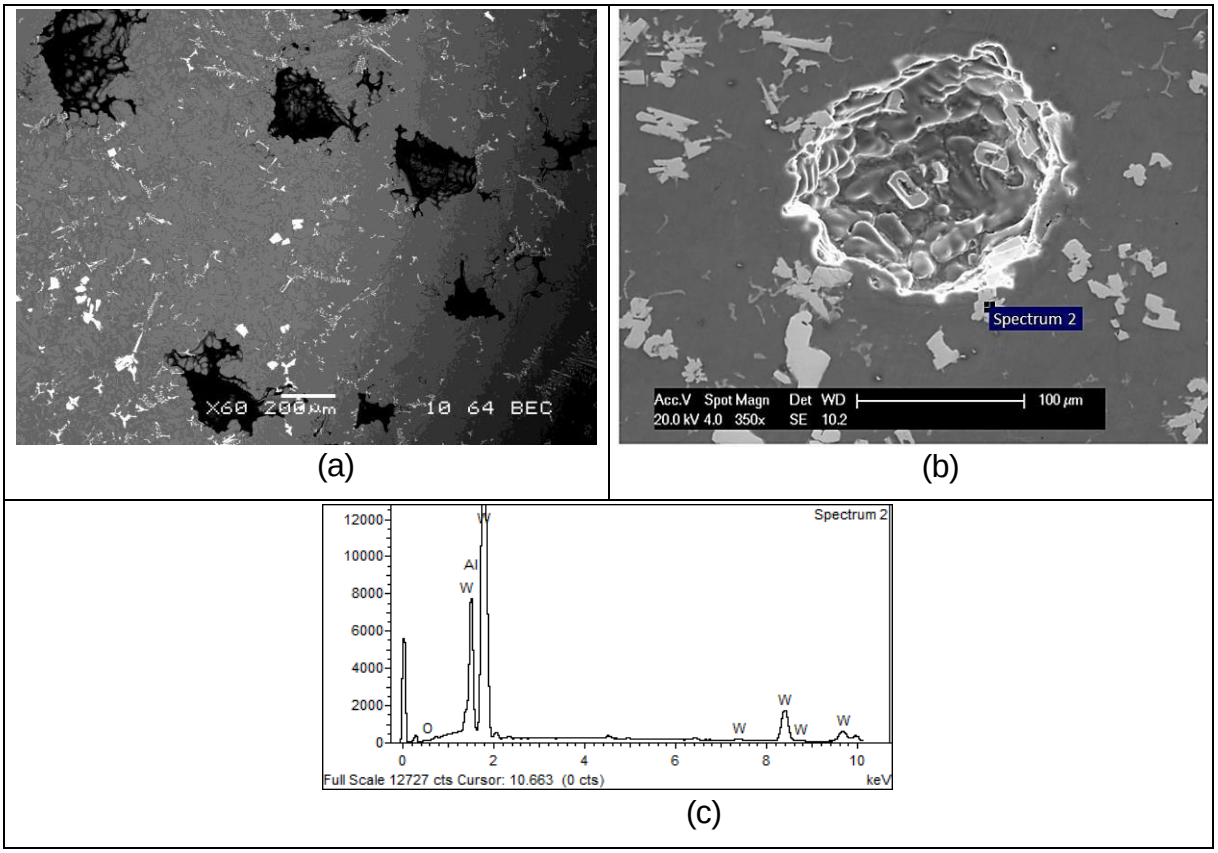


Figure 4-68: (a) and (b) low and high magnification of a typical SEM micrograph of the top of the polished surface of W masteralloy ingot with gas porosity, (c) EDX spectrum for the point marled as Spectrum 2

Table 4-72: EDX elemental composition of spectra in Figure 4-68 (b)

	Spectrum 2	
Element	Weight%	Atomic%
O K	0.29	1.70
Al K	33.28	75.10
W M	66.72	23.60

Figure 4-69 (b) shows Al $Si_{1.4}W_{1.2}$ with O varying from 20 µm to 300 µm in length blocky shaped and marked as Spectrum 6; the corresponding marked EDX spectrum is shown in Figure 4-69 (c), and EDX elemental compositions are presented in Table 4-73.

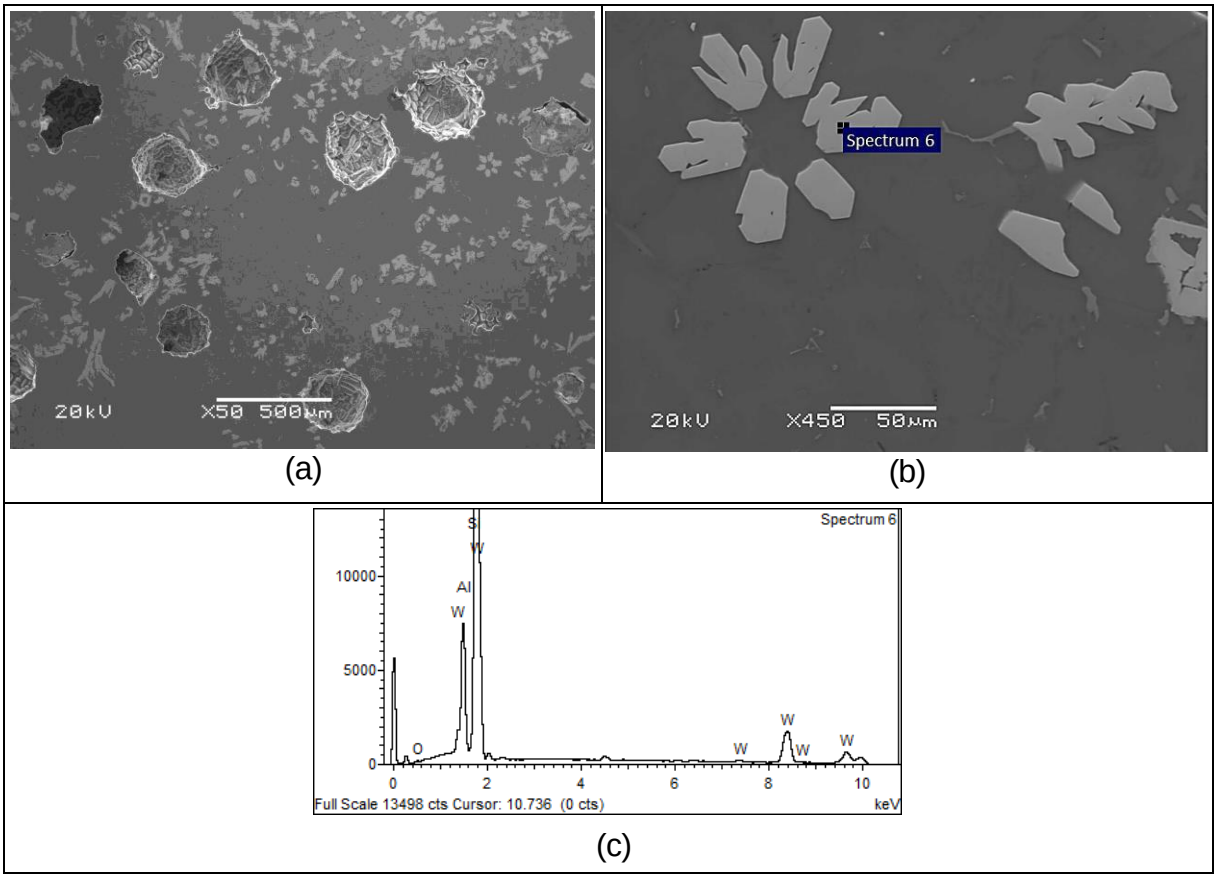


Figure 4-69: (a) and (b) low and high magnification of SEM image of the bottom of the W masteralloy ingot (c) EDX spectrum for the point marled as Spectrum 6

Table 4-73 EDX elemental composition of spectra in Figure 4-69 (b)

	Spectrum 6	
Element	Weight%	Atomic%
O K	0.63	3.04
Al K	8.90	25.36
Si K	14.55	39.85
W M	75.92	31.75

Summary of all the phases in the 2L99 +10 wt.% W masteralloy is presented in Table 4-74.

Table 4-74: Summary of the phases on the masteralloy of W (2L99 + 10 wt.% W)

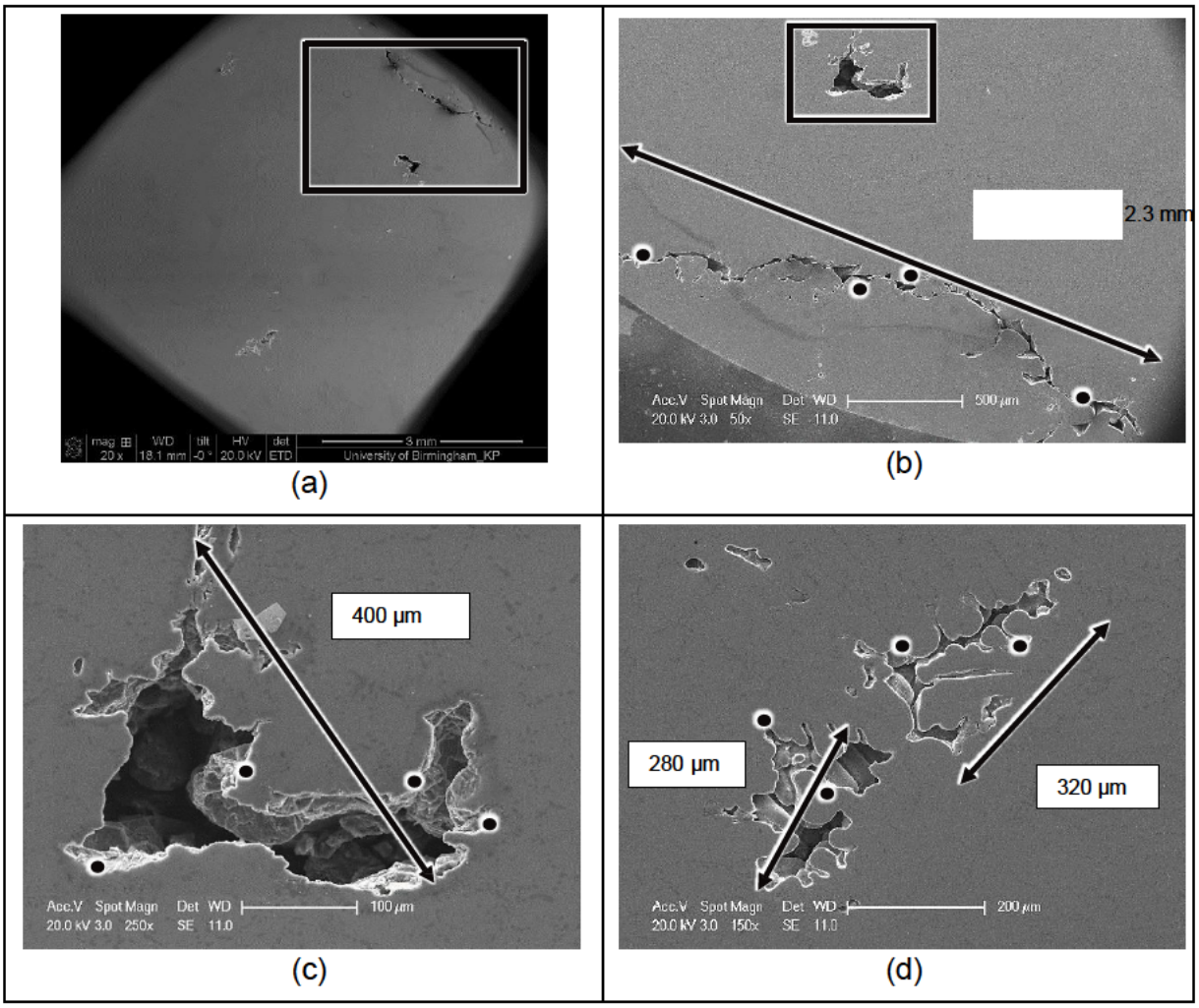
Masteralloy 2L99 + 10 wt.% W	Name	Size
Oxides on the fractured surface of the masteralloy	Mainly spinel, slightly SiO_2 and Mg O	-Cubic MgO 100 nm in with -SiO_2 100 µm in length -An oxide layer, probably MgO 12 µm in length
Nitrides	None	NA
Intermetallic Particles on the polished surface of the masteralloy	$W_4Al_{14}Si$ $W_4Al_{14}Si$ Al_3W AlW_2 $W_4Al_{14}Si$	approximately 40 µm in length approximately 60 µm in length approximately 12 µm in length approximately 30 µm in length approximately 20 µm in length
Intermetallic Particles on the fractured surface of the masteralloy	Al_4W $W_{1.5}AlSi_2$ $W_4Al_{14}Si$	approximately 50 µm in length approximately 35 µm in length approximately 50 µm in length
Masteralloy 2L99+10 wt.% W top and bottom	Al_3W $AlSi_{1.4}W_{1.2}$	approximately varying from 6 µm to 50 µm approximately varying from 20 µm to 300 µm

4.2.3.3 Characterisations of the phases on polished surfaces of 2L99 + 0.4 wt.% W

The morphology and composition of various phases, such as oxides, nitrides, and intermetallic compounds of polished surfaces of 2L99 + 0.4 wt.% W alloys were investigated using SEM and EDX. Figure 4-70 (a) to Figure 4-70 (e) show low to high magnification SEM micrographs of a representative low UTS (179 MPa) 2L99 + 0.4 wt.% W alloy testbar. Various bifilms with shrinkage porosities were observed, as shown in Figure 4-70 (a), ranging in length from 50 µm to 2300 µm with an overall average length of 500 µm positioned at various orientations.

Figure 4-70 (b) to Figure 4-70 (e) show high-magnification SEM micrographs of two of the largest bifilms. EDX composition of the points marked as black circles on these

bifilms (spinel) showed the presence of oxides on the edge of the defects with an average O content of 4 at.%. Figure 4-70 (f) shows a representative EDX composition of the points marked in Figure 4-70 (b) to Figure 4-70 (e). Table 4-75 presents the EDX elemental composition of the points marked with black circles in Figure 4-70 (b) to Figure 4-70 (e).



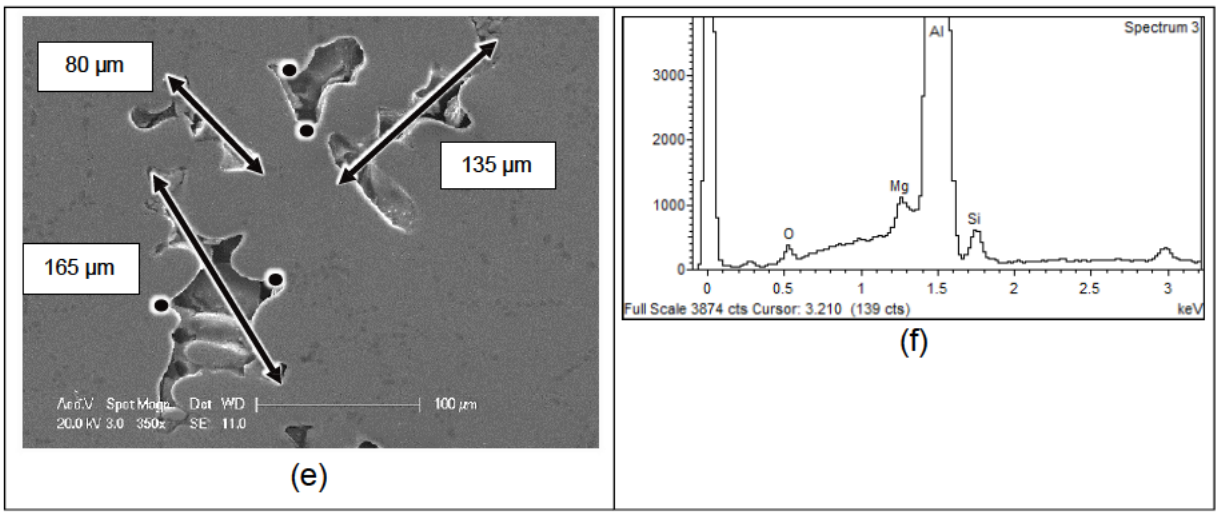


Figure 4-70: (a) the whole matrix SEM micrograph of the 2L99 + 0.4 wt.% W alloy polished cross-section with low UTS value (178.7 MPa), (b) to (e) High magnification SEM micrographs of the significant cavities detailed in (a), (f) Corresponding EDX Spectrum3 for black circles marked in (b) to (e)

Table 4-75: EDX elemental composition of the points marked in black in Figure 4-70 (b) to (e)

	Spectrum 3	
Element	Weight%	Atomic%
O K	2.60	4.30
Mg K	0.43	0.47
Al K	95.05	93.41
Si K	1.92	1.81

Figure 4-71 (a) to Figure 4-71 (c) show low to high magnification SEM micrographs of a representative high UTS (286.1 MPa) 2L99 + 0.4 wt.% W alloy testbar. Various bifilm defects were observed, as shown in Figure 4-71 (a), ranging in length from 30 µm to 160 µm (average 83 µm) with different orientations.

Figure 4-71 (b) and Figure 4-71 (c) show high-magnification SEM micrographs of three of the largest bifilms. EDX composition of the points marked on these bifilms showed the presence of oxides on the edge of the defects with an average O content of 4 at.%. Figure 4-71 (d) shows a representative EDX composition of the points marked in Figure 4-71 (b). An Iron intermetallic of W ($Al_{8.3}SiFe_{1.4}$) of approximately 10 µm was observed

on the polished surface, as shown in Figure 4-71 (c). Table 4-76 presents the EDX elemental composition of the points marked in black circles and Spectrum 2 in Figure 4-71 (b).

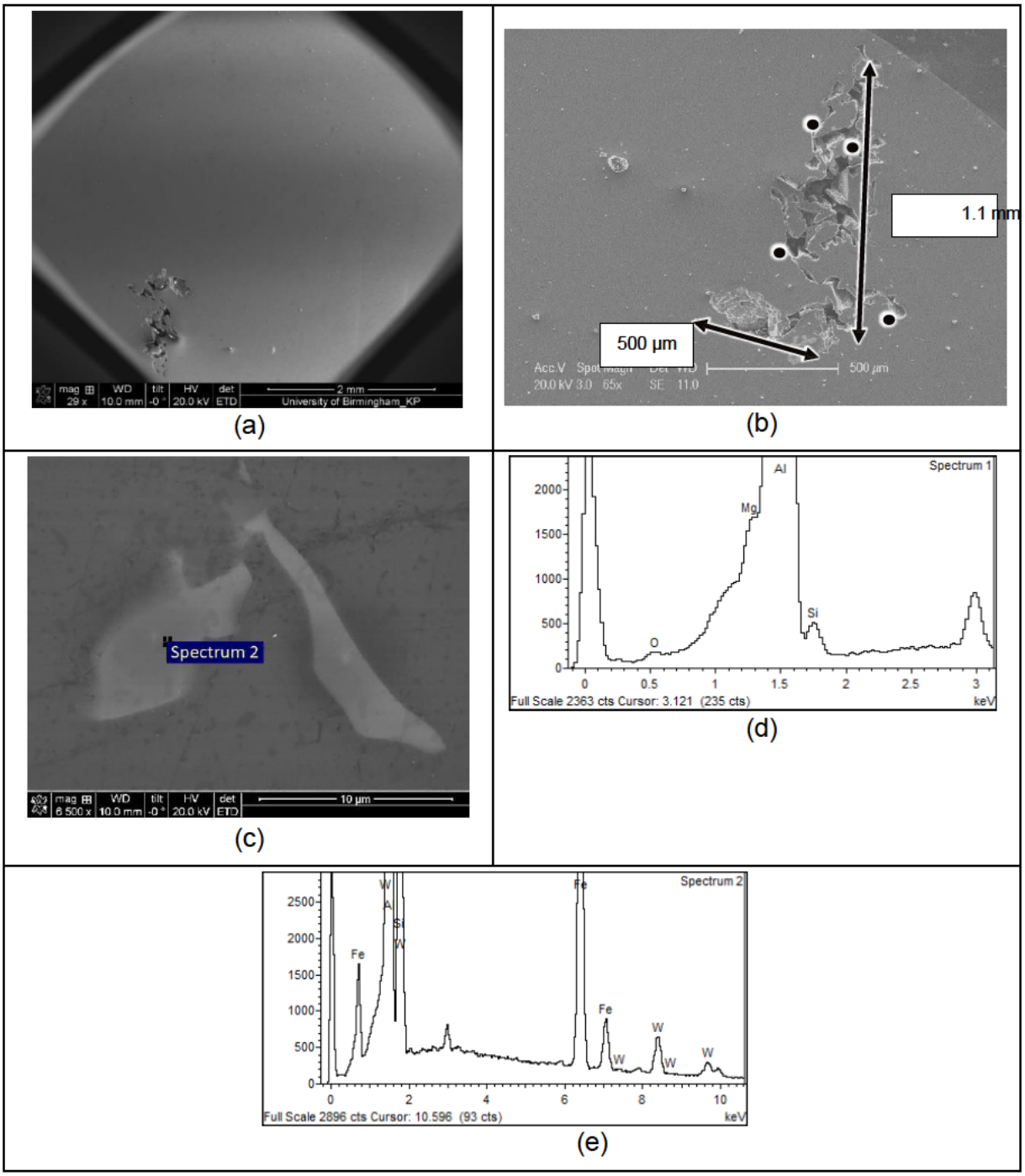


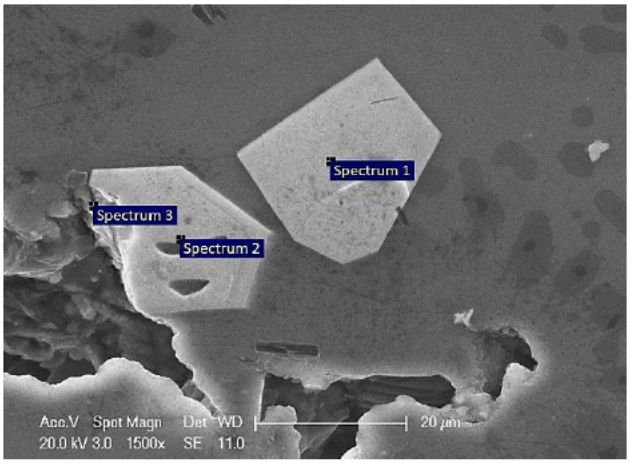
Figure 4-71: (a) Whole matrix SEM micrograph of a polished cross-section of the 2L99 + 0.4 wt.% W alloy with high UTS value (286.1 MPa), (b) and (c) High magnification SEM micrographs of the main cavities detailed in (a), (d) EDX Spectrumb1 as marked in (b) and (e) EDX Spectrum 2 as marked in (c)

Table 4-76: EDX elemental composition of the points marked in black in Figure 4-71 (b)

	Spectrum 1		Spectrum 2	
Element	Weight%	Atomic%	Weight%	Atomic%
O K	0.78	1.31	0.00	0.00
Mg K	0.56	0.62	0.00	0.00
Al K	97.22	96.70	58.99	75.63
Si K	1.44	1.38	7.21	8.88
Fe K	0.00	0.00	21.18	13.12
W M	0.00	0.00	12.62	2.37

Multi-facetted intermetallic compounds of $W_{1.2}AlSi_{1.2}$, as well as MgO, were observed on the polished surface of a 2L99 + 0.4 wt.% W alloy, as shown in Figure 4-72 (a), predominantly nucleating on the edge (wetted side) of the bifilm.

EDX compositions of the intermetallic compounds observed in Figure 4-72 (a) are presented in Figure 4-72 (b) to Figure 4-72 (d). The MgO with 1.3 at.% of W observed in Spectrum 3 located at the edge of the bifilm showed the presence of approximately 30 at.% O. The intermetallic compounds observed in this instance were approximately 20 µm and 30 µm in length. The intermetallics observed and marked up as Spectrum 1 and Spectrum 2 were revealed to have a similar composition of $W_{1.2}AlSi_{1.2}$ with O. Table 4-77 presents the EDX elemental composition of the points marked in Figure 4-72 (a).



(a)

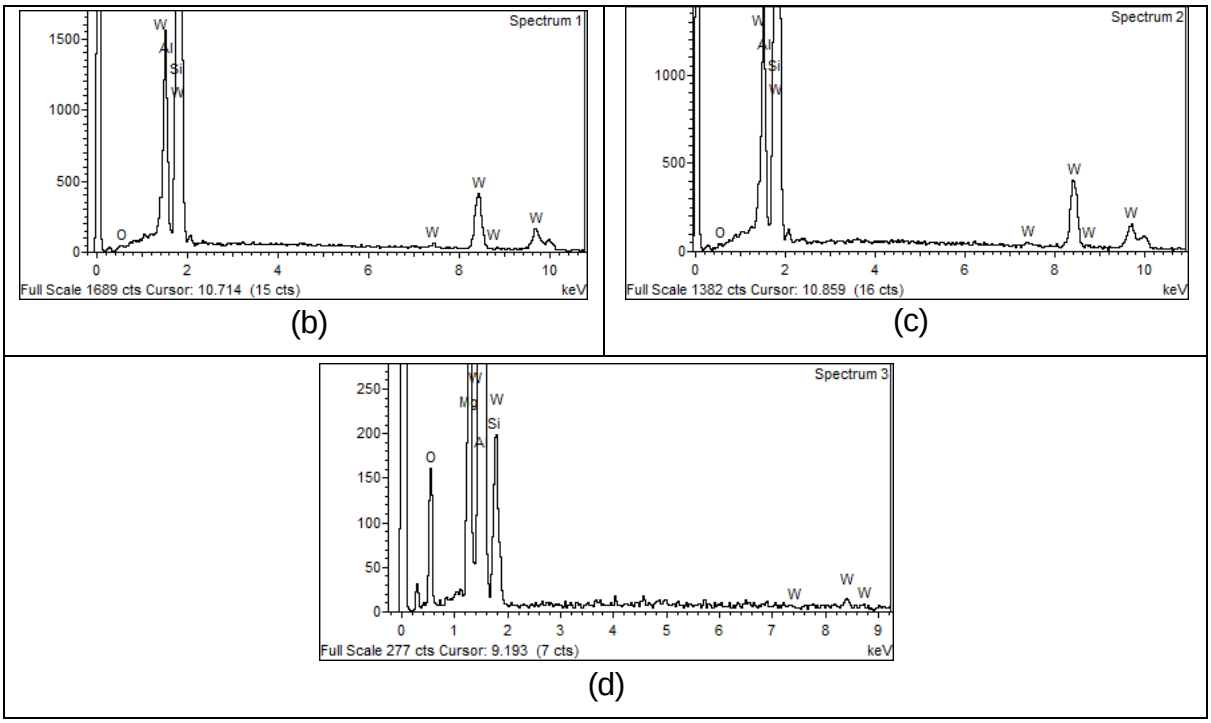


Figure 4-72: (a) SEM micrograph of a polished surface 2L99 + 0.4 wt.% W alloy showing the faceted intermetallic compounds grown on the bifilm (b) to (d) EDX spectra marked in (a)

Table 4-77: EDX elemental composition of the spectra marked in Figure 4-72 (a)

	Spectrum 3		Spectrum 2		Spectrum 1	
Element	Weight%	Atomic%	Weight%	Atomic%	Weight%	Atomic%
O K	18.38	29.45	1.17	5.91	0.64	3.26
Mg K	6.60	6.95	0.00	0.00	0.00	0.00
Al K	59.74	56.76	8.40	25.04	8.94	26.92
Si K	6.09	5.56	12.15	34.81	12.20	35.27
W M	9.19	1.28	78.27	34.24	78.22	34.55

Similar to Figure 4-72, multi-facetted (most likely irregular hexagonal) intermetallic compounds of $W(Al, Si)_2$ with oxides of approximately 25 µm length, marked as Spectrum 3, as well as bifilm (spinal) with a small amount of W (1.2 at.%) marked as Spectrum 4, was observed on a polished surface of a 2L99 + 0.4 wt. % W alloy, as shown in Figure 4-73 (a). It is important to note that the presence of the $W(Al, Si)_2$ intermetallic agrees with literature [3]. The intermetallic compounds were observed to have nucleated on the edge (or wetted side) of the bifilm, as shown in Figure 4-73 (a).

The EDX compositions of the intermetallic compounds observed in Figure 4-73 (a) are presented in Figure 4-73 (b) and Figure 4-73 (c). The spinel observed in Spectrum 4, located at the edge of the bifilm, showed the presence of approximately 45.2 at.% of O. The intermetallic compounds observed in this instance were between 30 µm in length and had with ranging from 10 to 25 µm in width. Table 4-78 presents the EDX elemental composition of the spectra marked in Figure 4-73 (a).

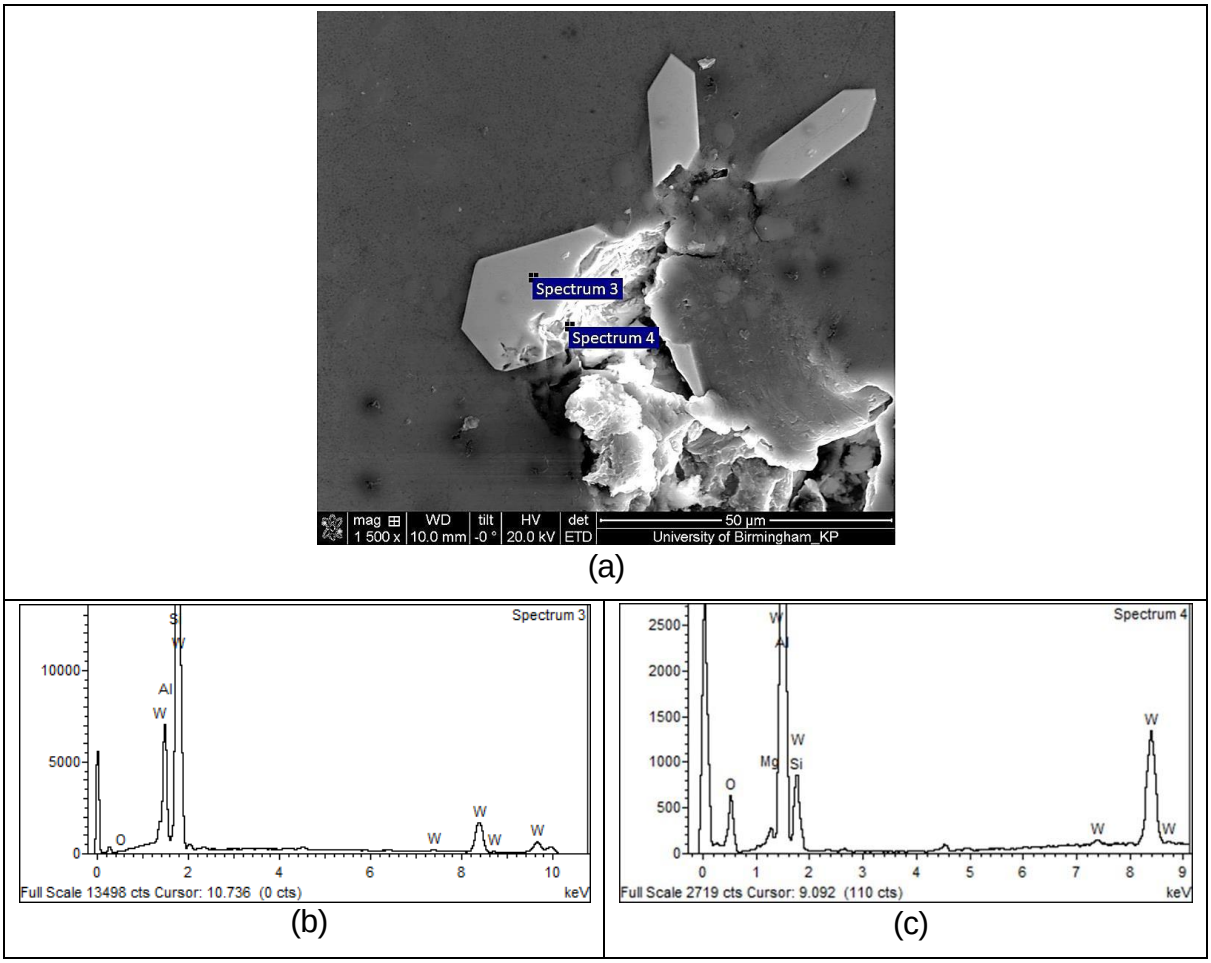


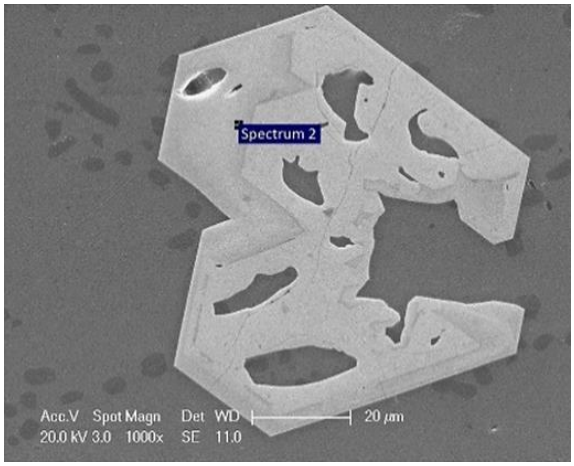
Figure 4-73: (a) SEM micrograph of a polished surface 2L99 + 0.4 wt.% W alloy showing the faceted intermetallic compounds grown on the bifilm (b) and (c) EDX spectra marked in (a)

Table 4-78: EDX elemental composition of the areas marked in Figure 4-73 (a)

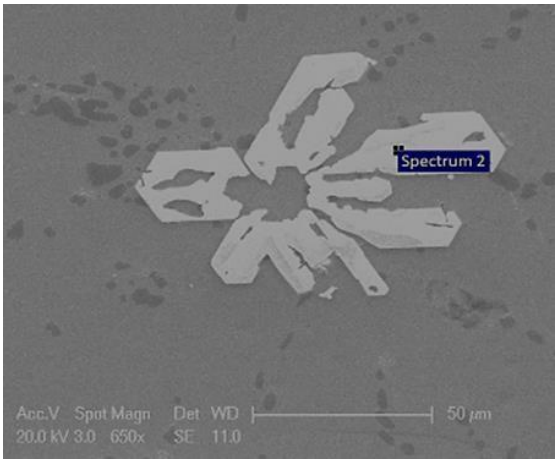
	Spectrum 3		Spectrum 4	
Element	Weight%	Atomic%	Weight%	Atomic%
O K	0.30	1.16	30.20	45.19
Mg K	0.00	0.00	1.49	1.47
Al K	8.59	39.61	48.78	43.27
Si K	14.90	39.58	10.42	8.88
W M	76.00	19.65	9.11	1.19

Figure 4-74 and Figure 4-75 show SEM micrographs and EDX compositions of numerous other intermetallic compounds observed on the surface of a polished 2L99+0.4 wt.% W alloy testbar. These intermetallic compounds were multi-faceted and possessed different morphologies varying between 20 µm and 80 µm in length.

The intermetallic compounds with O observed in Figure 4-74 (a) and Figure 4-74 (b) had the exact composition of $AlSi_{1.4}W_{1.2}$ with O . Figure 4-74 (c) and Figure 4-74 (d) show the EDX spectra of the areas marked in Figure 4-74 (a) and Figure 4-74 (b). Table 4-79 presents the EDX elemental composition of the points marked in Figure 4-74 (a) and Figure 4-74 (b).



(a)



(b)

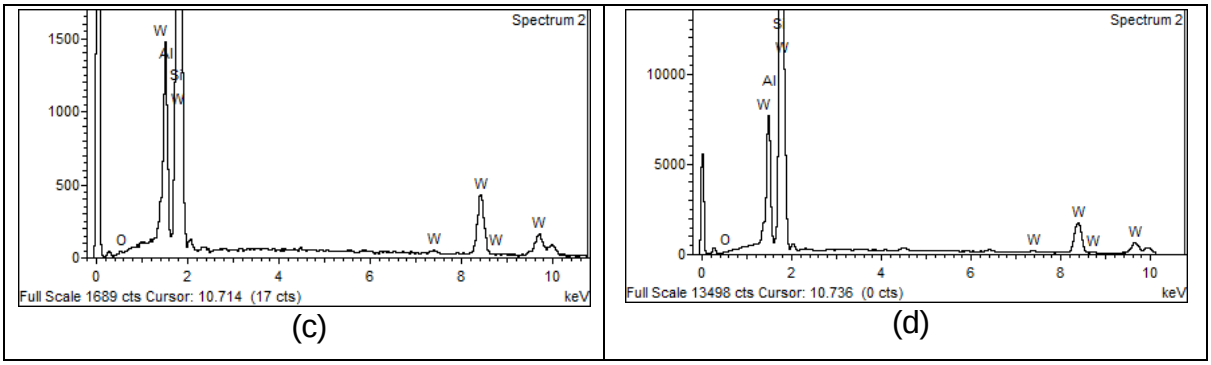


Figure 4-74: (a) and (b) SEM micrographs of a polished surface of 2L99 + 0.4 wt.% W alloy showing different single intermetallics with inverse three and flower shapes ($AlSi_{1.5}W_{1.5}$) intermetallic compounds, (c) and (d) corresponding EDX spectra marked in (a) and (b), respectively

Table 4-79: presents the EDX elemental composition of the spectra marked in Figure 4-74 (a) and (b)

	Spectrum 2		Spectrum 2	
Element	Weight%	Atomic%	Weight%	Weight%
O K	0.75	3.80	0.39	1.85
Al K	8.56	25.60	9.48	27.00
Si K	12.66	36.37	14.42	39.49
W M	78.02	34.23	75.71	31.66

In contrast to the intermetallic compounds observed in Figure 4-74 (a) and Figure 4-74 (b), the intermetallic compounds observed in Figure 4-75 (a) and Figure 4-75 (b) had different compositions of $AlW_{1.5}$ and $W(Al, Si)_2$ with O, 46 µm and 25 µm, respectively. The point marked as Spectrum 2 in Figure 4-75 (b) corresponded to oxides, probably spinel with a small amount of Fe (0.6 at.%). Figure 4-75 (c) to Figure 4-75 (e) show the EDX spectra of the areas marked in Figure 4-75 (a) and Figure 4-75 (b).

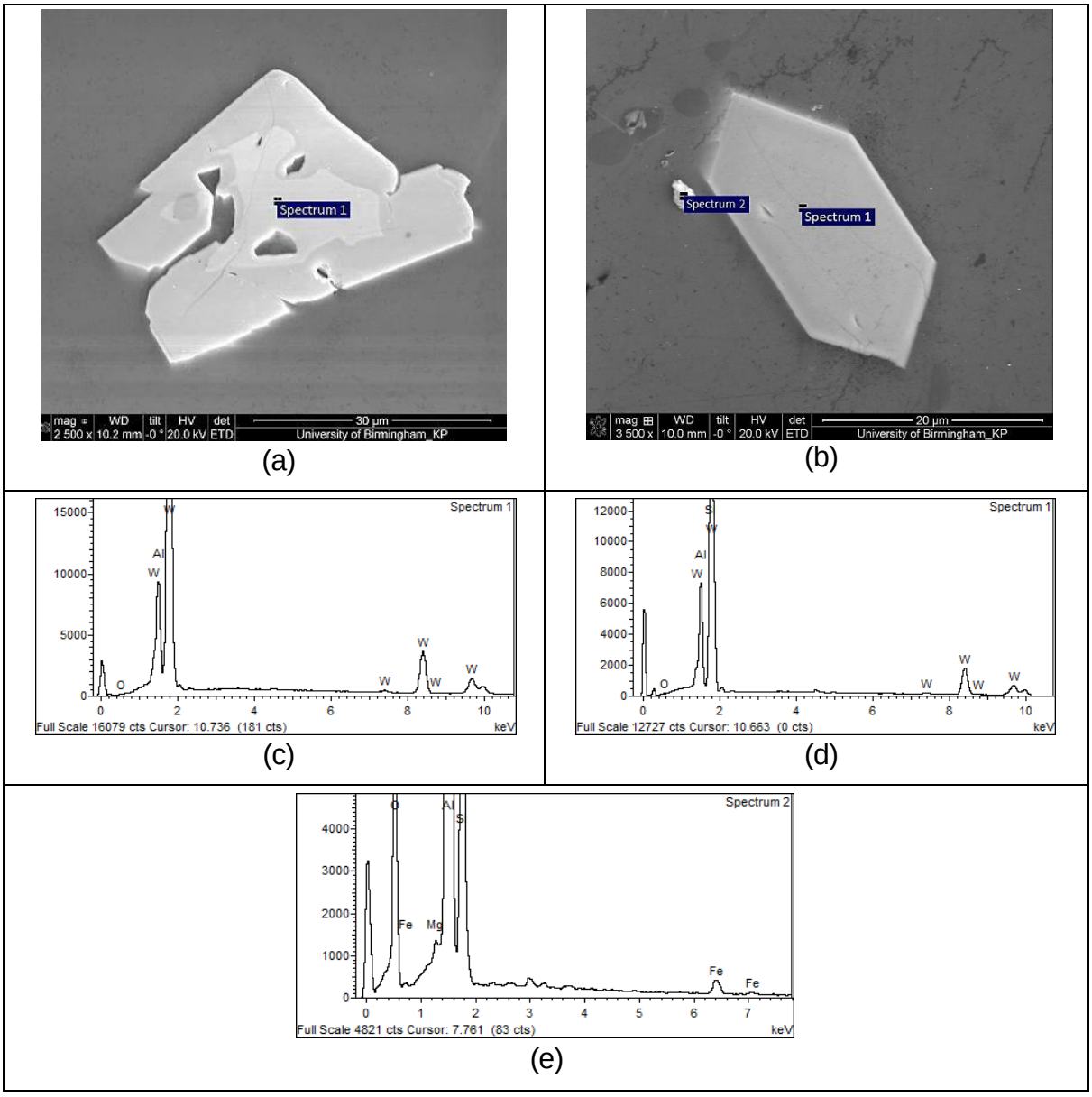
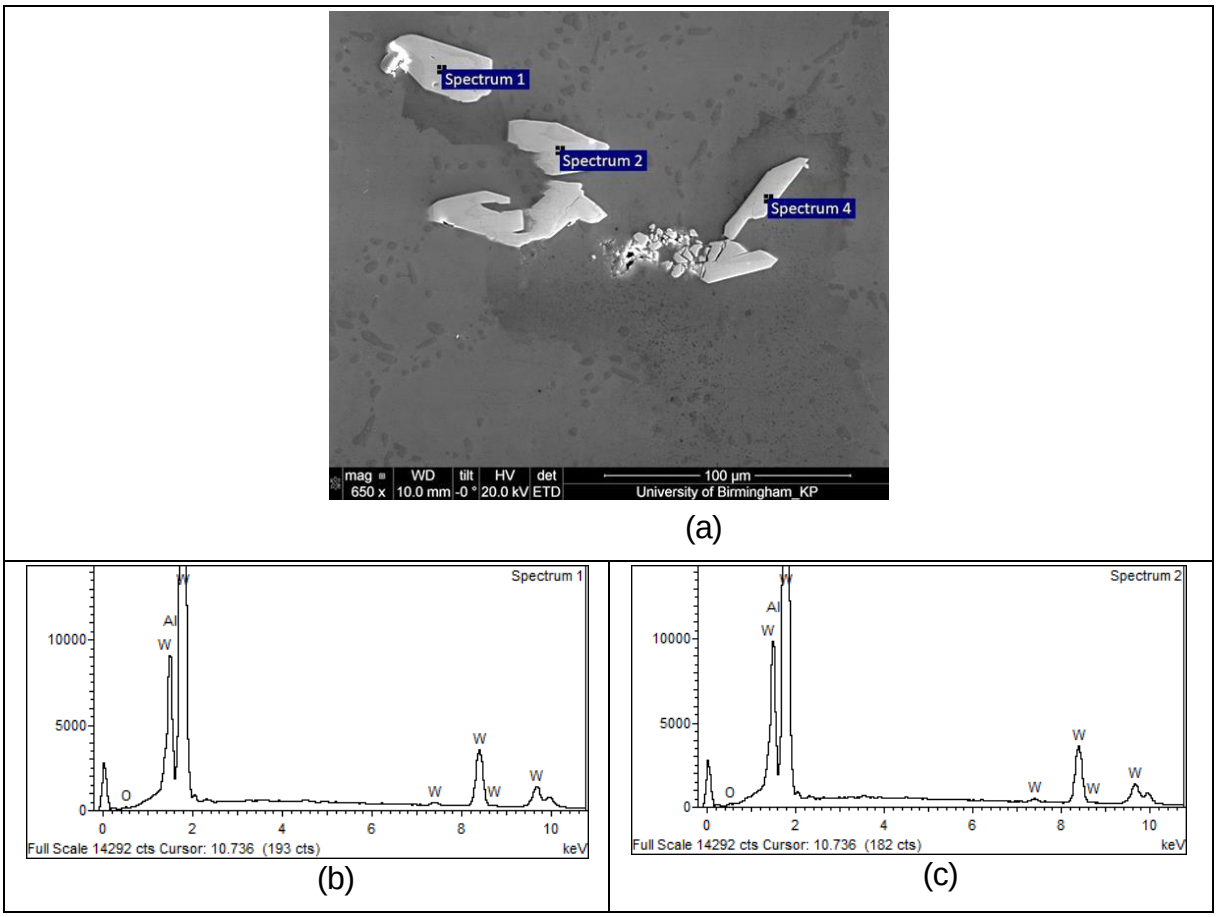


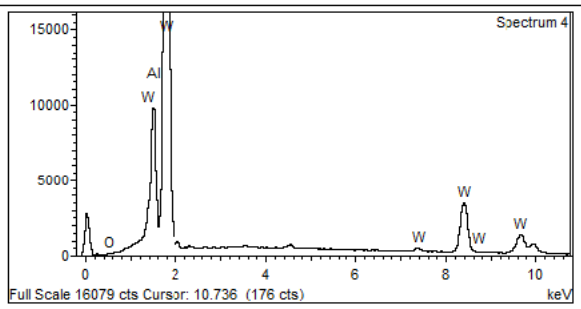
Figure 4-75: (a) and (b) SEM micrographs of a polished surface 2L99 + 0.4 wt.% W alloy showing different single intermetallics with inverse three and flower shapes ($AlW_{1.5}$, $AlSi_2W_{1.5}$) intermetallic compounds, (c) and (d) corresponding EDX spectra of the areas marked in (a) and (b), respectively.

Table 4-80: EDX elemental composition of the areas marked in Figure 4-75 (a) and (b)

	Spectrum 1		Spectrum 1		Spectrum 2	
Element	Weight%	Atomic%	Weight%	Atomic%	Weight%	Atomic%
O K	0.61	4.53	0.36	1.06	29.33	41.70
Al K	8.48	37.10	8.56	39.53	0.43	0.40
Si K	0	0	14.67	39.98	49.14	41.42
Fe K	0	0	0	0	19.58	15.86
W M	90.91	58.37	76.41	20.1	0	0

Further multi-faceted intermetallic compounds of $AlW_{1.5}$ with O were observed on the polished surface of a 2L99 + 0.4 wt.% W alloy as shown in low magnification in Figure 4-76 (a). The intermetallic compounds were not observed to nucleate on a bifilm, with some of the compounds showing signs of fracture. The EDX compositions of the intermetallic compounds observed in Figure 4-76 (a) are presented in Figure 4-76 (b) to (d). The intermetallic compounds observed in this instance measured approximately 70 µm in length and 20 µm to 30 µm in width. Table 4-81 presents the EDX elemental composition of the spectra marked in Figure 4-76 (a).





(d)

Figure 4-76: (a) SEM micrograph of a polished surface of 2L99 + 0.4 wt.% W alloy showing different faceted shapes $AlW_{1.5}$ intermetallic compounds, (b) to (d) EDX spectra of the areas marked in (a)

Table 4-81: EDX elemental composition of the spectra marked in Figure 4-76 (a)

	Spectrum 1		Spectrum 2		Spectrum 4	
Element	Weight%	Atomic%	Weight%	Atomic%	Weight%	Atomic%
O K	0.54	4.04	0.53	3.87	0.32	2.37
Al K	8.34	36.86	8.87	38.47	8.95	39.23
W M	91.12	59.09	90.60	57.67	90.73	58.39

Numerous small multi-facetted intermetallic compounds of $W_{1.1}AlSi_{1.3}$ and spinel (with 4.3 at.% of O content) were also observed on the polished surface of a 2L99 + 0.4 wt.% W alloy as shown in high magnification in Figure 4-77 (a). The intermetallic compounds were observed to be nucleating on the edge of the bifilm (wetted side). These intermetallic compounds were small, measuring approximately 1 µm to 5 µm in length. The EDX analysis for Spectra 1, 2 and 9 were similar, as shown in Figure 4-77 (b). Table 4-82 presents the EDX elemental composition of the points marked in Figure 4-77 (a).

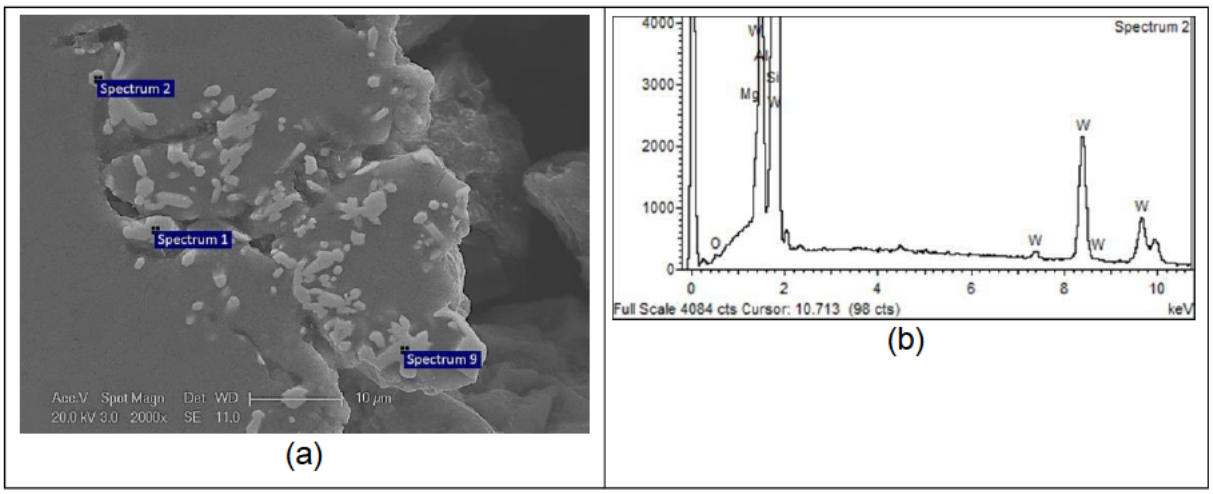


Figure 4-77: (a) SEM micrograph of a polished surface of 2L99 + 0.4 wt.% W alloy showing small-sized Al Si_2 W and Al-Si- W intermetallic compounds, (b) EDX spectra as marked in (a)

Table 4-82: EDX elemental composition of the areas marked in Figure 4-77 (a)

	Spectrum 2	
Element	Weight%	Atomic%
O K	0.88	4.33
Mg K	0.01	0.02
Al K	9.41	27.49
Si K	12.49	35.04
W M	77.22	33.11

A low to high magnification SEM micrograph of the inside of a bifilm defect observed on the polished surface of a 2L99 + 0.4 wt.% W testbar has been shown in Figure 4-78 (a) and Figure 4-78 (b). The bifilm was characterised using SEM and EDX, including a higher magnification of the area marked as X1, which is shown in Figure 4-78 (b). As shown in Figure 4-78 (a) and based on the EDX analysis, the composition of the material inside the bifilm was found to be spinel and nitride with an average O content of 28.6 at.% and N content of 12.5 at.%. As shown in Figure 4-78 (a), the width of the bifilm was approximately 90 µm, with nitride patches measuring approximately 5 µm in length. Table 4-83 presents the quantification of the spectra shown in Figure 4-78 (a).

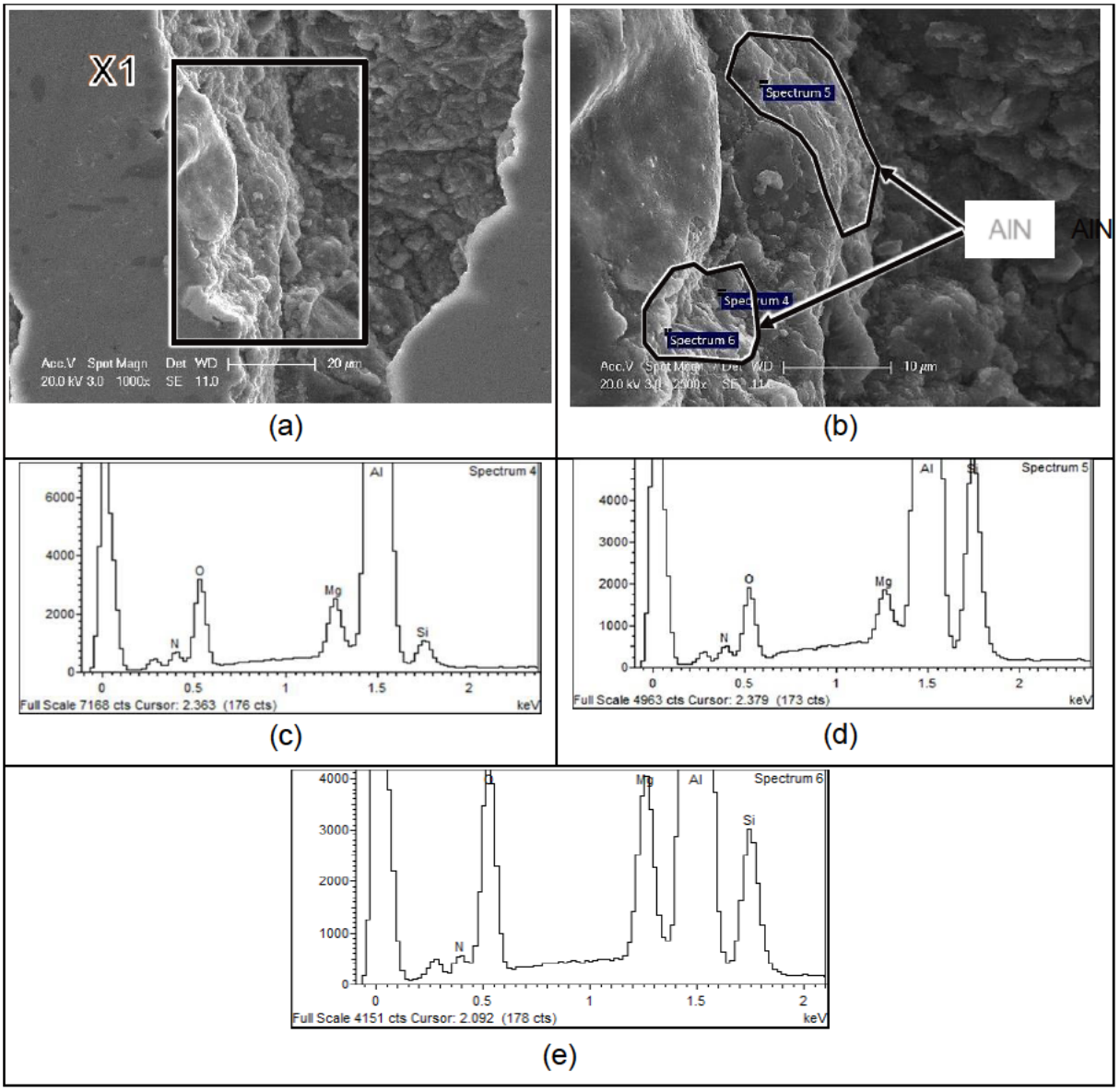
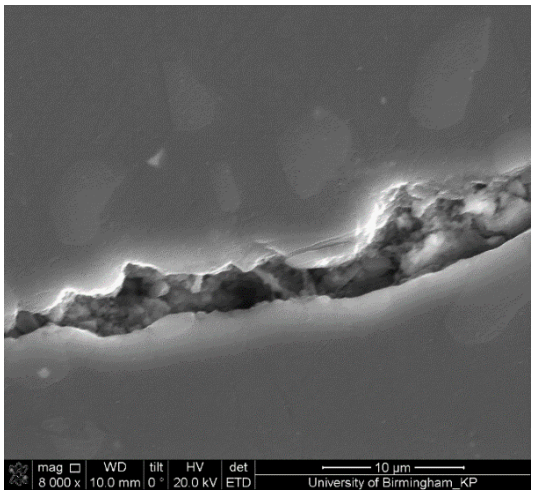


Figure 4-78: (a) SEM micrograph of a polished surface of 2L99 + 0.4 wt.% W alloy showing a bifilm with oxide and nitride layers, (b) High magnification of the area marked in (a), (c) to (e) EDX spectra as marked in (b)

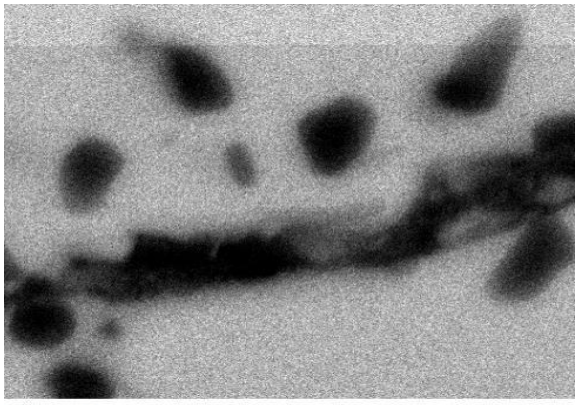
Table 4-83: EDX elemental composition of the areas marked in Figure 4-78 (a)

	Spectrum 4		Spectrum 5		Spectrum 6	
Element	Weight%	Atomic%	Weight%	Atomic%	Weight%	Atomic%
N K	9.42	14.68	7.66	12.70	6.61	10.19
O K	21.54	29.38	13.62	19.78	27.09	36.58
Mg K	0.64	0.58	0.89	0.87	1.52	1.39
Al K	64.85	52.44	66.33	57.12	56.60	45.32
Si K	2.05	1.84	1.15	1.10	3.73	3.31

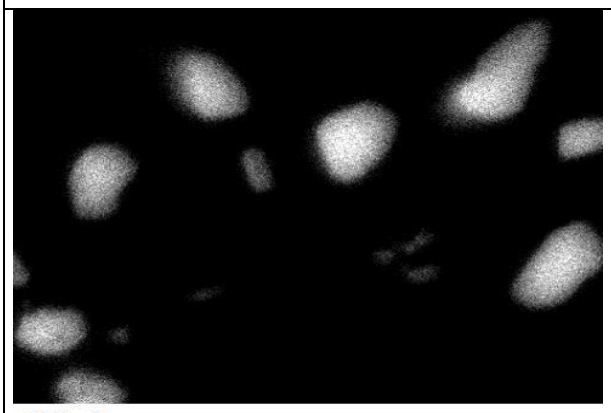
Figure 4-79 (a) to Figure 4-79 (f) show the EDX elemental mapping of a bifilm measuring 50 µm in length observed on the polished surface of a 2L99 + 0.4 wt.% W. The EDX elemental mapping was carried out to identify the areas where various elements such as Al, Si, O, Mg and N were present. Table 4-84 summarises the phases observed on the polished surface a 2L99 + 0.4 wt.% W alloy.



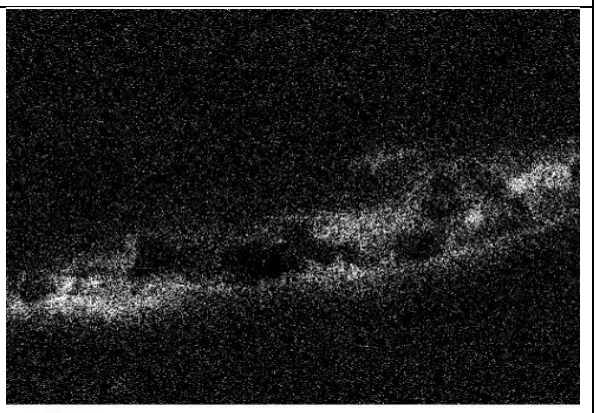
(a)



(b)



(c)



(d)

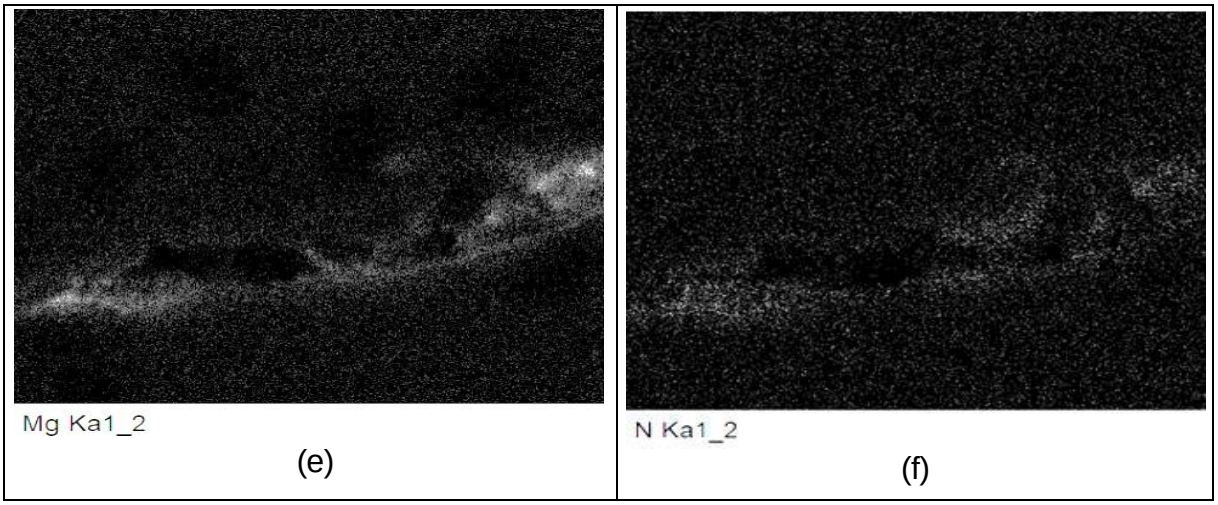


Figure 4-79: (a) to (f) EDX mapping of a bifilm on the polished surface of 2L99 + 0.4 wt.% W

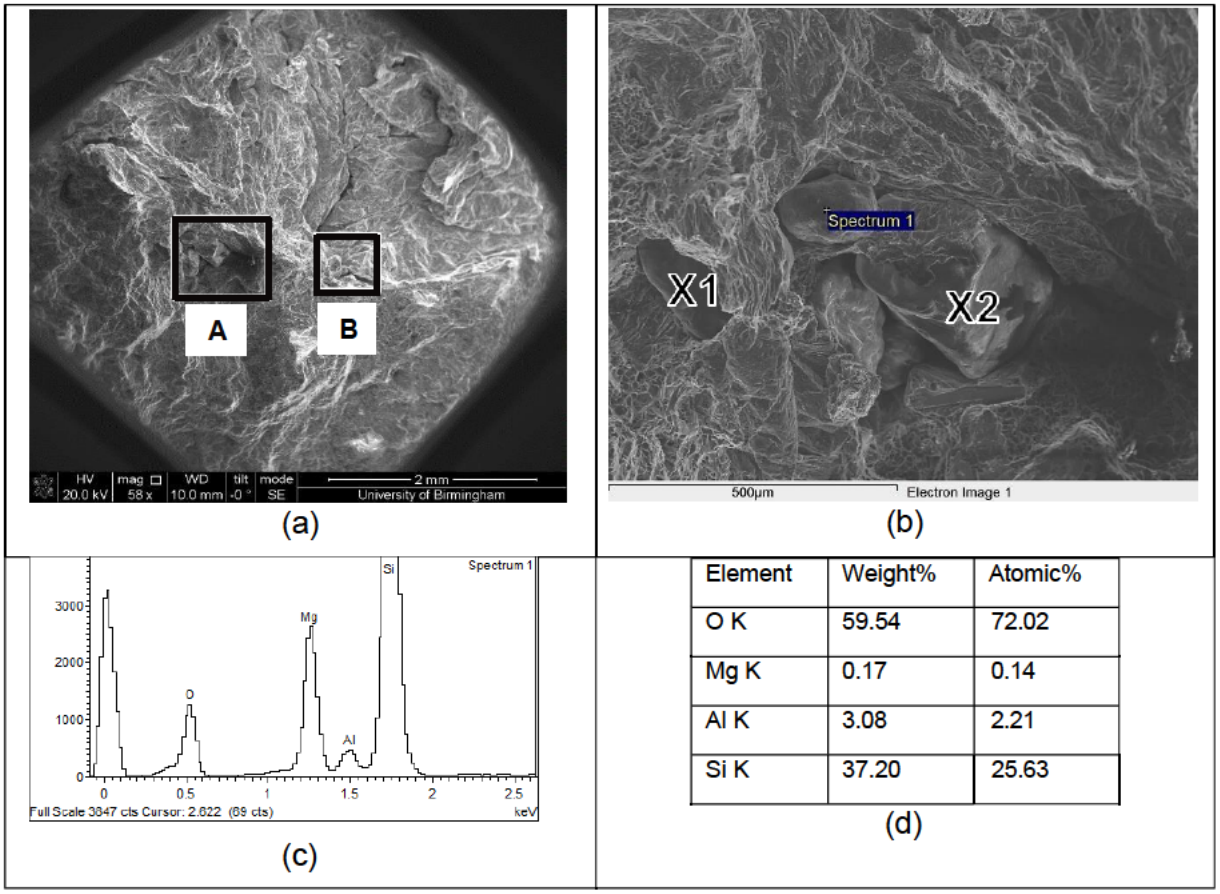
Table 4-84: Summary of the phases on polished flat surface 2L99 + 0.4 wt.% W alloy

Polished 2L99 + 0.4 wt.% W	Name	Size
Oxides	Mainly spinel	Average from 83 µm to 508 µm
Nitrides	AlN	5 µm in width
Intermetallic Particles	$W_{1.2}AlSi_{1.2}$ $W_{1.4}AlSi_{2.4}$ $W(Al,Si)_2$ $W_{1.5}Al$ $W_{1.1}AlSi_{1\ 3}$ $Al_{5.8}Si_{0.7}FeW_{0.2}$	approximately 20 µm and 30 µm 20 and 80 25 µm Vary between 20 µm to 70 µm approximately 1µm to 5 µm in width 70 µm in length and 20 µm to 30 µm in width

4.2.3.4 Characterisations of the phases on the fractured surfaces of 2L99 + 0.4 wt.% W

The fractured surface of a 2L99 + 0.4 wt.% W sample exhibited the presence of oxides and a visible long crack, approximately 2 mm in length, as depicted in Figure 4-80 (a). Among these oxides, the two largest bifilm inclusions containing significant Mg were identified and labelled as A and B on the fractured surface. In a more detailed view, Figure 4-80 (b) displayed a high-magnification image of the area, marked as A in Figure 4-80 (a).

Further analysis revealed the presence of oxides (SiO_2) with similar characteristics. Spectrum 1, X1, and X2 in Figure 4-80 (b) represent oxides with comparable EDX quantifications provided in Figure 4-80 (c) and (d). The EDX analysis showed O at 72 at.%, Mg at 0.14 at.%, Al at 2.21 at.%, and Si at 26 at.%. The average length of the oxide inclusions were to be 250 µm.

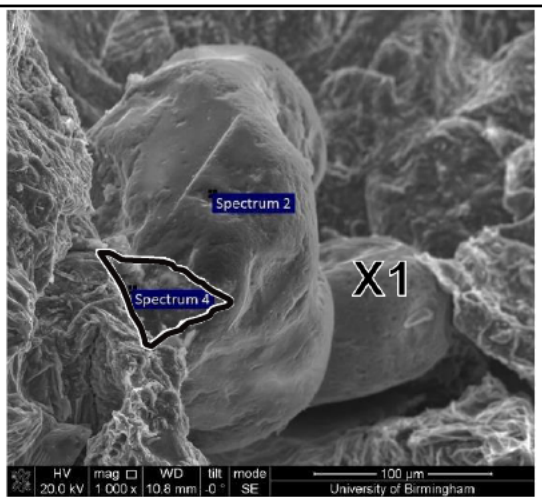


Element	Weight%	Atomic%
O K	59.54	72.02
Mg K	0.17	0.14
Al K	3.08	2.21
Si K	37.20	25.63

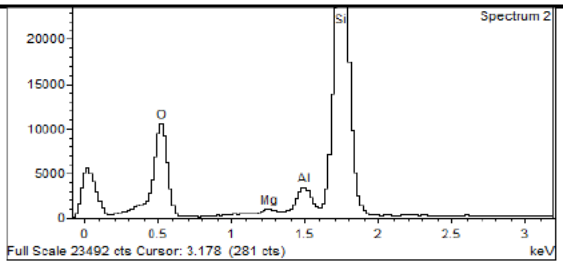
Figure 4-80: (a) Low magnification SEM image of the tensile test fractured surface of as-cast 2L99 + 0.4 wt.% W and (b) high magnification SEM image of area marked as A in Figure (a), (c) and (d) EDX analysis of spectrum1

To study the fractured surface further, high magnification of the area marked as B in Figure 4-80 (a) was investigated, as shown in Figure 4-81 (a). Oxide inclusions (SiO_2) with spinel patches were observed at points marked as Spectrum 2 and Spectrum 4. EDX spectrum and elemental composition of these locations are presented in Figure 4-81 (b), Figure 4-81 (d), Figure 4-81 (c) and Figure 4-81 (e). It was found that the areas marked

as X1 in Figure 4-81 (a) and Spectrum 2 (SiO_2) have the same elemental composition. The larger oxide inclusion, as shown in Figure 4-81 (a), was found to be 100 µm x 200 µm, whilst the smaller in the background was found to be 90 µm x 70 µm. The spinel patches around the Spectrum 4 area were approximately 30 µm in length and were observed to be on the exterior of the oxide inclusion, as shown in Figure 4-81 (a).



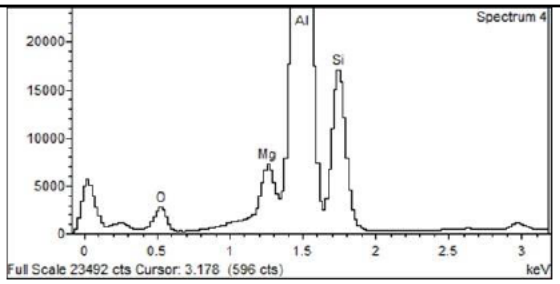
(a)



(b)

Element	Weight%	Atomic%
O K	53.37	66.67
Mg K	0.53	0.44
Al K	3.15	2.33
Si K	42.95	30.56

(c)



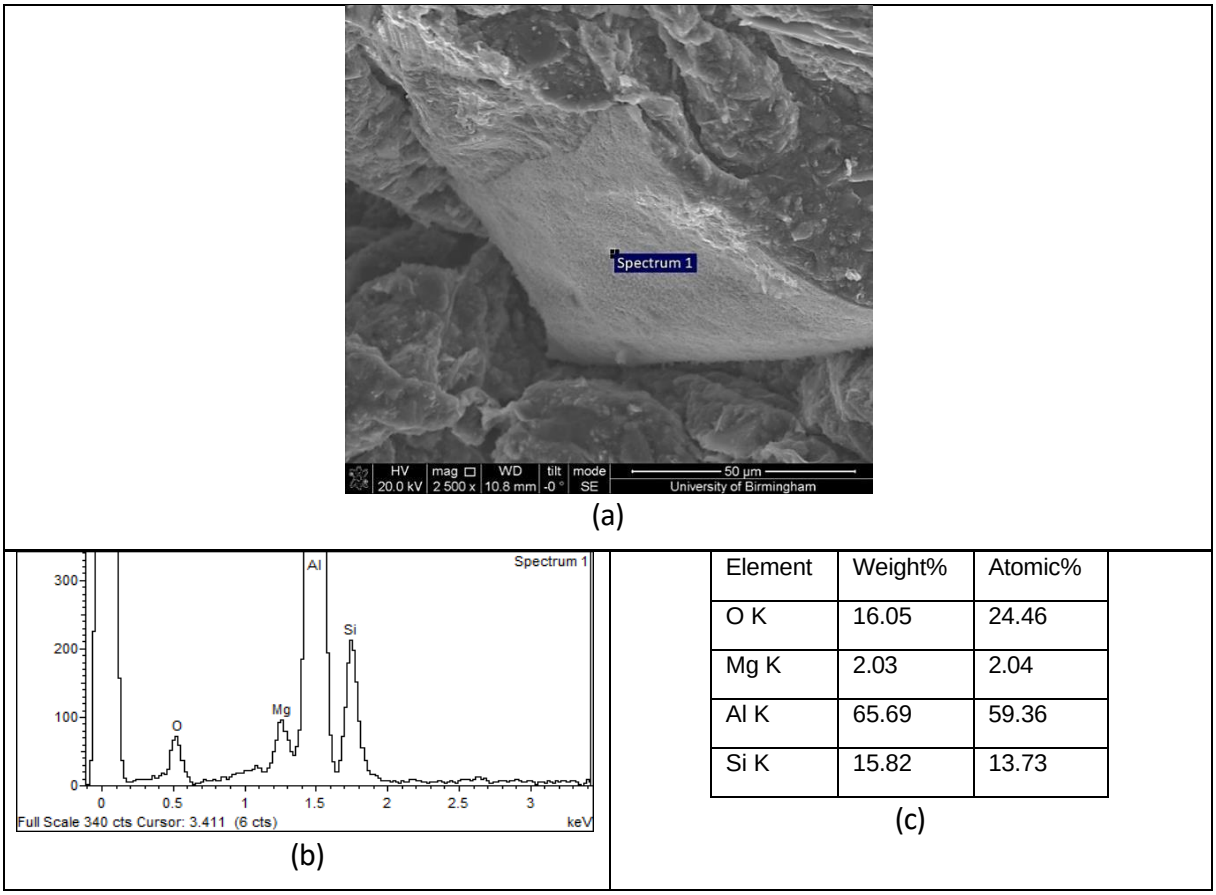
(d)

Element	Weight%	Atomic%
O K	11.22	17.65
Mg K	2.77	2.87
Al K	65.53	61.13
Si K	20.48	18.35

(e)

Figure 4-81: (a) SEM image of oxide inclusion on the fractured surface of as-cast 2L99 + 0.4 wt.% W, (b) and (c) EDX analysis of spectrum 2, (d) and (e) EDX analysis of spectrum 4

Figure 4-82 (a) shows an oxide probably spinel measuring approximately 80 µm x 50 µm on the fractured surface of the 2L99 + 0.4 wt.% W alloy with Mg content of 2 at.%. The EDX spectrum and quantification of the point marked as Spectrum 1 are presented in Figure 4-82 (b) and (c), respectively. The elemental composition of Spectrum 1 showed O constituted 24 at.%, while Mg accounted for 2 at.%, Al for 59 at.%, and Si for 14 at.%.



Element	Weight%	Atomic%
O K	16.05	24.46
Mg K	2.03	2.04
Al K	65.69	59.36
Si K	15.82	13.73

Figure 4-82: (a) SEM image of an oxide layer on the fractured surface of as-cast 2L99 + 0.4 wt.% W and (b) and (c) EDX analysis of spectrum1

Figure 4-83 (a) shows two types of oxide morphology of MgO with a nodular shape measuring approximately 16 µm and a whisker shape measuring approximately 6 µm on the fractured surface of the 2L99 + 0.4 wt.% W with a Mg content of 5 at.% and 10 at.%, respectively. The EDX spectra and quantification of Spectrum 1 marked in Figure

4-83 (a) and Figure 4-83 (b) are presented in Figure 4-83 (c) and Figure 4-83 (d), respectively, as well as Table 4-85.

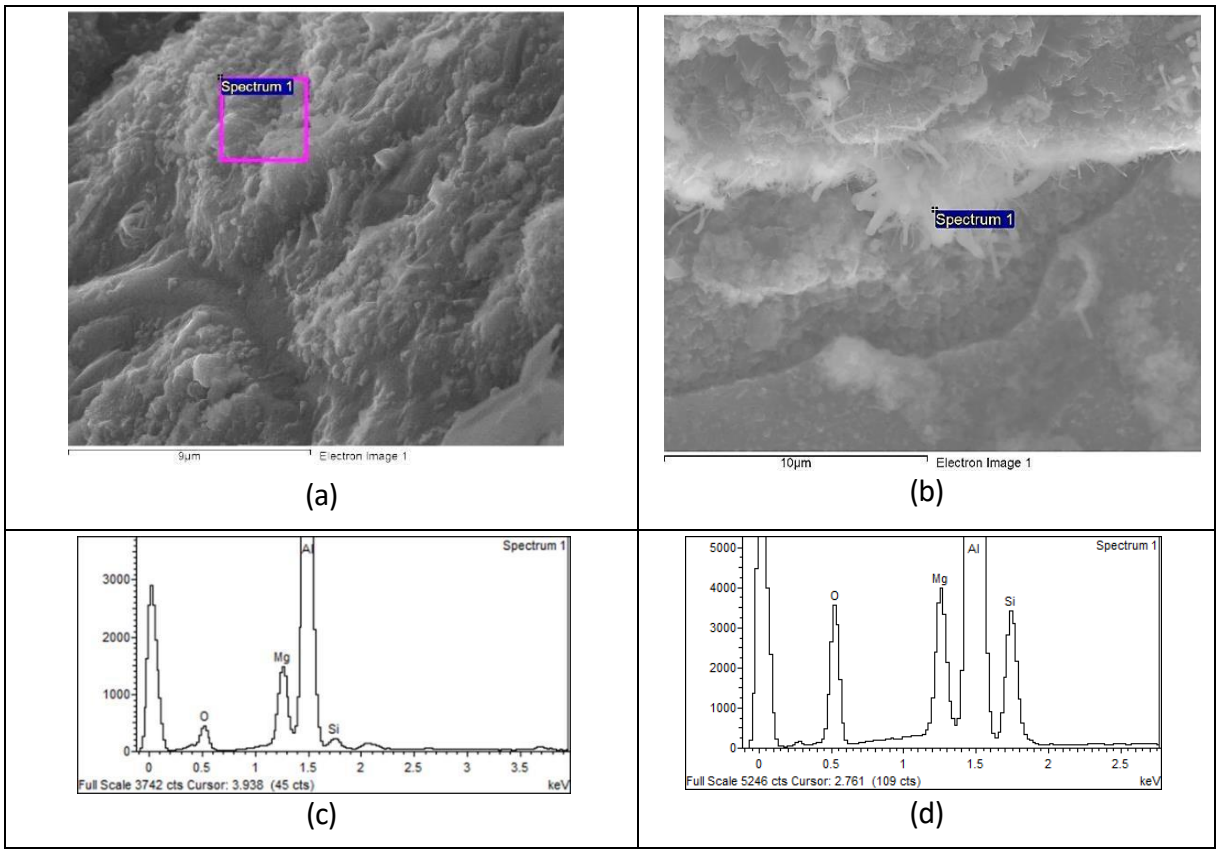


Figure 4-83: (a) and (b) SEM image of an oxide layer nodular and whisker on the fractured surface of as-cast 2L99 + 0.4 wt.% W and (c) and (d) corresponding EDX Spectra

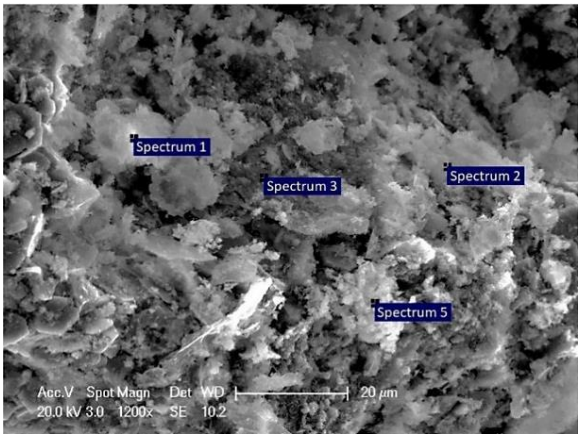
Table 4-85: EDX elemental composition of the areas and points marked in Figure 4-83 (a) and (b)

	Spectrum 1		Spectrum 1	
Element	Weight%	Atomic%	Weight%	Atomic%
O K	27.85	39.37	20.00	29.39
Mg K	5.50	5.12	10.87	10.51
Al K	56.45	47.31	65.33	56.92
Si K	10.19	8.21	3.80	3.18

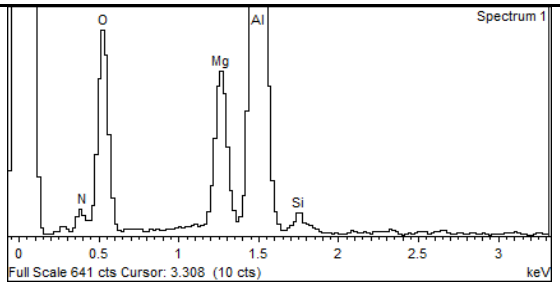
Aggregated nodular-shaped nitride patches with oxide (MgO), measuring on average 25 µm in width, were also observed on the fractured surface of 2L99 + 0.4 wt.% W alloy, as shown in Figure 4-84 (a). Elemental composition of the areas marked as Spectra 1,

2, 3 and 5 were determined by EDX, the results of which are presented in Figure 4-84 (b) to Figure 4-84 (i).

The average elemental composition of Spectra 1, 2, 3 and 5 showed N constituted 11 at.%, while O accounted for 53 at.%, Mg for 7.5 at.%, Al for 27 at.%, and Si for 1 at.%. It is thought that based on the EDX results, AlN and MgO with Al and Si from the main alloy (2L99). For the first time, AlN was observed with a high content of Mg content (7.5 at.%).



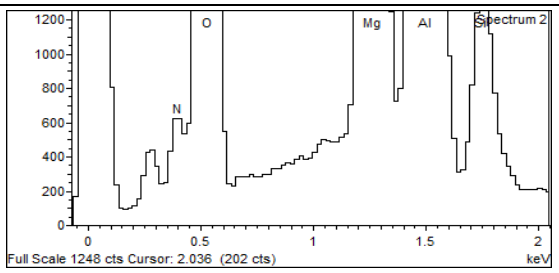
(a)



(b)

Element	Weight%	Atomic%
N K	11.53	15.75
O K	43.12	51.57
Mg K	7.17	5.64
Al K	37.06	26.28
Si K	1.12	0.76

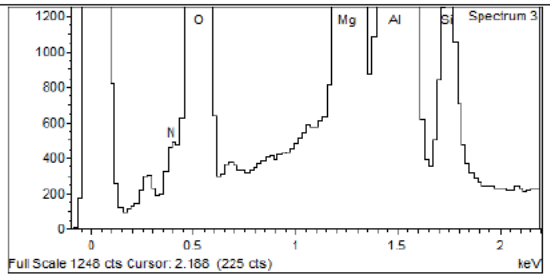
(c)



(d)

Element	Weight%	Atomic%
N K	6.67	9.38
O K	43.07	53.01
Mg K	12.36	10.01
Al K	35.78	26.11
Si K	2.12	1.49

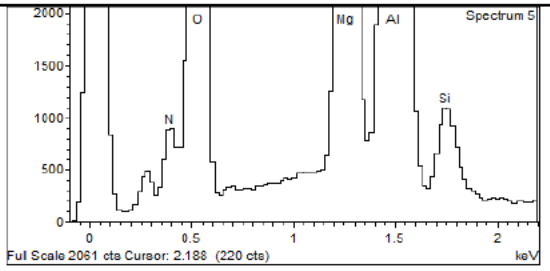
(e)



(f)

Element	Weight%	Atomic%
N K	4.96	7.12
O K	41.78	52.50
Mg K	9.01	7.46
Al K	42.40	31.59
Si K	1.85	1.33

(g)



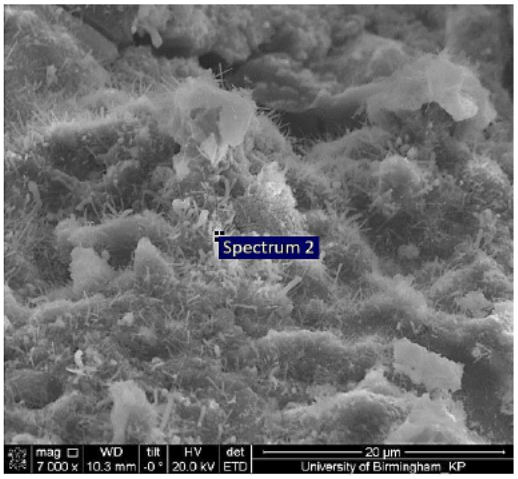
(h)

Element	Weight%	Atomic%
N K	8.28	11.36
O K	46.13	55.44
Mg K	9.35	7.40
Al K	35.02	24.96
Si K	1.22	0.84

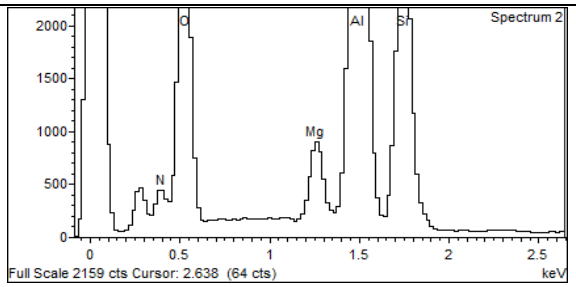
(i)

Figure 4-84: (a) SEM image of nitride layers on the fractured surface of as-cast 2L99 + 0.4 wt.% W, (b) and (c) EDX analysis of spectrum 1, (d) and (e) EDX analysis of spectrum 2, (f) and (g) EDX analysis of spectrum 3, (h) and (i) EDX analysis of spectrum 5

Nitride whisker shape patches and MgO were also observed on the fractured surfaces of the 2L99 + 0.4 wt.% W, as shown in Figure 4-85 (a). The EDX spectrum and quantification of the area marked as Spectrum 2 are presented in Figure 4-85 (b) and (c). The elemental composition of Spectrum 2 showed N constituted 9 at.%, while O accounted for 43 at.%, Mg for 2 at.%, Al for 32 at.% and Si for 14 at.%.



(a)



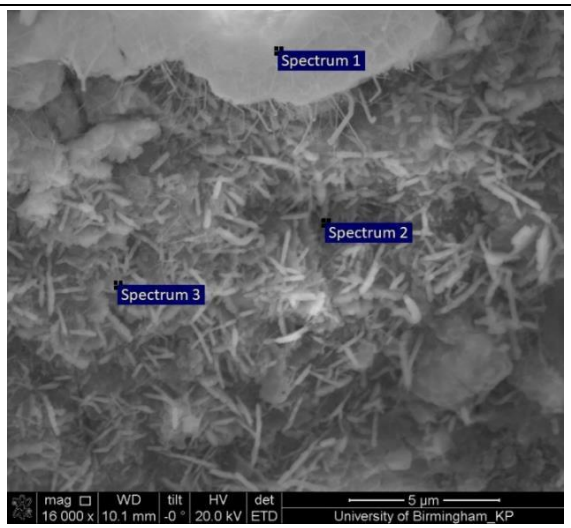
(b)

Element	Weight%	Atomic%
N K	6.06	9.16
O K	32.35	42.83
Mg K	2.69	2.34
Al K	40.54	31.82
Si K	18.36	13.85

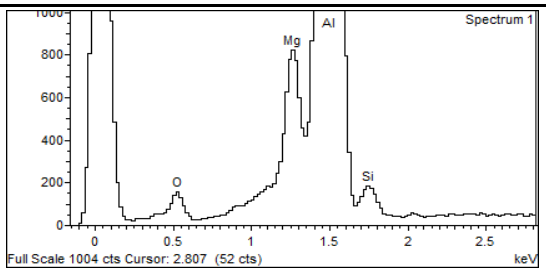
(c)

Figure 4-85: (a) SEM image of nitride layers on the fractured surface of as-cast 2L99 + 0.4 wt.% W and (b) and (c) EDX analysis of spectrum 2

Figure 4-85 (a) shows a high magnification of rod-shaped nitride patches. Nitrides were observed to be rod-shaped, measuring less than 5 µm, with an average size of 0.3 µm x 1.3 µm. The EDX spectrum and quantification of the pints marked spectra 1 to 3 are presented in Figure 4-86 (b) to (g). Spectrum 1 showed the presence of MgO, while Spectrum 2 and Spectrum 3 showed the presence of both AlN and MgO.



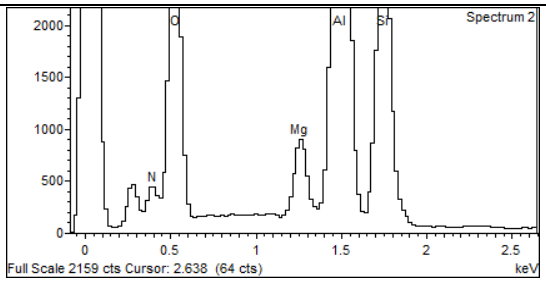
(a)



(b)

Element	Weight%	Atomic%
O K	6.23	10.05
Mg K	3.66	3.89
Al K	87.42	83.60
Si K	2.69	2.47

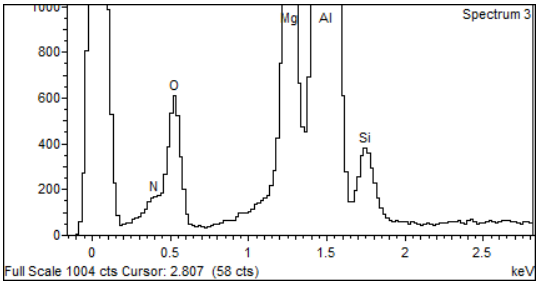
(c)



(d)

Element	Weight%	Atomic%
N K	12.08	18.39
O K	21.40	28.53
Mg K	6.73	5.90
Al K	56.66	44.80
Si K	3.13	2.38

(e)



(f)

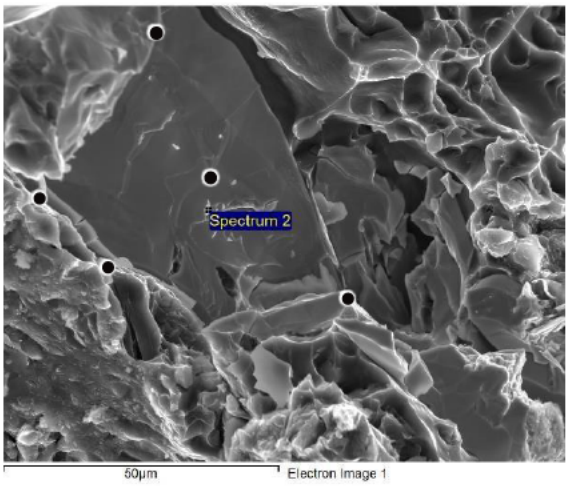
Element	Weight%	Atomic%
N K	9.79	15.06
O K	22.50	30.31
Mg K	7.54	6.68
Al K	56.61	45.21
Si K	3.56	2.73

(g)

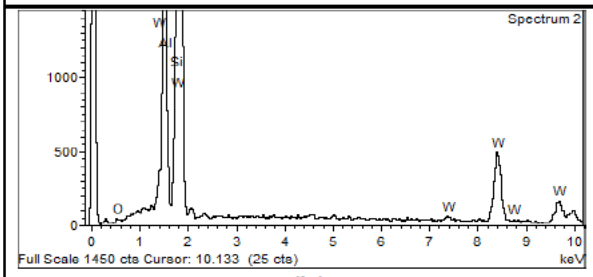
Figure 4-86: (a) SEM image of an oxide and nitride layers on the fractured surface of as-cast 2L99 + 0.4 wt.% W, (b) and (c) EDX analysis of spectrum 1, (d) and (e) EDX analysis of spectrum 2, (f) and (g) EDX analysis of spectrum 3

Figure 4-87 and Figure 4-88 show the two different intermetallics on the fractured surface of a 2L99 + 0.4 wt.% W alloy. Figure 4-87 reveals $W(Al, Si)_2$ with O intermetallic, which is in agreement with the literature [3], measuring approximately 46 µm in length. The intermetallic was observed to have a number of small cracks and was surrounded

by oxide film defects. The EDX analysis of the points marked with black circles was identical to the composition of Spectrum 3 presented in Figure 4-87 (d) and Figure 4-87 (e). This suggests that the W intermetallic could have nucleated on the bifilms.



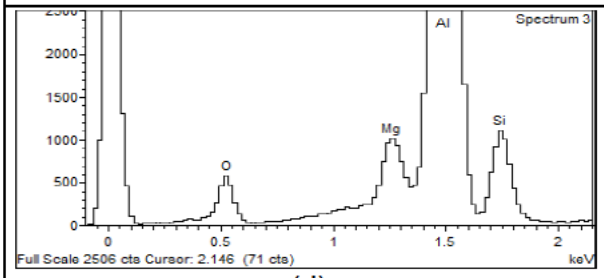
(a)



(b)

Element	Weight%	Atomic%
O K	1.10	1.63
Al K	14.80	39.55
Si K	14.91	39.38
W M	72.19	19.80

(c)



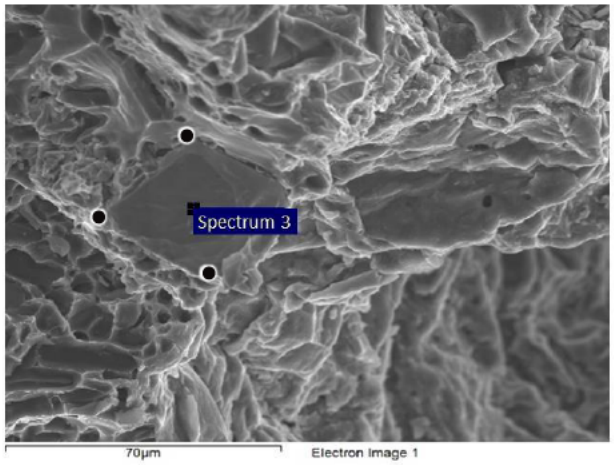
(d)

Element	Weight%	Atomic%
O K	13.59	20.99
Mg K	2.63	2.67
Al K	74.14	67.87
Si K	9.64	8.48

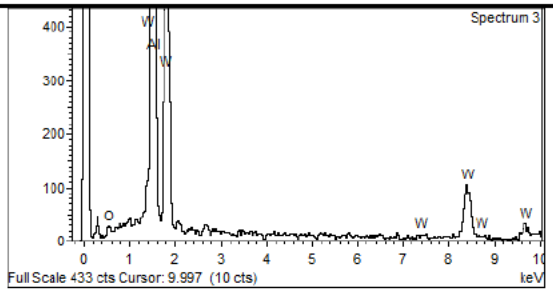
(e)

Figure 4-87: (a) SEM image of W intermetallic on the fractured surface of as-cast 2L99 + 0.4 wt.% W and (b) and (c) EDX analysis of spectrum 2

Figure 4-88 (a) shows $WAl_{3.5}$ intermetallic and oxide films on the fractured surface of the 2L99 + 0.4 wt.% W alloy. The intermetallic measured approximately 40 µm x 50 µm and is surrounded by bifilms similar to those shown in Figure 4-87.



(a)



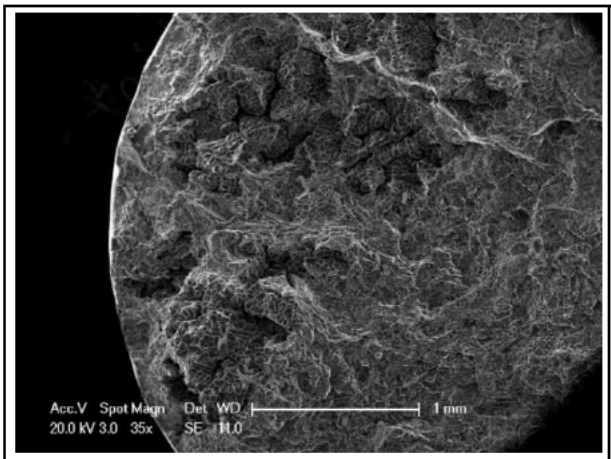
(b)

Element	Weight%	Atomic%
O K	3.08	10.74
Al K	33.99	70.19
W M	62.93	19.07

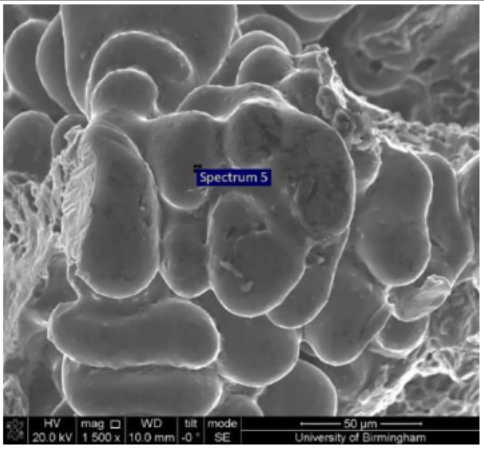
(c)

Figure 4-88: (a) SEM image of W intermetallic on the fractured surface of as-cast 2L99 + 0.4 wt.% W and (b) and (c) EDX analysis of spectrum 1

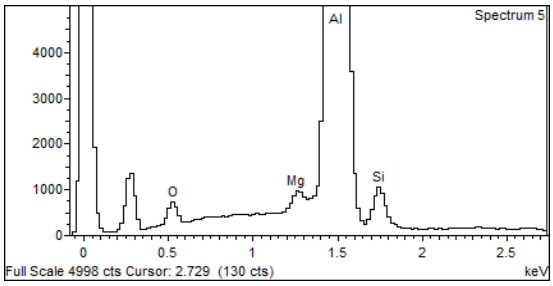
Figure 4-89 (a) and (b) revealed the presence of gas porosity defects on the fractured surface of a 2L99 + 0.4 wt.% W alloy measuring approximately 1.1 mm x 1.4 mm.



(a)



(b)



(c)

Element	Weight%	Atomic%
O K	5.50	8.94
Mg K	0.45	0.48
Al K	90.38	87.17
Si K	3.68	3.41

(d)

Figure 4-89: (a) Low magnification of the half of the fractured surface 2L99 + 0.4 wt.% W alloy with gas porosity (b) High magnification of gas porosity (c) and (d) EDX analysis of spectrum1 on gas porosity

A summary of the phases found in the fractured surfaces of 2L99 + 0.4 wt.% Mo is presented in Table 4-86.

Table 4-86: Summary of the phases on fractured surface 2L99 + 0.4 wt.% W alloy

Fractured 2L99+0.4 wt.% W	Name	Size
Oxides	Mainly spinel nodular shape, slightly SiO_2 slightly MgO nodular and whisker shape,	~80 µm x50 µm ~100 µm x 200 µm ~16 µm ~6 µm
Nitrides	AlN nodular, AlN Whisker shape	20 µm in width
Intermetallic Particles	W $(Al, Si)_2$ $WAl_{3.5}$	46 µm in length 49 µm x 42 µm
Gas porosity	H gas porosity	1.4 mm x 1.1 mm

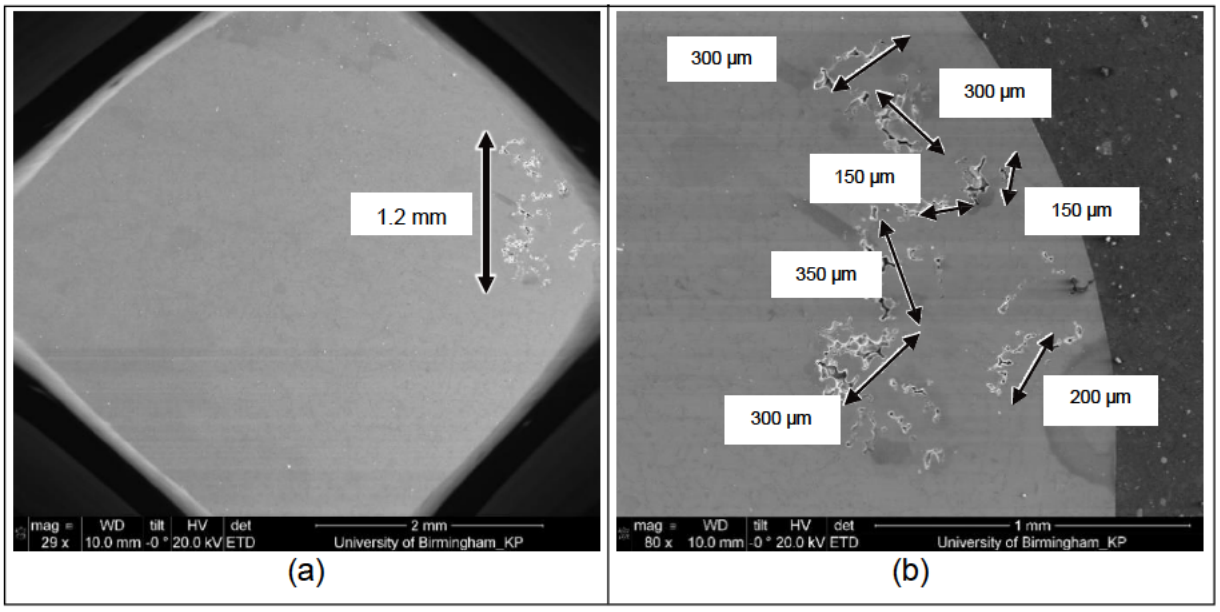
4.2.4 2L99 + V alloy

4.2.4.1 Characterisations of the phases on polished surfaces of 2L99 + 0.4wt.%V

The surfaces of 2L99 + 0.4 wt.% V were examined using SEM and EDX to investigate the composition of different phases, including oxides, nitrides, and intermetallic compounds. Figure 4-90 (a) to Figure 4-90 (d) displayed SEM micrographs at varying

magnifications of a representative low UTS (191.5 MPa) 2L99 + 0.4 wt.% V alloy testbar. Various bifilm defects were observed within these micrographs, as shown in Figure 4-90 (b). These defects ranged in length from 150 µm to 350 µm, with an average length of 240 µm, and exhibited different spatial orientations. Figure 4-90 (c) and Figure 4-90 (d) showed high-magnification SEM micrographs of three of the largest bifilms.

EDX elemental composition of the points marked with black circles on these figures showed the edge of the defects to be oxides with an average O content of 16 at.%. Figure 4-90 (e) shows a representative EDX spectrum and composition of the points marked in Figure 4-90 (c) and Figure 4-90 (d) shown in Table 4-87.



(a) (b)

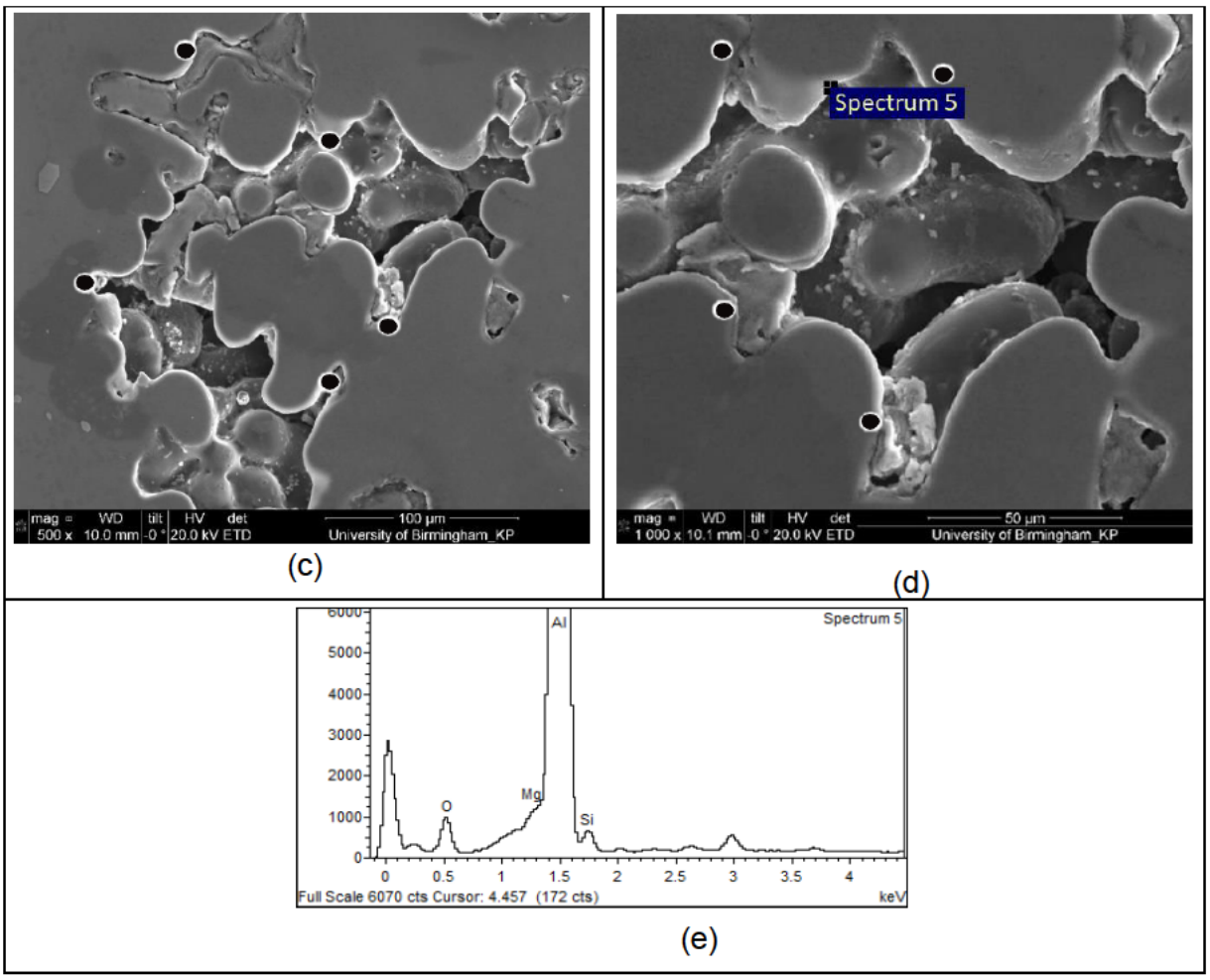


Figure 4-90: (a) Whole matrix SEM micrograph of a polished cross-section of the 2L99 + 0.4 wt.% V alloy with low UTS (191.5 MPa), (b) to (d) High magnification SEM micrographs of the main cavities detailed in (a), (e) EDX Spectrum 5 for (c) and (d)

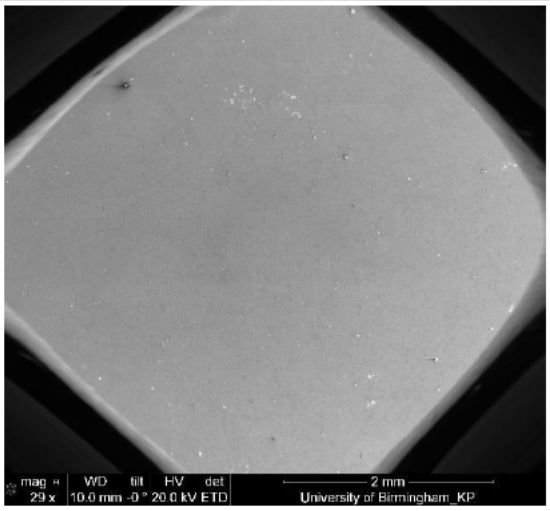
Table 4-87: EDX elemental composition of the points marked with black circles in Figure 4-90(c) and (d)

	Spectrum 5	
Element	Weight%	Atomic%
O K	10.11	15.95
Mg K	0.41	0.43
Al K	87.31	81.68
Si K	2.16	1.94

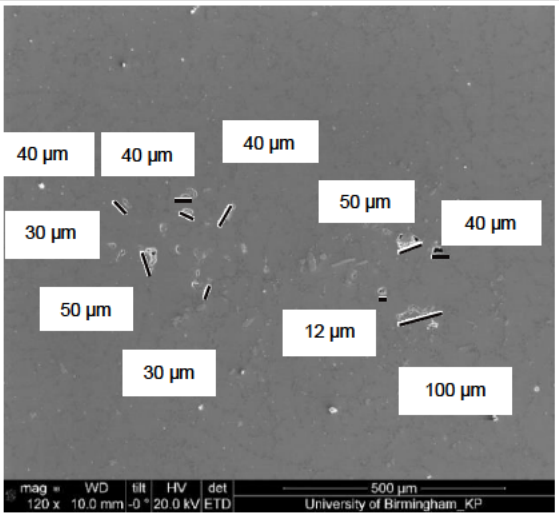
Figure 4-91 (a) displayed a low magnification SEM micrograph, revealing the polished surface of a high UTS (292.8 MPa) 2L99 + 0.4 V wt.% testbar. Compared to the low UTS testbar depicted in Figure 4-90, examining high UTS testbars revealed that the

observed defects were less common and smaller. These defects ranged from 12 μm to 100 μm in length, with an average length of 45 μm, as shown in Figure 4-91 (b). Figure 4-91 (c) shows high-magnification SEM micrographs of a few bifilms in Figure 4-91 (b). EDX elemental composition of the points marked with black circles in Figure 4-91 (c) shows the edge of the defects to be oxides with an average O content of 7 at.%.

Figure 4-91 (d) shows a few Chinese script morphology iron intermetallics of $Al_{28}Si_3Fe$, each approximately 5 μm in length, which is in agreement with literature [106]. This demonstrated that 0.2 wt.% V can affect the Fe plate intermetallics and change their morphology and type to Chinese script. Figure 4-91 (e) and Figure 4-91 (f) show representative EDX spectra, and Table 4-88 shows the composition of the points marked in Figure 4-91 (c) and Spectrum 9 in Figure 4-91 (d).



(a)



(b)

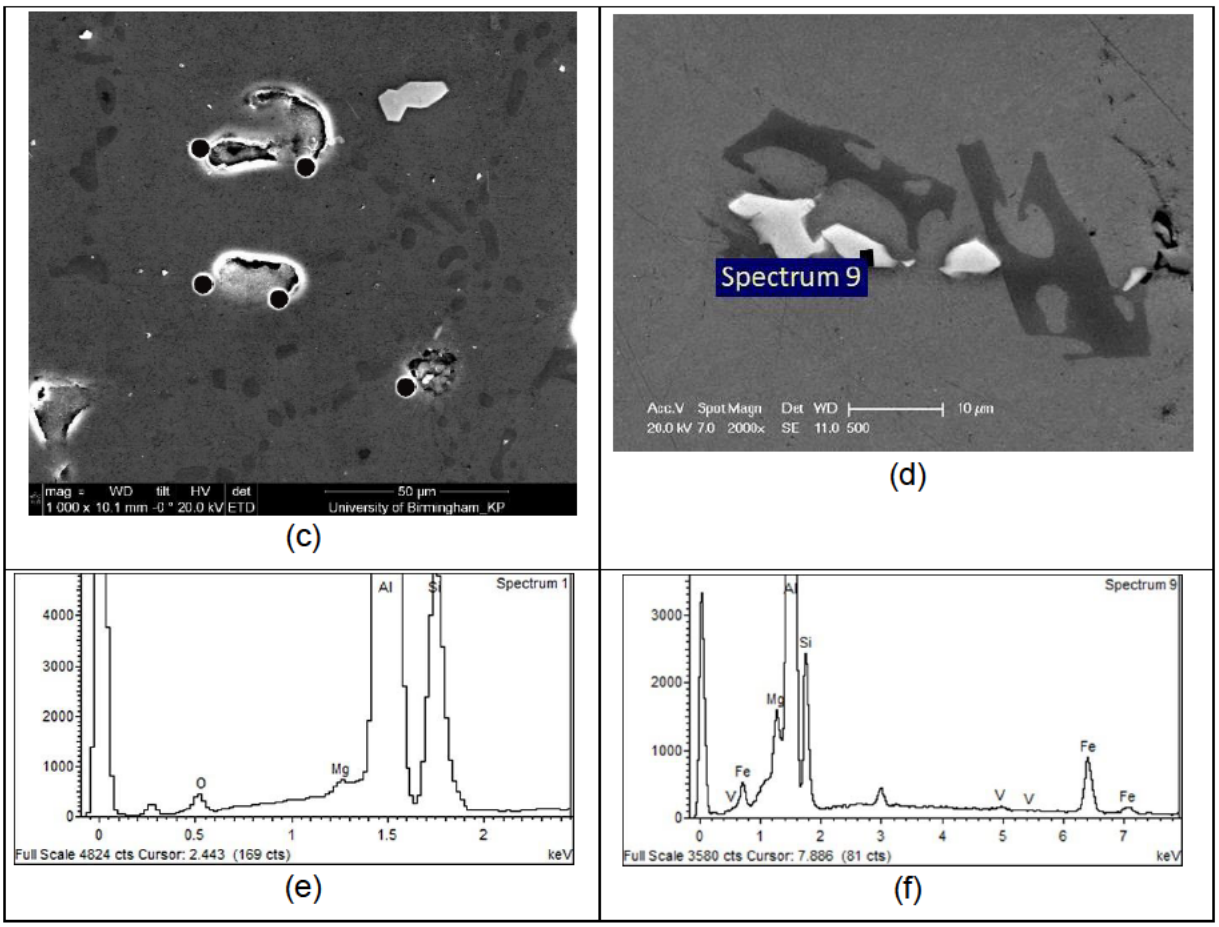


Figure 4-91: (a) Whole matrix SEM micrograph of a polished cross-section of the 2L99 + 0.4 wt.% V alloy with high UTS (292.8 MPa), (b) High magnification SEM micrographs of the main cavities detailed in (a), (c) High magnification SEM micrographs of the few cavities described in (b) and (d) EDX spectrum of the marked points

Table 4-88: EDX elemental composition of the points marked with black circles in Figure 4-91 (c) and Figure 4-91 (d)

	Spectrum 1		Spectrum 9	
Element	Weight%	Atomic%	Weight%	Atomic%
O K	4.14	6.84	0.00	0.00
Mg K	0.21	0.23	1.23	1.41
Al K	76.38	74.80	83.31	86.33
Si K	19.27	18.13	9.10	9.06
V K	0.00	0.00	0.19	0.10
Fe K	0.00	0.00	6.18	3.09

Figure 4-92 (a) showed the presence of two bifilms of approximately 40 µm in length each, as well as two $VAl_{1.1}Si_2$ intermetallic compounds of 23 µm and 9 µm in length with the largest compound nucleated on the wetted side of the bifilm as marked. The EDX spectra of the points marked as X1 and Spectrum 4 were identical; a representative Spectrum is shown in Figure 4-92 (c). A large crack of approximately 90 µm long formed on the outer side of both bifilms connecting them. The EDX spectra and quantification of the areas marked as X2, Spectrum 3, X3, X4 and X5 were similar, a representative EDX of Spectrum which is provided in Figure 4-92 (b). Table 4-89 presents the elemental composition of Spectra 3 and 4.

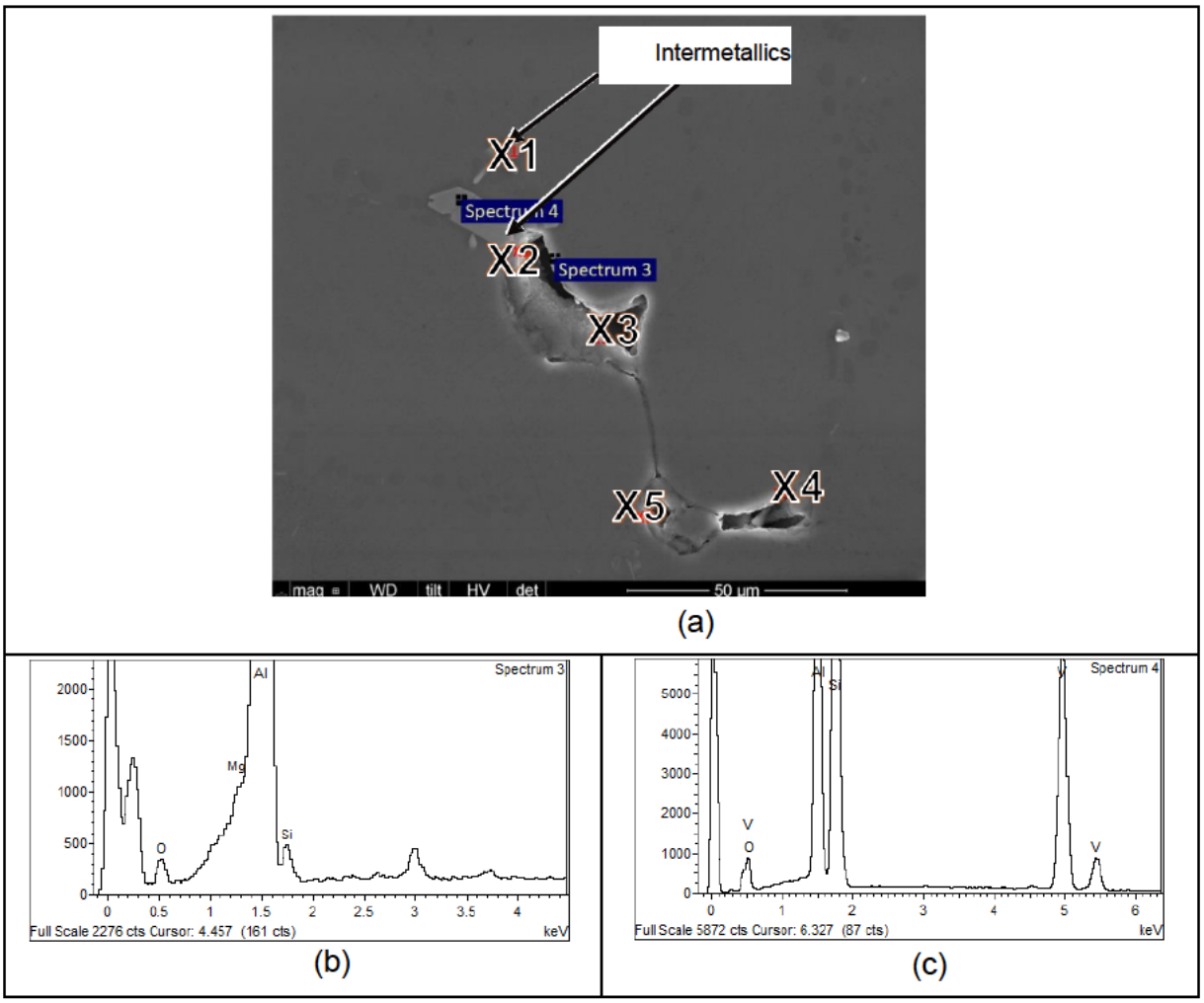


Figure 4-92: (a) SEM micrograph of a polished surface of 2L99 + 0.4 wt.% V alloy showing the faceted intermetallic compounds grown on the bifilm (b) and (c) EDX spectra of the areas marked in (a)

Table 4-89: EDX elemental composition of the points marked and Spectrum 3 and 4 in Figure 4-92 (a)

	Spectrum 3		Spectrum 4	
Element	Weight%	Atomic%	Weight%	Atomic%
O K	5.09	8.30	6.45	12.55
Mg K	0.46	0.49	0.00	0.00
Al K	92.67	89.55	21.54	24.86
Si K	1.78	1.66	37.26	41.32
V K	0.00	0.00	34.76	21.26

Figure 4-93 (a) shows the high-magnification SEM image of the larger $VAl_{1.1}Si_2$ intermetallic compound shown in Figure 4-92 (a) Spectrum 4. The image shows the intermetallic being nucleated on the wetted side of the bifilm as the O content of the point marked as Spectrum 4 is measured at 21 at.% (see Table 4-90). The EDX spectrum for the points marked as Spectrum 4 is presented in Figure 4-93 (b).

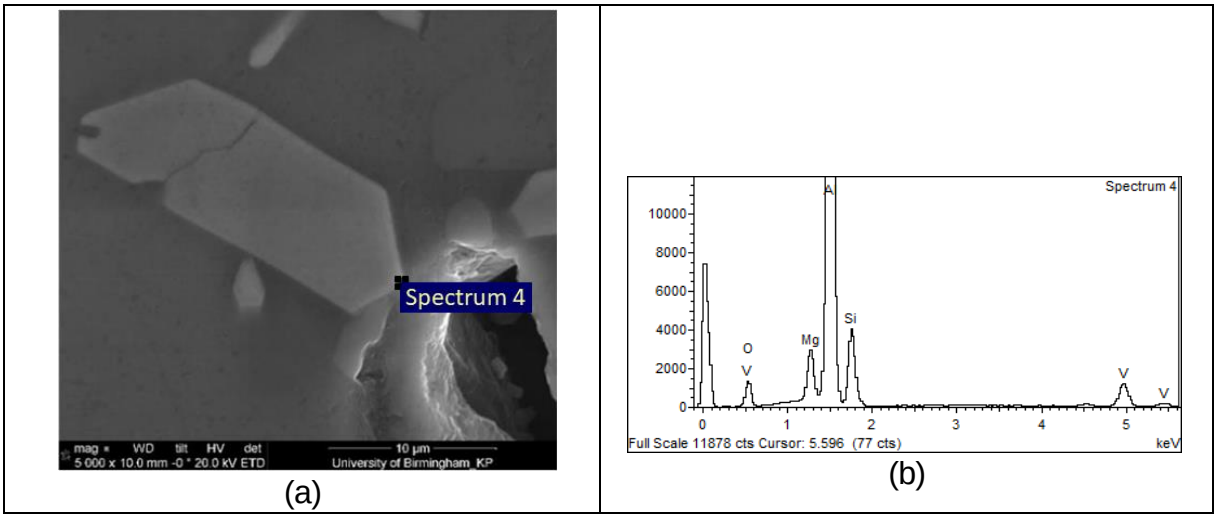


Figure 4-93: (a) SEM micrograph of a polished surface of 2L99 + 0.4 wt.% V alloy showing intermetallic compounds grew on the side of the bifilm, (b) EDX spectrum of the areas marked in (a)

Table 4-90: EDX elemental composition of the Spectrum 4 in Figure 4-93 (a)

	Spectrum 4	
Element	Weight%	Atomic%
O K	12.38	20.95
Mg K	0.92	1.03
Al K	42.44	42.59
Si K	27.54	26.55
V K	16.72	8.89

Figure 4-94 (a) shows two β shaped V_5AlSi_5 intermetallics of approximately 20 µm and 60 µm length. The EDX spectra for the points marked as X1 and Spectrum 3 were found to be similar, as presented in Figure 4-94 (b). Table 4-91 shows the elemental composition of Spectrum 3.

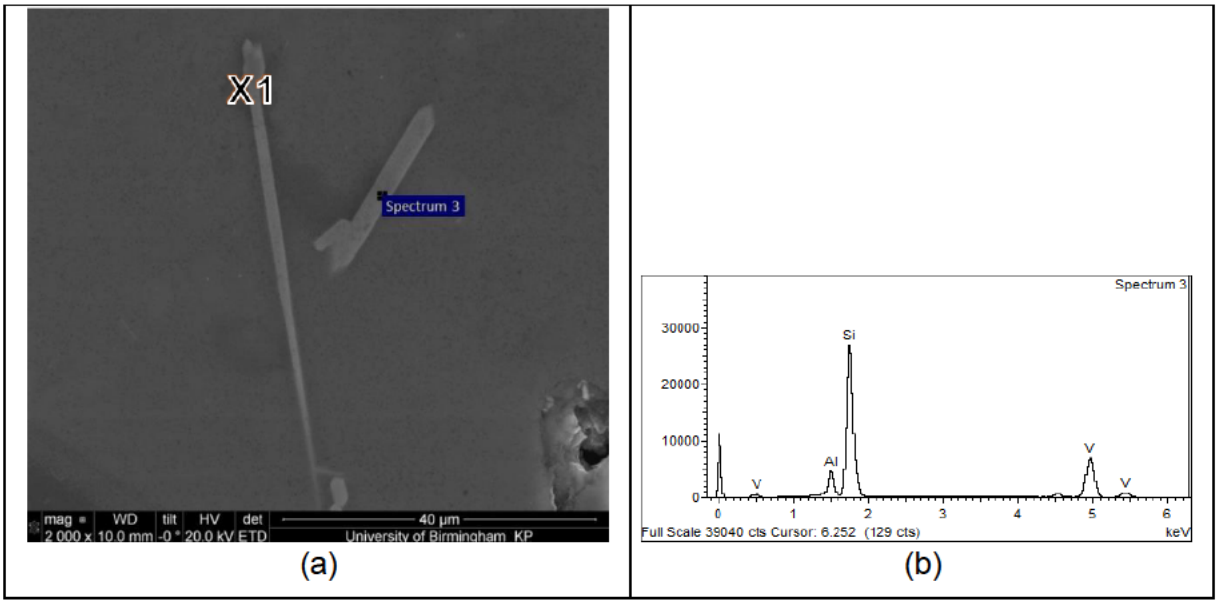


Figure 4-94: (a) SEM micrograph of a polished surface of 2L99 + 0.4 wt.% V alloy showing intermetallic compounds, (b) EDX spectrum of the areas marked in (a)

Table 4-91: EDX elemental composition of the Spectrum 3 in Figure 4-94 (a)

	Spectrum 3	
Element	Weight%	Atomic%
Al K	7.30	9.24
Si K	30.28	45.01
V K	32.42	45 .75

Figure 4-95 (a) shows the presence of five $Al_3VSi_{2.7}$ intermetallics with variable shapes of approximately 10 µm to 70 µm in length. The EDX spectra for the points marked as X1 to X4 and Spectrum 1 were similar, as representative EDX Spectrum is shown in Figure 4-95 (b). Table 4-92 shows the elemental composition of Spectrum 1.

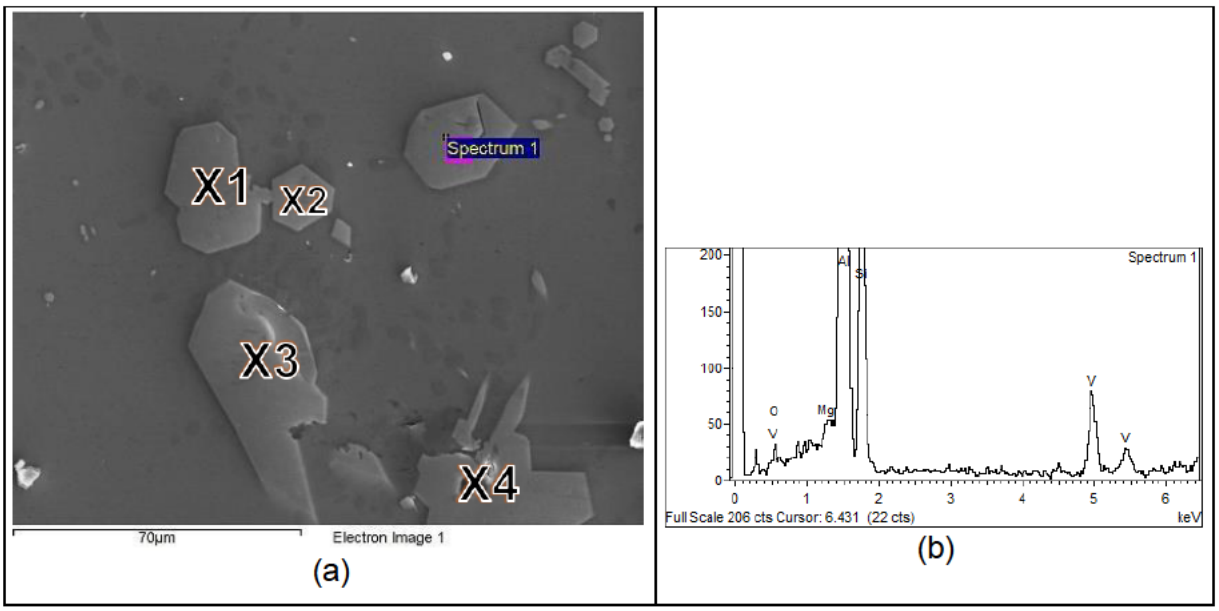


Figure 4-95: (a) SEM micrograph of a polished surface of 2L99 + 0.4 wt.% V alloy showing intermetallic compounds, (b) EDX spectrum of the areas marked in (a)

Table 4-92: EDX elemental composition of the Spectrum 1 in Figure 4-95 (a)

	Spectrum 1	
Element	Weight%	Atomic%
O K	0.51	1.02
Mg K	0.11	0.13
Al K	49.32	58.04
Si K	20.47	21.82
V K	29.88	19.01

Figure 4-96 (a) shows the presence of six $Al_3VSi_{4.2}$ intermetallics (with the same composition as Figure 4-95 intermetallics) of approximately 5 µm to 70 µm in length with variable shapes ranging from facetted rectangles to hexagons. The presence of Al_3V intermetallic is in agreement with the phase diagram [107]. The EDX spectra for the points marked as X1 to X4 and Spectrum 1 were identical, one of which is presented in Figure 4-96 (b). Table 4-93 shows the elemental composition of Spectrum 2.

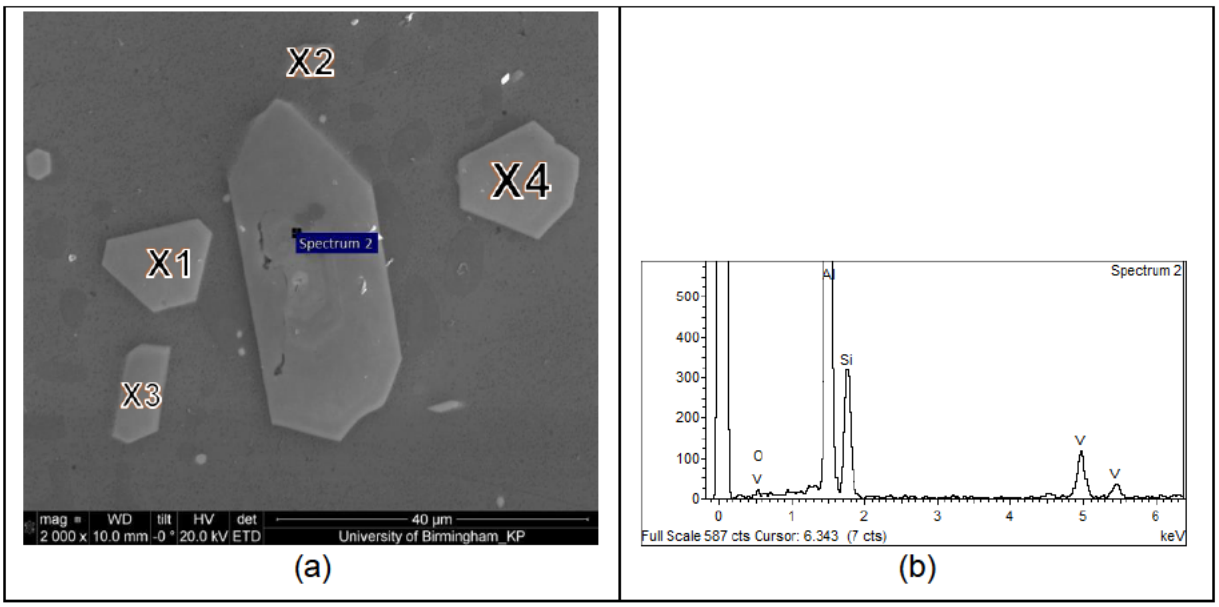


Figure 4-96: (a) SEM micrograph of a polished surface of 2L99 + 0.4 wt.% V alloy showing intermetallic compounds, (b) EDX spectrum of the areas marked in (a)

Table 4-93: EDX elemental composition of the Spectrum 1 in Figure 4-96 (a)

	Spectrum 1	
Element	Weight%	Atomic%
O K	3.51	4.01
Al K	48.32	60.04
Si K	12.47	14.97
V K	32.88	21.01

Figure 4-97 (a) shows the presence of $VAl_{1.4}Si_3$ intermetallics with a hexagonal shape of approximately 10 µm in length. The EDX spectrum for Spectrum 2 is presented in Figure 4-97 (b). Table 4-94 presents the elemental composition of points marked as Spectrum 2.

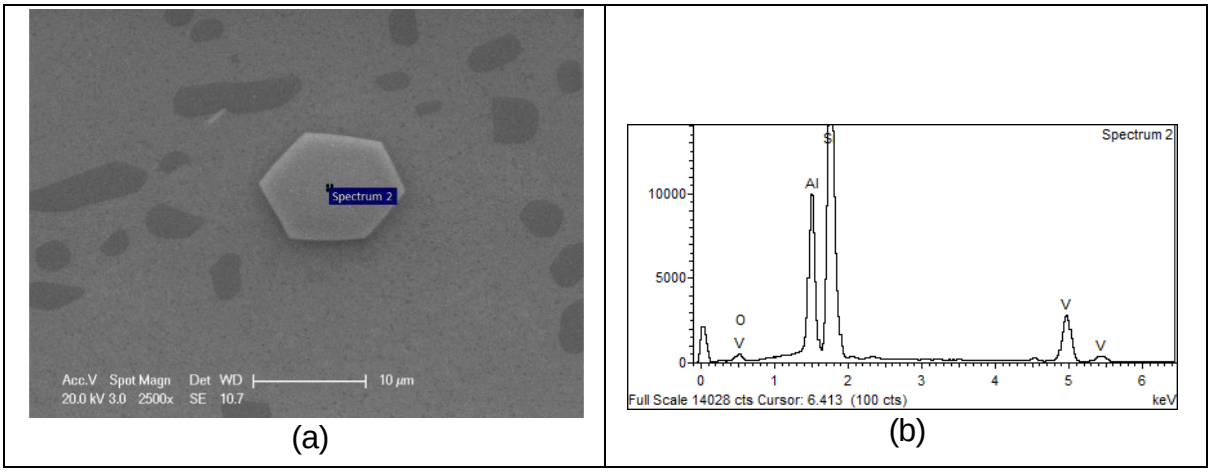


Figure 4-97: (a) SEM micrograph of a polished surface of 2L99 + 0.4 wt.% V alloy showing intermetallic compounds, (b) EDX spectrum of the areas marked in (a)

Table 4-94: EDX elemental composition of the Spectrum 2 in Figure 4-97 (a)

	Spectrum 2	
Element	Weight%	Atomic%
O K	3.47	6.72
Al K	21.11	24.25
Si K	46.69	51.54
V K	28.74	17.49

Figure 4-98 (a) shows the presence of a $V_{1.5}AlSi_{3.1}$ intermetallic approximately 16 µm in length, which is marked as Spectrum 6 nucleated on the wetted side of the bifilm marked as Spectrum 5. The point labelled as Spectrum 1 is a bifilm. The EDX spectra for the points labelled spectra 1, 5 and 6 are presented in Figure 4-98 (b) to Figure 4-98 (d). Table 4-95 shows the elemental composition of spectra 1, 5 and 6.

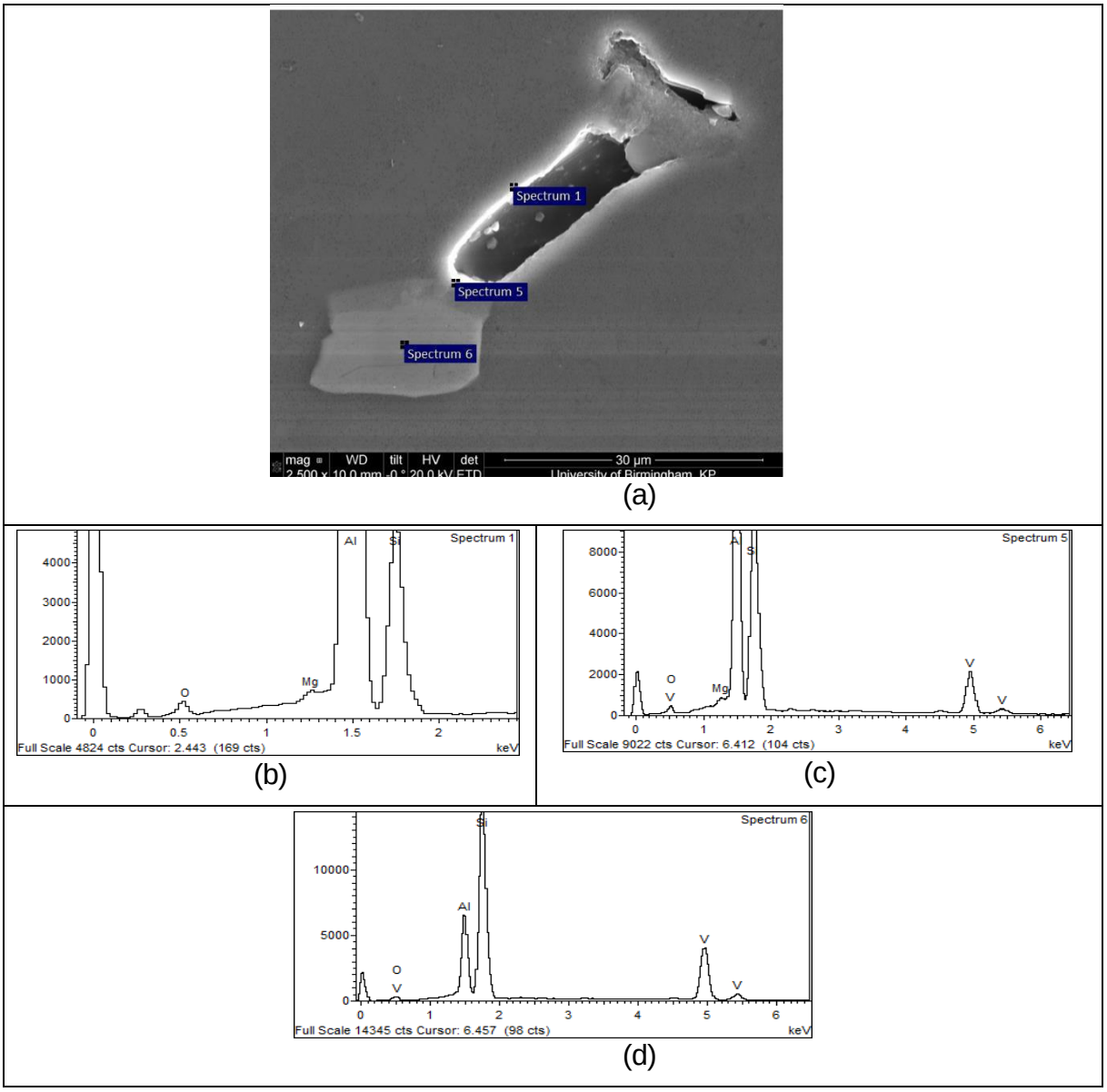


Figure 4-98: (a) SEM micrograph of a polished surface of 2L99 + 0.4 wt.% V alloy showing intermetallic compounds nucleated on the wetted side of a bifilm, (b) to (d) EDX spectra of the areas marked in Figure 4-98 (a)

Table 4-95: EDX elemental composition of the spectra 1, 5 and 6 in Figure 4-98 (a)

	Spectrum 1		Spectrum 5		Spectrum 6	
Element	Weight%	Atomic%	Weight%	Atomic%	Weight%	Atomic%
O K	8.14	10.84	4.76	8.68	1.69	3.53
Mg K	0.21	0.23	0.63	0.76	0.00	0.00
Al K	72.38	70.80	37.05	40.09	13.84	17.16
Si K	19.27	18.13	37.48	38.96	44.53	53.06
V K	0.00	0.00	20.08	11.51	39.94	26.24

Figure 4-99 (a) shows a high magnification image of a nodular AlN layer with spinel observed on the polished surface of 2L99 + 0.4 wt.% V. The EDX elemental composition in Table 4-96 shows N, O, Mg, Al, and Si contents of 6 at.%, 30 at.%, 2 at.%, 50 at.% and 13 at.%, respectively.

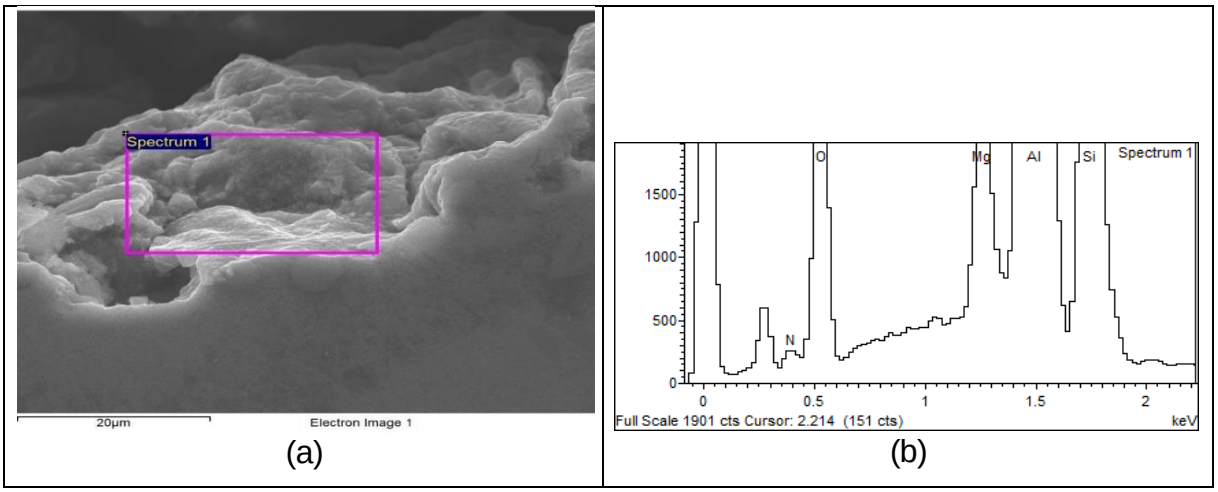


Figure 4-99: (a) SEM micrograph of high magnification of a polished surface of 2L99 + 0.4 wt.% V alloy showing oxide and nitride layers, (b) EDX spectrum of the areas marked in (a)

Table 4-96: EDX elemental composition of the Spectrum 1 in Figure 4-99 (a)

	Spectrum 1	
Element	Weight%	Atomic%
N K	3.63	5.99
O K	27.19	36.15
Mg K	1.86	1.77
Al K	58.15	49.79
Si K	5.91	5.08

Table 4-97 summarises the phases observed on the polished surface of the 2L99 + 0.4 wt.% V samples.

Table 4-97: Summary of the phases on polished surface 2L99 + 0.4 wt.% V alloy

Polished 2L99 + 0.4 wt.% V	Name	Size
Oxides	Mainly spinel	Ranging from 12 µm to 100 µm
Nitrides	AlN nodular shape	On average, covered 25 µm in a cavity on the polished surface
Intermetallic Particles	$VAl_{1.1}Si_2$ $VAl_{1.4}Si_3$ $VAl_3Si_{4.2}$ $Al_3VSi_{2.7}$ $V_{1.5}AlSi_{3.1}$ β-V_5AlSi_5 $Al_{28}Si_3Fe$	23 µm, 10 µm and 9 µm 10 µm 5 µm to 70 µm 10 µm to 70 µm 16 µm 20 µm and 60 µm long each 20µm
	Two types of intermetallics A and β, which β just observed 2.5 %	

4.2.4.2 Characterisations of the phases on the fractured surfaces of 2L99 + 0.4 wt.% V

Figure 4-100 to Figure 4-102 showed different oxide morphologies on the fractured surface of the 2L99 + 0.4 wt.% V. Figure 4-100 (a) is a high-magnification image of wrinkled oxides (spinel) covering approximately 30 µm of the fracture surface. These oxides have concentrations of V and Mg at 0.4 at.% and 0.8 at.%, respectively, and revealed the presence of O, Al, and Si, with atomic % of 8.5, 76, and 14 at.%, respectively. The EDX spectrum is shown in Figure 4-100 (b), and the elemental composition is shown in Table 4-98.

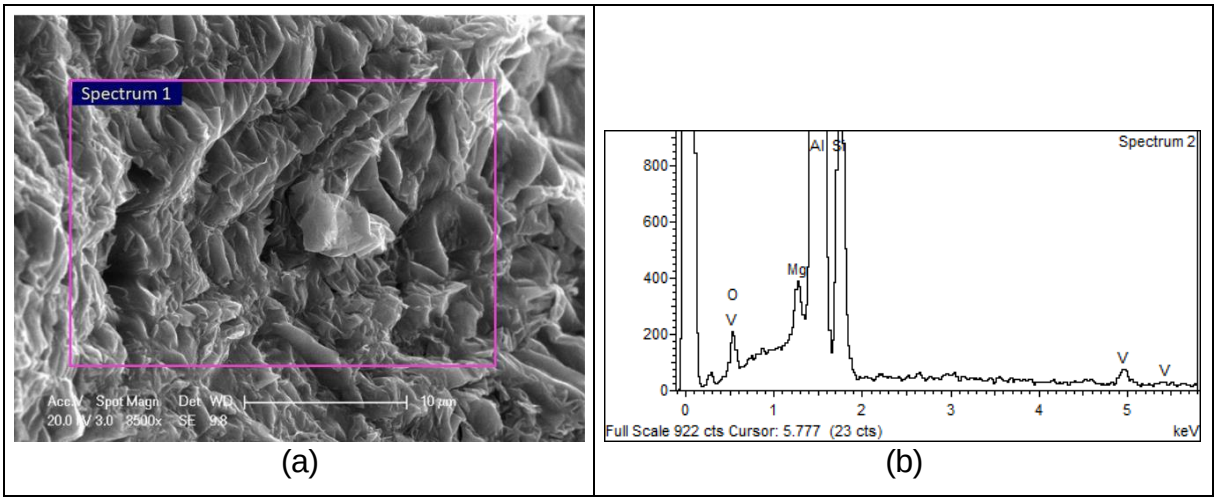
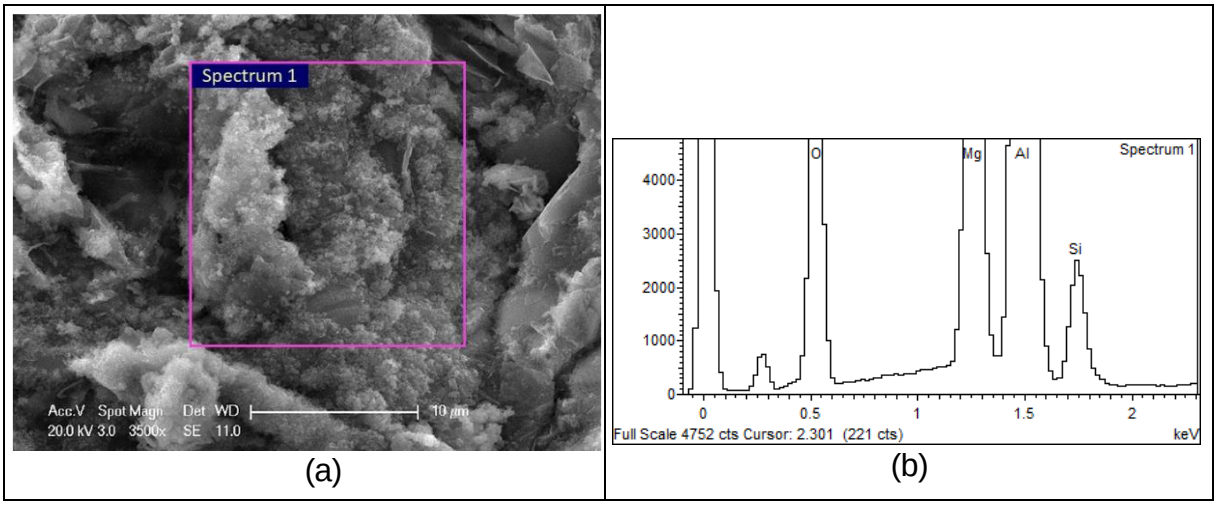


Figure 4-100: (a) High magnification of SEM image of an oxide layer on the fractured surface of as-cast 2L99 + 0.4 wt.% V, (b) EDX analysis of Spectrum 2

Table 4-98: EDX elemental spectrum of the area marked in Figure 4-100 (a)

	Spectrum 2	
Element	Weight%	Atomic%
O K	5.18	8.51
Mg K	0.74	0.80
Al K	78.16	76.14
Si K	15.09	14.13
V K	0.83	0.43

Figure 4-101 (a) shows Al oxides of nodular shape with a high amount of Mg (12 at.%) and the presence of other elements such as O, Al, and Si with the concentration of 46, 38 and 4 at.%, respectively. This type of oxide differs from Figure 4-100 wrinkle oxide in terms of morphology and amount of O, Mg, Al, and Si. The EDX spectrum is shown in Figure 4-101 (b), and the element's composition is shown in Table 4-99.



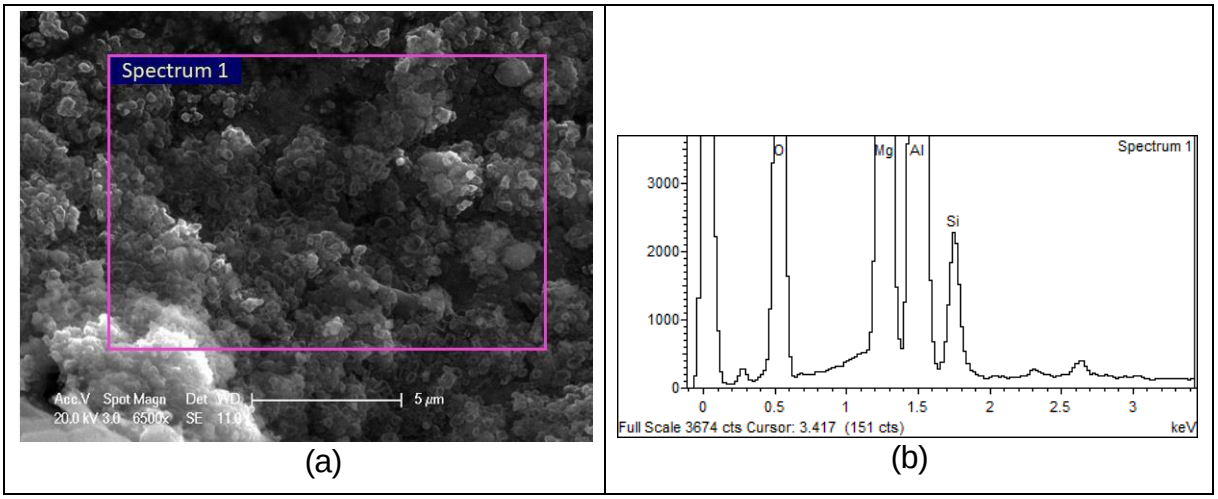
(a) (b)

Figure 4-101: (a) High magnification of SEM image of an oxide layer on the fractured surface of as-cast 2L99 + 0.4 wt% V, (b) EDX analysis of Spectrum 1

Table 4-99: EDX elemental spectrum of the area marked in Figure 4-101 (a)

	Spectrum 1	
Element	Weight%	Atomic%
O K	33.75	45.71
Mg K	13.87	12.36
Al K	47.52	38.17
Si K	4.87	3.75

Figure 4-102 (a) showed granular Al oxides, probably MgO, with an approximate diameter of 0.3 µm. These oxides demonstrated a high amount of Mg (18 at.%) and showed the presence of O, Al, and Si with concentrations of 53 at.%, 26 at.% and 3 at.%, respectively. This type of oxide differed from Figure 4-100 and Figure 4-101 wrinkle and sponge oxides respectively in terms of morphology and amount of O, Mg, Al and Si. The EDX spectrum is shown in Figure 4-102 (b), and the element's composition is shown in Table 4-100.



(a) (b)

Figure 4-102: (a) High magnification of SEM image of an oxide layer on the fractured surface of as-cast 2L99 + 0.4 wt.% V, (b) EDX analysis of Spectrum 1

Table 4-100: EDX elemental spectrum of the area marked in Figure 4-102 (a)

	Spectrum 1	
Element	Weight%	Atomic%
O K	41.13	53.21
Mg K	21.08	17.95
Al K	33.32	25.55
Si K	4.47	3.29

The surface of 2L99 + 0.4 wt.% V sample in Figure 4-103 (a) showed low magnification images of the fractured surface, indicating the presence of an area of AlN marked as X1 and AlN patches in X2. Figure 4-103 (b) and Figure 4-104 showed high magnification of X1 and X2. The AlN observed was nodular in shape and covered approximately 7 µm of the fractured surface. The amount of N was high (22 at.%), as well as Al (34 at.%), O (27 at.%) and Si (5 at.%) and a small amount of Mg (3 at.%). The EDX spectrum1 is shown in Figure 4-103 (c), and the element's composition is shown in Table 4-101.

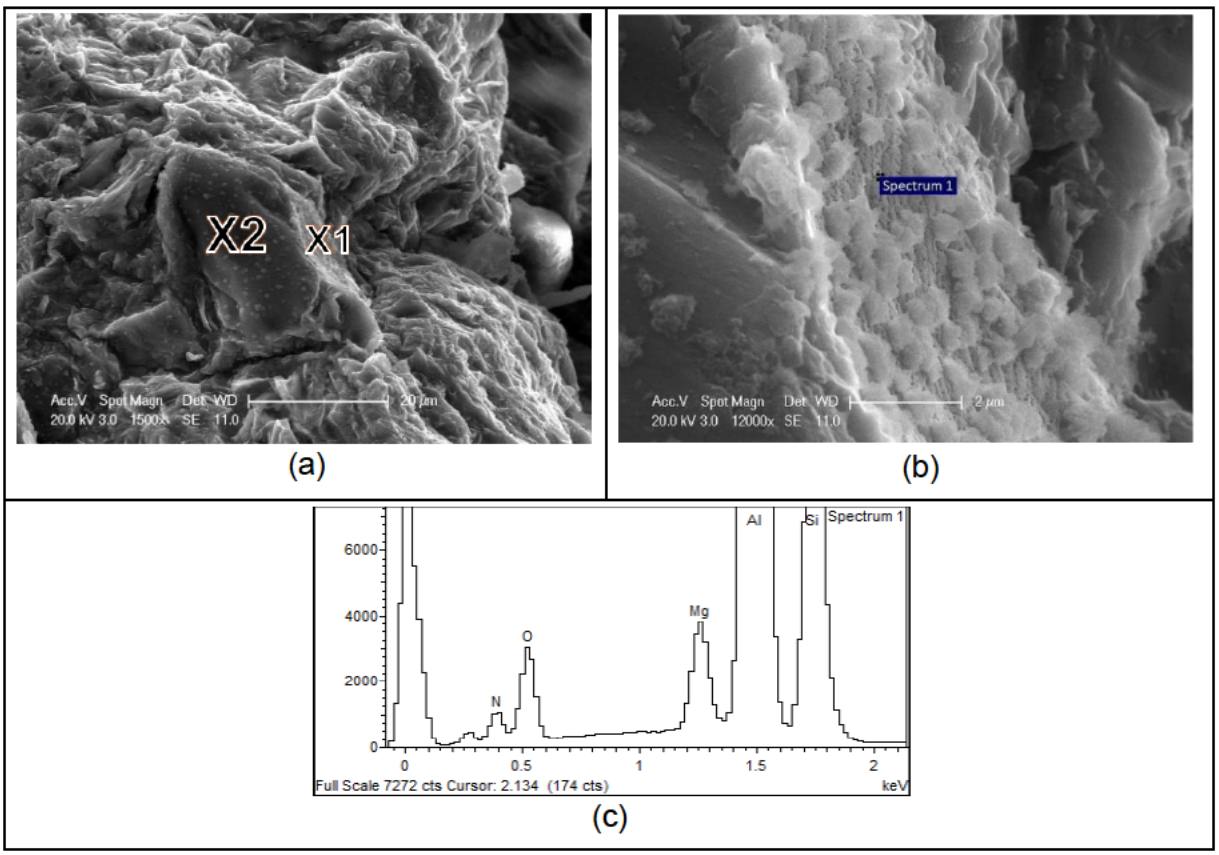


Figure 4-103: (a) SEM image of AlN layer on the fractured surface of as-cast 2L99 + 0.4 wt% V and (b) EDX analysis of Spectrum 1

Table 4-101: EDX elemental spectrum of the area marked in Figure 4-103 (a)

	Spectrum 1	
Element	Weight%	Atomic%
N K	14.37	21.88
O K	19.94	26.57
Mg K	2.98	2.62
Al K	43.07	34.03
Si K	5.93	4.92

The AlN patches observed were nodular on the spinel layer, covering approximately 20 µm x 30 µm of the fractured surface. The patches were approximately 1 µm length each. The amount of N was high (9 at.%), as was Al (64 at.%), O (21 at.%) and Si (3 at.%) with a small amount of Mg (2 at.%). The EDX analysis of patches is shown in Figure 4-104 (b) and Figure 4-104 (c), and the element's composition is shown in Table 4-102.

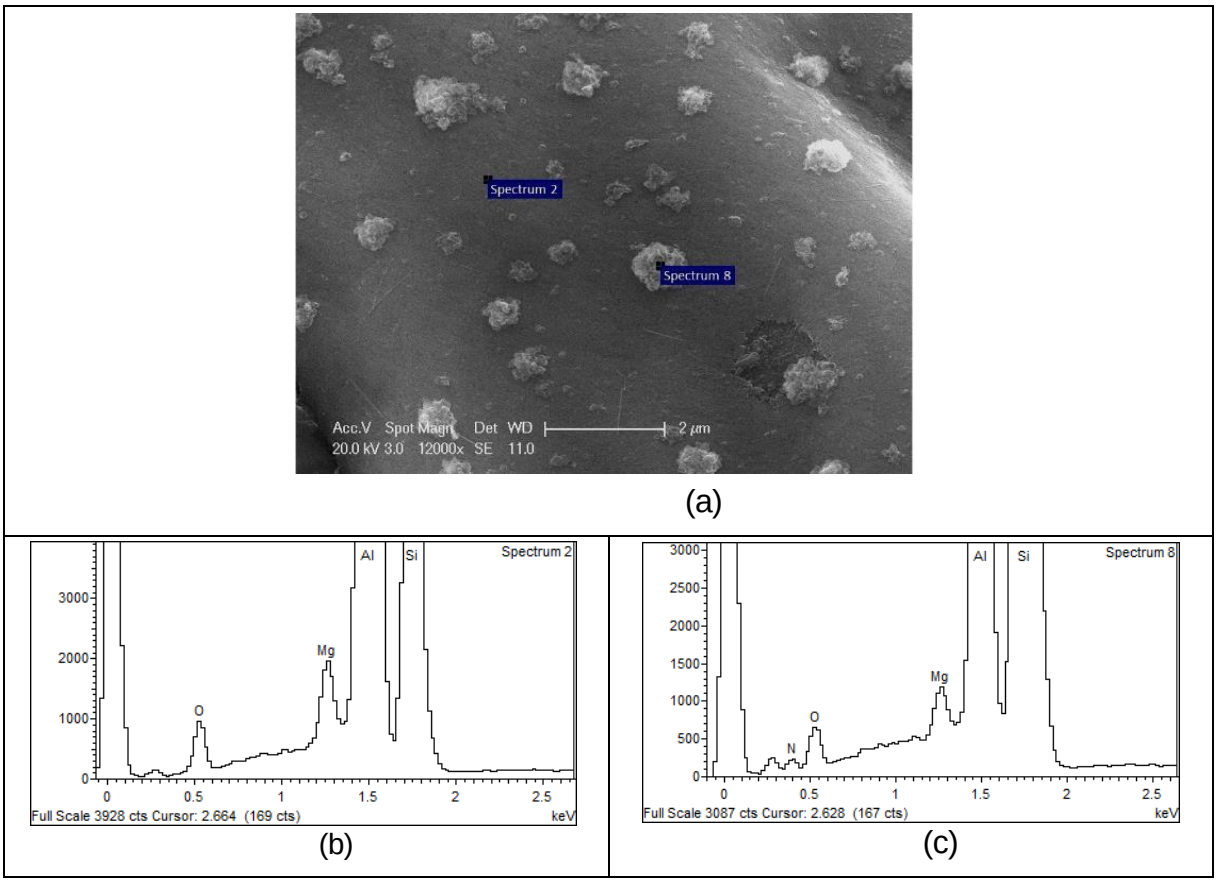


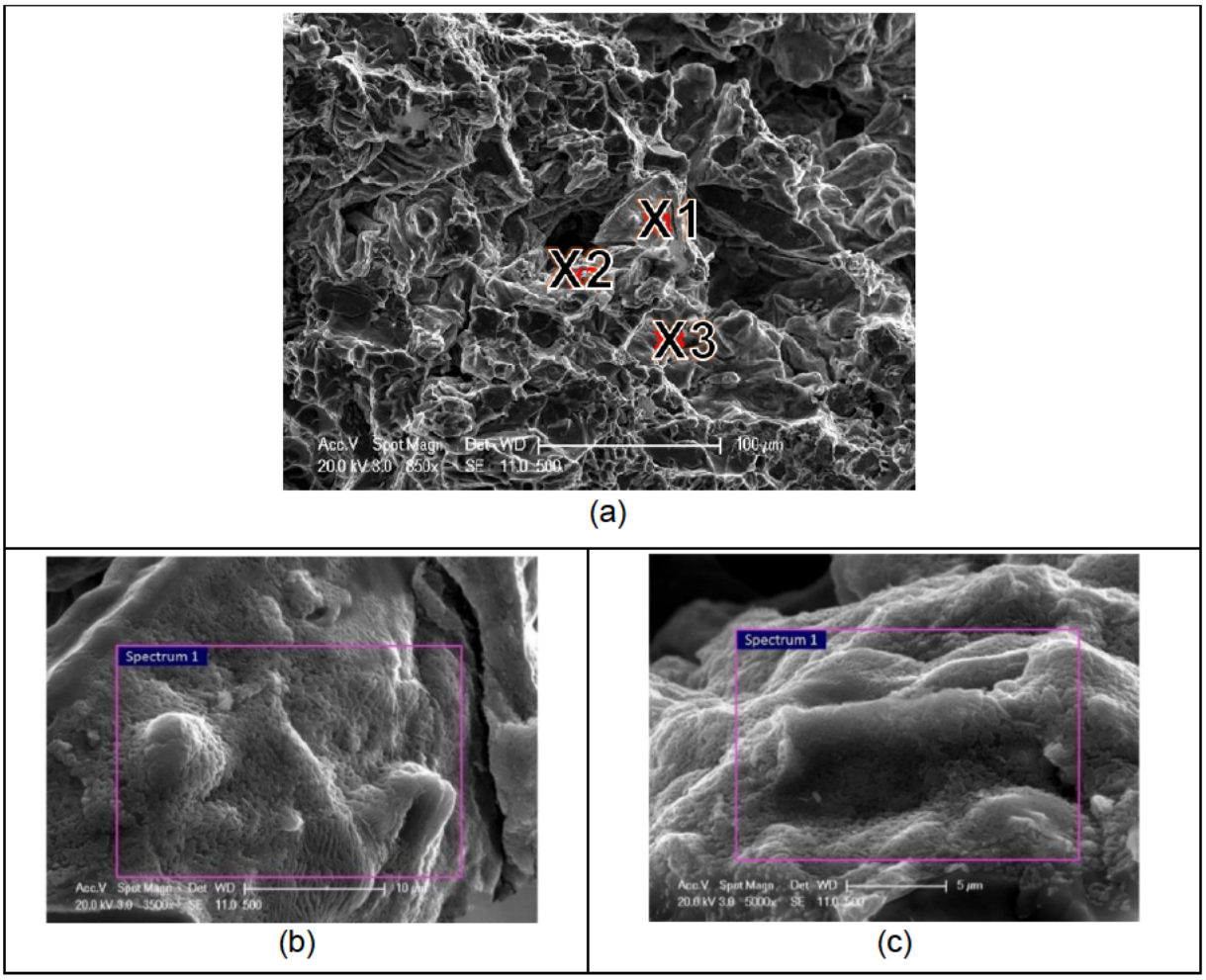
Figure 4-104: (a) SEM image of AlN patches and spinel on the fractured surface of as-cast 2L99 + 0.4 wt% V and (b) and (c) EDX analysis of Spectrum 2 and Spectrum 8

Table 4-102: EDX elemental spectrum of the points marked in Figure 4-104 (a)

	Spectrum 2		Spectrum 8	
Element	Weight%	Atomic%	Weight%	Atomic%
N K	0.00	0.00	5.70	8.93
O K	7.17	11.63	14.32	21.11
Mg K	1.37	1.47	1.28	1.99
Al K	61.03	58.75	74.09	64.77
Si K	30.44	28.15	3.81	3.20

Figure 4-105 (a) shows low-magnification images of the fractured surface of a 2L99 + 0.4 wt.% V, indicating the presence of areas of AlN marked as X1, X2, and X3. Figure

4-105 (b), Figure 4-105 (c), and Figure 4-105 (d) showed the high magnification of X1, X2, and X3, respectively, as marked in Figure 4-105 (a). These AlN were nodular and covered approximately 35 μm, 23 μm, and 48 μm of the fractured surface. The EDX analysis of points shown by X1, X2 and X3 were similar. The amount of N was high (22 at.%), as was Al (63 at.%), O (10 at.%), Si (4at.%) and a small amount of Mg (0.5 at.%). The EDX spectrum is shown in Figure 4-105 (e), whilst the elemental composition is presented in Table 4-103.



(a)

(b)

(c)

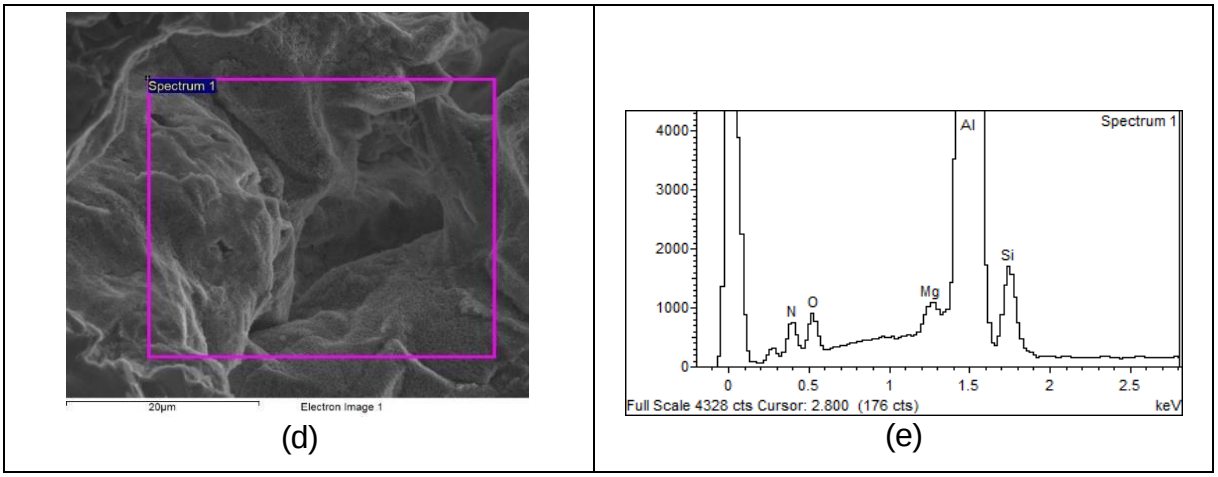


Figure 4-105: (a) SEM image of AlN layer on the fractured surface of as-cast 2L99 + 0.4 wt.% V and (b) EDX analysis of Spectrum 1

Table 4-103: EDX elemental spectrum of the area marked in Figure 4-105 (a)

Element	Weight%	Atomic%
N K	13.69	22.49
O K	6.83	9.82
Mg K	0.55	0.52
Al K	74.58	63.61
Si K	4.35	3.56

Figure 4-106 shows blocky multi-faceted V containing intermetallics on the fractured surfaces on a 2L99 + 0.4 wt.% V sample. The point marked as Spectrum 3 showed Mo containing intermetallic $V_{2.7}AlSi_{7.7}$, of 70 µm x 15 µm and the amount of Mo at 4.5 at.%, Al at 82 at.% and Si at 14 at.%, the corresponding EDX Spectrum 3 is shown in Figure 4-106 (b), and the element's composition is shown in Table 4-104.

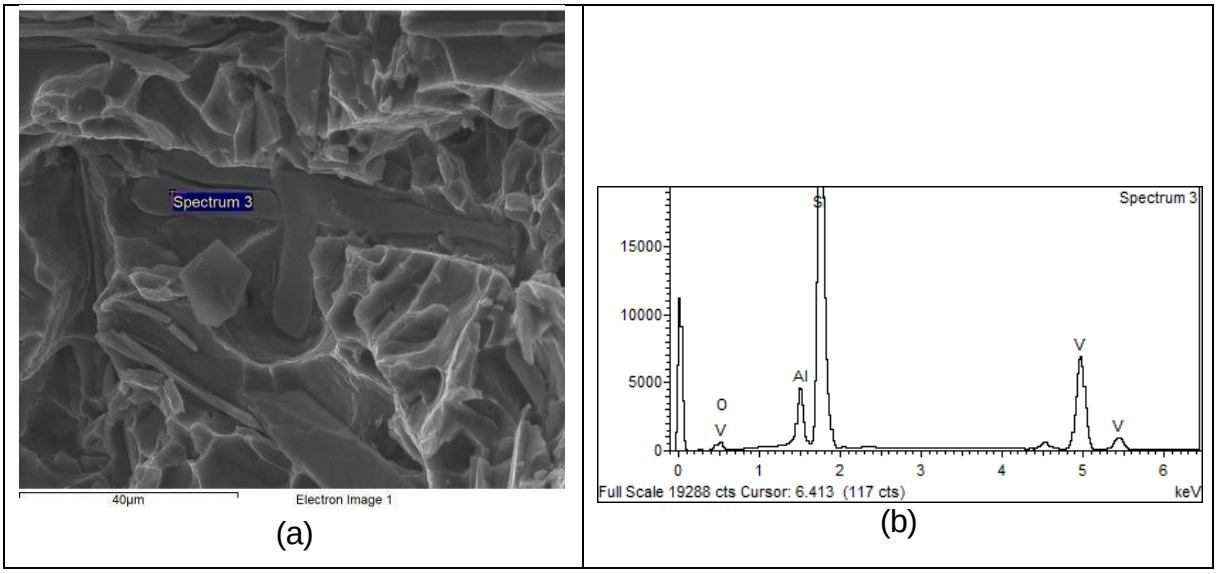


Figure 4-106: (a) SEM image of V intermetallic on the fractured surface of as-cast 2L99 + 0.4 wt.% V and (b) EDX analysis of spectrum 3

Table 4-104: EDX elemental spectrum of the area marked in Figure 4-106 (a)

Element	Weight%	Atomic%
O K	2.73	5.66
Al K	7.13	8.75
Si K	51.00	60.14
V K	39.14	25.44

Figure 4-107 showed a blocky faceted V containing intermetallic on the fractured surface on a 2L99 + 0.4 wt.% V sample. The point marked as Spectrum 1 showed a V containing intermetallic of $V_3AlSi_{3.3}$ 80 µm x 20 µm and containing V at 32 at.%, Al at 15 at.% and Si at 54 at.%, the corresponding EDX spectrum is shown in Figure 4-107 (b), and the elemental composition is shown in Table 4-105.

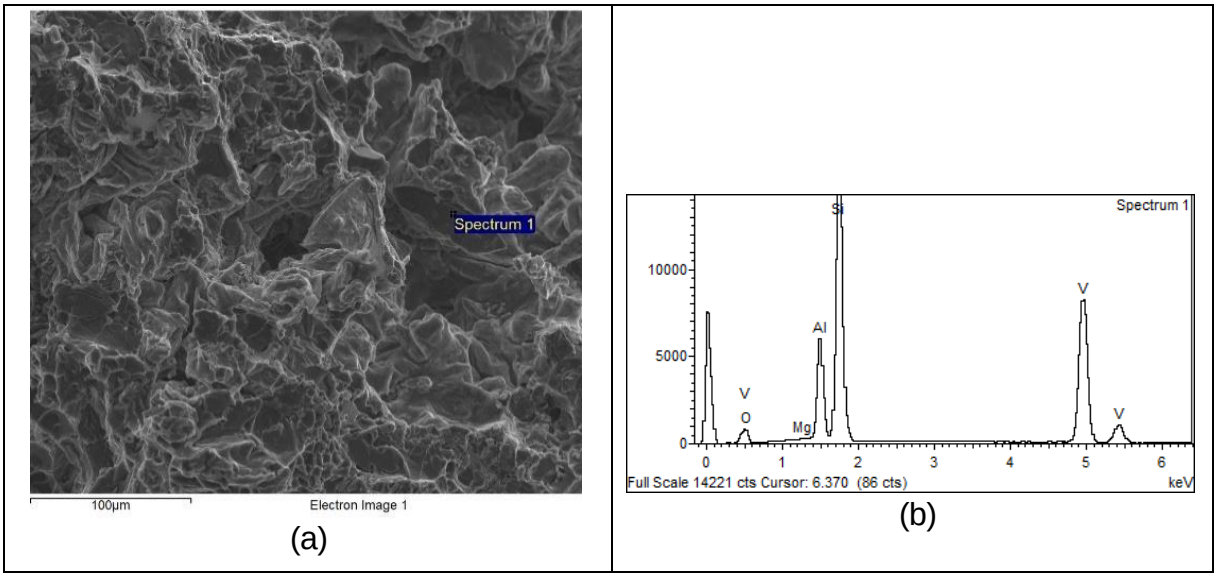


Figure 4-107: (a) SEM image of V intermetallic on the fractured surface of as-cast 2L99 + 0.4 wt.% V and (b) EDX analysis of spectrum 1

Table 4-105: EDX elemental spectrum of the area marked in Figure 4-107 (a)

Element	Weight%	Atomic%
O K	5.30	10.96
Mg K	0.05	0.07
Al K	10.58	12.97
Si K	38.93	40.8
V K	53.54	35.27

Figure 4-108 (a) to Figure 4-108 (i) show the EDX elemental mapping of an AlN measuring 20 µm in length observed on the fractured surface of a 2L99 + 0.4 wt.% V. The EDX elemental mapping was carried out to identify the areas where Al, Si, O, Mg, N and V were present.

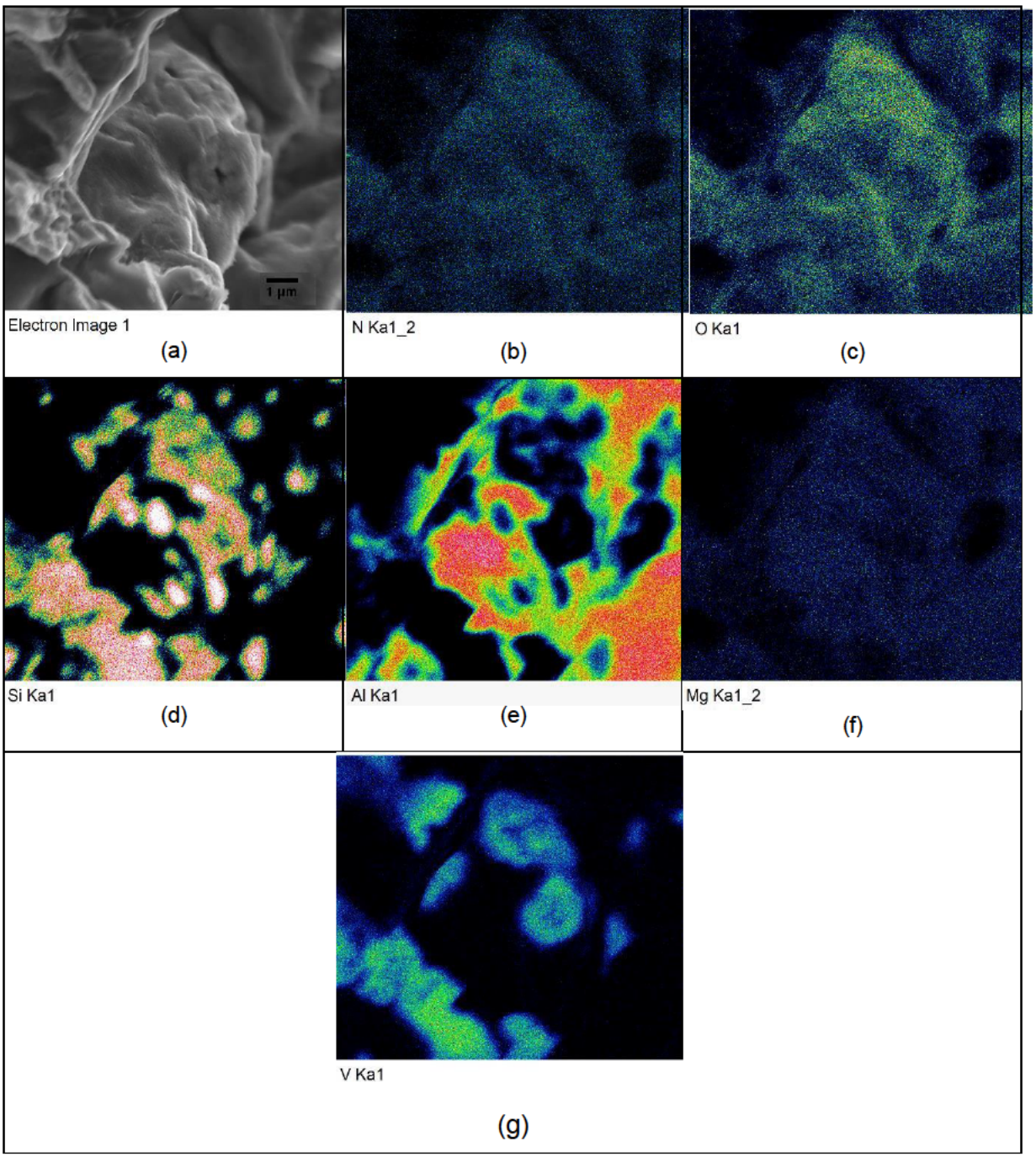


Figure 4-108: EDX mapping of an AlN on the fractured surface of 2L99 + 0.4 wt.% V

While the accuracy of EDX mapping on an alloy's fractured surface is not high, rough and irregular features, including cracks, voids, and roughness, will be exhibited. This is because surface topography can introduce challenges in collecting electron beam and X-ray signals during EDX mapping. However, EDX mapping can give valuable insights into the elemental composition and distribution within the fractured alloy.

Figure 4-109 (a) and Figure 4-109 (b) show low and high magnification of the largest gas porosity defects on the fractured surface of a 2L99 + 0.4 wt.% oxygen was detected within these V alloy at approximately 1.7 mm in diameter. The presence of H in these porosities was due to defects in the expanded oxide film. The EDX spectrum is shown in Figure 4-109 (c), and the elemental composition is shown in Table 4-106.

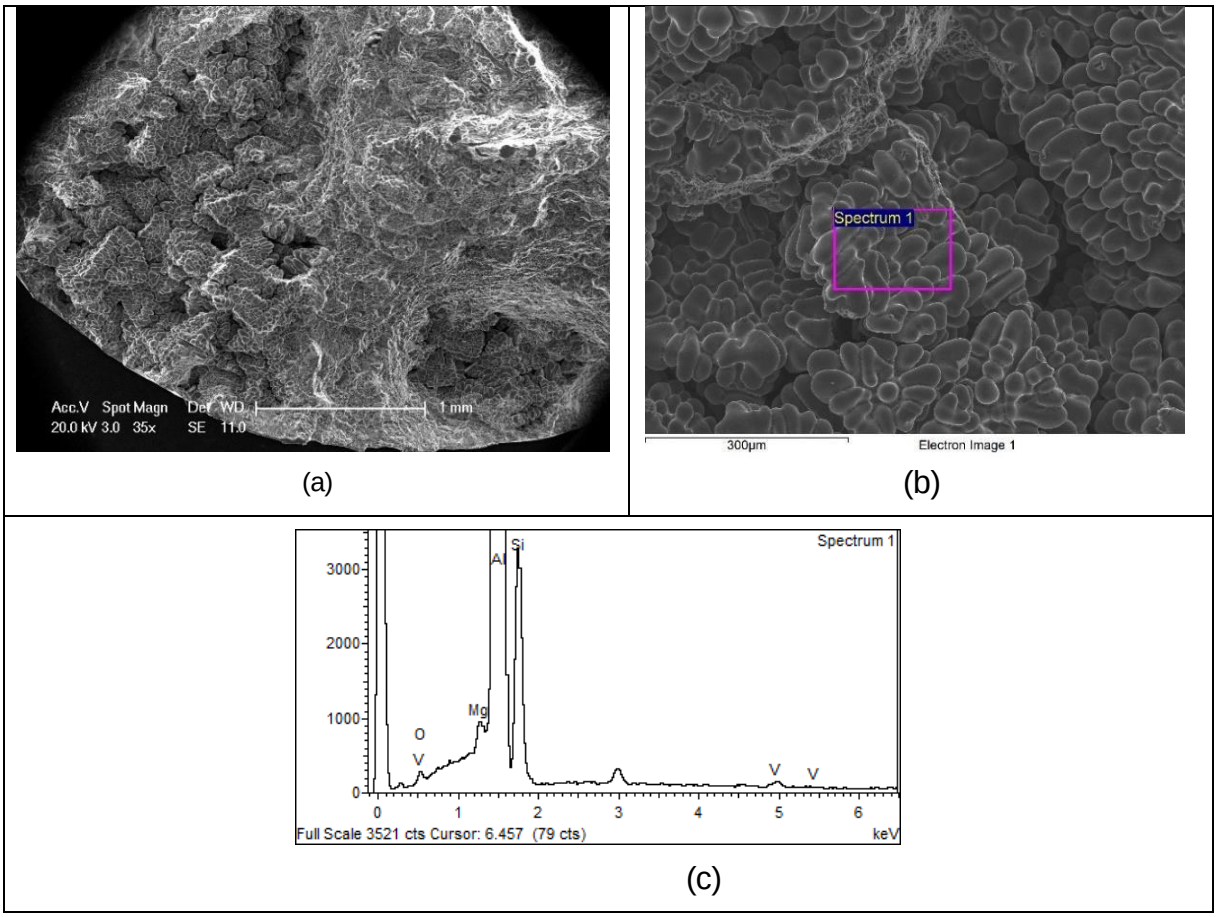


Figure 4-109: (a) SEM image of porosity on the fractured surface of as-cast 2L99 + 0.4 wt.% V and (b) EDX analysis of spectrum 3

Table 4-106: EDX elemental spectrum of the area marked in Figure 4-109 (a)

Element	Weight%	Atomic%
O K	1.47	2.47
Mg K	0.47	0.52
Al K	85.67	85.31
Si K	12.01	11.49
V K	0.38	0.20

EDX analysis of the 2L99 + 0.4 wt.% V alloys indicated the presence of the phases, shown in Table 4-107.

Table 4-107: Summary of the phases on fractured surface 2L99 + 0.4 wt.% V alloy

Fractured 2L99 + 0.4 wt.% V	Name	Size
Oxides	Mainly spinel nodular shape and slightly wrinkled shape MgO small granular	~50 µm ~36 µm 0.3 in diameter
Nitrides	AlN nodular shape	On average, it covered 28 µm of the fractured surface
Intermetallic Particles	$V_{2.77}$ Al $Si_{7.7}$ V_3 Al $Si_{3.3}$	70 x 15 µm 80 x 20 µm
Gas porosity	H gas porosity	2.4 x 1.4 mm 1.2 x 0.4mm

4.2.5 Summary

To summarise, SEM and EDX analysis was carried out on 40% (12 out of 30) of the polished and fractured surfaces of the 2L99 and 2L99 + 0.4 wt.% Mo, W and V testbars. A study of the polished surfaces showed that the percentage of the area covered by the bifilms gas porosity and shrinkage (able to observe on low, very low magnifications (30 magnification)) on the low and high UTS samples varied from 9% to 0.6% for 2L99, 0.7% to 0.08% for 2L99 + 0.4 wt.% Mo, 3% to 0.1% for 2L99 + 0.4 wt.% W and 0.8% to 0.09% for 2L99 + 0.4 wt.% V, which is in agreement with the changes in the measured UTS

Weibull moduli.

The results also showed various oxide, nitride, and intermetallic phases on both the polished and fractured surfaces. Polished surfaces of the alloy were primarily utilised to examine intermetallics, while the fractured surfaces were employed to identify the oxides and nitrides with their morphology.

On the polished surfaces of 2L99, the oxides observed were mainly spinel layers and cuboid particles of spinel, which were approximately 1 µm in length and found inside the pores. The oxide observed on the fractured surfaces of 2L99 were mainly nodular-shaped spinel layers, MgO particles of approximately 0.5 µm in length, and irregular granular SiO_2 oxides varying in length from 100 µm to 300 µm, observed on the sample with the lowest UTS 83 MPa.

Nitrides were only observed in patches on the fractured surfaces of 2L99, which were nodular in shape and measured approximately 15 µm in length. The intermetallics observed on the 2L99 polished surfaces were Mg_2Si and Al_5SiFe, measuring 60 µm in length each.

The polished surfaces of 2L99 + 0.4wt.% Mo showed the oxides were mainly spinel, ranging from 140 µm to 660 µm in length. Nodular nitrides were observed on the polished surfaces with an average length of 20 µm inside a cavity for the first time. Several types of intermetallics were detected by EDX having different compositions of Al-Si-Mo located on different areas of the samples and were mainly $Mo(Al, Si_2)_2$, in line with the relevant phase diagrams [108][109][110][111]. The oxides observed on the fractured surfaces of 2L99 + 0.4 wt.% Mo were mainly nodular spinel layers but occasionally granular or whisker- shaped MgO particles of approximately 0.5 µm in length. Nitrides were observed in patches on the fractured surfaces of 2L99 + 0.4wt.% Mo, exhibiting nodular

and feather shapes of approximately 8 µm and 30 µm length, respectively. The intermetallics observed on the fractured surfaces were $MoAlSi_2$, $Mo_7Al_5Si_7$ and $Mo_6Al_5Si_8$.

The polished surface of 2L99 + 0.4 wt.% W showed that oxides were mainly spinel ranging from 83 µm to 500 µm in length. Also, nodular AlN patches were observed on the polished surfaces similar to the Mo alloy, with an average 5 µm length of AlN found in cavities within the polished surface. The intermetallics suggested by EDX were several with different compositions of Al-Si-W located on various areas of the samples, mainly $W(Al, Si)_2$ composition measuring approximately 25 µm in length, which is in line with the literature [3][112].

The oxides observed on the fractured surfaces of 2L99 + 0.4 wt.% W were mainly nodular spinel or occasional granular MgO particles of approximately 0.5 µm, whisker-shaped MgO and SiO_2. The nitrides that were observed in patches on the fractured surfaces of 2L99 + 0.4 wt.% W exhibited nodular and whisker shapes and measured 20 µm in length. The nitrides were observed nucleating on MgO rather than spinel, as the Mg wt.% was more than 2.5. The intermetallics observed on the fractured surfaces of the W alloy were $W(Al, Si)_2$ and $WAl_{1.5}$ of approximately 46 µm and 50 µm, respectively.

The study of the polished surfaces of 2L99 + 0.4 wt.% V showed the oxides were mainly spinel ranging from 12 µm to 100 µm in length. Also, nodular AlN were observed on the polished surface, similar to Mo and W alloys, with an average length of 25 µm in length observed in cavities on the polished surface. The intermetallics suggested by EDX were several with different compositions of Al-Si-V observed in different areas of the samples analysed. These were α shape intermetallics such as Al_3V with Si_2 or Si_4 approximately varying from 5 µm to 70 µm in length, which is in line with the literature [107], and β shape

V_5AlSi_5 of approximately 20 µm and 60 µm length. The Fe intermetallic detected by EDX was $Al_{28}Si_3Fe$ of approximately 20 µm in length.

The oxide observed on the fractured surfaces of 2L99 + 0.4 wt.% V were mainly nodular spinel or occasional granular (0.3 µm) and nodular MgO oxides. The nitrides observed nucleating on spinel in patches were approximately 1 µm in length, covering 20 µm x 30 µm areas on the fractured surface of 2L99 + 0.4 wt.% V. The intermetallics observed on the fractured surfaces of the V alloy were $V_{2.77}AlSi_{7.7}$ and $V_3AlSi_{3.3,}$ measuring approximately 40 µm and 60 µm in length, respectively.

It is important to note that SEM and EDX characterisation revealed the presence of SiO_2 in a limited number of cases in each of the four alloys. The presence of SiO_2 is due to the sand particles released at the surface of the mould as a result of resin burn, coming into contact with the liquid metal (sand erosion).

This experimental study identified several distinct intermetallic compounds in the Mo, W and V alloying elements through EDX composition analysis. However, it is essential to acknowledge that the precision of the EDX results might be compromised by utilising a 20 kV voltage, and the predominant interaction volume for this specific alloy ranged from 2.5 µm to 5 µm. Consequently, the composition estimated based on the EDX data may exhibit some inaccuracy, as the obtained results could potentially stem from the primary matrix rather than solely representing the designated intermetallic phases within the specified area [113]. Furthermore, it is notable that the derived composition differed from the anticipated equilibrium phase diagram. As a result, XRD analysis was conducted to confirm the exact phase composition for these experimental results.

In summary, the differences between the experimental results and the equilibrium phase diagram can be attributed to non-equilibrium conditions, variations in alloy composition,

impurities, processing conditions, kinetic effects, and practical techniques.

4.3 Characterisation of the phases using XRD

XRD analysis was conducted on polished samples of 2L99, 2L99 + 10 wt.% Mo, 2L99 + 0.4 wt.% Mo, 2L99 + 10 wt.% W, 2L99 + 0.4 wt.% W, and 2L99 + 0.4 wt% V alloys to confirm crystal structure and composition, as shown in Figure 4-110, Figure 4-111, Figure 4-112, Figure 4-113, Figure 4-114, and Figure 4-115. Some of the peaks exhibited weak signals, likely attributed to the limited presence of these phases in the sample compared to the characteristic peaks of these phases provided by the HighScore software. Each phase correlates to a specific reference data code.

The XRD analysis presented in Figure 4-110 of the 2L99 alloy showed high-intensity peaks for spinel, AlN and Mg_2 Si and low-intensity peaks for MgO, SiO_2, and Al_5FeSi.

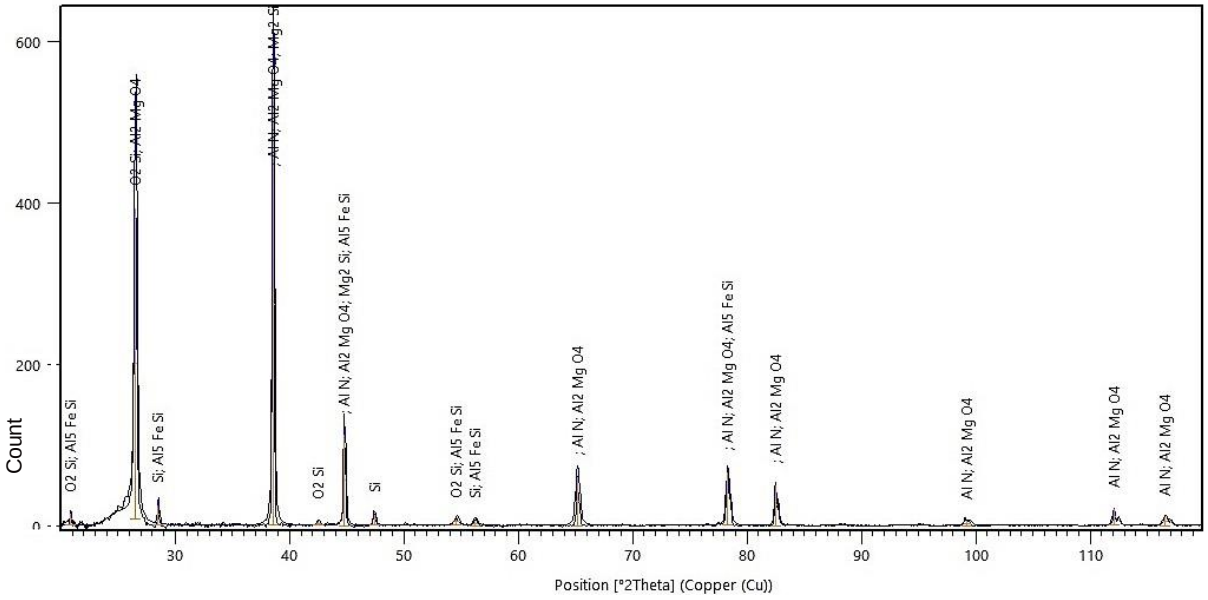


Figure 4-110: XRD Spectrum of 2L99

Figure 4-111 displays the XRD analysis of the 2L99 + 10wt.% Mo alloy, confirming the presence of the Al_4, Al, Al_2O_3, $AlMo_3$, MgO and SiO_2 phases with high-intensity peaks and lower-intensity peaks for $Al_{2.7}FeSi_{2.3}$ and Mo_2.

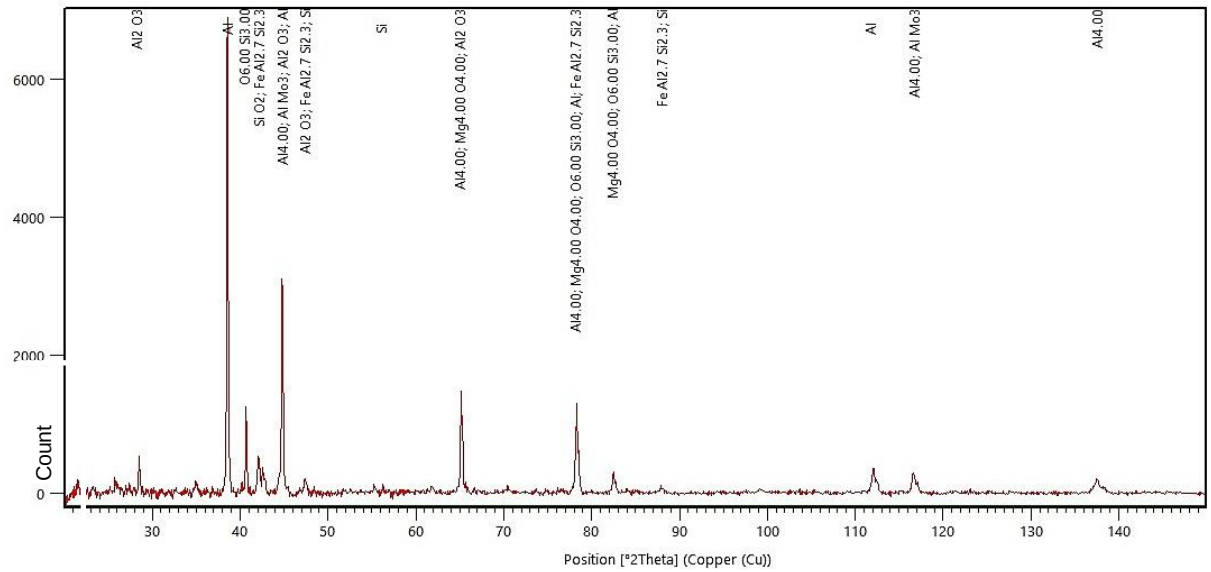


Figure 4-111: XRD spectrum for 2L99 + 10 wt.% Mo alloy

Figure 4-112 shows the XRD analysis of the 2L99 + 0.4 wt.% Mo alloy, confirming the presence of the AlN and $Mo(Si,Al)_2$ phases with high-intensity peaks and lower- intensity peaks for $MgAl_2O_4$, SiO_2, and $Fe_3Al_2Si_4$.

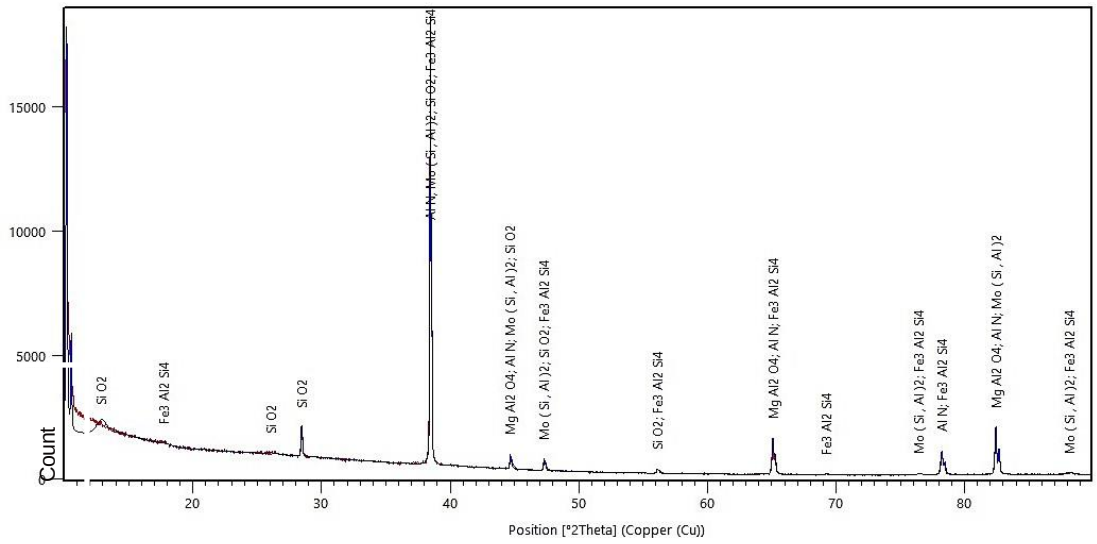


Figure 4-112: XRD spectrum for 2L99 + 0.4 wt.% Mo alloy

Figure 4-113 displays the XRD analysis of the 2L99 + 10 wt.% W alloy, confirming the presence of Al_4W, MgO, $MgAl_2O_4$ and SiO_2 phases with high-intensity peaks and lower-intensity peaks for Al_4, Si and Al_8Fe_2Si.

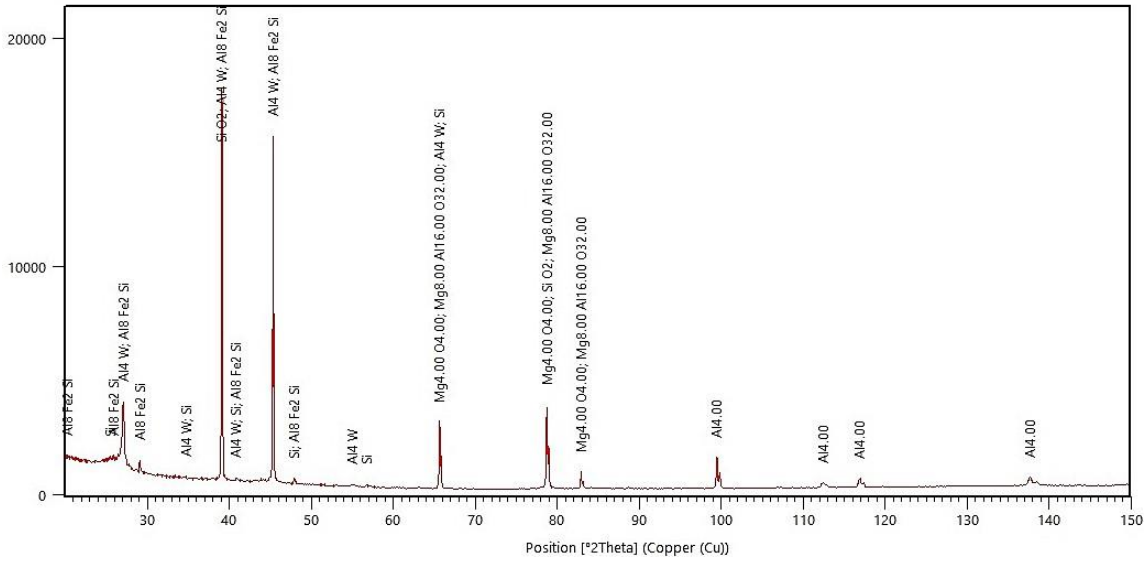


Figure 4-113: XRD spectrum for 2L99 + 10 wt.% W alloy

Figure 4-114 shows the XRD analysis of the 2L99 + 0.4 wt.% W alloy, confirming the presence of the AlN and $W(Si,Al)_2$ phases with high-intensity peaks and lower-intensity peaks for $MgAl_2O_4$, SiO_2, $Fe_3Al_2Si_3$ and Si8.

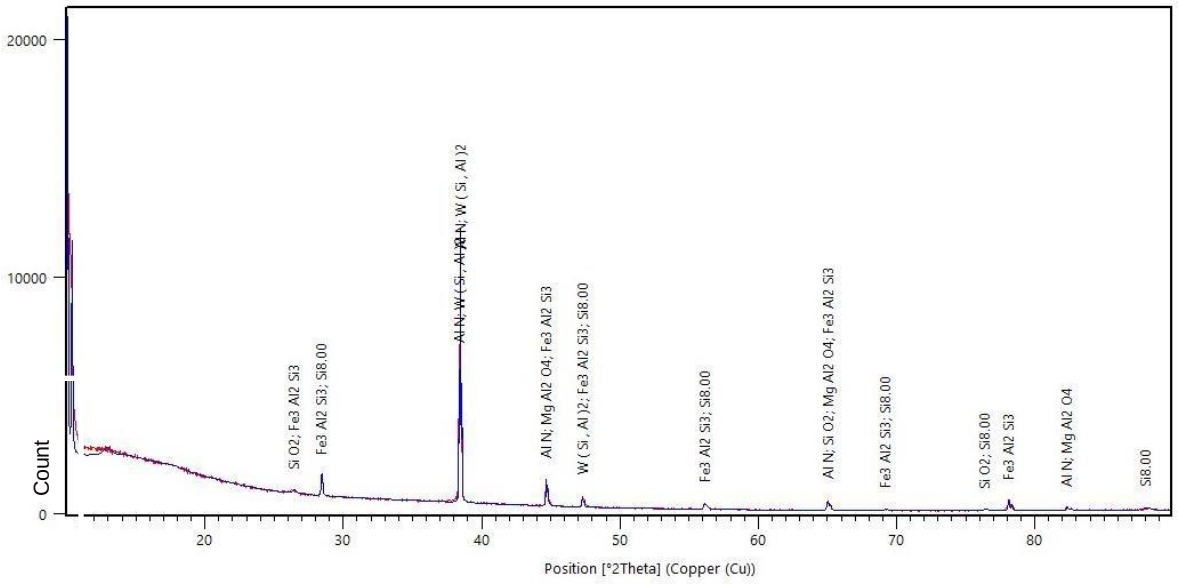


Figure 4-114: XRD spectrum for 2L99 + 0.4 wt.% W alloy

Figure 4-115 shows the XRD analysis of the 2L99 +0.4 wt.% V alloy, confirming the presence of the SiO_2, $MgAl_2O_4$, Al_9Si_3Fe, Al_3V, and $Al_{0.1}Si_{0.9}V_3$, phases with high-intensity peaks and lower-intensity peaks for MgO, AlV_3, AlN, and Si.

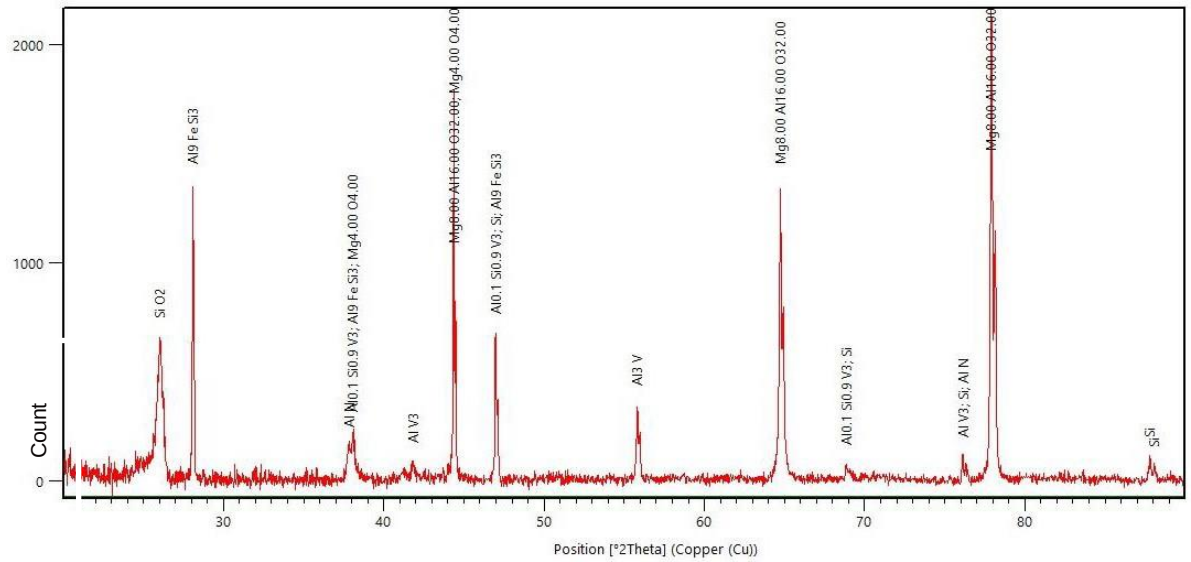


Figure 4-115: XRD spectrum for 2L99 + 0.4 wt.% V alloy

Since XRD is more accurate form of analysis (for intermetallics compositions) phases confirmed by XRD will be discussed.

4.4 Sedimentation

This section presents the findings from the sedimentation experiment and subsequent characterisation of different samples, as detailed in Section 3.3. The samples under investigation were Mo, W, and V alloys of 2L99 with various compositions of Mo (0.5%, 1.8% and 2.4%), W(1.6%, 1.9% and 4.8%), and V (1.2%, 2.1% and 5.1%) as determined by WD-XRF test results which are presented in Table 4-108, Table 4-109 and Table 4-110.

Table 4-108: XRF analysis results for 2L99 + Mo alloys

Alloys	2L99 + 0.4 wt.% Mo						2L99 + 1.77 wt.% Mo					2L99 + 2.4 wt.% MO				
Element Wt.%	Al	Si	Mo	Fe	Mg	O	Si	Mo	Fe	Mg	O	Si	Mo	Fe	Mg	O
Top	Bal	8.05	0.11	.003	0.26	2.5	8.23	0.48	0.04	0.27	2.9	8.05	0.5	0.04	0.28	3.8
Bottom	Bal	7.79	0.83	0.05	0.26	4.6	8.08	4.22	0.37	0.28	3.4	9.44	6.09	0.8	0.27	4.6

Table 4-109 XRF analysis results for 2L99 + W alloys

Alloys	2L99 + 1.6 wt. %W						2L99 + 1.9 wt. %W					2L99 + 4.7 wt.% W				
Element Wt.%	Al	Si	W	Fe	Mg	O	Si	W	Fe	Mg	O	Si	W	Fe	Mg	O
Top	Bal	8.3	0.3	0.16	0.29	2.9	7.9	0.4	0.27	0.24	3.9	5.6	0.5	0.04	0.19	3.2
Bottom	Bal	7.96	4.2	1.09	0.38	6.5	8.2	4.9	1.5	0.4	7.7	7.17	10.7	0.13	0.19	5.3

Table 4-110 XRF analysis results for 2L99 + V alloys

Alloys	2L99 + 1.2 wt. %V						2L99 + 2.1 wt.% V					2L99 + 5.1 wt.% V				
Element Wt.%	Al	S	V	Fe	Mg	O	Si	V	Fe	Mg	O	Si	V	Fe	Mg	O
Top	Bal	8.4	0.3	0.02	0.29	3.6	6.8	0.2	0.03	0.25	4.6	4.8	0.3	0	0.21	4.1
Bottom	Bal	9.4	1.7	0.15	0.27	4.6	10.6	3.3	0.05	0.27	5.6	12.4	7.7	0.1	0.21	4.8

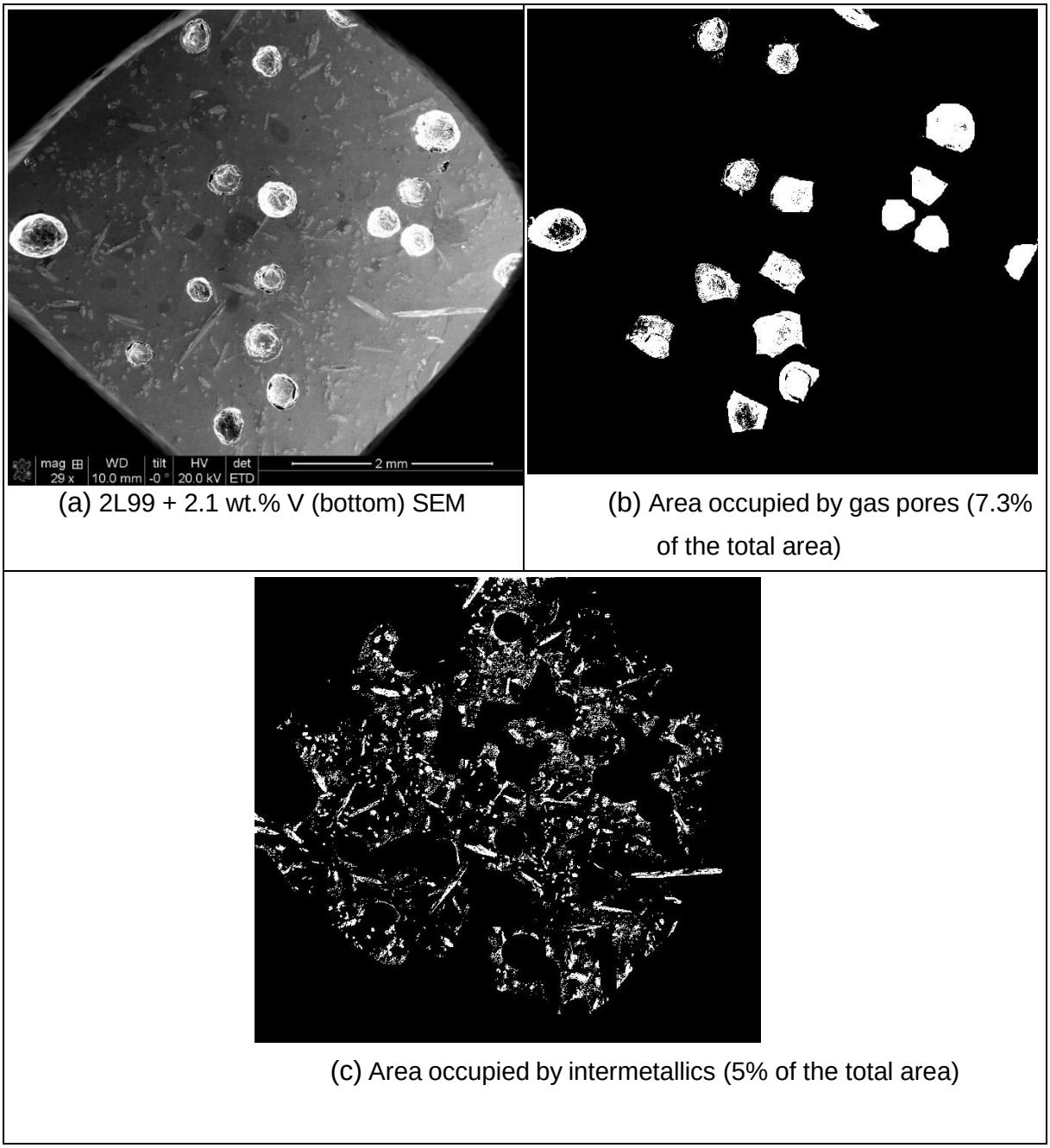
In order to characterise the phases of the sedimentation test samples, wedge samples of each alloy were taken from the top and bottom of a cylindrical bar measuring as described in section 3.3. These samples were polished to achieve a reflective, mirror-like surface and mounted in conductive Bakelite bases.

The primary objective of the sedimentation tests was to examine the effect of each different amount of alloy element on the various phases, such as gas pores/shrinkage defects and intermetallics, at both the top and bottom regions of the samples. Sedimentation testing was undertaken to examine the composition of the phases to explore the relationship between the sedimentation effects during casting and the impact of various alloying elements.

This section commences with reporting the extent of various defects, focusing on oxides and intermetallics, followed by a detailed characterisation of these defects and concludes with a summary of the results obtained.

It is important to clarify that the extent of defects was quantified as the area fraction, expressed as a percentage of the total sample area. This quantification was performed by analysing representative SEM images (with a low magnification of 30) in ImageJ software (version 1.54d). The bifilms (gas porosity) and intermetallics were digitally

distinguished based on their visual contrast. For clarity, Figure 4-116 (a) to Figure 4-116 (c) below provides an illustrative example of the results of the analysis conducted on a 2L99 + 2.1 wt.% V sample surface located at the bottom of the sedimentation sample.



(a) 2L99 + 2.1 wt.% V (bottom) SEM

(b) Area occupied by gas pores (7.3% of the total area)

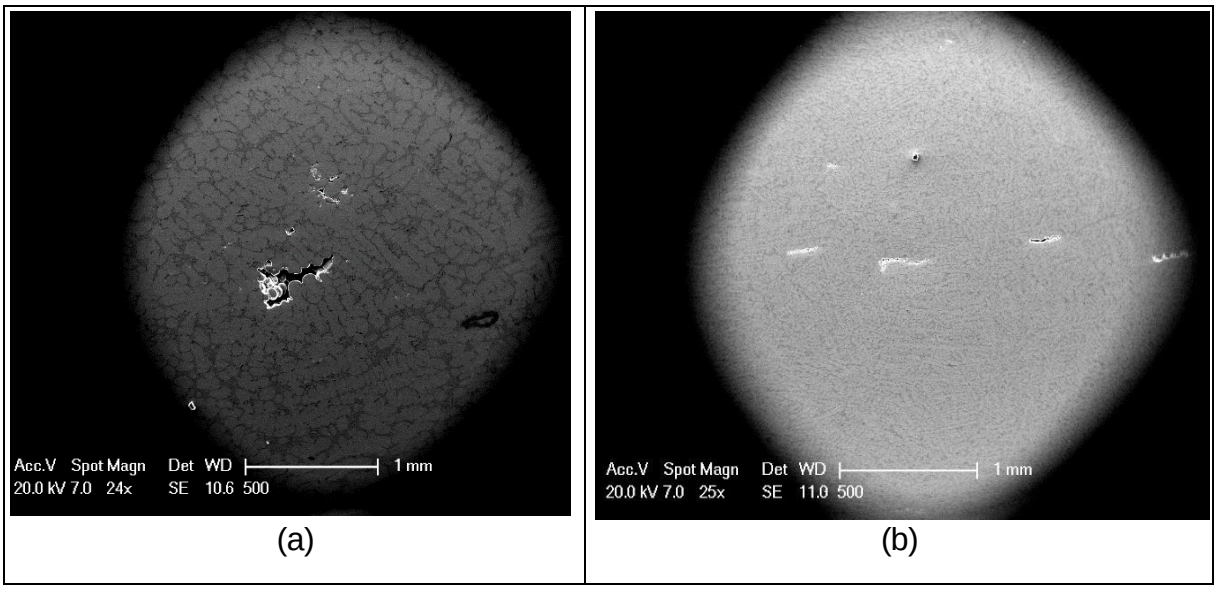
(c) Area occupied by intermetallics (5% of the total area)

Figure 4-116: (a) to (c) separation and calculation of the area fraction occupied by gas pores and intermetallics on a 2L99 + 2.1 wt.% V sample

4.4.1 2L99 + Mo alloy

4.4.1.1 2L99 + 0.5 wt.% Mo

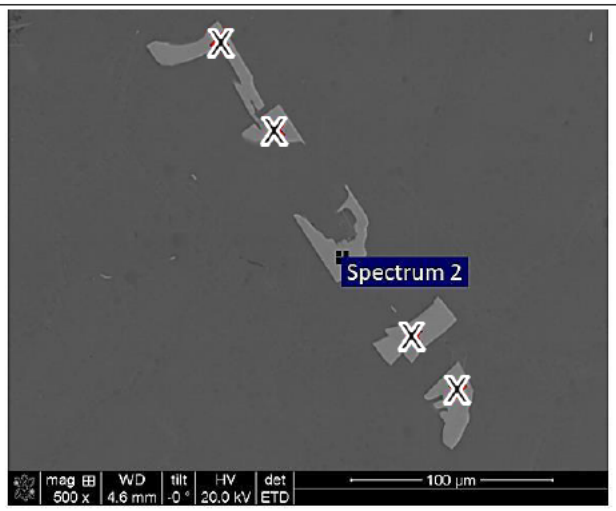
Figure 4-117 (a) and Figure 4-117 (b) depict low magnification SEM micrographs of the top and bottom samples of a 2L99 + 0.5 wt.% Mo. Figure 4-117 (a) illustrates the presence of shrinkage on the sample's surface, exhibiting varying sizes of defects ranging from 0.1 mm to 0.5 mm. The analysis revealed an equivalent area fraction of 0.35%, measured using ImageJ software, to be occupied by these defects. The characterisation of both the top and bottom samples did not indicate the presence of any significant amount of intermetallics.



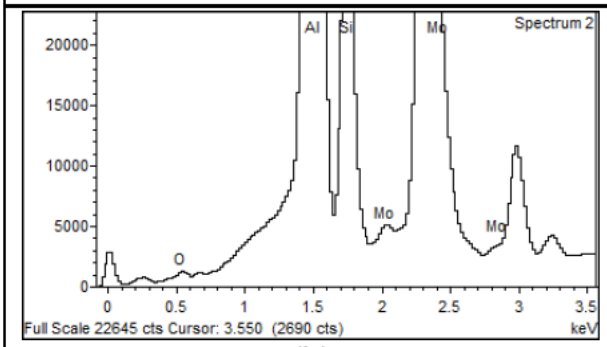
(a) (b)

Figure 4-117: (a) and (b) Low magnification of SEM images of 2L99 + 0.5 wt.% Mo top and bottom

Figure 4-118 (a) and Figure 4-118 (b) depicted high magnification SEM micrographs of the top surface of a 2L99 + 0.5 wt.% Mo sample displaying α shaped intermetallics. Figure 4-118 (b) and Figure 4-118 (c) present the EDX spectrum and elemental compositions of Spectrum 2 and the regions marked as “x”, which indicated to be $Al_6SiMo_{1.7}$.



(a)



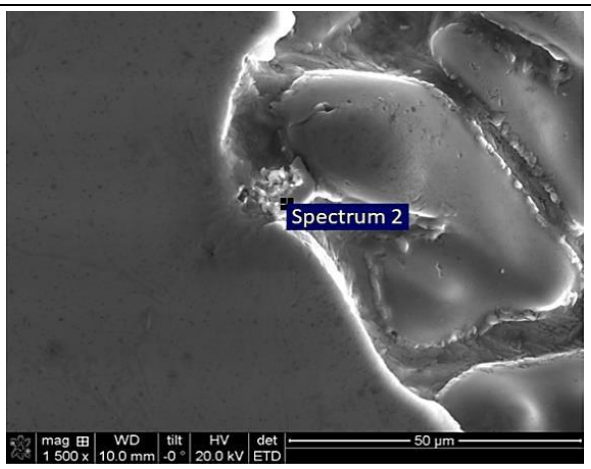
(b)

Element	Weight%	Atomic%
O K	0.89	2.03
Al K	53.41	71.89
Si K	9.60	12.41
Mo L	36.10	13.66

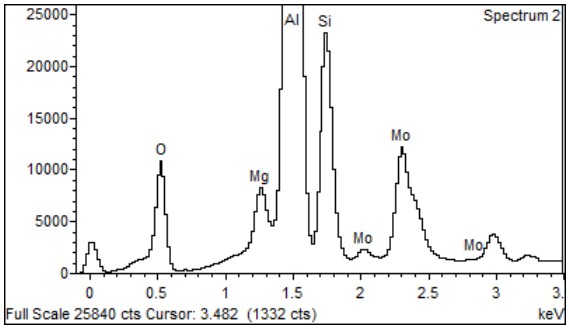
(c)

Figure 4-118: (a) High magnification SEM image of intermetallics on the top surface of a 2L99 + 0.5 wt.% Mo sample, (b) and (c)corresponding EDX elemental compositions

Figure 4-119 (a) depicts a high-magnification SEM micrograph of the base of a 2L99 + 0.5 wt.% Mo sample, displaying an α-shaped intermetallic on the wetted side of the bifilm inside the shrinkage pore. Figure 4-119 (c) and Figure 4-119 (d) present the corresponding information for points indicating Spectrum 2. The intermetallic marked as Spectrum 2 has grown on the wetted side of the shrinkage defect and comprises $Al_{3.5}SiMo_{1.2}$ plus 35.22 at.% of O (spinel).



(a)



(b)

Element	Weight%	Atomic%
O K	21.93	35.22
Mg K	1.66	1.76
Al K	41.32	38.87
Si K	11.50	10.52
Mo L	36.59	13.64

(c)

Figure 4-119: (a) High magnification SEM image of intermetallics on the bottom of a 2L99 + 0.5 wt.% Mo, (b) and (c)corresponding EDX elemental compositions

4.4.1.2 2L99 + 1.8 wt.% Mo

Figure 4-120 (a) and Figure 4-120 (b) are low magnification SEM micrographs of the top and bottom samples of 2L99 + 1.8 wt.% Mo. Figure 4-120 (a) shows the surface of the top sample, illustrating the presence of only shrinkage defects ranging significantly in length from 0.1 mm to 1.6 mm. Surface area analysis revealed an equivalent area fraction of 3.05% to be occupied by these bifilms. Figure 4-120 (b), however, demonstrates the presence of gas pores and intermetallic defects on the bottom sample. The observed gas pores exhibited a less variable range of sizes spanning from 0.05 mm to 0.2 mm in diameter. The intermetallics observed exhibited a length range of 0.01 mm

to 0.4 mm. As for the surface analysis of the bottom sample, it revealed that the shrinkage defects (i.e., the oxides) occupied an equivalent area fraction of 0.68%, whereas the intermetallics covered a larger area, accounting for 2.14% of the total sample area.

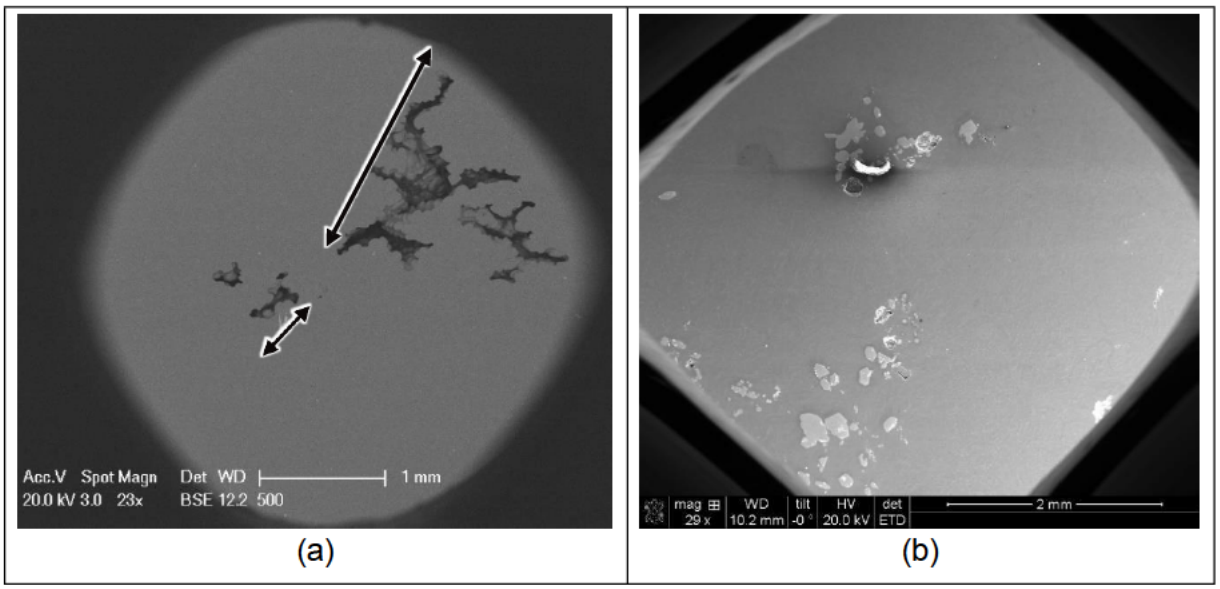
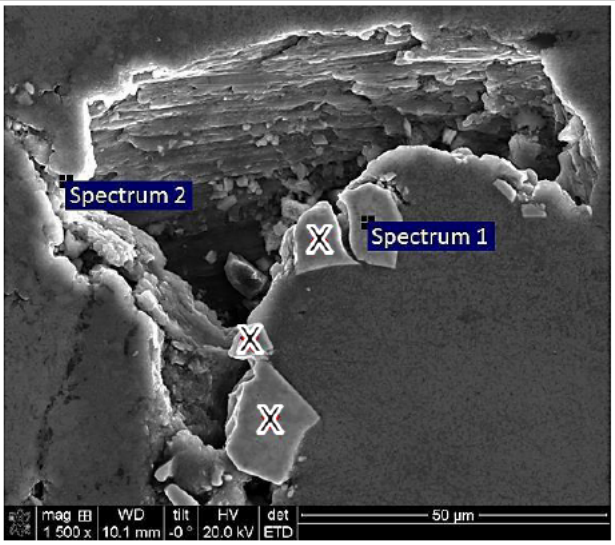
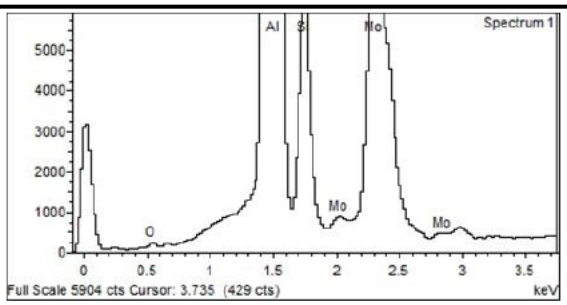


Figure 4-120 (a) and (b) Low magnification of SEM images of 2L99 + 1.8 wt.% Mo top and Bottom

Figure 4-121 (a) illustrates a high-magnification SEM micrograph of the top surface of a 2L99 + 1.8 wt.% Mo sample, revealing intermetallics of diverse α shapes and sizes but of similar composition of $Al_6SiMo_{1.2}$, labelled as Spectrum 1 and points “x” and spinel at the region marked as Spectrum 2. Figure 4-121 (b) and Figure 4-121 (c) present the EDX elemental composition of Spectrum 1 and points “x”, while Figure 4-121 (d) and Figure 4-121 (e) confirm the EDX elemental composition of Spectrum 2.



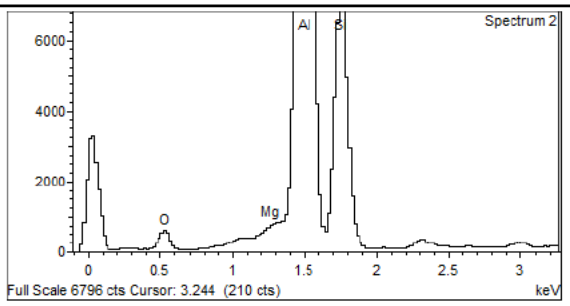
(a)



(b)

Element	Weight%	Atomic%
O K	1.00	2.27
Al K	52.86	71.22
Si K	9.87	12.77
Mo L	36.27	13.74

(c)



(d)

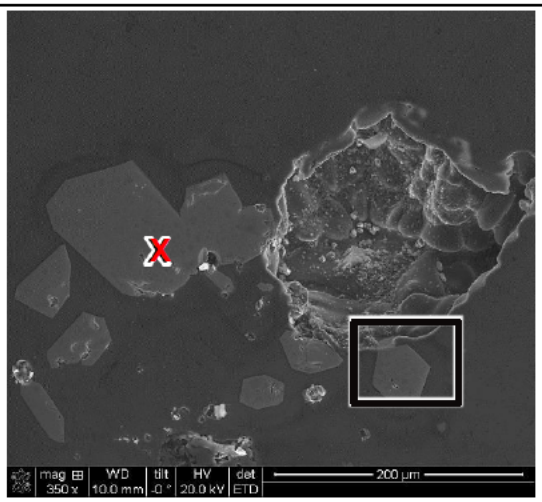
Element	Weight%	Atomic%
O K	7.83	12.65
Mg K	0.31	0.33
Al K	64.44	61.76
Si K	27.43	25.26

(e)

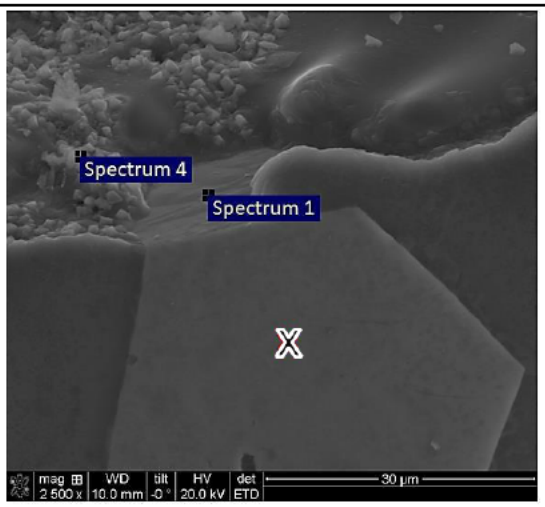
Figure 4-121: (a) to (e) Intermetallics observed on the top surface of a 2L99 + 1.8 wt.% Mo sample, accompanied by their respective EDX elemental compositions

Figure 4-122 (a) presents a low magnification SEM micrograph of the bottom surface of a 2L99 + 1.8 wt.% Mo sample, revealing the presence of intermetallics nucleating on the wetted surface of a gas pore, as shown in Figure 4-122 (b) at a higher magnification. Figure 4-122 (c) and Figure 4-122 (d) present the EDX elemental

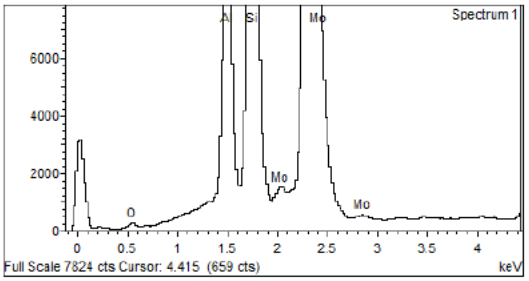
composition of Spectrum 1 and the point denoted as “x” in Figure 4-122 (a) and Figure 4-122 (b), revealing an intermetallic composition of $AlSi_{2.5}Mo_{1.7}$, while Figure 4-122 (e) and Figure 4-122 (f) present EDX elemental composition of Spectrum 4 as spinel particles.



(a)



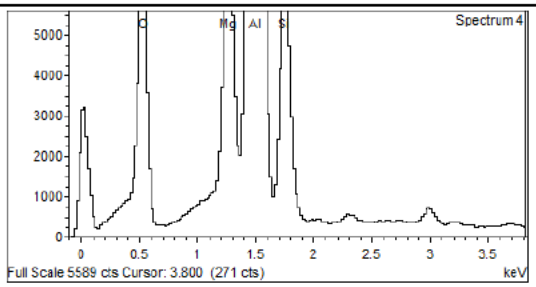
(b)



(c)

Element	Weight%	Atomic%
O K	1.82	5.52
Al K	10.07	18.12
Si K	25.99	44.92
Mo L	62.12	31.43

(d)



(e)

Element	Weight%	Atomic%
O K	26.86	38.16
Mg K	5.96	5.57
Al K	57.07	48.08
Si K	10.11	8.18

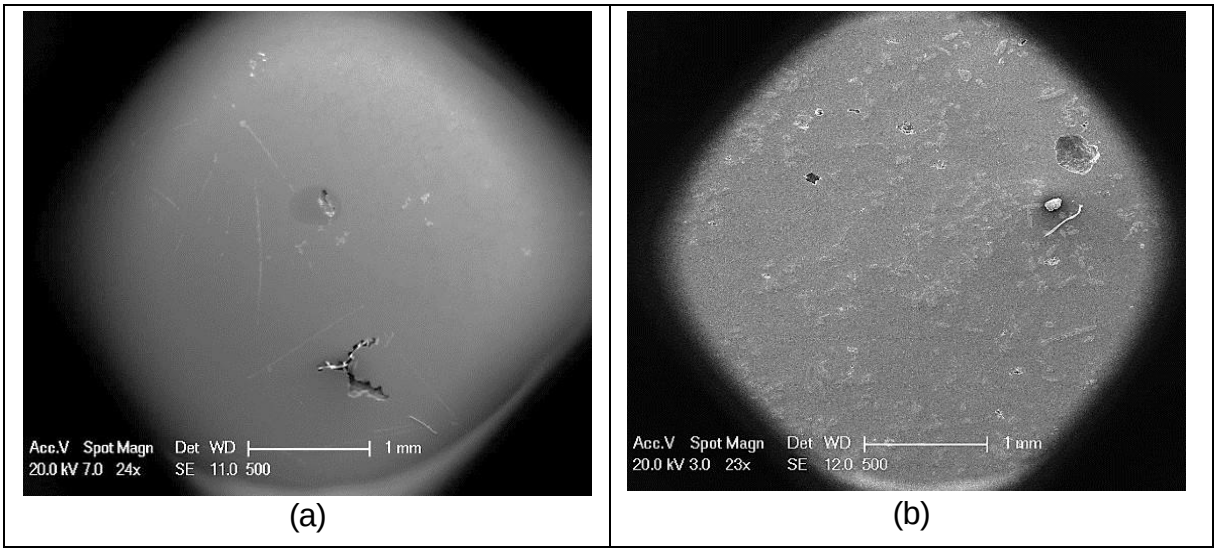
(f)

Figure 4-122: (a) to (f) Intermetallics observed on the bottom surface of a 2L99 + 1.8 wt.% Mo sample, accompanied by relevant EDX elemental composition

4.4.1.3 2L99 + 2.4 wt.% Mo

Figure 4-123 (a) and Figure 4-123 (b) depicted low magnification SEM micrographs of top and bottom samples of 2L99 + 2.4 wt.% Mo. Figure 4-123 (a) shows the surface of the top sample, illustrating the presence of shrinkage defects ranging in length from 0.2 mm to 0.5 mm, as well as intermetallic phases ranging in length from 0.01 mm to 1 mm. In Figure 4-123 (a), there was also a region with a darker colour that was due to sample contamination. Surface area analysis revealed an equivalent area fraction of 0.3% occupied by the shrinkage defects and 0.5% by the intermetallics.

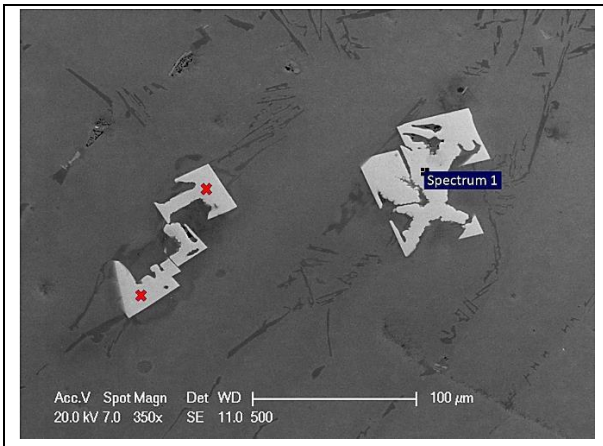
Figure 4-123 (b) demonstrated the presence of small amounts of bifilm and gas pores and a significant amount of intermetallics on the surface of the bottom sample. The gas pores observed varied in diameter between 0.1 mm and 0.4 mm. However, the observed intermetallics exhibited a wide length range of 0.01 mm to 0.5 mm. As for the surface analysis of the bottom sample, it revealed that the bifilms and shrinkage defects occupied an equivalent area fraction of 0.47%, whereas the intermetallics covered a much larger area, accounting for 5.5% of the total sample area.



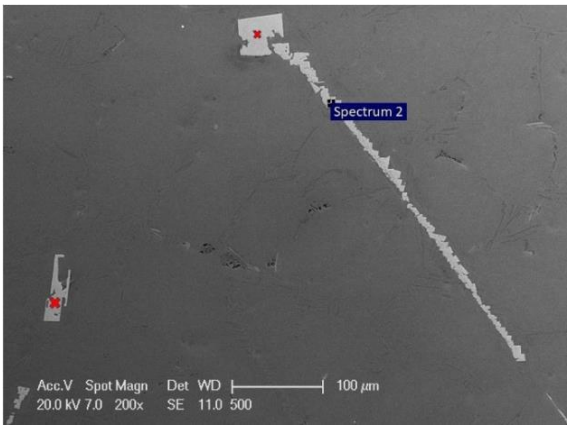
(a) (b)

Figure 4-123: (a) and (b) Low magnification of SEM images of 2L99 + 2.4 wt.% Mo top and Bottom

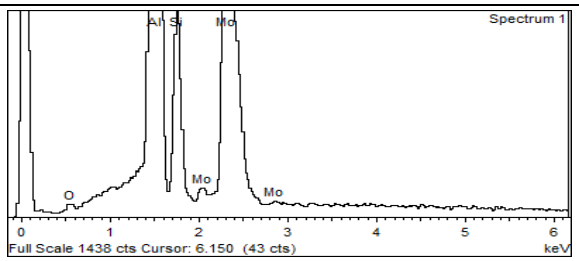
Figure 4-124 (a) and Figure 4-124 (b) illustrated high magnification SEM micrographs at the top surface of a 2L99 + 2.4 wt.% Mo sample, revealing intermetallics of diverse shapes and sizes but of similar composition marked as Spectrum 1, as well as points denoted as “x”, which were α phase. Figure 4-124 (b) showed a long needle shape (β-phase) marked as Spectrum 2. Figure 4-124 (c) to Figure 4-124 (f) confirmed the EDX spectrum and elemental composition of Spectrum 1, and the points denoted as “x” as $Al_{7.3}SiMo_{1.3}$ and Spectrum 2 as $Al_{5.4}Si_2Mo$.



(a)



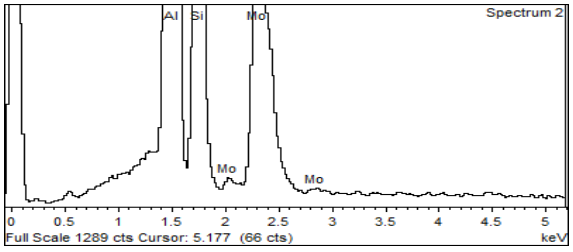
(b)



(c)

Element	Weight%	Atomic%
O K	1.36	3.06
Al K	54.62	73.08
Si K	8.02	10.31
Mo L	36.00	13.55

(d)



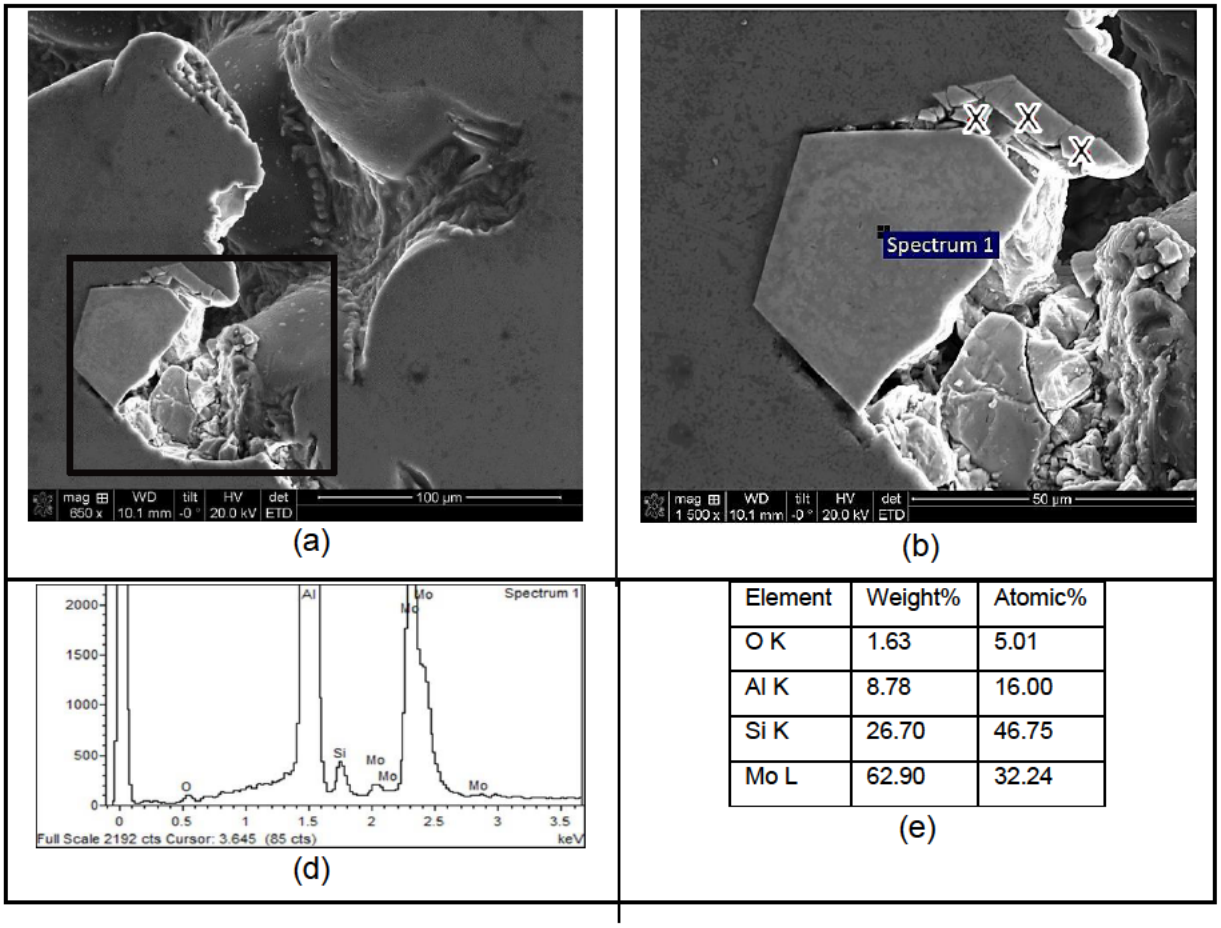
(e)

Element	Weight%	Atomic%
Al K	49.50	64.82
Si K	18.64	23.45
Mo L	31.86	11.73

(f)

Figure 4-124: (a) to (d) SEM image of the intermetallics on the top surface of a 2L99 + 2.4 wt.% Mo, (c) to (f) corresponding EDX spectra and elemental compositions

Figure 4-125 (a) and Figure 4-125 (b) illustrates a low and high-magnification SEM micrograph of an area at the base of a 2L99 + 2.4 wt.% Mo, showing intermetallics with diverse α shapes and at the edge of a pore. Figure 4-125 (d) and Figure 4-125 (e) present EDX elemental compositions of Spectrum 1 and the points denoted as “x” as Al Si_3Mo_2 with O (5 at.%).



Element	Weight%	Atomic%
O K	1.63	5.01
Al K	8.78	16.00
Si K	26.70	46.75
Mo L	62.90	32.24

(e)

Figure 4-125: (a) and (b) low and high SEM images of *intermetallics* in the pore at the base of a 2L99 + 2.4 wt.% Mo sample, (c) and (d) corresponding EDX elemental compositions

4.4.2 2L99 + W alloy

4.4.2.1 2L99 + 1.6 wt.% W

Figure 4-126 (a) and Figure 4-126 (b) depict low magnification SEM micrographs of

the top and bottom samples of 2L99 + 1.6 wt.% W. Figure 4-126 (a) illustrates the top surface of the sample, failing to indicate the presence of any significant bifilms or intermetallics at a low magnification of 30. Figure 4-126 (b), however, demonstrates the presence of bifilm and intermetallic defects on the bottom sample. The intermetallics observed exhibited a length range of 0.01 mm to 0.4 mm. The surface analysis of the bottom sample revealed that the intermetallics covered a larger area, accounting for 7.34% of the total sample area.

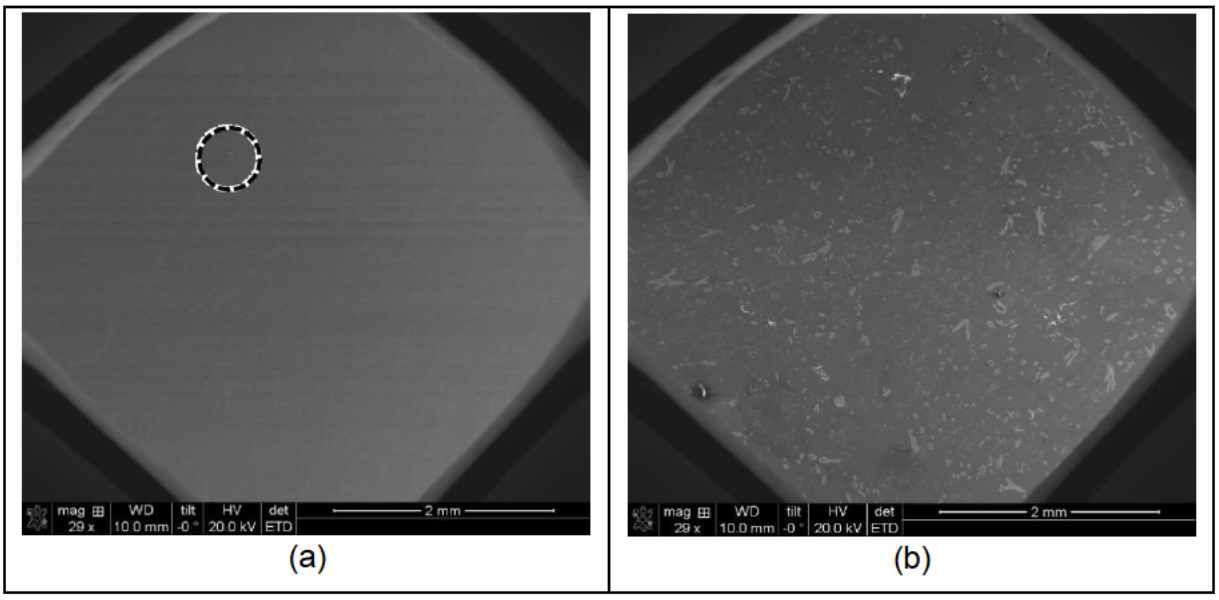
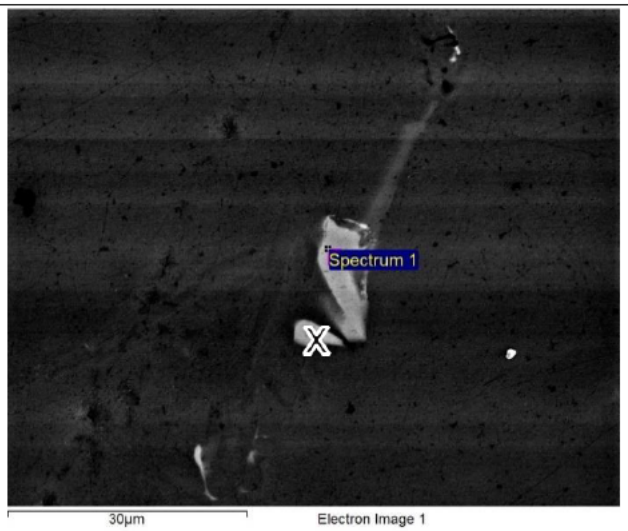
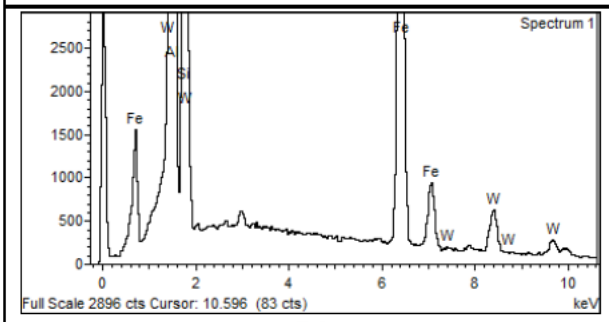


Figure 4-126 (a) and (b) Low magnification of SEM images of 2L99 + 1.6 wt.% W top and bottom

Figure 4-127 (a) depicts a high-magnification SEM micrograph of the upper surface of a 2L99 + 1.6 wt.% W sample, displaying two distinctively shaped intermetallics, labelled as Spectrum 1 and “x”, with matching $Al_{35}Si_6Fe_{7.5}W$ composition presented in Figure 4-127 (b) and (c).



(a)



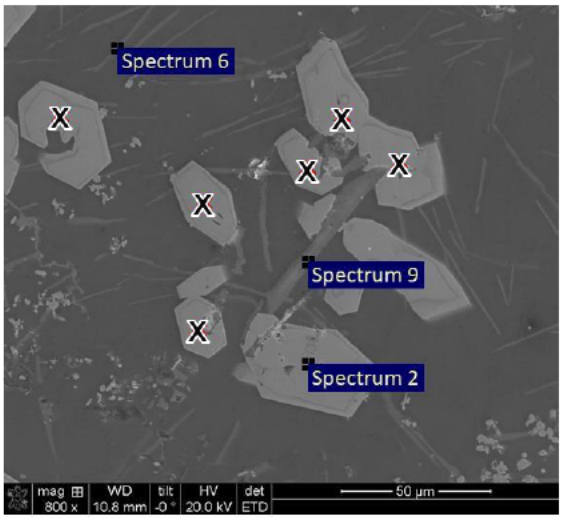
(b)

Element	Weight%	Atomic%
Mg K	0.40	0.58
Al K	54.05	69.89
Si K	9.68	12.02
Fe K	24.61	15.37
W M	11.27	2.14

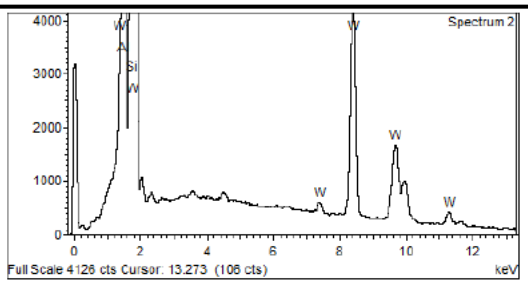
(c)

Figure 4-127: (a) High magnification SEM image of intermetallic on the top surface of a 2L99 + 1.6 wt.% W sample, (b) and (c) corresponding EDX spectrum and elemental composition

Figure 4-128 (a) illustrates a high-magnification SEM micrographs of a typical area at the base of a 2L99 + 1.6 wt.% W sample, showing numerous intermetallics with α-shapes and β-shapes with two different compositions, which had nucleated on the same bifilm marked as spectrum 9, as shown in Figure 4-128 (c). Figure 4-128 (b) and Figure 4-126 (c) presents EDX spectrum and elemental compositions of Spectrum 2, and the points denoted as “x” both are identical and identified as $Al_3Si_5W_4$; Figure 4-128 (d) and Figure 4-128 (e) present the EDX spectrum and elemental composition for Spectrum 6” as $Al_{10}Si_{1.5}Fe$, while Figure 4-128 (f) and Figure 4-128 (g) present EDX spectra and elemental compositions of Spectrum 9 as spinel.



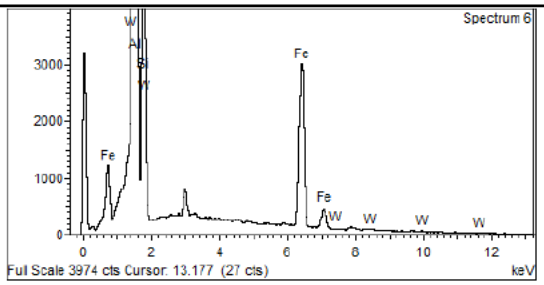
(a)



(b)

	Spectrum 2	
Element	Weight%	Atomic%
Al K	7.93	24.45
Si K	13.49	39.98
W M	78.58	35.57

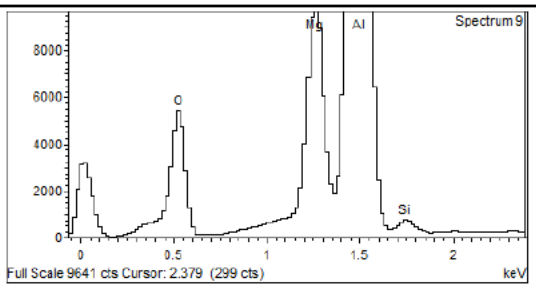
(c)



(d)

	Spectrum 6	
Element	Weight%	Atomic%
Al K	75.06	81.21
Si K	11.13	11.57
Fe K	13.81	7.22
W M	0.22	0.03

(e)



(f)

	Spectrum 9	
Element	Weight%	Atomic%
O K	26.05	37.00
Mg K	8.41	7.86
Al K	64.43	54.25
Si K	1.11	0.90

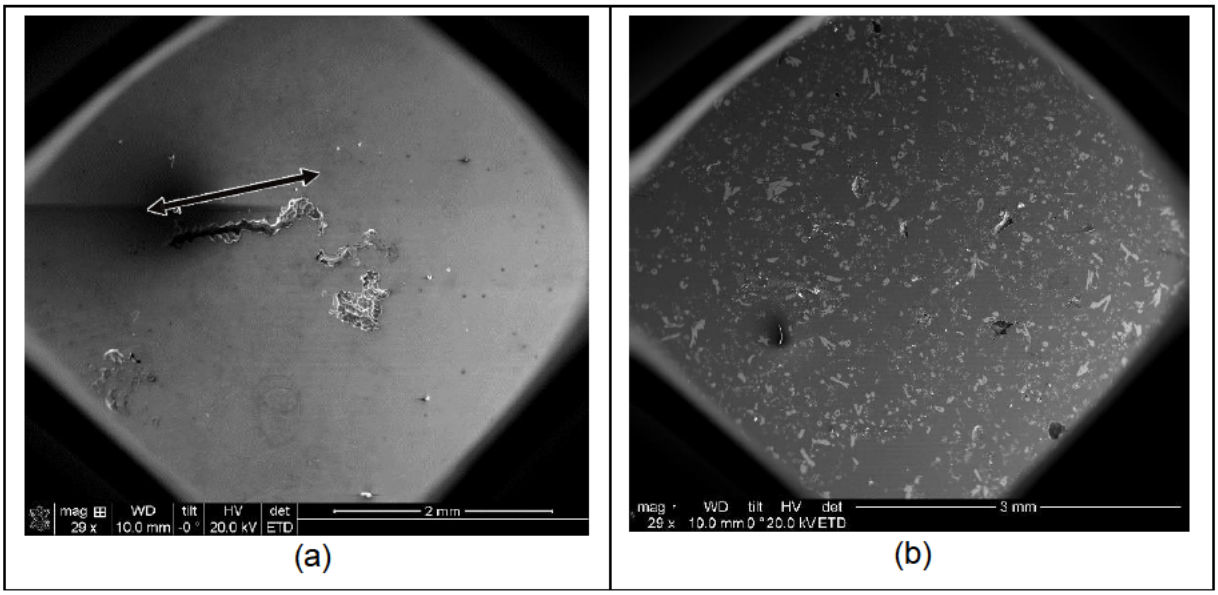
(g)

Figure 4-128: (a) High magnification of intermetallics and spinel observed on the bottom surface of a 2L99 + 1.6 wt.% W sample, (b) to (g) corresponding EDX spectra and elemental compositions

4.4.2.2 2L99 + 1.9 wt.% W

Figure 4-129 (a) and Figure 4-129 (b) depicted low magnification SEM micrographs of the top and bottom samples of 2L99 + 1.9 wt.% W. Figure 4-129 (a) shows the surface of the top sample, illustrating the presence of only shrinkage defects ranging significantly in length from 0.1 mm to 1.7 mm.

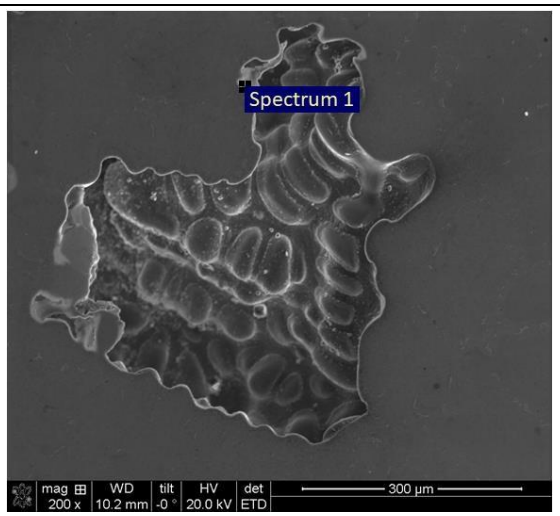
Figure 4-129 (b), however, demonstrated the presence of shrinkage defects and intermetallics on the surface of the bottom sample but, interestingly, did not reveal the presence of any large shrinkage defects. The shrinkage defects observed exhibit a less variable range of length from 0.05 mm to 0.3 mm. The intermetallics exhibited a length range of 0.01 mm to 0.3 mm. A surface analysis of the bottom sample revealed that the shrinkage defects occupied an equivalent area fraction of 0.08%, whereas the intermetallics covered a larger area, accounting for 8% of the total sample area.



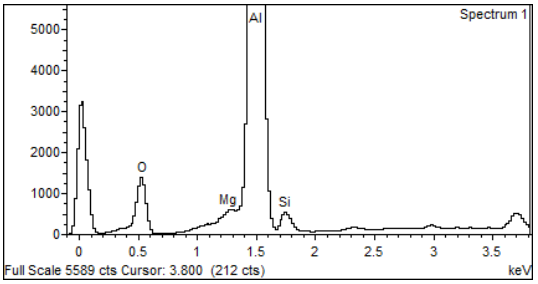
(a) (b)

Figure 4-129: (a) and (b) Low magnification SEM images of 2L99 +1.9 wt.% W top and bottom

Figure 4-130 (a) illustrates a high-magnification SEM micrograph of the top surface of a 2L99 +1.9 wt.% W sample, revealing shrinkage pores. Figure 4-130 (b) and Figure 4-130 (c) present the EDX elemental composition of Spectrum 1 as spinel.



(a)



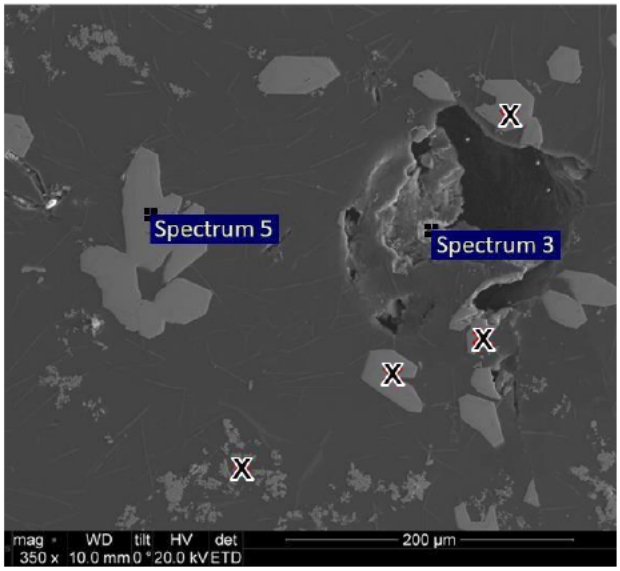
(b)

Element	Weight%	Atomic%
O K	22.57	32.97
Mg K	0.60	0.58
Al K	73.64	63.79
Si K	3.18	2.65

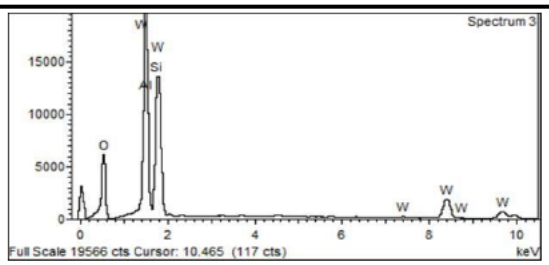
(c)

Figure 4-130: (a) SEM image of a shrinkage on the top surface of a 2L99 + 1.9 wt.% W sample, (b) and (c) corresponding EDX elemental composition

Figure 4-131 (a) illustrates a high-magnification SEM micrograph of the bottom surface of a 2L99 + 1.9 wt.% W sample, revealing intermetallics of diverse α shapes and sizes mostly nucleated on the same gas pore. Figure 4-131 (b) and Figure 4-131 (c) presented the EDX elemental composition of Spectrum 3 as spinel with W, the intermetallic located on the edge of the gas pore. Figure 4-131 (d) and Figure 4-131 (e) confirm the EDX elemental composition of Spectrum 5 as $AlSi_{2.3}W_{1.7}$ plus O.



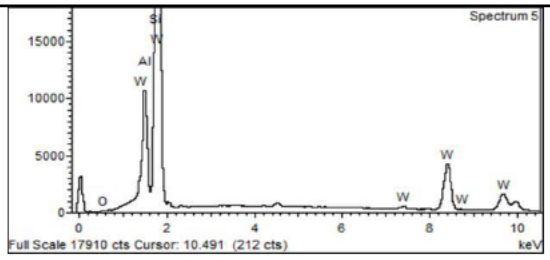
(a)



(b)

Element	Weight%	Atomic%
O K	34.17	63.14
Al K	21.04	23.06
Si K	7.40	7.79
W M	37.40	6.01

(c)



(d)

Element	Weight%	Atomic%
O K	0.91	4.53
Al K	6.36	18.69
Si K	15.37	43.40
W M	77.36	33.37

(e)

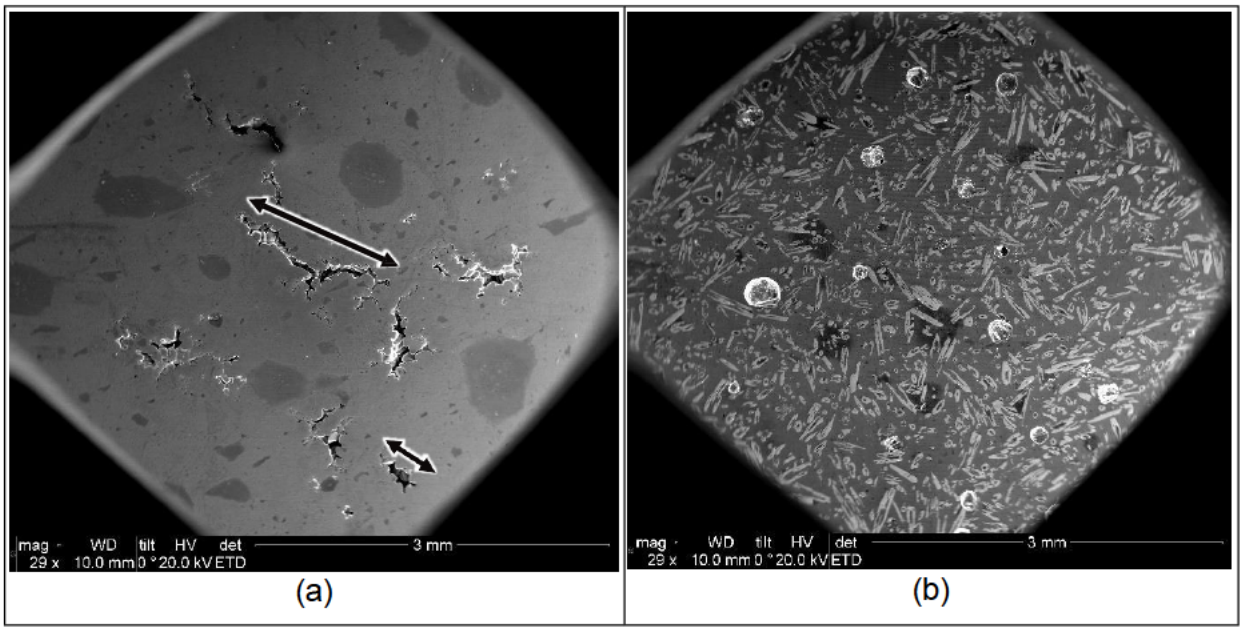
Figure 4-131: (a) SEM image of intermetallics and gas pore on the bottom surface of a 2L99 + 1.9 wt.% W sample, (b) to (e) corresponding EDX spectra and elemental composition

4.4.2.3 2L99 + 4.8 wt.% W

Figure 4-132 (a) and Figure 4-132 (b) depict low magnification SEM micrographs of the top and bottom samples of 2L99 + 4.8 wt.% W. Figure 4-132 (a) shows the surface of the top sample, illustrating the presence of shrinkage defects wide-ranging shrinkage defects 0.1 mm to 1.5 mm in length. Surface area analysis revealed an equivalent area

fraction of 4.2% occupied by these defects.

Figure 4-132 (b), however, demonstrated a significant presence of bifilms, gas pores and intermetallic defects on the surface of the bottom sample. The observed gas pores exhibited a less variable range of diameters from 0.1 mm and 0.3 mm. The intermetallics observed exhibited a length range of 0.01 mm to 0.4 mm. As for the surface analysis of the bottom sample, it revealed that the gas pores occupied an equivalent area fraction of 1%. In contrast, the intermetallics covered a significantly larger area, accounting for 16.4% of the total sample area.

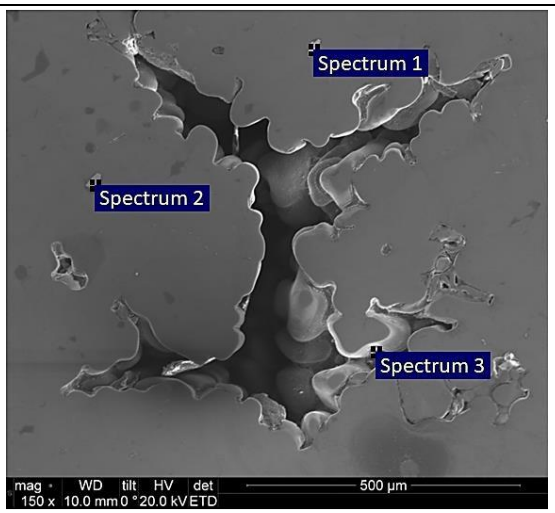


(a) (b)

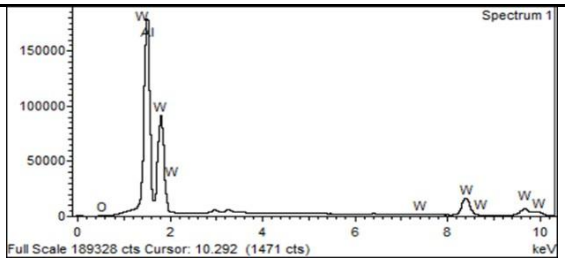
Figure 4-132 (a) and (b) Low magnification of SEM images of 2L99 + 4.8 wt.% W top and bottom

Figure 4-133 (a) illustrates a low magnification SEM micrograph at the top surface of a 2L99 + 4.8 wt.% W sample, showing a large shrinkage defect of approximately 800 µm in length. Figure 4-133 (a) revealed the presence of intermetallics (α shape) marked as Spectrum 1 and 2, and spinel, marked as Spectrum 3. Figure 4-133 (b) and Figure 4-133 (c) confirm the EDX elemental composition of Spectrum 1 as $Al_{24}SiW_7$. Figure 4-133 and Figure 4-133 (e) confirm the EDX elemental composition of Spectrum 2 as Al_5W. In

contrast, Figure 4-133 (f) and Figure 4-133 (g) confirm the presence of spinel marked as Spectrum 3.



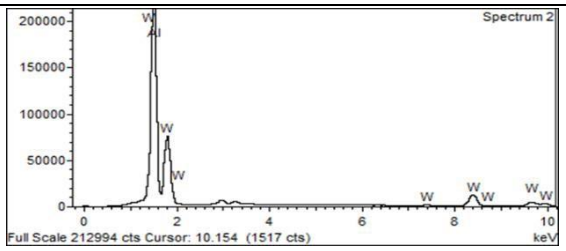
(a)



(b)

Element	Weight%	Atomic%
O K	0.62	2.35
Al K	32.27	72.71
Si K	1.50	3.24
W M	65.61	21.70

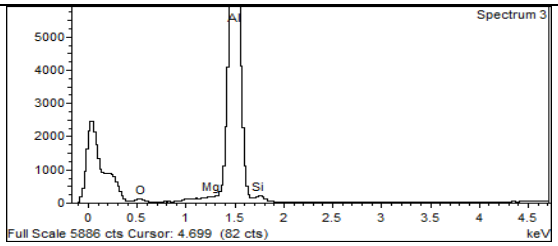
(c)



(d)

Element	Weight%	Atomic%
Al K	40.95	82.53
W M	59.05	17.47

(e)



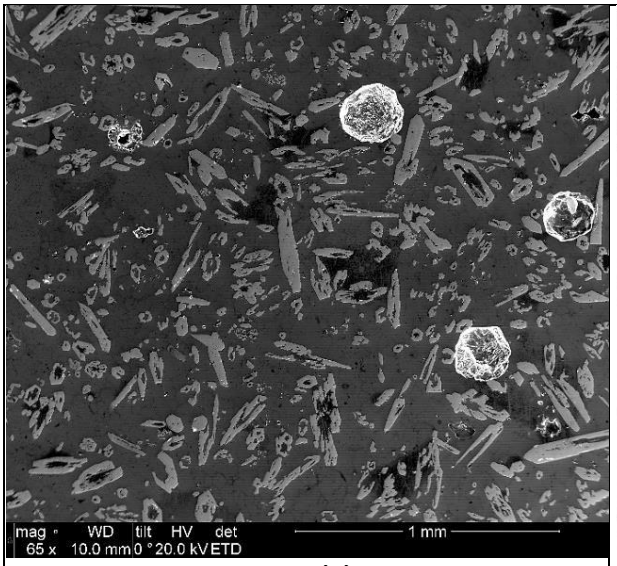
(f)

Element	Weight%	Atomic%
O K	11.58	18.11
Mg K	0.41	0.43
Al K	84.01	77.91
Si K	3.99	3.56

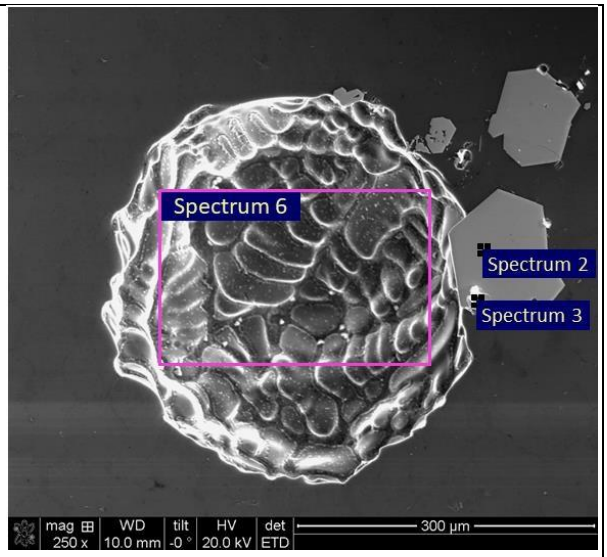
(g)

Figure 4-133: (a) Low magnification SEM micrograph at the top surface of a 2L99 + 4.8 wt.% W (b) to (g) corresponding EDX Spectra and EDX elemental compositions

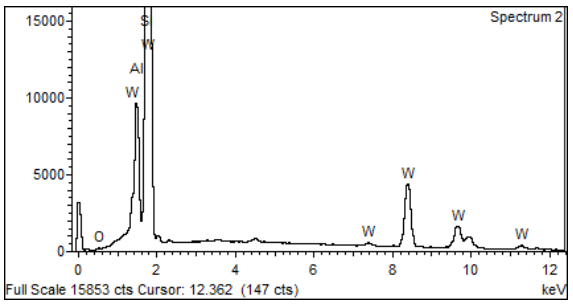
Figure 4-134 (a) and Figure 4-134 (b) show high and low magnification SEM micrographs at the base of a 2L99 + 4.8 wt.% W, showing gas pores of 360 µm diameter and a few intermetallics of α shaped and of various sizes. EDX spectra for the intermetallics and gas pore marked in Figure 4-134 (b) as Spectrum 2, Spectrum 3 and Spectrum 6 are shown in Figure 4-134 (c), Figure 4-134 (e) and Figure 4-134 (g). Figure 4-134 (d), Figure 4-134 (f) and Figure 4-134 (h) confirmed the EDX elemental composition of Spectrum 2 as $AlSi_{2.5}W_{1.8}$, while Spectrum 3 as spinel with small amount of W (1.9 at.%) and Spectrum 6 as oxides as spinel with Al and Si inside the pore, indicating nucleation of the intermetallics on the wetted side of the bifilm presented on the pore.



(a)



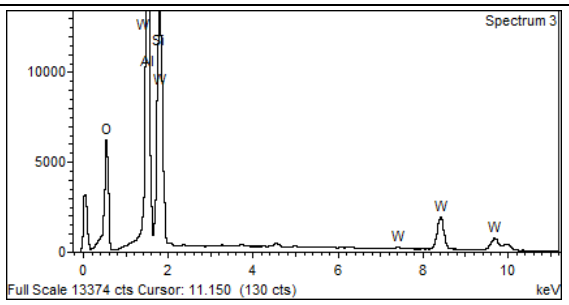
(b)



(c)

Element	Weight%	Atomic%
O K	0.50	2.48
Al K	6.09	17.96
Si K	16.29	46.17
W M	77.12	33.39

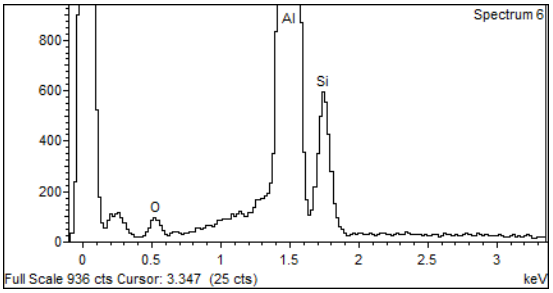
(d)



(e)

Element	Weight%	Atomic%
O K	43.09	62.61
Al K	37.62	32.42
Si K	3.61	2.99
W M	15.69	1.98

(f)



(g)

Element	Weight%	Atomic%
O K	16.67	20.82
Al K	69.34	66.26
Si K	13.99	12.92

(h)

Figure 4-134: (a) high (b) and (C) low magnification SEM micrographs at the base of a 2L99 + 4.8 wt.% W Intermetallics, (c) to (h) corresponding EDX spectra and their elemental composition

4.4.3 2L99 + V alloy

4.4.3.1 2L99 + 1.2 wt.% V

Figure 4-135 (a) and Figure 4-135 (b) depict low magnification SEM micrographs of the top and bottom samples of 2L99 + 1.2 wt.% V. Figure 4-135 (a) illustrate the surface of the top sample, showing the presence of only shrinkage defects ranging in length from 0.1 mm to 0.5 mm. It is important to note that in Figure 4-135 (a), areas of darker colour indicate sample contamination.

Figure 4-135 (b), however, demonstrated the presence of gas pores and intermetallic defects on the surface of the bottom sample. The observed gas pores have a less variable diameter range spanning from 0.1 mm to 0.3 mm. The intermetallics observed exhibited a length range of 0.01 mm to 0.4 mm. The surface analysis of the bottom sample revealed that the shrinkage defects occupied an equivalent area fraction of

0.56% and the intermetallics covered a larger area, accounting for 2.1% of the total sample area.

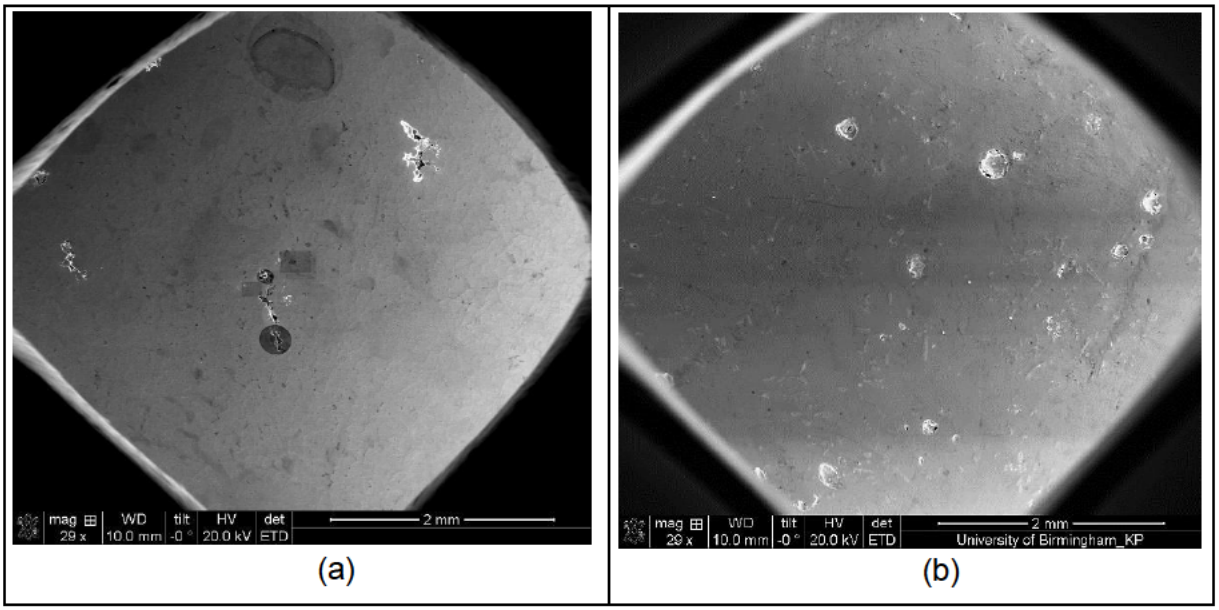
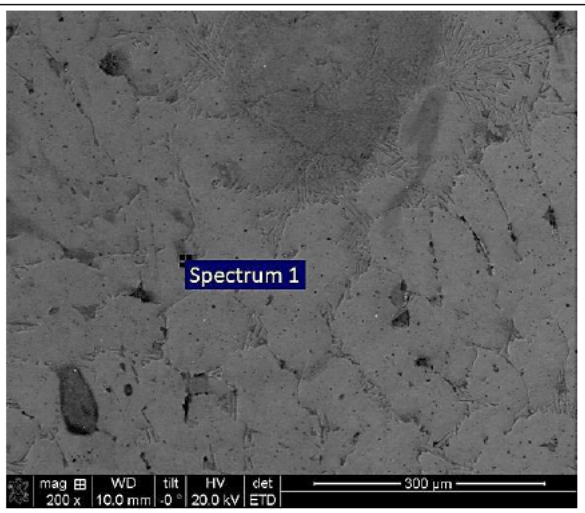
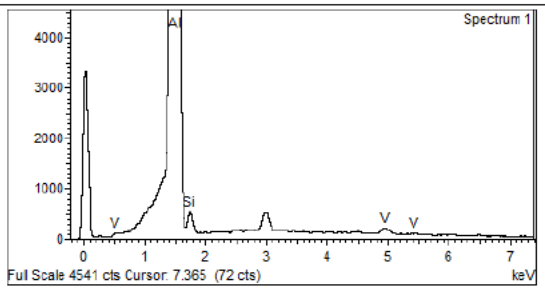


Figure 4-135: (a) and (b) Low magnification of SEM images of 2L99 + 1.2 wt.% V top and Bottom

Figure 4-136 (a) depicts a high-magnification SEM micrograph of the top surface of a 2L99 + 1.2 wt.% V sample, revealing an intermetallic composition of $Al_{49}SiV_{0.15}$ labelled as Spectrum 1. Figure 4-136 (b) and Figure 4-136 (c) present the EDX elemental composition of Spectrum 1.



(a)



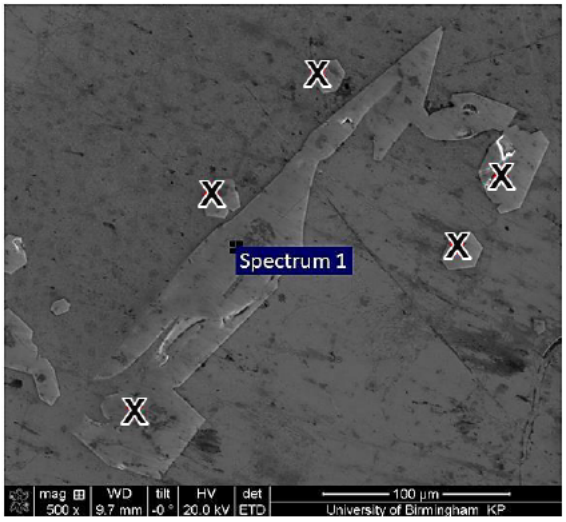
(b)

Element	Weight%	Atomic%
Al K	97.50	97.86
Si K	1.88	1.81
V K	0.62	0.33

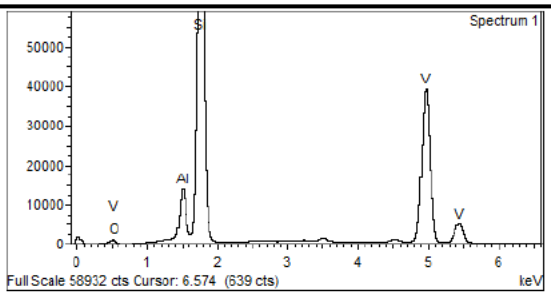
(c)

Figure 4-136: (a) to (c) Intermetallic observed on the top surface of a 2L99 + 1.2 wt.% V sample, accompanied by its respective EDX elemental composition

Figure 4-137 (a) illustrates high-magnification SEM micrographs of the bottom surface of a 2L99 +1.2 wt.% V sample, revealing α shaped intermetallics of diverse and sizes with the same composition of $AlSi_{6.2}V_{3.7}$ labelled as Spectrum 1 and points "x". Figure 4-137 (b) and Figure 4-137 (c) present the EDX elemental composition of Spectrum 1.



(a)



(c)

Element	Weight%	Atomic%
O K	2.73	5.92
Al K	5.95	7.65
Si K	43.65	53.95
V K	47.67	32.48

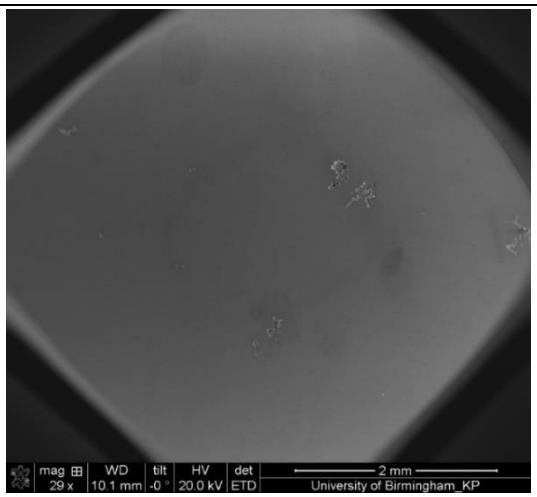
(d)

Figure 4-137: (a) SEM image of intermetallics on the bottom surface of a 2L99 + 1.2 wt.% V sample, (c) and (d) corresponding EDX spectrum and elemental composition

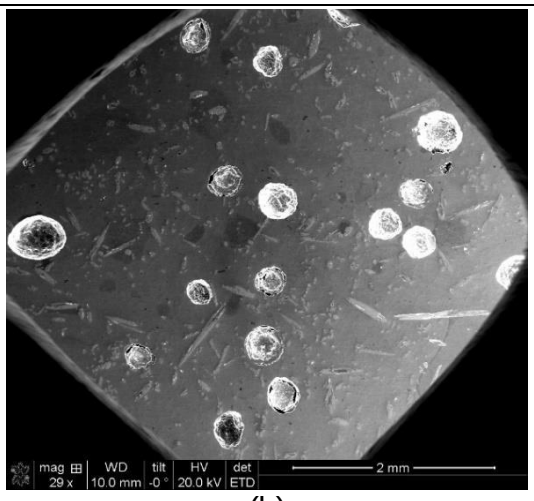
4.4.3.2 2L99 + 2.1 wt.% V

Figure 4-138 (a) and Figure 4-138 (b) depicted low magnification SEM micrographs of the top and bottom of a sample of 2L99 + 2.1 wt.% V. Figure 4-138 (a) shows the surface of the top sample, illustrating the presence of shrinkage defects ranging in length from 0.1 mm to 0.4 mm, as well as scarce amounts of intermetallics ranging in length from 0.01 mm to 0.2 mm. In Figure 4-138 (a), there are also regions with darker colours that are due to sample contamination. Surface area analysis revealed an equivalent area fraction of 0.24% occupied by the shrinkage defects and less than 0.02% by the intermetallics.

Figure 4-138 (b), however, demonstrates a significant presence of shrinkage and intermetallic defects at the base of the sample. The observed shrinkage defects exhibited a less variable range of diameters of between 0.2 mm and 0.4 mm. The intermetallics observed exhibited a wide length range of 0.01 mm to 1 mm. The surface analysis of the bottom sample revealed that the shrinkage defects occupied an equivalent area fraction of 7.3%, whereas the intermetallics covered a smaller area, accounting for 5% of the total sample area.



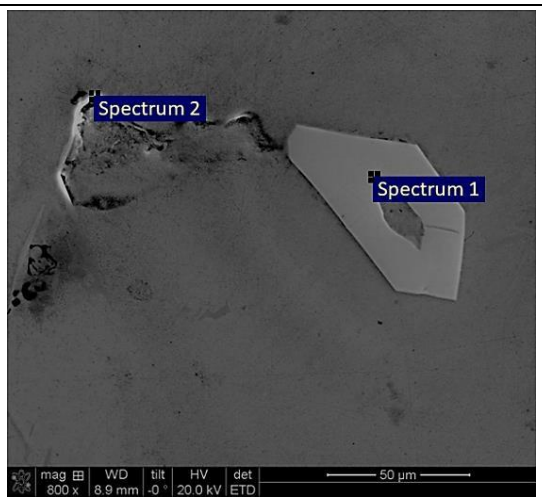
(a)



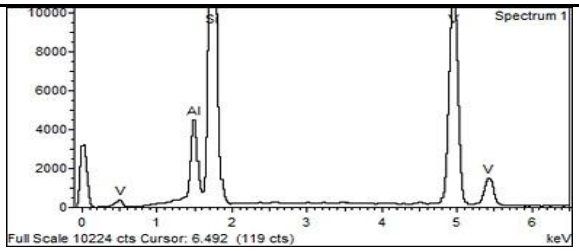
(b)

Figure 4-138: (a) and (b) Low magnification of SEM images of 2L99 + 2.1 wt.% V top and bottom

Figure 4-139 (a) illustrates a high-magnification SEM micrograph of the top surface of a 2L99 + 2.1 wt.% V sample, revealing an intermetallic α shape marked as Spectrum 1 with a composition of $AlSi_{10}V_4$ and a spinel phase marked as Spectrum 2. Figure 4-139 (b) and Figure 4-139 (c) present the EDX elemental composition of Spectrum 1, while Figure 4-139 (d) and Figure 4-139 (e) confirm the EDX elemental composition of spinel marked as Spectrum 2.



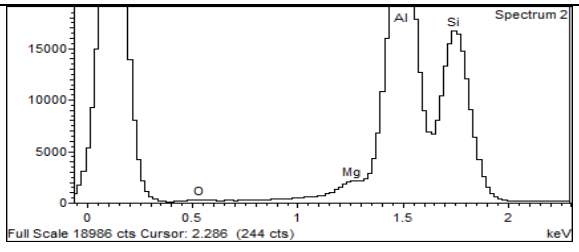
(a)



(b)

Element	Weight%	Atomic%
Al K	6.15	8.10
Si K	46.56	58.91
V K	47.29	32.99

(c)



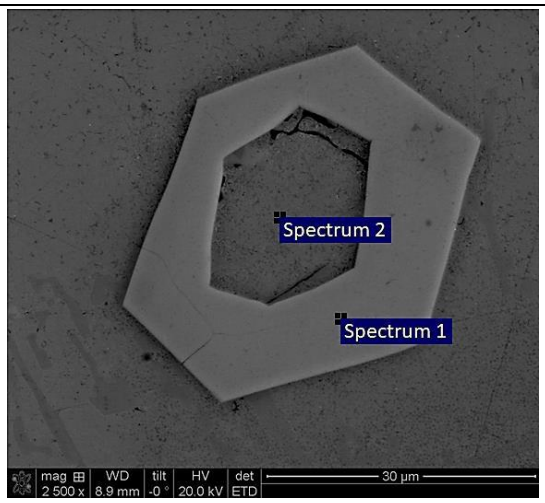
(d)

Element	Weight%	Atomic%
O K	6.94	11.35
Mg K	2.02	2.17
Al K	44.24	42.89
Si K	46.79	43.58

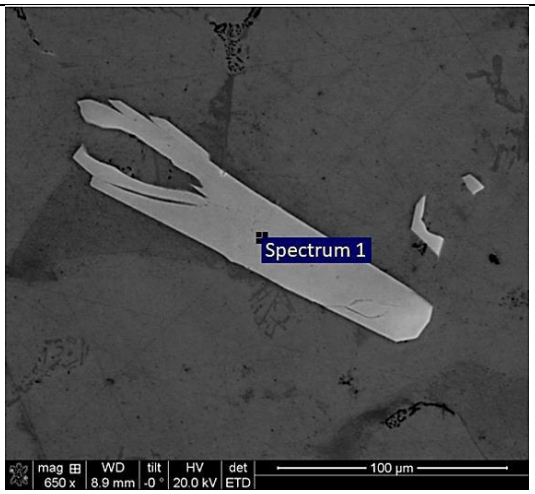
(e)

Figure 4-139: (a) Low magnification of SEM images of intermetallics on the top surface of a 2L99 + 2.1 wt.% V sample, (b) to (e) corresponding EDX spectra and elemental composition

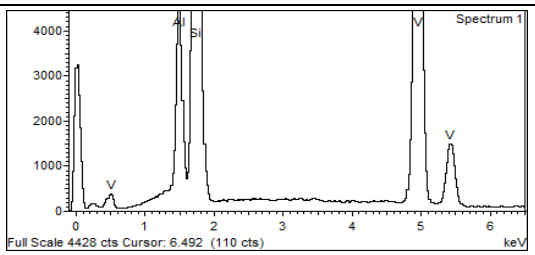
Figure 4-140 (a) and Figure 4-140 (b) illustrate high magnification SEM micrographs at the top surface of a 2L99 + 2.1 wt.% V sample, revealing α shaped intermetallics of diverse sizes. Figure 4-140 (c) and Figure 4-140 (d) present the EDX elemental composition of Spectrum 1 on both SEM micrographs, confirming the elemental composition of Spectrum 1 as $AlSi_{10}V_5$, while Figure 4-140 (e) and Figure 4-140 (f) confirm the EDX elemental composition of Spectrum 2 as the base alloy.



(a)



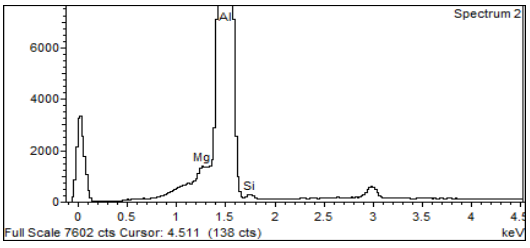
(b)



(c)

Element	Weight%	Atomic%
Al K	4.87	6.42
Si K	47.93	60.65
V K	47.20	32.93

(d)



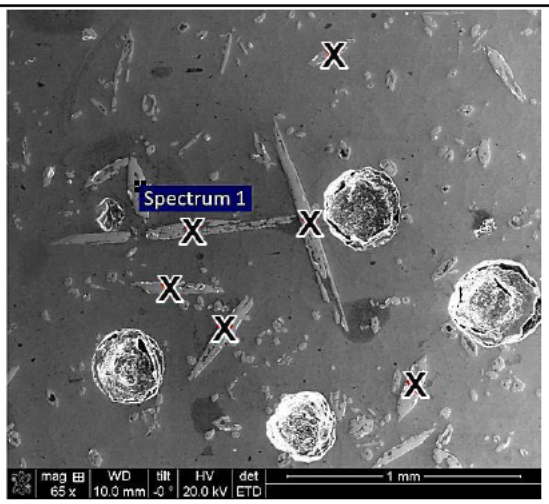
(e)

Element	Weight%	Atomic%
Mg K	0.67	0.74
Al K	98.45	98.42
Si K	0.88	0.84

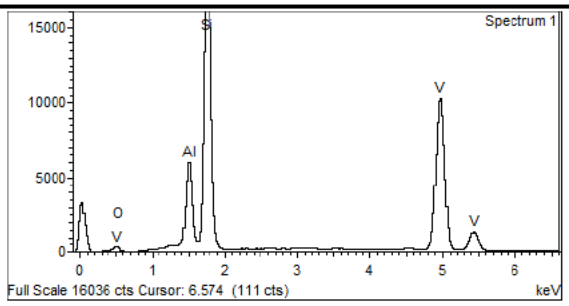
(f)

Figure 4-140: (a) Low magnification of SEM images of intermetallics on the top surface of a 2L99 + 2.1 wt.% V sample, (c) to (f) corresponding EDX spectra and elemental compositions

Figure 4-141 (a) illustrates a high-magnification SEM micrograph at the top surface of a 2L99 + 2.1 wt.% V sample, revealing numerous gas pores, bifilms and β shaped intermetallics of diverse sizes, marked as Spectrum 1 and points identified as “x”. Figure 4-141 (b) and Figure 4-141 (c) present the EDX elemental composition of Spectrum 1 and the points denoted as “x”, confirming the elemental composition of Spectrum 1 and points denoted as “X” as $Al_2Si_9V_5$.



(a)



(b)

Element	Weight%	Atomic%
O K	3.82	8.08
Al K	9.62	12.08
Si K	41.16	49.64
V K	45.40	30.19

(c)

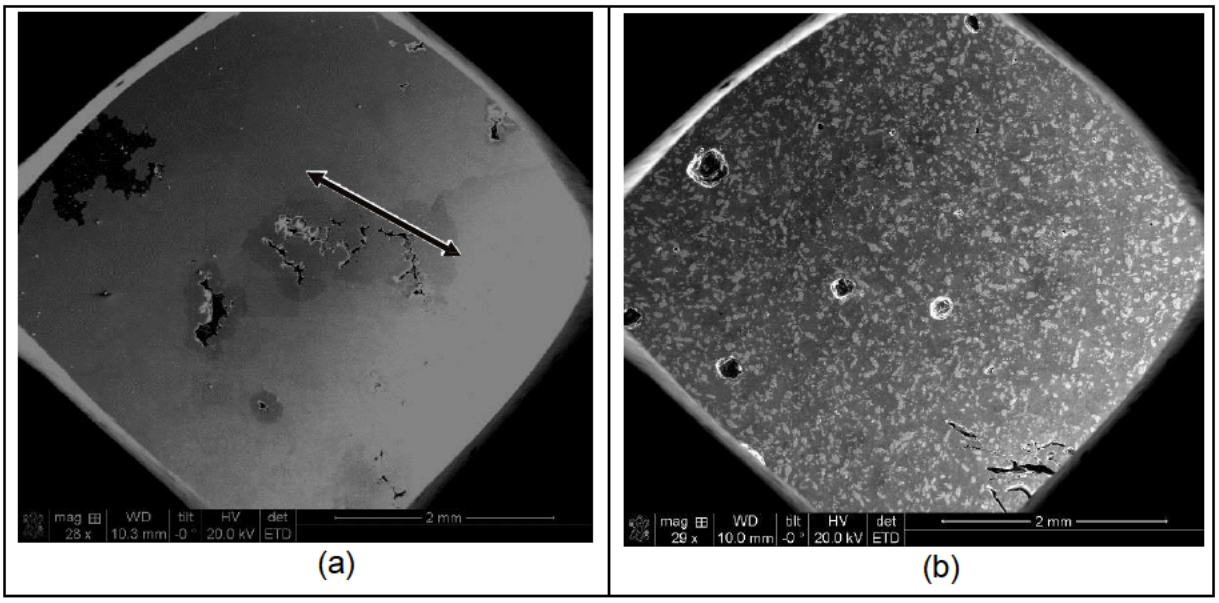
Figure 4-141: (a) Low magnification of SEM images on the bottom surface of a 2L99 + 2.1 wt.% V sample, (b) and (c) corresponding EDX spectra and elemental composition

4.4.3.3 2L99 + 5.1 wt.% V

Figure 4-142 (a) and Figure 4-142 (b) depict low magnification SEM micrographs of the top and bottom samples of a 2L99 + 5.1 wt.% V sample. Figure 4-142 (a) shows the

surface of the top sample, illustrating the presence of only shrinkage defects ranging significantly in size from 0.01 mm to 1.8 mm. Surface area analysis revealed an equivalent area fraction of 2.5% occupied by the shrinkage defects.

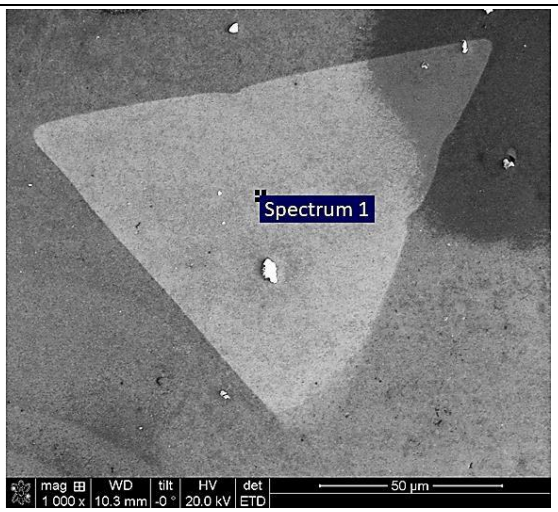
Figure 4-142 (b), however, shows the presence of gas pores and bifilms as well as a significant amount of intermetallics on the base of the sample. The gas pore defects exhibited a less variable range of diameters between 0.2 mm and 0.3 mm. The intermetallics observed exhibited a length range of 0.01 mm to 0.3 mm. As for the surface analysis of the bottom sample, it was revealed that the gas pores occupied an equivalent area fraction of 0.6%. In contrast, intermetallics covered a significantly larger area, accounting for 12.1% of the total sample area.



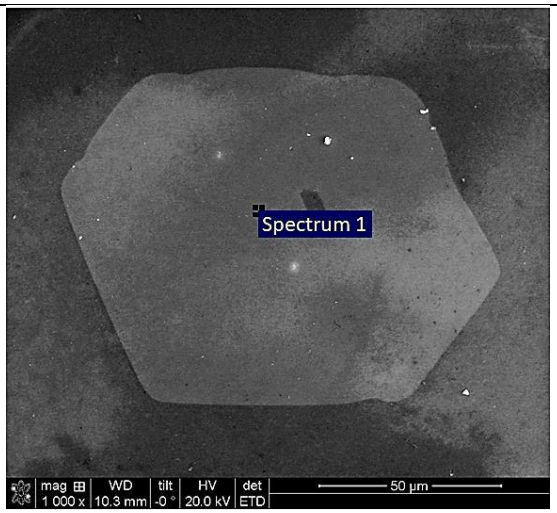
(a) (b)

Figure 4-142: (a) and (b) Low magnification of SEM images of 2L99 + 5.1 wt.% V top and Bottom

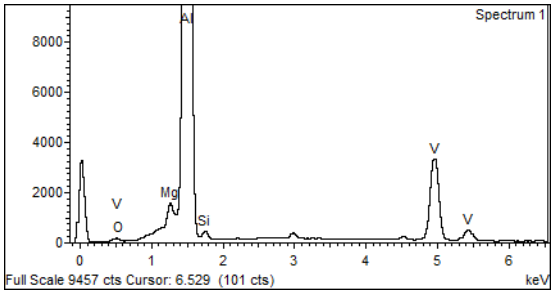
Figure 4-143 (a) and Figure 4-143 (b) illustrate high-magnification SEM micrographs at the upper surface of a 2L99 + 5.1 wt.% V sample, showing two α-shape V-intermetallics of approximately the same size but different shapes. Figure 4-143 (c) and Figure 4-143 (d) confirm the EDX elemental composition of both intermetallics marked as Spectrum 1 as $Al_{44}SiV_5$.



(a)



(b)



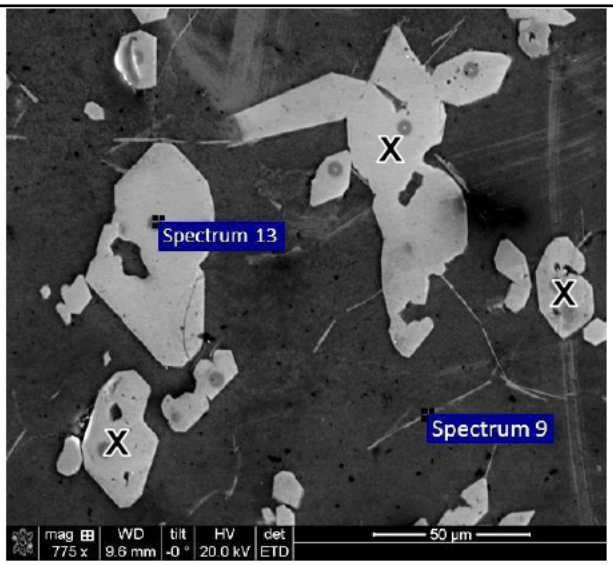
(c)

Element	Weight%	Atomic%
O K	0.67	1.22
Mg K	1.39	1.66
Al K	80.14	86.36
Si K	1.29	1.33
V K	16.51	9.42

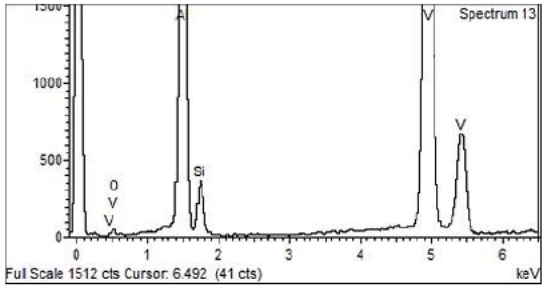
(d)

Figure 4-143: (a) and (b) low magnification SEM image of intermetallics on the top surface of a 2L99 + 5.1 wt.% V sample, (c) and (d) corresponding EDX spectra and elemental composition

Figure 4-144 (a) and Figure 4-144 (b) illustrated high magnification SEM micrographs at the bottom surface of a 2L99 + 5.1 wt.% V sample, showing various α and β shaped intermetallics of different sizes. Figure 4-144 (c) and Figure 4-144 (d) confirm the EDX elemental composition of the intermetallics labelled as Spectrum 13 (α shape) as “x” in $Al_{10}SiV_{11.5}$ with O. Figure 4-144 (e) and Figure 4-144 (f) confirm the EDX elemental composition of the intermetallics, labelled as Spectrum 9 (β shape) as“x” in $Al_{26}Si_3Fe$.



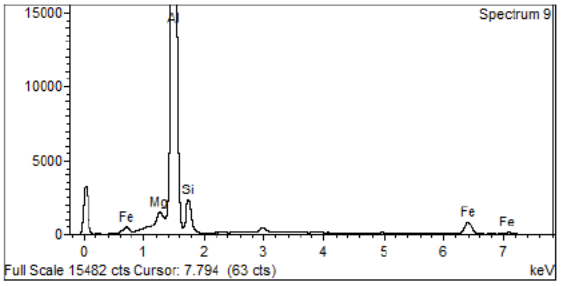
(a)



(c)

Element	Weight%	Atomic%
O K	4.16	9.64
Al K	28.85	39.64
Si K	3.32	4.39
V K	63.67	46.34

(d)



(e)

Element	Weight%	Atomic%
Mg K	1.23	1.41
Al K	83.44	86.40
Si K	9.13	9.08
Fe K	6.20	3.10

(f)

Figure 4-144: (a) and (b) SEM image of intermetallics on the bottom surface of a 2L99 + 5.1 wt.% V sample, (c) to (f) corresponding EDX spectra and elemental compositions

4.4.4 Summary

Sedimentation tests were carried out on 2L99 (plus Mo/W/V) alloys. XRF analysis was carried out on the top and bottom samples from the tests, the results of which are presented in Table 4-108, Table 4-109, and Table 4-110. Low magnification SEM

image was used to compare the top and bottom of different samples, the increase in the amount of O and intermetallics was measured using XRF and analysed by ImageJ software, as presented in Table 4-111, Table 4-112, Table 4-113, and Table 4-114.

Table 4-111: the amount of O measured by XRF on all studied alloys

	Mo			W			V		
O Wt.% at the top	2.5	2.9	3.8	2.9	3.9	3.2	3.6	4.6	4.1
O Wt.% at the bottom	4.6	3.4	4.6	6.5	7.7	5.3	4.6	5.4	4.8
Average. composition of intermetallics per sample wt.%	0.47	2.35	3.31	2.26	2.67	5.6	1.05	1.76	4
% increase of O at the bottom of the sample	84.0	17.2	21.1	124.1	97.4	65.6	27.8	17.4	17.1

Table 4-112: XRF amount and ImageJ analysis results for Mo intermetallics at the base of the sample

Sample	Wt.% of Mo composition on the Top of the sample based on XRF	Wt.% of Mo composition on the Bottom of the sample based on XRF	Increase Mo-IMC at the bottom	Average. of composition of Mo in wt.% based on XRF	Mo-IMC% area at the bottom based on ImageJ
1	0.11	0.83	635%	0.47	0.17
2	0.48	4.22	773%	2.35	2.01
3	0.53	6.09	1045%	3.31	6.53

Table 4-113: XRF amount and ImageJ analysis results for W intermetallics at the base of the sample

Sample	Wt.% of W composition on the Top of the sample based on XRF	Wt.% of W composition on the Bottom of the sample based on XRF	Increase W-IMC at the bottom	Average. of composition of W in wt.% based on XRF	W-IMC% area at the bottom based on ImageJ
1	0.32	4.21	1227%	2.26	6.34
2	0.37	4.98	1244%	2.67	7.72
3	0.58	10.70	1735%	5.64	17.43

Table 4-114: XRF amount and ImageJ analysis results for V intermetallics at the base of the sample

batch	Wt.% of V composition on the Top of the sample based on XRF	Wt.% of V composition on the Bottom of the sample based on XRF	Increase V-IMC at the bottom	Average. of composition of V in wt.% based on XRF	V-IMC% area at the bottom based on ImageJ
1	0.36	1.74	377%	1.05	2.09
2	0.20	3.33	1575%	1.76	4.99
3	0.31	7.70	2397%	4	12.13

4.5 Nitride growth[5]

The results of the aluminium nitride growth tests carried out, as described in section 3.4, are presented in this section. Table 4-115 shows the elemental composition of the various alloys used.

Table 4-115: Elemental composition of the alloys based on XRF analysis

Element Weight%	Mo	W	V	Mg	Si	Fe	Ti	Cu	Zn	Pb	Sn	Rh	Se	La	Al
2L99	0	0	0	0.3	9.8	0.03	0.14	0	0	0	0	0	0	0	Bal.
CP-Al	0	0	0	0.01	0.10	0.10	0.02	0.01	0.01	0.01	0.01	0	0	0	Bal.
2L99 + 0.6 wt.% Mo	0.64	0	0	0.32	8.55	0.06	0.11	0	0	0	0	0	0	0	Bal.
2L99 + 0.2 wt.% W	0	0.21	0	0.29	9.42	0.14	0	0	0	0	0	0	0	0	Bal.

4.5.1 Rod- Shape AlN

Figure 4-145 (a) to Figure 4-145 (h) show micrographs and EDX spectra of rod-shaped nitrides, which have an average width of 2 µm and a length of approximately 6 µm. These nitrides were observed on the surfaces of all four alloys of CP-Al, 2L99, 2L99 + 0.6 wt.% Mo and 2L99 + 0.2 wt.% W subjected to a 24-hour exposure to nitrogen gas. The largest rod-shaped nitride observed in CP-Al measured approximately 12 µm in length and 2 µm in width. Table 4-116 provides the quantification results for the spectra corresponding to the areas marked as Spectrum 1 in Figure 4-145 (a) to Figure 4-145 (d). The rod-shaped AlN patches observed on the alloy surfaces had an average size of approximately 30 µm by 50 µm.

[5] The results presented in this section have been published by the author in the paper provided in Appendix A.

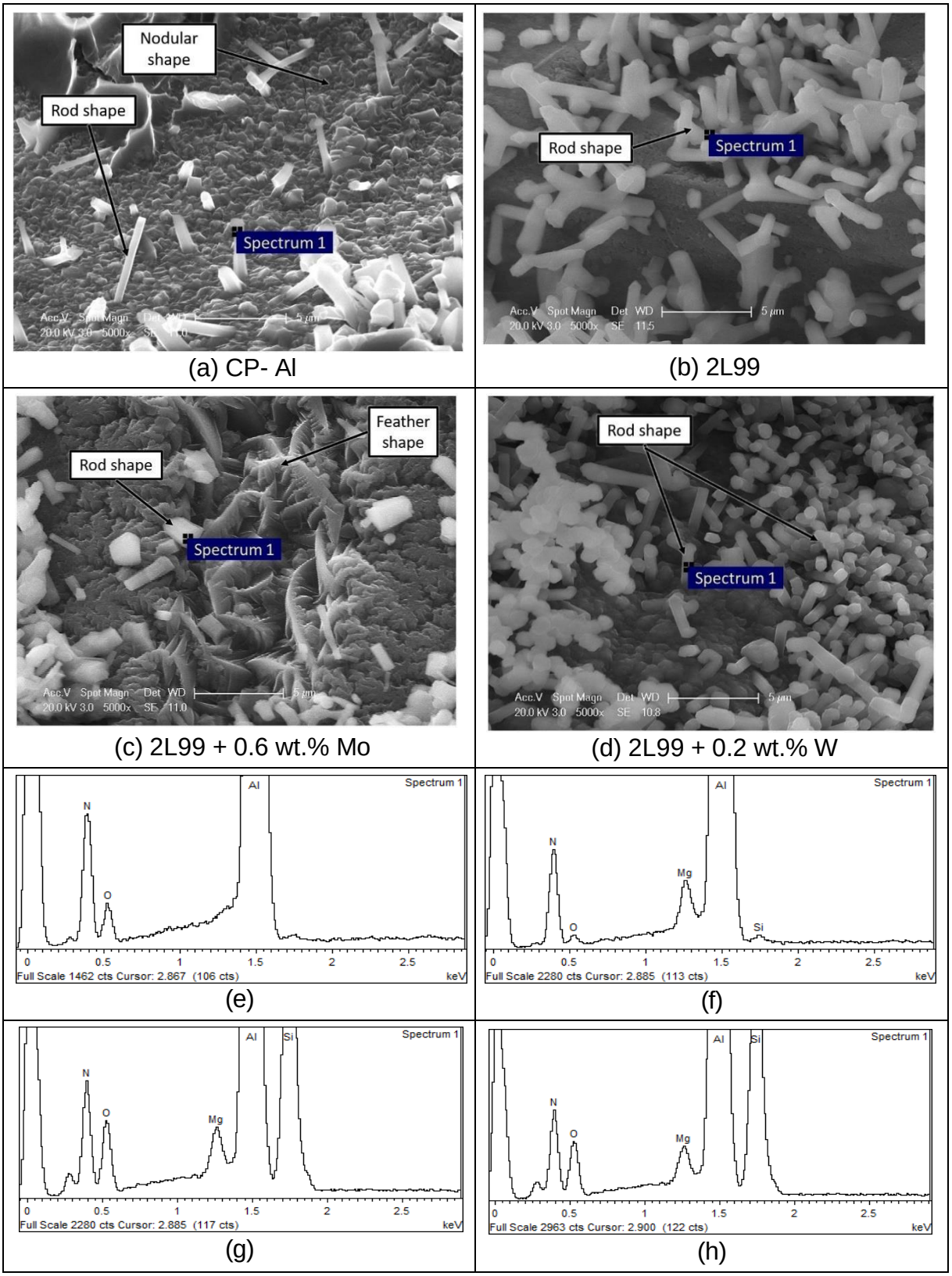


Figure 4-145: (a) to (d) SEM micrographs of rod-shaped AlN on the surface of CP-Al, 2L99 alloy, 2L99 + 0.6 wt.% Mo alloy and 2L99+0.2 wt pct W alloy, with 24 hours holding time in N at 850 °C (e) to (h) the EDX spectra for the marked areas in (a) to (d)

Table 4-116: Quantification of spectra for Figure 4-145 (a) to (d)

Description	Figure 4-145 (a) Spectrum 1		Figure 4-145 (b) Spectrum 1		Figure 4-145 (c) Spectrum 1		Figure 4-145 (d) Spectrum 1	
	Weight %	Atomic %	Weight%	Atomic %	Weight %	Atomic %	Weight %	Atomic %
N	33.35	47.29	35.94	51.20	29.92	41.96	29.92	41.96
O	7.20	8.94	2.65	3.31	14.60	17.92	14.60	17.92
Mg	0	0	1.10	0.90	0.92	0.75	0.92	0.75
Al	59.45	43.77	60.02	44.39	41.95	30.54	41.95	30.54
Si	0	0	0.29	0.21	12.61	8.82	12.61	8.82

In addition to the rod-shaped nitrides, feather shaped AlN was also observed, as depicted in Figure 4-145 (c).

4.5.2 Whisker-shaped AlN

Figure 4-146 (a) to Figure 4-146 (h) present micrographs and EDX spectra of whisker-shaped nitrides observed on the surfaces of all four alloys (CP-Al, 2L99, 2L99+0.6 wt.% Mo and 2L99+0.2 wt.% W), which were exposed to nitrogen for a duration of 12 hours. Notably, these nitrides exhibited a distinct whisker shape. The EDX spectra analysis showed that the amount of oxygen was more than three times greater than the amount of nitrogen in the whisker-shaped nitrides. Table 4-117 provides the quantification results for the spectra corresponding to areas as denoted as Spectrum 1, 2, and 3, as shown in Figure 4-146 (a) to Figure 4-146 (d). The average dimensions of the whisker-shaped AlN patches observed on the surfaces of the examined alloys were measured to be approximately 60 µm by 90 µm.

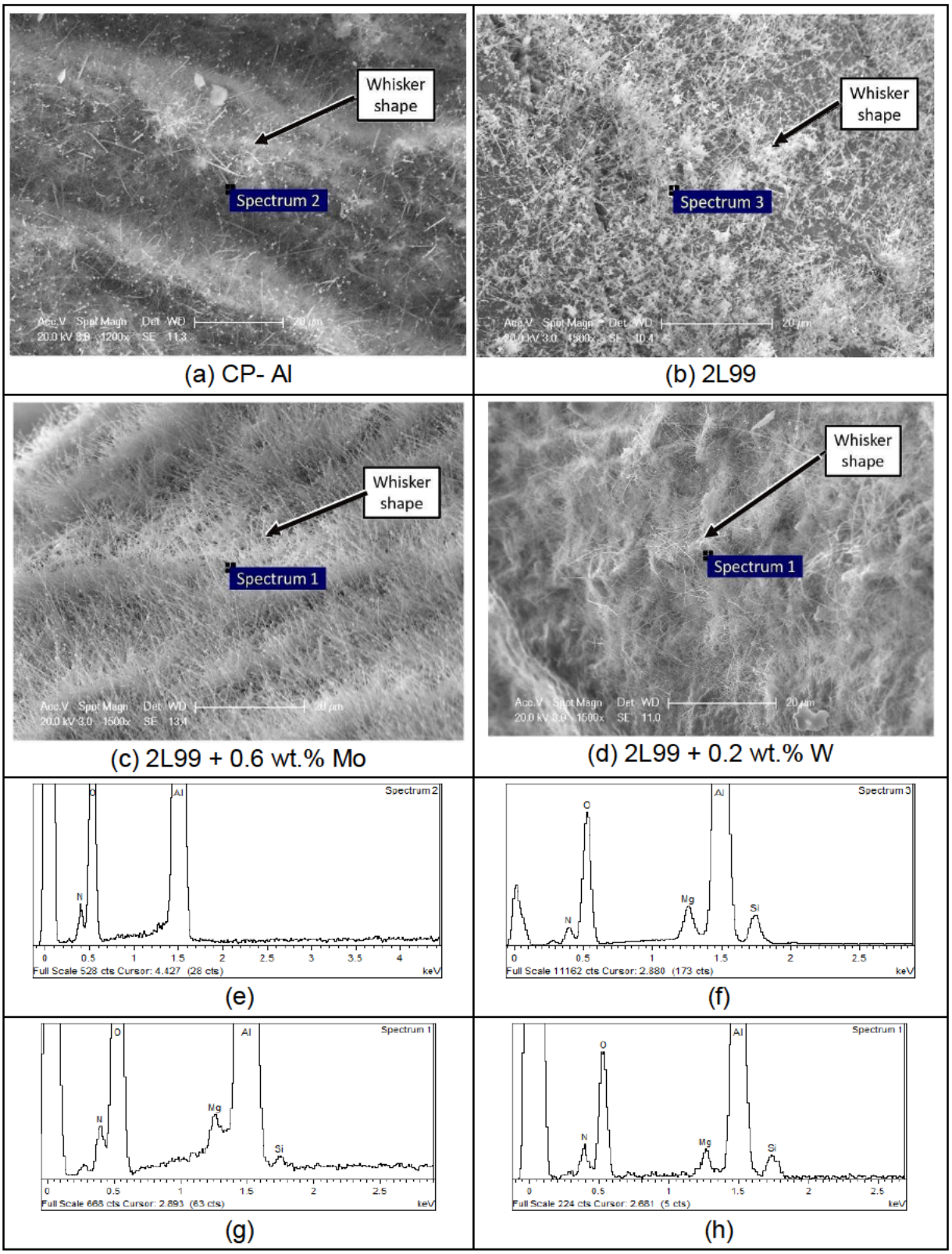


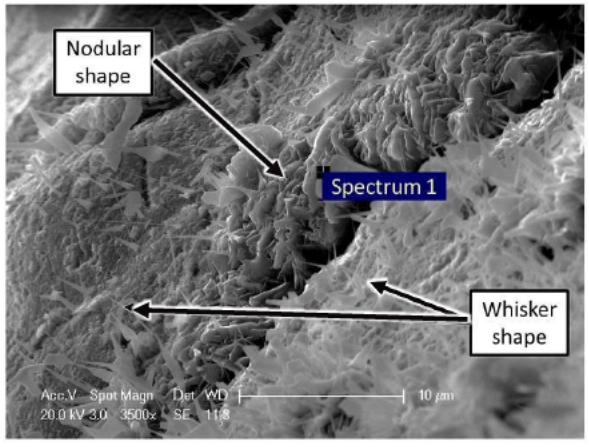
Figure 4-146: (a) to (d) SEM micrographs of whisker-shaped AlN on the surfaces of CP- Al, 2L99 alloy, 2L99 + 0.6 wt.% Mo alloy and 2L99 + 0.2 wt.% W alloy respectively, with 12 hours of holding time in N at 850 °C (e) to (h) the EDX spectra for the marked areas shown in (a) to (d)

Table 4-117: Quantification of spectra for Figure 4-146 (a) and (b)

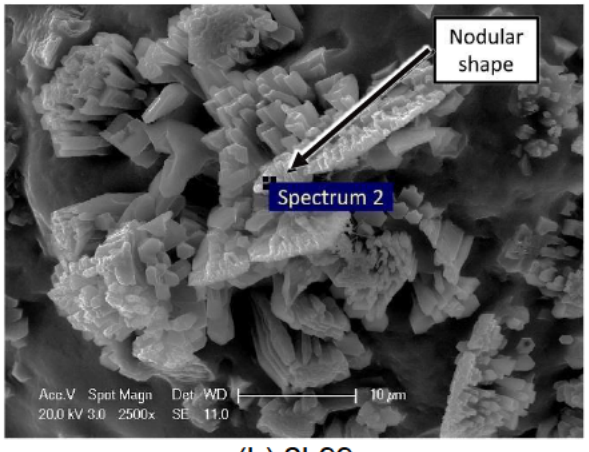
Description	Figure 4-146 (a) Spectrum 2		Figure 4-146 (b) Spectrum 3		Figure 4-146 (c) Spectrum 1		Figure 4-146 (d) Spectrum 1	
	Weight%	Atomic%	Weight%	Atomic%	Weight%	Atomic%	Weight%	Atomic%
N	10.98	14.85	11.92	16.54	8.63	11.98	14.87	15.94
O	47.07	55.71	40.23	48.89	44.88	54.51	43.31	54.86
Mg	0	0	1.96	1.57	0.43	0.34	1.74	1.35
Al	41.94	29.44	43.29	31.20	45.87	33.04	37.91	26.40
Si	0	0	2.61	1.81	0.19	0.13	2.17	1.45

4.5.3 Nodular-shaped AlN

Figure 4-147 (a) to Figure 4-147 (h) exhibit a nodular morphology for nitrides, with an average length of approximately 250 nm. These nodular nitrides were observed on the surfaces of all four alloys (CP-Al, 2L99, 2L99+0.6 wt.% Mo and 2L99+0.2 wt.% W) after a 3-hour exposure to nitrogen. Interestingly, the nodular shapes were similar to those observed in the as-cast condition, as shown in Figure 4-25 (e), Figure 4-26 (c), Figure 4-27 (b) and Figure 4-28 (b). Additionally, whisker-shaped nitrides were observed between the nodular-shaped nitrides, as shown in Figure 4-147 (a). Table 4-118 presents the quantification results for the spectra corresponding to the areas denoted as Spectrum 1 and 2 in Figure 4-147 (a) to Figure 4-147 (d). The average dimensions of the nodular-shaped AlN patches observed on the surfaces of the examined alloys were measured to be approximately 15 µm by 25 µm.



(a) CP- Al



(b) 2L99

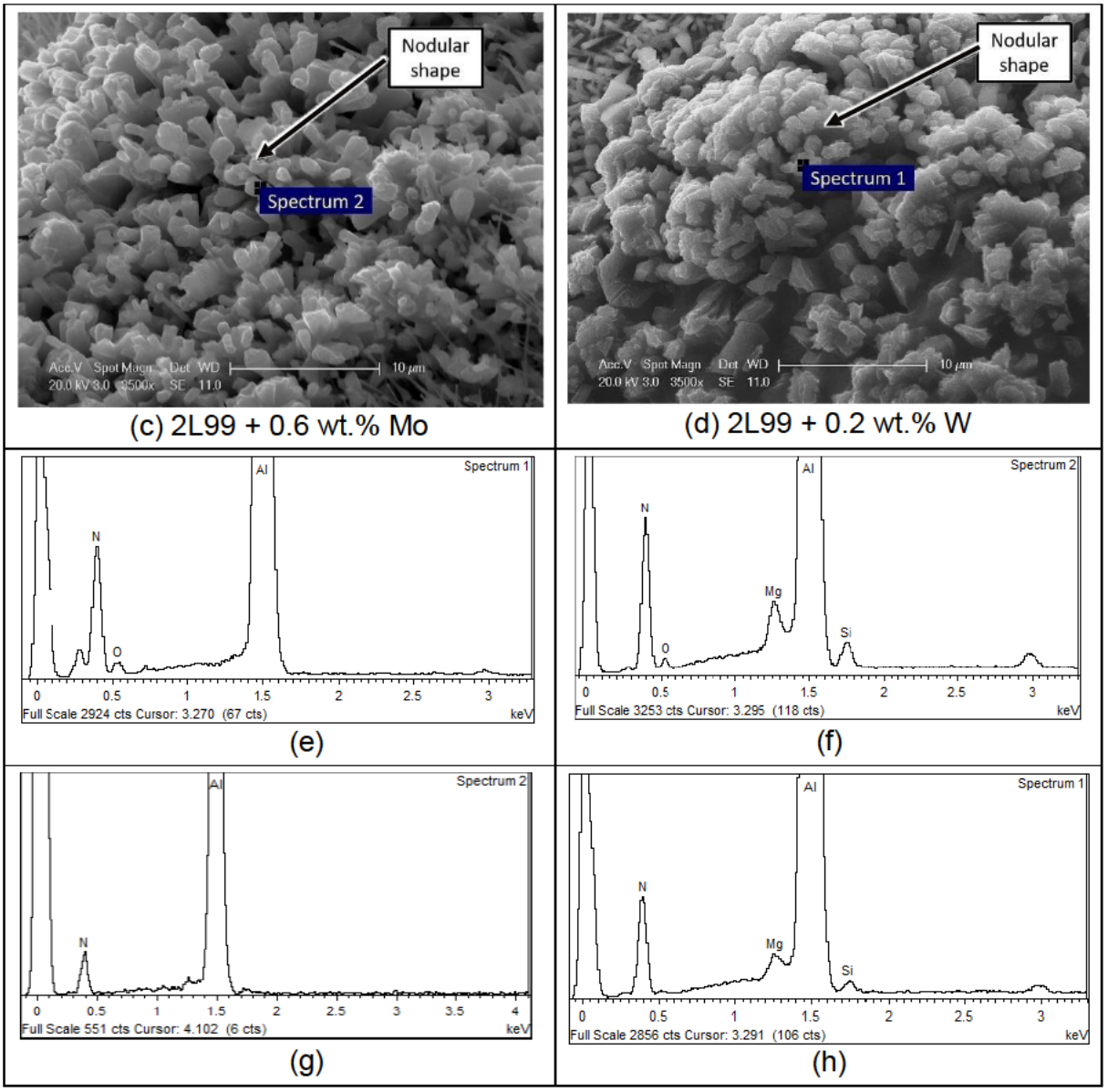


Figure 4-147: (a) to (d) SEM micrographs of nodular-shaped AlN on the surfaces of CP- Al, 2L99 alloy, 2L99 + 0.6 wt.% Mo alloy and 2L99 + 0.2 wt.% W alloy, respectively, with 3 hours of holding time in N at 850 °C (e) to (h) are EDX spectra of the marked areas shown in (a) to (d)

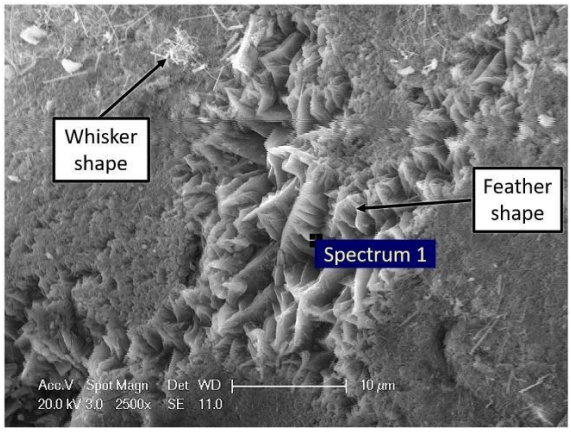
Table 4-118: Quantification of spectra for Figure 4-147 (a) and (b)

Description	Figure 4-147 (a) Spectrum 1		Figure 4-147 (b) Spectrum 2		Figure 4-147 (c) Spectrum 2		Figure 4-147 (d) Spectrum 1	
	Weight%	Atomic %	Weight%	Atomic %	Weight%	Atomic %	Weight%	Atomic %
N	42.41	57.54	35.94	51.36	37.82	53.95	36.34	52.36
O	3.94	4.68	2.15	2.69	0	0	0	0
Mg	0	0	0.64	0.53	0	0	0.44	0.37
Al	53.65	37.78	60.43	44.83	62.18	46.05	62.76	46.94
Si	0	0	0.84	0.60	0	0	0.46	0.33

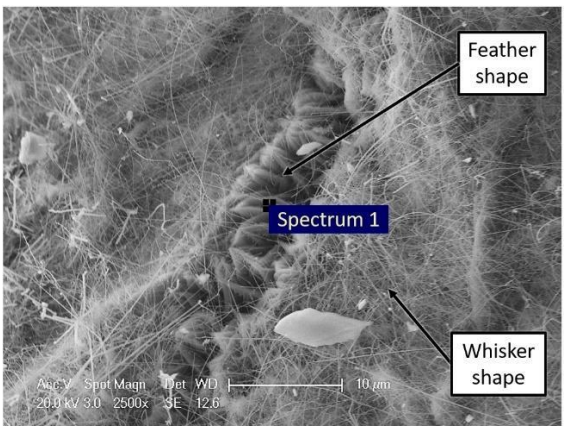
4.5.4 Feather-shaped AlN

Figure 4-148 (a) to Figure 4-148 (h) depict micrographs and EDX spectra of feather-shaped nitrides with an average length of approximately 10 µm. These nitrides can be seen in the central portion of the image, as marked, and cover an area of approximately 9 µm by 38 µm in length and with an alloy surface. They were observed on the surfaces of all four alloys (CP-Al, 2L99, 2L99 + 0.6 wt.% Mo and 2L99 + 0.2 wt.% W) after being exposed to nitrogen for 6 hours. Table 4-119 provides the corresponding quantification results for the areas denoted as Spectrum 1 and 2 in Figure 4-148 (a) to Figure 4-148 (d).

The average dimensions of the feather-shaped AlN patches observed on the surfaces of the examined alloys were measured to be approximately 15 µm by 30 µm. These feather-shaped morphologies are consistent with other researchers' findings concerning AlN. Similar feather-shaped morphologies have been observed in experiments involving trapped air bubbles after 8 hours of holding time [10][61][114]. Additionally, feather-shaped morphologies have been observed on the fractured surfaces of 2L99 + 0.4 wt.% Mo in the as-cast condition [3][65].



(a) CP- Al



(b) 2L99

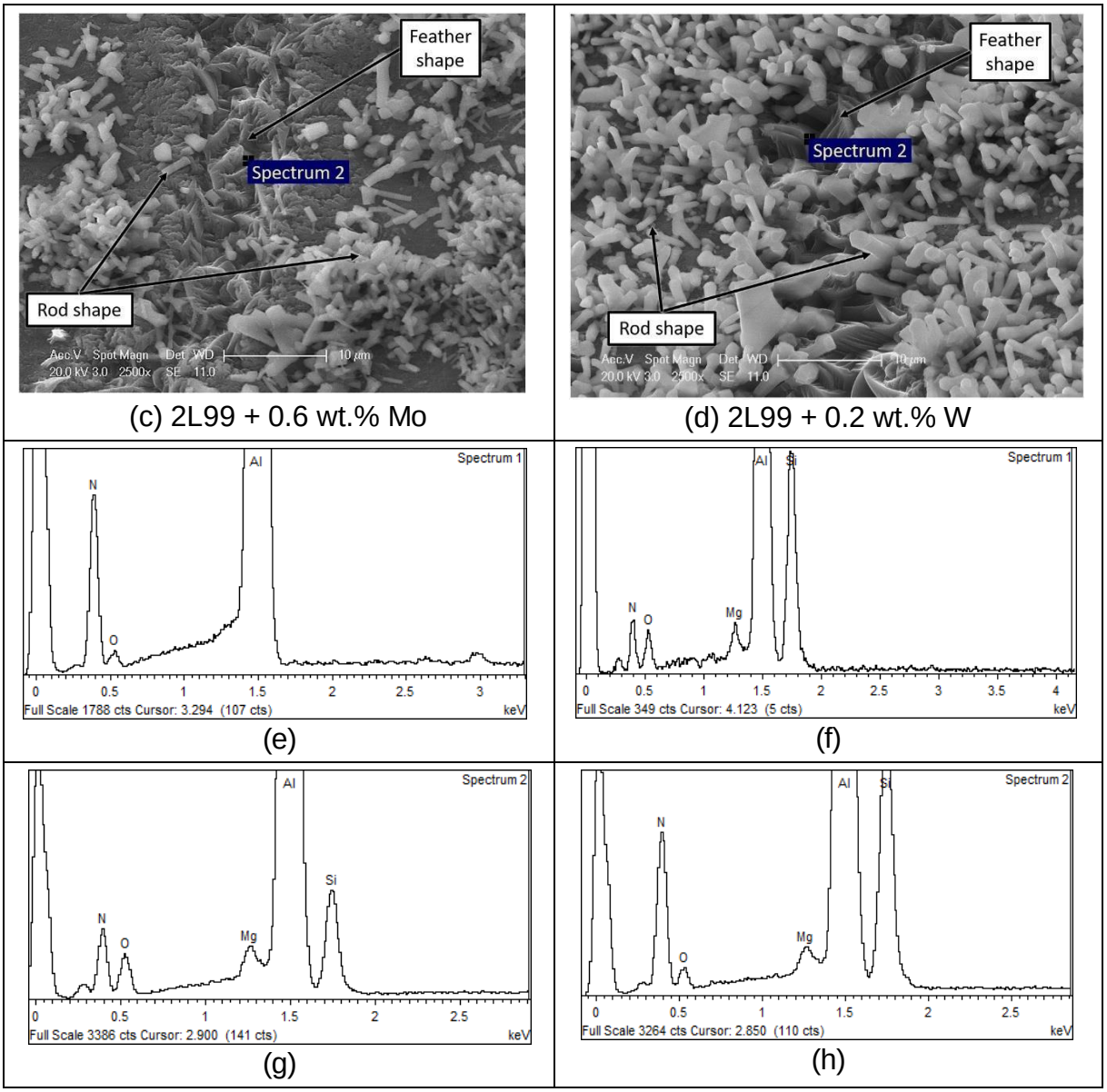


Figure 4-148: (a) to (d) are SEM micrographs of feather-shaped AlN on the surfaces of CP- Al, 2L99 alloy, 2L99 + 0.6 wt.% Mo alloy and 2L99 + 0.2 wt.% W alloy, respectively, with 6 hours holding time in N at 850 °C (e) to (h) are EDX spectra of the marked areas shown in (a) to (d)

Table 4-119: Quantification of spectra for Figure 4-148 (a) and (b)

Description	Figure 4-148 (a) Spectrum 1		Figure 4-148 (b) Spectrum 1		Figure 4-148 (c) Spectrum 2		Figure 4-148 (d) Spectrum 2	
	Weight%	Atomic %	Weight%	Atomic %	Weight%	Atomic %	Weight%	Atomic %
N	37.66	53.04	24.20	36.13	24.98	37.15	42.01	56.93
O	2.73	3.36	10.18	13.31	9.46	12.32	5.18	6.15
Mg	0	0	0.74	0.64	0.67	0.57	0.48	0.38
Al	59.61	43.59	52.69	40.84	60.01	46.34	43.12	30.33
Si	0	0	12.20	9.08	4.89	3.62	9.21	6.22

4.5.5 Summary

To summarise, in this study, AlN with a feather-shaped morphology was consistently observed in combination with other morphologies such as rod, whisker, and nodular morphologies. These different morphologies were observed in all the Al alloys examined, CP-Al, 2L99, 2L99 + 0.6 wt.% Mo, and 2L99 + 0.2 wt.% W.

These morphologies were observed under different holding times and appeared in small patches rather than covering the entire surface. No consistent pattern of AlN distribution was observed across the alloys. However, the nitrogen growth experiments confirmed the presence of AlN with four different morphologies in all the examined alloys at each holding period.

5 DISCUSSION

5.1 Phases in 2L99 alloy

This section will discuss the various phases observed on the as-cast polished and fractured surfaces of T6 heat-treated 2L99 alloys. Table 4-5 shows the tensile strength of the 2L99 alloy after heat treatment, showing a mean UTS of 227 MPa, %Elongation of 1.07 and a yield strength of 203.5 MPa. In Table 4-6, the Weibull modulus of UTS was calculated to be 4, %Elongation as 1.35, and yield as 4.28. It is important to note that the 2L99 alloy used in the experiment had a high H content (6 ppm).

The mean UTS value measured in this study was lower than the 271 MPa reported by Chen [3]. Similarly, the Weibull modulus of UTS was lower at 4 compared to the value of 18 reported by Chen [3]. The reason for this difference is thought to be due to the difference in the H content of the 2L99 alloy tested. The 2L99 alloy cast by Chen [3] was subject to effective Ar lance de-gassing and was reported to have 0.225 ppm H, compared to the 6 ppm of H in the 2L99 alloy used in this research.

The detrimental effects of the high H content in the alloy can be demonstrated by reference to Figure 4-19 (a), which shows a large gas pore (1400 µm x 800 µm) on a low UTS 2L99 sample. Similar gas porosities may have the potential to develop into a shrinkage pore and be further influenced by the amount of dissolved H present in the melt [115], such as the one seen in Figure 4-19 (b). Figure 4-23 (d) shows the distribution of O on the same large shrinkage pore on a polished surface of 2L99. It is reported that effective degassing can decrease the level of porosity by approximately 90% [115]. Intermetallic phases found on 2L99 in this study consisted of Al_5-Fe-Si, Mg_2-Si, oxides, in line with literature [116], and nitrides.

i) Al_5-Fe-Si: The Fe-containing intermetallic particles in Al-Si alloys are concluded to pose a deleterious effect on the mechanical properties of the alloys as these particles are more vulnerable to fracturing under tensile stress compared to the aluminium matrix or small silicon particles. Fe particles often serve as initiation points for micro-cracks, facilitating the propagation of macro-cracks [117]. Figure 4-20 (b) displays a large (60 μm) β-Al_5FeSi intermetallic observed in this study by SEM and EDX on a polished surface of 2L99 and is confirmed by the XRD result shown in Figure 4-110.

Furthermore, and at high Fe content, the formation of large β-platelets of Fe-intermetallics has been suggested to facilitate the nucleation of Si-eutectics [118][119][45]. This is considered to lead to the formation of less frequent but larger Al-Si eutectic cells. These enlarged Al-Si eutectic cells, combined with the substantial β-platelets, may be a cause of blockage of feeding channels, thereby enhancing casting porosity [117] [45]. It can be argued that an increase in both H and Fe contents of the melts decreased the mechanical properties and the relevant Weibull moduli in 2L99 alloys.

ii) Mg_2Si: The Mg_2Si phase was suggested based on the EDX results on the polished surface of 2L99 alloys, as shown in Figure 4-20 (b). This phase is considered detrimental to the ductility of 2L99 alloys [100].

iii)Oxides: Several oxides in the form of mostly spinel layers (Figure 4-21), spinel particles (Figure 4-22 (b)), MgO (Figure 4-29 (g)) and SiO_2 (Figure 4-31) were found on the polished and fractured surfaces of the 2L99 alloy samples using SEM and EDX. These were confirmed with XRD results, as shown in Figure 4-110. The presence of these phases also corresponds to what has

been reported in the literature previously, with the primary 2L99 oxide observed as spinel [17] [120]. Table 5-1 summarises the thermodynamic stability of oxides in Al-Mg alloys under varying temperatures and magnesium concentrations. It is widely recognised that when the magnesium concentration is below 0.1 wt.%, Al_2O_3 is the most stable oxide. Within the range of 0.1 to 1.5 wt.% magnesium concentration, spinel ($MgAl_2O_4$) becomes the preferred oxidation product, while for magnesium concentrations exceeding 1.5 wt.%, magnesium oxide (MgO) is the most favourable outcome.

Table 5-1: Oxide stability under varying temperatures and Mg concentrations from a thermodynamic perspective [121]

Temperature	**Al_2O_3 stable**	**$MgAl_2O_4$ stable**	**MgO stable**
500 °C (solid)	0 – 0.14 wt.% Mg	0.14 – 0.93 wt.% Mg	> 0.93 wt.% Mg
700 °C (liquid)	0 – 0.058 wt.% Mg	0.058 – 2.17 wt.% Mg	> 2.17 wt.% Mg
725 °C (liquid)	0 – 0.0089 wt.% Mg	0.0089 – 1.34 wt.% Mg	> 1.34 wt.% Mg
800 °C (liquid)	0 – 0.038 wt.% Mg	0.038 – 1.46 wt.% Mg	> 1.46 wt.% Mg

In addition, the Gibbs Free Energy of spinel is less than other oxides at 727°C (1000 k), as shown in Table 5-2.

Table 5-2: Gibbs Free Energy data for oxides kJ/mol [122]

T (°C)	MgO	Al_2O_3	$MgAl_2O_4$	SiO_2
627	-504.289	-1393.908	-1929.739	-747.785
727	-492.952	-1361.437	-1886.914	-730.236
827	-481.399	-1328.286	-1843.219	-712.805
927	-469.844	-1295.228	-1799.655	-695.426

Sylvia and Talbot [17] suggested that for magnesium contents exceeding 1.5 wt.%, MgO is the most stable oxide due to its equilibrium with the lowest oxygen pressure. For Mg in the 0.02 to 1.5 wt.% range, $MgAl_2O_4$ was reported to be the most stable oxide [17].

iv) Nitrides: The AlN shown in Figure 4-25 to Figure 4-28 found on the fractured surface of a heat-treated 2L99 alloy in as-cast alloy conditions was observed in this study for the first time. This was the only 2L99 batch of samples cast with Ar lance degassing for a 20-minute duration, reducing the melt's hydrogen content to below 0.1 mm^3/100 g, as measured by a Severn Science hydrogen gas analyser during casting. Also, Figure 4-29 and Figure 4-30 shows AlN on a 2L99 as-cast alloy with a high H amount (6 ppm). The observed AlN particles were nodular and seemed impermeable, which contrasts with previously more permeable feather-shaped AlN particles.

The most impermeable AlN phase observed in this research, in the as-cast condition, is suggested to be of a nodular morphology. When the AlN layer is impermeable, it may act as a hindrance to the passage of reaction gases between the entrapped atmosphere of a bifilm and the surrounding liquid metal. This impermeable AlN layer may also reduce the hydrogen diffusion through the bifilm and prevent further expansion of the bifilm, supporting Nyahumwa’s hypothesis.

5.2 Phases of 2L99 + transitional alloys Mo, W and V

5.2.1 2L99 + Mo phases

This section will discuss the various phases observed on the polished and fractured surfaces of 2L99 + 10 wt.% Mo masteralloy and T6 heat treated 2L99 + 0.4 wt.% Mo alloys. In Table 4-23, the addition of 0.4 wt.% of Mo to 2L99 resulted in an increase of 7%, 13% and 8% in the mean UTS, %Elongation and yield strength parameters, respectively, of the alloy compared to 2L99 alloy. The results also showed an increase of 173%, 68% and 302% in the Weibull modulus of the UTS, %Elongation and yield stress, respectively, as shown in Table 4-24. Notably, the 2L99+0.4 wt.% Mo alloy used in the experiment had a high H content (8 ppm).

As shown in Table 4-50, the phases observed on the ingot, polished and fractured surfaces of a 2L99 + 10 wt.% Mo masteralloy, characterised with SEM and EDX, were mainly spinel oxide and a small amount of alumina and SiO_2 with α shaped $Mo_{1.5}AlSi_2$, $MoAl_2Si$, $Mo_{1.2}AlSi_{1.5}$, and β shaped $Mo_4Al_{11}Si$ and $Mo_{7.3}Al_{24}Si$ intermetallics.

As shown in Table 4-62 and Table 4-65, the phases observed using SEM and EDX on the polished surface of 2L99 + 0.4 wt.% Mo alloy were $Mo_{1.5}AlSi_2$, $MoAl_8Si_3$, $MoAl_{10}Si$, $Mo_{0.6}(Al,Si)$, Mo $(Al,Si_2)_2$, $Mo_7Al_5Si_8$, Mo_2AlSi_2, $Mo(Al,Si)_2$ and $Al_2FeSi_{2.6}$ intermetallics. However, the phases observed on the fractured surfaces were $MoAlSi_2$, $Mo_7Al_5Si_7$ and $Mo_6Al_5Si_8$ intermetallics.

The intermetallics observed on the polished and fractured surfaces of 2L99 + 0.4 wt.% Mo were α-Mo intermetallics with an irregular multi-faceted morphology. The numerous intermetallics were reported, and these were suggested by EDX analysis. Although

EDX is considered a strong technique to detect elements, it is not considered to be the most suitable technique to measure elemental composition due to its limited observation area on the sample [113].

In addition to the above, it is also known that the beam acceleration voltage utilised in EDX analysis can impact the volume of the interaction between the electron beam and the sample. Lower voltages improve resolution but limit the range of observable elements, a decrease in signal strength, and the number of counts. Consequently, an acceleration voltage of 20 kV was frequently employed in the EDX analysis in this research to ensure the detection of the transition metals.

The main intermetallics observed in 2L99 + 0.4 wt.% Mo alloys were $Mo(Al, Si)_2$ as confirmed by XRD, and are shown in Figure 4-112. It was concluded that $Mo(Al, Si)_2$ could nucleate on spinel, which is the main oxide phase in 2L99, as explained in section 5.1. This was in line with the ternary Al-Mo-Si phase diagram [108][109][110][111]. As can be seen in Figure 4-58, the Mo intermetallic had nucleated on the wetted side of the oxide film, which agreed with the observations reported by previous researchers [3]. It is important to note that the lattice mismatch calculations carried out in this research are based on the XRD database developed by HighScore.

As shown in Figure 4-112, the XRD pattern of $Mo(Si, Al)_2$ included two deep peaks at 38.43° and 84.6° are related to the (110) and (115) planes, respectively. The relative XRD intensity of the (110) plane was higher than the (115) plane. The (110) plane has an interplanar spacing of 2.34 (reference code: 00-010-0277). The intense peaks for $MgAl_2O_4$ in the 2L99 + 0.4 wt.% Mo alloy occurred at 38.7° and 68.9°, corresponding to the (222) and (153) planes, with the (222) plane having a higher intensity than the (153) plane, with an interplanar spacing of 2.32 (reference code: 96-101-130). Using

equation (5-1) [3], the lattice mismatch between (222)//$MgAl_2O_4$ and (110)//$Mo(Si, Al)_2$ was calculated to be -0.7%.

$$\delta = \frac{d\beta - d\alpha}{d\alpha} \quad (5\text{-}1)$$

$d\alpha$: interplanar spacing for the matrix [3]

$d\beta$: interplanar spacing for the phase [3]

δ: lattice mismatch [3]

The XRD pattern of the $Fe_3Al_2Si_4$ included two deep peaks at 38.3° and 65.2° that related to the (024) and (243) planes, respectively, with the (024) plane having a higher intensity than the (243) plane, with an interplanar spacing of 2.35 (reference code: 01- 087-1921). Using equation (5-1), the lattice mismatch between (222)//$MgAl_2O_4$ and (024)//$Fe_3Al_2Si_4$ was calculated to be -1.1%.

The XRD pattern of AlN in the 2L99 + 0.4 wt.% Mo alloy included two deep peaks at 38.43° and 65.18° related to the (111) and (220) planes, respectively. The relative XRD intensity of the (111) plane was higher than the (220) plane. The (111) plane has an interplanar spacing of 1.43 (reference code: 00-046-1200). The intense peaks for $MgAl_2O_4$ in the 2L99 + 0.4 wt.% Mo alloy occurred at 38.7° and 68.9°, corresponding to the (222) and (153) planes, respectively, with the (222) plane having a higher intensity than the

(153) plane, with an interplanar spacing of 2.32 (reference code: 96-101-130). Using equation (5-1) [3], the lattice mismatch between (222)//$MgAl_2O_4$ and (111)//AlN was calculated to be -0.5%.

The calculated lattice mismatch between Mo(Al, Si)2 with a hexagonal structure and spinel (cubic) was -0.7%; this suggests that the spinel is a suitable substrate for nucleation and growth of Mo(Al, Si)2 [3]. Since a lattice mismatch of less than 7%

indicates that the oxide (spinel) phase will provide a potent substrate for $Mo(Al, Si)_2$ and Fe3Al2Si4 intermetallics nucleation (<7% [66]). Figure 4-44 shows a Mo intermetallic with a Fe-intermetallic ($Al_2FeSi_{2.6}$) at 10 µm in length. Compared with the Fe-intermetallic in 2L99 shown in Figure 4-20 (b), which was a 60 µm β phase Al_5-Fe-Si, it seemed that the addition of 0.4 wt.% Mo to 2L99 alloy modified the Fe-intermetallic to a different composition and morphology in agreement with literature [91]. Dichtl [123] reported that Mo converted β-phase Fe-intermetallics to compact star-shaped compounds [119].

As shown in Figure 4-111, XRD detected the $Fe_3Al_2Si_4$ intermetallic, which is understood to be less detrimental to the mechanical properties of the alloy compared to Al_5FeSi, which was observed in 2L99, as previously reported in literature [100].

Several oxides in the form of spinel (Figure 4-56) and MgO (Figure 4-55 (b)) were found on the polished and fractured surfaces of the 2L99 + 0.4 wt.% Mo samples using SEM and EDX. The XRD, as shown in Figure 4-112, however, picked up only the spinel from the phases described before, as well as SiO_2, which was not detected by SEM and EDX.

A significant difference could not be identified in the amount of the oxides found in 2L99 and 2L99 + 0.4 wt.% Mo. However, different additional oxide morphologies were observed on the fractured surfaces of the 2L99 + 0.4 wt.% Mo alloy samples, such as granular and whisker shapes, as shown in Figure 4-55 and wrinkled shapes in Figure 4-56. It is important to note that Mo was not detected by EDX analysis as part of an oxide phase.

AlN was found on both polished and fractured surfaces of 2L99 + 0.4 wt.% Mo and was detected by XRD (Figure 4-112). AlN is shown in Figure 4-52 and Figure 4-53 on the polished surfaces with a nodular shape and 20 µm in length, positioned in a cavity on the polished surface. On the fractured surface, AlN with different morphologies of nodular (Figure 4-56) and feather-shaped morphologies (Figure 4-57) were observed measuring 8 µm and 30 µm in length, respectively.

A limited number of Mo-intermetallics identified by EDX and SEM characterisation were observed to have migrated from the masteralloy to the as-cast alloy of 0.4 wt.% Mo, namely $MoAl_2Si$, $Mo_{1.5}AlSi_2$ α-shaped. None of the intermetallics that migrated into the as-cast alloy were observed to have a β shape. With regards to oxides, the main phases observed in the masteralloy were spinel and a limited amount of alumina and SiO_2. However, only spinel and MgO were observed in the as-cast alloy. It is important to note that no Al nitrides were observed in any of the masteralloys at any stage.

This indicates that AlN potentially forms during the cooling stage [124] of the as-cast alloy due to the consumption of the gases inside the bifilm rather than forming at high temperatures in the masteralloy. Figure 4-111 shows the 2L99 + 10 wt.% Mo masteralloy phases characterised by XRD.

5.2.2 2L99 + W phases

This section will discuss the various phases observed on the polished and fractured surfaces of 2L99 + 10 wt.% W masteralloy and T6 heat treated 2L99 + 0.4 wt.% W alloy. Table 4-23 shows that adding 0.4 wt.% of W to the 2L99 alloy resulted in an increase of 7%, 33% and 6% in the mean UTS, %Elongation and yield strength parameters, respectively, of the alloy compared to 2L99. The results also showed an increase of

109%, 12% and 227% in the Weibull moduli of UTS, %Elongation and yield stress results, respectively, as shown in Table 4-24. It is important to note that the 2L99 + 0.4 wt.% W alloy used in the experiment had a high H content (8 ppm). It is worth noting that adding 0.8 wt.% nanoparticle tungsten to Al-5Mg has been reported to increase the UTS from 155 to 194 MPa and reduce the gain size of AL-5Mg alloys [125].

A summary of the phases observed on the ingot, polished and fractured surfaces of 2L99 + 10 wt.% W masteralloy, characterised with SEM and EDX, predominantly showed the presence of spinel oxide and a slight amount of SiO_2 with $W_4Al_{14}Si$, Al_3W, AlW_2, $W_4Al_{14}Si$, Al_4W, $W_{1.5}Si_2$ and $W_{1.2}AlSi_{1.4}$ intermetallics as shown in Table 4-74.

A summary of the phases observed on the polished and fractured surfaces of 2L99 + 0.4 wt.% W alloy, characterised with SEM and EDX, on a polished surface showed $W_{1.2}AlSi_{1.2}$, $W_{1.4}AlSi_{2.4}$, $W_{1.5}Al$, $W_{1.1}AlSi_{1.3}$, $W(Al, Si)_2$ and $Al_{8.3}SiFe_{1.4}$ intermetallics. $W(Al, Si)_2$ and $WAl_{3.5}$ intermetallics were observed on the fracture surface, as shown in Table 4-84 and Table 4-86.

The intermetallics observed on the polished and fractured surfaces of 2L99+0.4 wt.% W were α-W intermetallics with an irregular multi-faceted morphology, similar to Mo. As explained in 5.2.1, although EDX can detect elements, it is not considered to be the strongest technique for determining the precise composition of the phase. The main intermetallics observed in 2L99+0.4 wt.% W alloys were considered to be $W(Al, Si)_2$, as confirmed by XRD and shown in Figure 4-114.

The XRD pattern of the $W(Si, Al)_2$ included two deep peaks at 38.43° and 47.31° that related to the (110) and (112) planes, respectively. The relative XRD intensity of the (112) plane was higher than the (110) plane. The (112) plane has an interplanar spacing of 1.92 (reference code: 00-010-0242). The intense peaks for $MgAl_2O_4$ in the

2L99 + 0.4 wt.% W alloy occurred at 38.35° and 44.57° corresponding respectively to the (222) and (040) planes, with the (040) plane having a higher intensity than the (222) plane, with an interplanar spacing of 2.03 (reference code: 96-900-2134). Using equation (5-1), the lattice mismatch between (040)//$MgAl_2O_4$ and (112)//$W(Si, Al)_2$ was calculated to be 5.7%.

The XRD pattern of the $Fe_3Al_2Si_3$ included two deep peaks at 44.89° and 28.5° that related to the (022) and (110) planes, respectively, with the (022) plane having a higher intensity than the (110) plan with an interplanar spacing of 2.02 (reference code: 01-087-1920). Using equation 5-1, the lattice mismatch between (222)//$MgAl_2O_4$ and (024)//$Fe_3Al_2Si_4$ was calculated to be 0.7%.

The XRD pattern of the AlN included two deep peaks at 38.53° and 47.56° that related to the (111) and (200) planes, respectively. The relative XRD intensity of the (111) plane was higher than the (200) plane. The (111) plane has an interplanar spacing of 2.32 (reference code: 00-046-120). The intense peaks for $MgAl_2O_4$ in the 2L99 + 0.4 wt.% W alloy occurred at 38.35° and 44.57° corresponding respectively to the (222) and (040) planes, with the (040) plane having a higher intensity than the (222) plane, with an interplanar spacing of 2.03 (reference code: 96-900-2134). Using equation (5- 1), the lattice mismatch between (040)/$MgAl_2O_4$ and (111)//AlN was calculated to be 0.4%.

As shown in Figure 4-72 and Figure 4-73, similar to Mo, the W intermetallics had nucleated on the wetted side of the oxide film. This is in line with the results of the lattice mismatch of 5.7% calculated between $W(Al, Si)_2$ and spinel and 0.7% between $Fe_3Al_2Si_4$ and spinel, suggesting the spinel would be a suitable substrate for nucleation and growth of $W(Al, Si)_2$ [3][112] due to a lattice mist match difference of less than 7 [66]. It can be concluded that $W(Al, Si)_2$ and $Fe_3Al_2Si_4$ could nucleate on spinel as the main

oxide phase in 2L99, as explained in section 5.1.

Figure 4-71 showed a W intermetallic, with a Fe-intermetallic ($Al_{8.3}SiFe_{1.4}$), approximately 10 µm in length, observed on the polished surface of the W alloy. In comparison with the Fe intermetallic in 2L99, as shown in Figure 4-20 (b), which was a 60 µm length β phase Al_5FeSi (similar to Mo), it seems that the addition of 0.4 wt.% W modified the Fe intermetallic to a different composition and morphology [91].

It was not possible to find the ternary phase diagram of Al-Si-W in published literature. As shown in Figure 4-114, XRD detected $Fe_3Al_2Si_3$ intermetallic, which was similar to the intermetallic detected in 2L99 + 0.4 wt.% Mo, and is understood to be less detrimental to the mechanical properties of the alloy compared to the Al_5FeSi, which was observed on 2L99 [100]. Both the intermetallics detected on Mo and W alloys are understood to be less detrimental.

Several oxides in the form of spinel (Figure 4-82), nodular and whisker-shaped MgO (Figure 4-58 (a) and (b)) and SiO_2 (Figure 4-81) were found on the polished and fractured surfaces of the 2L99 + 0.4 wt.% W samples using SEM and EDX. XRD (Figure 4-114), however, only identified the spinel and SiO_2 phases (Figure 4-114).

Similar to Mo, the amount of O found in 2L99 + 0.4 wt.% W oxides were not significantly different from the O amount in 2L99 alloys. However, different additional oxide morphologies were observed on the fractured surface of the W alloy samples, including nodular and whisker-shaped, wrinkled-shaped MgO particles of 100 µm in length, as shown in Figure 4-82. Note that similar to Mo, W was also not detected by the EDX analysis as part of an oxide phase. Similar to 2L99 + 0.4 wt.% Mo alloy, no nitrides were observed on any of the masteralloys at any stage. Figure 4-113 shows the masteralloy

phases confirmed by XRD. However, AlN was found on both polished and fractured surfaces of 2L99 + 0.4 wt.% W and was also detected by XRD (Figure 4-114). AlN was found on the polished surface in Figure 4-52, with AlN mapping in Figure 4-79. This was 5 µm in length (less than the AlN observed on the polished surface of the Mo alloy) with a nodular shape positioned in a cavity on the polished surface.

On the fractured surface, AlN with different morphologies of nodular (Figure 4-84) and whisker shapes (Figure 4-85 and Figure 4-86) were observed, measuring 20 µm and 0.3 µm x 1.5 µm, respectively.

Tungsten intermetallics were observed to have migrated from the masteralloy to the as-cast alloy of 0.4 wt.% W, namely $W_{1.5}AlSi_2$ and $W_{1.2}AlSi_{1.4}$, both α shaped. Similar to the Mo alloy, none of the intermetallics that migrated into the as-cast alloy were observed to have a β shape. With regard to oxides, the main phases observed on the W masteralloy were spinel, with a limited amount of SiO_2, cubic MgO particles and a MgO layer. However, mainly spinel, SiO_2 and MgO were observed on the as-cast alloy.

5.2.3 2L99 + V phases

This section will discuss the various phases observed on the polished and fractured surfaces of T6 heat-treated 2L99 + 0.4 wt.% V alloy. Table 4-23 shows that the addition of 0.4 wt.% of V to a 2L99 alloy resulted in a negligible increase of 2%, 0% and 3% in the mean UTS, %Elongation and yield strength parameters, respectively, of the alloy compared to 2L99. The results also showed an increase of 168%, 83% and 241% in the Weibull modulus of the UTS, %Elongation and yield stress results, respectively, as shown in Table 4-24, which is considered to be in line with the literature [85]. It is important to note that the 2L99 + 0.4 wt.% V alloy used in the experiment had a high H

content (8 ppm).

A summary of the phases observed on the polished and fractured surfaces of 2L99 + 0.4 wt.% V alloy, characterised with SEM and EDX, are shown in Figure 4-94 and Figure 4-102. The intermetallics observed on the polished and fractured surfaces of 2L99 + 0.4 wt.% V were in the majority α shaped V intermetallics with the exception of a β- shape V-intermetallic (Figure 4-94).

The main intermetallic detected in a 2L99 + 0.4 wt.% V alloy is considered to be $Al_{0.1}Si_{0.9}V_3$, as confirmed by XRD, shown in Figure 4-115, which was in agreement with the literature [107]. Although several other intermetallic compositions were suggested by the EDX, as explained in section 5.2.1.

The XRD pattern of the AlV_3 included two deep peaks at 41.74° and 76.2° that related to the (110) and (211) planes, respectively. The relative XRD intensity of the (110) plane was higher than the (211) plane, with an interplanar spacing of 1.25 (reference code: 03-065-5142). The intense peaks for $MgAl_2O_4$ in the 2L99 + 0.4 wt.% V alloy occurred at 38.31° and 44.53° corresponding respectively to the (222) and (040) planes, with the (040) plane having a higher intensity than the (222) plane, with an interplanar spacing of 2.03 (reference code: 96-900-2107). Using equation 5-1, the lattice mismatch between (040)//$MgAl_2O_4$ and (110)//AlV_3 was calculated to be -6%.

The XRD pattern of the $Al_3Si_{0.9}V_3$ included two deep peaks at 38.01° and 47.7° that related to the (200) and (211) planes, respectively. The relative XRD intensity of the (211) plane was higher than the (200) plane, with an interplanar spacing of 1.93 (reference code: 03-065-8557). Using equation 5-1, the lattice mismatch between (040)/$MgAl_2O_4$ and (211)//$Al_3Si_{0.9}V_3$ was calculated to be 5.2%. The XRD pattern of the

Al_3V included two peaks at 25.86° and 55.96° that related to the (101) and (114) planes, respectively. The relative XRD intensity of the (114) plane was higher than the (101) plane, with an interplanar spacing of 1.64 (reference code: 03-065-5860). Using equation (5-1), the lattice mismatch between (040)//$MgAl_2O_4$ and (114)//Al_3V was calculated to be 23.8%.

The XRD pattern of the $FeAl_9Si_3$ included two deep peaks at 28.6° and 47.1° that related to the (003) and (310) planes, respectively, with the (310) plane having a higher intensity than (003), with an interplanar spacing of 1.93 (reference code: 00-020-0033). Using equation 5-1, the lattice mismatch between (040)/$MgAl_2O_4$ and (310)/$Fe_3Al_2Si_4$ was calculated to be 5.5%.

The XRD pattern of the AlN included two deep peaks at 37.8° and 33.1° that related to the (101) and (100) planes, respectively. The relative XRD intensity of the (101) plane was higher than the (100) plane, with an interplanar spacing of 2.4 (reference code: 01-089-3446). The intense peaks for $MgAl_2O_4$ in the 2L99 + 0.4 wt.% V alloy occurred at 38.31° and 44.53° corresponding respectively to the (222) and (040) planes, with the (040) plane having a higher intensity than the (222) plane, with an interplanar spacing of 2.03 (reference code: 96-900-2107). Using equation (5-1), the lattice mismatch between (040)/$MgAl_2O_4$ and (101)/AlN was calculated to be -14%.

As shown in Figure 4-92 and Figure 4-93, similar to Mo and W, the intermetallics have nucleated on the wetted side of the oxide films. This is in line with the results of a lattice mismatch of 5.2% calculated between cubic $Al_{0.1}Si_{0.9}V_3$ and spinel suggesting the spinel to be a suitable substrate for nucleation and growth of $Al_{0.1}Si_{0.9}V_3$ as the lattice mist matched is less than 7 % [66][126]. It can be concluded that $Al_{0.1}Si_{0.9}V_3$ could nucleate on spinel as the main oxide phase in 2L99, as explained in section 5.1. Therefore, spinel

will provide a potent nucleation substrate for AlV_3, $Al_3Si_{0.9}V_3$ and Fe_3Al2Si_4 but not a potent substrate for the nucleation of Al_3V.

Figure 4-91 (d) shows V intermetallic with $Al_{28}Si_3Fe$, approximately 20 µm in length, observed on a polished surface of 0.4 wt.% V alloy. In comparison with the Fe-intermetallic in 2L99, as shown in Figure 4-20 (b), which was a β phase of Al_5-Fe- Si of length 60 µm. Similar to Mo and W, it seems that the addition of 0.4 wt.% V modified the Fe- intermetallic to a different composition and morphology [91]. Qin et al. reported that the addition of 1 wt.% V to Al-Si alloy promoted the transformation of β-phase to α-phase Fe-intermetallics through the increase of melt temperature [113].

As shown in Figure 4-115, the XRD detected an Al_9Si_3Fe intermetallic on the 0.4 wt.% V alloy, which is understood to be less detrimental to the mechanical properties of the alloy compared to Al_5FeSi, as observed on 2L99; this is in agreement with literature [100].

Several oxides in the form of wrinkle-shaped spinel (Figure 4-100) and granular-shaped MgO (Figure 4-102) were found on the polished and fractured surfaces of the 2L99 + 0.4 wt.% V samples using SEM and EDX. As seen in Figure 4-115, XRD identified spinel from the phases described above in addition to SiO_2 (sand erosion).

Similar to Mo and W, the amount of O found in 2L99 + 0.4 wt.% V oxides was not significantly different from the O amount in 2L99. However, different additional oxide morphologies (granular morphologies and wrinkled spinel layer) were observed on the fractured surface of the V alloy samples, as shown in Figure 4-102 and Figure 4-100, respectively. Note that similar to Mo and W, V was also not detected by EDX analysis as part of any oxide phase.

Similar to Mo and W alloys, AlN was found on both polished and fractured surfaces of

2L99 + 0.4 wt.% V and was also detected by XRD (Figure 4-115). AlN can be seen on the polished surface of 2L99+0.4 wt.% V as shown in Figure 4-99 with the length of 25 µm nodular shape within cavities on the polished surface.

On the fractured surface, only AlN with a nodular morphology of up to 28 µm in length was observed (Figure 4-103 (b), Figure 4-104 and Figure 4-105). Figure 4-108 shows the EDX mapping of the nitrides as well as other elements such as Al, Mg, Si, O and V on the fractured surface of the V alloy.

The 2L99 + 10 wt.% V masteralloy was not characterised as part of this research. This was not considered necessary as the characterisation of Mo and W masteralloys showed that AlN could not be formed at high temperatures during the casting of the masteralloys. Therefore, AlN was not transferred from the masteralloys to the as-cast alloys of Mo, W and we assume V. By conducting a comprehensive characterisation of both Mo and W masteralloys, this confirmed that AlN would not occur in the masteralloy.

5.3 Nitrogen growth impact on AlN morphology[6]

As discussed in section 4.5, the AlN phase exhibited various morphologies, including rod, nodular, feather, and whisker shapes observed in CP-Al, 2L99, 2L99 + 0.6 wt.% Mo, and 2L99 + 0.2 wt.% W these were observed under different holding times and appeared in small patches rather than covering the entire surface. No consistent pattern of AlN distribution was observed across the different alloys. However, nitrogen growth experiments confirmed the presence of AlN in all the alloys examined at each holding period.

[6] The results discussion presented in this section has been published by the author in the paper provided in Appendix A.

As shown in Figure 2-13 and as per the eutectoid Al_2O_3–AlN phase diagram, AlN was not expected to occur at temperatures below 1640 °C. Considering that the testbars were cast at 730 °C or heated in the growth experiments to 850 °C, it has been deduced that the presence of nitrogen in the EDX results is due to the presence of AlN and not AlON.

A small difference in lattice size and structure is required for AlN to nucleate on Al and other Al oxide substrates. The interatomic spacing misfit (*fr*) influences grain refinement and nucleation, with an *fr* difference of up to 7%, as suggested by Wang and Fan [66].

The *fr* calculated between AlN and Al oxides based on the crystallographic data is presented in Table 2-2 [66]. This was found to be 10.9% for ɣ-alumina, 13.1% for α-alumina, and 8.7% for spinel, suggesting spinel not to be a potent substrate for AlN nucleation if considering a lattice misfit of less than 7% [66]. This is in contrast to Wang and Fan's [66] research as well as the observations in this study, where EDX analysis suggested both O and N would nucleate on oxide particles, as shown in Figure 2-21 (c), Figure 4-25 (f), Figure 4-26 (d), Figure 4-27 (c) and Figure 4-28 (c). According to Campbell [44], the reinterpretation of Bramfitt's data for predominantly metallically bonded materials showed any lattice mismatch of up to 12 % could be a potent nucleation substrate.

Chen's study [3] of the fractured surfaces 2L99 + 0.4 wt.% Mo alloys suggest that AlN may have formed at high temperatures (1300 °C) during the production of the masteralloy and subsequently migrated over to the as-cast testbars. However, in this study, no evidence of AlN was observed during the characterisation of the ten testbars in 2L99 + 10 wt.% Mo and the 10 of 2L99 + 10 wt.% W masteralloy testbars.

As described in section 5.2, AlN was observed for the first time to the research's knowledge in this study on the fractured surfaces of a 2L99 alloy in an as-cast condition at 730 °C. The observed AlN particles were of a nodular morphology and appeared to be impermeable, which is in contrast with the previously reported AlN particles in samples cast under various conditions reported as feather-shaped and appearing to be more permeable, as shown in Figure 2-16 (a), Figure 2-17 (a), Figure 2-19 (a). Table 5-3 summarises the different nitrides observed by other researchers under laboratory conditions[3] [61] [114] [65].

Table 5-3: various AlN morphologies reported by other researchers, mainly in pure Al and 2L99 + 0.4 wt.% Mo

Researcher/s	Alloy	Temperature	Holding Time	Morphology	AlN Weight%/ atomic%	Width
Raeiszadeh [10] [61] [114]	Pure Al	850°C	8 Hours	Feather shaped	28 wt.%	-
Gerrard [11] [63]	Pure Al	700°C	15 minutes	Feather shaped	17 wt.%	8.6 µm
Chen [3]	2L99+ 0.4wt%Mo	730°C	N/A (fractured surface, as-cast alloy)	Feather shaped	36 at.%	15 µm
Wang & Fan [66]	CP-Al	750°C - 850°C	N/A (Pressure melt filtration technique)	Rod Shape	-	104 nm

The seemingly impermeable AlN phase observed on the 2L99 as-cast alloy suggests that the presence of AlN may hinder the passage of reaction gases between the entrapped atmosphere of the bifilm and the external liquid melt. Additionally, the impermeable AlN layer may limit hydrogen diffusion through the bifilm, preventing further expansion of the bifilm and supporting the Nyahumwa hypothesis [3][41].

The feather-shaped AlN particles observed in various alloys seemed to be more easily formed in the CP-Al alloy compared to the 2L99, 2L99 + 0.6 wt.% Mo, and 2L99 + 0.2

wt.% W alloys. This might be due to the absence of the alloying elements Si and Mg in CP-Al. It is important to point out that in all aforementioned alloys, the observation of feather and nodular AlN particles was less frequent compared to the rod and whisker-shaped morphologies.

It is also of interest that feather-shaped AlN was regularly observed to be trapped between rod or whisker-shaped AlN, as shown in Figure 4-148 (a) to Figure 4-148 (d). In contrast, the nodular and rod-shaped AlN particles observed on the fractured surfaces of various alloys where AlN growth was carried out were often observed alone or in combination with a whisker or feather-shaped morphologies, as shown in Figure 4-147 (a) to Figure 4-147 (d) and Figure 4-145 (a) to Figure 4-145 (d), while whisker-shaped AlN morphologies were observed alone, as depicted in Figure 4-146 (a) to Figure 4-146 (d).

5.4 The mechanism for improvement of mechanical properties of 2L99 with the addition of 0.4 wt.% Mo, W and V

As discussed in section 5.2, the addition of 0.4 wt.% of the alloying elements Mo, W and V led to considerable improvement in both measured properties and data scatter (Weibull moduli) of the mechanical properties measured; UTS, %Elongation and yield strength.

This improvement in mechanical properties is considered to be due to a combination of the following factors:

i) Sedimentation: SEM and EDX analysis revealed nucleation of Mo intermetallics in varying quantities on the bifilms in the samples with different Mo contents, as shown on 0.5 wt.% Mo in Figure 4-119, 1.8 wt.% Mo in Figure 4-121, Figure 4-122 and 2.4 wt.% Mo in Figure 4-125. Similar to Mo, W intermetallics in varying quantities nucleated on the bifilms as revealed with SEM and EDX as shown on 1.6 wt.% W in Figure 4-128, 1.9 wt.% in Figure 4-131, and 4.8 wt.% in Figure 4-134. SEM and EDX showed Nucleation of V intermetallics on bifilms with the addition of 2.1 wt.% V, as shown in Figure 4-139.

Furthermore, XRF analysis showed the amount of transition metals (Mo, W and V) as well as O to be higher at the bottom of the samples (compared to the top), as shown in Table 4-108, Table 4-109, and Table 4-110.

As shown in Figure 5-1, the addition of 0.5 to 3.3 wt.% Mo to 2L99 showed a steady increase in the amount of intermetallics from 0.2% to 6.5% and the addition of 2.3 to 5.6 wt.% W to 2L99 showed an increase in the amount of intermetallics from 6.3% to 17.5%. For V, the addition of 1 to 4 wt.% of the metal showed a steady increase in the amount of intermetallics from 2.1% to 12.1%. The addition of W and V was shown to have a larger impact on the amount of intermetallics present at the base of the samples. The addition of W and V was shown to have a larger impact on the amount of intermetallics present at the base of the samples.

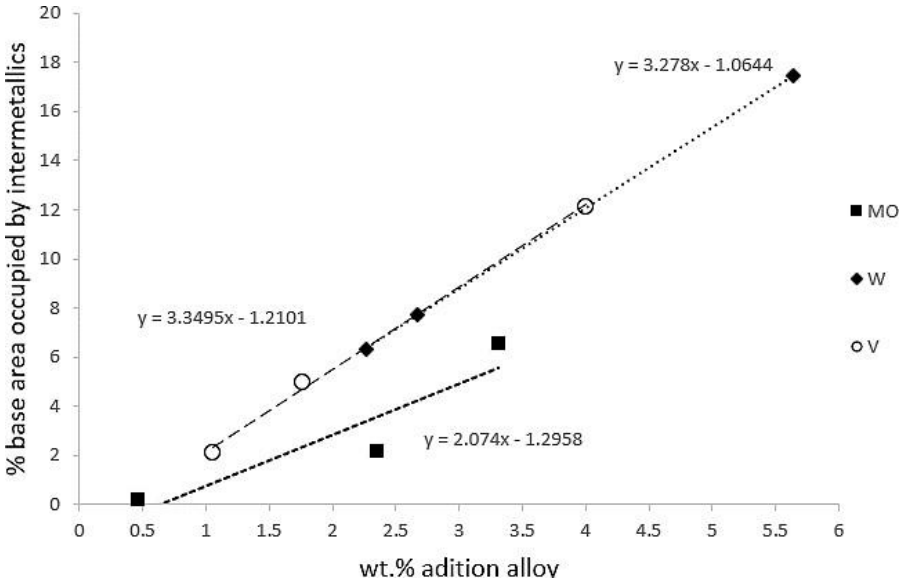


Figure 5-1: XRF measured wt.% of transition metal additions vs. the area occupied by the intermetallics at the base of the samples

Similar to the above, Figure 5-2 presents the XRF measured wt.% of the transition metals versus the percentage of wt.% increase of O at the base compared to the top of the sedimentation test samples. It could be observed that the addition of 0.5 wt.% resulted in an 84% increase in the measured amount of O. Addition of 2.35 wt.% and 3.3 wt.% Mo showed an increase in the amount of O by around 20% measured at the base of the sample compared to the top. It could also be observed that the addition of W at 2.2 wt.%, 2.8 wt.% and 5.6 wt.% resulted in a 124%, 97% and 66%, respectively increase in the measured amount of O at the bottom of the sample compared to the top. Addition of 2.35 and 3.3 wt.% Mo showed an increase in the amount of O by around 20%.

In the case of V, the results showed that addition of 1.1 wt.%, 1.8 wt.% and 5 wt.% resulted in a 28%, 17.4% and 17.1% increase in the measured amount of O at the bottom of the sample compared to the top.

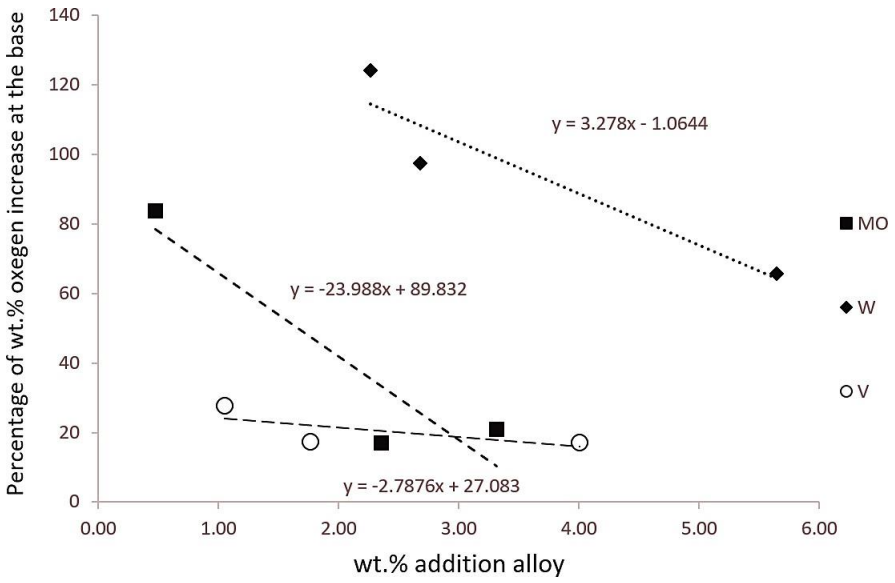


Figure 5-2: XRF measured wt.% of transition metal additions vs. the % increase in XRF measured wt.% of O at the base of the samples compared to the top

The results showed a considerable increase in the amount of O at the base of the samples as a result of the addition of the transition metals. It is important to note that the amount of the XRF measured O at the base samples showed a reduction in all metals with an increase in wt.% addition. This is thought to be due to the formation of more diverse intermetallics, which may not identify the bifilms as a potent substrate for nucleation.

The addition of V was shown to have less of an effect on the amount of XRF measured O at the base of the samples. This is thought to be due to the presence of the additional intermetallics, Al_3V, which is less likely to nucleate on the bifilms due to large differences in their lattice mismatch.

Overall, the addition of Mo, V and W significantly increased the amount and size of the intermetallics settling to the base of the samples, with W showing the highest increase, followed by V and Mo. Furthermore, in all samples analysed gas porosity and bifilms were observed to have a collapsed morphology at the top, in

contrast to a spherical morphology at the bottom of the sample. This is thought to be due to the diffusion of H downwards from the top pores during the solidification process.

Figure 4-121, Figure 4-122 and Figure 4-139 show intermetallics having nucleated on the bifilms. Due to the higher mass density of the intermetallics, the nucleation of the bifilms is thought to promote the settling of the bifilms, together with their intermetallics, to the base of the melt, resulting in an increase in mechanical properties of the alloys [127][128][20]. The amount of intermetallics observed at the base of the melt was highest for W, followed by V and Mo. This is in line with the mechanical property tests carried out in this research and previous research on Ti by Gyarmati et al. [129] and research on Al_8Mn_5 by Peng et al. [93].

ii) Changes in β intermetallic phases in addition to alloys compared to 2L99 may have resulted in less harmful intermetallics. As discussed in section 5.2, the addition of Mo, W and V resulted in changes to the β intermetallic of Al_5FeSi to $Fe_3Al_2Si_4$ in the Mo alloy, $Fe_3Al_2Si_3$ in the W alloy and $FeAl_2Si$ in the V alloy. The modified intermetallic phases detected using XRD are reported to be metastable and less harmful to the mechanical properties of the alloy compared to β-Al_5FeSi observed on the 2L99 [100][91].

iii) An increase in quantity, as well as changes to the morphology of AlN phases, suggest a reduction in the size of the bifilms due to enhanced consumption of the internal gases and prevention of diffusion of H into the bifilms. In addition to this, and compared to the 2L99 alloy, far more frequent morphologies of AlN were observed on both the fractured and polished surfaces of the 2L99 + Mo, W and V alloys. The AlNs observed were of various shapes, such as

feather and nodular shapes in Mo alloy, nodular and whisker shapes in W alloy and nodular shapes in V alloy. The increase in the amount and diversity in the shape of the nitrides observed is thought to improve the mechanical properties of the alloys [130].

This is because intermetallics can nucleate on bifilms; this may cause a rupture in the bifilms and increase the rate of the consumption of the gases inside the bifilms, resulting in the presence of more AlN in the alloys.

The nodular-shaped AlNs, considered impermeable, might also serve as a sealing point to the rupture of the oxide layer, preventing diffusion of H into the bifilms. Therefore, the formation of AlN may play an important role in preventing an increase in the size of the bifilms and therefore reduce their detrimental effect on the mechanical properties of Al alloys.

6 CONCLUSIONS

This study aimed to investigate the effects of additional alloying elements Mo, W and V on tensile properties (UTS, %Elongation and yield strength) of 2L99 alloy, focusing on observation of the changes in key phases such as bifilms, intermetallics and nitrides.

The results showed the tensile properties (UTS, %Elongation and yield stress) all increased with the addition of 0.4 wt.% of the alloying elements Mo and W, leading to meaningful improvement in the mechanical properties of 2L99 alloy, with V showing a negligible increase. The addition of all the transition metals showed considerable improvement in the Weibull Moduli of the mechanical properties of 2L99. This enhancement is thought to be the result of a combination of the following factors:

a. Settling of a considerable amount of Mo and W intermetallics to the base of the melt, and subsequent settlement of the bifilms through nucleation of the intermetallics on the bifilms (84% increase in O amount at the base Mo alloy, and 124% increase in O amount for W alloy as confirmed by XRF). The increase in the amount of O at the base of the V alloy was 27.7%, which was lower compared to Mo and W.

b. An increase in the amount of gas consumption within the bifilm of the alloys due to the formation of various intermetallics promoted the consumption of O first, followed by the consumption of N, and the formation of AlN as compared to the 2L99 alloys was observed. The increase in the amount of impermeable nodular AlN morphology on the bifilms is thought to prevent the diffusion of H into the bifilms, leading to a reduction in their size. The formation of other AlN morphologies, such as feather and

whisker shapes on Mo and W alloys, may be due to the alloys' exposure to longer cooling periods, leading to the formation of the different AlN morphologies.

c. Modifying the β-Fe intermetallic phases of 2L99 alloys reduces the detrimental effects of Al_5FeSi.

6.1 Effect of alloying elements on tensile properties of 2L99 alloy

1. Mechanical test results on a high H content (6 ppm) T6 heat-treated as-cast 2L99 alloy (30 testbars) showed a mean UTS of 227 MPa, %Elongation of 1.07 and yield strength of 203.5 MPa. The Weibull modulus of UTS was calculated as 4, %Elongation as 1.35, and yield strength as 4.28.
2. The addition of 0.4 wt.% of Mo to 2L99 led to an increase of 7%, 13% and 8% in the mean UTS, %Elongation and yield strength parameters, respectively, of the alloy compared to 2L99. This also resulted in an increase of 173%, 68% and 302% in the Weibull modulus of the UTS, %Elongation and yield stress results.
3. The addition of 0.4 wt.% of W to 2L99 resulted in an increase of 7%, 33% and 6% in the mean UTS, %Elongation and yield strength parameters, respectively, of the alloy compared to 2L99. The results also showed an increase of 109%, 12% and 227% in the Weibull modulus of the UTS, %Elongation and yield stress.
4. The addition of 0.4 wt.% of V to 2L99 resulted in an increase of 2% and 3% in the mean UTS yield strength parameters of the alloy compared to 2L99, respectively. The results also showed an increase of 168%, 83% and 241% in the Weibull modulus of the UTS, %Elongation and yield stress, respectively.

6.2 Effects of alloying elements on the bifilms

1. XRD analysis confirmed AlN, Mg_2Si, spinel, MgO, SiO_2 and Al_5FeSi phases on the polished surface of 2L99 alloy. The SEM and EDX suggested several oxides to be spinel, a thin layer of MgO and a moderate amount of SiO_2 phases in general. The most stable and dominant oxide in 2L99 was spinel.

2. Phases that were detected and confirmed by XRD analysis in 2L99 + 0.4 wt.% Mo were $Mo(Al,Si)_2$, AlN, spinel, SiO_2 and $Fe_3Al_2Si_4$. The oxides observed on the polished and fractured surfaces of Mo masteralloy (2L99 + 10 wt.% Mo) were mainly layered or spherical (<1 μm in diameter) spinel, accompanied by a small amount of alumina (80 μm length) and SiO_2 (150 μm diameter). XRD, however, detected alumina and SiO_2 as well as MgO. No AlN was found on any of the surfaces of the Mo masteralloy. SEM and EDX also suggested the presence of mainly nodular-shaped spinel and a small amount of granular and whisker-shaped MgO on the fractured and polished surfaces of 2L99 + 0.4 wt.% Mo.

3. Phases that were detected and confirmed by XRD analysis on 2L99 + 0.4 wt.% W were $W(Al,Si)_2$, AlN, spinel, SiO_2 and $Fe_3Al_2Si_3$. The oxides observed on the fractured and polished surfaces of W masteralloy (2L99 + 10 wt.% W) were mainly spinel, accompanied by a small amount of SiO_2 and MgO. SEM and EDX also suggested the presence of oxides of mainly nodular-shaped spinel and a small amount of nodular and whisker-shaped MgO, as well as a small amount of SiO_2 (150 μm diameter) on the fracture and polished surfaces of 2L99 + 0.4 wt.% W.

4. Phases that were detected and confirmed by XRD analysis in 2L99 + 0.4 wt.% V were spinel, SiO_2, Al_3V, Al_9Si_3Fe, $Al_{0.1}Si_{0.9}V_3$, MgO, AlV_3 and AlN. On the polished surface of 2L99 + 0.4 wt.% V, EDX suggested $VAl_{1.1}Si_2$, $VAl_{1.4}Si_3$, $VAl_3Si_{4.2}$, $Al_3VSi_{2.7}$, $V_{1.5}AlSi_{3.1}$, β shaped V_5AlSi_5 and $Al_{28}Si_3Fe$ intermetallics. On the fracture surface of the V alloy, EDX suggested $V_{2.7}AlSi_{7.7}$ and $V_3AlSi_{3.3}$ intermetallics. SEM and EDX also suggested the presence of oxides of mainly wrinkled and nodular spinel and a small amount of granular MgO on the fractured and polished surfaces of 2L99 + 0.4 wt.% V.

6.3 Effects of the alloying elements on nitrides

1. This research observed AlN for the first time on the fracture surface of heat-treated as-cast 2L99 alloy (i.e. in a casting). The AlN observed had a nodular impermeable morphology and was 15 μm in length. The presence of AlN particles in the as-cast condition supported Nyahumwa et al. hypothesis [41] and suggested a potential role of hydrogen within the bifilms, depending on the hydrogen content in the liquid melt. These factors can lead to significant differences in bifilm size and variations in the mechanical properties of the alloys.
2. The AlN observed on both fracture and polished surfaces of 2L99 + 0.4 wt.% Mo alloys were nodular, whilst the nitrides on the fracture surfaces were nodular and feather-shaped.
3. The AlN observed on both fracture and polished surfaces of 2L99 + 0.4 wt.% W were nodular, whilst the nitrides on the fracture surfaces were observed to be nodular and whisker-shaped.

4. The AlNs observed on both fractured and polished surfaces of 2L99 + 0.4 wt.% V were nodular in shape.

5. AlN in 2L99+0.4 wt% Mo and 2L99+0.4 wt% W alloys was found to be nucleating on spinel with a lattice misfit of -0.5% and 0.4%, respectively. However, AlN was not observed to have nucleated on spinel in 2L99+0.4 wt.% V alloys due to the large lattice mismatch between the spinel and AlN (-14%).

6.3.1 Nitrogen growth experiment[7]

1. In 2L99 + 0.6 wt.% Mo and 2L99 + 0.2 wt.% W alloys, AlN was found to nucleate only on spinel with an Mg content of <1.5 wt.% on nitride growth samples. AlN was found nucleating on alumina in CP-AL as part of the nitride growth experiment reported in section 4.5. The lattice mismatch between AlN and spinel, γ-alumina and α-alumina was calculated as 8.7%, 10.9% and 13.1%, respectively. According to Wang and Fan [66], the calculated lattice mismatch means the above oxide phases can not be a potent substrate for AlN nucleation with spinel. On the other hand, according to Campbell [44], the oxides listed above can be a potent substrate for nucleation of AlN based on their lattice mismatch. The detection of both N and O by EDX in this research confirms the nucleation of AlN on oxides and aligns with the lattice mismatch specified by Campbell (12%).

[7] The conclusions presented in this section have been published by the author in the paper provided in Appendix A.

2. Various morphologies of AlN, such as rod, whisker, nodular, and feather-shaped, were observed in CP-Al, 2L99, 2L99 + 0.6 wt.% Mo and 2L99 + 0.2 wt.% W alloys that underwent N growth.
3. The presence of nodular nitrides in the as-cast condition suggests the consumption of oxygen within the bifilms and the formation of nitrides, as suggested by Nyahumwa et al. [41].

6.4 Effects of alloying elements on intermetallics

1. Characterisation of 2L99 alloys showed the presence of Al_5FeSi (60 µm) in length, Mg_2Si (60 µm) in length, oxides and nitrides.
2. The intermetallics suggested by SEM and EDX in the Mo masteralloy were α shaped $Mo_{1.5}AlSi_2$, $MoAl_2Si$, $Mo_{1.2}AlSi_{1.5}$, and β-shaped $Mo_4Al_{11}Si$ and $Mo_{7.3}Al_{24}Si$.
3. On the polished surface of 2L99 + 0.4 wt.% Mo, EDX suggested the phases $Mo_{1.5}AlSi_2$, $MoAl_8Si_3$, $MoAl_{10}Si$, $Mo_{0.6}(Al,Si)$, Mo $(Al,Si_2)_2$, $Mo_7Al_5Si_8$, $Mo_2Al\ Si_2$, $Mo(Al, Si)_2$ and $Al_2\ FeSi_{2.6}$ intermetallics. On the fracture surface of the 0.4 wt.% Mo alloy, EDX suggested $MoAlSi_2$, $Mo_7Al_5Si_7$ and $Mo_6Al_5Si_8$ intermetallics.
4. The intermetallics suggested by EDX on a W masteralloy were observed on the top and bottom of polished masteralloy ingot and polished and fracture surfaces of the masteralloy testbars and included $W_4Al_{14}Si$, Al_3W, AlW_2, $W_4Al_{14}Si$, Al_4W, $W_{1.5}Si_2$ and $W_{1.2}AlSi_{1.4}$. The oxides suggested by EDX on Mo masteralloy were mostly layered spinel or spherical (<1 µm in diameter). Small amounts of alumina (80 µm length) and SiO_2 (150 µm diameter) were also observed. The

intermetallics detected by XRD on W masteralloy were Al4W as well as oxides such as spinel, MgO and SiO_2.

5. On the polished surface of 2L99 + 0.4 wt.% W, EDX suggested $W_{1.2}AlSi_{1.2}$, $W_{1.4}AlSi_{2.4}$, $W_{1.5}Al$, $W_{1.1}AlSi_{1.3}$, $W(Al, Si)_2$ and $Al_{8.3}SiFe_{1.4}$ intermetallics. On the fracture surface of the W alloy, EDX suggested $W(Al, Si)_2$ and $WAl_{3.5}$ intermetallics.
6. Molyndenium intermetallics were found to be nucleating on the spinel phase. The lattice mismatch between $Mo(Al, Si)_2$ and spinel was calculated as -0.7%, suggesting spinel to be a potent substrate for Mo intermetallic nucleation as suggested by EDX results and confirmed by XRD.
7. Tungsten intermetallics were found to be nucleating on the spinel phase. The lattice mismatch between $W(Al, Si)_2$ and spinel was calculated as 5.7%, suggesting spinel to be a potent substrate for W intermetallic nucleation as suggested by EDX results and confirmed by XRD.
8. Vanadium intermetallics were found to be nucleating on a spinel phase. The lattice mismatch between ($Al_{0.1}Si_{0.9}V_3$, AlV_3, Al_9FeSi_3) and spinel was calculated to be 5.2%, -6% and 5.5%, respectively, suggesting spinel to be a potent substrate for $Al_{0.1}Si_{0.9}V_3$, AlV_3, Al_9FeSi_3 intermetallics. However, the lattice mismatch between Al_3V and spinel was calculated as 23.8%, suggesting spinel to be an unsuitable substrate for Al_3V intermetallic nucleation, as suggested by EDX results and confirmed by XRD.
9. It was found that the addition of Mo, W and V resulted in the settlement of a considerable amount of intermetallics in the melt. As spinel phases were found to

be a suitable substrate for intermetallics nucleation, it can be concluded that sedimentation of the intermetallics could result in settling some of the floating spinels in the melt, particularly for Mo and W and can improve the mechanical properties of the 2L99 alloy.

7 FUTURE WORKS

In this study, appreciable progress was made towards understanding the mechanisms by which transition metals contribute to improving the mechanical properties of 2L99 alloys and proving the mechanism by which nitrides contribute to the consumption of gases within the bifilms.

Moving forward, the following are considered necessary to advance the research further:

1. It is recommended that further research is carried out only on as-cast alloys with H content control (using Sevren Science), limiting the H content to a maximum of 0.1 ppm to improve the accuracy and reliability of the mechanical test results.
2. More experimental work can be conducted on adding up to 1% vanadium to 2L99 alloys to determine the optimum addition amount for enhancing the mechanical properties of 2L99 alloys.
3. Carry out Transmission Electron Microscopy (TEM) on ultra-thin (~100 nm) specimens to observe intermetallics and nitrides at higher-resolution images to obtain atomic and crystallographic data. Such specimens can be analysed in TEM with an X-ray spectrometer to provide more information on the crystallography of phases such as intermetallics, nitrides and oxides. This can potentially lead to a more certain explanation of the effect of each phase.

4. Conduct a Reduced Pressure Test (RPT) on each alloying element to assess the melt quality and changes to the size and number of the bifilms (bifilm index measurement).
5. Run Differential Scanning Calorimetry (DSC) to accomplish the thermal analysis of the (2L99+0.4 wt.% Mo/W/V) alloys to understand the thermal behaviour of the intermetallics and assess the potential impact on enhancing the consumption of the gases inside the bifilms.
6. Conduct fatigue testing on various Mo, W and V alloys of 2L99 to understand the long-term performance of these alloys and the effects of transition metals additions on the fatigue characteristics of 2L99 alloys.

8 References

[1] Arya SM, Griffiths WD. Aluminum Nitride in Al–Si–Mg Alloy. Metallurgical and Materials Transactions B: Process Metallurgy and Materials Processing Science 2023;54:1965–84. https://doi.org/10.1007/s11663-023-02810-8.

[2] Campbell J. Castings. Elsevier 2001.

[3] Chen Q. The effect of transition metal additions on double oxide film defects in Al alloy castings. Doctor of Philosophy. PhD thesis, University of Birmingham, 2017.

[4] Dignam MJ. Oxide Films on Aluminum I. Ionic Conduction and Structure. Journal of Electrochemical Society 1962;109:184–91.

[5] Wang Yun, Li Hu-Tian, Fan Zhongyun. Oxidation of Aluminium Alloy Melts and Inoculation by Oxide Particles n.d. https://doi.org/10.1007/s12666-012-0194-x.

[6] Wightman G, Fray DJ. The dynamic oxidation of aluminum and its alloys. Metallurgical Transactions B 1983;14:625–31. https://doi.org/10.1007/BF02653948/METRICS.

[7] Hinton EM. The oxidation of liquid aluminium and the potential for oxides in grain refinement of aluminium alloys. PhD thesis, University of Birmingham, 2016.

[8] Akagwu I, Brooks R, Fan Z, Ralph B, Quested P. Liquid state oxidation of aluminium, 2014.

[9] Sleppy WC. Oxidation of Molten High-purity Aluminum in Dry Oxygen. J Electrochem Soc 1961;108:1097. https://doi.org/10.1149/1.2427963.

[10] Raeiszadeh R. A method to study the behaviour of double oxide film defects in aluminium alloys. PhD thesis, University of Birmingham, 2005.

[11] Gerrard AJ. Inclusions and Hydrogen and Their Effects on the Quality of Direct Chill Cast and Flat Rolled Aluminium Alloys for Aerospace Applications. PhD thesis, University of Birmingham, 2014.

[12] Nyahumwa C, Green NR, Campbell J. Effect of Mold-Filling Turbulence on Fatigue Properties of Cast Aluminum Alloys. Transaction of the American Foundry Society 1998;106:215–24.

[13] Dholiwar R. The Oxidation of Liquid Aluminium. PhD Thesis, Brunel University, 1985.

[14] Impey S, Stephenson DJ, Nicholls JR. A study of the effect of magnesium additions on the oxide growth morphologies on liquid aluminium alloys, CRC press; 2023, p. 238–44.

[15] Stephenson DJ. The Absorption of Hydrogen from Humid Atmospheres by Molten Aluminium and an Aluminium Magnesium Alloy. PhD thesis, Brunel University, 1978.

[16] Cochran C, Belitskus D, Kinosz D. Oxidation of aluminum-magnesium melts in air, oxygen, flue gas, and carbon dioxide. Metall Trans B 1977;8(1):323–32.

[17] Silva MP, Talbot DEJ. Oxidation of Liquid Aluminum — Magnesium Alloys. In Essential Readings in Light Metal. Essential Readings in Light Metals 2016;3:137–42.

[18] Campbell J. Complete casting handbook : metal casting processes, metallurgy, techniques and design. Butterworth-Heinemann; 2015.

[19] Campbell J. Thin wall castings. Materials Science and Technology 1988;4(3):194–204.

[20] Dispinar D, Kahruman C, Campbell J. Correlation between Bifilm Index and Toughness of Aluminum Alloys. Shape Casting: 5th International Symposium 2014 2014:171–6. https://doi.org/10.1007/978-3-319-48130-2_21.

[21] Campbell J. Castings - 2nd Edition. Butterworth-Heinemann; 2003.

[22] Griffiths WD, Lai N-W. Double Oxide Film Defects in Cast Magnesium Alloy. Metallurgical and Materials Transactions A 2007;38:190–6. https://doi.org/10.1007/s11661-006-9048-7.

[23] Fox S, Campbell J. VISUALISATION OF OXIDE FILM DEFECTS DURING SOLIDIFICATION OF ALUMINIUM ALLOYS. Scripta Mater 2000;43:881–6.

[24] Campbell J. Complete Casting Handbook : Metal Casting Processes, Techniques and Design. 1st ed. Oxford: Elsevier Science; 2011.

[25] Weibull W. A Statistical Distribution Function of Wide Applicability. J Appl Mech 1951;18:293–7.

[26] Salem Z, Nashwan MH. SURFACE TURBULENCE AND THE TENSILE PROPERTIES, REPRODUCIBILITY AND RELIABILITY OF CAST IRONS-A STUDY OF ENTRAINMENT. DEFECTS. PhD thesis, University of Birmingham, 2022.

[27] Peirce F. 32—X.—Tensile tests for cotton yarns v.—“The Weakest Link” Theorems on the strength of long and of composite specimens. Journal of the Textile Institute Transactions 1926;17:355–68. https://doi.org/10.1080/19447027.1926.10599953.

[28] Hallinan AJ. A Review of the Weibull Distribution. Journal of Quality Technology 1993;25:85–93. https://doi.org/10.1080/00224065.1993.11979431.

[29] Bantle M, Kolsaker K, Eikevik TM. Modification of the Weibull Distribution for Modeling Atmospheric Freeze-Drying of Food. Drying Technology 2011;29:1161–9. https://doi.org/10.1080/07373937.2011.574242.

[30] Campbell J. Properties of Castings. In: Complete Casting Handbook. Elsevier; 2015.

[31] Sullivan J, Lauzon P. Experimental probability estimators for Weibull plots. J Mater Sci Lett 1986;5(12):1245–7.

[32] Lawless J. Statistical models and methods for lifetime data. John Wiley & Sons 2011;362.

[33] Khalili A, Kromp K. Statistical properties of Weibull estimators. J Mater Sci 1991;26(24):6741– 52.

[34] Tiryakioglu M, Hudak D. Unbiased estimates of the Weibull parameters by the linear regression method. J Mater Sci 2008;43(6):1914–9.

[35] Tiryakioglu M, Hudak D, Okten G. On evaluating Weibull fits to mechanical testing data. Materials Science and Engineering A 2009;527(1-2):397–9.

[36] Green N, Campbell J. Statistical distributions of fracture strengths of cast Al7SiMg alloy. Materials Science and Engineering A 1993;173(1-2):261–6.

[37] Byczynski GE. THE STRENGTH AND FATIGUE PERFORMANCE OF 319 ALUMINUM ALLOY CASTINGS. PhD thesis, University of Birmingham, 2002.

[38] Nyahumwa C. Multiple Defect Distributions On Weibull Statistical Analysis Of Fatigue Life Of Cast Aluminium Alloys. African Journal of Science and Technology (AJST) Science and Engineering Series 2005;6:43–54.

[39] Tiryakioglu M. Weibull Analysis of Mechanical Data for Castings II: Weibull Mixtures and Their Interpretation. Metall Mater Trans A Phys Metall Mater Sci 2015;46(1):270–80.

[40] Cox M, Wickins M, Kuang JP, Harding RA, Campbell J. Effect of top and bottom filling on reliability of investment castings in Al, Fe, and Ni based alloys. Materials Science and Technology 2000;16:1445–52. https://doi.org/10.1179/026708300101507442.

[41] Nyahumwa C, Green N, Campbell J. Influence of casting technique and hot isostatic pressing on the fatigue of an Al-7Si-Mg alloy. Metall Mater Trans A Phys Metall Mater Sci 2001;32(2):349– 58.

[42] Weibull W. A statistical theory of the strength of materials. IVB-Handl 1939;15.

[43] Ravi M, Pillai UTS, Pai BC, Damodaran AD, Dwarakadasa ES, Dwarakadasat ES. Mechanical properties of cast Al-7Si-0.3Mg (LM 25/356) alloy. International Journal of Cast Metals Research 1998;11:113–25. https://doi.org/10.1080/13640461.1998.11819265.

[44] Cao X, Campbell J. The nucleation of Fe-rich phases on oxide films in Al-11.5Si-0.4Mg cast alloys. Metall Mater Trans A Phys Metall Mater Sci 2003;34 A:1409–20. https://doi.org/10.1007/s11661-003-0253-3.

[45] Lu L, Dahle AK. Iron-Rich Intermetallic Phases and Their Role in Casting Defect Formation in Hypoeutectic Al-Si Alloys. Metallurgical and Materials Transactions A 2005;36:819–35.

[46] Li J, An Q, Wu S, Li F, Lü S, Guo W. Relationship of Mg2Si morphology with Mg2Si content and its effect on properties of in-situ Mg2Si/Al–Cu composites. J Alloys Compd 2019;808. https://doi.org/10.1016/j.jallcom.2019.151771.

[47] Kim B, Hwang J, Park Y, Lee Y. Microstructural improvement of eutectic Al + mg2si phases on Al–Zn–Si–Mg cast alloy with TiB2 particles additions. Materials 2021;14. https://doi.org/10.3390/ma14112902.

[48] Li C, Liu X, Wu Y. Refinement and modification performance of Al-P master alloy on primary Mg2Si in Al-Mg-Si alloys. J Alloys Compd 2008;465:145–50. https://doi.org/10.1016/j.jallcom.2007.10.111.

[49] Li C, Liu X, Zhang G. Heterogeneous nucleating role of TiB2 or AlP/TiB2 coupled compounds on primary Mg2Si in Al-Mg-Si alloys. Materials Science and Engineering A 2008;497:432–7. https://doi.org/10.1016/j.msea.2008.07.034.

[50] Emamy M, Khorshidi R, Raouf AH. The influence of pure Na on the microstructure and tensile properties of Al-Mg2Si metal matrix composite. Materials Science and Engineering A 2011;528:4337–42. https://doi.org/10.1016/j.msea.2011.02.010.

[51] Yu HC, Wang HY, Chen L, Zha M, Wang C, Li C, et al. Spheroidization of primary Mg2Si in Al-20Mg2Si-4.5Cu alloy modified with Ca and Sb during T6 heat treatment process. Materials Science and Engineering: A 2017;685:31–8. https://doi.org/10.1016/j.msea.2016.12.080.

[52] Zheng Q, Wu B, Reddy RG. In-Situ Processing of Al Alloy Composites. Adv Eng Mater 2003;5:167–72.

[53] Aghajanian MK, Rocazella MA, Burke JT, Keck SD. The fabrication of metal matrix composites by a pressureless infiltration technique. J Mater Sci 1991;26:447–54. https://doi.org/10.1007/BF00576541.

[54] Nagendra N, Rao BS, Jayaram V. Microstructures and properties of Al2O3/Al–AlN composites by pressureless infiltration of Al-alloys. Materials Science and Engineering: A 1999;269:26–37. https://doi.org/10.1016/S0921-5093(99)00180-X.

[55] Han YS, Kalmykov KB, Dunaev SF, Zaitsev AI. Solid-state phase equilibria in the Titanium-Aluminum-Nitrogen system. Journal of Phase Equilibria and Diffusion 2004 25:5 2004;25:427–36. https://doi.org/10.1007/S11669-004-0134-5.

[56] Willems HX, Hendrix MMRM, de With G, Metselaar R. Thermodynamics of Alon II: Phase relations. J Eur Ceram Soc 1992;10:339–46. https://doi.org/10.1016/0955-2219(92)90089-V.

[57] Willems HX, Hendrix MMRM, Metselaar R, de With G. Thermodynamics of Alon I: Stability at lower temperatures. J Eur Ceram Soc 1992;10:327–37. https://doi.org/10.1016/0955- 2219(92)90088-U.

[58] Zheng Q, Reddy RG. Mechanism of in situ formation of AlN in Al melt using nitrogen gas. Journal of Materials Science 2004 39:1 2004;39:141–9. https://doi.org/10.1023/B:JMSC.0000007738.14116.FD.

[59] El-Sayed MAM. Double oxide film defects and mechanical properties in aluminium alloys. PhD thesis, University of Birmingham, 2012.

[60] El-Sayed MA, Salem HAG, Kandeil AY, Griffiths WD. Determination of the lifetime of a double-oxide film in al castings. Metallurgical and Materials Transactions B: Process Metallurgy and Materials Processing Science 2014;45:1398–406.

[61] Raiszadeh R, Griffiths WD. Estimation of the Duration of the Atmosphere Within a Double Oxide Film Defect in Pure Aluminium. World Foundry Congress, Istanbul, Turkey 2005;8:464–71.

[62] Griffiths WD, Gerrard AJ, Yue Y. Oxide film defects in Al alloys and the formation of hydrogen-related porosity. IOP Conf Ser Mater Sci Eng 2016;117:012070. https://doi.org/10.1088/1757-899X/117/1/012070.

[63] Griffiths WD, Gerrard AJ, Yue Y. Oxide film defects in Al alloys and the formation of hydrogen-related porosity. IOP Conf Ser Mater Sci Eng 2016;117. https://doi.org/10.1088/1757-899X/117/1/012070.

[64] Griffiths WD, Elsayed A, El-Sayed MA. Metallurgical and Materials Transaction B. Metallurgical and Materials Transactions B: Process Metallurgy and Materials Processing Science 2016;47:3459–68.

[65] Chen Q, Griffiths WD. Modification of Double Oxide Film Defects with the Addition of Mo to An Al-Si-Mg Alloy. Metallurgical and Materials Transactions B: Process Metallurgy and Materials Processing Science 2021;52:502–16. https://doi.org/10.1007/S11663-020-02038-W/TABLES/7.

[66] Wang F, Fan Z. Characterization of AlN Inclusion Particles Formed in Commercial Purity Aluminum. Metall Mater Trans A Phys Metall Mater Sci 2019;50:2519–26. https://doi.org/10.1007/s11661-019-05150-y.

[67] Talbot DEJ. Effect of Hydrogen in Aluminium, Magnesium, Copper and their alloys. International Metallurgical Review 1975;(20):166–84.

[68] Ransley C, Neufeld H. The solubility of hydrogen in liquid and solid aluminium. Journal of the Institute of Metals 1948;74(12):599–620.

[69] Shivkumar S, Apelian D, Zhou J. Modeling of microstructure evolution and micro porosity formation in cast aluminium alloys. AFS Transactions 1990;98:897–904.

[70] El-Sayed MA, Griffiths WD. Hydrogen, bifilms and mechanical properties of al castings. International Journal of Cast Metals Research 2014;27:282–7. https://doi.org/10.1179/1743133614Y.0000000113.

[71] Gerrard AJ, Griffiths WD. The Formation of Hydrogen Related Porosity by Double Oxide Film Defects in Al Alloys , in Shape Casting: 5th International Symposium. John Wiley & Sons, Inc 2014:269–76.

[72] Griffiths WD, Caden AJ, Chen Q. Effects of transition metal additions on double-oxide film defects in an Al–Si–Mg alloy. Materials Science and Technology (United Kingdom) 2017;33:2212–22. https://doi.org/10.1080/02670836.2017.1346911.

[73] Bourkhina A inventor, Caterpillar Inc assignee. Aluminum alloy with improved tribological characteristics. United States Patent 1999.

[74] Kawahara, H. et al. Method for manufacture of aluminum alloy casting 1981.

[75] Szymczak T, Gumienny G, Pacyniak T. Effect of Vanadium and Molybdenum on the Crystallization, Microstructure and Properties of Hypoeutectic Silumin. Archives of Foundry Engineering 2015;15:81–6. https://doi.org/10.1515/AFE-2015-0084.

[76] Okamoto H. Al-Mo (Aluminum-Molybdenum). J Phase Equilibria Diffus 2010;31:492–3. https://doi.org/10.1007/s11669-010-9758-9.

[77] Gronostajski J, Matuszak A. The recycling of metals by plastic deformation: an example of recycling of aluminium and its alloys chips. J Mater Process Technol 1999;92:35–41.

[78] Cao X, Campbell J. Effect of precipitation and sedimentation of primary α-Fe phase on liquid metal quality of cast Al-11·1Si-0·4Mg alloy. International Journal of Cast Metals Research 2004;17:1–11. https://doi.org/10.1179/136404604225014792.

[79] Raskolenko LG, Gerul'skii AYu. Compounds WAl4, WAl3, W3Al7, and WAl2 and Al-W-N combustion products. Inorganic Materials 2008 44:1 2011;44:30–9. https://doi.org/10.1134/S0020168508010056.

[80] Elhadari HA, Patel HA, Chen DL, Kasprzak W. Tensile and fatigue properties of a cast aluminum alloy with Ti, Zr and V additions. Materials Science and Engineering A 2011;528:8128–38. https://doi.org/10.1016/J.MSEA.2011.07.018.

[81] Meng Y, Cui J, Zhao Z, Zuo Y. Effect of vanadium on the microstructures and mechanical properties of an Al–Mg–Si–Cu–Cr–Ti alloy of 6XXX series. J Alloys Compd 2013;573:102–11. https://doi.org/10.1016/J.JALLCOM.2013.03.239.

[82] Lech-Grega M, Szymański W, Boczkal S, Gawlik M, Bigaj M. The effect of vanadium addition on structure and material properties of heat treated 6xxx series aluminium alloys. TMS Light Metals 2015;2015-January:173–8. https://doi.org/10.1007/978-3-319-48248-4_31/COVER.

[83] Boczkal S, Lech-Grega M, Morgiel J, Piela K. Effect of vanadium additions on the structure of aluminium (AL99.5) and 6xxx aluminium alloys. TMS Light Metals 2014:261–4. https://doi.org/10.1007/978-3-319-48144-9_45/COVER.

[84] Camero S, Puchi ES, Gonzalez G. Effect of 0.1% vanadium addition on precipitation behavior and mechanical properties of Al-6063 commercial alloy. J Mater Sci 2006;41:7361–73. https://doi.org/10.1007/s10853-006-0794-0.

[85] Wu Y, Liao H, Zhou K. Effect of minor addition of vanadium on mechanical properties and microstructures of as-extruded near eutectic Al-Si-Mg alloy. Materials Science and Engineering: A 2014;602:41–8. https://doi.org/10.1016/j.msea.2014.02.053.

[86] Okamoto H. Al-V (Aluminum-Vanadium). J Phase Equilibria Diffus 2012;33:491. https://doi.org/10.1007/s11669-012-0090-4.

[87] Zhu S, Yao JY, Sweet L, Easton M, Taylor J, Robinson P, et al. Influences of nickel and vanadium impurities on microstructure of aluminum alloys. JOM 2013;65:584–92. https://doi.org/10.1007/S11837-013-0572-9/FIGURES/9.

[88] Bangyikhan K. Effects of Oxide film, Fe-rich phase, Porosity and their Interactions on Tensile Properties of Cast Al-Si-Mg Alloys. PhD thesis, University of Birmingham, 2005.

[89] Dhinakar A, Lu PY, Tang NK, Chen JK. Iron Reduction in 356 Secondary Aluminum Alloy by Mn and Cr Addition for Sediment Separation. International Journal of Metal Casting 2021;15:182–92. https://doi.org/10.1007/s40962-020-00433-2.

[90] Park JM. Behaviours of Bifilms in A356 Alloy during Solidification: Developing Observation Techniques with 3D Micro X-ray Tomography. Engineering 2009:97.

[91] Callegari B, Lima TN, Coelho RS. The Influence of Alloying Elements on the Microstructure and Properties of Al-Si-Based Casting Alloys: A Review. Metals (Basel) 2023;13:1174. https://doi.org/10.3390/met13071174.

[92] Zhou Y. Solidification behaviour of Fe-rich intermetallic compounds in aluminium alloys. PhD thesis, Brunel University London, 2018.

[93] Peng L, Zeng G, Su TC, Yasuda H, Nogita K, Gourlay CM. Al8Mn5 Particle Settling and Interactions with Oxide Films in Liquid AZ91 Magnesium Alloys. JOM 2019;71:2235–44. https://doi.org/10.1007/s11837-019-03471-2.

[94] Cao X, Sauders N, Campbell J. Effect of iron and manganese contents on convection-free precipitation and sedimentation of primary a-Al(FeMn)Si phase in liquid Al-11.5Si-0.4Mg alloy. J Mater Sci 2004;39:2303–14. https://doi.org/10.1023/B.

[95] Lazaro-Nebreda J, Patel JB, Chang ITH, Stone IC, Fan Z. Solidification processing of scrap Al-alloys containing high levels of Fe. IOP Conf Ser Mater Sci Eng 2019;529. https://doi.org/10.1088/1757-899X/529/1/012059.

[96] Li T, Davies J, Luo D. Consumption of entrained gases within bifilms during a Mg-alloy casting process. METALLURGICAL AND MATERIALS TRANSACTIONS B 2021;52 (5):3093–106. https://doi.org/10.1007/s11663-021-02237-z.

[97] Friedrich B, Kräutlein C, Krone K. Melt treatment of Copper and Aluminium-The complex step before casting. Proceedings of the International Conference on Continuous Casting of Non-Ferrous Metals 2005:1–22.

[98] El-Sayed MA. The behaviour of bifilm defects in cast Al-7Si-Mg alloy. PLoS One 2016;11. https://doi.org/10.1371/journal.pone.0160633.

[99] Samuel AM, Samuel E, Songmene V, Samuel FH. A Review on Porosity Formation in Aluminum-Based Alloys. Materials 2023;16:2047. https://doi.org/10.3390/ma16052047.

[100] Ebhota WS, Jen T-C. Intermetallics Formation and Their Effect on Mechanical Properties of Al- Si-X Alloys. Intermetallic Compounds - Formation and Applications, InTech; 2018. https://doi.org/10.5772/intechopen.73188.

[101] Mathew J, Remy G, Williams MA, Tang F, Srirangam P. Effect of Fe Intermetallics on Microstructure and Properties of Al-7Si Alloys. JOM 2019. https://doi.org/10.1007/s11837-019-03444-5.

[102] Campbell J. Castings 2nd ed. Butterworth-Heinemann, Oxford; 2001.

[103] Divandari Mehdi, Campbell John. A new technique for study of aluminum oxide films 2000;2:233–8.

[104] Mashifana T, Sithole T. Recovery of Silicon Dioxide from Waste Foundry Sand and Alkaline Activation of Desilicated Foundry Sand. Journal of Sustainable Metallurgy 2020;6:700–14. https://doi.org/10.1007/s40831-020-00303-5.

[105] Campbell J. The origin of griffith cracks. Metallurgical and Materials Transactions B: Process Metallurgy and Materials Processing Science 2011;42:1091–7. https://doi.org/10.1007/S11663-011-9575-5/FIGURES/6.

[106] Lin B, Li H, Xu R, Xiao H, Zhang W, Li S. Effects of Vanadium on Modification of Iron-Rich Intermetallics and Mechanical Properties in A356 Cast Alloys with 1.5 wt.% Fe. J Mater Eng Perform 2019;28:475–84. https://doi.org/10.1007/s11665-018-3798-4.

[107] Raghavan V. Al-Si-V (Aluminum-Silicon-Vanadium). J Phase Equilibria Diffus 2013;34:39–42. https://doi.org/10.1007/s11669-012-0160-7.

[108] Ponweiser N, Paschinger W, Ritscher A, Schuster JC, Richter KW. Phase equilibria in the Al- Mo-Si system. Intermetallics (Barking) 2011;19:409–18. https://doi.org/10.1016/j.intermet.2010.11.010.

[109] Ding Z, Brouwer JC, Kwakernaak C, Hermans MJM, Popovich V, Quadakkers WJ, et al. Selective oxidation of aluminium in Mo(Al,Si)2. Corros Sci 2023;211. https://doi.org/10.1016/j.corsci.2022.110884.

[110] Nanko M, Kitahara A, Ogura T, Kamata H, Maruyama T. Formation of Mo(Si, Al) 2 layer on Mo dipped in Al melt saturated with Si and the effects of transition metals added in the melt. Intermetallics (Barking) 2001;9:637–46.

[111] Systems B, Equilibria TP. Al-Mo-Si (Aluminum-Molybdenum-Silicon) 2012;33:329–33. https://doi.org/10.1007/s11669-012-0069-1.

[112] Angermann H, Van Der Biest O, Froyen L. INVESTIGATION OF THE AL UMINIUM-RICH CORNER IN THE Al-Si-W PHASE DIAGRAM. Scripta Metallurgica et Materialia 1995;32:1423– 8.

[113] Qin R, Yan RF, Guan ZP, Zhang GQ, Song JW, Ren MW, et al. Effect of vanadium on Fe-rich phase, mechanical properties and thermal conductivity of hypoeutectic Al-Si alloy. Mater Res Express 2021;8. https://doi.org/10.1088/2053-1591/abe5f0.

[114] Raiszadeh R, Griffiths WD. A method to study the history of a double oxide film defect in liquid aluminum alloys. Metallurgical and Materials Transactions B: Process Metallurgy and Materials Processing Science 2006;37:865–71. https://doi.org/10.1007/BF02735007.

[115] Gagnon D, M. Samuel A, H. Samuel F, H. Abdelaziz M, W. Doty H. Melt Treatment-Porosity Formation Relationship in Al-Si Cast Alloys. Casting Processes and Modelling of Metallic Materials 2021;113. https://doi.org/10.5772/intechopen.94595.

[116] Ibrahim M. Effects of Be, Sr, Fe and Mg interactions on the microstructure and mechanical properties of aluminum based aeronautical alloy. PhD thesis, University of Quebec at Chicoutimi , 2015.

[117] Taylor JA. Iron-Containing Intermetallic Phases in Al-Si Based Casting Alloys. Procedia Materials Science 2012;1:19–33. https://doi.org/10.1016/J.MSPRO.2012.06.004.

[118] Lazaro-Nebreda J, Patel JB, Chang ITH, Stone IC, Fan Z. Solidification processing of scrap Al-alloys containing high levels of Fe. IOP Conf Ser Mater Sci Eng 2019;529. https://doi.org/10.1088/1757-899X/529/1/012059.

[119] Zhang L, Gao J, Damoah LNW, Robertson DG. Removal of iron from aluminum: A review. Mineral Processing and Extractive Metallurgy Review 2012;33:99–157. https://doi.org/10.1080/08827508.2010.542211.

[120] Cao X, Campbell J. OXIDE INCLUSION DEFECTS IN Al-Si-Mg CAST ALLOYS. Canadian Metallurgical Quarterly 2005;44:435–48. https://doi.org/10.1179/CMQ.2005.44.4.435.

[121] Li C, Gökelma M, Dang T, Huang J, Huang C, Li J, et al. Assessment of Melt Cleanliness of Secondary 5000 Aluminum Alloy Via Non-metallic Inclusions Characterization. Metallurgical and Materials Transactions B: Process Metallurgy and Materials Processing Science 2023;54:578–92. https://doi.org/10.1007/S11663-022-02710-3/FIGURES/14.

[122] Hu B, Li D, Ying T, Yu N, Zeng X. Oxidation mechanism of molten Al–5Mg–2Si–Mn alloy. J Mater Sci 2020;55:12554–67. https://doi.org/10.1007/s10853-020-04874-2.

[123] Dichtl HJ. Use of molybedenum to compensate for the adverse effect of iron in aluminium-silicon alloys. Aluminium 1970;46(5):362–4.

[124] Borgonovo C, Apelian D, Makhlouf MM. Aluminum nanocomposites for elevated temperature applications. JOM 2011;63:57–64. https://doi.org/10.1007/s11837-011-0030-5.

[125] Khrustalyov A, Kakhidze N, Platov V, Zhukov I, Vorozhtsov A. Influence of Tungsten Nanoparticles on Microstructure and Mechanical Properties of an Al-5%Mg Alloy Produced by Casting. Metals (Basel) 2022;12:989. https://doi.org/10.3390/MET12060989.

[126] Huber B, Effenberger HS, Richter KW. Phase equilibria in the Al-Si-V system. Intermetallics (Barking) 2010;18:606–15. https://doi.org/10.1016/j.intermet.2009.10.016.

[127] Cao X, Campbell J. Effect of melt superheating on convection-free precipitation and sedimentation of primary α-Fe phase in liquid al-11.5Si-0.4Mg alloy. International Journal of Cast Metals Research 2003;15:595–608. https://doi.org/10.1080/13640461.2003.11819546.

[128] Cao X, Campbell J. The solidification characteristics of Fe-rich intermetallics in Al-11.5Si-0.4Mg cast alloys. Metallurgical and Materials Transactions A 2004;35:1425–35. https://doi.org/10.1007/s11661-004-0251-0.

[129] Gyarmati G, Bogoly L, Stawarz M, Fegyverneki G, Kéri Z, Tokár M, et al. Grain Refiner Settling and Its Effect on the Melt Quality of Aluminum Casting Alloys. Materials 2022;15. https://doi.org/10.3390/ma15217679.

[130] Arya SM, Griffiths WD. Aluminum Nitride in Al–Si–Mg Alloy. Metallurgical and Materials Transactions B: Process Metallurgy and Materials Processing Science 2023;54:1965–84. https://doi.org/10.1007/s11663-023-02810-8.

[131] Campbell J. Entrainment defects. Materials Science and Technology 2006;22:127–45. https://doi.org/10.1179/174328406X74248.

[132] J. Campbell. Casting 2nd ed. Butterworth-Heinemann, Oxford 2001:pp.17-67. https://books.google.co.uk/books?hl=en&lr=&id=8yqaLGr-bIgC&oi=fnd&pg=PP1&ots=ClTMiSMU2T&sig=R_c3kEtsLM7T_XQN80Xwub6_cTg&redir_esc=y#v=onepage&q&f=false (accessed August 19, 2022).

Appendix A

University of Birmingham

Title: Aluminum Nitride in Al-Si-Mg alloy

Samira M. Arya and W. D. Griffiths

Corresponding author: Samira Moghadam Arya
PhD Student with the School of Metallurgy and Materials, College of Engineering and Physical Sciences,
University of Birmingham, Edgbaston, Birmingham,
United Kingdom. B15 2TT [redacted]
Email: [redacted]

Co-author: Dr W. D. Griffiths
Associated Professor lecturer School of Metallurgy and Materials, College of Engineering and Physical Sciences,
University of Birmingham, Edgbaston, Birmingham,
United Kingdom. B15 2TT [redacted]
Email: [redacted]

Aluminum Nitride in Al-Si-Mg alloy

Samira Moghadam Arya and W. D. Griffiths.
School of Metallurgy and Materials, College of Engineering and Physical Sciences, University of Birmingham, Edgbaston, Birmingham, United Kingdom, B15 2TT. Corresponding author: Samira Moghadam Arya

Abstract

When liquid aluminum is exposed to air, an oxide layer instantaneously forms on the surface of the melt, which, when enfolded, becomes a double oxide film defect (bifilm), producing entrained air pockets forming voids, cracks, and areas of stress. Studies of the reactions between the air trapped inside the bifilms and the surrounding melt have produced reaction products such as AlN.

In this study, examination of the fracture surfaces of an Al-7Si-0.3Mg (2L99) as-cast alloy revealed AlN apparently of a different "nodular" morphology of approximately 15 µm in length. In contrast to the "feather-shaped" AlN morphology grown through holding in nitrogen or the addition of Mo to 2L99 observed in previous research, the observed nodular morphology in this study was thought to be less permeable. This confirmed the hypothesis of Nyahumwa, Green and Campbell (1998), who suggested that the entrapped air in bifilms can react with the surrounding liquid melt by initially consuming oxygen to form oxides, such as spinel ($MgAl_2O_4$), followed by the consumption of the nitrogen to form AlN. The AlN observed has been proposed to reduce the size of bifilms and correspondingly improve the mechanical properties of the alloy. In this work, AlN was also grown by holding alloys in a controlled nitrogen gas environment at 850°C at various holding times to reveal AlN morphologies.

Keywords— Aluminum alloys, AlN morphology, double oxide film defects, sand casting.

I. Introduction

Aluminum alloys are widely used in the aerospace and automotive industries owing to their castability and high strength-to-weight ratio. During the casting process, liquid Al reacts with air to create a surface oxide layer almost instantaneously. Provided the oxide layer stays at the surface, it can be seen as beneficial as it protects the bulk liquid metal from further reaction. However, with any surface turbulence of the melt, the surface oxides can be entrained into the bulk liquid forming double oxide film defects (bifilms) containing air or other mold gases [131,132] (see Figure 1). The internal surfaces of the bifilms form as dry-side to dry-side crevices in the final casting, reducing the mechanical properties, fatigue, and areas of stress concentration [131,132].

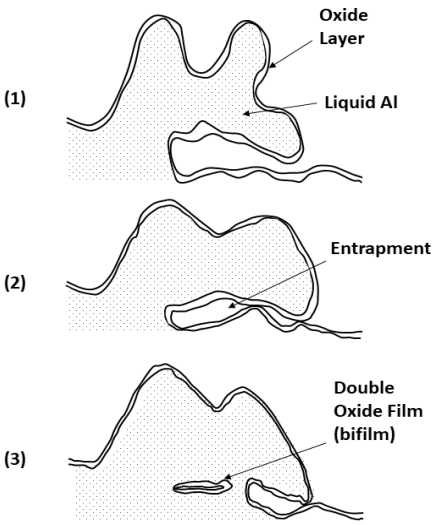


Fig. 1- Sketch of an oxide layer leading to entrapment and bifilms in Al melt. Reprinted from [131,132].

Nyahumwa et al. [131,132] studied the effects of surface turbulence during casting on the fatigue life of cast A356 (Al-7Si-Mg) commercial aluminum alloy, suggesting that the gradual consumption of the entrapped gases (air) in the bifilms was caused by the reaction of internal gases with the surrounding liquid metal, as shown in Figure 2. They proposed that, initially, oxygen was consumed by reaction with the liquid metal to give spinel, followed by the reaction between the liquid metal and the entrapped N_2 to form AlN.

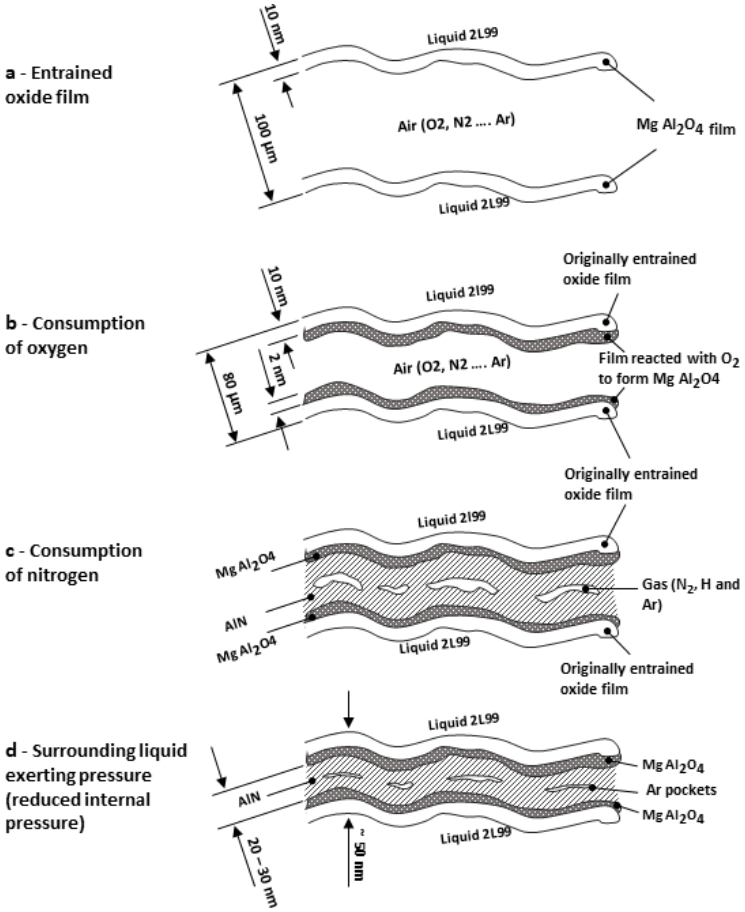


Fig. 2-Nyahumwa sketch of the conception of gases inside the bifilm in 2L99 alloy. Reprinted with permission from [131,132].

Apart from alumina, spinel and MgO, AlON is a possible phase. However, Figure 3 shows a eutectoid Al_2O_3–AlN phase diagram [131,132]. The phase diagram shows that AlON is not to be expected to occur at temperatures below 1640 °C [131,132]. At room temperature, AlON is not stable and only occurs at extremely restricted pressures of O and N of approximately 10^{-10} bar [131,132].

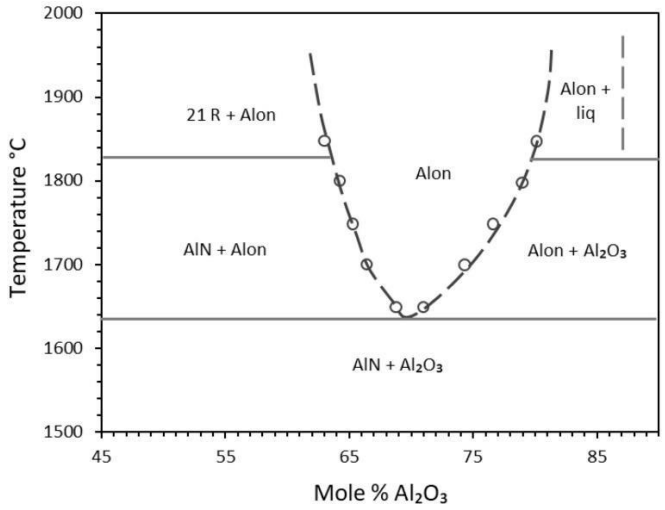


Fig. 3-Phase diagram of eutectoid Al_2O_3-AlN reprinted from [131,132]

Nyahumwa et al. [131,132] further suggested that the phase transformation of alumina from ɣ to α-alumina could cause a 24 % reduction in the oxide volume and consequently cause a rupture of the oxide surface of the bifilm.

Impey et al. [131,132] reported that the phase transformation from ɣ to α-alumina largely depended on the presence of water vapor associated with the humidity of the air and time. They reported that oxidation starts immediately, and the rate of oxidation reduces to a lower rate after 30 - 60 minutes. However, after approximately 5 hours, the breakaway transformation from gamma to alpha alumina occurs following hydrogen absorption, which leads to the natural removal of hydroxyl ions that function as a stabilizer for gamma alumina. The transformation is reported by Impey et al. [131,132] to continue for up to 24 hours and is more pronounced in dry air [131,132]. El Sayed et al. [131,132] studied the rate of consumption of the gases inside air bubbles in various alloys. They claimed that the type of oxide, which was in turn defined by the alloy composition, affected the consumption rate of oxygen and nitrogen and the rate of hydrogen diffusion into the bifilm. The time estimated for the consumption of O and N in a bifilm defect in Al-5Mg alloy was reported to be approximately 6 minutes, 9 minutes for CP-Al and 25 minutes for 2L99, respectively [131,132].

The consumption of the internal gases proposed by Nyahumwa et al. [131,132] was thought to begin a reaction with oxygen, forming Al_2O_3 in the case of pure Al, $MgAl_2O_4$ in the case of 2L99, or MgO in the case of Al-5Mg alloy, followed by nitrogen to form AlN. El Sayed et al. [131,132] observed granular (described by them as nodular) AlN structures in CP-Al (held for 40 minutes) and 2L99 (held for 32 minutes) at 720 °C, as shown in Figures 4(a) and (b). Figures 4(c) and (d) show the EDX spectra, respectively. It was also reported that hydrogen might diffuse into the entrapped bifilm defects during their residence in the melt [131,132].

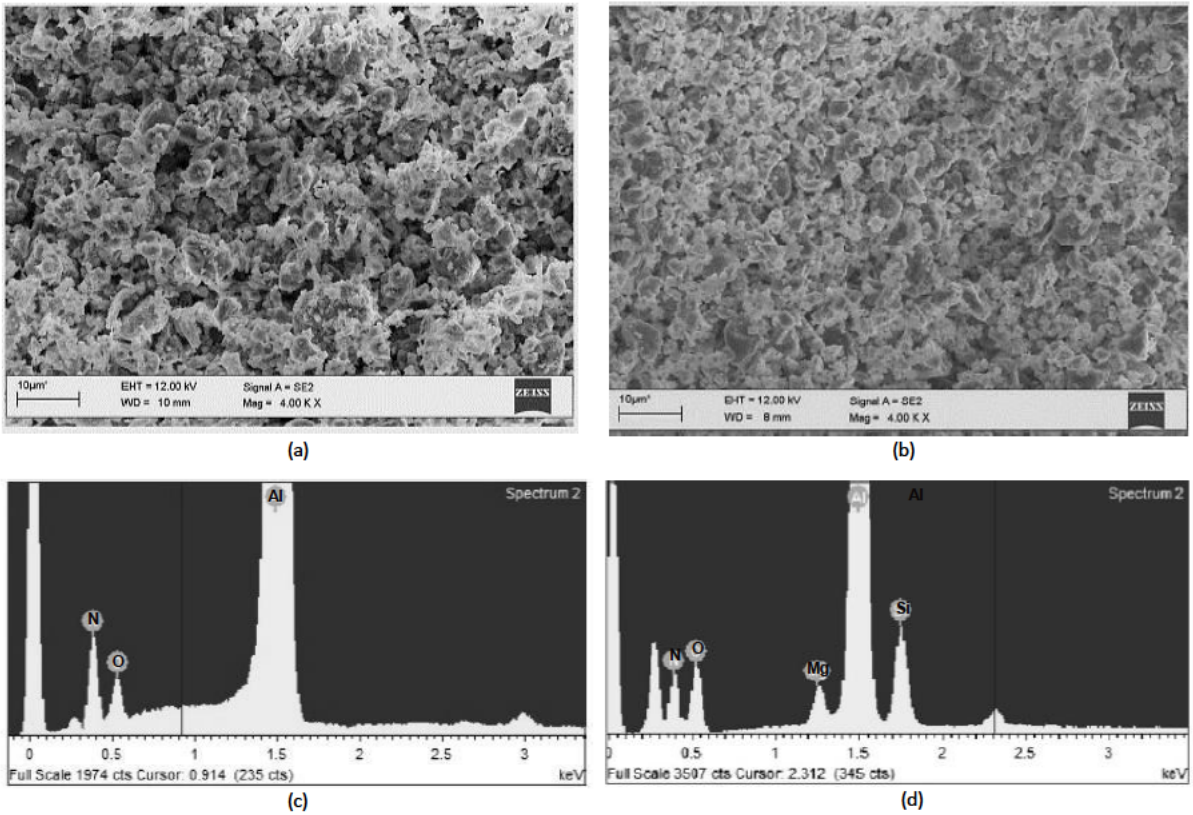


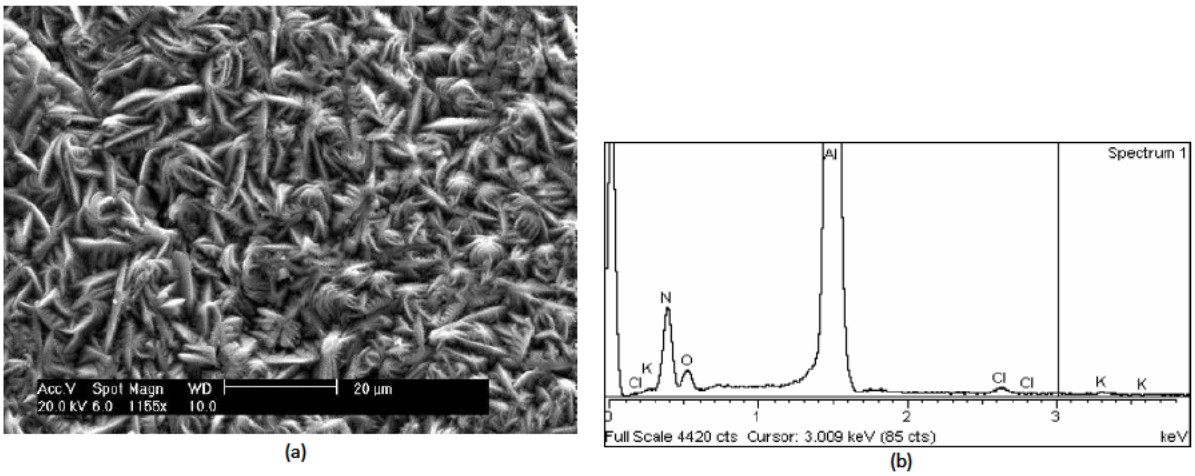
Fig. 4-(a) SEM micrograph shows granular AlN on CP-Al after 40 minutes holding time (b) SEM micrograph of granular AlN on 2L99 after 32 minutes holding time (c) and (d) EDX spectrum of Figures 4(a) and 4(b). Reprinted from [131,132]

It is worth noting that aluminum nitride can form when liquid Al is reacted directly with nitrogen gas (Equation (1)) in the production of a reinforced Metal Matrix Composite (MMC), obtained by blowing N gas into the melt at a pre-determined rate [131,132].

Equation (1) $2Al + N_2 \rightarrow 2AlN$

Zheng et al. [131,132] reported having formed smaller than 10 µm spherical dendritic AlN particles by bubbling N_2 directly into a pure Al melt for 6 hours at 1200°C.

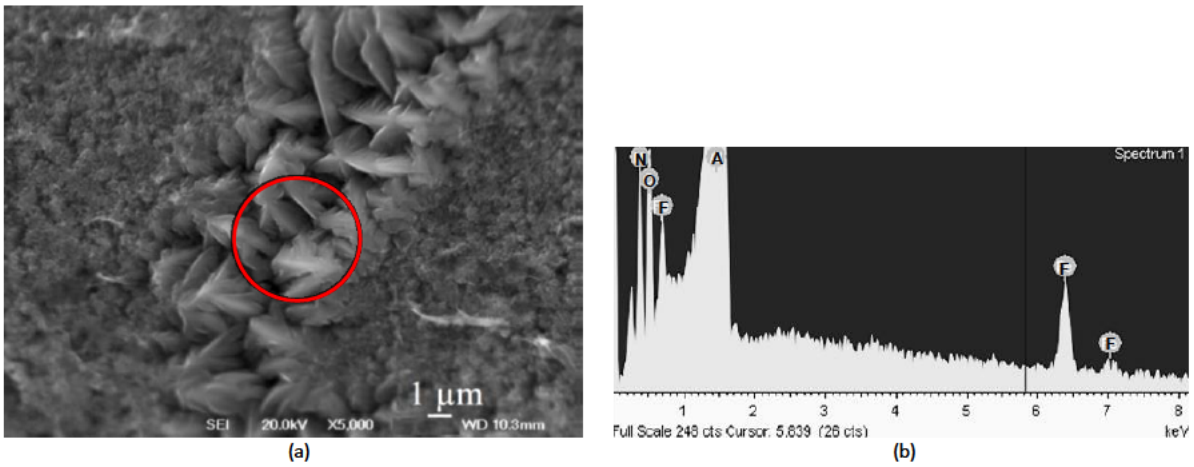
Raeiszadeh and Griffiths [131,132] studied the reaction rate of a trapped air bubble in pure (CP) liquid Al, using real-time x-ray radiography to record changes in the volume of air when in contact with liquid Al at 850 °C. They concluded that all O was consumed within about the first 4 hours, followed by complete consumption of N for a further 4 hours (8 hours in total), forming feather-like nitrides of approximately 10 µm in length. Figure 5(a) shows an SEM micrograph of the AlN layer, and Figure 5(b) shows an EDX spectrum of the whole area of Figure 5(a).



(a) (b)

Fig. 5-(a) SEM micrograph of feather AlN layer (b) EDX spectrum of the whole area of figure 5(a). Reprinted from [131,132]

Gerrard et al. [131,132] also observed feather-shaped AlN on CP-Al, by first degassing a LECO sample to remove existing hydrogen from the metal, followed by heating the sample to above its melting point at 700 °C and holding it for 15 minutes in a nitrogen atmosphere, as shown in Figure 6(a). Figures 6(b) shows an EDX analysis of Figure 6(a). The composition of spectrum1 showed the presence of oxides at 5 wt pct, nitrides at 12 wt pct and Fe at 2 wt pct[131,132].



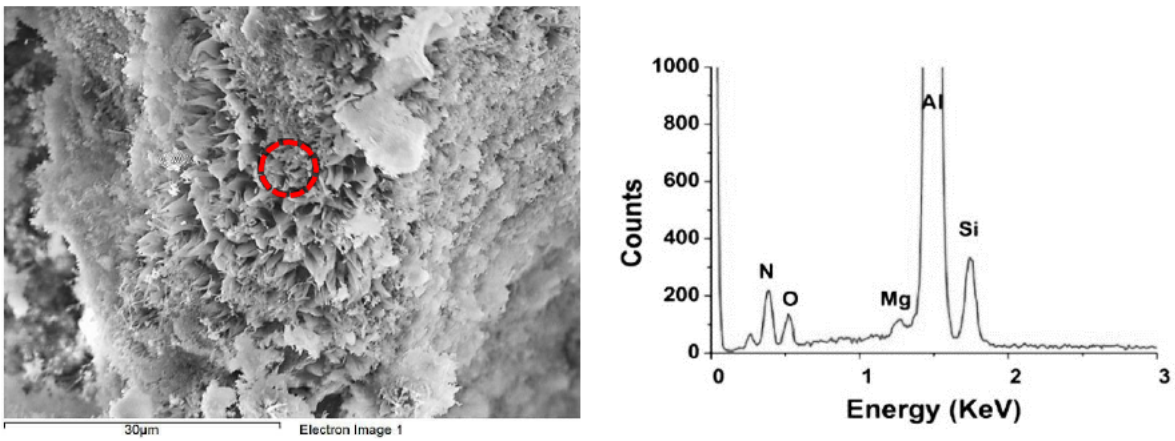
(a) (b)

Fig. 6-(a) SEM micrograph of feather shaped AlN layer (b) EDX spectrum of the Figure 6(a). Reprinted from [131,132] under the terms of Creative Commons CC-BY license.

Griffiths et al. [131,132] studied the fracture surfaces of CP-Al, and Al-5Mg alloy and observed the whisker structure of alumina and magnesium oxide inside pores after 20 minutes of melt holding time. Their study suggested that the whisker shapes could have been formed due to the evaporation of oxides within the pores, followed by condensation. Chen and Griffiths [131,132] also observed feather-shaped AlN, of about 14 µm thickness, on the fracture surface of 2L99+0.4 wt pct Mo alloy, cast at 730°C, followed by a T6 heat treatment. They reported that, with the addition of 0.4 wt pct Mo to 2L99 alloy, the Weibull modulus of the Ultimate Tensile Strength (UTS) was increased from 277 MPa to 304 MPa, and %Elongation increased from 2.1 % to 3.6 %.

The feather-shaped AlN morphology shown in Figure 7(a) was considered to be permeable, which could promote the consumption of the entrapped gases leading to a reduction in the sizes of the bifilms. As a result, a certain degree of bonding between the two un-wetted oxide surfaces might then occur, thereby improving the mechanical properties of the alloy. Figure 7(b) shows the EDX spectrum of the area marked in Figure 7(a). The

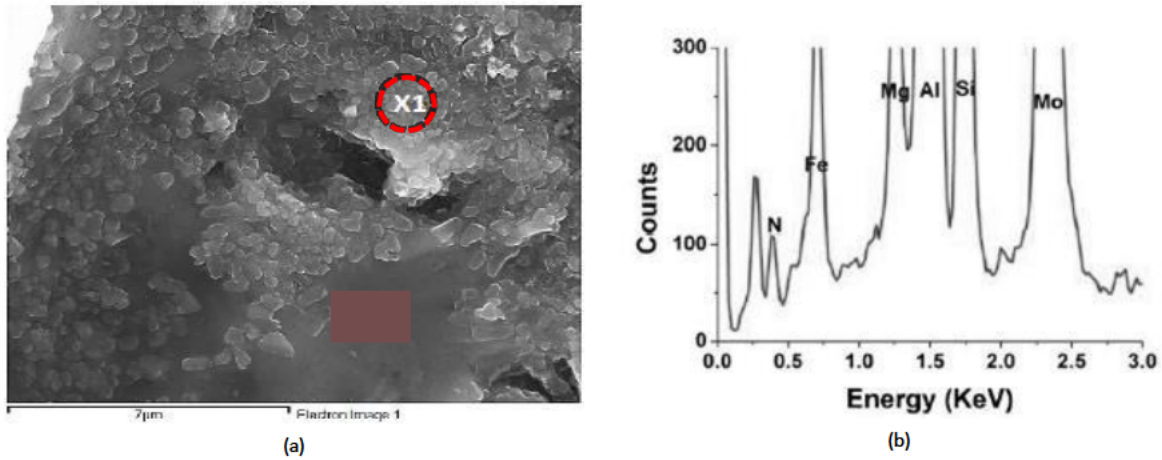
EDX analysis of this area showed the presence of O at 9 at pct, N at 36 at pct, Si at 5 at pct, Al at 49.6 at pct and Mg at 0.4 at pct.



(a) (b)

Fig. 7-(a) SEM micrograph of nitride on the fracture surface of un heat treated 2L99+ 0.4 wt pct Mo alloy (b) EDX spectrum and of the marked area in Figure 7(a). Reprinted from [131,132]

A granular AlN structure was also reported by Chen and Griffiths on the surface of 2L99+0.4 wt pct Mo alloy using a trapped air bubble experiment. The sample was held for 1 hour at 725 °C (as shown in figure 8(a)). The granular AlN structure shown in Figure 8(a) contrasts with the feather-shaped morphology presented in Figure 7(a) and may be considered impermeable. Figure 8(b) shows the EDX spectrum for the area marked X1 in Figure 8(a).



(a) (b)

Fig. 8-(a) SEM micrographs of granular nitride layer on the surface of 2L99+ 0.4 wt pct Mo alloy, sample from the bubble-growth experiment. Figures 8(b) EDX spectra of the marked area in Figures 8(a). Reprinted from [131,132]

Wang and Fan [131,132] reported the characterization of nitride particles formed in CP-Al at 750°C and 850°C, as shown in Figures 9(a) and (b). Their characterization was conducted using analytical electron microscopy on samples derived from a pressure melt filtration technique using a Prefil-Footprinter device. The EDX spectra are presented in Figure 9(c) for all particles marked in Figures 9(a) and (b). The morphology of the observed AlN particles was that of short (1µm) rod-shaped objects, measured to be 104 nm and 375 nm in width and length, respectively. The observed AlN particles were described as hexagonal wurtzite AlN with a close-packed plane [131,132]. Based on Figures 9(a) and (b), it might be concluded that the AlN particles may have nucleated on an oxide film.

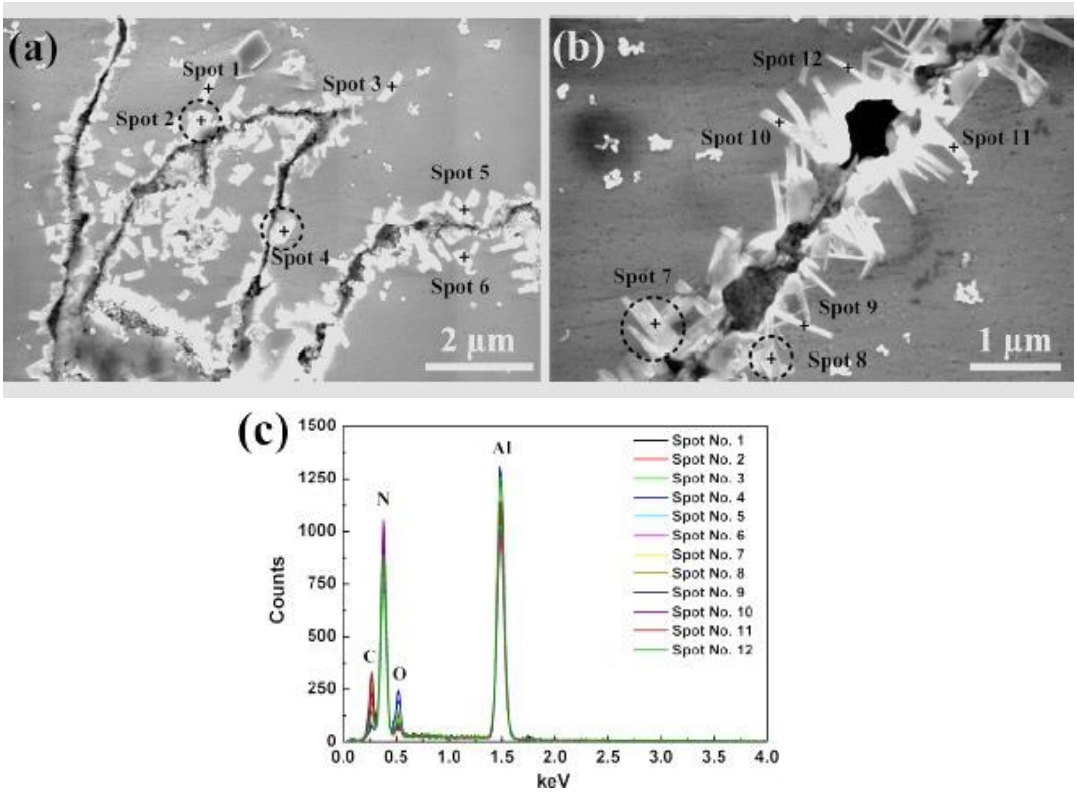


Fig. 9-(a) SEM micrograph of nitride inclusion particles held at (a) 750°C and (b) 850°C (c) the EDX spectrum of the marked areas and points in (a) and (b). Reprinted from [131,132]

Based on the crystallography of the observed AlN particles, they calculated the lattice matching potency of the particles as a nucleating substrate for α-Al grains, using Equations (2) and (3).

Equation (2) $fr = rAl - rp * \frac{1}{rp} \times 100pct,$

Equation (3) $fd = dAl - dp * \frac{1}{dp} \times 100pct,$

Where rAl and rp are the interatomic spacings along the most close-packed directions, and dAl and dp are the interplanar spacings of the most close-packed planes of Al, oxides, borides and AlN. fr represents the interatomic spacing misfit, and fd represents the interplanar misfit of close-packed planes. Wang and Fan [131,132] calculated that the interatomic spacing misfit (see Table I) with the close-packed directions of the close-packed planes between AlN and Al was 6.66 pct, indicating that AlN was a reasonably potent nucleating substrate for α-Al grains, having an fr of less than 7%. However, comparing the size of AlN with oxide and boride particles ($MgAl_2O_4$, γ-Al_2O_3, TiB_2, α-Al_2O_3). Wang and Fan concluded that AlN particles were not as potent for nucleation as other particles in the melt [131,132].

Table I. Crystallographic data of Al, AlN and common oxides and borides at 660°C. Reprinted from [131,132]

Phase	*Structure*	*Lattice Parameter*		*Close-Packed Plane*	*Close-Packed Row*	$d_{(hkl)}(nm)$	fd *(Pct)*	$r_{[uvw]}nm$	fr *(Pct)*
		a	*C*						
Al	Cubic	0.4121	-	{111}	<110>	{111} 0.2379	N/A	0.2914	N/A
AlN	Hexagonal	0.3122	0.4992	{0001}	<2110>	{0002} 0.2496	4.67	0.3122	6.66
γ-Al_2O_3	Cubic	0.7963	-	{111}	<110>	{222} 0.2299	3.50	0.2815	3.50
α-Al_2O_3	Rhomb	0.4782	1.3057	{0001}	<1100>	{0006} 0.2176	9.33	0.2761	5.54
$MgAl_2O_4$	Cubic	0.8126	-	{111}	<110>	{222} 0.2346	1.43	0.2873	1.43
TiB_2	Hexagonal	0.3037	0.3237	{0001}	<2110>	{0001} 0.3237	26.49	0.3037	4.05

This research aimed to investigate further the presence of AlN in an as-cast alloy, specifically Al-7Si-0.3Mg (2L99) and to study its morphology in both as-cast and laboratory-produced samples under an atmosphere of nitrogen. Understanding the morphology and prevalence of AlN in relation to bifilms is crucial as it is thought to have a considerable effect on the behavior of bifilms, perhaps more so than in the case of oxides [131,132] through direct consumption of nitrogen or diffusion of hydrogen inside the bifilms. It is understood that this phenomenon has not been widely reported, and further research in this area is needed.

II. EXPERIMENTAL PROCEDURE

Initially, experiments were carried out to produce testbars cast in resin-bonded sand molds. The alloys used were based upon CP-AL, 2L99 alloy (Al-7Si-0.3Mg), 2L99 + 0.6 wt pct Mo, and 2L99 + 0.2 wt pct W reflecting the composition of alloys in which AlN had been detected in earlier work. The composition of the alloys has been shown in Table II, measured by a BRUKER S8 Tiger wavelength dispersive X-ray fluorescence (XRF) with a test duration of 7 minutes.

Table II. Composition of the 2L99, 2L99+0.6 wt pct Mo and 2L99+0.2 wt pct W alloy

Element Weight pct	*Mo*	*W*	*Mg*	*Si*	*Fe*	*Ti*	*Cu*	*Zn*	*Pb*	*Sn*	*Al*
2L99	0.00	0.00	0.3	9.8	0.03	0.14	0.00	0.00	0.00	0.00	Balance
2L99+0.6 wt pct Mo	0.64	0.00	0.32	8.55	0.06	0.11	0.00	0.00	0.00	0.00	Balance
2L99+0.2 wt pct W	0.00	0.21	0.29	9.42	0.14	0.00	0.00	0.00	0.00	0.00	Balance

Grade 60 silica sand and (0.6 wt pct resin (types 5112 and 5230) were used to make the sand molds. The running systems of the molds were deliberately badly-designed with a long-running bar, and no filters to both encourage the creation of bifilms in the testbars due to surface turbulence and air entrapment in the melt, as shown in Figure 10.

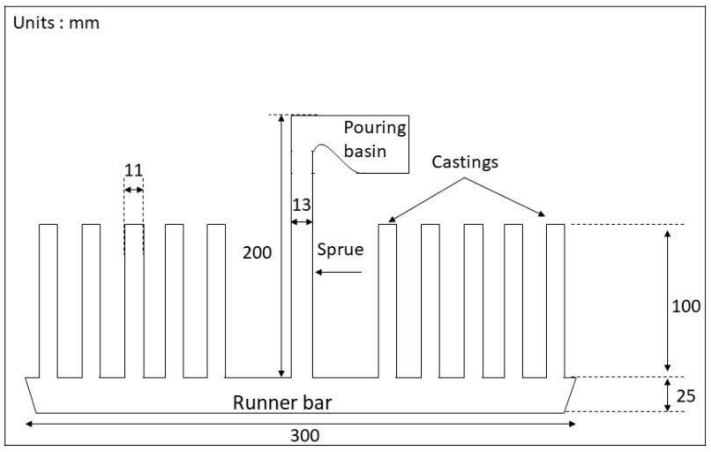


Fig. 10 - Sketch of the "badly-designed" running system. Reprinted from [131,132]

The sand molds were made two weeks before casting to allow the evaporation of solvents from the resin-bonded sand molds, reducing hydrogen pick-up and gas porosity in the castings. Alloying elements Mo and W were used based on previous research. Chen [131,132] reported that the addition of about 0.4 wt pct Mo and about 0.4 wt pct W, brought about a beneficial effect on the mechanical properties of the alloys; specifically, an improvement in the Weibull Modulus and a reduction in the scatter of measured UTS values [131,132]. This research reported in this paper aimed to determine the influence of Mo and W on AlN, if any.

Masteralloys of nominal compositions 2L99+10 wt pct Mo and 2L99+10 wt pct W were made by the addition of 200g of pure Mo, or 200g of pure W, to 1800g of 2L99 liquid metal carried out at a melt temperature of 1300°C, held for 40 minutes before pouring the masteralloy into a steel ingot mold.

Subsequently, 2 kg of 2L99 was melted in a C80 clay graphite crucible in a 175-kW induction furnace heated to 730°C. Ar lance degassing was applied for 20 minutes to decrease the hydrogen content of the melt to less than 0.1 mm^3/100g, measured using a Severn Science hydrogen gas analyzer. Testbars from the sand molds, of composition 2L99+0.6 wt pct Mo and 2L99+0.2 wt pct W, were then cast by the addition of the masteralloys, made as described above, to 2L99 liquid metal, with Ar lance degassing, cast at a melt temperature of 730°C.

Each casting provided ten testbars of composition 2L99, 2L99+0.6 wt pct Mo and 2L99+0.2 wt pct W. These were machined to a standard size of 100 mm in length, with a gauge length of 37 mm and 26 mm radius on the gauge length. Tensile strength tests were conducted on 2L99 samples using a Zwick tensile strength testing machine carried out at 1 mm/min strain rate. After breaking the 2L99 samples, each half of the broken testbar was cut 5 mm below the fracture surface and characterized using a Philips XL-30 FEG Environmental Scanning Electron Microscopy (SEM) equipped with an Inca Oxford Energy Dispersive X-ray (EDX). It was reasonable to assume that the fracture surfaces represented the area with the largest concentration of defects; however, an additional study of AlN morphology on fracture surfaces was carried out using a Focused Ion Beam (FIB), dual beam FIB- SEM, equipped with an Electron Dispersive X-ray.

In a separate experiment conducted to grow oxides and nitrides on CP-Al, 2L99, 2L99+0.6 wt pct Mo and 2L99+0.2 wt pct W, samples held in a melt (see Figure 11), cylindrical samples of diameter 15 mm and height 25 mm, were placed in a cylindrical sintered alumina crucible of 20 mm outer diameter, 16 mm inner diameter and 30 mm in height. The crucibles were then inserted into a custom-made vertically oriented cylindrical stainless steel tube designed to allow control of the atmosphere of the melt, (see Figure 11). The steel tube was placed inside a sealed vertical tube furnace, and the lid sealed with an O-ring and screws. An Inconel-sheathed Type-K

thermocouple (0.5 mm diameter) was inserted through a valve into the tube and positioned adjacent to the crucible. Nitrogen gas was fed through a high-pressure tube to an inlet valve at a flow rate of ~13 cm^3/min, while a high-pressure hose was connected to an outlet valve to discharge the nitrogen. The furnace was set to 850°C and then held for 15 minutes to stabilize its temperature. The sample was then held at various holding times of 1.5, 3, 6, 12 and 24 h, after which the sample was left in the furnace to cool. The unaltered top surfaces of the samples undergoing growth and as recovered from the furnace were characterized using SEM.

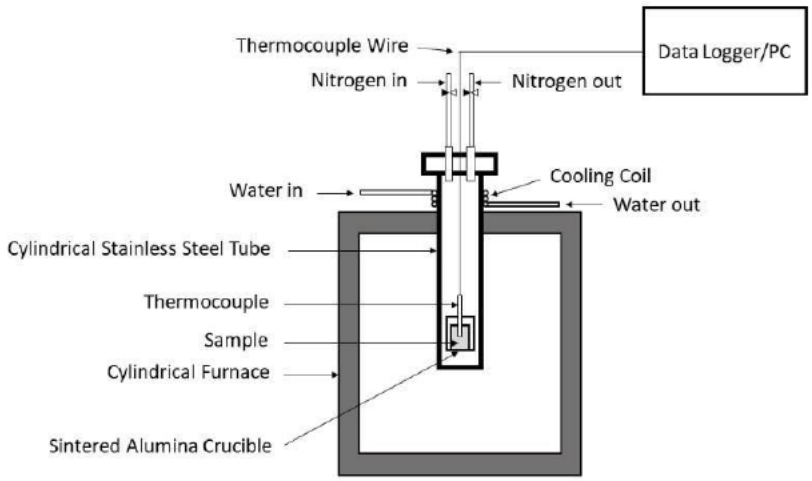
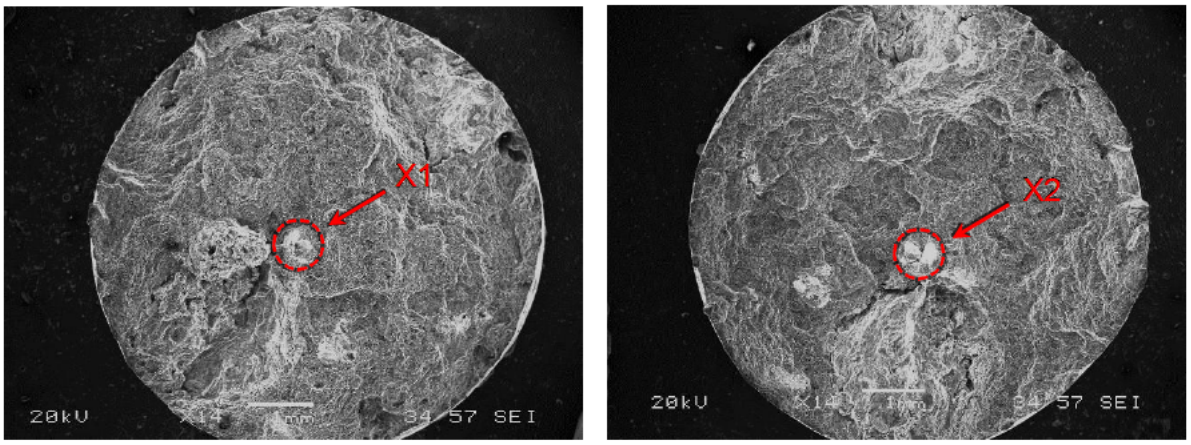


Fig. 11 – Nitrogen growth experiment set-up

III. Results

A. Characterization of 2L99 alloy at 730°C (as-cast) conditions

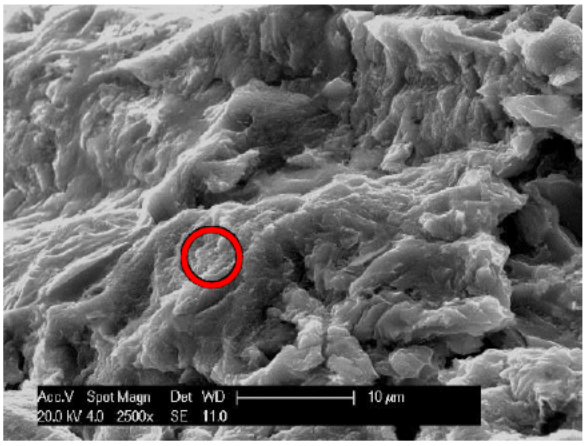
Figures 12(a) and (b) show two halves of a testbar fracture surface of as-cast 2L99 alloy observed using SEM at low magnification. As mentioned in the experimental procedure, each half of the broken testbar was cut 5 mm below the fracture surface. High magnification and EDX results of areas marked X1 and X2 in Figures 12(a) and (b) are shown in Figures 13 and 14. The fracture surfaces revealed the presence of 220 µm long bifilms, with small patches of aluminum nitrides of about 15 µm in length. This suggested symmetrical oxides and nitrides present on both halves of the fracture surfaces of the as-cast 2L99 alloy.



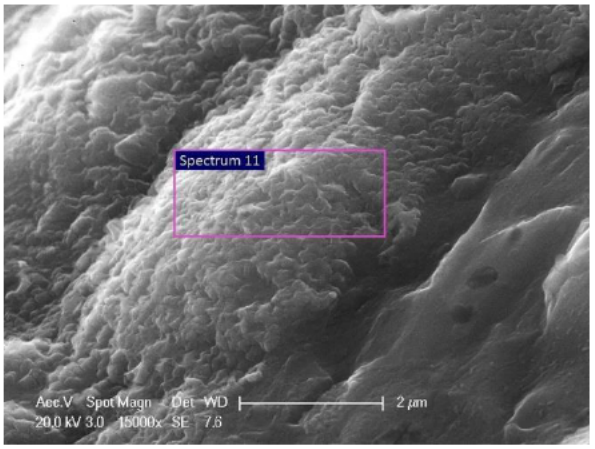
(a) (b)

Fig. 12-(a) and (b) Low magnification of SEM micrographs of two halves of fracture surfaces of as-cast 2L99 testbar, showing bifilm defects and nitrides at the marked areas X1 and X2.

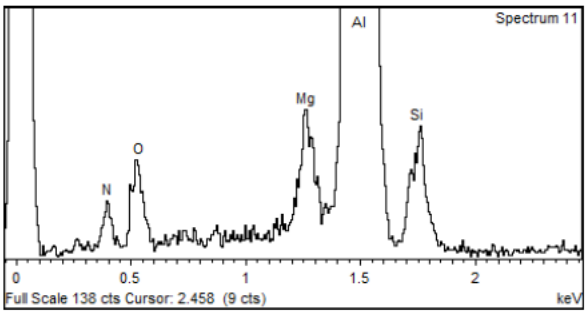
Figures 13(a) and (b) show the morphology and EDX quantification of nitride/oxide patches observed on a fracture surface of a 2L99 testbar (as marked in X1 in Figure 12(a)). The composition (Table III) for the marked area in Figure 13(b) confirms the presence of oxides at 14 at pct and nitrides at 20 at pct. The nitride patches had a nodular shape and covered approximately 15 µm of the fracture surface (Figure 13(b)).



(a)



(b)



(c)

Fig. 13-(a) and (b) show SEM micrograph of a layer of oxide and nitride on the fracture surface of as-cast 2L99 (c) EDX analysis of spectrum11 (the marked area) in Figure 13(b).

Table III. Quantification of the marked area (Spectrum11) in Figure 13(b)

Description	*Spectrum11 in Figure 13(b)*	
	Weight %	*Atomic %*
N	12.54	20.39
O	10.04	14.29
Mg	1.43	1.34
Al	71.98	60.73
Si	4.01	3.25

The area marked in Figure 14(a) shows the area of nitride on the other half of the testbar marked X2 in Figure 12(b). Figure 14(b) shows a high-magnification image of the same marked area in Figure 14(a). Figure 14(c) is the EDX spectrum, and Table IV shows the quantification of spectrum 2 marked in Figure 14(b).

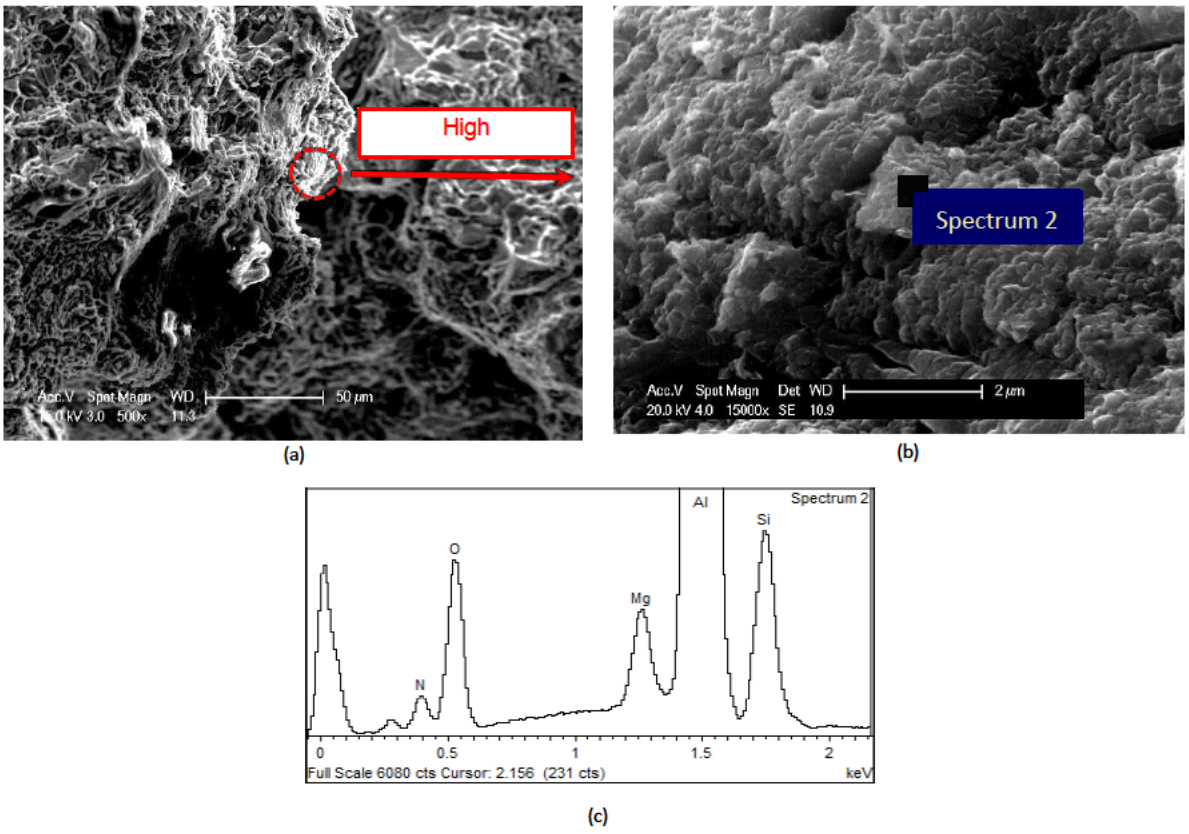
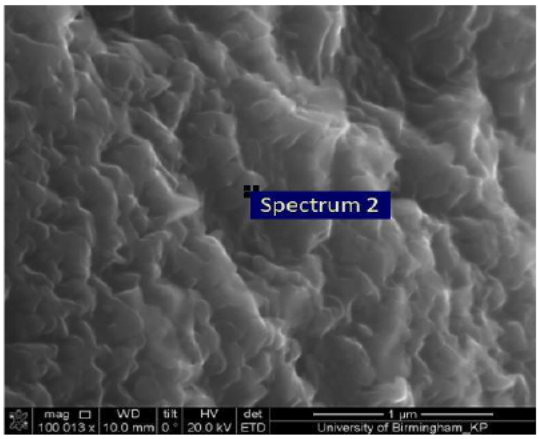


Fig. 14-(a) SEM micrograph showing a low magnification of the oxide layers and nitride on the fracture surface of 2L99 (as-cast condition) (b) higher magnification of SEM micrograph of the marked area in Figure 14(a), (c) EDX analysis of spectrum2 of the marked area in Figure 14(b).

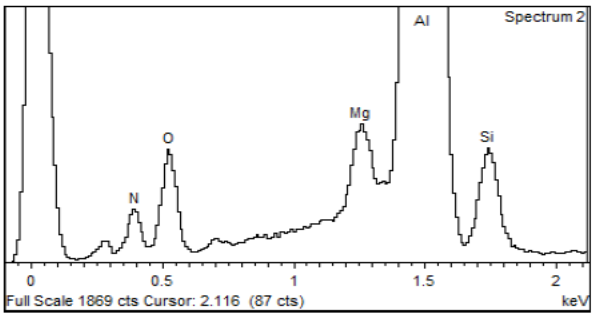
Table IV. Quantification of the market area (Spectrum 2) in Figure 14(b)

Description	*Spectrum 2 in Figure 14(b)*	
	Weight%	*Atomic %*
N	11.44	17.43
O	23.19	30.93
Mg	1.88	1.65
Al	56.25	44.49
Si	7.25	5.51

To more accurately define the shape and thickness of the nitride phases present on the fracture surface of the 2L99 alloy, the region represented in Figure 13(b) was investigated using FIB. Figure 15(a) displays a higher magnification of the nitride prior to milling, while Figure 16(a) shows the same area after milling, which was used to determine the nitride's thickness. This confirmed the nodular shape of AlN, where each nodule measured approximately 250 nm. Figure 14(b) shows the EDX analysis, and Table V shows the quantification of the spectrum2 for Figure 14(a).



(a)



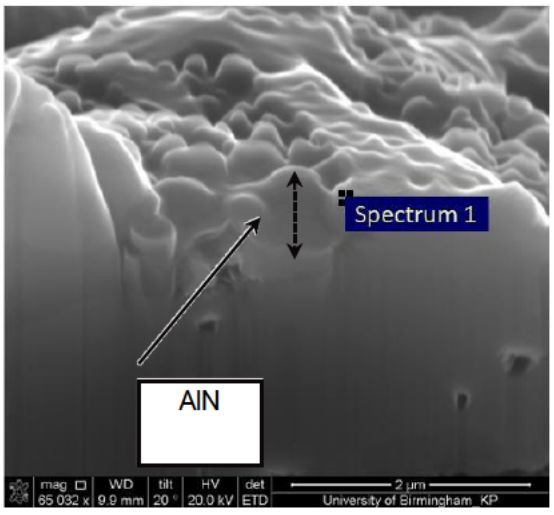
(b)

Fig. 15-(a) High magnification of SEM image of a nitride and oxide layer on the fracture surface of as-cast 2L99 and (b) EDX analysis of spectrum2

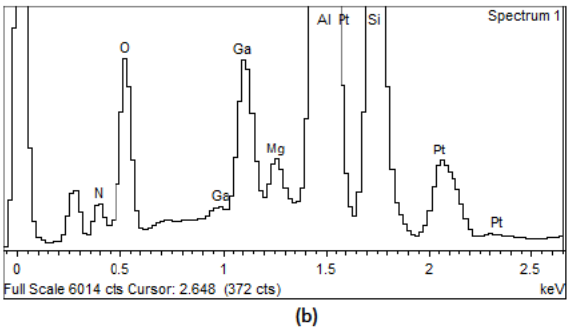
Table V. Quantification of the marked area (Spectrum 2) in Figure 15(b)

Description	*Spectrum2 in Figure 15(a)*	
	Weight %	*Atomic %*
N	10.93	17.95
O	10.53	15.13
Mg	1.02	0.96
Al	74.62	63.59
Si	2.90	2.38

Figure 16(a) shows the FIB cross-section of Figure 15(a). The thickness of the AlN layer was measured to be approximately 0.7 µm. Figure 16(b) shows an EDX analysis, and Table VI provides quantification of spectrum 1 as marked in Figure 15(a).



(a)



(b)

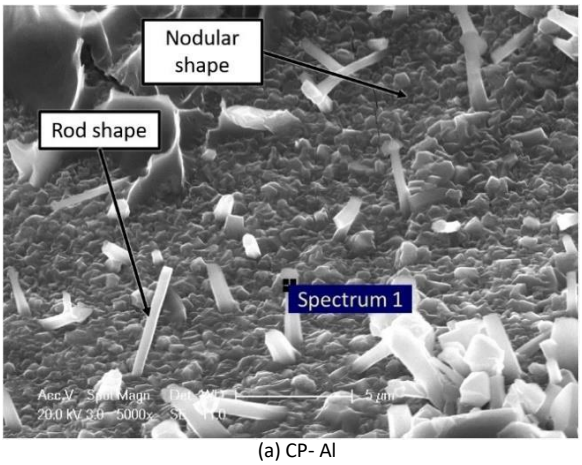
Fig. 16-(a) Cross-section of the nitride layer on the fracture surfaces of 2L99 (as-cast condition) without Pt coating (b) EDX analysis of Spectrum 1 showing both O and N as well as a small amount of Pt and Ga.

Table VI. Quantification of the marked area (Spectrum 1) in Figure 16(b)

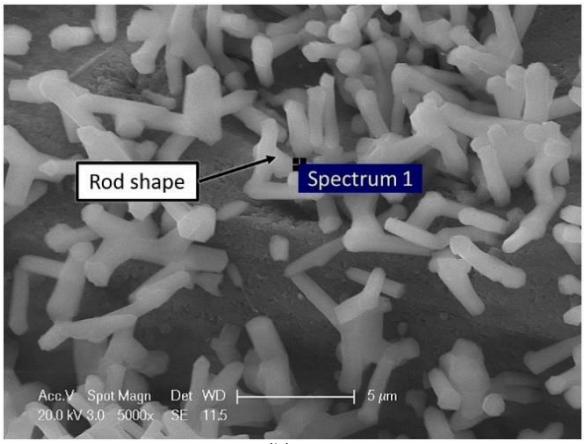
Description	*Spectrum1 in Figure 16(b)*	
	Weight%	*Atomic %*
N	10.93	17.95
O	10.53	15.13
Mg	1.02	0.96
Al	74.62	63.59
Si	2.90	2.38
Ga	4.33	1.50
Pt	7.00	0.87

B. AlN morphologies in the nitrogen growth experiment B1. Rod Shaped AlN

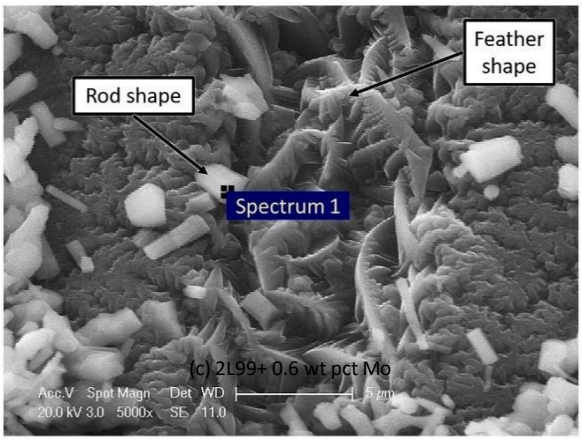
Figures 17(a) to 17 (h) show the micrographs and EDX spectra of rod-shaped nitrides with an average of 2 µm in width and about 6 µm in length. They were observed on the surfaces of all four different alloys, held for 24 hours in nitrogen gas. The largest rod shape, measured in CP-Al, was about 12 x 2 µm. Table VII shows the quantification of the spectra for Figures 17(a) to (d). The average dimensions of the rod-shaped AlN patches observed on the surface of the alloys examined were measured to be approximately 30 by 50 µm.



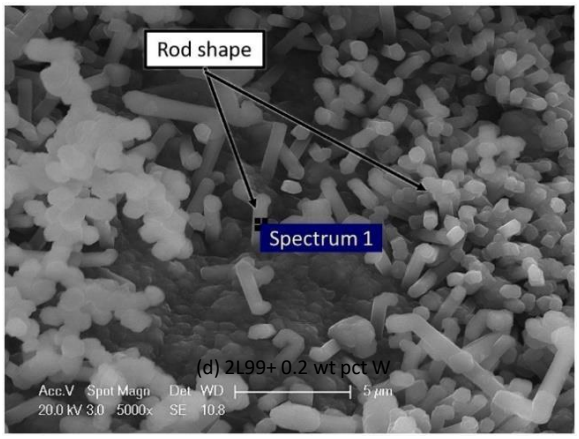
(a) CP- Al



(b) 2L99



(c) 2L99+ 0.6 wt pct Mo



(d) 2L99+ 0.2 wt pct W

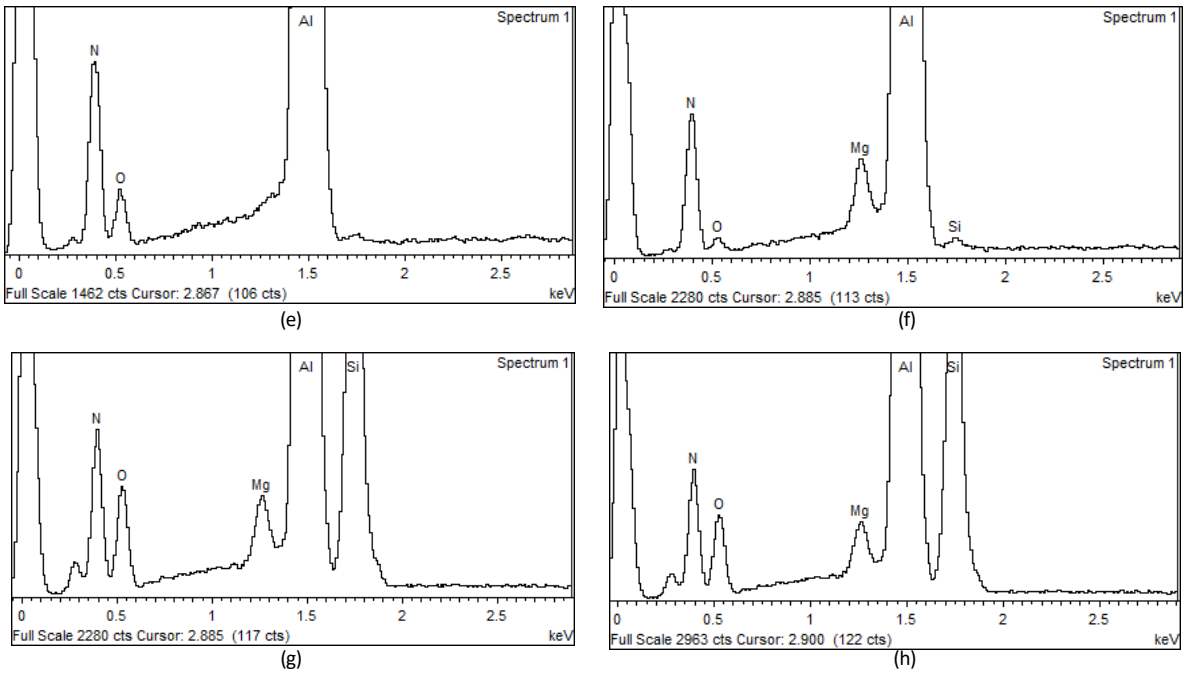


Fig. 17-(a) to (d) show SEM micrographs of rod-shaped AlN on the surface of CP- Al, 2L99 alloy, 2L99+0.6 wt pct Mo alloy and 2L99+0.2 wt pct W alloy, respectively with 24 hours holding time in N at 850°C. Figures 17(e) to (h) are the EDX spectra for the marked areas shown in Figures 17(a) to (d).

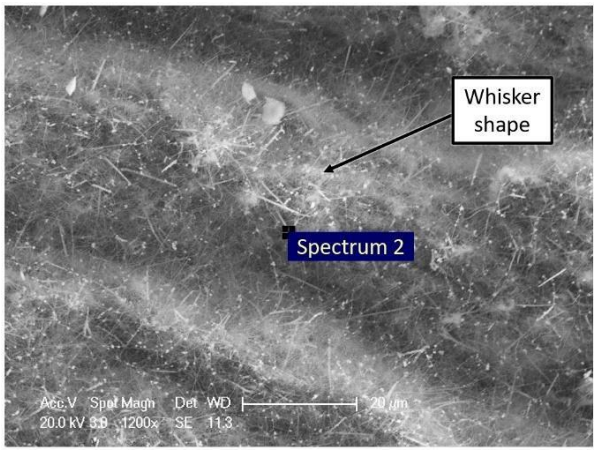
Table VII. Quantification of spectra for Figure 17(a) to (d)

Description	*Figure 17(a) Spectrum 1*		*Figure 17(b) Spectrum 1*		*Figure 17(c) Spectrum 1*		*Figure 17(d) Spectrum 1*	
	Weight%	*Atomic%*	*Weight%*	*Atomic%*	*Weight%*	*Atomic%*	*Weight%*	*Atomic %*
N	33.35	47.29	35.94	51.20	29.92	41.96	29.92	41.96
O	7.20	8.94	2.65	3.31	14.60	17.92	14.60	17.92
Mg	0	0	1.10	0.90	0.92	0.75	0.92	0.75
Al	59.45	43.77	60.02	44.39	41.95	30.54	41.95	30.54
Si	0	0	0.29	0.21	12.61	8.82	12.61	8.82

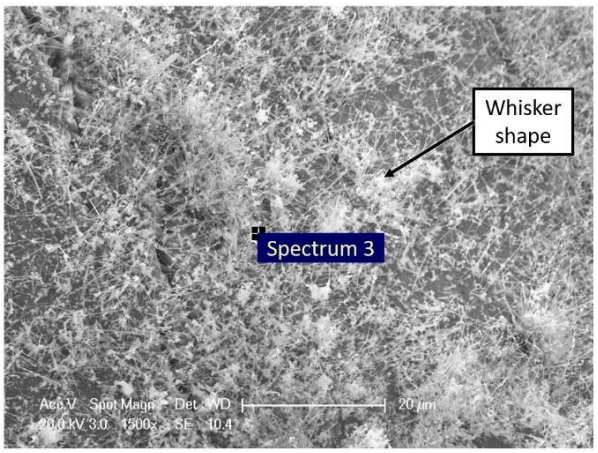
Feather-shaped AlN was also observed between the rod-shaped nitrides, shown in Figure 17(c). The rod-shaped AlN appeared to be similar to that observed by Wang and Fan [131,132] in CP-Al (see Figures 9(a) and (b)), although the latter was obtained from a polished cross-section.

B2. Whisker-shaped AlN

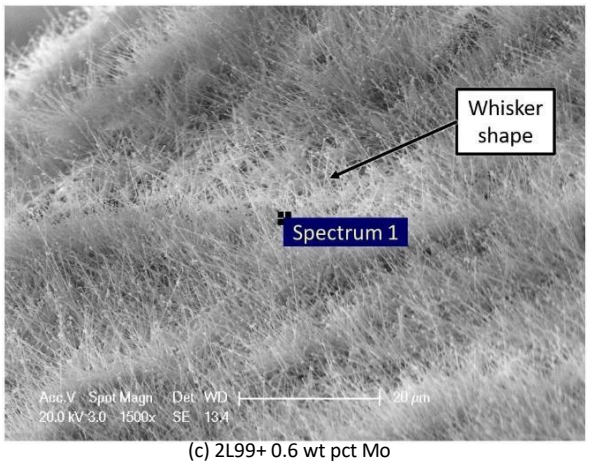
Figures 18(a) to 18(h) show micrographs and EDX spectra of whisker-shaped nitrides on the surfaces of all four alloys, which were held for 12 hours in nitrogen. Exclusively to whisker shapes, the results from the EDX spectra show the amount of O to be more than three times larger than the amount of N. Table VIII shows the quantification of spectra for Figures 18(a) to (d). The average dimensions of the whisker shape AlN patches observed on the surface of the alloys examined were measured to be approximately 60 by 90 µm.



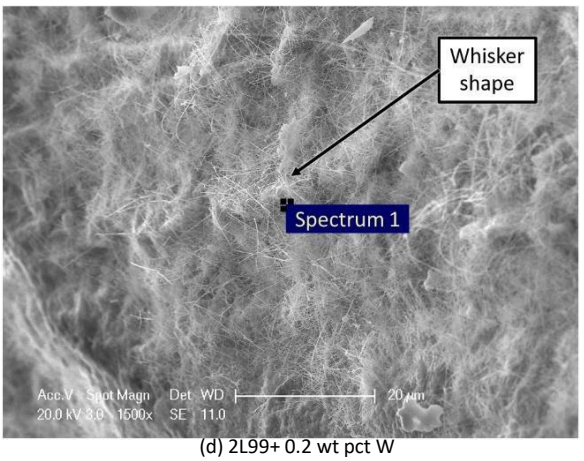
(a) CP- Al



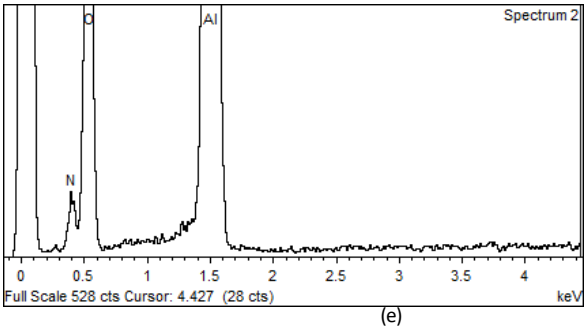
(b) 2L99



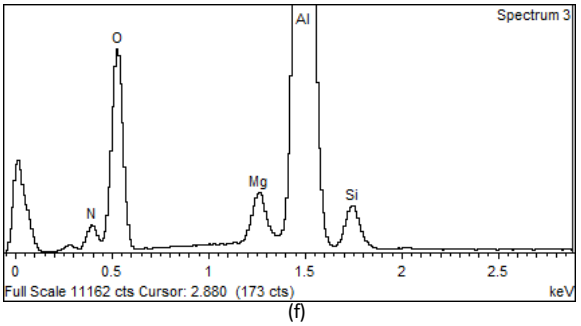
(c) 2L99+ 0.6 wt pct Mo



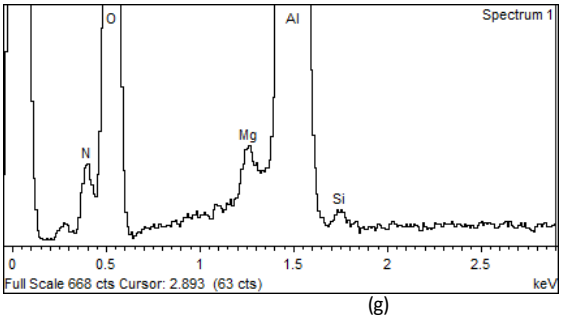
(d) 2L99+ 0.2 wt pct W



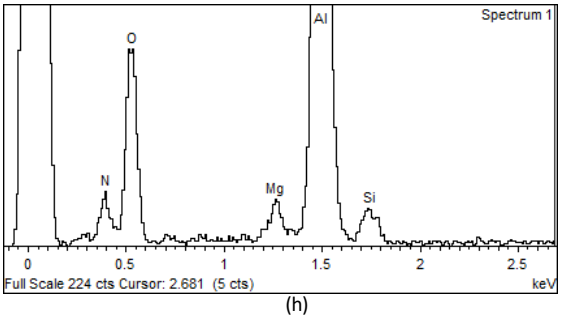
(e)



(f)



(g)



(h)

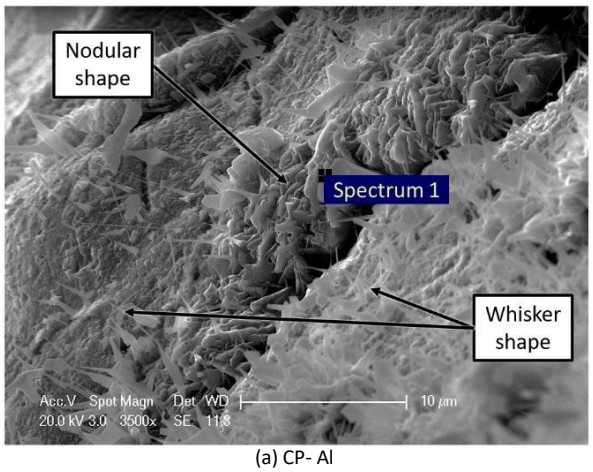
Fig. 18-(a) to (d) show the SEM micrographs of whisker-shaped AlN on the surfaces of CP- Al, 2L99 alloy, 2L99+0.6 wt pct Mo alloy and 2L99+0.2 wt pct W alloy respectively, with 12 hours of holding time in N at 850°C. Figures 18(e) to (h) are the EDX spectra for the marked areas shown in Figures 18(a) to (d).

Table VIII. Quantification of spectra for Figure 18(a) and (b)

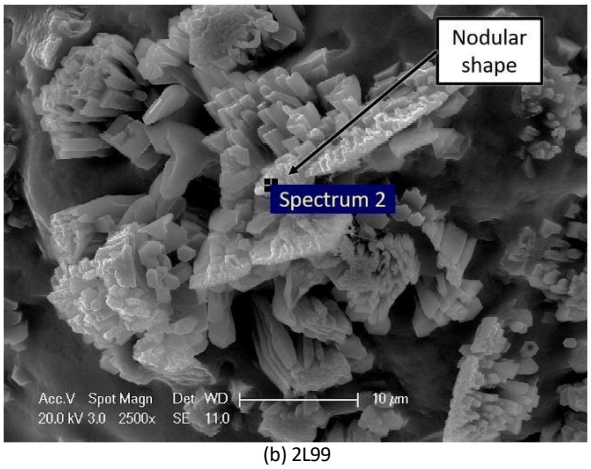
Description	*Figure 18(a) Spectrum 2*		*Figure 18(b) Spectrum 3*		*Figure 18(c) Spectrum 1*		*Figure 18(d) Spectrum 1*	
	Weight%	*Atomic%*	*Weight%*	*Atomic%*	*Weight%*	*Atomic%*	*Weight%*	*Atomic %*
N	10.98	14.85	11.92	16.54	8.63	11.98	14.87	15.94
O	47.07	55.71	40.23	48.89	44.88	54.51	43.31	54.86
Mg	0	0	1.96	1.57	0.43	0.34	1.74	1.35
Al	41.94	29.44	43.29	31.20	45.87	33.04	37.91	26.40
Si	0	0	2.61	1.81	0.19	0.13	2.17	1.45

C. Nodular-shaped AlN

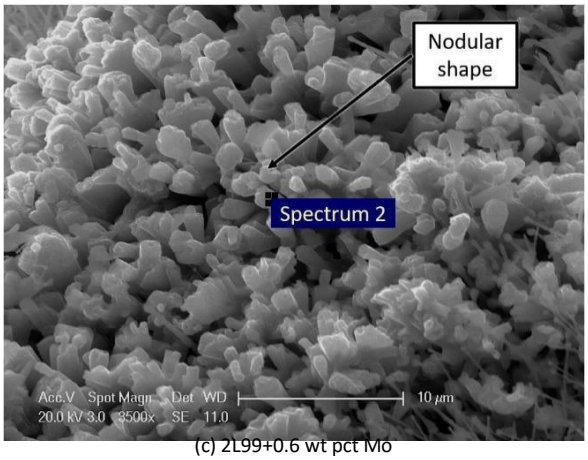
Figures 19(a) to 19(h) showed a nodular morphology obtained in a nitrogen atmosphere with a mean of approximately 250 nm. They were observed on the surfaces of all four alloys after holding for 3 hours in nitrogen. The nodular shapes were similar to those found in the as-cast condition described earlier (Figures 13(b), 14(a), 15(a) and 16(b)). Whisker-shaped nitrides were also observed occurring between the nodular-shaped nitrides (see Figure 19(a)). Table IX shows the quantification of the spectra for Figures 19(a) to (d). The average dimensions of the nodular shape AlN patches observed on the surface of the alloys examined were measured to be approximately 15 by 25 µm.



(a) CP- Al



(b) 2L99



(c) 2L99+0.6 wt pct Mo



(d) 2L99+0.2 wt pct W

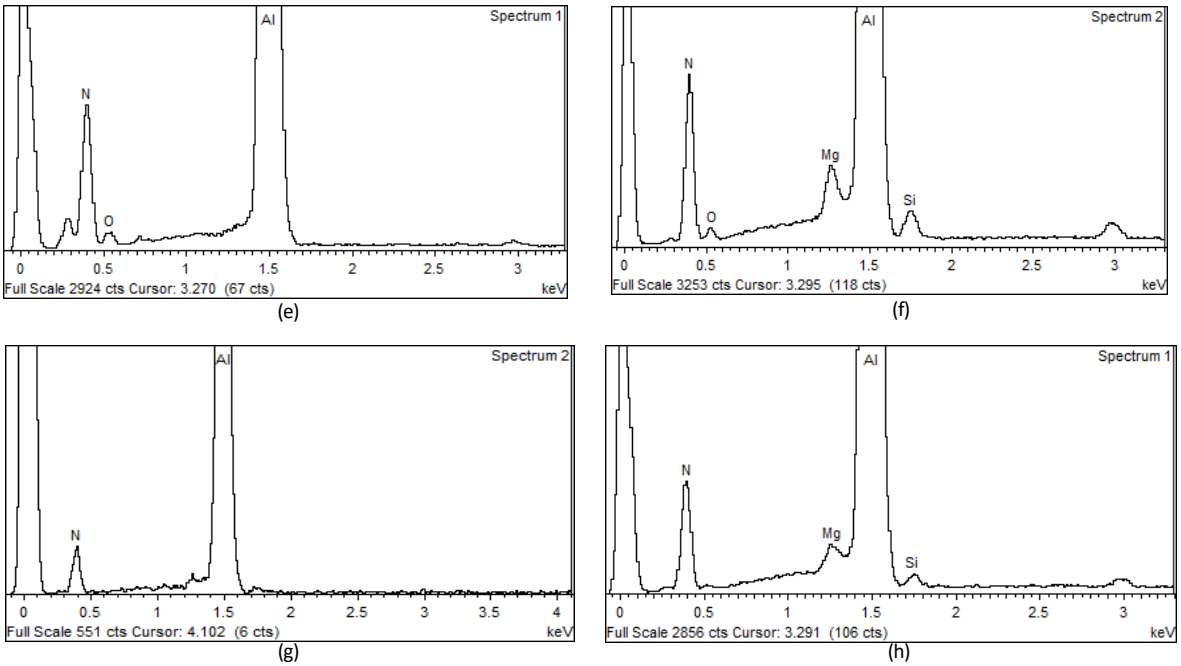


Fig. 19-(a) to (d) are the SEM micrographs of nodular-shaped AlN on the surfaces of CP- Al, 2L99 alloy, 2L99+0.6 wt pct Mo alloy and 2L99+0.2 wt pct W alloy respectively, with 3 hours of holding time in N at 850°C. Figures 19(e) to (h) are EDX spectra of the marked areas shown in figures 19(a) to (d).

Table IX. Quantification of spectra for Figure 19(a) and (b)

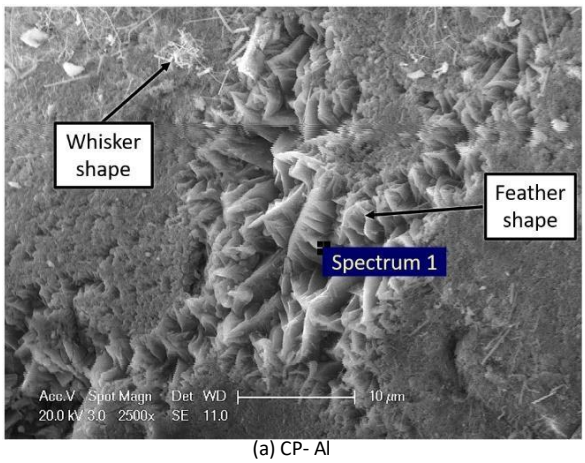
Description	*Figure 19(a) Spectrum3*		*Figure 19(b) Spectrum1*		*Figure 19(a) Spectrum3*		*Figure 19(b) Spectrum1*	
	Weight%	*Atomic %*	*Weight%*	*Atomic %*	*Weight%*	*Atomic %*	*Weight%*	*Atomic %*
N	42.41	57.54	35.94	51.36	37.82	53.95	36.34	52.36
O	3.94	4.68	2.15	2.69	0	0	0	0
Mg	0	0	0.64	0.53	0	0	0.44	0.37
Al	53.65	37.78	60.43	44.83	62.18	46.05	62.76	46.94
Si	0	0	0.84	0.60	0	0	0.46	0.33

D. Feather-shaped AlN

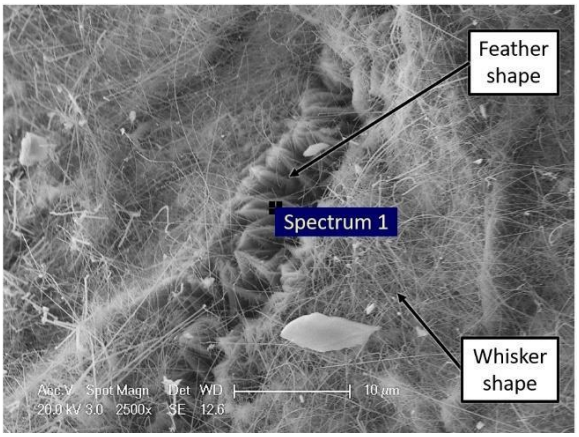
Figures 20(a) to (h) show micrographs and EDX spectra for feather-shaped nitrides with a mean dimension of around 10 µm in length, which ran through the central portion of the image (as marked). They covered an area of approximately 9 x 38 µm of the surface. They were observed on the surfaces of all four alloys after being held for 6 hours in nitrogen. Table X shows the quantification of the spectra for Figures 20(a) to (d).

The average dimensions of the feather shape AlN patches observed on the surface of the alloys examined were measured to be approximately 15 by 30 µm.

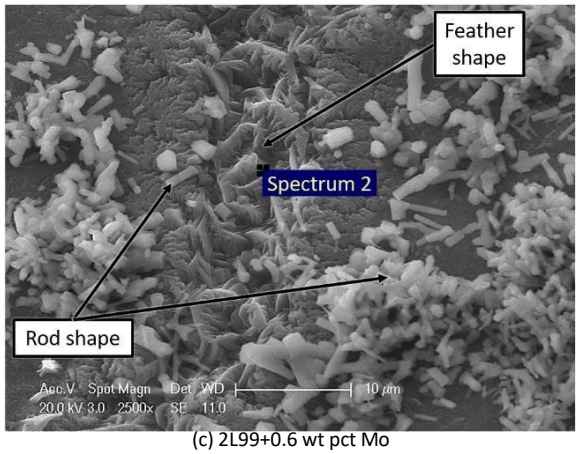
The feather-shaped morphologies were similar to the findings of other researchers' AlN. Specifically, after 8 hours of holding time in the trapped air bubbles experiment, [131,132] and on the fracture surfaces of 2L99+0.4 wt pct Mo in an as-cast condition [131,132]. In this study, a feather-shaped morphology was consistently observed in combination with other morphologies, such as the rod, whisker, and nodular morphologies. To summarize, the feather-shape morphology may be promoted by more extended holding periods (in this case, 6 h) at 850°C.



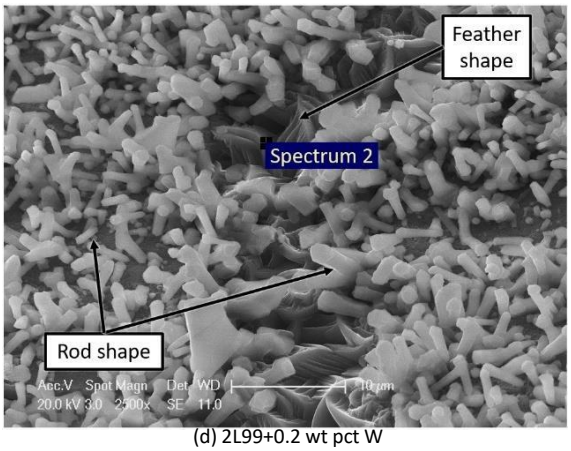
(a) CP- Al



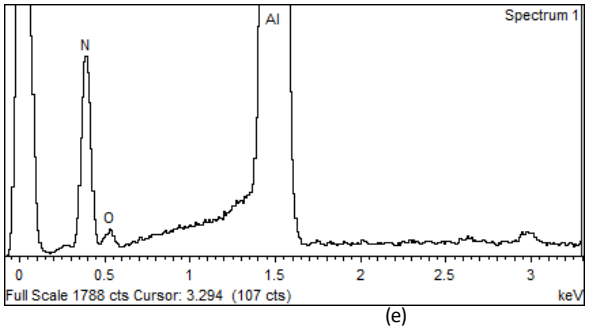
(b) 2L99



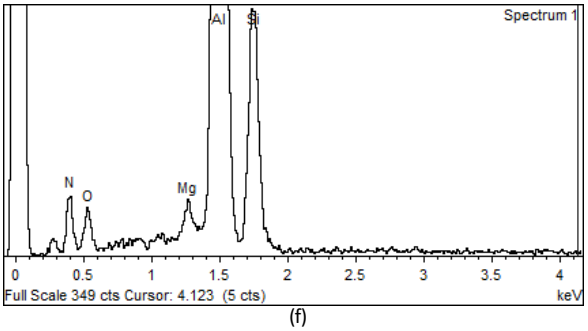
(c) 2L99+0.6 wt pct Mo



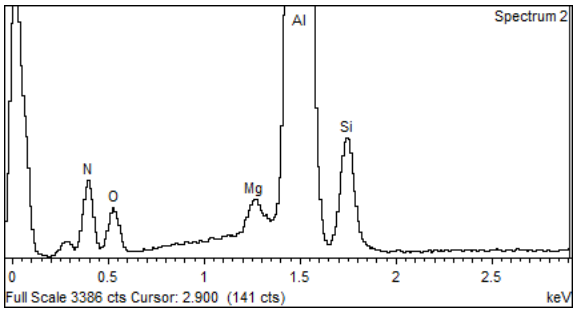
(d) 2L99+0.2 wt pct W



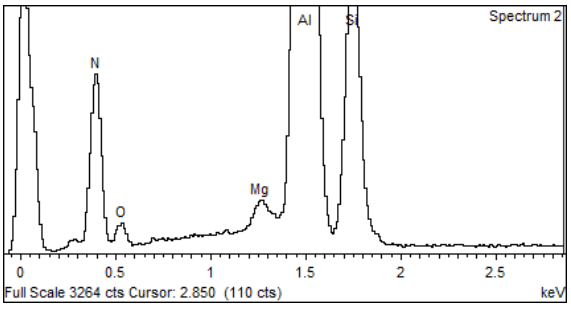
(e)



(f)



(g)



(h)

Fig. 20-(a) to (d) are SEM micrographs of feather-shaped AlN on the surfaces of CP- Al, 2L99 alloy, 2L99+0.6 wt pct Mo alloy and 2L99+0.2 wt pct W alloy, respectively with 6 hours holding time in N at 850°C. Figures 20(e) to (h) are EDX spectra of the marked areas shown in Figures 20(a) to (d).

Table X. Quantification of spectra for Figures 20(a) and (b)

Description	*Figure 20(a) Spectrum2*		*Figure 20(b) Spectrum1*		*Figure 20(a) Spectrum2*		*Figure 20(b) Spectrum1*	
	Weight%	*Atomic %*	*Weight%*	*Atomic %*	*Weight%*	*Atomic %*	*Weight%*	*Atomic %*
N	37.66	53.04	24.20	36.13	24.98	37.15	42.01	56.93
O	2.73	3.36	10.18	13.31	9.46	12.32	5.18	6.15
Mg	0	0	0.74	0.64	0.67	0.57	0.48	0.38
Al	59.61	43.59	52.69	40.84	60.01	46.34	43.12	30.33
Si	0	0	12.20	9.08	4.89	3.62	9.21	6.22

IV. Discussion

As shown in Figure 3 and on the eutectoid Al_2O_3–AlN phase diagram, AlON is not to be expected to occur at temperatures below 1640 °C. Therefore, the nitrogen detected by EDX has been concluded to be AlN, as the testbars were cast at 730°C or were heated in the growth experiments at 850°C.

For nucleation of AlN on Al, and other Al oxide substrates, there should be a small difference between lattice size and structure. Interatomic spacing misfit f_r is fundamental to grain refinement and nucleation, with an optimal f_r (calculated interatomic spacing misfit) difference of 7% being suggested [131,132]. The interatomic spacing misfit between AlN and Al oxides was calculated based on the crystallographic data shown in Table I [131,132]. The interatomic spacing misfit was calculated to be 10.9% for ɣ-alumina, 13.1 % for α-alumina, and 8.7 % for spinel, all of which were greater than the value of 7% mentioned above. This suggests that AlN may not be a potent substrate for Al oxide nucleation, in contrast with Wang and Fan's research [131,132] as well as this research's observations, which showed AlN may nucleate on oxide particles confirmed by EDX analysis detecting both O and N elements, shown in Figures 9(c), 13(c), 14(b), 15(b) and 16(c).

In previous research, a feather-shaped AlN morphology was found on the surface of pure Al [131,132] and on the fracture surfaces of 2L99+0.4 wt pct Mo [131,132] but not on the fracture surfaces of 2L99 testbars. Based on Chens' observations of the patches of AlN on the fracture surfaces of 2L99+0.4 wt pct Mo, it was suspected that AlN might have formed at high temperatures (1300°C) in the production of the masteralloy, to be carried through to the as-cast testbars. However, in this research, no evidence of AlN was observed in the characterization of ten testbars of 2L99+10 wt pct Mo and ten testbars of 2L99+10 wt pct W master alloys.

In this research, AlN has been found, for the first time, on the fracture surfaces of a 2L99 alloy in the as-cast condition at 730°C rather than in laboratory experiments. The AlN particles observed were nodular and appeared to be impermeable. This is in contrast with previously observed AlN particles in samples cast in different conditions [131,132], which have been described as feather-shaped and appeared to be more permeable (as shown in Figures 5(a), 6(a), and 7(a)). Table XI shows a summary of the different nitrides observed by other researchers, created under laboratory conditions.

Table XI. Summary of different AlN morphologies found by other researchers, mainly in pure Al and 2L99+0.4 wt pct Mo.

Researcher	*Alloy*	*Temperature*	*Holding Time*	*Morphology*	*AlN Weight/ atomic%*	*Width*
Raeiszadeh [131,132]	Pure Al	850°C	8 Hours	Feather shaped	28 wt%	-
Gerrard [131,132]	Pure Al	700°C	15 minutes	Feather shaped	17 wt%	8.6 µm
Chen [131,132]	2L99+ 0.4wt%Mo	730°C	N/A (fracture surface, as cast alloy)	Feather shaped	36 at%	15 µm
Wang & Fan [131,132]	CP-Al	750°C- 850°C	N/A (Pressure melt filtration technique)	Rod Shape	-	104 nm

The most impermeable AlN phase observed in this research, in the as-cast condition, is suggested to be of a nodular morphology. In this case, AlN may act as a hindrance to the passage of reaction gases between the entrapped atmosphere of a bifilm and the surrounding liquid metal. The impermeable AlN layer may also lead to a reduction in hydrogen diffusion through the bifilm preventing further expansion of the bifilm, supporting the Nyahumwa hypothesis [131,132].

The AlN phase in this study showed them to be of various morphologies, such as rod, nodular, feather and whisker. These morphologies were observed in all Al alloys of CP-Al, 2L99, 2L99+0.6 wt pct Mo and 2L99+0.2 wt pct W, with different holding times and in small patches rather than over the entire surface, as presented in section B of this paper. No consistent pattern of AlN distribution was observed. The nitrogen growth experiments showed the existence of AlN in all the alloys examined at every holding period.

The observed morphologies of AlN particles suggested that the feather-shaped AlN particles were more readily formed in the CP-Al alloy than in the 2L99, 2L99+0.6 wt pct Mo and 2L99+0.2 wt pct W alloys. This may have been caused by the lack of the alloying elements Si and Mg in CP-Al. It was challenging to observe the feather and nodular-shaped AlN in all alloys, while the rod and whisker-shaped morphologies were more frequently observed. The feather-shaped morphology was generally found sandwiched between either rod or whisker- shaped morphologies, as shown in Figures 20(a) to (d). Nodular and rod-shaped AlN were found to occur alone and with whisker or feather-shaped AlN on the fracture surfaces, as shown in Figures 19(a) to (d) and Figures 17(a) to (d), whereas whisker-shaped morphology was observed alone, as shown in Figures 18(a) to (d).

V. Conclusions.

1. Four AlN morphologies were observed after various holding times under nitrogen gas in all the different Al alloys such as CP-Al, 2L99, 2L99+0.6 wt pct Mo and 2L99+0.2 wt pct W. These were rod, whisker, nodular and feather-shaped.
2. Nodular AlN particles were observed in as-cast alloy conditions on the fracture surfaces of 2L99 alloy, measuring approximately 15 µm in length. Observation of AlN particles in as-cast alloy conditions supports Nyahumwa's et al. hypothesis [131,132] of consumption of the gases within the bifilms and the presence of nitrides in the process.
3. The presence of nodular nitrides observed in as-cast conditions in this study suggests (i). the consumption of oxygen within the bifilms, (ii). nucleation of nitrides and their growth, as Nyahumwa et al. [131,132] suggested, and (iii). a possible role for hydrogen within the bifilms, depending on whether there was a considerable hydrogen content in the solution in the liquid metal. These considerations may result in a notable difference in the bifilm size and a change in the mechanical properties of the alloys.

Acknowledgements

The authors wish to acknowledge the financial support of the EPSRC (grant reference EP/L016206/1). The authors also would like to thank Mr. Adrien Caden and Mr. Jonathan Davies from the School of Metallurgy and Materials, the University of Birmingham, for their technical assistance in this research work. The authors would also like to thank Ms. Theresa Morris and Dr Ludwig Schneider for their assistance in the operation of the various Scanning Electron Microscopes in the department.

CONFLICT OF INTEREST

The authors declare that they have no conflict of interest.

References

1. J. Campbell: Castings 2nd ed., Butterworth-Heinemann, Oxford, 2001, pp. 17-67.

2. C. Nyahumwa, N.R. Green and J. Campbell: AFS Trans., 1998, vol. 106, pp. 215-223.

3. H. X. Willems, M. M. R. M. Hendrix, G. de With, and R. Metselaar: Journal of the European Ceramic Society, 1992, vol. 10, pp. 339-346.

4. H. X. Willems, M. M. R. M. Hendrix, R. Metselaar, and G. de With: Journal of the European Ceramic Society, 1992, vol. 10, pp. 327-337.

5. S. A. Impey, D. J. Stephenson, and J. R. Nicholls: Materials Science and Technology (United Kingdom*)*, Dec. 1988, vol. 4, no. 12, pp. 1126–1132.

6. M.A. El-Sayed, H.G. Salem, A.Y. Kandeil and W.D. Griffiths: Metallurgical and Materials Transactions B, 2014, vol. 45(4), pp. 1398-1406.

7. Q. Zheng, B. Wu, and R.G. Reddy: Advanced Engineering Materials. John Wiley & Sons, Ltd., 2003, vol. 5, pp. 167–72.

8. N. Nagendra, B.S. Rao, and V. Jayaram: Materials Science and Engineering: A. Elsevier.,1999, vol. 269, pp .26–37.

9. Q. Zheng and R.G. Reddy: Journal of Materials Science., 2004, vol. 39, pp. 141-149.

10. R. Raeiszadeh, PhD Thesis, University of Birmingham, UK, 2005.

11. R. Raiszadeh, W.D. Griffiths: Conf. on Estimation of the Duration of the Atmosphere Within a Double Oxide Film Defect in Pure Aluminum, 2005, The University of Birmingham, UK, pp. 464–71.

12. R. Raiszadeh, W.D. Griffiths: Metallurgical and Materials Transactions B, 2006, vol. 37, pp. 865–871.

13. A.J. Gerrard, PhD Thesis, University of Birmingham, UK, 2014.

14. W.D. Griffiths, A.J. Gerrard, and Y. Yue: Conf. On Oxide film defects in Al alloys and the formation of hydrogen-related porosity, Materials Science and Engineering, 2016, The University of Birmingham, UK.

15. W.D. Griffiths, A. Elsayed and M.A. El-Sayed: Metallurgical and Materials Transactions B, 2016, vol. 47, pp. 3459.

16. Q. Chen and W.D. Griffiths: Metallurgical and Materials Transactions B, 2021, vol. 52, pp. 502–16.

17. Q. Chen, PhD Thesis, University of Birmingham, UK, 2017.

18. F. Wang and Z. Fan: Metallurgical and Materials Transactions A, 2019, vol. 50, pp. 2519–26.